

XXI RINEM

Riunione Nazionale di Elettromagnetismo

September 12-14, 2016

Parma, Italy



Proceedings

Under the patronage of:



UNIVERSITÀ
DEGLI STUDI
DI PARMA



COMUNE DI PARMA

Organized by:

GAEM | Group of
Applied
ElectroMagnetics
University of Parma Information Engineering Department


siem
SOCIETÀ ITALIANA
DI ELETTROMAGNETISMO

XXI RINEM

Parma, Italy

September 12-14, 2016

Conference Chair

Stefano Selleri, *University of Parma*

Promoting Committee

Graziano Cerri, *Marche Polytechnic University*

Andrea Galtarossa, *University of Padua*

Tommaso Isernia, *Mediterranea University of Reggio Calabria*

Michele Midrio, *University of Udine*

Luca Perregrini, *University of Pavia*

Stefano Selleri, *University of Parma*

Luciano Tarricone, *University of Salento*

Organizing Committee

Annamaria Cucinotta, *University of Parma*

Stefano Selleri, *University of Parma*

Federica Poli, *University di Parma*

Luca Vincetti, *University of Modena and Reggio Emilia*

Conference Venue:

Santa Elisabetta Congress Center

Parma University Campus,

Viale G. P. Usberti 93, Parma Italy

+39 0521 905527

Info at: <http://rinem2016.unipr.it/>

ISBN: 978-88-907599-1-8

Organizers



Sponsors



Under the Patronage of



**UNIVERSITÀ
DEGLI STUDI
DI PARMA**



COMUNE DI PARMA

Invited Speakers

Fulvio Ricci: *"Universe observation through gravitational waves"*



Biography: Fulvio Ricci is full professor of Experimental Physics at the university of Rome La Sapienza since 2000 and research associate to the Italian Institute of Nuclear Physics (INFN). He started his scientific career in 1975 joining the gravitational wave (g.w.) group of Professor E. Amaldi at Rome University. He spend two years at the CNR laboratory of Frascati to put in operation a 400 kg g.w. antenna, cooled at cryogenic temperature. Then for fifteen years he was at CERN, where he had the responsibility of the installation and operation of the 2300 kg g. w. detector EXPLORER, which achieved the

sensitivity goal of $h=7 \cdot 10^{-19}$ for g.w. burst of 1 ms of duration (Action Evading transducer) in order to circumvent the limitation imposed by the quantum mechanical nature of the antenna. In 1995 he joined the VIRGO collaboration, the French-Italian project for the construction of a 3 km laser interferometer to detect the gravitational waves. He was data analysis coordinator of the VIRGO international collaboration and then since 2007 the Italian coordinator for the INFN of the VIRGO collaboration. Since 2014 he is the spokesperson of the VIRGO international collaboration. In 2016 he announced the first direct detection of a gravitational wave signal, a result obtained in the context of the collaboration between the USA project LIGO and Virgo.

Abstract: La prima e la seconda rilevazione diretta di un segnale di onda gravitazionale è avvenuta grazie ai due rivelatori avanzati LIGO a cui presto si affiancherà Virgo in Europa. Nel prossimo futuro sarà possibile osservare segnali provenienti da supernovae, stelle di neutroni rotanti, coalescenze di sistemi binari formati da oggetti collassati, distanti di milioni di milioni di chilometri come è già avvenuto nel caso di due buchi neri trenta volte più pesanti del Sole. In questa presentazione sintetizzeremo il principio di misura e le caratteristiche degli apparati sperimentali che sono stati sviluppati in questi anni. Quindi illustreremo i risultati ottenuti.

Invited Speakers

Hubregt J. Visser: *"Practical Applications of Radiative Wireless Power Transfer"*



Biography: Hubregt J. Visser was born in 1964. He received the M.Sc. degree in electrical engineering from Eindhoven University of Technology, The Netherlands, in 1989. In 2009 he obtained a Ph.D. from Eindhoven University of Technology, The Netherlands and Katholieke Universiteit Leuven, Belgium. He is part-time full professor at Eindhoven University of Technology where he teaches antenna theory. Hubregt is author of the books 'Array and Phased Array Antenna Basics' (Wiley, 2005), 'Approximate Antenna Analysis for CAD' (Wiley, 2009) and 'Antenna Theory and Applications' (Wiley, 2012).

Abstract: in the presentation the principle of Radiative Wireless power Transfer (RWPT) will be given. In RWPT radio waves are used to transfer energy over a distance of several meters. It is a technology different from inductive power transfer that is used for near-contact applications. After the principle of RWT has been explained, a detailed discussion of rectifying antenna (rectenna) design and optimization will be presented. Then, pairing rectenna technology to (ultra) low-power wireless sensor technology – using commercially available components- will be treated and demonstrators of the technology will be shown.

Invited Speakers

Aydogan Ozcan: *"Democratization of Next-Generation Microscopy, Sensing and Diagnostics Tools through Computational Photonics"*



Biography: Dr. Aydogan Ozcan received his Ph.D. degree at Stanford University Electrical Engineering Department. After a short post-doctoral fellowship at Stanford University, he was appointed as a research faculty at Harvard Medical School, Wellman Center for Photomedicine in 2006. Dr. Ozcan joined UCLA in the summer of 2007 as an Assistant Professor, and was promoted to Associate and Full Professor ranks in 2011 and 2013, respectively. He is currently the Chancellor's Professor at UCLA and an HHMI Professor with the Howard Hughes Medical Institute, leading the Bio- and Nano-Photonics

Laboratory at UCLA Electrical Engineering and Bioengineering Departments, and is also the Associate Director of the California NanoSystems Institute (CNSI) at UCLA. Dr. Ozcan holds 32 issued patents (all of which are licensed) and more than 20 pending patent applications for his inventions in nanoscopy, wide-field imaging, lensless imaging, nonlinear optics, fiber optics, and optical coherence tomography. Dr. Ozcan gave more than 250 invited talks and is also the author of one book, the co-author of more than 400 peer reviewed research articles in major scientific journals and conferences. In addition, Prof. Ozcan is the founder and a member of the Board of Directors of Holomic LLC. Prof. Ozcan received several major awards including the 2011 Presidential Early Career Award for Scientists and Engineers (PECASE), which is the highest honor bestowed by the United States government on science and engineering professionals in the early stages of their independent research careers. Dr. Ozcan received this prestigious award for developing innovative optical technologies and signal processing approaches that have the potential to make a significant impact in biological science and medicine; addressing public health needs in less developed countries; and service to the optical science community including mentoring and support for underserved minority undergraduate and graduate students. Dr. Ozcan also received the 2015 UCLA Postdoctoral Scholars Mentoring Award for his dedicated efforts to training and mentoring of postdoctoral researchers. In addition, Dr. Ozcan received the 2015 International Commission for Optics (ICO) Prize, the 2013 SPIE BioPhotonics Technology Innovator Award, the 2011 Army Research Office Young Investigator Award, 2011 SPIE Early Career Achievement Award, the 2010 NSF CAREER Award, the 2009 NIH Director's New Innovator Award, the 2009 Office of Naval Research (ONR) Young Investigator Award, the 2009 IEEE Photonics Society Young Investigator Award and the MIT's Technology Review TR35 Award for his seminal contributions to near-field and on-chip imaging, and telemedicine based diagnostics.

Prof. Ozcan is also the recipient of the 2013 and 2015 Microscopy Today Innovation Awards, 2012 Popular Science Brilliant 10 Award, 2012 National Academy of Engineering (NAE) The Grainger Foundation Frontiers of Engineering Award, 2011 Innovators Challenge Award presented by the Rockefeller Foundation and mHealth Alliance, the 2010 National Geographic Emerging Explorer Award, the 2010 Gates Foundation Grand Challenges Award, the 2010 Popular Mechanics Breakthrough Award, the 2009 Wireless Innovation Award (Vodafone Americas Foundation) and the 2008 Okawa Foundation Award.

Invited Speakers

Prof. Ozcan was selected as one of the top 10 innovators by the U.S. Department of State, USAID, NASA, and NIKE as part of the LAUNCH: Health Forum organized in 2010. He also received the 2012 World Technology Award on Health and Medicine, which is presented by the World Technology Network in association with TIME, CNN, AAAS, Science, Technology Review and Fortune. Dr. Ozcan is elected Fellow of SPIE and OSA, and is a Lifetime Member of AAAS.

Abstract: My research focuses on the use of computation/algorithms to create new optical microscopy, sensing, and diagnostic techniques, significantly improving existing tools for probing micro- and nano-objects while also simplifying the designs of these analysis tools. In this presentation, I will introduce a new set of computational microscopes which use lens-free on-chip imaging to replace traditional lenses with holographic reconstruction algorithms. Basically, 3D images of specimens are reconstructed from their "shadows" providing considerably improved field-of-view (FOV) and depth-of-field, thus enabling large sample volumes to be rapidly imaged, even at nanoscale. These new computational microscopes routinely generate >1–2 billion pixels (giga-pixels), where even single viruses can be detected with a FOV that is >100 fold wider than other techniques. At the heart of this leapfrog performance lie self-assembled liquid nano-lenses that are computationally imaged on a chip. These self-assembled nano-lenses are stable for >1 hour at room temperature, and are composed of a biocompatible buffer that prevents nano-particle aggregation while also acting as a spatial "phase mask." The field-of-view of these computational microscopes is equal to the active-area of the sensor-array, easily reaching, for example, >20 mm² or >10 cm² by employing state-of-the-art CMOS or CCD imaging chips, respectively. In addition to this remarkable increase in throughput, another major benefit of this technology is that it lends itself to field-portable and cost-effective designs which easily integrate with smartphones to conduct giga-pixel tele-pathology and microscopy even in resource-poor and remote settings where traditional techniques are difficult to implement and sustain, thus opening the door to various telemedicine applications in global health. Some other examples of these smartphone-based biomedical tools that I will describe include imaging flow cytometers, immunochromatographic diagnostic test readers, bacteria/pathogen sensors, blood analyzers for complete blood count, and allergen detectors. Through the development of similar computational imagers, I will also report the discovery of new 3D swimming patterns observed in human and animal sperm. One of this newly discovered and extremely rare motion is in the form of "chiral ribbons" where the planar swings of the sperm head occur on an osculating plane creating in some cases a helical ribbon and in some others a twisted ribbon. Shedding light onto the statistics and biophysics of various micro-swimmers' 3D motion, these results provide an important example of how biomedical imaging significantly benefits from emerging computational algorithms/theories, revolutionizing existing tools for observing various micro- and nano-scale phenomena in innovative, high-throughput, and yet cost-effective ways.

Invited Speakers

Fetah Benabid: *"Hollow core photonic crystal fibre: Novel light guidance and myriad of gas-photonic applications"*



Biography: Fetah Benabid is a CNRS director of research and honorary professor at the universities of Bath (UK) and Western Australia (Australia). He is the group founder and leader of Gas-Phase Photonic and Microwave Materials (GPPMM) at the CNRS UMR Xlim, Limoges, France. Fetah Benabid has pioneered the development of hollow-core photonic crystal fibres (HC-PCF) and their incorporation into scientific and technological applications. He is the inventor of Kagome HC-PCF and an all-fibre gas cells, coined photonic microcell (PMC). He is the inceptor of new optical guidance mechanism called inhibited coupling optical guidance that led to low loss optical fiber with

negative curvature core-contour, and the "photonic tight-binding model" to explain the formation of photonic bandgap in photonic crystal fibres. Fetah Benabid research interests covers guided photonics, gas-phase based nonlinear and coherent optics. Fetah Benabid is also the founder of the start-up GLOphotonics ([www://http.glophotonics.fr](http://http.glophotonics.fr)) market leader in hollow-core fibers for industrial applications.

Abstract: In 2002 the development of a new type of hollow-core photonic crystal fibre (HC-PCF), coined Kagome fibre, paved the way to a new manner to guide light within a hollow core. The fibre guides light via a new mechanism that doesn't require a photonic bandgap in the fibre cladding. Instead, the light is confined within the fibre core, and prevented from leaking out through the cladding by a strong coupling inhibition between the core guided mode and the cladding mode continuum. This guidance mechanism, called Inhibited Coupling (IC), is the guided photonic analogue of the concept of bound or quasi-bound state in a continuum established within the field of solid-state quantum physics. The IC guidance offered a design tool to the seminal introduction of hypocycloid core-contour (i.e. negative curvature) hollow-core photonic crystal fibre, which allowed a dramatic reduction in transmission loss of IC guiding HC-PCF. This improvement is such that IC guiding HC-PCF, which previous typical loss figure was in the range of 0.5 -1 dB/m, outperforms photonic bandgap (PBG) guiding HC-PCF in optical transmission. Today, the lowest loss figures at the benchmark wavelengths of the NIR-VIS spectral range are all set by IC guiding HC-PCF, such as the records of 17 dB/km $\sim 1\mu\text{m}$ wavelength or 7.7 dB/km at ~ 750 nm. Furthermore, because of the intrinsic properties of the IC guidance, the reduction in loss means systematically a reduction in the power overlap with the silica core-surround. As a result high optical power handling is expected with the transmission loss reduction. This has been illustrated in the recent results in ultra-short pulse transportation and compression, leading to the record 1 mJ energy pulse delivery. Here, 1 milli-Joule energy, gigawatt peak power and close-to pettawatt/cm² intensity ultra-fast laser-pulses from 600 fs Yb fiber-laser were successfully guided and compressed in HC-PCF.

Invited Speakers

The guidance was achieved with low loss and in a single-mode fashion, and the pulse compression is achieved in a self-compression manner. Another result in high optical-field is the self-compression down to sub-cycle regime of 80 fs USP operating at 1.8 μm and with several tens of μJ pulse-energy. These results open exciting prospects in fibre based high field photonics and laser micromachining. As a matter of fact, IC guiding Kagome HC-PCF is currently commercially available from GLOphotonics and is strongly used as a fibre beam delivery of high power ultra-short pulse lasers.

Invited Speakers

Qing Huo Liu: *"Subsurface Sensing and Super-Resolution Imaging: Application of Computational Acoustics and Electromagnetics"*



Biography: Qing Huo Liu (S'88-M'89-SM'94-F'05) received his B.S. and M.S. degrees in physics from Xiamen University in 1983 and 1986, respectively, and Ph.D. degree in electrical engineering from the University of Illinois at Urbana-Champaign in 1989. His research interests include computational electromagnetics and acoustics, inverse problems, and their applications in geophysics, nanophotonics, and biomedical imaging. He has published over 300 refereed journal papers and 450 conference papers in conference proceedings, and his H-index is 48 (Google Scholar). He was with the Electromagnetics Laboratory at the University of Illinois at Urbana-Champaign as a Research Assistant from

September 1986 to December 1988, and as a Postdoctoral Research Associate from January 1989 to February 1990. He was a Research Scientist and Program Leader with Schlumberger-Doll Research, Ridgefield, CT from 1990 to 1995. From 1996 to May 1999 he was an Associate Professor with New Mexico State University. Since June 1999 he has been with Duke University where he is now a Professor of Electrical and Computer Engineering. Dr. Liu is a Fellow of the IEEE, Fellow of the Acoustical Society of America, Fellow of Electromagnetics Academy, and Fellow of the Optical Society of America. Currently he serves as the founding Editor in Chief of the *IEEE Journal on Multiscale and Multiphysics Computational Techniques*, the Deputy Editor in Chief of *Progress in Electromagnetics Research*, an Associate Editor for *IEEE Transactions on Geoscience and Remote Sensing*, and an Editor for the *Journal of Computational Acoustics*. He was recently a Guest Editor in Chief of *the Proceedings of the IEEE* for a 2013 special issue on large-scale electromagnetics computation and applications. He received the 1996 Presidential Early Career Award for Scientists and Engineers (PECASE) from the White House, the 1996 Early Career Research Award from the Environmental Protection Agency, and the 1997 CAREER Award from the National Science Foundation. He serves as an IEEE Antennas and Propagation Society Distinguished Lecturer for 2014-2016.

Abstract: Acoustic/seismic and electromagnetic waves have widespread applications in geophysical subsurface sensing and imaging. In these applications, often the problems of understanding the underlying wave phenomena, designing the sensing and imaging measurement systems, and performing data processing and image reconstruction require large-scale computation in acoustics and electromagnetics. It is very challenging to solve such problems with the traditional finite difference and finite element methods. In this presentation, several high-performance computational methods and super-resolution imaging in acoustics and electromagnetics will be discussed along with their applications in oil exploration and subsurface imaging.

Program Overview

	Monday Sept. 12	Tuesday Sept. 13	Wednesday Sept. 14				
8:30-8:45		Registration	Registration				
8:45-9:00			Session 5 Integrated and nonlinear optics	Session 6 Metamaterials and nanomaterials	Session 9 Optical fibers	Session 10 Remote sensing	
9:00-9:30							Registration
9:30-10:00							
10:00-10:30	Session 1 EMF propagation	Session 2 Microwaves					
10:30-11:00			Coffee Break				
11:00-11:15				Coffee Break			
11:15-11:30					Session 7 Numerical methods	Session 8 Antenna design and measurement	Start-up and Spin-off
11:30-11:45	Lunch						
11:45-12:00		Lunch					
12:00-12:30			Lunch				
12:30-13:00				Session 3 Antennas	Session 4 RFID		
13:00-13:15	Siem Meeting (CS, CD) + Poster 2					Session 11 EMF for energy and environment applications	Session 12 Bioelectromagnetism and biomedical applications
13:15-13:30		Poster 2 + Coffee break					
13:30-14:00			CNIT Meeting + Siem Meeting (AS)				
14:00-14:15				Closing and awards			
14:15-14:30	Poster 1 + Coffee Break						
14:30-15:00		Social Dinner					
15:00-15:30			Visit at CSAC + cocktail party				
15:30-15:45							
15:45-16:00							
16:00-16:30							
16:30-17:00							
17:00-17:30							
17:30-17:45							
17:45-18:00							
18:00-18:30							
18:30-20:00							
20:00-20:30							
20:30-21:00							
21:00-23:00							

Plenary Session

12th Sep. 10:30-11:00 Room "Auditorium"

Chairman: Stefano Selleri, *University of Parma*

Session 1: EMF propagation

12th Sep. 11:00-13:15 Room "Auditorium"

Chairman: Luca Perregrini, *University of Pavia*

11:00-11:40 Invited presentation, Room "Auditorium"

UNIVERSE OBSERVATION THROUGH GRAVITATIONAL WAVES

F. Ricci

"La Sapienza" University of Rome

p. 2

11:45-12:00 1.1

GENERATION OF LIMITED-DIFFRACTIVE TWISTED PULSES

D. Comite¹, W. Fuscaldo^{1,2}, S.C. Pavone³

¹*Department of Information Engineering, Electronics and Telecommunications, "La Sapienza" University of Rome*

²*Institut d'Électronique et de Télécommunications de Rennes, Université de Rennes 1, France*

³*Department of Information Engineering and Mathematics, University of Siena*

p. 35

12:00-12:15 1.2

"BLIND" FIELD SEPARATION OF 2D FAR ZONE DATA

G. Leone, A. Natale,

Department of Industrial and Information Engineering, Second University of Naples

p. 39

12:15-12:30 1.3

INHOMOGENEOUS WAVES GENERATION FOR THE ELECTROMAGNETIC DEEP PENETRATION INTO LOSSY MEDIA

V. Pascale, F. Pelorossi, N. Tedeschi, F. Frezza

Department of Information Engineering, Electronics and Telecommunications, "La Sapienza" University of Rome

p. 43

12:30-12:45 1.4

ITERATED VIRTUAL EXPERIMENTS AND COMPRESSIVE SENSING FOR QUANTITATIVE INVERSE SCATTERING PROBLEMS

R. Palmeri¹, M.T. Bevacqua¹, L. Crocco², T. Isernia^{1,2}, L. Di Donato³

¹*DIIES, Università Mediterranea di Reggio Calabria*

²*CNR-IREA, Naples*

³*DIEEI, Università di Catania*

p. 47

XXI RINEM – CONFERENCE SESSIONS

12:45-13:00	1.5	ELECTROMAGNETIC MODELING OF FORWARD SCATTER RADAR	
M.T. Falconi, D. Comite			
<i>Department of Information Engineering, Electronics and Telecommunications, "La Sapienza" University of Rome</i>			
p.			51
13:00-13:15	1.6	ELECTROMAGNETIC SCATTERING BY PERFECTLY CONDUCTING BURIED OBJECTS	
F. Di Murro, M. Lucido, G. Panariello, C. Santomassimo, F. Schettino			
<i>Department of Electrical and Information Engineering, University of Cassino and Southern Lazio</i>			
p.			55
Session 2: Microwaves			
<i>12th Sep. 11:00-13:15 Room "Master"</i>			
Chairman: Gino Sorbello, <i>University of Catania</i>			
11:00-11:40		Invited presentation, <i>Room "Auditorium"</i>	
UNIVERSE OBSERVATION THROUGH GRAVITATIONAL WAVES			
<i>F. Ricci</i>			
<i>"La Sapienza" University of Rome</i>			
p.			2
11:45-12:00	2.1	ON THE DESIGN OF AN ANTENNA ARRAY FOR CUBE SATS OPERATING IN THE KA-FREQUENCY BAND	
G. Buttazoni, M. Comisso, A. Cuttin, R. Vescovo			
<i>Department of Engineering and Architecture, University of Trieste</i>			
p.			59
12:00-12:15	2.2	THE ALPHASAT PROPAGATION EXPERIMENT: INTERIM RESULTS FROM ASI AND NASA GROUND STATIONS	
C. Riva ^{1,2} , L. Luini ^{1,2} , R. Nebuloni ² , J. Nessel ³ , G. Codispoti ⁴ , G. Parca ⁴ , A. Tuozi ⁴			
¹ <i>Dipartimento di Elettronica, Informazione e Bioingegneria, Politecnico di Milano</i>			
² <i>Istituto di Elettronica e di Ingegneria dell'Informazione e delle Telecomunicazioni, Consiglio Nazionale delle Ricerche, Milano</i>			
³ <i>NASA Glenn Research Center, Cleveland, OH, USA</i>			
⁴ <i>Italian Space Agency, Rome</i>			
p.			63
12:15-12:30	2.3	A NOVEL MICROWAVE FREQUENCY SWEEP INTERFEROMETER FOR ECR PLASMA ELECTRON DENSITY MEASUREMENTS	
G. Torrisi ^{1,2} , O. Leonardi ¹ , G. Sorbello ^{1,3} , D. Mascali ¹ , G. Castro ¹ , L. Celona ¹ , S. Gammino ¹			
¹ <i>INFN - Laboratori Nazionali del Sud, Catania</i>			
² <i>Università Mediterranea di Reggio Calabria</i>			
³ <i>Università degli Studi di Catania</i>			
p.			67

12:30-12:45 2.4
X-BAND WAVEGUIDE DIPLEXER DESIGN WITH RELAXED FABRICATION TOLERANCE
 E. Agastra
Department of Electronics and Telecommunications, Polytechnic University of Tirana, Albania
 p. 71

12:45-13:00 2.5
X/KA-B AND DUAL-POLARIZED DIGITAL BEAMFORMING SYNTHETIC APERTURE RADAR
 C. Mao¹, S. Gao¹, C. Tienda², S. Glisic³, E. Arneri⁴, P. Penkala⁵, M. Krstic⁶, A. Dominuez⁷, A. Patyuchenko², F. Qin¹, U. Yodprasit³, O. Schrape⁶, L. Boccia⁴, G. Amendola⁴, M. Younis², E. Celton⁷, V. Petrovic⁶
¹*School of Engineering and Digital Arts, University of Kent, UK*
²*Microwaves and Radar Institute, German Aerospace Center (DLR), Germany*
³*Silicon Radar GmbH, Germany*
⁴*DIMES, Università della Calabria*
⁵*Evatronix S.A. Bielsko-Biala, Poland*
⁶*IHP, Germany*
⁷*Innovative Solutions In Space BV, Netherlands*
 p. 75

13:00-13:15 2.6
ADDITIVE MANUFACTURING OF METAL PASSIVE WAVEGUIDE COMPONENTS
 M. Lumia¹, M. Lorusso²
¹*Istituto di Elettronica e di Ingegneria dell'Informazione e delle Telecomunicazioni, Consiglio Nazionale delle Ricerche, Turin*
²*Center for Space Human Robotics, Istituto Italiano di Tecnologia, Turin*
 p. 79

Session 3: Antennas

12th Sep. 14:15-16:30 Room "Auditorium"

Chairman: Graziano Cerri, *Marche Polytechnic University*

14:15-14:55 Invited presentation, *Room "Auditorium"*
PRACTICAL APPLICATIONS OF RADIATIVE WIRELESS POWER TRANSFER
 H.J. Visser
 TU Eindhoven
 p. 3

15:00-15:15 3.1
A CPW-FED PRINTED LPDA FOR WIRELESS COMMUNICATIONS
 G.A. Casula, G. Montisci, P. Maxia, G. Muntoni, G. Mazzarella
Dipartimento di Ingegneria Elettrica ed Elettronica, Università degli Studi di Cagliari
 p. 83

15:15-15:30 3.2
NONREDUNDANT SPHERICAL NEAR-FIELD-FAR-FIELD TRANSFORMATION FOR A NONCENTRED ANTENNA
 F. D'Agostino, F. Ferrara, C. Gennarelli, R. Guerriero, M. Migliozzi
Dipartimento di Ingegneria Industriale, Università di Salerno
 p. 87

XXI RINEM – CONFERENCE SESSIONS

15:30-15:45	3.3	IMMUNITY TEST SIMULATION IN A MULTIPLE ANTENNA SOURCE STIRRED REVERBERATION CHAMBER	
A. De Leo, V. Mariani Primiani, P. Russo, G. Cerri			
<i>Dipartimento di Ingegneria dell'Informazione, Università Politecnica delle Marche</i>			
p.			91
15:45-16:00	3.4	BROADBAND TEST-SOURCE FOR ANTENNA MEASUREMENTS WITH UNMANNED AERIAL VEHICLES	
F. Paonessa			
<i>Istituto di Elettronica e di Ingegneria dell'Informazione e delle Telecomunicazioni, Consiglio Nazionale delle Ricerche, Torino</i>			
p.			95
16:00-16:15	3.5	A SINGLE-LAYER PENTAGONAL ARRAY BASED ON THE SEQUENTIAL ROTATION ARRANGEMENT OF FIVE ELEMENTS	
S. Maddio, G. Pelosi, M. Righini, S. Selleri			
<i>Department of Information Engineering, University of Florence</i>			
p.			99
16:15-16:30	3.6	TAPERED EBG SUPERSTRATES FOR HIGH-GAIN EBG RESONATOR ANTENNAS	
C. Ponti ¹ , S. Ceccuzzi ¹ , P. Baccarelli ² , G. Schettini ¹			
¹ <i>Department of Engineering, Roma Tre University</i>			
² <i>Department of Information Engineering, Electronics and Telecommunications, "La Sapienza" University of Rome</i>			
p.			103

Session 4: RFID

12th Sep. 14:15-16:30 Room "Master"

Chairman: Luciano Tarricone, *University of Salento*

14:15-14:55		Invited presentation, Room "Auditorium"	
PRACTICAL APPLICATIONS OF RADIATIVE WIRELESS POWER TRANSFER			
H.J. Visser			
<i>TU Eindhoven</i>			
p.			3
15:00-15:15	4.1	UWB-UHF RFID TAG ON PAPER FOR SIMULTANEOUS COMMUNICATION AND RF ENERGY HARVESTING	
M. Fantuzzi ¹ , D. Masotti ¹ , A. Costanzo ²			
¹ <i>DEI, University of Bologna</i>			
² <i>DEI, Cesena Campus, University of Bologna</i>			
p.			107

XXI RINEM – CONFERENCE SESSIONS

15:15-15:30	4.2	PASSIVE RFID SENSOR NETWORK FOR INDUSTRIAL INTERNET OF THINGS	
C. Occhiuzzi ¹ , S. Amendola ^{1,2} , S. Manzari ¹ , G. Marrocco ^{1,2}			
¹ RADIO6ENSE			
² Pervasive Electromagnetics Lab, University of Tor Vergata			
p.			111
15:30-15:45	4.3	MODULAR ANTENNAS FOR NEAR-FIELD UHF-RFID SYSTEMS	
A. Michel, P. Nepa, G. Manara			
<i>Department of Information Engineering, University of Pisa</i>			
p.			115
15:45-16:00	4.4	ENHANCED BATTERY-FREE AUGMENTED RFID TAG	
R. Colella, L. Catarinucci, L. Tarricone			
<i>Department of Innovation Engineering, University of Salento</i>			
p.			119
16:00-16:15	4.5	CHIPLESS RFID TAGS AND SENSORS FOR WIRELESS SENSOR NETWORKS	
F. Costa ^{1,2} , S. Genovesi ^{1,2} , M. Borgese ^{1,2} , F.A. Dicandia ^{1,2} , A. Monorchio ^{1,2} , G. Manara ^{1,2}			
¹ Department of Information Engineering, University of Pisa			
² Consorzio Nazionale Interuniversitario per le Telecomunicazioni, Parma			
p.			123
16:15-16:30	4.6	EXPERIMENTAL TOOL FOR RFID TAG ELECTROMAGNETIC ANALYSIS	
R. Colella			
<i>Department of Innovation Engineering, University of Salento</i>			
p.			127

Poster Session 1

12th Sep. 16:30-17:45

P1.1	ANALYSIS OF THE ROBUSTNESS OF WEARABLE PIFAS TO THE HUMAN BODY COUPLING	
G.A. Casula ¹ , A. Michel ² , G. Montisci ¹ , P. Nepa ² , G. Mazzearella ¹		
¹ Dipartimento di Ingegneria Elettrica ed Elettronica, Università degli Studi di Cagliari		
² Department of Information Engineering, University of Pisa		
p.		131
P1.2	A CENTRALISED ADS-B SYSTEM FOR EN-ROUTE AND LOW LEVEL COVERAGE	
M. Arpaio ¹ , S. Selleri ²		
¹ Thales Italia Spa, Air Traffic Management Domain		
² Department of Information Engineering, University of Parma		
p.		135

P1.3
CHARACTERIZATION OF LOCALIZED AND STATIONARY DYNAMIC BRILLOUIN GRATINGS
 F. Chiarello, L. Palmieri, M. Santagiustina
Department of Information Engineering, University of Padua
 p. 140

P1.4
EXPLOITING FREQUENCY DIVERSITY IN PROPAGATION-BASED WIRELESS LOCALIZATION OF MOBILE DEVICES
 A. Polo
ELEDIA Research Center ELEDIA@UniTN, University of Trento
 p. 144

P1.5
WIRELESS SENSOR NETWORK AND DOPPLER RADAR TECHNOLOGIES FOR WILDLIFE ROAD CROSSING MONITORING
 F. Robol
ELEDIA Research Center ELEDIA@UniTN, University of Trento
 p. 148

P1.6
INVERSE SCATTERING METHODOLOGIES AND APPLICATIONS @ ELEDIA RESEARCH CENTER
 N. Anselmi¹, M. Donelli¹, M.A. Hannan¹, G. Oliveri^{1,2}, L. Poli¹, P. Rocca¹, M. Salucci^{1,2}, L. Tenuti¹, A. Massa^{1,2}
¹*ELEDIA Research Center ELEDIA@UniTN, University of Trento*
²*ELEDIA Research Center ELEDIA@L2S, UMR8506 [CNRS-CS-UPS], France*
 p. 152

P1.7
DISTRIBUTED WIRELESS SENSING, MONITORING, AND DECISION SUPPORT: CURRENT ACTIVITIES @ ELEDIA RESEARCH CENTER
 H. Ahmadi¹, M. S. Dao², E. Giarola³, A. Polo³, F. Robol³, F. Viani³, A. Massa^{3,4}
¹*ELEDIA Research Center ELEDIA@Innov'COM Sup'Com Tunis, Tunisia*
²*ELEDIA Research Center ELEDIA@UTB, Universiti Teknologi Brunei, Brunei Darussalam*
³*ELEDIA Research Center ELEDIA@UniTN, University of Trento*
⁴*ELEDIA Research Center ELEDIA@L2S, UMR 8506 [CNRS-CS-UPS], France*
 p. 156

P1.8
WIRELESS-BASED DECISION SUPPORT SYSTEMS AND FLEET MANAGEMENT @ ELEDIA RESEARCH CENTER
 A. Polo¹, A. Massa²
¹*ELEDIA Research Center ELEDIA@UniTN, University of Trento*
²*ELEDIA Research Center ELEDIA@L2S, UMR 8506 [CNRS-CS-UPS]*
 p. 160

P1.9	DESIGN AND OPTIMIZATION OF ADVANCED RADAR AND COMMUNICATIONS SYSTEMS AND ARCHITECTURES @ ELEDIA RESEARCH CENTER	
	N. Anselmi ¹ , M. Donelli ¹ , M.A. Gelmini ¹ , G. Gottardi ¹ , G. Oliveri ^{1,2} , L. Poli ¹ , P. Rocca ¹ , L. Tenuti ¹ , A. Massa ^{1,2}	
	¹ ELEDIA Research Center ELEDIA@UniTN, University of Trento	
	² ELEDIA Research Center ELEDIA@L2S, UMR8506 [CNRS-CS-UPS], France	
p.		164
P1.10	JOINT EFFECTS OF CLOUDS AND RAIN ON EHF SATELLITE COMMUNICATION SYSTEMS	
	L. Luini, C. Capsoni	
	<i>Dipartimento di Elettronica, Informazione e Bioingegneria, Politecnico di Milano</i>	
p.		168
P1.11	RFIDRONES : PRELIMINARY EXPERIMENTS AND ELECTROMAGNETIC MODELS	
	G. Casati, M. Longhi, D. Latini, F. Carbone, F. Del Frate, A. Perrone, G. Schiavon, G. Marrocco	
	<i>Civil Engineering and Computer Science, University of Rome Tor Vergata</i>	
p.		172
P1.12	LOW-COST WIRELESS SENSING BY MEANS OF RECONFIGURABLE RFID SYSTEMS	
	M.C. Caccami, G. Marrocco	
	<i>Department of Civil and Information Engineering, University of Rome Tor Vergata</i>	
p.		176
P1.13	COPRIME SYNTHETIC ARRAYS	
	G. Di Martino, A. Iodice	
	<i>Department of Electrical Engineering and Information Technology, University of Naples "Federico II"</i>	
p.		180
P1.14	MICROWAVE CHARACTERIZATION OF A DILUTED WATER-BASED FERROFLUID IN PRESENCE OF AN EXTERNAL POLARIZING MAGNETIC FIELD FOR BIOMEDICAL APPLICATIONS	
	G. Bellizzi ^{1,2} , G.G. Bellizzi ^{2,3} , O.M. Bucci ^{3,4}	
	¹ DIETI, Università di Napoli "Federico II"	
	² IREA, Consiglio Nazionale delle Ricerche, Napoli	
	³ DIIES, Università Mediterranea della Calabria	
	⁴ Consorzio Nazionale Interuniversitario sulle Telecomunicazioni, Parma	
p.		184
P1.15	EXPERIMENTAL VALIDATION OF MAGNETIC NANOPARTICLE ENHANCED MICROWAVE IMAGING OF BREAST CANCER	
	O.M. Bucci ^{1,4} , G. Bellizzi ^{2,4} , A. Borgia ³ , S. Costanzo ³ , L. Crocco ¹ , G. Di Massa ³ , R. Scapatucci ²	
	¹ IREA, Consiglio Nazionale delle Ricerche, Napoli	
	² DIETI, Università di Napoli "Federico II"	
	³ DIMES, Università della Calabria	
	⁴ Consorzio Nazionale Interuniversitario sulle Telecomunicazioni, Parma	
p.		188

P1.16

A SPECTRAL-DOMAIN METHOD FOR THE ELECTROMAGNETIC SCATTERING FROM A MULTILAYERED SPHERE BURIED IN A STRATIFIED LOSSY MEDIUMF. Mangini^{1,2}¹Enrico Fermi Research Center, Rome²Department of Information Engineering, Electronics and Telecommunications, "La Sapienza" University of Rome

p. 192

P1.17

ANALYSIS OF DB UNIT CELL AND EXTRACTION OF ITS EFFECTIVE CONSTITUTIVE PARAMETERS

M. Khalid, N. Tedeschi, F. Frezza

Department of Information Engineering, Electronics and Telecommunications, "La Sapienza" University of Rome

p. 196

P1.18

ELECTROMAGNETIC INTERACTION WITH A MISALIGNED BROKEN PIPEP.P. Di Gregorio¹, V. Ferrara¹, F. Frezza¹, F. Mangini^{1,2}, M. Muzi¹¹Department of Information Engineering, Electronics and Telecommunications, "La Sapienza" University of Rome²Enrico Fermi Research Center, Rome

p. 200

P1.19

RECONFIGURABLE FABRY-PEROT CAVITY LEAKY-WAVE ANTENNAS BASED ON NEMATIC LIQUID CRYSTALS FOR THZ APPLICATIONSW. Fuscaldo^{1,2}, S. Tofani^{1,3}, P. Burghignoli¹, P. Baccarelli¹, D.C. Zografopoulos², R. Beccherelli³, A. Galli¹¹Department of Information Engineering, Electronics and Telecommunications, "La Sapienza" University of Rome²Institut d'Électronique et de Télécommunications de Rennes, UMR CNRS 6164, Université de Rennes 1, France³Institute for Microelectronics and Microsystems, National Research Council, Rome

p. 204

P1.20

CELLULAR VOLUME FRACTION ESTIMATION THROUGH COMPLEX DIELECTRIC PERMITTIVITY MEASUREMENT AND MONTE CARLO ALGORITHM

F. Mangini, M. Muzi, N. Tedeschi

Department of Information Engineering, Electronics and Telecommunications, "La Sapienza" University of Rome

p. 208

P1.21

EARTHQUAKE DAMAGE DETECTION IN URBAN AREAS FROM VHR SAR IMAGERYR. Anniballe¹, M. Chini², N. Pierdicca¹¹Department of Information Engineering, Electronics and Telecommunications, "La Sapienza" University of Rome²Luxembourg Institute of Science and Technology, Belvaux, Luxembourg

p. 212

P1.22

HTS FILTERS FOR THE SARDINIA RADIO TELESCOPE

P. Bolli¹, L. Cresci¹, F. Huang², S. Mariotti³, D. Panella⁴

¹*Arcetri Astrophysical Observatory, INAF, Florence*

²*School of EESE, University of Birmingham, Birmingham, UK*

³*Institute of Radio Astronomy, INAF, Bologna*

p. 216

P1.23

ORTHO-MODE TRANSDUCERS FOR MULTI-FEED RECEIVERS

G. Addamo, G. Virone, O. A. Peverini, M. Lumia, R. Tascone

CNR-IEIIT, c/o Politecnico di Torino

p. 220

P1.24

DESIGN OF ERBIUM DOPED CHALCOGENIDE MICRODISK EMITTING AT 4.5 μm WAVELENGTH

G. Palma¹, M.C. Falconi¹, F. Starecki², V. Nazabal², L. Bodiou³, Y. Dumeige³, J. Lemaitre³, J. Charrier³, F. Prudenzeno¹

¹*Dipartimento di Ingegneria Elettrica e dell'Informazione, Politecnico di Bari*

²*ISCR, UMR UR1-CNRS 6226, Université de RENNES 1, France*

³*FOTON-UMR-CNRS 6082, ENSSAT BP80518, Lannion, France*

p. 224

P1.25

MONTE CARLO MODEL OF CLOUD SCATTERING OF SOLAR RADIATION FOR VLC AIRCRAFT SYSTEMS

D. Tagliaferri¹, R. Nebuloni², L. Luini^{1,2}, C. Capsoni¹

¹*Dipartimento di Elettronica, Informazione e Bioingegneria, Politecnico di Milano*

²*IEIIT-CNR, Milano*

p. 228

P1.26

PRELIMINARY RESULTS ON A MINIATURIZED QUADRATURE HYBRID COUPLER USING SLOW-WAVE TRANSMISSION LINES

G. Aciri¹, P. Ferrari², L. Boccia¹, D. Calzona¹, G. Amendola¹

¹*Department of Telecommunication Engineering, University of Calabria*

²*IMEP-LAHC, University Grenoble-Alpes, France*

p. 232

P1.27

ANALYSIS AND DESIGN OF IN-PACKAGE TRANSMIT-ARRAYS

G.R. Chamba Romero, F. Greco, L. Boccia, G. Amendola, E. Arneri

DIMES – Microwave laboratory Rende, University of Calabria

p. 236

P1.28

LINEAR PROGRAMMING RELAXATION IN 3D ELECTROMAGNETIC CONSTRAINED POWER FOCUSING

D.A.M. Iero

DIIES, Università Mediterranea di Reggio Calabria

p. 240

P1.29

A STEP-WISE MICROWAVE IMAGING STRATEGY FOR LANDMINE DETECTION MODELLING AND NUMERICAL ASSESSMENT

A. Brancaccio^{1,7}, G. Maiello^{1,7}, M.D. Migliore^{2,7}, D. Pinchera^{2,7}, F. Schettino^{2,7}, T. Isernia^{3,7}, M. Ambrosiano^{4,7}, V. Pascazio^{4,7}, L. Di Donato^{5,7}, L. Crocco^{6,7}

¹*DIII, Seconda Università di Napoli*

²*DIEI, Università di Cassino e del Lazio Meridionale*

³*DIIES, Università Mediterranea di Reggio Calabria*

⁴*Dipartimento di Ingegneria, Università di Napoli Parthenope*

⁵*DIEEI, Università di Catania*

⁶*IREA-CNR, Napoli*

⁷*Consorzio Nazionale Interuniversitario per le Telecomunicazioni, Parma*

p. 244

P1.30

NEAR-FIELD WPT TO LOOSELY-COUPLED SMALL IMPLANTS

A. Pacini, F. Berra, A. Costanzo, F. Mastri, D. Masotti

DEI, University of Bologna

p. 248

Session 5: Integrated and nonlinear optics

13th Sep. 9:00-11:15 Room "Auditorium"

Chairman: Gaetano Bellanca, *University of Ferrara*

9:00-9:40 Invited presentation, *Room "Auditorium"*

DEMOCRATIZATION OF NEXT-GENERATION MICROSCOPY, SENSING AND DIAGNOSTIC TOOLS THROUGH COMPUTATIONAL PHOTONICS

A. Ozcan

University of California, Los Angeles, CA, USA

p. 4

9:45-10:00 5.1

ALL-OPTICAL UNSCRAMBLING OF MIXED SPATIAL MODES ON A SILICON PHOTONIC CHIP

F. Morichetti¹, A. Annoni¹, S. Grillanda¹, N. Peserico¹, M. Carminati¹, P. Ciccarella¹, G. Ferrari¹, E. Guglielmi¹, M. Sorel², A. Melloni¹

¹*Dipartimento di Elettronica, Informazione e Bioingegneria, Politecnico di Milano*

²*School of Engineering, University of Glasgow, Glasgow, UK*

p. 252

10:00-10:15 5.2

INVESTIGATING THE USE OF A HYBRID PLASMONIC-PHOTONIC NANORESONATOR FOR OPTICAL TRAPPING USING FINITE-DIFFERENCE TIME-DOMAIN METHOD

M. Mossayebi², G. Bellanca¹, A.J. Wright², A. Parini¹, M.G. Somekh³, E.C. Larkins²

¹*Department of Engineering, University of Ferrara*

²*Department of Electrical and Electronic Engineering, University of Nottingham, Nottingham, UK*

³*Department of Electrical and Information Technology, Hong Kong Polytechnic University, Kowloon, Hong Kong, China*

p. 256

10:15-10:30	5.3	OPTICAL KERR DARK-LUMP DYNAMICS OF HYDRODYNAMIC ORIGIN F. Baronio ¹ , C. De Angelis ¹ , S. Wabnitz ¹ , Y. Kodama ² ¹ INO CNR and Department of Information Engineering, University of Brescia ² Department of Mathematics, Ohio State University, Columbus, OH, USA	260
10:30-10:45	5.4	DESIGN OF MESOSCOPIC PHOTONIC CRYSTAL MICROCAVITY BASED SENSORS DEVOTED TO OPTICAL TWEEZING APPLICATIONS B. Ferrara ¹ , M. Grande ¹ , G. Calò ¹ , A. D’Orazio ¹ , V. Petruzzelli ¹ , G. Magno ² , B. Dagens ² , A. Monmayrant ³ , O. Gauthier-Lafaye ³ ¹ Dipartimento di Ingegneria Elettrica e dell’Informazione, Politecnico di Bari ² IEF, CNRS, University Paris-Sud, University Paris-Saclay, Orsay, France ³ CNRS, LASS, Toulouse, France; University De Toulouse, LAAS, Toulouse, France	264
10:45-11:00	5.5	A DESIGN TOOL FOR INTEGRATED OPTICAL SEGMENTED WAVEGUIDES A.E. Kaplan ¹ , G. Bellanca ² , P. Bassi ¹ ¹ Department of Electrical, Electronic and Information Engineering, University of Bologna ² Department of Engineering, University of Ferrara	268
11:00-11:15	5.6	EFFECT OF ETCHING SLOPE IN HIGH Q-FACTOR OPTICAL NANOBEAMS D. Panettieri ¹ , L. O’Faolain ² , M. Grande ¹ ¹ Dipartimento di Ingegneria Elettrica e dell’Informazione, Politecnico di Bari ² SUPA, School of Physics and Astronomy, University of St. Andrews, UK	272

Session 6: Metamaterials and nanomaterials
13th Sep. 9:00-11:15 Room "Master"

Chairman: Federica Poli, *University of Parma*

9:00-9:40	Invited presentation, Room "Auditorium"	DEMOCRATIZATION OF NEXT-GENERATION MICROSCOPY, SENSING AND DIAGNOSTIC TOOLS THROUGH COMPUTATIONAL PHOTONICS A. Ozcan <i>University of California, Los Angeles, CA, USA</i>	4
9:45-10:00	6.1	DESIGN AND ANALYSIS OF AN ULTRA-THIN DUAL-BAND METAMATERIAL ABSORBER FOR THZ APPLICATIONS M.D. Astorino, N. Tedeschi <i>Department of Information Engineering, Electronics and Telecommunications, "La Sapienza" University of Rome</i>	276

10:00-10:15	6.2		
MATERIAL-BY-DESIGN PHASED ARRAYS SYNTHESIS			
L. Tenuti			
<i>ELEDIA Research Center ELEDIA@UniTN, University of Trento</i>			
p.			280
10:15-10:30	6.3		
EFFECT OF EXTREME ANISOTROPY ON THE REFLECTION FROM THE INTERFACE OF A MATCHED UNIAXIAL MEDIUM			
M. Khalid			
<i>Department of Information Engineering, Electronics and Telecommunications, "La Sapienza" University of Rome</i>			
p.			284
10:30-10:45	6.4		
INFLUENCE OF DISORDER ON LASING ONSET IN PLANAR MEDIA			
C. Molardi ¹ , X. Yu ² , H.K. Liang ² , A. Cucinotta ¹ , S. Selleri ¹			
¹ <i>Information Engineering Department, University of Parma</i>			
² <i>Precision Measurement Group, Singapore Institute of Manufacturing Technology, Singapore</i>			
p.			288
10:45-11:00	6.5		
A SIMPLE WIDE-ANGLE METAMATERIAL ABSORBER			
E. Sassolini, N. Tedeschi, M. Khalid, E. Lia, M.D. Astorino, F. Frezza			
<i>Department of Information Engineering, Electronics and Telecommunications, "La Sapienza" University of Rome</i>			
p.			292
11:00-11:15	6.6		
SIW FILTERS BASED ON PERFORATED DIELECTRIC SUBSTRATE			
L. Silvestri ¹ , E. Massoni ¹ , M. Bozzi ¹ , L. Perregrini ¹ , C. Tomassoni ² , A. Coves ³			
¹ <i>Department of Electrical, Computer and Biomedical Engineering, University of Pavia</i>			
² <i>Department of Engineering, University of Perugia</i>			
³ <i>Departamento de Ingenieria de Comunicaciones, Universidad Miguel Hernandez, Elche, Spain</i>			
p.			296

Session 7: Numerical methods

13th Sep. 11:45-13:15 Room "Auditorium"

Chairman: Stefano Selleri, *University of Florence*

11:45-12:15	Invited presentation		
EM MODELING OF COMPLEX AND ELECTRICALLY LARGE ELECTROMAGNETIC SYSTEMS FROM A RF AND EMC POINT OF VIEW			
E. Leroux			
<i>CST Italy srl</i>			

12:15-12:30	7.1	SINGULARITY EXTRACTION FOR WEAKLY SINGULAR INTEGRALS ON HIGH ORDER ELEMENTS	
		G. Borzì	
		<i>Department of Engineering, Messina University</i>	
p.			300
12:30-12:45	7.2	A FINITE-ELEMENT BASED FIELD ESTIMATION VIA A KALMAN FILTERING APPROACH	
		G. Battistelli, L. Chisci, N. Forti, G. Pelosi, S. Selleri	
		<i>Department of Information Engineering, University of Florence</i>	
p.			304
12:45-13:00	7.3	ELECTROMAGNETIC IMAGING IN LP BANACH SPACES: 3D FREE SPACE RECONSTRUCTIONS	
		A. Fedeli, M. Pastorino, A. Randazzo, E. Tavanti	
		<i>Department of Electrical, Electronic, Telecommunications Engineering, and Naval Architecture, University of Genoa</i>	
p.			308
13:00-13:15	7.4	THE BI-RME METHOD COMBINED WITH THE SEGMENTATION TECHNIQUE APPLIED TO THE MODELING OF 3D COMPONENTS	
		S. Battistutta, M. Bozzi, M. Bressan, M. Pasian, L. Perregrini	
		<i>Department of Electrical, Computer and Biomedical Engineering, University of Pavia</i>	
p.			312

Session 8: Antenna design and measurement

13th Sep. 11:45-13:15 Room "Master"

Chairman: Raffaele Solimene, *Second University of Naples*

11:45-12:00	8.1	THE SYSTEM-BY-DESIGN APPROACH FOR SOLVING HIGH-COMPLEXITY EM DESIGN PROBLEMS	
		M. Salucci ^{1,2}	
		¹ <i>ELEDIA Research Center ELEDIA@UniTN, University of Trento</i>	
		² <i>ELEDIA Research Center ELEDIA@L2S, UMR8506 [CNRS-CS-UPS], France</i>	
p.			316
12:00-12:15	8.2	ϵ-ENTROPY OF SCATTERED FIELD	
		M.A. Maisto, R. Solimene, R. Pierri	
		<i>Dipartimento di Ingegneria Industriale e dell'Informazione, Seconda Università di Napoli</i>	
p.			320

12:15-12:30	8.3	
ANTENNA NEAR FIELD PHASE RECOVERY BY IMPROVED INDIRECT HOLOGRAPHIC METHOD		
G. Di Massa, S. Costanzo, <i>Dipartimento di Ingegneria Informatica, Modellistica, Elettronica e Sistemistica, Università della Calabria</i>		
p.		324
12:30-12:45	8.4	
SYNTHESIS OF DIELECTRIC CLOAKS VIA INVERSE SCATTERING DESIGN WITHOUT METAMATERIAL COATINGS		
G. Labate ¹ , L. Di Donato ² ¹ <i>Dipartimento di Elettronica e Telecomunicazioni, Politecnico di Torino</i> ² <i>Dipartimento di Ingegneria Elettrica, Elettronica e Informatica, Università di Catania</i>		
p.		328
12:45-13:15	Invited presentation	
DESIGN ED ANALISI DI ANTENNE IN MATLAB		
Stefano Olivieri <i>MathWorks Italy</i>		

Poster Session 2
13th Sep. 14:15-16:00

P2.1		
DEEP PENETRATION PROPERTIES OF INHOMOGENEOUS WAVES		
P. Baccarelli, F. Frezza, P. Simeoni, N. Tedeschi <i>Department of Information Engineering, Electronics and Telecommunications, "La Sapienza" University of Rome</i>		
p.		332
P2.2		
ANALYSIS OF LEAKY-WAVE THZ ANTENNAS BASED ON GRAPHENE		
W. Fuscaldo ^{1,2} , P. Burghignoli ¹ , P. Baccarelli ¹ , A. Galli ¹ ¹ <i>Department of Information Engineering, Electronics and Telecommunications, "La Sapienza" University of Rome</i> ² <i>Institut d'Électronique et de Télécommunications de Rennes, UMR CNRS 6164, Université de Rennes 1, France</i>		
p.		336
P2.3		
WIRE-MEDIUM LOADED FABRY-PEROT CAVITY ANTENNAS		
D. Comite, P. Burghignoli, P. Baccarelli, A. Galli <i>Department of Information Engineering, Electronic and Telecommunications, "La Sapienza" University of Rome</i>		
p.		340

P2.4

A HIGH GAIN DIELECTRIC RESONATOR ANTENNA FOR WIDEBAND WIRELESS APPLICATIONS

R. Cicchetti, E. Miozzi, O. Testa

Department of Information Engineering, Electronics and Telecommunications, "La Sapienza" University of Rome

p. 344

P2.5

COMPUTATIONAL MODELLING OF THE INDUCED FIELDS DURING CEREBELLAR AND SPINAL DIRECT CURRENT STIMULATION IN CHILDRENS. Fiocchi¹, P. Ravazzani¹, A. Priori², M. Parazzini¹¹*Istituto di Elettronica e di Ingegneria dell'Informazione e delle Telecomunicazioni IEIIT, CNR Consiglio Nazionale delle Ricerche*²*Dipartimento di Scienze della Salute, Università degli studi di Milano, Ospedale San Paolo*

p. 348

P2.6

DESIGN OF PATTERN RECONFIGURABLE SPARSE ANTENNA ARRAYS

G. Buttazoni

Department of Engineering and Architecture, University of Trieste

p. 352

P2.7

POLARIMETRIC SAR RAW SIGNAL SIMULATION

G. Di Martino, A. Iodice, D. Poreh, D. Riccio

Department of Electric Engineering and Information Technology, University of Naples "Federico II"

p. 356

P2.8

TWO-PORT WPT LINK USING THREE COUPLED INDUCTORSG. Monti¹, A. Costanzo², F. Mastri², M. Mongiardo³, L. Tarricone¹¹*DII, University of Salento*²*DEI, University of Bologna*³*DE, University of Perugia*

p. 360

P2.9

MONOPOLE ARRAY WITH PARASITIC ELEMENTS AND CORPORATE-FEED NETWORKM. Farran¹, S. Boscolo², A. Locatelli¹, A.D. Capobianco³, M. Midrio², V. Ferrari¹, D. Modotto¹¹*Dipartimento di Ingegneria dell'Informazione, Università di Brescia*²*Dipartimento di Ingegneria Elettrica, Gestionale e Meccanica, Università di Udine*³*Dipartimento di Ingegneria dell'Informazione, Università di Padova*

p. 364

P2.10

PATH-LOSS STATISTICAL MODEL FOR URBAN MOBILE BACKHAULING AT MM-FREQUENCIESF. Fuschini¹, M. Barbiroli¹, M. Zoli¹, A. Perikleous², V. Petrini³, C. Carciofi³¹*DEI, University of Bologna*²*Consorzio Elettra2000, Pontecchio Marconi (BO)*³*Fondazione Ugo Bordononi, Pontecchio Marconi (BO)*

p. 368

P2.11	FREQUENCY RECONFIGURABLE SELF-ADAPTING CONFORMAL ARRAY FOR CHANGING SURFACES	
	G. Mansutti ¹ , M.S. Khan ¹ , B.D. Braaten ² , A.D. Capobianco ¹	
	¹ <i>Department of Information Engineering, University of Padua</i>	
	² <i>Department of Electrical and Computer Engineering, North Dakota State University, ND, USA</i>	
p.		372
P2.12	FRACTIONAL-CALCULUS-BASED FDTD MODEL FOR SIMULATING ARBITRARY DISPERSIVE DIELECTRIC MATERIALS	
	P. Bia ¹ , L. Mescia ¹ , D. Caratelli ²	
	¹ <i>Dipartimento di Ingegneria Elettrica e dell'Informazione, Politecnico di Bari</i>	
	² <i>The Antenna Company Nederland B.V., AE Eindhoven, The Netherlands</i>	
p.		376
P2.13	A SIMPLIFIED RADIATION MODEL OF A WAVEGUIDE SLOT	
	G. Buonanno, G. Leone	
	<i>Department of Industrial and Information Engineering, Second University of Naples</i>	
p.		380
P2.14	INVERSE SOURCE IMMERSSED IN INHOMOGENEOUS MEDIUM	
	M.A. Maisto, R. Solimene, R. Pierri	
	<i>Dipartimento di Ingegneria Industriale e dell'Informazione, Seconda Università di Napoli</i>	
p.		385
P2.15	COUPLING STRUCTURES FOR ON-CHIP MODE-DIVISION MULTIPLEXING SIGNAL PROCESSING	
	A. Parini ¹ , Y.G. Boucher ¹ , G. Bellanca ² , C. Peucheret ¹	
	¹ <i>FOTON Laboratory, CNRS UMR 6082, Lannion, France</i>	
	² <i>Department of Engineering, University of Ferrara</i>	
p.		389
P2.16	ELECTROMAGNETIC SCATTERING BY ROTATING AXISYMMETRIC OBJECTS	
	P.K. Ramakrishnan, M. Raffetto	
	<i>Department of Electrical, Electronic, Telecommunications Engineering, and Naval Architecture, University of Genoa</i>	
p.		393
P2.17	A LOW-PROFILE ULTRAWIDEBAND ANTENNA FOR AUTOMOTIVE APPLICATIONS	
	A. Michel ¹ , V. Franchina ¹ , P. Nepa ¹ , G. Manara ¹ , M. Gallo ² , I. Moro ² , D. Zamberlan ²	
	¹ <i>Department of Information Engineering, University of Pisa</i>	
	² <i>Calero Antenne S.p.A., Isola Vicentina (VI)</i>	
p.		397
P2.18	NUMERICAL ANALYSIS OF THE RFID PRINTER ENCODER ANTENNAS PERFORMANCE	
	A. Michel, A. Buffi, P. Nepa, G. Manara	
	<i>Department of Information Engineering, University of Pisa</i>	
p.		401

P2.19

SIMPLE TOOLS FOR UNDERSTANDING THE LIMITATIONS OF ORBITAL ANGULAR MOMENTUM ANTENNAS

A.F. Morabito¹, L. Di Donato²

¹*DIIES Department, University of Reggio Calabria and CNIT Consortium*

²*DIEEI Department, Università degli Studi di Catania*

p. 405

P2.20

A NEW APPROACH TO THE DIAGNOSTICS OF ARRAY ANTENNAS BY MEANS OF A SMALL NUMBER OF PHASELESS MEASUREMENTS

A.F. Morabito, R. Palmeri

DIIES Department, University of Reggio Calabria, and CNIT Consortium

p. 409

P2.21

FURTHER APPROACH TO PHASE RETRIEVAL THROUGH CONSTRAINED POWER INFLATION AND FLIPPING

A.R. Laganà , T. Isernia

LEMMA Research Group @ DIIES, Università Mediterranea di Reggio Calabria

p. 413

P2.22

LATTICE OPTIMIZATION FOR A MULTI-ARRAY ANTENNA SYSTEM AIMED AT SPACE DEBRIS SURVEILLANCE

G. Siciliano¹, M. Mendijur², P. Besso², M. Pasian¹, M. Bozzi¹, L. Perregrini¹

¹*Department of Electrical, Electronic and Biomedical Engineering, University of Pavia*

²*Department of Ground Stations and Operations, European Space Operations Center (ESOC), Darmstadt, Germany*

p. 417

P2.23

ADDITIVE MANUFACTURING OF SUBSTRATE INTEGRATED WAVEGUIDE COMPONENTS

E. Massoni, L. Silvestri, S. Moscato, M. Pasian, M. Bozzi, L. Perregrini

Department of Electrical, Computer and Biomedical Engineering, University of Pavia

p. 421

P2.24

RADIATION OF AN APERTURE ON THE FACE OF A PERFECTLY ELECTRIC CONDUCTING WEDGE-SHAPED SCREEN

M. Righini

Department of Information Engineering, University of Florence

p. 425

P2.25

A BACK PROJECTION ALGORITHM TO FOCUS SYNTHETIC APERTURE RADAR DATA ACQUIRED FROM STRONGLY NON-RECTILINEAR TRAJECTORIES

S. Perna^{1,2}, A. Natale², P. Berardino²

¹*DI, Università degli Studi di Napoli "Parthenope"*

²*IREA – CNR, Napoli*

p. 429

P2.26

INVESTIGATION OF THE PATH REDUCTION FACTOR ON TERRESTRIAL LINKS FOR THE DEVELOPMENT OF A PHYSICALLY-BASED RAIN ATTENUATION MODEL

R. Ghiani¹, L. Luini^{2,3}, A. Fanti¹

¹*DIEE, Università di Cagliari*

²*DEIB, Politecnico di Milano*

³*IEIIT, Consiglio Nazionale delle Ricerche, Milano*

p. 433

P2.27

MICROWAVE BESSEL BEAM LAUNCHER FOR PLANETARY DRILLING OPERATIONS

S. Costanzo, G. Di Massa, A. Borgia, A. Raffo

DIMES, University of Calabria

p. 437

P2.28

DI-SILICATE DENTAL CERAMIC SURFACE PREPARATION BY FIBER LASER: ULTRASTRUCTURAL ANALYSIS

C. Fornaini^{1,2}, F. Poli¹, E. Merigo², M. Valentini³, L. Romoli³, F. Bondioli³, S. Selleri¹, A. Cucinotta¹

¹*Information Engineering Department, University of Parma*

²*Micoralis Laboratory, Faculty of Dentistry, University of Nice, France*

³*Department of Industrial Engineering, University of Parma*

p. 441

P2.29

OPTIMIZATION OF STRAIGHT AMPLIFIER ERBIUM DOPED WAVEGUIDES WITH THE IMPLEMENTATION OF AN ADIABATIC INPUT TAPER

V. Vaiti

Information Engineering Department, University of Parma

p. 445

P2.30

PLASMONIC NANOANTENNA FOR POSSIBLE CMOS INTEGRATION

M. Celli¹, A. Polemi^{1,2}, L. Vincetti¹

¹*Department of Engineering "Enzo Ferrari", University of Modena*

²*Department of Material Science and Engineering, Drexel University, Philadelphia, PA, USA*

p. 449

Session 9: Optical Fibers

14th Sep. 8:45-11:00 Room "Auditorium"

Chairman: Luca Vincetti, *University of Modena and Reggio Emilia*

8:45-9:25 Invited presentation, Room "Auditorium"

HOLLOW CORE PHOTONIC CRYSTAL FIBRE: NOVEL LIGHT GUIDANCE AND MYRIAD OF GAS-PHOTONIC APPLICATIONS

F. Benabid

Research Institute XLIM - UMR CNRS n°7252, Limoges, France

p. 6

9:30-9:45	9.1	REDUCTION OF HARMONIC DISTORTION IN RADIO OVER FIBER LINKS THROUGH DIGITAL PREPROCESSING	
F. Fuochi, M.U. Hadi, J. Nanni, P.A. Traverso, G. Tartarini			
<i>Department of Electrical, Electronic and Information Engineering, University of Bologna</i>			
p.			453
9:45-10:00	9.2	DYSPROSIUM-DOPED CHALCOGENIDE FIBER LASER FOR MEDICAL APPLICATIONS	
M.C. Falconi ¹ , G. Palma ¹ , F. Starecki ² , V. Nazabal ² , J. Troles ² , S. Taccheo ³ , M. Ferrari ⁴ , F. Prudeniano ¹			
¹ <i>Department of Electrical and Information Engineering, Politecnico di Bari</i>			
² <i>Institut des Sciences Chimiques de Rennes, UMR 6226, Université de Rennes 1, France</i>			
³ <i>Institute of Advanced Telecommunications, Swansea University, Wales, UK</i>			
⁴ <i>CSMFO Laboratory, Consiglio Nazionale delle Ricerche Istituto di Fotonica e Nanotecnologie, Trento</i>			
p.			457
10:00-10:15	9.3	MULTI-MODE PROPAGATION IN OPTICAL FIBERS FOR SPACE-DIVISION MULTIPLEX TRANSMISSION	
C. Antonelli ¹ , A. Mecozzi ¹ , M. Shtai ²			
¹ <i>Department of Physical and Chemical Sciences, University of L'Aquila</i>			
² <i>Department of Physical Electronics, Tel Aviv University, Tel Aviv, Israel</i>			
p.			461
10:15-10:30	9.4	A PRELIMINARY NUMERICAL ANALYSIS OF THE DIFFERENTIAL GROUP DELAY OF A 6-SPATIAL-MODES SPUN FIBER	
L. Palmieri, G. Guerra, L. Marcon, M. Santagiustina, A. Galtarossa			
<i>Department of Information Engineering, University of Padua</i>			
p.			465
10:30-10:45	9.5	INFLUENCE OF INNER CLADDING GEOMETRY ON SYMMETRY-FREE PHOTONIC CRYSTAL FIBER PROPERTIES UNDER SEVERE HEAT LOAD	
F. Poli, G. Ciletti, E. Coscelli, A. Cucinotta, S. Selleri			
<i>Information Engineering Department, University of Parma</i>			
p.			469
10:45-11:00	9.6	A QUASI-D ISTRIBUTED OPTICAL FIBER LOAD SENSOR	
L. Schenato ¹ , A. Pasuto ¹ , A. Galtarossa ^{2,3} , L. Palmieri ²			
¹ <i>Research Institute for Geo-Hydrological Protection, National Research Council, Padua</i>			
² <i>Department of Information Engineering, University of Padua</i>			
³ <i>IIUSE, Southeast University, Nanjing, China</i>			
p.			473

Session 10: Remote Sensing

14th Sep. 8:45-11:00 Room "Master"

Chairman: Daniele Riccio, *University of Naples "Federico II"*

8:45-9:25 Invited presentation, Room "Auditorium"

HOLLOW CORE PHOTONIC CRYSTAL FIBRE: NOVEL LIGHT GUIDANCE AND MYRIAD OF GAS-PHOTONIC APPLICATIONS

F. Benabid

Research Institute XLIM - UMR CNRS n°7252, Limoges, France

p. 6

9:30-9:45 10.1

DEVELOPING A LOW COST MULTIPURPOSE X-BAND FMICW RADAR

C. Lucianaz¹, S. Bertoldo¹, P. Petrini¹, M. Allegretti²

¹*Department of Electronics and Telecommunications, Politecnico di Torino*

²*CINFAI (Consorzio Interuniversitario Nazionale per la Fisica delle Atmosfere e delle Idrosfere) c/o Politecnico di Torino, Torino*

p. 477

9:45-10:00 10.2

ELECTROMAGNETIC SCATTERING AND A NEW PERSPECTIVE IN SAR DESPECKLING

G. Di Martino, A. Di Simone, A. Iodice, D. Riccio, G. Ruello

Department of Information Technology and Electrical Engineering, University of Naples "Federico II"

p. 481

10:00-10:15 10.3

OPTIMAL TILING FOR NEW GENERATION RADAR SYSTEMS

N. Anselmi

ELEDIA Research Center ELEDIA@UniTN, University of Trento

p. 485

10:15-10:30 10.4

EXPERIMENTAL ASSESSMENT OF SOFTWARE DEFINED RADAR FOR LANDSLIDE EARLY WARNING

S. Costanzo, G. Di Massa, A. Costanzo, A. Borgia, A. Raffo

DIMES – University of Calabria

p. 489

10:30-10:45 10.5

COLOR-CODING OF SAR IMAGES USING MULTITEMPORAL

D. Amitrano, G. Di Martino, A. Iodice, D. Riccio, G. Ruello

Department of Electrical Engineering and Information Technology, University of Napoli "Federico II"

p. 493

10:45-11:00 10.6

NEURAL NETWORKS ARCHITECTURES FOR OIL SPILL MONITORING USING FULLY POLARIMETRIC SAR DATA

V. Scappiti, D. Latini, A. Ghezzi, F. Del Frate, G. Schiavon

Department of Civil Engineering and Computer Science Engineering, University of Rome Tor Vergata

p. 497

Start-up and Spin-off

14th Sep. 11:30-13:15 Room "Auditorium"

Chairman: Annamaria Cucinotta, *University of Parma*

11:30-11:40 **Welcome and opening remarks**

11:40-12:00

VISLAB UN'ESPERIENZA DA RIPETERE..!

G. Gandolfi

University of Parma

12:00-12:20

START UP E SPIN OFF: RISCHI E OPPORTUNITÀ DURANTE IL PERCORSO DI CRESCITA

S. Vurro

Università del Salento

12:20-12:40

"SENZA FILI SENZA CONFINI". IL SUCCESSO DELL'INNOVAZIONE SOCIALE A BASE POPOLARE

D. Trincherò

Politecnico di Torino

12:40-13:00

UN'ESPERIENZA DI SPINOFF UNIVERSITARIO NEL CAMPO DELLE RF

R. Sorrentino

Università degli Studi di Perugia

13:00-13:10

WE LAB

A. Tonelli

DNAPhone s.r.l.

13:10-13:15 **Concluding remarks**

**Session 11: EMF for energy
and environment applications**

14th Sep. 14:15-16:30 Room "Auditorium"

Chairman: Lorenzo Crocco, *CNR*

14:15-14:55 Invited presentation, Room "Auditorium"

SUBSURFACE SENSING AND SUPER-RESOLUTION IMAGING: APPLICATION OF COMPUTATIONAL ACOUSTICS AND ELECTROMAGNETICS

Q.H. Liu

Duke University, Durham, NC, USA

p. 8

15:00-15:15	11.1	A PORTABLE WIRELESS CHARGER FOR THIN-FILM BATTERIES G. Monti, L. Corchia, E. De Benedetto, L. Tarricone <i>Department of Engineering for Innovation, University of Salento</i> p. 501	501
15:15-15:30	11.2	A PRELIMINARY STUDY OF EBG HOLLOW-CORE STRUCTURES FOR HIGH VOLTAGE APPLICATION O. Leonardi ¹ , G. Castorina ² , G. Sorbello ² , G. Torrisci ¹ , L. Di Donato ² , L. Celona ¹ , S. Gammino ¹ ¹ <i>Istituto Nazionale di Fisica Nucleare - Laboratori Nazionali del Sud, Catania</i> ² <i>DIEEI, Università degli Studi di Catania</i> p. 505	505
15:30-15:45	11.3	A UHF PASSIVE SENSING LINK IN A NEAR-FIELD WIRELESS POWER TRANSFER SYSTEM R. Trevisan ¹ , A. Costanzo ² ¹ <i>Innovation R&D – IMA SpA, Ozzano dell'Emilia (BO)</i> ² <i>Department of Electrical, Electronic and Information Engineering, University of Bologna</i> p. 509	509
15:45-16:00	11.4	INTERLEAVED ISOPHORIC ARRAY ARCHITECTURES FOR RECONFIGURABLE FULL-EARTH COVERAGE FROM GEO SATELLITES O.M. Bucci ^{1,4} , S. Perna ^{2,3,4} , D. Pinchera ^{3,4} ¹ <i>IREA, Consiglio Nazionale delle Ricerche, Napoli</i> ² <i>DI, Università degli Studi di Napoli "Parthenope"</i> ³ <i>DIEI, Università degli Studi di Cassino e del Lazio Meridionale</i> ⁴ <i>Consorzio Nazionale Interuniversitario per le Telecomunicazioni, Parma</i> p. 513	513
16:00-16:15	11.5	UNMANNED AERIAL VEHICLE FOR THE MEASUREMENT OF 3D ELECTROMAGNETIC FIELDS DISTRIBUTION D. Latini ¹ , F. Carbone ² , J. Bulli ³ , A. Saitto ⁴ , F. Del Frate ¹ , G. Schiavon ¹ ¹ <i>Earth Observation Laboratory, Department of Civil Engineering and Computer Science Engineering, University of Rome Tor Vergata</i> ² <i>GEO-K s.r.l., Rome</i> ³ <i>Mpb s.r.l., Rome</i> ⁴ <i>Consorzio NITEL, Rome</i> p. 517	517
16:15-16:30	11.6	SOIL MOISTURE RETRIEVALS FROM RADAR DATA AT L-BAND THROUGH A MULTI-TEMPORAL APPROACH F. Fascetti ¹ , N. Pierdicca ¹ , L. Pulvirenti ² ¹ <i>Department of Information Engineering, Electronics and Telecommunications, "La Sapienza" University of Rome</i> ² <i>Cima Research Foundation, Savona</i> p. 521	521

**Session 12: Bioelectromagnetism
and biomedical applications**

14th Sep. 14:15-16:45 Room "Master"

Chairman: Marta Cavagnaro, *"La Sapienza" University of Rome*

14:15-14:55 Invited presentation, Room "Auditorium"

SUBSURFACE SENSING AND SUPER-RESOLUTION IMAGING: APPLICATION OF COMPUTATIONAL ACOUSTICS AND ELECTROMAGNETICS

Q.H. Liu

Duke University, Durham, NC, USA

p. 8

15:00-15:15 12.1

SUPERPARAMAGNETIC SCAFFOLDS FOR TISSUE ENGINEERING

M. B. Lodi¹, A. Fanti¹, B. Bisceglia², G. Mazzarella¹

¹*Department of Electric and Electronic Engineering, University of Cagliari*

²*Department of Industrial Engineering, University of Salerno*

p. 525

15:15-15:30 12.2

INDUCTIVE LINK FOR RECHARGEABLE PULSE GENERATORS IMPLANTED IN THE CHEST

G. Monti, M. V. De Paolis, L. Tarricone

Department of Engineering for Innovation, University of Salento

p. 529

15:30-15:45 12.3

TISSUE SHRINKAGE IN MICROWAVE THERMAL ABLATION

L. Farina, M. Cavagnaro

Department of Information Engineering, Electronics and Telecommunications, "La Sapienza" University of Rome

p. 533

15:45-16:00 12.4

EPIDERMAL UHF ANTENNAS FOR SKIN SENSING: FUNDAMENTAL LIMITATIONS AND OPTIMAL PERFORMANCE

S. Amendola, G. Marrocco

Department of Civil Engineering and Informatics, University of Rome Tor Vergata

p. 537

16:00-16:15 12.5

FEASIBILITY STUDY ON THE USE OF MICROWAVE TOMOGRAPHY FOR TEMPERATURE MONITORING IN ABLATION TREATMENTS

R. Scapatucci¹, G.G. Bellizzi^{1,2}, O.M. Bucci^{1,3}, M. Cavagnaro⁴, L. Crocco¹, V. Lopresto⁵

¹*IREA, National Council of Research of Italy, Naples*

²*DIIES, Mediterranea University of Reggio Calabria*

³*CNIT - National Interuniversity Consortium on Telecommunications, Parma*

⁴*DIET, "La Sapienza" University of Rome*

⁵*ENEA, Division of Health Protection Technologies, Rome*

p. 541

XXI RINEM – CONFERENCE SESSIONS

16:15-16:30 12.6

MICROWAVE HYPERTHERMIA OF PHOENIX CANARIENSIS FOR RED PALM WEEVIL PEST CONTROL

R. Massa¹, M.D. Migliore², G. Panariello², D. Pinchera², F. Schettino², E. Caprio³, R. Griffo⁴

¹Physics Department "Ettore Pancini", University of Naples "Federico II"

²DIEI, University of Cassino and Southern Lazio

³Department of Agricultural Sciences, University of Naples "Federico II"

⁴Plant Protection Service of Campania Region

p. 545

16:30-16:45 12.7

FIBER-BASED BIOSENSOR FOR DNA DETECTION

M. Barozzi¹, S. K. M. Al-Hayali², A. Candiani³, A. Vannucci¹, A. H. Al-Janabi², A. Cucinotta¹, S. Selleri¹

¹Information Engineering Department, University of Parma

²Institute of Laser for Postgraduate Studies, University of Baghdad

³DNAPhone s.r.l.

p. 549

16:45 – 17:30

Closing remarks and awards

GENERATION OF LIMITED-DIFFRACTIVE TWISTED PULSES

D. Comite⁽¹⁾, W. Fuscaldo^(1,2), S. C. Pavone⁽³⁾

⁽¹⁾ Department of Information Engineering, Electronic and Telecommunications, Sapienza University of Rome
00184 Rome, Italy.

comite, fuscaldo@diet.uniroma1.it

⁽²⁾ Institut d'Électronique et de Télécommunications de Rennes,
UMR CNRS 6164, Université de Rennes 1,
35042 Rennes, France.

⁽³⁾ Department of Information Engineering and Mathematics,
University of Siena, 53100 Siena, Italy.

santi.pavone@unisi.it

Abstract

In this work, we investigate the possibility to generate a limited-diffractive electromagnetic twisted pulse carrying an orbital angular momentum (OAM). To this aim, a higher-order Bessel beam with an azimuthal phase variation is generated by enforcing an inward cylindrical travelling wave aperture distribution over a finite aperture. The normal component of the electric field is first computed within the Fresnel region, at a single frequency in the microwave range. Then, the electric field is evaluated for different frequencies over a limited fractional bandwidth centered around the carrier frequency. Finally, the time-domain description of the electric field is obtained by means of an inverse Fourier transform of the previously generated electric fields. Numerical results demonstrate the peculiar twisted shape of a pulse with limited spatio-temporal broadening over the propagating axis.

Index Terms – Near field, non-diffracting waves, Bessel beams, orbital angular momentum (OAM).

I. INTRODUCTION

In the last decades, the possibility to generate localized electromagnetic waves as well as the capability to transfer orbital angular momentum by means of electromagnetic radiation has been investigated by various authors (see [1] and Refs. therein). Non-diffracting waves are exact solutions of the wave equation that do not exhibit either time or spatial broadening as they propagate. The spatial and temporal confinements of electromagnetic waves have been widely investigated in optics and acoustics [1]. However, at microwaves, it still lacks evidence of either non-diffractive beams (monochromatic solutions) with an azimuthal phase variation, or twisted pulses (polychromatic solutions). In particular, to the authors' best knowledge, a realistic device which is able to launch non-diffractive waves in the microwave range has never been proposed. To this aim, we discuss here the possibility to generate a non-diffractive electromagnetic pulse at microwaves by means of a radiating aperture

able to carry on an orbital angular momentum (OAM) [2]. The main result of the work relies in the fact that, even when dispersion effects cannot be neglected, as typical for conventional microwave devices, we are able to generate a limited-diffraction electromagnetic twisted pulse over a well-defined area. This approach may pave the way for the first experimental realization of localized transmission of pulses carrying an OAM in the microwave range.

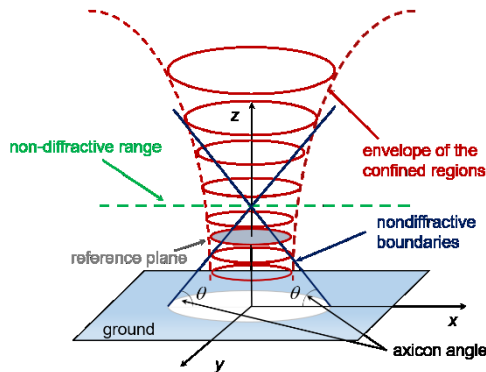


FIG. 1 – A circular aperture is considered over the transverse (xy) plane. The non-diffractive boundaries are defined as the transverse planes at which the amplitude of the normal component E_z is -20 dB with respect to the central peak. Their section slowly increases beyond the non-diffracting range due to the limited spatio-temporal dispersion of the pulse.

This paper is organized as follows. In Section II, the exact aperture field distribution required to generate a monochromatic Bessel beam with an azimuthal phase variation is introduced along with the theoretical steps supporting the generation of a twisted pulse. In Section III numerical results are shown. Conclusion follows.

II. THEORETICAL BACKGROUND

The longitudinal component of a transverse magnetic (TM^z) electric field E_z describing a higher-order Bessel beam can be written as

$$E_z = E_0 J_n(k_\rho \rho) e^{jn\phi} e^{-jk_z z} \quad (1)$$

being $J_n(\cdot)$ the n -th order Bessel function of the first kind, whereas k_ρ , k_z , and k_0 are the transverse, longitudinal, and free-space wavenumbers, respectively; ρ , ϕ , and z are the coordinates of a cylindrical reference system. If $n = 0$, a zeroth-order azimuthally symmetric beam is generated, i.e., showing a maximum on the axis of symmetry of the aperture and having both amplitude and phase azimuthally invariant, whereas for $n = 1$ a first-order azimuthal phase variation is generated.

Let us consider a finite circular radiating aperture of radius ρ_{ap} with its origin centered in the aperture. It can be shown [3] that, when an inward cylindrical traveling-wave aperture distribution is considered, the E_z

component is accurately described by a Bessel beam within a well-defined conical region close to the axis of symmetry of the radiating aperture. In this work, the aperture distribution along the transverse electric field E_ρ takes the following form (mathematical details regarding this formulation will be given at the conference):

$$E_\rho = -j \frac{k_z}{k_\rho^2} E_0 H_1'(k_\rho \rho) e^{-j\phi} e^{-jk_z z} \quad (2)$$

Let us stress that we consider an inward traveling-wave Hankel distribution to avoid resonance Bessel aperture distributions and in turns exploit the wide-band nature provided by the Hankel distributions [2]. Eq. (2) describes the transverse aperture field able to generate an ideal non-diffractive-beam, and is still accurate provided that the definition is restricted to the aperture diameter $d_{\text{ap}}=2\rho_{\text{ap}}$ and to the non-diffractive range, defined as $z_{\text{ndr}}=\rho_{\text{ap}} k_z/k_\rho$ [1,3].

The near-field distribution of E_z is obtained by numerically evaluating the radiation integral given by the aperture field described by Eq. (2) [4]. As is shown in Fig. 2, E_z takes the form of Eq. (1). Once such a higher-order Bessel beam is generated at a single frequency, an ideal non-diffractive pulse can be synthesized by superposing monochromatic fields over a certain frequency range, assuming that k_ρ and k_z frequency dispersion is almost linear (as frequently assumed in optics [1]). The mathematical description of such ideal pulse is given by:

$$\chi(\rho, \phi, z, t) = \int_{-\infty}^{+\infty} F(\omega) J_n[k_\rho \rho] e^{jn\phi} e^{-jk_z z} e^{j\omega t} d\omega \quad (3)$$

where $F(\omega)$ is the pulse frequency spectrum. However, when Bessel beams are generated at microwaves, the frequency dispersion of both k_ρ and k_z must be taken into account. Hence, for a uniform frequency spectrum $F(\omega) = 1$ and $\omega \in [\omega_0 - \Delta\omega/2, \omega_0 + \Delta\omega/2]$ (0 elsewhere), being $\omega_0 = 2\pi f_0$ and $\Delta\omega$ the bandwidth, from Eq. (3) it holds

$$\chi(\rho, \phi, z, t) = \text{Re}[\chi^+(\rho, \phi, z, t)] = \text{Re} \left[\int_{\omega_0 - \Delta\omega/2}^{\omega_0 + \Delta\omega/2} J_n[k_\rho(\omega)\rho] e^{jn\phi} e^{-jk_z(\omega)z} e^{j\omega t} d\omega \right] \quad (4)$$

where k_ρ and k_z generally depends on ω , and $\chi^+(\rho, \phi, z, t)$ is the analytic signal. By comparison with Eq. (2), it is clear that Eq. (4) for $n = 1$ represents the inverse Fourier transform of E_z ; once the aperture field in Eq. (3) is enforced over the aperture, a non-diffractive pulse carrying an orbital angular momentum of order $n = 1$ is generated within the non-diffractive range.

III. NUMERICAL RESULTS

In Fig. 2, the amplitude and phase of a monochromatic non-diffracting field evaluated for $f_0 = 12.5$ GHz and $\rho_{\text{ap}} = 25$ cm are presented. The phase azimuthal dependence is clearly visible and the singularity for $z = 0$ of

the amplitude distribution is in agreement with Eq. (1). In Fig. 3, three time instants representing the spatial distribution on the reference plane (see Fig. 1) of the intensity of the twisted pulse generated for $\Delta\omega = 0.2\omega_0$ are presented. The peculiar rotating behavior is clearly visible.

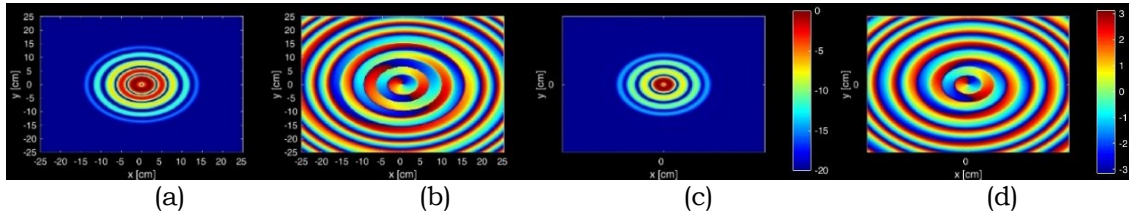


FIG. 2 – Amplitude and phase distribution of the near field radiated over different transverse planes: (a) amplitude $d=28$ cm, (b) phase $d=28$ cm, (c) amplitude $d=32$ cm, (d) phase $d=32$ cm.

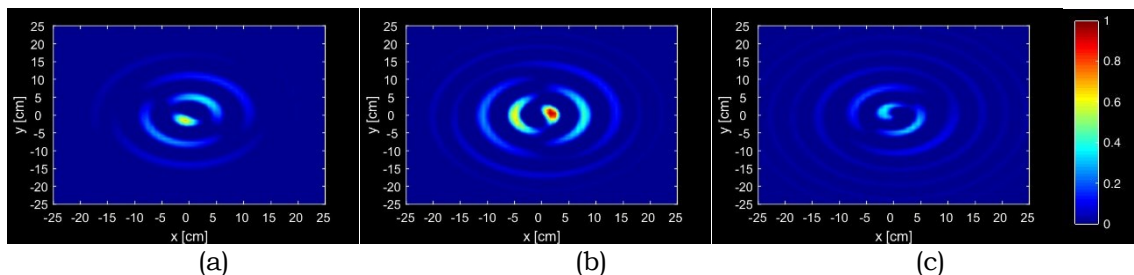


FIG. 3 – Time screenshots of the twisted electromagnetic pulse observed on the reference plane (see Fig. 1): (a) $t_1 = 0.85$ ns, (b) $t_2 = 1.06$ ns, (c) $t_3 = 1.27$ ns.

IV. CONCLUSION

The generation of a monochromatic higher-order Bessel beam with an azimuthal phase variation has been presented in this paper in order to investigate the possibility of generating twisted electromagnetic limited-diffraction pulses. Numerical results have shown that, with the frequency superposition of such fields over a 20% fractional bandwidth, it is possible to generate twisted pulses showing limited spatio-temporal broadening along the propagating axis. The proposed solution may be of interest for near-field applications exploiting pulses carrying OAM.

REFERENCES

- [1] H. E. Hernandez-Figueroa, M. Zamboni-Rached, and E. Recami, “Non-diffracting Waves,” John Wiley & Sons, 2013.
- [2] M. Ornigotti, C. Conti, and A. Szameit, “Effect of orbital angular momentum on non-diffracting ultrashort optical pulses,” *Phys. Rev. Lett.*, vol. 115, 100401-5, 2015.
- [3] M. Albani, S. C. Pavone, M. Casaletti, and M. Ettore, “Generation of non-diffractive Bessel beams by inward cylindrical traveling wave aperture distributions,” *Opt. Express*, vol. 22, no. 15, pp. 18354–18364, 2014.
- [4] R. F. Harrington, “Time-harmonic Electromagnetic Fields,” Wiley, 1961.

"BLIND" FIELD SEPARATION OF 2D FAR ZONE DATA

G. Leone, A. Natale

Department of Industrial and Information Engineering
Second University of Naples
via Roma 29, Aversa, Italy
giovanni.leone@unina2.it

Abstract

Source radiation or target scattering can be badly affected by parasite nearby objects. An algorithm for the extraction of the individual contributions is introduced by founding on an appropriate field representation. The expansion coefficients can be found by solving an over determined system of linear equations. The source separation plays an important role in ensuring to obtain a well-conditioned problem. Numerical results for plane wave scattering confirm the feasibility of the approach.

Index Terms—Linear inverse problem, Parasite elements.

I. INTRODUCTION

Source radiation or target scattering can be affected by the presence of a nearby parasite object contributing to the total field. For instance in antenna testing a secondary source or a nearby passive scatterer can contaminate the collected data and make it impossible to reconstruct the antenna pattern [1]. A similar problem arise in microwave imaging when a parasite object affects the field scattered by a target of interest in a complicated way [2].

With reference to a simplified 2D scattering geometry composed of two Perfectly Electric Conducting cylinders, we show that, under some hypothesis about the geometry of the scattering scenario, it is possible to separate the field scattered by each object from the total scattered field. Founding on an appropriate representation of the scattered field [3], a linear inverse problem is set up and solved numerically.

II. THE PROBLEM

For the sake of illustration the scattering scenario is composed of two PEC cylinder of circular cross section, whose centers are at O_i and radii are ρ_i $i=1,2$. The centers are separated by a distance d each other (Fig. 1). Under TM_z plane wave incidence, be E_t^0 the available far zone total field within the reference system with origin O (which is assumed midway between O_1 and O_2) and E_t^j the unknown fields scattered in far zone by the i -th (subscript) object represented in the reference system with center at the j -th (superscript) point. Because of the problem

geometry all fields are represented under the scalar cylindrical wave expansion, consisting essentially in a Fourier series expansion in far zone. As well known, because of the analytical properties of radiated fields, the highest significant field harmonic is provided by the order nearest to $\beta\rho_{max}$ where ρ_{max} is the radius of the minimum circle enclosing the scatterer and β is the free space wavenumber. Therefore each scattered field can be well approximated within an appropriate finite dimension space.

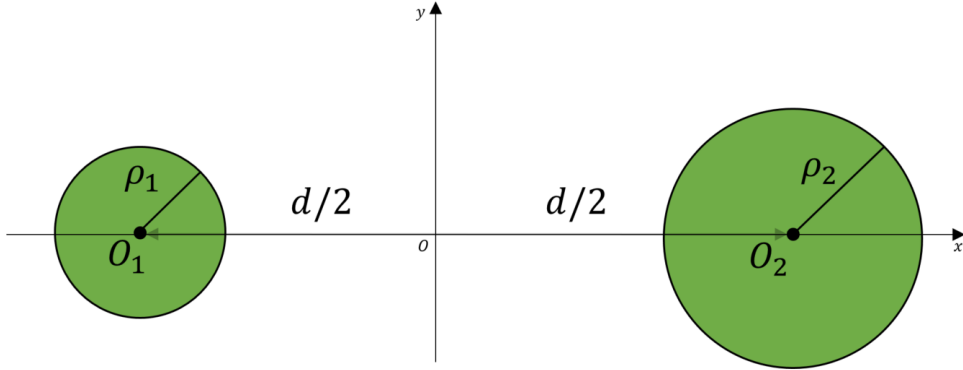


FIG. 1—The relevant geometry.

Let us point out that the number of relevant harmonics depends on the choice of the reference system origin. This gives rise to redundancy in the field representation for a generic choice since the actual minimum number of independent harmonics is provided when the origin lies at the center of the object in correspondence of the minimum radius. However this redundancy can be exploited to identify different contributions to the total field and possibly separate the one of an individual object.

III. THE APPROACH

Let us define as $\{a_n, |n| \leq N\}$, $\{b_m, |m| \leq M\}$ and $\{c_l, |l| \leq L\}$ the expansion coefficients of E_t^0 , E_t^1 and E_t^2 , respectively, where $N \cong \lceil \beta(d/2 + \max(\rho_1, \rho_2)) \rceil$, $M \cong \lceil \beta\rho_1 \rceil$ and $L \cong \lceil \beta\rho_2 \rceil$ ($\lceil \cdot \rceil$ stands for the nearest integer operator). In principle each a_n coefficients depends in an intricate way on all the b_m and c_l coefficients.

As a first step the total field is recast under a reference system with a different origin, say O_1 , which can be accomplished by a simple multiplication for a phase factor. Be E_t^1 the new far zone total field. It is expressed always under a Fourier series with $\{a'_i, |i| \leq N'\}$ coefficients, where $N' \cong \lceil \beta(d + \rho_2) \rceil$ is the maximum order of the corresponding harmonic. Note that, while the first M coefficients depend on both objects, the remaining $N'-M$, in turn, depend only on the second object.

So the problem arise about whether and how to extract the field scattered by the second object from the latter ones.

The second step concerns the expansion of E_2^2 under the same reference system with origin in O_1 . This gives rise to the field E_2^1 approximated by the $\{c'_k, |k| \leq N'\}$ harmonics. However the actual independent pieces of information are provided by the c_l coefficients which can be explicitly connected to the c'_k 's by a linear operator, i.e. a matrix \mathbf{T} whose terms are $\{t_{kl} = j^{k-l} J_{k-l}(\beta d)\}$, where $J_n(\cdot)$ is the Bessel function of first kind and order n .

We are now in the position to observe that since $a'_i = c'_i, M < |i| \leq N'$, a linear relationship \mathbf{L} can be established between the $N'-M$ higher Fourier coefficients of E_1^1 and the L ones of E_2^2 as

$$\underline{a}' = \mathbf{L}\underline{c} \quad (1)$$

where \mathbf{L} is represented as a $2(N'-M) \times 2L$ rectangular matrix with the same elements as \mathbf{T} , to be inverted by a standard regularized approach, as for instance the Singular Value Decomposition algorithm.

Note that the only compatibility condition is not enough to guarantee to achieve the solution of the problem. In fact the actual rank of the over determined system of linear equations (1) depends on the distance d and must be investigated numerically. This can be done in advance for an assigned separation d between the scatterers and assigned maximum dimensions ρ_i by examining the number of significant singular values of \mathbf{L} : if it is very close to L the problem admits a solution.

It is difficult to establish a priori conditions to achieve this result. As a rule of thumb the larger the scatterers, the larger the distance between them is required to achieve accurate separation between the fields of the scatterers. Fig. 3 depicts the behavior of the condition number.

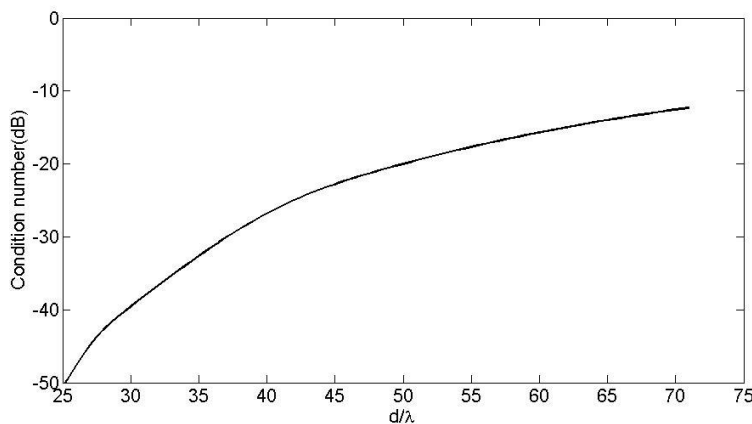


FIG. 2—Condition number of \mathbf{L} ($\rho_1=5\lambda$ and $\rho_2=7\lambda$).

As a test example we consider the scattering by two PEC cylinders with circular cross section, with $\rho_1=5\lambda$ and $\rho_2=7\lambda$, separated by $d=50\lambda$ as in fig.1 and illuminated by a plane wave impinging from the negative x axis. Fig 3 shows the total scattered field, the actual and the reconstructed ones.

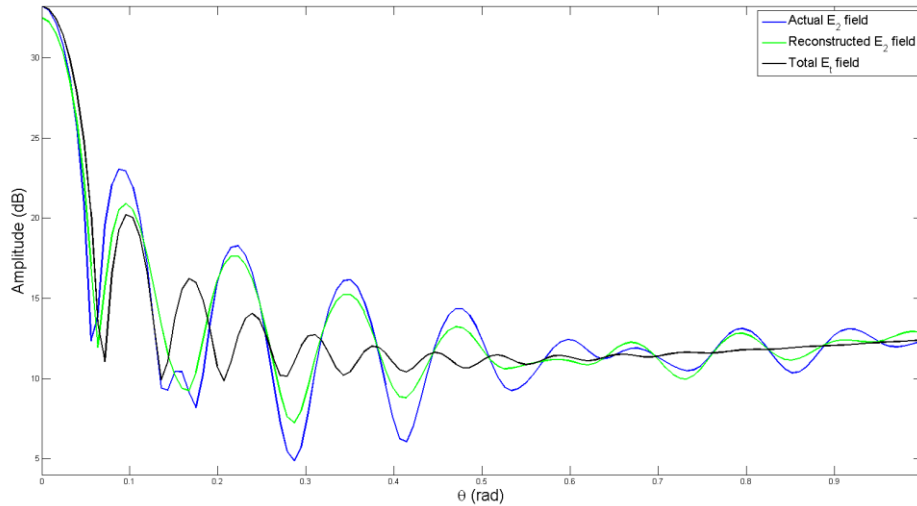


FIG. 3—Amplitude of the total field, the actual and reconstructed fields scattered by the second object.

IV. CONCLUSION

The possibility of separating the field scattered by two objects into individual contributions is introduced and its feasibility related to the geometrical parameters of the scenario. The approach can be applied also to generic scattering objects and extended to account for near zone data. To establish the solution of the separation problem is a preliminary task in order to deal with the related inverse source problem and discuss correctly the resolution issues.

REFERENCES

- [1] R.J. Pogorzelski, "Analysis and Demonstration of Two Spherical Mode Expansion Resolution Algorithms", *IEEE Transactions on Antennas and Propagation*, vol 63(3), pp. 1098-1105, March 2015.
- [2] A. Natale, M. A. Maisto, R. Solimene, R. Pierri, "Separating the Contributions of Two Sources from Their Radiated Fields Over a Single Domain, *36th Progress In Electromagnetics Research Symposium*, July 2015, Prague, Czech Republic.
- [3] T. Laitinen, S. Pivnenko, "Separation of radiation from two sources from their known radiated sum field", *2011 XXXth URSI General Assembly and Scientific Symposium*, Aug 2011, Istanbul, Turkey.

Inhomogeneous waves generation for the electromagnetic deep penetration into lossy media

Vincenzo Pascale¹, Fabio Pelorossi¹, Nicola Tedeschi¹ and Fabrizio Frezza¹

¹Department of Information Engineering, Electronics and Telecommunications, Sapienza University of Rome, via Eudossiana 18, 00184 Roma, Italy
e-mail: vincenzo.pascale@uniroma1.it, fabio.pelorossi@uniroma1.it, nicola.tedeschi@uniroma1.it, fabrizio.frezza@uniroma1.it

Abstract— The generation of inhomogeneous electromagnetic waves in a lossless medium is generally associated to leaky-wave antennas. In the present paper it is shown how such waves can be also easily generated by the transmission of a homogeneous wave through a dissipative dielectric layer. In particular, a dissipative triangular prism in the free space, whose first interface is fed by a homogeneous wave can be employed to generate an inhomogeneous wave emerging at the second interface. The phase and attenuation vectors obtained are evaluated against the geometry and the material of the prism. The results illustrate a novel approach in generating inhomogeneous waves in lossless media which finds applications for the deep penetration of lossy materials.

I. INTRODUCTION

Inhomogeneous waves are typical solutions of the Maxwell equations at the interface between two semi-infinite media [1], [2]. Inhomogeneous waves can be generated in lossless media by means of appropriate radiative structures, in which the field shows a complex wave number. These field solutions are also known as leaky waves. In fact, their generation is generally made possible by introducing some leakage effect in the travelling-wave path, like opening the guiding structure, creating the so-called leaky-wave antennas. Such antennas are traveling-wave antennas: designed in order to make a radiating mode (leaky mode) the dominant one [3]. Nevertheless, in recent studies, it has been pointed out that an inhomogeneous wave can also be obtained by illuminating with a homogeneous wave a dissipative dielectric [4]. Let us consider a lossy two-dimensional triangular prism immersed in the free space as a dissipative dielectric with two non-parallel interfaces, forming an angle χ , as shown in Fig. 1. We consider a quasi-plane wave incident at an angle ξ_{1i} on the left side (vertical side) of the prism. We suppose that, using a geometrical-optics approximation, given the characteristics of a quasi-plane wave, the wave does not interact with the prism's wedges. In other words, a finite beam is considered impinging on the prism. The described system is considered to work at X-band (10.6 GHz) aiming at reducing the dimensions for the prism and at investigating the viability of generating an inhomogeneous wave for the deep penetration through lossy media at such frequencies, as never done before in the literature.

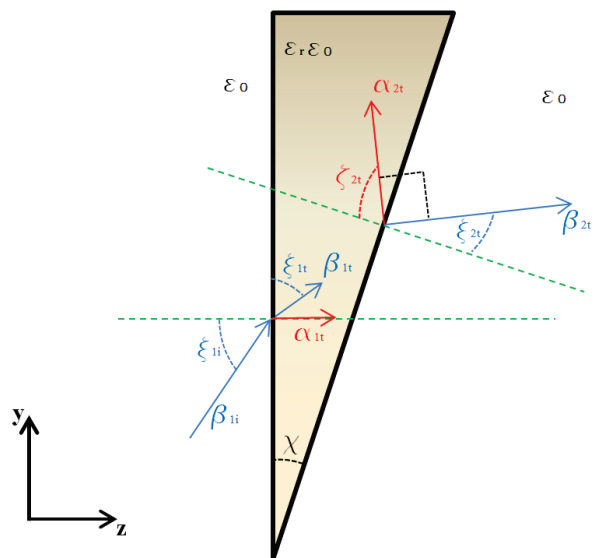


Fig. 1. Geometry of the problem.

II. THEORETICAL MODEL

The reflected and transmitted waves in the system of Fig. 1 can be easily computed at both interfaces with well-known relations [5]. While the incident vector has a null attenuation vector (lossless medium), the wave transmitted after each interface has both non-null attenuation (α) and phase (β) vectors. At the first interface (vertical side) of the prism, the phase vector forms an angle ξ_{1i} with respect to the z -axis, while the attenuation vector must be perpendicular to the interface. The wave impinges then on the second interface (oblique side) of the prism with an angle of the phase vector equal to $(\xi_{1i} + \chi)$ with respect to the normal direction to the interface. The attenuation vector impinges on the second interface with an angle χ with respect to the normal direction to the interface. The reflected and transmitted waves at the second interface can be computed using the results presented in [6]–[8]. In particular, the transmitted wave results as an inhomogeneous wave. In fact, in a lossless medium (the free

space), the attenuation vector and the phase vector computed after the second interface result orthogonal, meaning that the equi-phase planes and the equi-amplitude planes are perpendicular to each other.

If we consider the case of a prism with the real part of the relative permittivity $\varepsilon' = 4.3$ and the loss tangent $\text{tg}\delta = 0.025$ (FR4 dielectric material), we can obtain the theoretical prediction of the properties of the transmitted wave: both magnitudes and direction (i.e. angles) of the phase and attenuation vectors. Since the prism is dissipative, we can suppose that the wave is strongly attenuated as far as reflections are concerned. Therefore, the contribution to the transmitted wave (after the second interface) is only given by from the direct wave and any reflection is neglected.

III. RESULTS AND CONSIDERATIONS FROM THE THEORETICAL MODEL

Varying the four characteristic parameters of the system (χ , ξ_{1i} , ε' and $\text{tg}\delta$), relevant numerical results can be obtained. In particular, it will be highlighted how the angle of incidence ξ_{1i} appears paramount in defining the characteristics of the system. For this reason, all the figures reported depend on such quantity. In Figs. 2 and 3 the magnitudes of the attenuation and phase vectors are shown, respectively, as functions of the angle of incidence and of the angle of the prism considering a FR4 dielectric. A step-behaviour of the magnitudes can be noted. The vectors are approximately constant and equal to zero and k_0 , respectively, for a wide spectrum of the incident angles but the magnitude of both starts to increase for values larger than a specific angle. This behaviour is of extreme interest: in fact, as it has been pointed out in the literature [7], inhomogeneous waves with attenuation and phase components higher than a defined thresholds are able to deeply penetrate in lossy materials and they can be of interest in several applications. Fig. 2 pins some critical angles corresponding to each defined case of χ . We have to emphasize that the magnitude of the attenuation vector is never zero before the critical angle, but it is considerably smaller than one, as typical for inhomogeneous waves generated by leaky-wave antennas. In this regard, the plot of the ratio β/α (see Fig. 4) is very handy. Furthermore, it gives a comprehensive indication of the step behaviour individuated by the present analysis, with respect to the characteristic parameters. Fig. 4 shows a strong dependence of the ratio β/α and of the critical angle on the angle of the prism. In particular, increasing the angle of the triangular prism, reduces the possibility of having a high β (necessary for the deep penetration) and the range of incident angles for which the transmitted wave is a usable wave according to Figs. 5 and 6. In these figures, the transmitted angles of the attenuation and phase vectors are, respectively, shown as functions of the incident angle and the prism angle. An analogous step behaviour is noted. The attenuation vector's angle grows with

the initial incident angle and reaches a direction almost perpendicular to the oblique interface starting from the critical angle. Similarly, the phase vector becomes quasi-parallel to the oblique interface starting from a critical initial angle of incidence. In other words, after a critical angle the transmitted wave behaves like a surface wave.

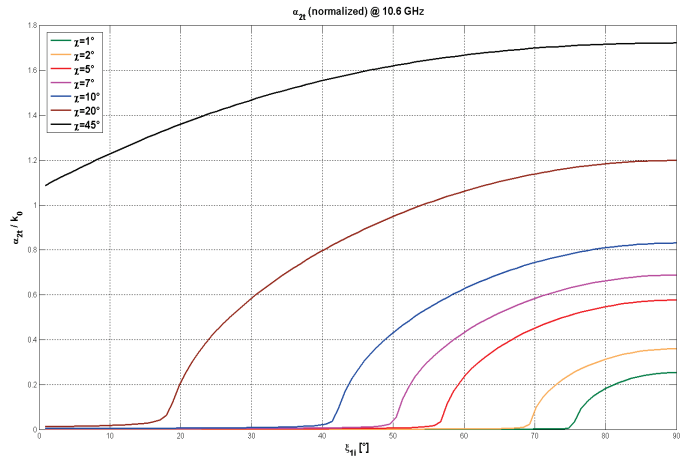


Fig. 2. α_{2t} as a function of ξ_{1i} for some cases of χ .

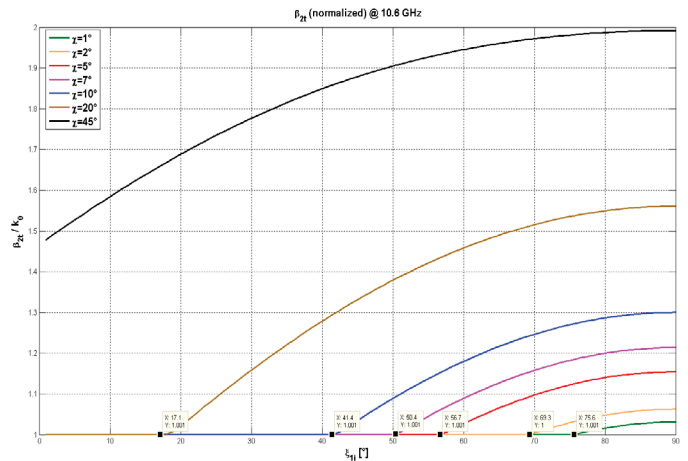


Fig. 3. β_{2t} as a function of ξ_{1i} for some cases of χ .

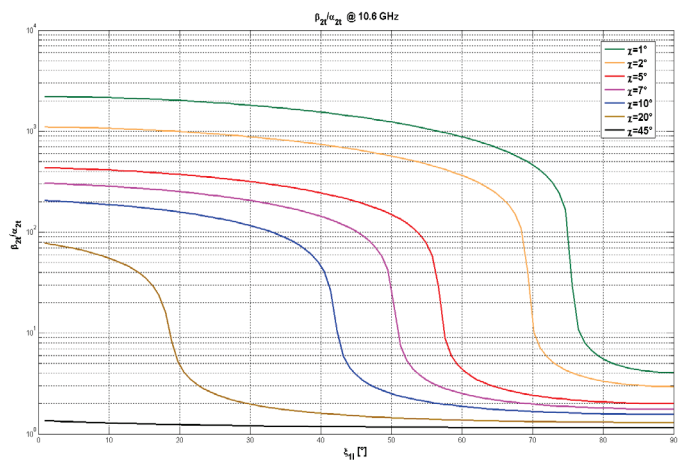


Fig. 4. β_{2t}/α_{2t} as a function of ξ_{1i} for some cases of χ .

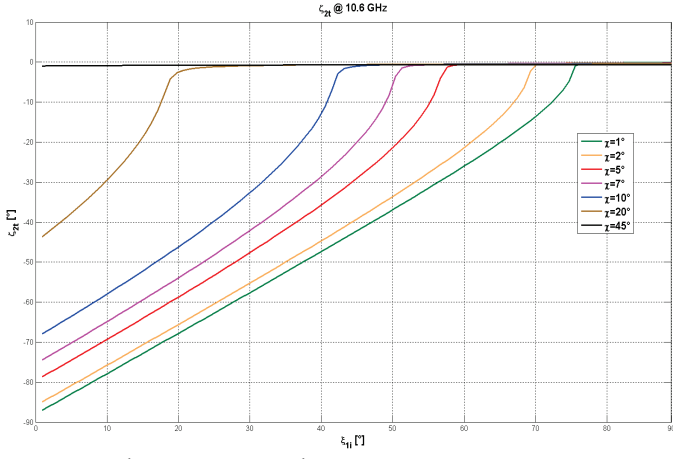


Fig. 5. ξ_{2t} as a function of ξ_{1t} for some cases of χ .

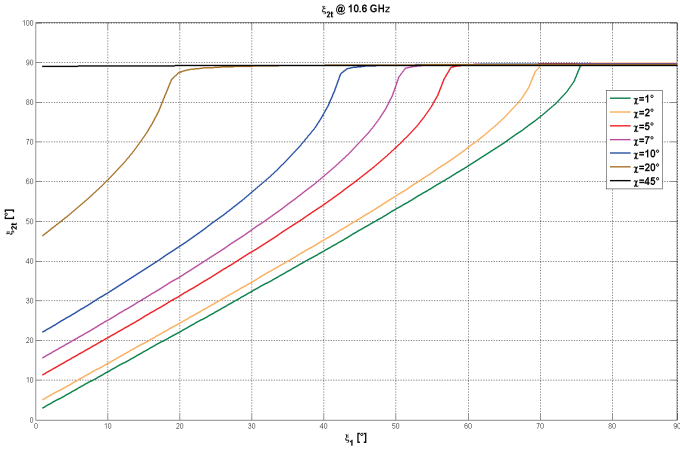


Fig. 6. ξ_{2t} as a function of ξ_{1t} for some cases of χ .

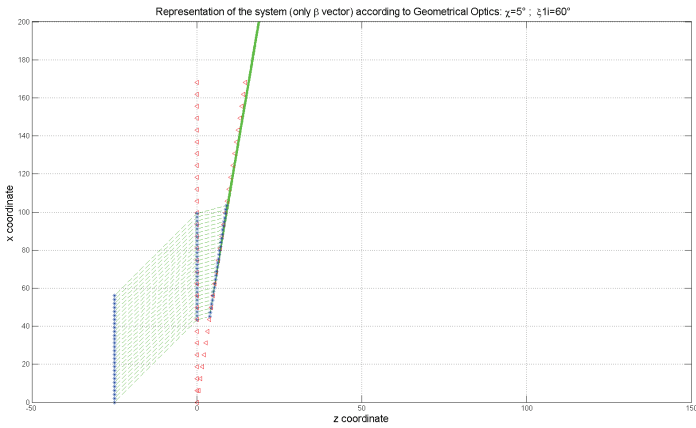


Fig. 7. Ray tracing representation of the surface wave generation condition.

Fig. 7 depicts this condition assuming a pure geometrical-optics approximation of the system and confirms that the wave is not exactly parallel to the prism side, then it is not a bounded wave, but it is able to propagate in the free space. As expected, the phase vector of the transmitted wave is in general deflected from the initial direction, being this deflection higher with larger prism's angles. Ultimately, the material of the prism is varied as well. Figs. 8 and 9 complete

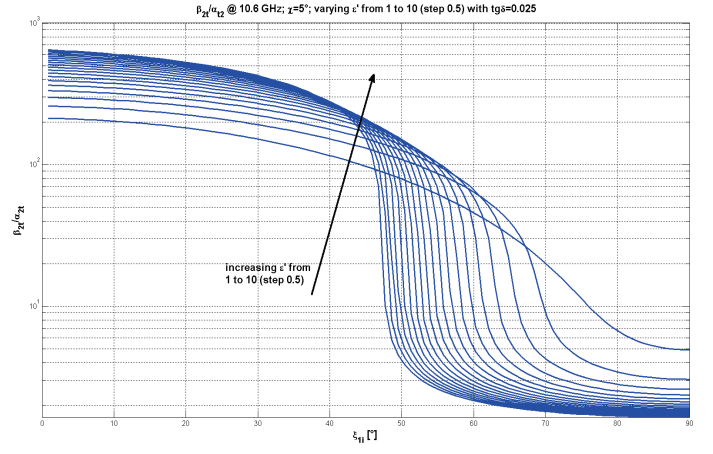


Fig. 8. β_{2t}/α_{2t} as a function of ξ_{1t} and ε' .

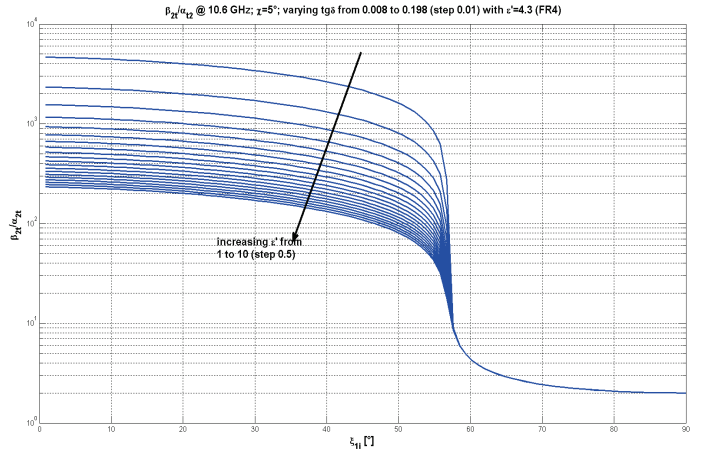


Fig. 9. β_{2t}/α_{2t} as a function of ξ_{1t} and $\text{tg}\delta$.

the analysis showing the variation of the ratio β/α depending on the relative permittivity and on the loss tangent, respectively, with a $\chi = 5^\circ$. An increase and saturation of the ratio β/α with the increase of ε' and a marked dependence of the critical angle on ε' can be noted. On the contrary, the increase of $\text{tg}\delta$ causes a decrease of the ratio β/α , while the critical-angle results not affected.

IV. ELECTROMAGNETIC MODEL

We considered a rectangular tapered (WR90) horn antenna working at 10.6 GHz. The horn is placed at a distance from the prism, L_m , which allows to consider the radiated beam as a finite-section quasi-plane wave at the prism interface. We considered a prism with squared transverse section, $\chi = 5^\circ$ and made of FR4 material. The vertical side is 556.9 mm long, computed as the horn HPBW footprint at a distance L_m plus a margin evaluated as $\text{FFd}/2$, being FFd the far field distance of the horn antenna, equal to 1013 mm at the working frequency. The single horn and the system horn+prism have been simulated with the commercial software CST.

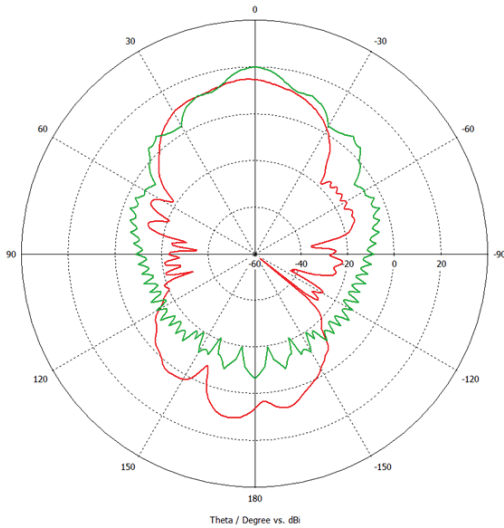


Fig. 10. CST pattern single tapered horn (green) and system horn+prism (red).

The radiation patterns depicted in Fig. 10, green-lined for the single horn, red-lined for the system, show the impact of the dielectric prism on the radiating characteristics of the source used for the boresight case. As expected, the dielectric prism substantially impacts on the radiating performances. In Table 1, the cases of interest, where the impinging angle ξ_{li} is non-null, are added. Figs. 11 and 12 show the electric field propagating in the y - z plane for the single horn and the system with $\xi_{li}=5^\circ$, respectively.

Table 1: Main radiated characteristics of the single horn compared to the horn+prism system for various cases of incidence

Target	Single Horn	Horn+prism ($\xi_{li} 0^\circ$)	Horn+prism ($\xi_{li} 5^\circ$)	Horn+prism ($\xi_{li} 45^\circ$)	Horn+prism ($\xi_{li} 65^\circ$)
Main lobe magnitude	20.1 dB	14.8 dB	14.4 dB	15.2 dB	17.3 dB
Main lobe direction	0.0°	3°	6°	57°	88°
HPBW	14.3°	29.2°	37.8°	31.1°	5.6°

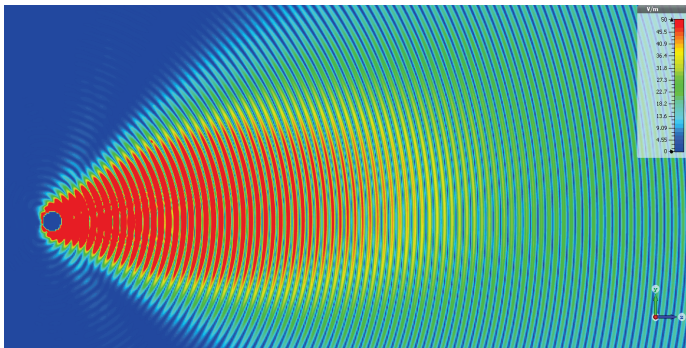


Fig. 11. Electric field along the propagation y - z plane of the single tapered horn modeled for angle $\xi_{li}=5^\circ$ with respect to the z -axis.

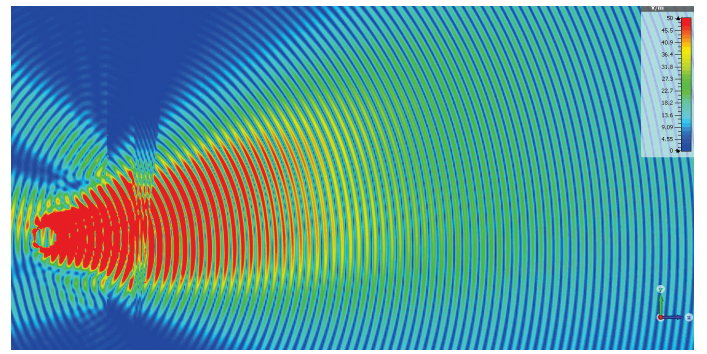


Fig. 12. Electric field along the propagation y - z plane with dielectric FR4 prism and incidence $\xi_{li}=5^\circ$.

V. CONCLUSION

In this paper we considered a novel approach for inhomogeneous waves generation in lossless media based on the illumination of a dissipative triangular prism by a homogeneous wave. We discussed the behaviour of the magnitudes and angles of the transmitted attenuation and phase vectors. The analyses showed a dual behaviour defined by a critical incident angle. Below such incident angle, the inhomogeneous wave which emerges from the prism is not a surface wave and presents magnitudes typical of the leaky waves; therefore, usable for the deep penetration of lossy media. Moreover, the magnitudes and the angles of this inhomogeneous wave can be tuned by the choice of the prism's geometry (angle of aperture) and material. The incident critical angle is defined as well by the prism's properties. In particular, it is primarily dependant on the angle of aperture of the prism and secondarily on its relative permittivity, while independent of the loss tangent of the material. Finally, we considered the electromagnetic simulations with a rectangular tapered horn antenna illuminating a lossy prism of FR4 material, quantifying the insertion losses caused by the dielectric prism on a realistic electromagnetic source, so to pave the floor for more in depth analyses of the deep penetrating potentiality of the system presented.

REFERENCES

- [1] T. Tamir, "Inhomogeneous waves types at planar structures: III. Leaky waves," *Optik*, Vol. 38, No. 3, pp. 269-297, 1973.
- [2] F. Frezza and N. Tedeschi, "Electromagnetic inhomogeneous waves at planar boundaries," *J. Opt. Soc. Am. A*, vol. 32, no. 8, pp. 1485-1501, 2015.
- [3] D.R. Jackson and A.A. Oliner, "Leaky-Wave Antennas", Ch. 7, *Modern Antenna Handbook*, Edited by C.A. Balanis, Wiley, 2008.
- [4] N. Tedeschi and F. Frezza, "An analysis of the inhomogeneous wave interaction with plane interfaces," in *Proc. URSI GASS'14*, 2014, paper BP1.25, p. 109.
- [5] J.A. Stratton, *Electromagnetic Theory*, McGraw-Hill, New York, 1941.
- [6] J.E. Roy, "New results for the effective propagation constants of nonuniform plane waves at the planar interface of two lossy media," *IEEE Trans. Antennas Propag.*, vol. 51, pp. 1206-1215, 2003.
- [7] F. Frezza and N. Tedeschi, "Deeply penetrating waves in lossy media" *Opt. Lett.* vol. 37, pp. 2616-2618, 2012.
- [8] F. Frezza and N. Tedeschi, "On the electromagnetic power transmission between two lossy media: discussion," *J. Opt. Soc. Am. A*, vol. 29, pp. 2281-2288, 2012.

ITERATED VIRTUAL EXPERIMENTS AND COMPRESSIVE SENSING FOR QUANTITATIVE INVERSE SCATTERING PROBLEMS

Roberta Palmeri⁽¹⁾, Martina T. Bevacqua⁽¹⁾, Lorenzo Crocco⁽²⁾, Tommaso Isernia^(1,2) and Loreto Di Donato⁽³⁾

⁽¹⁾ DIIES, Univ. Mediterranea di Reggio Calabria, Italy,
(martina.bevacqua, tommaso.isernia, roberta.palmeri)@unirc.it

⁽²⁾ CNR-IREA, Naples, Italy, crocco.l@irea.cnr.it

⁽³⁾ DIEEI, Univ. di Catania, Italy, loreto.didonato@dieei.unict.it

Abstract

In this contribution the solution of non linear inverse scattering problems is tackled by means of a novel iterative approach based on the emerging virtual scattering experiments' paradigm. The proposed method is also enhanced by using the compressive sensing (CS) paradigm, up to now adopted only in linear inverse scattering procedures.

Index Terms – Compressive Sensing, Distorted Born Iterative Method, Linear Sampling Method, Non-linear Inverse Scattering, Virtual Experiments.

I. INTRODUCTION

In inverse scattering problems one amounts to retrieve the location, shape and electromagnetic properties of unknown targets illuminated by means of known incident fields. Although they are relevant for a large number of imaging applications, the development of effective and reliable inversion procedures still represents an open issue, due to the non-linearity and ill-posedness of the problem [1,2]. As a countermeasure to non-linearity, the Born Approximation (BA) [3] could be very attractive, although it is safely applicable only in the weak scattering regime. A possible way to overcome these limitations is represented by the Distorted Born Iterative Method (DBIM) [4], which relies on iterated linear approximations of the scattering equations.

In this paper, in the same spirit of DBIM, an iterative method is proposed, wherein at each iteration the problem is linearized by means of a recently introduced field approximation based on the emerging framework of the virtual scattering experiments (VE) [5-8]. The resulting *Distorted Iterated Virtual Experiments* (DIVE) scheme is intrinsically different from DBIM and it is expected to outperform this latter because of the wider range of validity of the intermediate linearizations [6]. Moreover, as countermeasure to ill-posedness, the relevant paradigm of Compressive Sensing (CS) is exploited in order to obtain nearly optimal reconstruction of extended but piecewise homogeneous scatterers.

II. STATEMENT OF THE PROBLEM AND VIRTUAL EXPERIMENTS

Let us consider the canonical 2D TM scalar problem and an unknown nonmagnetic object embedded in a nonmagnetic homogeneous medium with complex permittivity ε_b . Let the unknown object with support Ω and complex permittivity ε_s . The scatterer is probed by means of some antennas located in the far-field of Ω on a closed curve Γ and the measurements of the resulting scattered fields are taken on Γ by adopting a multiview-multistatic configuration.

The equations describing the relevant scattering problem are:

$$E_s(\mathbf{r}_m, \mathbf{r}_t) = k^2 \int_{\Omega} G_b(\mathbf{r}_m, \mathbf{r}') \chi(\mathbf{r}') E(\mathbf{r}', \mathbf{r}_t) d\mathbf{r}' = \mathcal{A}_e[\chi E], \quad \mathbf{r}_t, \mathbf{r}_m \in \Gamma \quad (1)$$

$$E(\mathbf{r}, \mathbf{r}_t) = E_i(\mathbf{r}, \mathbf{r}_t) + k^2 \int_{\Omega} G_b(\mathbf{r}, \mathbf{r}') \chi(\mathbf{r}') E(\mathbf{r}', \mathbf{r}_t) d\mathbf{r}' = E_i + \mathcal{A}_i[\chi E], \quad \mathbf{r} \in \Omega, \mathbf{r}_t \in \Gamma \quad (2)$$

where E_i , E_s and E are the incident, scattered and total field, respectively, $k = \omega\sqrt{\mu_b\varepsilon_b}$ is the wavenumber in the host medium, $G_b(\mathbf{r}, \mathbf{r}')$ is the Green's function pertaining to the background and \mathcal{A}_e and \mathcal{A}_i are a short notation for the integral radiation operators.

In the inverse scattering problem the aim is to estimate the unknown contrast function χ from measured scattered fields E_s . Due to the properties of the involved operator in (1), the problem is ill-posed [2] and, as the total field also depends on the unknown contrast, it is also non-linear. In the adopted formulation, multiple experiments have been considered to increase as much as possible the amount of independent information [8] and improve the performances of the inversion strategy. Once collected, this amount of independent information can be re-organized in a different way by taking advantage from the linearity of the scattering phenomenon. Starting from this simple linear 'transformation' of the scattering data, one can re-arrange the original experiments into virtual experiments (VE) [5-7] without requiring additional measurements.

III. DISTORTED ITERATED VIRTUAL EXPERIMENTS

The idea of transforming the original experiments into VE opens the way to a new iterative procedure in which the nonlinear inverse problem is solved through successive linearizations, in the same spirit of DBIM. Since the VE are conveniently derived from a smart processing of the scattering data (rather than on a priori assumption), the DIVE approach reaches better and better performance with respect to DBIM. The procedure can be summarized in five steps.

1) *Initialization*: a first estimate χ^1 of the contrast function is achieved by using the VE based linear approximation introduced in [5]. Obviously,

other more favorable starting guesses can be considered with respect to the a priori information.

2) *Scenario update*: the forward scattering problem pertaining to χ^k , the background medium at the k^{th} iteration, is solved in order to update the total (background) field E_b^k and compute the anomalous field ΔE_s^k (that is the difference between E_s and the field scattered when $\chi = \chi^k$). Then, the Green's function G_b^k with respect to χ^k is numerically computed by exploiting the reciprocity theorem.

3) *Convergence control*: a stopping rule is considered by defining the relative residual error (RRE) at k^{th} iteration as $RRE^k = \|\Delta E_s^k\|_2 / \|E_s\|_2$. If RRE^k is less than a set threshold (10^{-5}) or is larger than the RRE^{k-1} , the procedure terminates. Otherwise, the iterative procedure continues.

4) *VE update*: in order to identify and localize possible perturbation and corrections $\Delta\chi^k$ with respect to the current reference scenario χ^k , we solve in each sampling point \mathbf{r}_s , the (distorted) linear sampling method (LSM) equation [9,10]:

$$\sum_{t=1}^N \Delta E_s^k(\mathbf{r}_t, \mathbf{r}_m) \alpha^k(\mathbf{r}_t, \mathbf{r}_s) = G_b^k(\mathbf{r}_m, \mathbf{r}_s) \quad (3)$$

wherein $\alpha^k(\mathbf{r}_t, \mathbf{r}_s)$ are the sought auxiliary excitations coefficients which allow to define the support indicator of the perturbation and to select on it some *pivots points* \mathbf{r}_p , in order to build the new VE [5].

5) *Contrast update via linear inversion*: the relevant data equation (1) is applied to the case of partially known scenario and recast in terms of VE as:

$$\Delta E_s^k(\mathbf{r}_m, \mathbf{r}_p) = \int_{\Omega} G_b^k(\mathbf{r}_m, \mathbf{r}') \Delta\chi^k(\mathbf{r}') \mathcal{E}^k(\mathbf{r}', \mathbf{r}_p) d\mathbf{r}' \quad (4)$$

where ΔE_s^k and \mathcal{E}^k are the anomalous and total fields arising in the VE, respectively. By considering the physical meaning of (regularized) eq.(3) [9,10], the unknown total field in eq.(4) can be approximated by:

$$\mathcal{E}^k(\mathbf{r}, \mathbf{r}_p) = \mathcal{E}_b^k(\mathbf{r}, \mathbf{r}_p) + LP\{G_b^k(\mathbf{r}, \mathbf{r}_p)\} \quad (5)$$

where \mathcal{E}_b^k is the virtual background field obtained by recombining E_b^k through the coefficients α^k , and the second addendum is a low pass filtered version of G_b^k . Note that approximation (5), unlike the DBA, is a "scatterer aware" approximation as it takes into account the contribution of the anomaly through \mathcal{E}_b^k at each step.

In order to solve the linearized distorted problem (4), we use the CS theory as regularization technique and suppose to deal with extended

targets exhibiting piecewise constant dielectric profiles, which can be conveniently represented in terms of step functions [11]. Finally, a new profile is generated by adding the reconstruction to the current reference scenario, that is $\chi^{k+1} = \chi^k + \Delta\chi^k$.

6) *Return to step 2.* The iteration continues until the stopping criterion is fulfilled.

IV. CONCLUSION

A new iterative inversion scheme is introduced, in which the inverse scattering problem is solved through successive linearizations based on the virtual experiments framework. The new proposed method is able to outperform the usual DBIM and allows to exploit the Compressive Sensing paradigms for the solution of non linear inverse problem.

Further details on the approach together with numerical examples (with numerical and experimental data) will be presented at the Conference.

REFERENCES

- [1] D. Colton and R. Kress. "Inverse Acoustic and Electromagnetic Scattering Theory", Springer-Verlag, Berlin, Germany, 1998.
- [2] M. Bertero and P. Boccacci. "Introduction to Inverse Problems in Imaging", Institute of Physics, Bristol, UK, 1998.
- [3] A. J. Devaney, "Geophysical diffraction tomography," IEEE Trans. Geosci. Remote Sensing, vol. GE-22, no. 1, pp. 3–13, 1984.
- [4] W. C. Chew and Y. M. Wang, "Reconstruction of two-dimensional permittivity distribution using the distorted Born iterative method," IEEE Trans. Med. Imaging, vol. 9, no. 2, pp. 218–225, 1990.
- [5] L. Crocco, I. Catapano, L. Di Donato and T. Isernia, "The linear sampling method as a way to quantitative inverse scattering", IEEE Trans. Antennas Propag., vol. 60, no. 4, pp. 1844-1853, Apr. 2012.
- [6] L. Di Donato, R. Palmeri, G. Sorbello, T. Isernia, and L. Crocco, "Assessing the capabilities of a new linear inversion method for quantitative microwave imaging". Int. J. Antennas Propag., vol. 2015, no. ID:403760, 2015.
- [7] L. Di Donato, M. Bevacqua, L. Crocco, and T. Isernia, "Inverse Scattering via Virtual Experiments and Contrast Source Regularization", IEEE Trans. Antennas Propag., vol. 63, no. 4, pp. 1669-1677, 2015.
- [8] O. M. Bucci and T. Isernia, "Electromagnetic inverse scattering: Retrievable information and measurement strategies", Radio Sci., vol. 32, no. 6, pp. 2123–2138, 1997.
- [9] D. Colton, H. Haddar, and M. Piana, "The linear sampling method in inverse electromagnetic scattering theory," Inv. Probl., vol. 19, no. 6, pp. 105–137, 2003.
- [10] I. Catapano and L. Crocco, "An imaging method for concealed targets", IEEE Trans. Geosci. Remote Sens., vol. 47, no. 5, pp. 1301–1309, 2009.
- [11] M. Bevacqua, L. Crocco, L. Di Donato, and T. Isernia, "Microwave imaging of non-weak targets via compressive sensing and virtual experiments," IEEE Antennas Wireless Propag. Letters, vol. 14, pp. 1035–1038, 2015.

ELECTROMAGNETIC MODELING OF FORWARD SCATTER RADAR

M. T. Falconi and D. Comite

Department of Information Engineering, Electronics and
Telecommunications (DIET) - Sapienza University of Rome
Via Eudossiana 18, 00184, Rome, Italy
falconi@diet.uniroma1.it

Abstract

The forward scattering (FS) phenomenon is investigated in this work referring to a typical radar scenario where a metallic target crosses the baseline while is illuminated by a transmitting source. A straightforward electromagnetic (EM) analytical model is provided to predict the received signal both in near- and far-field conditions. The effect of different distances between target and receiving antenna are analyzed in terms of scattered and total EM fields. The results have been validated through an ad-hoc numerical implementation of a full-wave solution. Physical insight into the FS effect and restrictions on the applicability of the EM model are also discussed.

Index Terms – Forward Scatter Radar (FSR), Forward Scattering, Electromagnetic Modeling, Numerical Simulations.

I. INTRODUCTION

The Forward Scatter Radar (FSR) is a specific class of bistatic radars with the peculiar capability to enhance the detection in particular scenarios [1]. The radar cross section (RCS) enhancement is exploited by the forward scattering (FS) phenomenon occurring when the bistatic angle is close to the baseline, i.e., near 180° [1], [2]. From a physical viewpoint, such improvement is produced in the forward direction, due to the co-phase interference between the incident electromagnetic (EM) wave and the secondary wave re-irradiated by the target. The signal formation is different from the monostatic configuration and results from the direct and forward-scattered contributions. Furthermore, the FS signature is related to the electrical dimensions of the involved target along with the distance between the transmitting (Tx) and receiving (Rx) antennas [2], [3].

The FSRs are increasingly considered as a viable alternative to monostatic or bistatic radar systems, being able to improve the detection of low-signature targets in the presence of clutter interferences and also for applications to passive radar configurations [1],[2]. To profitably exploit such advantageous features, it is essential to properly detect the received signal and consequently achieve an optimal signal processing. Up to now, the FS signal has extensively studied in far-field conditions [2], but never removing this limiting hypothesis. To this aim, we introduce here an EM model of the forward scattering integrated in a flexible FSR geometry valid also in near-field conditions.

II. BACKGROUND FSR THEORY

The evaluation of the FS field is a standard diffraction problem. When an EM wave impinges on an object, following the physical theory of diffraction (PTD), the scattered (diffracted) field is generated by surface sources induced in the object by the incident wave. In the forward direction, if the target dimensions are larger than the operating wavelength, a shadow region exists due to scattered field that cancels the incident field. Beyond this zone, directly opposite the object, there is a forward region in which the fields add in phase, generally producing a strong radiation peak responsible to the enhanced RCS. The pattern of this forward radiation is similar to the scattered pattern of a metallic screen having the same silhouette of the object and identical incident field. The physical explanation of the phenomenon can be derived through the well-known Babinet's principle (BP): by applying the equivalence theorem when the target is replaced with the silhouette, the induced currents on the target must be equal to the surface current on an infinite plane. The restrictions underlying this EM approach are that, as said, the main target dimension must be larger than the wavelength, and also that the reciprocity theorem is valid only if the bistatic angle is near 180° or when the Rx and Tx are interchanged. Despite such restrictions, which are however reasonably satisfied for FSR applications, in the next section we exploit this theory [4] in a general EM model capable to predict the overall performance of FSR systems.

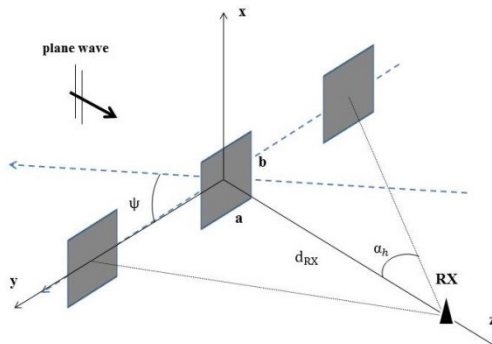


FIG. 1 – Simulated scenario for the analysis of the forward scatter radar.

III. FS GEOMETRY AND MODEL

The basic FSR geometry considered is sketched in Fig. 1, where the target is illuminated by a radiation source while crosses a baseline (BL). The moving target has an arbitrary linear trajectory in a plane (yz) described by a tilt angle (ψ) and a horizontal angle (α_h). The Tx and the Rx antennas look at each other along the BL (i.e., bistatic angle near to 180°) and, without the target, the received signal corresponds to the direct wave, while it is gradually reduced by the target shadow as the object reaches the central position ($\alpha_h = 0^\circ$). The complexity of the scattering problem can be reduced significantly as follows.

We locate the Tx in far-field region and consequently a plane wave illuminates a metallic target, which acts as a secondary source of radiation. Therefore, the target size (a rectangle of a and b dimensions along y and x , respectively, is considered here) and the Rx-distance (d_{RX}) become the essential geometrical parameters of the EM model. When the target is getting close to the Rx, or equivalently the target size increases for a fixed wavelength λ , the amplitude of the forward signal increases and the width decreases. The electric field of the incident plane wave is x -polarized (see Fig. 1): $E_x(z, w) = E_0 x_0 e^{+jkz}$, where E_0 is a complex value taking into account also the initial phase of the wave. By exploiting the BP for the forward electric-field component, we have [4]:

$$E_x^{RX}(r, w) = E_x(d_{RX}, w) - \frac{1}{2\pi} \iint_a^b E_x(z, w) \frac{e^{-jk|r-r'|}}{|r-r'|} \left(jk + \frac{1}{|r-r'|} \right) \frac{d_{RX}}{|r-r'|} dx' dy' \quad (1)$$

Using suitable approximations, after some algebra, we obtain a closed-form expression for the received field:

$$E_x^{RX}(r, w) \approx E_x(d_{RX}, w) - \frac{1}{4\pi} E_x(z, w) e^{-jk d_{RX}} \left(jk + \frac{1}{r} \right) \frac{d_{RX}^2}{r^2} [-C(P_1) + jS(P_1) + C(P_2) - jS(P_2)] [-C(Q_1) + jS(Q_1) + C(Q_2) - jS(Q_2)] \quad (2)$$

where C and S are the cosine and sine Fresnel integrals [4], in which the parameters are $P_1, P_2 = (y \pm a/2) \sqrt{k/(\pi d_{RX})}$, $Q_1, Q_2 = (x \pm b/2) \sqrt{k/(\pi d_{RX})}$. Eq. 2 allows us to reach a straightforward analytical model for the evaluation of the FS signal by canonical shapes both in near- and far-field configurations, when the distance r is larger than λ . The next section presents some results obtained through this EM formulation for a simulated scenario (see Fig. 1), in conjunction with a validation using a numerical commercial EM code.

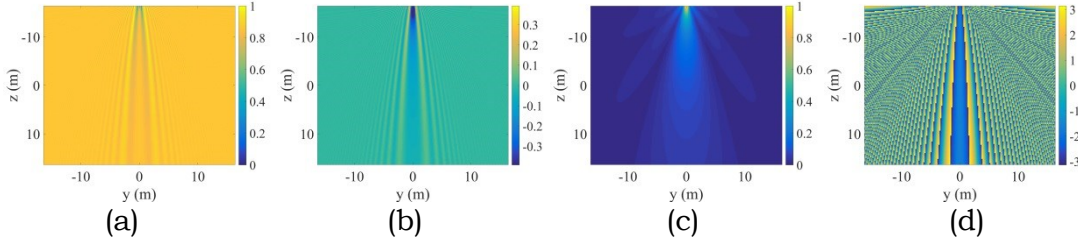


FIG. 2 – Maps of the total received (a, b) and scattered fields (c, d), in terms of normalized signal magnitude (a, c) and signal phase (b, d).

IV. NUMERICAL RESULTS

The results are referred here to a 2-D target, a square shape ($a=b=3\lambda$) crossing the baseline in a FS scenario (Fig. 1) where the carrier frequency for the plane wave is fixed at $f = 1.75$ GHz. Fig. 1 shows the EM model applied considering not only a Rx but an entire Rx area with a Rx-distance from 10λ to 100λ . Fig. 2(a) and (c) show, respectively, the normalized magnitude for the total received field (Eq. (2)) and for the scattered field (i.e., Eq. (2) minus the direct wave) obtained with a

numerical EM commercial code. In both cases the magnitude increases when the target is getting close to the receiver. The first observed feature is the typical *sinc* function in the 2-D Rx area for the scattered field magnitude (Fig. 2(c)). Looking at Fig. 2(b) and (d), respectively (the phase of the total received field and of the scattered field), the second one gradually increases the width of the hole due to the re-irradiation effect of the aperture from near to far field. Those FS effects confirm that the target basically acts as a re-irradiating antenna illuminated by the incident field. In Fig. 3, a comparison is shown between the numerical formulation (Eq. (1)) and the analytical EM model (Eq. (2)): a validation of the results is presented both for the magnitude (Fig. 3(a)) and for the phase (Fig. 3(b)) of the scattered field. The case analyzed is for a target crossing the baseline with a tilt angle of $\psi = 45^\circ$, starting from $d_{RX} = 10 \lambda$ to $d_{RX} = 100 \lambda$, considering in this way both far-field and near-field effects. An excellent agreement of the results is demonstrated until a horizontal angle $\alpha_h = 20^\circ$ for this geometry.

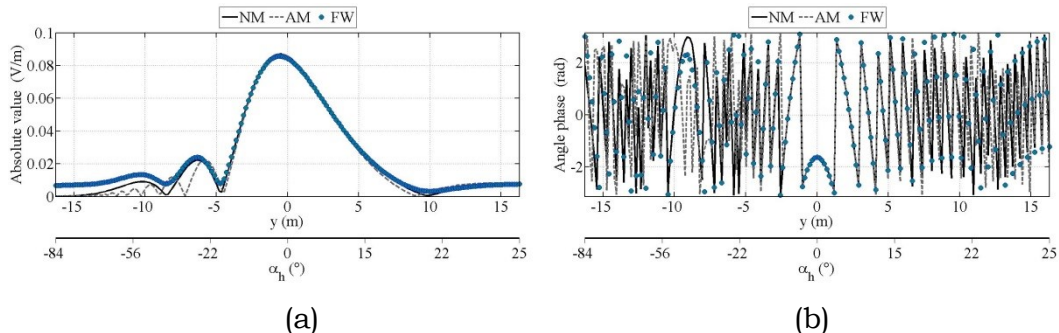


FIG. 3 – Comparison of the results obtained with the numerical model (NM), analytical model (AM) and full-wave validation (FW) for the scattered field in magnitude (a) and phase (b) when a target crosses the BL ($\psi=45^\circ$).

V. CONCLUSION

A simple electromagnetic model for the forward scattering generated by canonical shapes has been proposed and tested. This is a fundamental step for setting up a framework to detect and classify targets with FSR systems in both far-field and near-field conditions.

REFERENCES

- [1] N. J. Willis, *Bistatic Radar*. SciTech Publishing, 2007.
- [2] M. Gashinova, L. Daniel, V. Sizov, E. Hoare, and M. Cherniakov, “Phenomenology of Doppler forward scatter radar for surface targets observations,” *IET Radar, Sonar Navigation*, vol. 7(4), pp. 422-432, Apr. 2013.
- [3] M. T. Falconi, D. Comite, A. Galli, P. Lombardo, and F. S. Marzano, “Forward scatter radar modeling: effects of near field for canonical targets,” *IEEE Antennas Propag. & USNC/URSI Nat. Radio Science Meeting*, Jul. 2015.
- [4] A. Ishimaru, *Electromagnetic Wave Propagation, Radiation, and Scattering*. Prentice Hall, 1991.

ELECTROMAGNETIC SCATTERING BY PERFECTLY CONDUCTING BURIED OBJECTS

F. Di Murro⁽¹⁾, M. Lucido⁽¹⁾, G. Panariello⁽¹⁾, C. Santomassimo⁽¹⁾,
F. Schettino⁽¹⁾

⁽¹⁾ Department of Electrical and Information Engineering, University
of Cassino and Southern Lazio,
Via G. di Biasio, 43, Cassino (FR), Italy
francescadimurro@gmail.com, lucido@unicas.it, panariello@unicas.it,
chiara89santomassimo@alice.it, schettino@unicas.it

Abstract

The aim of this paper is to present the accurate and efficient analysis of the electromagnetic scattering by some canonical shape, perfectly conducting objects entirely buried in a lossy half-space. The problem, formulated as an electric field integral equation in the spectral domain for the surface current density on the metallic object, is discretized by means of the Galerkin's method with a set of orthonormal analytically transformable basis functions factorizing the correct behavior of the unknown at the edges. In this way fast convergence is achieved even for scatterers size of some wavelengths.

Index Terms – Scattering, regularization, Galerkin's Method.

I. INTRODUCTION

The analysis of the electromagnetic scattering by buried objects is an important issue due to the numerous applications in areas such as communications, geophysical exploration, remote sensing, target identification, and so on. Due to the complexity of the problem, it is necessary to resort to numerical methods even when dealing with canonical shape objects. Consequently convergence and error control are issues to be faced. This paper addresses such issues for both rectangular and circular geometries, by means of a regularizing procedure ensuring quick convergence and high accuracy.

The problem is formulated as an electric field integral equation in the spectral domain, and is discretized by means of the Galerkin's method with expansion functions factorizing the correct behavior of the unknowns at edges. In this paper, three examples are presented: a strip, a rectangular and a circular plates.

II. FORMULATION

In Fig. 1 two interfacing half-spaces, of dielectric permittivity, magnetic permeability and wavenumber $\varepsilon_1 = \varepsilon_0 \varepsilon_{r1}$, $\mu_1 = \mu_0 \mu_{r1}$, $k_1 = k_0 \sqrt{\varepsilon_{r1} \mu_{r1}}$ and

$\varepsilon_2 = \varepsilon_0 \varepsilon_{r2}$, $\mu_2 = \mu_0 \mu_{r2}$, $k_2 = k_0 \sqrt{\varepsilon_{r2} \mu_{r2}}$ respectively, are depicted, where ε_0 , μ_0 and $k_0 = 2\pi/\lambda = \omega \sqrt{\varepsilon_0 \mu_0}$ are the dielectric permittivity, the magnetic permeability and the wavenumber of the vacuum, λ is the wavelength and ω is the angular frequency. An arbitrarily oriented perfectly conducting object, such as a rectangular plate, a strip or a disk, is completely dipped in the half-space 2. The section view is the same for all the objects, with parameter $2a$ representing the rectangular plate width, the strip width or the disk diameter respectively.

A global coordinate system (x, y, z) and a local coordinate system (x_0, y_0, z_0) are introduced as in Fig. 1. A plane wave of electric field $\underline{E}^{inc}(\underline{r})$ travelling through the half-space 1 impinges on the discontinuity surface. Hence, a reflected wave arises in the half-space 1 ($\underline{E}^{ref}(\underline{r})$) and a damped transmitted wave arises in the half-space 2 ($\underline{E}^{tr}(\underline{r})$) inducing a current density $\underline{J}(\underline{r})$ in the scatterer that, in turn, generates a scattered field in both the half-spaces.

Starting from the spectral domain Green's function, the components of the scattered electric field in the half-space 2 parallel to the scatterer surface can be readily expressed as

$$\begin{aligned} \underline{E}^{sc}(\underline{r}_0) = & \int_{-\infty}^{+\infty} \int_{-\infty}^{+\infty} \underline{\underline{G}}^{(P)}(u, v) \underline{\underline{J}}(u, v) e^{-j[u\hat{x}_0 + v\hat{y}_0 + \sqrt{k_2^2 - u^2 - v^2}|z_0|]} dudv \\ & + \int_{-\infty}^{+\infty} \int_{-\infty}^{+\infty} \underline{\underline{G}}^{(S)}(u, v) \underline{\underline{J}}(f^+(u, v) \cdot \hat{x}_0, f^+(u, v) \cdot \hat{y}_0) e^{-j\underline{f}^-(u, v) \cdot \underline{r}_0} dudv \end{aligned} \quad (1)$$

$\underline{\underline{G}}(u, v)$ being the spectral Green function for a stratified medium ("P" stands for the primary or free space contribution while "S" stands for the scattered contribution due to the non-homogeneity of the medium), $\underline{\underline{J}}(u, v)$ being the double Fourier transform of the induced current and $\underline{f}^+(u, v) = u\hat{x} + v\hat{y} \pm \sqrt{k_2^2 - u^2 - v^2}\hat{z}$. An integral equation can be obtained by imposing the tangential components of the electric field to be vanishing on the scatterer surface.

III. REGULARIZED SOLUTION OF THE PROBLEM

Following the procedure outlined by Nosich in [1], the analytical regularization of the problem can be achieved by splitting the integral operator into two parts, and by resorting to the Galerkin's method with a complete set of expansion functions making the most singular part of the integral operator invertible. In the present cases, the most singular part of the problem is represented by the free space contribution, and

basis functions ensuring the regularization have been found and are given in [2]-[4]. They are not repeated here due to lack of space. The efficiency of the proposed method can be appreciated by introducing a normalized truncation error, comparing different orders of reconstruction of the unknown currents. Some examples are shown in Figs. 2-4 for the different geometries, showing a fast decaying of the error.

IV. CONCLUSION

Some examples of regularized problems have been presented in this paper, with particular reference to the scattering by buried objects. The regularization procedure is very powerful in that it allows to achieve an high efficiency and error control. The generalization to 3D structures will be the next step and will be the object of future work.

REFERENCES

- [1] A. I. Nosich, "Method of Analytical Regularization in wave-scattering and eigenvalue problems: Foundations and review of solutions," *IEEE Antennas Propag. Mag.*, vol. 42, no. 3, pp. 34–49, 1999.
- [2] M. Lucido, "Electromagnetic Scattering by a Perfectly Conducting Rectangular Plate Buried in a Lossy Half-Space," *IEEE Transactions on Geoscience and Remote Sensing*, vol. 52(10), pp. 6368-6378, Oct. 2014.
- [3] F. Di Murro, M. Lucido, G. Panariello, F. Schettino, "Guaranteed-Convergence Method of Analysis of the Scattering by an Arbitrarily Oriented Zero-Thickness PEC Disk Buried in a Lossy Half-Space," *IEEE Transactions on Antennas and Propagation*, vol. 63(8), pp. 3610-3620, Aug. 2015.
- [4] M. Lucido, "Scattering by a tilted strip buried in a lossy half-space at oblique incidence," *Progress In Electromagnetics Research M*, Vol. 37, 51-62, 2014.

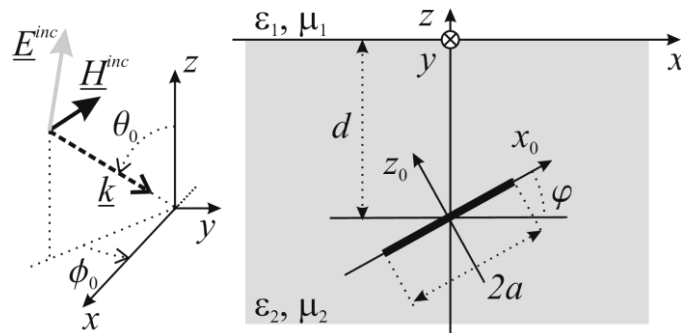


FIG. 1 – Section view of the geometry, representing a rectangular plate of dimensions $2a \times 2b$ (the second dimension is not visible in the figure), or a strip of width $2a$ or a disk of radius a .

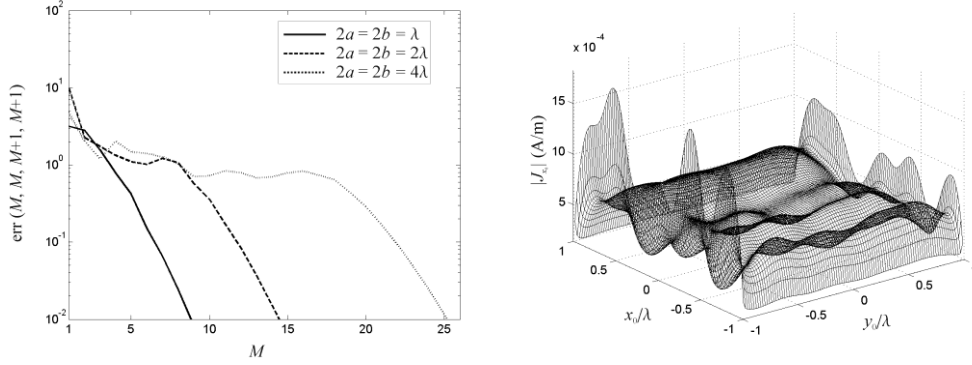


FIG. 2 – Rectangular plate, with $\varepsilon_{r1}=\mu_{r1}=\mu_{r2}=1$, $\varepsilon_{r2}=3-j0.3$, $d=3\lambda$, $\vartheta_1=\vartheta_2=\vartheta_3=30$, $\underline{E}_0=(3\sqrt{2}\hat{x}+4\sqrt{2}\hat{y}-7\sqrt{3}\hat{z})/\sqrt{197}$, $\theta_0=60^\circ$, $\phi_0=45^\circ$: (a) error defined as $er(N,M,Q,P)=\|\mathbf{J}_{N,M}-\mathbf{J}_{Q,P}\|/\|\mathbf{J}_{N,M}\|$, where $\mathbf{J}_{N,M}$ is the vector of the expansion coefficients evaluated by using N expansion functions along the x_0 axis and M along the y_0 axis; (b) example of current distribution.

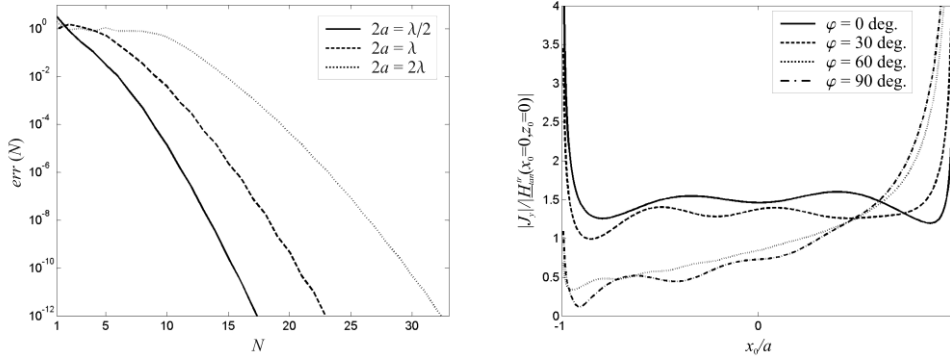


FIG. 3 – Strip, with $2a=\lambda$, $\varepsilon_{r1}=\mu_{r1}=\mu_{r2}=1$, $\varepsilon_{r2}=4-j0.5$, $d=\lambda$, $\theta_0=60^\circ$, $\phi_0=45^\circ$, $\underline{E}_0=(3\sqrt{2}\hat{x}+4\sqrt{2}\hat{y}-7\sqrt{3}\hat{z})/\sqrt{197}$ V/m: (a) error defined as $er(N)=\|\mathbf{j}_{N+1}-\mathbf{j}_N\|/\|\mathbf{j}_N\|$, where \mathbf{j}_N is the vector of the expansion coefficients evaluated by using N expansion functions for each component; (b) example of current distribution.

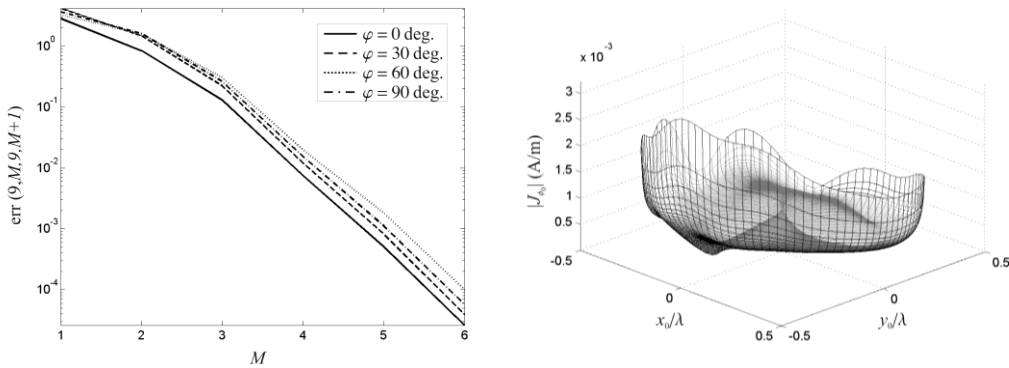


FIG. 4 – Disk, with $a=\lambda/2$, $\varepsilon_{r1}=\mu_{r1}=\mu_{r2}=1$, $\varepsilon_{r2}=3-j0.3$, $d=3\lambda$, $\theta_0=60^\circ$, $\phi_0=45^\circ$, $\underline{E}_0=(\hat{x}+j\hat{y})/\sqrt{5}-(1+j)\sqrt{3}/10\hat{z}$ V/m: (a) error defined as $er(N,M,Q,P)=\|\mathbf{J}_{N,M}-\mathbf{J}_{Q,P}\|/\|\mathbf{J}_{N,M}\|$, where $\mathbf{J}_{N,M}$ is the vector of the expansion coefficients evaluated by using $2N-1$ cylindrical harmonics and M expansion functions for each component; (b) example of current distribution.

ON THE DESIGN OF AN ANTENNA ARRAY FOR CUBE SATS OPERATING IN THE KA-FREQUENCY BAND

G. Buttazzoni⁽¹⁾, M. Comisso⁽¹⁾, A. Cuttin⁽¹⁾, R. Vescovo⁽¹⁾

⁽¹⁾ Department of Engineering and Architecture, University of Trieste
Via A. Valerio 10, 34127, Trieste, Italy

[gbuttazzoni\(mcomisso,vescovo\)@units.it](mailto:gbuttazzoni(mcomisso,vescovo)@units.it), alessandro.cuttin@phd.units.it

Abstract

This paper describes the design of an antenna array of microstrip patches for CubeSats operating in the Ka-frequency band. To the best of authors' knowledge, this design represents one of the first proposals of direct radiating array for the support of CubeSat communications in the Ka-band, which is becoming of growing interest to sustain commercial, civil, and military high data rate applications by small satellites.

Index Terms – CubeSats, direct radiating arrays, Ka-frequency band, millimeter-wave antennas.

I. INTRODUCTION

CubeSats belong to the class of nano satellites. Born in 1999, they were initially thought to serve as educational tools for universities, and have experienced a very fast and huge spread in recent years. The potential of a CubeSat mission has grown beyond the original expectations, so that, nowadays, the number of commercial missions has overcome that of the educational ones [1].

Planar antennas have been recognized to be particularly suited for CubeSats. In [2], 66 planar antennas for CubeSats have been analyzed and mutually compared. However, beside one antenna working in the Ku-frequency band, all the others operate at lower frequencies. This is relevant since the transition to the Ka-frequency band would provide a significant increase in the data throughput. This would meet the capacity demand of current payloads, which are now capable of generating up to several Gbytes of data per day [3]. Unfortunately, really few antennas for CubeSats operating in the Ka-band have been proposed in the literature so far [3]-[5].

In this paper we present an introductory study to optimize the geometry of a direct radiating array composed by square patches, which fits on a side panel of a CubeSat and radiates a right-hand-circularly-polarized (RHCP) field at 37.25 GHz. The procedure adopted to design the array structure is detailed step-by-step in the next section, which also discusses the achievable performance.

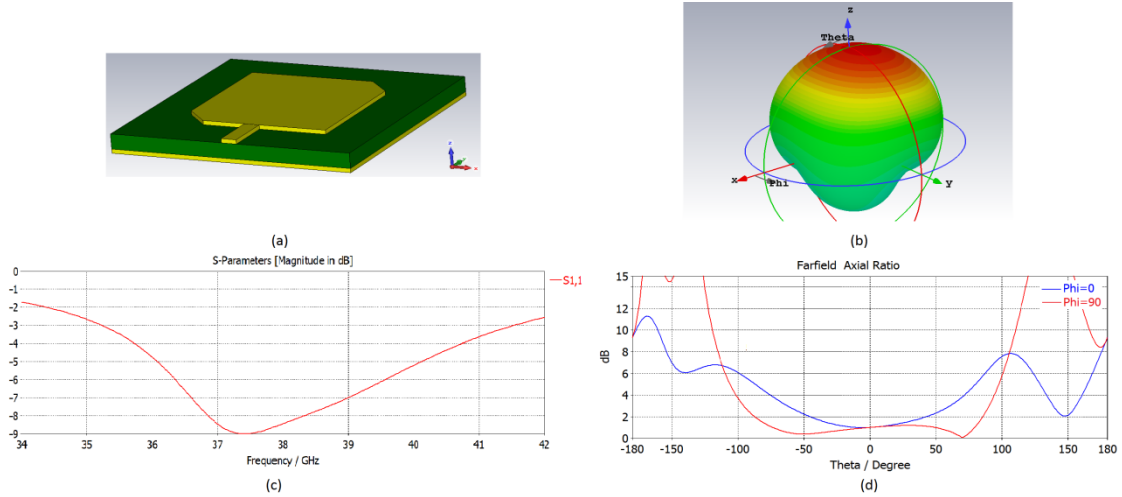


FIG. 1 – Single element: (a) square patch, (b) 3D far-field pattern, (c) return loss in dB, (d) axial ratio principal cuts.

II. THE ADOPTED DESIGN PROCEDURE

The design of the array has been carried out following a well-established procedure in the field of microstrip antenna arrays [6]. Precisely, the design of the overall structure is performed in three successive steps. Firstly, the single element of the array is optimized to radiate at the desired frequency. Secondly, four elements are grouped to form a subarray according to the *sequential rotation technique*. Thirdly, the available surface of one side of a 1U CubeSat¹ is filled with the maximum possible number of subarrays. In each of these steps, the internal CST optimizer is used.

For low-cost reasons, a common substrate composed by Duroid 5880 ($\epsilon_r = 2.2$, $\tan\delta = 9 \cdot 10^{-4}$) with a thickness of 0.254 mm is considered. To meet the efficiency requirements typical of satellite applications, a circularly polarized element is designed by selecting a square patch with truncated corners. A careful optimization of this structure is carried out to obtain the structure in Fig. 1, which reports the designed patch (Fig. 1(a)), the 3D far-field pattern (Fig. 1(b)), the return loss (Fig. 1(c)), and the axial ratio principal cuts (Fig. 1(d)).

The subarray building block is then designed moving from the single element and applying the sequential rotation technique. Accordingly, four replicas of the basic element are arranged sequentially in orientation and in phases. More precisely, the four elements are phased 0° , 90° , 180° and 270° , and configured as shown in Fig. 2, which shows the subarray (Fig. 2(a)), the 3D far-field pattern (Fig. 2(b)), the return loss (Fig. 2(c)), and the axial ratio principal cuts (Fig. 2(d)).

¹ As available surface we consider a square of 85x85 mm².

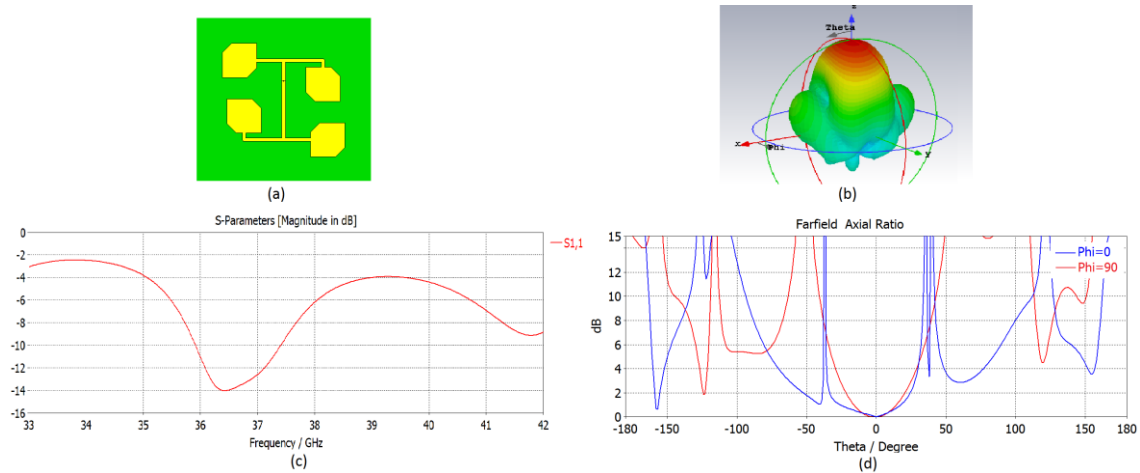


FIG. 2 – Building block: (a) subarray, (b) 3D far-field pattern, (c) return loss in dB, (d) axial ratio principal cuts.

Once the subarray is available, the complete array is obtained by placing the subarrays on an 8x8 grid with 1.3λ spacing between the centers of adjacent subarrays. The radiation pattern and the axial ratio principal cuts shown in Fig. 3 are evaluated by Matlab[®], taking into account the mutual coupling effects among adjacent subarrays and assuming a uniform amplitude for the 64 excitations. This figure reveals a relevant result concerning the axial ratio: its value is below 1 dB in the 3dB-beamwidth, which is 4° , whereas a polarization is generally accepted to be circular when the axial ratio is lower or equal to 3 dB. This result is encouraging, since it is due to the designed physical antenna system, and leaves space to further possible improvements achievable using suitable algorithms for the synthesis of the excitations.

III. CONCLUSION

A square direct radiating array of patch antennas has been designed to be installed on a face of a CubeSat. The array, whose structure has been optimized by the CST tools, operates in the Ka-band, thus enabling a significant potential increase of the transmission rate of the spacecraft. The obtained results are promising to foster the design of high directivity antennas for small satellites of CubeSat class developed to exploit the licensed Ka-frequencies.

ACKNOWLEDGEMENT

This work is partly supported by the European Space Agency (ESA Contract No. 4000108924/13/NL/FE: “Design Tool for SAR Instruments based on Aperiodic Phased Arrays”), and by the Italian Ministry of University and Research (project FRA 2015, Univ. of Trieste, Italy: “Peer-to-peer Millimeter-Wave Communications in 5G Networks: Theoretical Modeling and Algorithms for Massive MIMO Systems”).

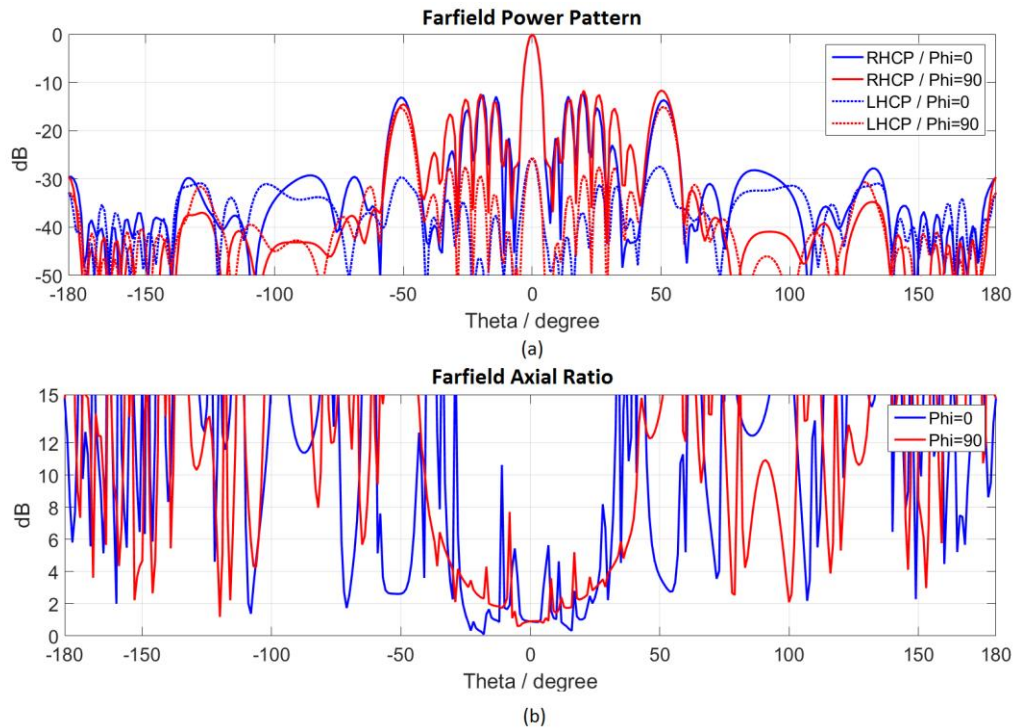


FIG. 3 – Radiation pattern (a) and axial ratio cuts (b) of the complete array.

REFERENCES

- [1] E. Buchen, "Small satellite market observations," AIAA/USU Conf. on Small Satellites, Logan, UT, 2015.
- [2] F. E. Tubbal, R. Raad, and K.-W. Chin, "A survey and Study of Planar Antennas for Pico-Satellites," *IEEE Access*, vol. 3, pp. 22590-2612, 2015.
- [3] J. A. King, J. Ness, G. Bonin, M. Brett, and D. Faber, "Nanosat Ka-Band Communications - A Paradigm Shift in Small Satellite Data Throughput," in AIAA/USU Conf. on Small Satellites, Logan, UT, 2012.
- [4] J. F. Sauder, N. Chahat, R. Hodges, E. Peral, Y. Rahmat-Samii, and M. Thomson, "Designing, Building, and Testing a Mesh Ka-band Parabolic Deployable Antenna (KaPDA) for CubeSats," in AIAA Aerospace Sciences Meeting, San Diego, California, USA, 2015.
- [5] R. Hodges, B. Shah, D. Muthulingham, and T. Freeman, "ISARA Integrated Solar Array and Reflectarray Mission Overview," in AIAA/USU Conf. on Small Satellites, Logan, UT, 2013.
- [6] A. Chen, Y. Zhang, Z. Chen, and S. Cao, "A Ka-Band High-Gain Circularly Polarized Microstrip Antenna Array," *IEEE Antennas and Wireless Propagation Letters*, vol. 9, pp. 1115-1118, 2010.

THE ALPHASAT PROPAGATION EXPERIMENT: INTERIM RESULTS FROM ASI AND NASA GROUND STATIONS

C. Riva⁽¹⁾⁽²⁾, L. Luini⁽¹⁾⁽²⁾, R. Nebuloni⁽²⁾, J. Nessel⁽³⁾, G. Codispoti⁽⁴⁾,
G. Parca⁽⁴⁾, A. Tuozi⁽⁴⁾

⁽¹⁾ Dipartimento di Elettronica, Informazione e Bioingegneria (DEIB),
Politecnico di Milano, Piazza L. Da Vinci 32, Milano, Italy
lorenzo.luini@polimi.it

⁽²⁾ Istituto di Elettronica e di Ingegneria dell'Informazione e delle
Telecomunicazioni (IEIIT), Consiglio Nazionale delle Ricerche, Via
Ponzio 34/5, Milano
roberto.nebuloni@ieiit.cnr.it

⁽³⁾ NASA Glenn Research Center, 21000 Brookpark Rd. MS 54-1,
Cleveland, OH, USA
james.a.nessel@nasa.gov

⁽⁴⁾ Italian Space Agency, Via del Politecnico 00133,
Rome – Italy
giuseppe.codispoti@asi.it

Abstract

This contribution presents results obtained from the Italian ground stations in the frame of the Alphasat propagation experiment. Yearly statistics of the atmospheric attenuation as inferred from the received beacon signals (19.7 and 39.4 GHz) are reported and discussed for the two receiving stations installed in Spino d'Adda and Milan, whose experimental data are also combined to evaluate the advantage that would originate from a two-station diversity configuration.

Index Terms – Atmospheric effects, Electromagnetic wave propagation, Experimental activities, Satellite communications.

I. INTRODUCTION

Near future broadband satellite communication systems will aim at providing extremely high capacity and very high data rates. This calls for very large bandwidths, which, in turn, is driving the adoption of higher carrier frequencies in the Ka or Q/V bands and beyond. In this scenario, the Alphasat Aldo Paraboni propagation experiment was conceived and supported by the Italian Space Agency (ASI) to better characterize the electromagnetic propagation in the atmosphere using two beacon signals at 19.7 (Ka band) and 39.4 GHz (Q band). Specifically, goals are the investigation of first and second order statistics

of attenuation, joint depolarization and attenuation measurements, sky noise temperature, instantaneous frequency scaling law and so on. This contribution addresses interim results obtained in the frame of the Alphasat experiment from the ASI equipment deployed at Spino d'Adda, and from the NASA receivers, hosted at Politecnico di Milano.

II. THE ALPHASAT ALDO PARABONI PROPAGATION EXPERIMENT

Building upon the heritage of past experimental campaigns such as Sirio and ITALSAT, the Alphasat Aldo Paraboni propagation experiment aims at a more accurate description of the propagation channel at Ka and Q bands, and at demonstrating the effectiveness of some Propagation Impairment Mitigation Techniques (PIMTs) to counteract the relevant atmospheric impairments foreseen at mm waves in the design of new satellite TLC systems [1]. The experiment payload, embarked aboard the Alphasat satellite since July 2013, consists of two beacons operating at 39.4 GHz and 19.7 GHz, and covering the whole Europe. As for the ground segment, two ASI stations are installed in Italy, located in Tito Scalco (near Potenza) and Spino d'Adda (near Milan), both of which are equipped with a monopulse auto tracking system and measure co-polar signals at the two frequencies (the cross-polar signal is also received at 39.4 GHz) with 16 Hz sampling rate, using a 4.2 m diameter antenna with an average elevation angle of 42.1° (Tito Scalco) and 35.5° (Spino d'Adda). A profiler radiometer, a tipping bucket rain gauge and an ancillary meteorological station complete the equipment of both stations. In addition, NASA Glenn Research Center (GRC) developed and installed receivers at the Politecnico di Milano campus in Milano, Italy: 1.2-m K-band and 0.6-m Q-band antennas, satellite open-loop tracking, 8-Hz sampling rate [2]. A weather station with an optical disdrometer is also available to characterize rain drop size distribution.

III. MEASUREMENT DATA BASE AND DATA PROCESSING

A full year of measurements (2015) collected by the two ground stations have been processed to obtain statistics of the signal attenuation in the two sites, as well as to evaluate the advantage originating from the joint use of both stations in site-diversity configuration.

The first processing step consisted in calculating the reference attenuation level A_{ref} required to convert the received power levels (dBm) into total tropospheric attenuation (dB). This task was performed by taking advantage of the collocated radiometer (brightness temperatures collected at various frequencies) for the Spino d'Adda station, while being radiometric data unavailable in Milan, we have applied for the latter site an alternative procedure involving the use of atmospheric profiles (derived from radiosonde observations, RAOBS, and/or

operational Numerical Weather Predictions, NWP) and mass absorption models (e.g. Liebe's MPM93 [3]) to estimate the total atmospheric attenuation in clear sky conditions. Full details on this approach can be found in [4].

Fig. 2 shows a sample of calibrated attenuation data (Q band) collected during a rainy day (November, 30th 2015) in Spino d'Adda and in Milan (distance between the stations \approx 23 km), together with the attenuation that would be experienced by a two-site diversity configuration, for which the lowest attenuation between the two stations is always selected.

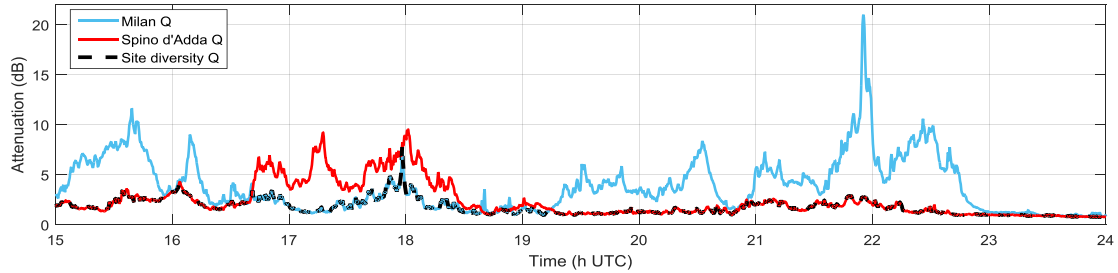


Fig. 2 – Example of calibrated attenuation data for Spino d'Adda and for Milan (Q band). Also shown is the two-site diversity attenuation level.

IV. STATISTICAL RESULTS

Statistics of the total tropospheric attenuation in the two ground stations have been calculated from the strictly concurrent calibrated database for both frequencies. Fig. 3 compares the Complementary Cumulative Distribution Functions (CCDFs) obtained for the two sites ((a) Ka band, (b) Q band): as expected, given the limited distance between Spino d'Adda and Politecnico di Milano main campus (\approx 23 km), attenuation statistics are similar. Notwithstanding this, some discrepancies between the curves arise, mainly as a consequence of the differences in the equipment (e.g. receiver architecture and dynamics), in the outage periods, as well as in the climate affecting the two sites, one lying in the city and the other in the open countryside.

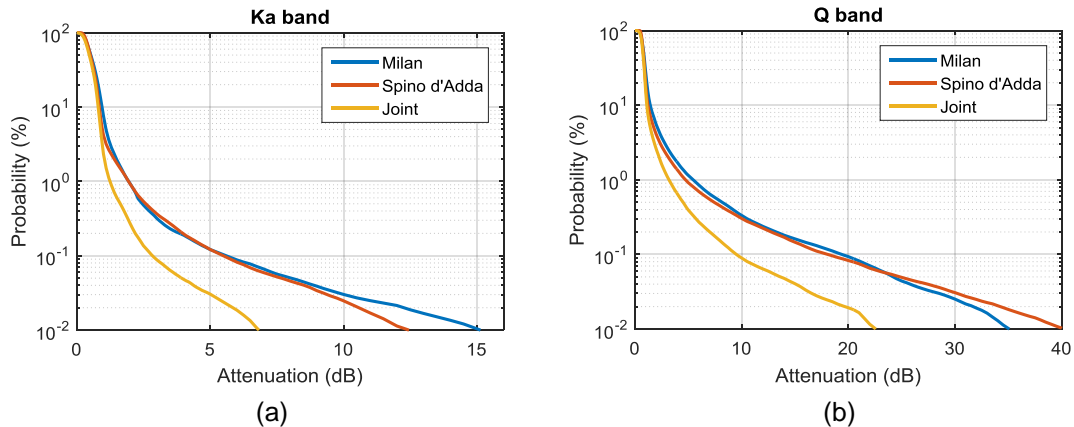


Fig. 3 – CCDFs of total tropospheric attenuation obtained for Spino d'Adda, Milan, and the joint two-site diversity system.

Fig. 3 also gives a hint about the advantage of the site diversity scheme consisting in the joint use of both stations: as an example, considering the Q band, the same yearly system availability of 99.9% could be achieved with a power margin of 10 dB when taking advantage of the site-diversity configuration, while 20 dB would be required when using only one site.

V. CONCLUSION

This paper presents interim results on the total tropospheric attenuation data collected by the ASI equipment installed at Spino d'Adda, Italy, and by the NASA receivers deployed at the main Politecnico di Milano campus (1 year of data in the frame of the Alphasat propagation experiment). As expected, results indicate a similar trend for the attenuation CCDFs measured at the two sites, the differences being mainly ascribable to the different environment (city and open countryside) and some differences in the equipment (e.g. receiver architecture and dynamics). Given the short distance between the station (roughly 23 km), we have also investigated the site diversity concept: as expected, results show a strong reduction in the power margin required to guarantee a given system high-availability target, mainly due to the uneven spatial distribution of rain. Future work includes the investigation of other propagation effects (e.g. depolarization) and results (e.g. frequency scaling), as well as the use of the experimental data to develop new propagation models and/or improve existing ones.

REFERENCES

- [1] C. Riva, M. Schönhuber, G. Codispoti, A. Martellucci, C. Capsoni, M. D'Amico, L. Luini, L. Resteghini, R. Nebuloni, F. Teschl, F. Cuervo, K. Plimon, "The Alphasat Aldo Paraboni scientific experiment: objectives and preliminary results", The 20th Ka and BroadBand Communications, Navigation and Earth Observation Conference, Vietri, Italy, October 1-3, 2014, pp. 347-355.
- [2] Nessel J., J. Morse, M. Zemba, C. Riva, L. Luini, "Preliminary results of the NASA beacon receiver for Alphasat Aldo Paraboni TDP5 propagation experiment", The 20th Ka and BroadBand Communications, Navigation and Earth Observation Conference, Vietri, Italy, October 1-3, 2014, pp. 357-365.
- [3] H. J. Liebe, G. A. Hufford, M. G. Cotton, "Propagation modeling of moist air and suspended water/ice particles at frequencies below 1000 GHz," in Proc. AGARD 52nd Spec. Meeting EM Wave Propag.
- [4] J. Nessel, J. Morse, M. Zemba, C. Riva, L. Luini, "Preliminary Results of the NASA Beacon Receiver for Alphasat Aldo Paraboni TDP5 Propagation Experiment", pp. 1-8, IEEE Aerospace Conference 2015, 7-14 March 2015, Big Sky, Montana, USA.

A NOVEL MICROWAVE FREQUENCY SWEEP INTERFEROMETER FOR ECR PLASMA ELECTRON DENSITY MEASUREMENTS

Giuseppe Torrìsi^{(1),(2)}, Ornella Leonardi⁽¹⁾, Gino Sorbello^{(1),(3)}, David Mascali⁽¹⁾, Giuseppe Castro⁽¹⁾, Luigi Celona⁽¹⁾, Santo Gammino⁽¹⁾

(1) INFN - Laboratori Nazionali del Sud, Via S. Sofia 62, 95125
Catania, peppetorrìsi@lns.infn.it

(2) Università Mediterranea di Reggio Calabria, Via Graziella, 89100
Reggio Calabria, Italy

(3) Università degli Studi di Catania, Viale Andrea Doria 6, 95125,
Catania, Italia

Abstract

We present the experimental results collected by a novel microwave interferometer for plasma density measurements in compact Electron Cyclotron Resonance Ion Sources (ECRIS). Microwave interferometry represents the best candidate for non-intrusive plasma diagnostics in these devices, where the plasma under test is contained in a microwave resonant cavity. The developed K-band microwave interferometry system is based on the so-called “frequency sweep” or FMCW method. This method is robust with respect to the uncontrolled disturbances of the spurious reflections introduced by the cavity. The paper includes the description of the calibration and preliminary tests performed on a known scenario, “a holed paraffin wax”, as well as the first measurements on a magnetized microwave-heated plasma in a compact ion source.

Index Terms – microwave interferometry, diagnostics, plasma

I. INTRODUCTION

Interferometry is a well-known diagnostic technique for measuring the line averaged electron density of a plasma from its refraction index, obtained by measuring the interference between two waves [1].

For densities in the range 10^{11} - 10^{13} cm⁻³ (plasmas for thermonuclear fusion and/or heavy ion sources for accelerators [2]), the relation $L_p \sim L_c \sim \lambda_0$ (where L_p and L_c are the plasma and plasma chamber lengths, and λ_0 the RF vacuum wavelength) holds, that greatly complicates the measurement due to multi-component signals caused by reflections on the metallic walls of the compact metallic plasma chamber. In the present paper we will just focus on the first results of the refraction index measurements performed in microwave resonant cavity, in the following cases:

- refraction index $N = 1$ calibration in empty/vacuum cavity;
- refraction index N_{HP} measurement in cavity filled by holed paraffin wax, modelling an “artificial” plasma having a less-than-one refraction index;

- refraction index N_P measurement for a microwave generated plasma. For more details about the interferometer design and ECRIS characteristics see [3].

Figure 1a) shows the interferometer assembly.

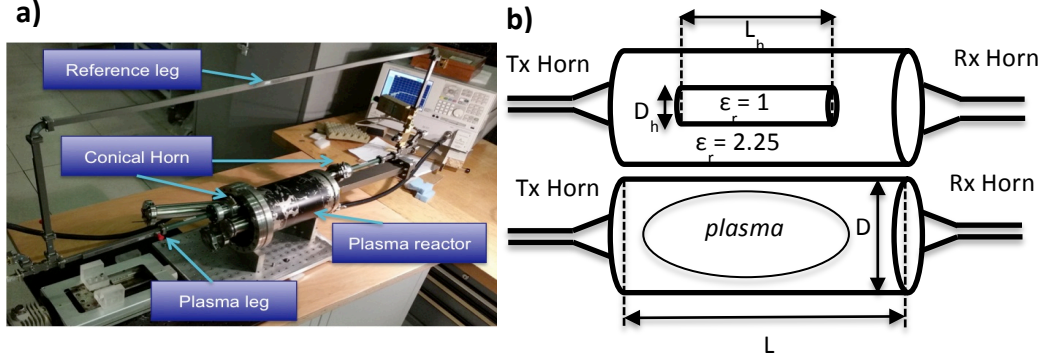


FIG. 1 a) K-band (18-26.5 GHz) microwave interferometer. **b)** Top: Holed paraffin experiment. Bottom: real plasma experiment.

II. SWEEP -FREQUENCY INTERFEROMETRY

According to the “Mach-Zehnder” swept-frequency scheme [1], the density measurement is based on the evaluation of the beating signal $S(t) \propto \cos^2(\Delta\phi(t))$ obtained as the superposition of the signal which crosses the plasma with a reference one.

The signal launched from the transmitting conical horn antenna along two paths, is “up-chirped” (from 22.5 to 26.5 GHz). The detected signal $S(t)$ can be described in terms of a “beat” frequency, i.e., $S(t) \propto \cos^2(\omega_{beat}t)$, where ω_{beat} is the time rate of changing of the relative phase $\Delta\phi$:

$$\omega_{beat} = \frac{\partial \Delta\phi(t)}{\partial t} = \frac{\partial \omega}{\partial t} \frac{\partial \Delta\phi(t)}{\partial \omega} = \frac{\partial \omega}{\partial t} \left(\Delta L \frac{\partial k_g}{\partial \omega} - \int_L \frac{\partial k_p}{\partial \omega} dl \right) \quad (1)$$

where ΔL is the difference in length between the reference leg and the plasma leg, k_g the wave number in the waveguide, k_p is the plasma wave number. For a magnetized plasma, as it is typical of ion sources, the probing wave has the following constant of propagation:

$$k_p = \frac{\omega}{c} N_p = \frac{\omega}{c} \frac{1}{2} \left(\sqrt{1 - \frac{\omega_p^2}{\omega(\omega - \omega_g)}} + \sqrt{1 - \frac{\omega_p^2}{\omega(\omega + \omega_g)}} \right) \quad (2)$$

where $\omega_p^2 = n_e e^2 / m \epsilon_0$. Therefore, in the same way of the range profile computation of FMCW radar, by applying the Fast Fourier Transform (FFT) on the beating signal, the beating frequency ω_{beat} shift is used to determine the plasma refraction index N_P , which depends on the plasma frequency ω_p and, in turn, on the electron density n_e .

IV. EXPERIMENTAL RESULTS

The plasma chamber has length $L = 266$ mm and diameter $D = 120$ mm. The measured beating frequency of the empty cavity was: $\omega_{beat_V} = 2\pi(0.3974)$ rad/s. This “in vacuum” measurement has been used as an absolute calibration. Eq. (1), can be rearranged in following way:

$$\omega_{beat_V} = \frac{\Delta\omega}{\Delta t} \left(C_F - \frac{L}{c} N \right) \quad (3)$$

where $C_F = \Delta L \frac{\partial k_g}{\partial \omega}$ is a calibration factor incorporating eventual unknown parameters in the reference leg, the waveguide dispersion, etc. It can be found by imposing $N = 1$ (vacuum refraction index) in the empty cavity measurement: the obtained C_F can be then applied in the successive experiments, such as the paraffin bulk refraction index measurement. When filling the cavity with paraffin, as expected the measured beating frequency downshifts to $\omega_{bBP} = 2\pi(0.3802)$ rad/s. By inverting equation (3) (now the unknown parameter is right N), we obtain:

$$N_{BP} = C_F \frac{c}{L} - \omega_{beat_{BP}} \frac{\Delta t}{\Delta \omega} \frac{c}{L} \quad (4)$$

Replacing C_F with the experimental value obtained above, and using the measured beating frequency, we obtain: $N_{BP} = 1.43$, in good agreement – although slightly underestimated – with the literature values lying in the range 1.48–1.5.

Before measuring the plasma refraction index, we made another intermediate step, validating the calibration procedure by introducing into the cavity a holed paraffin cylinder (see Fig. 1b) where $L_h = 150$ mm and $D_h = 50$ mm). This virtual plasma experiment allowed us to test the setup in a simpler and well-known (controllable) scenario, before to deal with more complicated unknown plasma measurements. A plasma can be in facts simulated (it is often called “analog” experiment) by cutting holes in a block of low-loss dielectric [1]: we realized a cylindrical hole cut in paraffin ($\epsilon_r = 2.25$). The dielectric constant ratio vacuum/paraffin corresponds to a plasma of $X=0.56$, i.e. of a density equal to the 56% of the critical density at the probing frequency. The “simulation” resembles the plasma case (the wave propagates from the vacuum to the less-than-one N of the plasma), since we tried to probe an internal region of vacuum ($N=1$) surrounded by a background of larger refractive index (for paraffin $N \sim 1.5$). This “analogy” requires to calibrate the system by treating the bulk paraffin as it would be vacuum; we started from the $\omega_{beat_{BP}}$ formula:

$$\omega_{beat_{BP}} = \frac{\Delta\omega}{\Delta t} \left(C_F - \frac{L}{c} N_{BP} \right) \quad (5)$$

Imposing $N_{BP} = N_V = 1$ as normalization condition to “convert” the bulk paraffin scenario in the vacuum one. We then obtained a new calibration factor:

$$C'_F = \omega_{beat_{BP}} \frac{\Delta t}{\Delta \omega} + \frac{L}{c}$$

Hence, the holed paraffin beating frequency becomes:

$$\omega_{beat_{HP}} = \frac{\Delta \omega}{\Delta t} \left(C'_F - \frac{L_h}{c} N_{HP} - \frac{L - L_h}{c} N_{BP} \right)$$

Thus, the holed paraffin refraction index N_{HP} “simulating” the plasma was obtained from:

$$N_{HP} = C'_F \frac{c}{L_h} - \omega_{beat_{HP}} \frac{\Delta t}{\Delta \omega} \frac{c}{L_h} - \frac{L - L_h}{L_h} N_{BP}$$

resulting in $N_{HP}=0.59$, in very good agreement with the expected value. The last step was to switch-on the plasma. A nitrogen-oxygen plasma at 10^{-4} mbar and in presence of a 0.1 T magnetic field has been heated by 150 W microwave power coming out from a TWT-Amplifier at 3.75 GHz. This time, the measured beating frequency was upshifted to $\omega_p = 2\pi(0.406) \pm 3.6589 \cdot 10^4$ rad/s. From the following equation:

$$N_p = C'_F \frac{c}{L} - \omega_{beat_p} \frac{\Delta t}{\Delta \omega} \frac{c}{L}$$

we obtained the plasma refraction index of $N_p = 0.7905 \pm 0.111$ applying a standard error propagation procedure. The obtained refraction index corresponds to an electron density of $2 \cdot 10^{12}$ cm⁻³.

III. CONCLUSION

The paper has summarized the experimental results of plasma refraction index measurements performed by means of a microwave interferometer able to operate inside compact metallic resonators. The frequency sweep and the FFT on resulting beating allows the analysis of the very noisy spectrum of the beating signal detected in presence of the cavity, allowing filtering the direct-path signal from the ones coming from walls reflections. This strategy has been numerically tested [3] and finally experimentally validated in a ion source prototype, obtaining the first interferometric measurement of plasma density in these devices.

REFERENCES

- [1] M. A. Heald and C. B. Wharton, “Plasma diagnostic with microwaves”, Robert E. Krieger, 1996.
- [2] S. Gammino, L. Celona, G. Ciavola, F. Maimone, and D. Mascali, “Review on high current 2.45 GHz electron cyclotron resonance sources (invited),” *Review of Scientific Instruments*, vol. 81, no. 2, 2010.
- [3] G. Torrisi, D. Mascali, L. Neri, O. Leonardi, G. Sorbello, L. Celona, G. Castro, R. Agnello, A. Caruso, S. Passarello, A. Longhitano, T. Isernia, and S. Gammino, “Microwave frequency sweep interferometer for plasma density measurements in ECR ion sources: Design and preliminary results,” *Review of Scientific Instruments*, vol. 87, no. 2, 2016.

X-BAND WAVEGUIDE DIPLEXER DESIGN WITH RELAXED FABRICATION TOLERANCE

Elson Agastra

Department of Electronics and Telecommunications,
Polytechnic University of Tirana
Sheshi Nënë Tereza, No. 1, Tirana, Albania
eagastra@fti.edu.al

Abstract

In this contribution, an X-band diplexer geometry based in multiple coupling resonators is presented. The frequency analysis is carried out not only toward S-parameters analysis and requirements satisfaction, but also for their sensitivity to fabrication errors. For relaxing fabrication tolerance requirements without introducing significant frequency response modification, a larger coupling resonator is introduced. Simulations shows that using larger resonators (about one wavelength), the sensitivity of S-parameters due to fabrication errors is reduced with respect of the conventional (half wavelength) resonator.

Index Terms – coupled resonator, diplexer, microwave fabrication tolerance.

I. INTRODUCTION

In modern radio-communication transceivers front end, diplexers are a key element able to separate the RX and TX signals and connect the receiver and transmitter circuits to a single antenna port. Most of the standard waveguide diplexers are composed by a conventional three-port power divider and two bandpass filters, one for each channel [1-5]. In recent years, different typologies based on all-coupled resonators have been proposed [1-3]. Most of these devices are fabricated using CNC techniques. The fabrication tolerance can produce significant errors in frequency response resulting in a poor production yield [4-5]. Reducing the fabrication tolerance can be a practicable solution, but due to the required tolerance, this can be uneconomical solution. For this purposes, using resonator geometries exhibiting a frequency response tolerant to fabrication errors is a possible interesting solution [4-5].

The aim of this contribute is in analyzing a practical diplexer solution from fabrication tolerance point of view and propose a new design with better frequency response to the same fabrication errors.

II. RESONATOR DIPLEXER STRUCTURE

The primary layout of analyzed diplexer typology [2] is shown in Fig. 1(a). Geometrical dimension for X-band design are shown in Table 1.

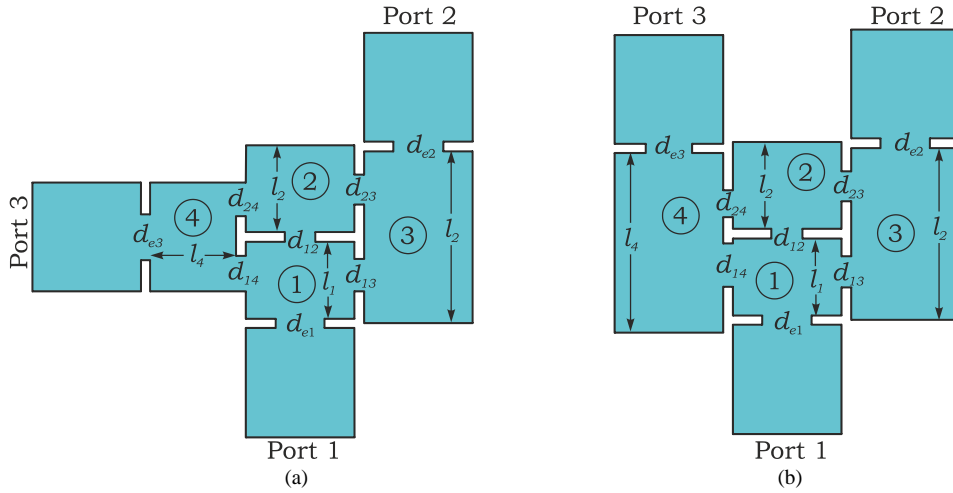


FIG. 1 – X-Band diplexer with physical parameters inside; (a) reference geometry [2]; (b) proposed diplexer geometry.

In this contribute, only inductive irises are used as to facilitate the CNC milling fabrication. Use of H-plane inductive iris discontinuities produce a more sensitive frequency response to the fabrication tolerance rather using E-Plane discontinuities [4, 5]. Frequency response error can be theoretically reduced using capacitive discontinuities rather than inductive ones or by increasing the length of inductive resonators [4].

TABLE I – X-BAND DIPLEXER DIMENSIONS, WAVEGUIDE: WR90.

Symbol	Reference [2] Fig. 1(a) (mm)	Proposed Fig. 1(b) (mm)	Symbol	Reference [2] Fig. 1(a) (mm)	Proposed Fig. 1(b) (mm)
l_1	16.15	16.15	d_{e3}	9.47	9.729
l_2	18.27	18.27	d_{12}	6.56	6.52
l_3	36.11	36.11	d_{13}	6.64	6.64
l_4	18.09	37.59	d_{14}	7.41	9.41
d_{e1}	10.41	10.53	d_{23}	6.35	6.35
d_{e2}	10.39	10.39	d_{24}	7.03	5.90

Analyzing the geometry presented in Fig. 1(a), the fourth resonator have a length approximatively $\lambda/2$. Increasing the length up to full wavelength can significantly reduce the filter sensitivity to tolerance effect [4]. In Fig. 1(b) is shown the modified geometry.

Changing resonator typology will automatically introduce a different frequency response witch need to be tuned to the desired central frequency. For re-tuning the new structure response to the desired center frequency, a local optimization search technique is used.

Using this typology, with a noticeable increase of l_4 of the structure in Fig. 1(b), permits more independent coupling between resonators 1-4 and resonators 2-4. This typology also reduce the footprint of the entire geometry.

III. EXPERIMENTAL RESULTS

Both geometries are analyzed using 3D-FEM software developed at University of Florence [6,7] where perfect matching of the frequency response is obtained to the reference [2] for geometry in Fig. 1(a).

S-parameters for both structures can be compared in Fig. 2. The frequency response of Fig. 2(b) have been obtained after a preliminary tuning of the geometrical dimensions relative to resonator 4 and its coupling apertures to resonator 1 and 2. Final dimensions of this procedure are reported in Table 1 where coupling width for all apertures is considered fixed at 2mm.

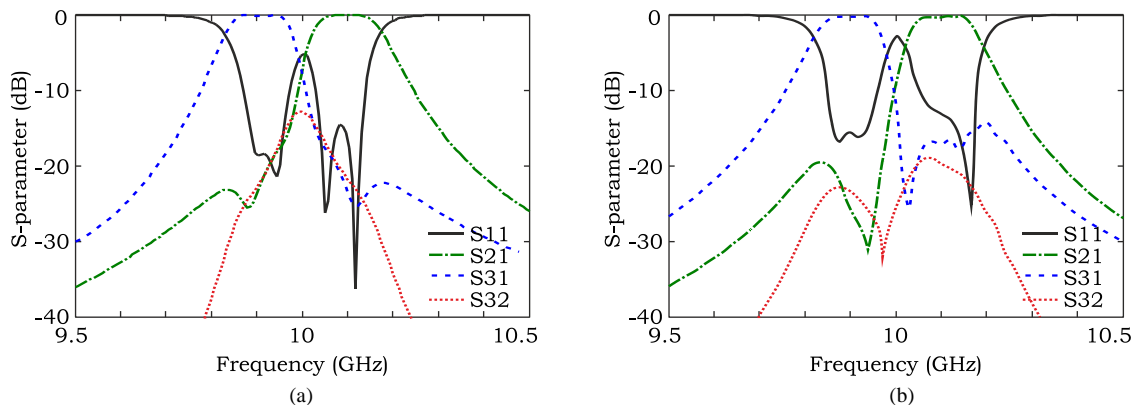


FIG. 2 – S-parameter response for reference geometry [2] (a); S-parameter response for proposed geometry.

The difference in frequency response, especially for 10.1GHz (Fig. 2) is due to the fact that the coupling of resonator 3 to resonator 1 and 2 is also influenced partially by resonator 4 geometry. Modifying only parameters regarding resonator 1, 2 and 4 in the new geometry, this also influences to the energy stored in the third resonator. Hence, a fine tuning of all 12 geometrical parameters is required.

Results of frequency response for both geometries to fabrication tolerance of 0.2mm are reported in Fig. 3. For the first geometry (Fig. 1(a)) it is evident a greater sensitivity of the lower band response (S21 and S31). This is coherent as the coupling resonator 4 that connects port 3 to port 1 is approximatively half wavelength. Increasing this resonator volume (Fig. 1(b)) and analyzing its frequency response to the same fabrication tolerance, is evident from Fig. 3(e,f) where a more reduced frequency variation have been obtained for frequency smaller than 10GHz.

IV. CONCLUSION

The present work shows a proof of concept design of a microwave diplexer with relaxed fabrication tolerances. The simulated structure shows that increasing the length of the resonators up to one wavelength sensitivity to fabrication errors can be reduced. This also corresponds to

greater energy stored in each resonator and as consequence; larger coupling windows are required for maintaining the same frequency response.

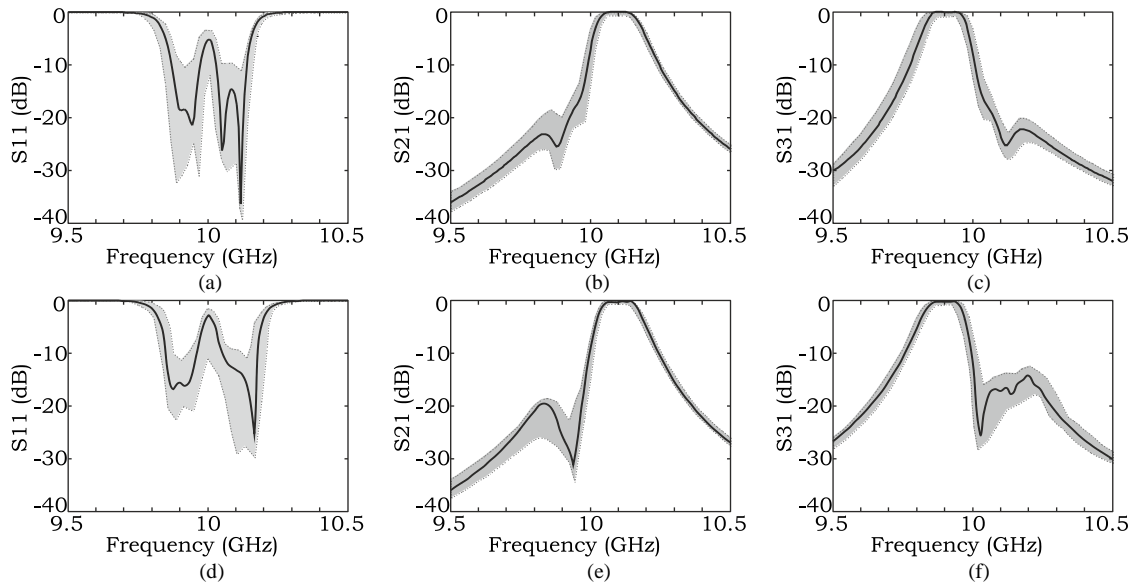


FIG. 3 – S-parameter subject to systematic fabrication errors: reference geometry [2] (a, b, c); Proposed geometry (d, e, f).

REFERENCES

- [1] X. Shang, Y. Wang, W. Xia and M. J. Lancaster, "Novel Multiplexer Topologies Based on All-Resonator Structures," *IEEE Transactions on Microwave Theory and Techniques*, vol. 61, no. 11, pp. 3838-3845, Nov. 2013
- [2] W. Xia, X. Shang and M. J. Lancaster, "All-resonator-based waveguide diplexer with cross-couplings," *Electronics Letters*, vol. 50, no. 25, pp. 1948-1950, 2014
- [3] T. F. Skaik, M. J. Lancaster and F. Huang, "Synthesis of multiple output coupled resonator circuits using coupling matrix optimization," in *IET Microwaves, Antennas & Propagation*, vol. 5, no. 9, pp. 1081-1088, June 27 2011
- [4] J. R. Aitken and J. Hong, "Tolerance considerations for wireless backhaul diplexer circuits," *Proc. 44th European Microwave Conference (EuMC)*, pp. 620-623, Rome, 2014
- [5] J. R. Aitken and J. Hong, "Design of millimeter wave diplexers with relaxed fabrication tolerances," *IET Microwaves, Antennas & Propagation*, vol. 9, no. 8, pp. 802-807, 2015
- [6] G. Pelosi, R. Coccioli, and S. Selleri, "Quick finite elements for electromagnetic waves," *Artech House*, Norwood, MA, 2009
- [7] G. Guarnieri, G. Pelosi, L. Rossi, S. Selleri, "An Efficient Perturbative Approach for Finite-Element Analysis of Microwave Devices Exhibiting Small Geometrical Variations," *IEEE Transactions on Microwave Theory and Techniques*, Vol. 57, No. 2, Feb. 2009, pp. 395-405

X/KA-BAND DUAL-POLARIZED DIGITAL BEAMFORMING SYNTHETIC APERTURE RADAR

Chunxu Mao⁽¹⁾, Steven Gao⁽¹⁾, Carolina Tienda⁽²⁾, Srdjan Glisic⁽³⁾, Emilio Arnieri⁽⁴⁾, Piotr Penkala⁽⁵⁾, Milos Krstic⁽⁶⁾, Arancha Dominuez⁽⁷⁾, Anton Patyuchenko⁽²⁾, Fan Qin⁽¹⁾, Uroschanit Yodprasit⁽³⁾, Oliver Schrape⁽⁶⁾, Luigi Boccia⁽⁴⁾, Giandomenico Amendola⁽⁴⁾, Marwan Younis⁽²⁾, Elisabeth Celton⁽⁷⁾, Vladimir Petrovic⁽⁶⁾

⁽¹⁾ School of Engineering and Digital Arts, University of Kent, Canterbury, UK (email: cm688@kent.ac.uk; s. gao@kent.ac.uk).

⁽²⁾ Microwaves and Radar Institute, German Aerospace Center (DLR), 82234 Wessling, Germany.

⁽³⁾ Silicon Radar GmbH, 15236 Frankfurt (Oder), Germany.

⁽⁴⁾ DIMES, Università della Calabria, 87036 Arcavacada di Rende Cosenza, Italy.

⁽⁵⁾ Evatronix S.A. Bielsko-Biala, 43-300 Bielsko-Biala, Poland.

⁽⁶⁾ IHP, 15236 Frankfurt (Oder), Germany.

⁽⁷⁾ Innovative Solutions In Space BV, 629 JD, Delft, Netherlands.

emilio.arnieri@unical.it

Abstract

This paper presents the concept, design and development of a novel digital beamforming (DBF) space-borne synthetic aperture radar (SAR). The target of the DBF-SAR system is to realize a low cost, light weight, low power consumption and dual-band dual-polarized SAR system for future small/micro satellite applications. The concepts of multi-static SAR system, reflector-based aperture-shared dual-band array and chip on board highly integration are presented.

Index Terms – Digital beamforming (DBF) Dual-band, dual-polarized, synthetic aperture radar (SAR).

I. INTRODUCTION

This paper present a novel X/Ka-band digital beamforming SAR (DBF-SAR) system proposed in the project DIFFERENT. DIFFERENT is abbreviated of “digital beam forming for low-cost multi-static space-borne synthetic aperture radars”. The project currently still in progress, is collaborated amongst several leading universities, research institutes and companies in Europe. The aim of DIFFERENT project is to develop a low-cost, low weight, highly integrated, dual-band dual-polarized DBF-SAR instrument to overcome the limitations of current SAR systems and pave the way to small satellites formation flying missions.

To solve the existing problems of traditional SAR systems, a multi-static SAR system based on formation flying small satellites [1],[2] is proposed in this paper. In this SAR system, the transmitting and receiving antennas are separated and mounted on separate satellites,

enabling a larger freedom of operation and increasing the sensitivity due to the reduction of transmitter/receiver switches.

Up to now, all of the SAR systems for small satellites are operating at single band, which limits SAR applications in earth observation. A shared-aperture, dual-band dual-polarized SAR radiation board will not only lead to a compact size, low cost SAR system, but also versatile applications. To meet the requirements of the future SAR missions, the bandwidth of each band should be larger than 5 %. In addition, the dual-band antenna with excellent cross polarization discrimination (XPD) and high isolation between elements are required.

II. DBF-SAR SYSTEM

DIFFERENT has a dual-band (X- and Ka-bands) performance which enables it apply in new mission scenarios [3]. The project is planned for operating in a constellation with two or more satellites involved.

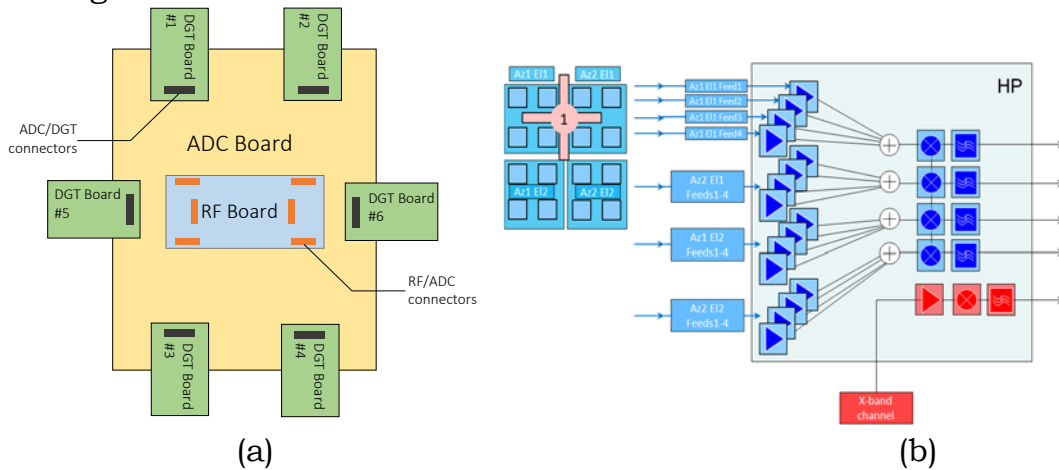


FIG. 1 – (a) Architecture of radar module in DIFFERENT: RF board, ii) analog to digital converters (ADC) board and iii) digital (DGT) boards. (b) Block diagram of active summation of the RF frontend.

The DIFFERENT concept mission could not only fly in tandem with an existing X-band master satellite but also as a swarm of small platforms to collect the Ka-band data. The architecture of DIFFERENT radar module demonstrator consists of four main blocks: i) RF board, ii) analog to digital converters (ADC) board and iii) digital (DGT) board. These blocks are connected through interfaces, as shown in Fig. 1 (a). The RF board is composed of 6 X-band and 96 Ka-band (24 in elevation and 4 in azimuth) dual-polarized antenna elements. Every 2×2 Ka-band elements are active combined and formed a channel, as shown in Fig. 1 (b). The function of each RF MMIC unit is to down-convert the received V- and H-pol signals to an intermediate frequency (IF) band. The down-converted signals are processed in the digital backend block, which contains 60 ADCs (see ADC board in Fig. 1). After digitization, the IF signals are pre-processed in the Digital Beamforming Network (DBFN). There are in total

4 × 2 DBFN blocks. In each DBFN unit, the digitized data corresponding to all elevation channels, specific azimuth channel and polarization are weighted and combined.

III. RF BOARD

A. Stack-Up Structure

The RF Board consists of a 16 layers PCB hybrid stack-up where are integrated the radiating elements, the MMICs and the distribution networks. Fig. 2 shows the stack-up configuration of the proposed RF board. The radiating elements are implemented using metal layers from layer 1 to layer 8. A laser cavity is realized in the upper part to accommodate MMICs. The striplines and microstrips are connected to the microstrips on L16 via the vertical transition to give access the active devices (MMIC).

LAYER NAME		TICKNESS	MATERIAL
L16	MICROSTRIP	0,114mm	Copper
L15	GROUND	0,127mm	Rogers 3001
L14	GROUND	0,114mm	Copper
L13	STRIPLINE (LO)	0,127mm	Rogers 5880
L12	GROUND	0,114mm	Copper
L11	STRIPLINE1	0,127mm	Rogers 5880
L10	GROUND	0,038mm	Rogers 3001
L9	STRIPLINE2	0,127mm	Rogers 5880
L8	GROUND	0,038mm	Rogers 3001
L7	STRIPLINE_KA	0,254mm	Rogers 5880
L6	GROUND	0,038mm	Rogers 3001
L5	KA PATCH DRIVEN, X FEED	0,127mm	Rogers 5880
L4	X BAND DIPOLE, KA PATCH	0,038mm	Rogers 3001
L3	X BAND DIPOLE	1mm	Rohacell
L2	X BAND DIPOLE, KA PATCH	0,038mm	Rogers 3001
L1	X BAND DIPOLE, KA PATCH	0,127mm	Rogers 5880

FIG. 2 – The stack-up of the proposed RF Board.

B. Integrated X/Ka-Band Dual-Polarized Array Feed

Fig. 3 shows the configuration of the X- and Ka-band radiating elements and their stack-up structures (from layer 1 to layer 8 of the RF board). The X-band radiating element is a pair of cross-dipole antenna, which is printed on the both sides of a substrate, as shown in Fig. 3(a). The dipoles are proximately coupled using microstrips. The X band antenna is designed to work at 9.6 GHz with bandwidth of 300 MHz. To further enhance the radiation performance, parasitic dipoles are added above the driven dipoles with a foam of 2 mm between them.

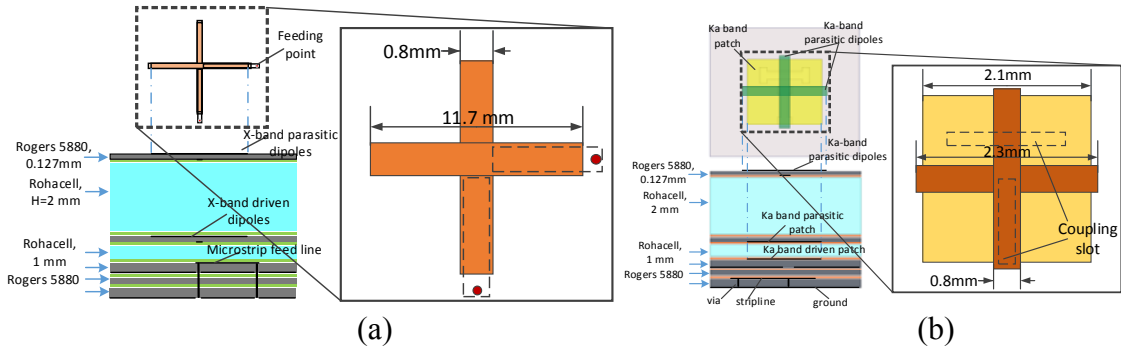


FIG. 3 – Configuration of radiating elements: (a) X-band, (b) Ka-band.

The Ka-band radiating element is a patch antenna, which is fed using stripline through the slots in the ground plane as shown in Fig. 3(b). The patch is designed to work at 35.75 GHz with the bandwidth over 1 GHz. The driven patch of Ka-band and the feed of X-band are in the same layer. A pair of cross parasitic dipoles are added on the uppermost board for improving the performance of radiation and gain.

IV. ADC BOARD

The purpose of the ADC board is to digitalize the baseband signals provided by the RF board. A 10 layers PCB stackup has been used to integrate Analog to Digital Converters (ADCs), distribution networks, filters, capacitors and connectors. The ADC board is composed by two sections: analog section and digital section. The baseband signals coming from the analog section are digitalized by 60 ADCs (Texas Instruments ADS5527) integrated in the upper layer of the board. Proper synchronization between ADCs is guaranteed by a clock distribution network.

V. CONCLUSION

A novel X/Ka-band dual-polarized DBF-SAR system within the DIFFERENT project is presented. The aim of DIFFERENT is to develop next-generation space-borne SAR systems applied in the future small or micro satellites. The SAR concept and techniques such as multi-static, digital beam-forming, reflector-based dual-band dual-polarized aperture-shared antenna array and the integration are presented.

REFERENCES

- [1] P. Zebker, T. Farr, R. Salazar and T. Dixon, "Mapping the world's topography using radar interferometry: the TOPSAR mission," Proc. IEEE, vol. 82, no. 12, pp. 1774-1786, Dec. 1994.
- [2] M. Martin, P. Klupar, S. Kilberg and J. Winter, "Techsat 21 and revolutionizing space missions using microsattellites," 15th Am. Inst. Of Aeronaut. And Astronaut Conf. on Small Satellites 2001, Utah, USA, 2001.
- [3] James Tsui: Digital techniques for wideband receivers. SciTech Publishing, 2004.

ADDITIVE MANUFACTURING OF METAL PASSIVE WAVEGUIDE COMPONENTS

M. Lumia⁽¹⁾, M. Lorusso⁽²⁾

- 1) Istituto di Elettronica e di Ingegneria dell'Informazione e delle Telecomunicazioni (IEIIT), Consiglio Nazionale delle Ricerche (CNR), Corso duca degli Abruzzi 24, 10129 Turin, Italy
mauro.lumia@ieiit.cnr.it
- 2) Center for Space Human Robotics, Istituto Italiano di Tecnologia (IIT), C.so Trento 21, 10129 Turin, Italy
Massimo.Lorusso@iit.it

Abstract

This paper reports a study on the applicability of Direct Metal Laser Sintering to the manufacturing of passive waveguide components. Different test RF benchmarks in K-band [17.5, 19.5] GHz, Ka-band [26, 34] GHz and Q-band [35, 50] GHz have been developed. Subsequently, two stop-band filters in Ku/K-band [12, 22] GHz have been designed, manufactured and tested. This study has been carried out jointly by CNR-IEIIT and IIT.

Index Terms – Additive manufacturing, Direct metal laser sintering, Ku/K band, Stop-band filters

I. INTRODUCTION

Additive manufacturing (AM) allows the production of complex shape and structures without molds directly from a three-dimensional (3D) computer aided design (CAD) model. Direct Metal Laser Sintering (DMLS) is an AM technology that enables the manufacturing of 3D components from metal powders [1], [2]. It offers several advantages, such as the integration of RF functionalities in a single part with complex shape, minimization of mass and envelope, reduction of lead time and costs [3], [4]. However, the application of DMLS to the manufacturing of passive waveguide components is currently limited by some technological aspects. The most important factors to evaluate are roughness, accuracy, electrical conductivity and repeatability. In order to assess the impact of these parameters on the RF performance, test lines in Ka and Q-bands, and a resonant cavity in Ku/K band has been designed. Then, two different Ku/K-band filters have been designed and tested. An aluminum alloy (AlSi10Mg) and a titanium alloy (Ti6Al4V) have been used in this work, both processed via an EOSINT M270 Xtended machine.

II. DMLS TECHNOLOGY

DMLS is an AM technology that uses a high-energy laser beam to heat and melt the metal powder, which has been racked across the build

area using a blade powder levelling roller. After finishing a layer, the built platform is lowered by one layer thickness and a new powder bed is spread. The process is realized in a protected atmosphere (normally argon). [1], [4].

Generating a CAD model of the part to be manufactured is the first step in the DMLS process. After generating the CAD model, a sequence of process planning steps is needed to enable an efficient and accurate manufacture of the part: orientation determination, support structure generation and slicing. The first two steps are interrelated. Support generation depends on the orientation since, only after an orientation is specified, can be determined the overhanging parts of the object that need support. An overhang zone corresponds to a down-facing part surface where powder has to be melted on top of loose powder particles instead of an earlier solidified part. The melt pool created during scanning rests on loose powder rather than on solid material. The poor thermal conductivity of powder material leads to higher temperatures in the overhang areas and in the associated higher residual stresses after final cooling. These diverse effects can cause various quality problems such as curling, warping, distortion, undesired surface roughness and complete fabrication failure in certain cases [5], [2]. However, the build orientation is chosen to be the one that has the least area to be supported. Orientation also affects the mechanical properties of the part, since the mechanical properties are anisotropic in nature.

III. TEST COMPONENTS

Several rectangular, circular and square waveguide lines in Ka-band [26, 34] GHz and Q-band [35, 50] GHz have been designed. The lines have been made of AlSi10Mg alloy powder. The dimensional uncertainties is in the order of 50 μm and the equivalent surface resistivity has been estimated at roughly 10 $\mu\Omega$ cm. These parameters have been evaluated by applying a non-linear best-fitting procedure between the measured and the simulated value of the scattering parameters.

Two prototypes of a resonant cavity operating in the K band [17.5, 19.5] GHz have been manufactured. The two components are made of Ti64 and AlSi10Mg alloy, respectively. The cavity has been designed with a narrow bandwidth in order to increase the sensitivity of its electrical response to the process parameter. The dimensional uncertainties for the AlSi10Mg prototype is in the order of 60÷100 μm , while it is in the order of 40÷60 μm for the Ti64 sample. The two cavities have been measured via a Vector Network Analyzer (VNA) before and after silver plating. The equivalent surface resistivity of the AlSi10Mg prototype has been estimated at 40 $\mu\Omega$ cm. This value is higher than the one estimated for AlSi10Mg waveguide lines because of the cavity sensitivity to geometrical errors and surface roughness. The equivalent surface resistivity of the Ti64 prototype has been estimated at roughly 250 $\mu\Omega$

cm. The value is significant higher than the AlSi10Mg one due to the different electrical resistivity of the two materials. After silver plating, the two prototypes exhibit the same estimated electrical conductivity of $8 \mu\Omega$ cm.

IV. KU/K-BAND FILTERS

On the basis of the experimental results of the test components, two different waveguide stop-band filter configurations, suitable for satellite communication systems operating in Ku/K-band [12, 22] GHz, have been developed. The pass-band is [12.5, 15.3] GHz and the stop-band is [17.5, 22] GHz.

A fifth-order filter in WR51 waveguide has been the first configuration developed (FIG. 1). Step/stub resonators have been arranged along alternating sides of the main waveguide channel. Edges and corners have been rounded in order to reduce thermal stress concentrations and to increase the accuracy of the process. In order to minimize supports and overhanging structures, a sixth-order step/stub filter has subsequently been developed. Thanks to the geometrical optimized design, this component has been manufactured in a vertical position. Indeed, supports have only been used for the WR51 flanges. Different prototypes of the two filter configurations have been manufactured and measured via a VNA. The overall properties of the two configurations are summarized in Table I.

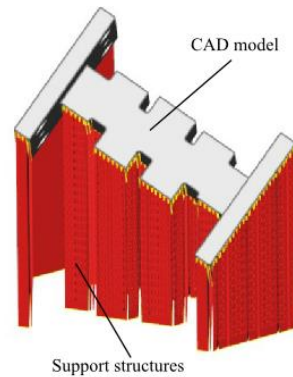


FIG. 1 - Orientation and support structures for the fifth-order Ku/K-band filter.

TABLE I - PROPERTIES OF KU\K-BAND FILTER PROTOTYPES

Parameter	AlSi10Mg 5 th -order	AlSi10Mg 5 th -order	AlSi10Mg 6 th -order	AlSi10Mg 6 th -order
<i>Coating</i>	No Coating	Silver	No Coating	Silver
<i>Return loss</i>	≥ 23 dB	≥ 23 dB	≥ 25 dB	≥ 25 dB
<i>Insertion loss</i>	≤ 0.1 dB	≤ 0.07 dB	≤ 0.1 dB	≤ 0.07 dB
<i>Rejection</i>	≥ 40 dB	≥ 40 dB	≥ 50 dB	≥ 50 dB
<i>Estimated resistivity</i>	$20 \mu\Omega$ cm	$8 \mu\Omega$ cm	$14 \mu\Omega$ cm	$8 \mu\Omega$ cm

In addition to provide a higher out-of-band rejection, the sixth-order filter has been assessed to allow for a more reliable manufacturing process. Moreover, the difference in the estimated equivalent surface resistivity suggests a better surface finish and accuracy of the sixth-order filter. This configuration has further been improved by optimizing the mechanical design in order to eliminate the supports for the WR51 flange. More details on geometry and measurements of both configurations of the sixth-order filter will be presented during the conference.

V. CONCLUSIONS

DMLS technology has been successfully applied to the manufacturing of passive waveguide components. Two stop-band filters have been designed, manufactured and tested. Geometrical optimization has been used in order to improve the accuracy and the electrical performances of the components. Future works will consist in a more detailed study of Q-band components and in the development of a compact antenna feed-chain for satellite communication systems.

REFERENCES

- [1] D. Manfredi, F. Calignano, M. Krishnan, R. Canali, E. P. Ambrosio, S. Biamino, D. Ugués, M. Pavese and P. Fino, "Additive Manufacturing of Al Alloys and Aluminium Matrix Composites (AMCs)," in *Light Metal Alloys Applications*, Waldemar A. Monteiro, 2014.
- [2] F. Calignano, «Design optimization of supports for overhanging structures in aluminum and titanium alloys by selective laser melting,» *Materials & Design*, vol. 64, pp. 203-213, 2014.
- [3] P. Booth and E. V. Lluch, "Performance Enhancement for Waveguide Filters Using Additive Manufacturing," in *International Workshop on Microwave Filters*, Toulouse, France, 2015.
- [4] J. A. Lorente, M. M. Mendoza, A. Z. Petersson, L. Pambaguian, A. A. Melcon and C. Ernst, "Single part microwave filters made from selective laser melting," in *39th European Microwave Conference (EuMC)*, Rome, 2009.
- [5] A. Uriondo, M. Esperon-Miguez and S. Perinpanayagam, "The present and future of additive manufacturing in the aerospace sector: A review of important aspects," *Journal of Aerospace Engineering*, vol. 229, no. 11, pp. 2132-2147, Sept 2015.
- [6] T. Craeghs, S. Clijsters, E. Yasa, F. Bechmann, S. Berumen and J. P. Kruth, "Determination of geometrical factors in layerwise laser melting using optical process monitoring," *Optics and Lasers in Engineering*, vol. 49, no. 12, pp. 1440-1446, July 2011.

A CPW-FED PRINTED LPDA FOR WIRELESS COMMUNICATIONS

G. A. Casula⁽¹⁾, G. Montisci⁽¹⁾, P. Maxia⁽¹⁾, G. Muntoni⁽¹⁾, G. Mazzarella⁽¹⁾

⁽¹⁾ Dipartimento di Ingegneria Elettrica ed Elettronica , Università degli Studi di Cagliari, 09123 Cagliari, Italy
e-mails: a.casula@diee.unica.it, giorgio.montisci@unica.it,
paolo.maxia@gmail.com chuckn@tiscali.it, mazzarella@diee.unica.it

Abstract

A dual-band printed Log-periodic dipole array (LPDA) antenna for wireless communications, designed on a PET substrate and implemented by inkjet printing using a conductive ink, is presented. The LPDA has been designed using a general purpose 3D CAD, CST Microwave Studio.

Index Terms—Log-periodic arrays, Multiband Antennas, PET Inkjet-Printed Antenna, Wireless communications

I. INTRODUCTION

The recent developments in mobile communications and wireless industry, require the use of multiband antennas able to cover the whole WLAN services, and ensure also a wideband behavior in order to obtain high data rate transmission. The use of printed technology is the best choice, since it allows the design of planar antennas with high performance, compact size, and low cost, and which can be easily integrated into front-end circuits [1, 2], providing low profile and a relatively simple fabrication. In the past literature, a number of printed multiband antennas have been proposed, and implemented using robust and cheap materials as dielectric substrates [1-3], and the current leading technology for designing cheap antennas makes use of plastic or paper substrates, with metal tracks realized through conductive inks [4-6]. In this work, we present a multiband printed log-periodic dipole array (LPDA) fed by a grounded coplanar waveguide (GCPW), working both in the S and C frequency bands (from 2.4 to 2.484 GHz, and from 5.2 to 5.8 GHz), designed on a PET substrate and implemented by inkjet printing using a conductive ink. Although the radiating structure is similar to the one proposed by the same authors in [3], and the feeding network is based on the configuration presented in [7], the design of the proposed antenna cannot be considered an easy application based on our previous works [3, 7]. A number of significant problems, in fact, have been faced, and addressed, during the design process of this antenna, which have not involved the antennas discussed in [3, 7]. These difficulties are due both to the chosen substrate and technology, and to the multiband radiating structure. The designed LPDA presented here, shares all the advantages of the configurations proposed in [3] and [7], and, in addition, it has a very low production cost, thanks to the use of a PET substrate and conductive ink in the fabrication process. The LPDA design has been performed

using a general purpose 3D CAD, CST Microwave Studio, and then manufactured. The measured results are in very good agreement with the simulations.

II. ANTENNA DESIGN

The proposed printed LPDA is fed by a GCPW printed on the two sides of a PET dielectric slab, and the array dipoles are alternately connected on the two layers of the GCPW (Fig.1). In order to obtain the typical alternate feeding of the elements of the LPDA, necessary to radiate an end-fire radiation pattern, the central conductor of the coplanar waveguide is connected to the ground of the through a via-hole. The structure resembles a standard LPDA, therefore the standard design of a CPW-fed LPDA [7] has been applied, separately, to two different groups of dipoles [3], designed to operate each one in a specific frequency band (namely in the S-band and in the C- band). The two groups of dipoles have been then connected together, obtaining the configuration shown in Fig. 1. We require an average directivity of 8 dBi for both the groups of dipoles of the printed LPDA, obtaining $\tau = 0.88$ and $\sigma = 0.16$. Following [8], we get $N = 4$ dipoles for the S-Band, and $N = 8$ dipoles for the C-Band, with a log-periodic antenna aperture angle 2α equal to 10.62° . The distance d between the two groups of dipoles has subsequently been optimized, aiming at the best input match of the whole antenna. The final distance $d = 12.39$ mm is relatively small, and comparable to the spacing between two adjacent dipoles of the LPDA, resulting in a very compact multiband antenna. The antenna substrate is a PET film, with a dielectric constant $\epsilon_r = 3.0$, a thickness of 1 mm and a loss tangent of 0.002. The metallization is made by inkjet printing, using a silver-based ink (Cabot Conductive Ink CCI-300) which has a conductivity of 90 MS/m. The electrical contact between SMA and conductive ink has been realized through conductive glue. Figure 1c shows a photo of the manufactured LPDA antenna. We have selected the characteristic impedance of the GCPW feeding line equal to 50Ω , so as to obtain an easy matching with the standard SMA connectors. The GCPW parameters a and b , shown in Fig. 1b, are computed using the well-known GCPW design equations [9]. The spacings S_n are computed according to [8].

TABLE I - GEOMETRY OF THE PRINTED LPDA. ALL UNITS ARE IN [MM].

Dipole	$L_{n,\text{SBand}}$	$W_{n,\text{SBand}}$	$S_{n,\text{SBand}}$	$L_{n,\text{CBand}}$	$W_{n,\text{CBand}}$	$S_{n,\text{CBand}}$
8	-	-	-	9.50	1.92	6.08
7	-	-	-	8.36	1.69	5.35
6	-	-	-	7.36	1.48	4.71
5	-	-	-	6.48	1.31	4.14
4	23.00	3.10	14.72	5.70	1.15	3.65
3	20.24	2.73	12.95	5.02	1.01	3.21
2	17.81	2.40	11.40	4.41	0.89	2.82
1	15.67	2.11		3.88	0.78	

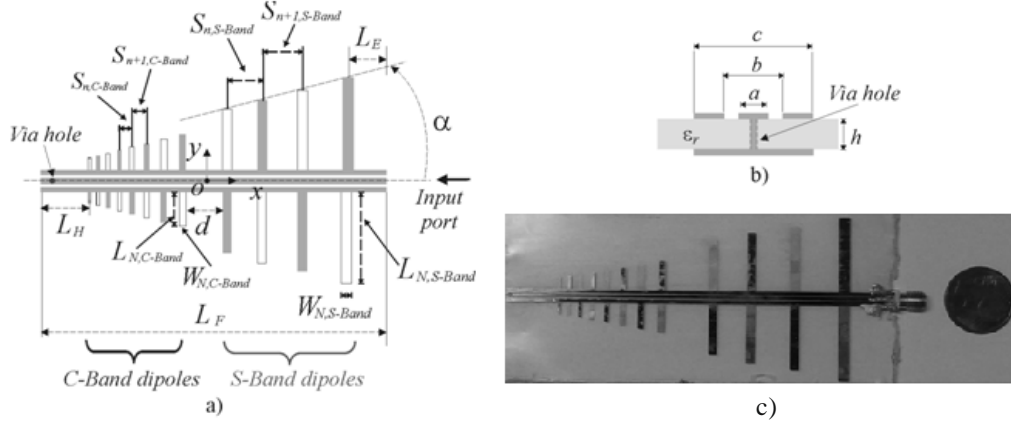


FIG. 1–(a) Antenna Layout (Top Layer). $L_F = 111.60$ mm, $L_H = 15.60$ mm, $L_E = 12.55$ mm. (b) Grounded Coplanar Waveguide transverse section, with the via hole connecting the central conductor of the GCPW with the bottom feeding line: $a=1.125$ mm; $b=1.575$ mm; $c=4.027$ mm. (c) Photo of the LPDA antenna.

III. RESULTS

The LPDA antenna, designed in Section II, has been realized (see Fig. 1c) and fully characterized. The comparison between the simulated and measured reflection coefficient of the antenna is shown in Fig. 2a, and it is below -10 dB both in the S and C band (2.4–2.484 GHz, 5.2–5.8GHz). The numerical and experimental data are in good agreement, and the out-of-band rejection is satisfactory, especially considering that no stop-band filters have been used in the antenna design. The simulated and measured realized gain of the complete antenna are reported in Fig. 2b. The antenna realized gain is about equal to 5.5 dB in the S-Band, varies from 6 to 7 dB in the C-Band, and quickly decreases out of the operating frequency bands. The simulated E-Plane and H-Plane far field patterns of the designed antenna are reported in Fig. 2c. The antenna has an end-fire radiation pattern within the design frequency bands (2.4–2.484 GHz and 5.2–5.8 GHz), while it quickly deteriorates very rapidly out-of-band, presenting also unsatisfactory values for both SLL and Front-to-Back ratio.

IV. CONCLUSION

A multiband printed Log-periodic dipole array (LPDA) antenna for wireless communications, covering both the WLAN-UHF band from 2.4 GHz to 2.5 GHz and the WLAN-SHF band from 5.2 GHz to 5.8 GHz has been presented. The antenna is fed by a GCPW and implemented by inkjet-printing conductive ink on a PET substrate. The simulated and measured results are in a good agreement, showing a very good input matching, an end-fire radiation pattern, and a good rejection out of its operating frequency bands.

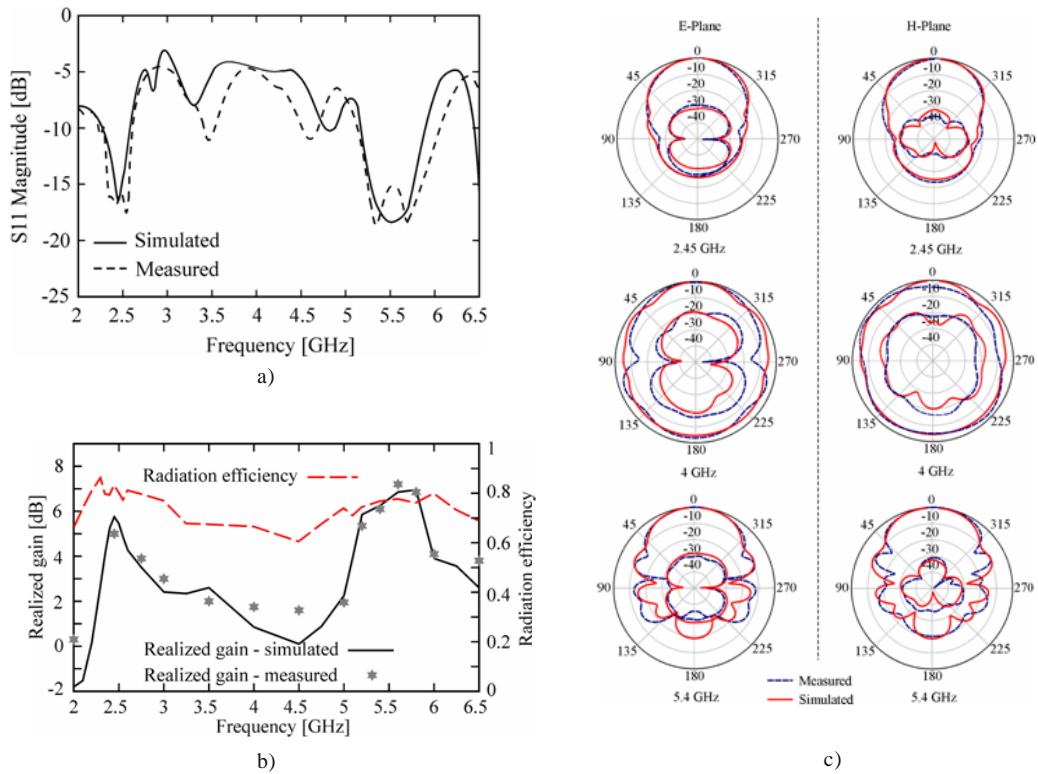


FIG. 2—(a) Reflection coefficient of the designed LPDA antenna. (b) Realized Gain of the designed LPDA antenna. (c) Simulated Co-Polar and Cross-Polar normalized radiation pattern of the designed LPDA antenna.

REFERENCES

- [1] R. K. Joshi and A. R. Harish, "A modified bow-tie antenna for dual band applications," *IEEE Antennas Wir. Prop. Lett.*, vol.6, pp.468–471, Oct. 2007.
- [2] X. Q. Zhang, Y. C. Jiao, and W. H. Wang, "Compact wide tri-band slot antenna for WLAN/WiMAX applications," *El. Lett.*, vol.48, Jan. 2012.
- [3] G. A. Casula, P. Maxia, "A Multiband Printed Log-Periodic Dipole Array for Wireless Communications," *International Journal of Antennas and Propagation*, vol. 2014, Article ID 646394, 6 pages, 2014.
- [4] Tursunjan Yasin and Reyhan Baktur, "Inkjet Printed Patch Antennas on Transparent Substrates", 2010 APS-URSI Intern. Symp., Toronto, Canada.
- [5] G. A. Casula, G. Montisci and G. Mazzarella "A Wideband PET Inkjet-Printed Antenna for UHF RFID", *IEEE Ant. Wir. Prop. Lett.*, vol.12, 2013.
- [6] T.W.Koo, D.Kim, J.I.Ryu, H.M.Seo, J.G.Yook, and J.C.Kim, "Design of a label typed UHF RFID tag antenna for metallic objects," *IEEE Antennas Wireless Propag. Lett.*, vol. 10, pp. 1010–1014, 2011.
- [7] G.A. Casula., P. Maxia, G. Montisci, G. Mazzarella, F. Gaudiomonte, "A Printed LPDA Fed by a Coplanar Waveguide for Broadband Applications", *IEEE Antennas and Wireless Prop. Letters*, vol. 12, p. 1232-1235, 2013.
- [8] R. Carrel, "The Design of Log-Periodic Dipole Antennas," *IRE International Convention Record*, Vol.9, pp. 61-75, March 1961.
- [9] B.C. Wadell, *Transmission Line Desing Handbook*, Artech House, 1991.

NONREDUNDANT SPHERICAL NEAR-FIELD – FAR-FIELD TRANSFORMATION FOR A NONCENTRED ANTENNA

F. D’Agostino, F. Ferrara, C. Gennarelli, R. Guerriero, M. Migliozi

D.I.In., Università di Salerno, via Giovanni Paolo II, 132 - 84084 Fisciano, Italy
{fdagostino, flferrara, cgennarelli, rguerriero, mmigliozi}@unisa.it

Abstract

An efficient probe compensated near-field – far-field (NF–FF) transformation technique with spherical scanning for noncentred antennas, which requires a minimum number of NF data, is developed in this work, by applying the nonredundant sampling representations of electromagnetic field and modelling the antenna under test (AUT) by a sphere. The interest for it arises from the fact that, for practical constraints, it could be not possible a centred mounting of the AUT on the scanning sphere centre. In fact, the number of NF data needed by classical spherical NF–FF transformation can considerably grow for an offset mounting, due to the increase of the radius of the minimum sphere containing the AUT and centred on the scanning sphere centre.

Index Terms – Antenna measurements, NF–FF transformations, nonredundant representations of electromagnetic fields, spherical scanning.

I. INTRODUCTION

Among the near-field–far-field (NF–FF) transformations, that adopting the spherical scanning [1] is particularly appealing, because of its unique characteristics to allow the complete antenna pattern recovery and to avoid the error due to the scanning zone truncation. The classical spherical NF–FF transformation [1] has been modified in [2] by exploiting the spatial quasi-bandlimitation properties of the electromagnetic (EM) fields [3]. In particular, the choice of the highest spherical wave has been rigorously determined by these properties instead to be fixed by a rule-of-thumb related to the minimum sphere enclosing the antenna under test (AUT), and the number of NF data to be acquired on the parallels has resulted to be decreasing towards the poles. The nonredundant sampling representations of the EM fields [4] have been properly applied in the same paper to develop effective NF–FF transformations, requiring a number of NF data remarkably lower than that needed by the classical transformation [1] when considering a quasi-planar or an elongated AUT, which has been modelled by a prolate or an oblate ellipsoid, respectively. In fact, the NF data required by the classical transformation are efficiently recovered from the acquired nonredundant ones by means of optimal sampling interpolation (OSI) expansions. It is so possible to obtain a remarkable measurement time saving. Alternative nonredundant NF–FF transformations for nonvolumetric antennas have been proposed in [5] by using very flexible modellings to shape them. At last, the aforementioned transformation techniques [2] and [5] have been experimentally assessed in [6] and [7], respectively.

Aim of this work is to properly exploit the nonredundant representations of EM fields to develop a nonredundant NF–FF transformation with spherical scanning for noncentred antennas, namely a NF–FF transformation that requires a minimum number of NF data also when the AUT is mounted in an offset configuration with respect to the scanning sphere centre. In fact, it is not always possible for practical constraints to mount the AUT in such a way that it is centred on the scanning sphere centre. In such a case, the number of NF data

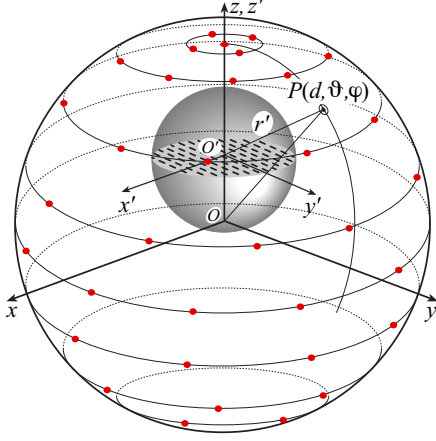


FIG. 1 – Spherical scanning for a noncentred AUT.

needed by the classical NF–FF transformation [1] and the related measurement time can considerably grow, due to the corresponding increase of the radius of the minimum sphere. Accordingly, the development of a nonredundant transformation requiring the same number of NF data in both cases of centred and offset mounting of the AUT is surely worthy.

Let us consider an AUT enclosed in the smallest sphere Σ of radius a able to contain it and a nondirective probe scanning a sphere in the antenna NF region having radius d . The spherical coordinate system $S(r, \vartheta, \varphi)$, with the origin on the scanning sphere centre at O , is adopted to denote an observation point P . The centre O' of the AUT is on the axis z at distance d_s from O . A spherical coordinate system $S'(r', \vartheta', \varphi')$ with the origin at O' and the axis z' coincident with z is also introduced (see Fig. 1). Since the voltage V measured by a nondirective probe has the same effective spatial bandwidth of the antenna field, the nonredundant sampling representations of EM fields [4] can be applied to it. According to these representations, it is convenient to describe the observation surface (the scanning sphere) by meridian curves and azimuthal circumferences, so that in the following we deal with the voltage representation on a curve C described by a parameterization $\underline{r} = \underline{r}(\xi)$. Note that the nonredundant sampling representation for the voltage is relevant to the S' system, wherein the meridian curves and azimuthal circumferences describing the scanning sphere are no longer meridians and parallels. It is also convenient to introduce the “reduced voltage” $\tilde{V}(\xi) = V(\xi) e^{j\gamma(\xi)}$, where $V(\xi)$ is the voltage V_p or V_r measured by the probe or by the rotated probe and $\gamma(\xi)$ is a proper phase function. The error, occurring when $\tilde{V}(\xi)$ is approximated by a band-limited function, becomes negligible as the bandwidth exceeds a critical value W_ξ [4]. Therefore, it can be effectively controlled by choosing a bandwidth equal to $\chi' W_\xi$, where $\chi' > 1$ is an enlargement bandwidth factor.

II. NONREDUNDANT SAMPLING REPRESENTATION ON A SPHERE FOR A NONCENTRED AUT

The bandwidth W_ξ and parameterization ξ relevant to a meridian curve, and the corresponding phase function γ are [4]:

$$W_\xi = \beta a ; \quad \xi = \vartheta' ; \quad \gamma = \beta \sqrt{r'^2 - a^2} - \beta a \cos^{-1}(a/r') \quad (1)$$

where β is the wavenumber.

On an azimuthal circumference, due to the symmetry, γ is constant and it is convenient to choose the angle φ' as parameter. The related bandwidth [4] is

$$W_{\varphi'}(\vartheta') = \beta a \sin \vartheta' \quad (2)$$

In light of the above results, the voltage at P can be evaluated [4] by means of the following two-dimensional OSI expansion:

$$\tilde{V}(\vartheta', \varphi') = \sum_{n=n_0-q+1}^{n_0+q} \left\{ G(\vartheta', \vartheta'_n, \bar{\vartheta}', N, N'') \sum_{m=m_0-p+1}^{m_0+p} \tilde{V}(\vartheta'_n, \varphi'_{m,n}) G(\varphi', \varphi'_{m,n}, \bar{\varphi}', M_n, M''_n) \right\} \quad (3)$$

where $2q$, $2p$ are the numbers of retained samples along ϑ' and φ' , respectively, $n_0 = \text{Int}(\vartheta'/\Delta\vartheta')$, $m_0 = \text{Int}(\varphi'/\Delta\varphi'_n)$, $\vartheta' = q\Delta\vartheta'$, $\bar{\varphi}' = p\Delta\varphi'_n$,

$$\vartheta'_n = n\Delta\vartheta' = 2\pi n/(2N''+1); \quad N'' = \text{Int}(\chi N') + 1; \quad N' = \text{Int}(\chi' W_\xi) + 1 \quad (4)$$

$$\varphi'_{m,n} = m\Delta\varphi'_n = 2\pi m/(2M''+1); \quad M'' = \text{Int}(\chi M'_n) + 1; \quad M'_n = \text{Int}[\chi^* W_{\varphi'}(\vartheta'_n)] + 1 \quad (5)$$

$$\chi^* = 1 + (\chi' - 1)[\sin \vartheta'_n]^{-2/3}; \quad N = N'' - N'; \quad M_n = M'' - M'_n \quad (6)$$

$\chi > 1$ is an oversampling factor needed to control the truncation error [4], $\text{Int}(x)$ denotes the integer part of x , and

$$G(\alpha, \alpha_k, \bar{\alpha}, L, L'') = \Omega_L[(\alpha - \alpha_k), \bar{\alpha}] D_{L''}(\alpha - \alpha_k) \quad (7)$$

Moreover,

$$D_{L''}(\alpha) = \frac{\sin[(2L''+1)\alpha/2]}{(2L''+1)\sin(\alpha/2)}; \quad \Omega_L(\alpha, \bar{\alpha}) = \frac{T_L[2\cos^2(\alpha/2)/\cos^2(\bar{\alpha}/2) - 1]}{T_L[2/\cos^2(\bar{\alpha}/2) - 1]} \quad (8)$$

are the Dirichlet and Tschebyscheff sampling functions, respectively, $T_L(\alpha)$ being the Tschebyscheff polynomial of degree L .

By using the OSI expansion (3), it is possible to accurately evaluate V_p or V_r at any point on the scanning sphere and, in particular, at the points needed by the spherical NF-FF transformation in its original version [1] or as modified in [5].

To practically apply the described procedure, in the measurement step, the coordinates of the sampling points (known in the reference system S') must be expressed in the S one, whereas, in the post-processing step, the coordinates of the points needed by the NF-FF transformation (given in S) must be determined in S' . It is easy to verify that the coordinates in S and S' are related by:

$$\varphi = \varphi'; \quad \vartheta = \tan^{-1}[r'\sin\vartheta'/(r'\cos\vartheta' + d_s)]; \quad r' = -d_s\cos\vartheta' + \sqrt{d^2 - (d_s\sin\vartheta')^2} \quad (9)$$

$$\vartheta' = \tan^{-1}[d\sin\vartheta/(d\cos\vartheta - d_s)] \quad (10)$$

III. NUMERICAL RESULTS

The effectiveness of the proposed nonredundant spherical NF-FF transformation for noncentred antennas has been assessed by several numerical tests. The reported simulations refer to a scanning sphere having radius $d = 30\lambda$ (λ being the wavelength) and to a uniform planar circular array with diameter $2a = 31.2\lambda$, lying in the plane $z = d_s = 11\lambda$. Its elements, symmetrically placed with respect to the plane $x = 0$, are elementary Huygens sources linearly polarized along y and spaced of 0.6λ along the radial and azimuthal lines. Such an AUT has been considered as enclosed in a sphere with radius $a = 15.6\lambda$, centred in O' , whose Cartesian coordinates are $(0, 0, 11\lambda)$. Figures 2 and 3 show representative reconstruction examples of the amplitude and phase of the voltage V_r on the meridian at $\varphi = 90^\circ$. As can be seen, the exact and recovered voltages are practically indistinguishable.

At last, the developed interpolation algorithm has been applied to recover the NF data needed to perform the spherical NF-FF transformation [1], as modified in [5]. The reconstructed FF patterns in the principal planes E and H are compared in Figs. 4 and 5 with the exact ones. As can be seen, the FF reconstruction is everywhere very accurate, in spite of the significantly reduced number of employed NF samples, 27347 instead of 130562 required by the classical

NF–FF transformation with spherical scanning [1].

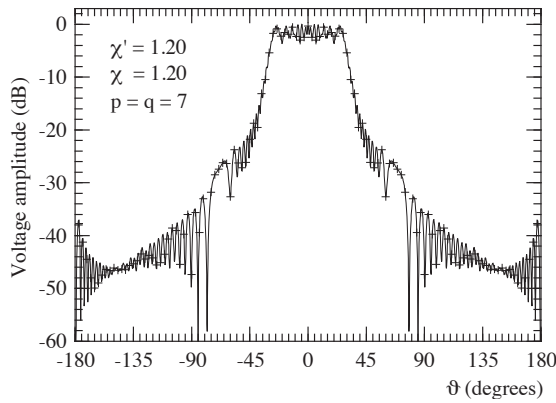


FIG. 2 – Amplitude of V_r on the meridian at $\varphi = 90^\circ$. Solid line: exact. Crosses: interpolated.

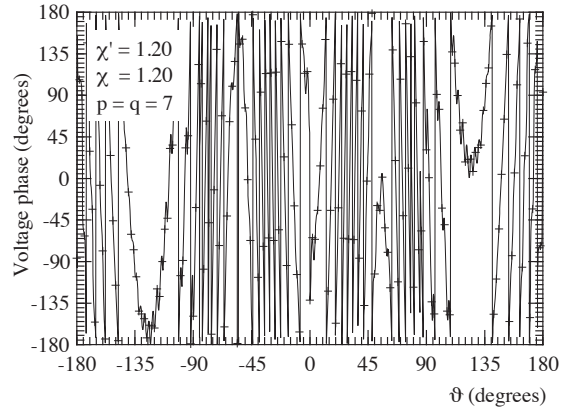


FIG. 3 – Phase of V_r on the meridian at $\varphi = 90^\circ$. Solid line: exact. Crosses: interpolated.

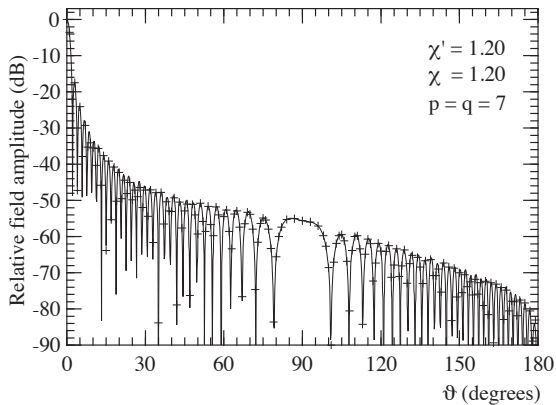


FIG. 4 – E-plane pattern. Solid line: exact. Crosses: reconstructed from NF data.

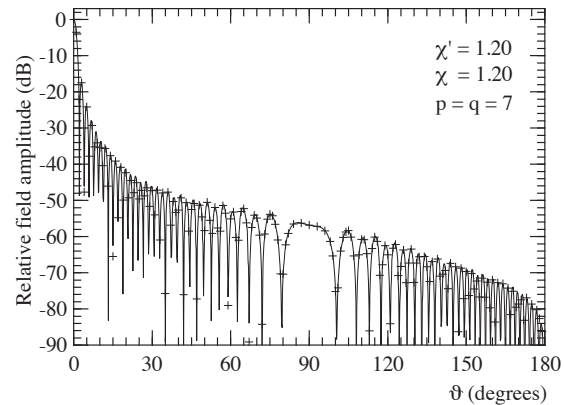


FIG. 5 – H-plane pattern. Solid line: exact. Crosses: reconstructed from NF data.

REFERENCES

- [1] J. Hald, J.E. Hansen, F. Jensen, and F.H. Larsen, “Spherical near-field antenna measurements,” J.E. Hansen Ed., Peter Peregrinus, London, 1998.
- [2] O.M. Bucci, F. D’Agostino, C. Gennarelli, G. Riccio, and C. Savarese, “Data reduction in the NF–FF transformation technique with spherical scanning,” *J. Electromagn. Waves Appl.*, vol. 15, pp. 755-775, 2001.
- [3] O.M. Bucci and G. Franceschetti, “On the spatial bandwidth of scattered fields,” *IEEE Trans. Antennas Prop.*, vol. AP-35, pp. 1445-1455, Dec. 1987.
- [4] O.M. Bucci, C. Gennarelli, and C. Savarese, “Representation of electromagnetic fields over arbitrary surfaces by a finite and nonredundant number of samples,” *IEEE Trans. Antennas Prop.*, vol. 46, pp. 351-359, March 1998.
- [5] F. D’Agostino, F. Ferrara, C. Gennarelli, R. Guerriero, and M. Migliozi, “Effective antenna modellings for a NF–FF transformation with spherical scanning using the minimum number of data,” *Int. Jour. Antennas Prop.*, vol. 2011, ID 936781, 11 pages, 2011.
- [6] F. D’Agostino, F. Ferrara, C. Gennarelli, R. Guerriero, and M. Migliozi, “Non-redundant spherical NF – FF transformations using ellipsoidal antenna modeling: experimental assessments,” *IEEE Antennas Prop. Magaz.*, vol. 55, pp. 166-175, Aug. 2013.
- [7] F. D’Agostino, F. Ferrara, C. Gennarelli, R. Guerriero, and M. Migliozi, “Experimental testing of nonredundant near-field to far-field transformations with spherical scanning using flexible modellings for nonvolumetric antennas,” *Int. Jour. Antennas Prop.*, vol. 2013, ID 517934, 10 pages, 2013.

IMMUNITY TEST SIMULATION IN A MULTIPLE ANTENNA SOURCE STIRRED REVERBERATION CHAMBER

A. De Leo⁽¹⁾, V. Mariani Primiani⁽¹⁾, P. Russo⁽¹⁾, G. Cerri⁽¹⁾

⁽¹⁾ Dipartimento di Ingegneria dell'Informazione, Università Politecnica delle Marche, Via B. Bianche, 60131 Ancona, Italy
g.cerri@univpm.it

Abstract

Multiple antenna source stirring is an alternative technique to realize a reverberation chamber: in the proposed case, 62 monopoles are distributed on the chamber walls and fed two at time, so achieving 1891 combinations. The electromagnetic field distribution and the self and mutual impedances are analytically determinable, and statistics can be predicted through the computation of Cumulative Distribution Functions and Polar Plots. The model can be also extended to simulate an immunity test by inserting a DUT inside the working volume of the chamber. Both a monopole and a loop are analytically modeled to simulate common and differential mode noise. It must be highlighted that all mutual coupling among the transmitting antennas and the DUT are accounted for, in terms of mutual impedances. In the lower frequency range, undermoded condition, the technique takes benefit from the adoption of an out-of-phase feeding of each active couple of antennas that enhances field strength.

Index Terms – reverberation chamber; source stirring; immunity test.

I. INTRODUCTION

Reverberation Chambers (RC) are widely used for Electromagnetic Compatibility (EMC) immunity testing [1], since statistical uniformity and isotropy of the electromagnetic field ensure a significant interference signal. The traditional stirring technique is the mechanical one, based on rotating paddles [2] [3]; reverberation can be also achieved by vibrating the chamber walls [4]. Source stirring techniques represent a valid alternative because they allow nothing moves in the chamber, including fixed walls. In those tests where the frequency stirring is not allowed, therefore multiple antenna radiating into the chamber must be used. The electromagnetic modelling of this stirring method can be carried out by a modal expansion of the field chamber [5], [6]. In [7] the method was theoretically investigated for 62 equally spaced monopoles mounted on the chamber walls, fed two a time, for a total of 1891 combinations. Two simulations of an immunity test in a source stirred reverberation chamber will be presented: in the first one the Device Under Test (DUT) is modeled as a monopole, so investigating the common mode noise effect. In the second one a loop is inserted to evaluate the differential mode immunity. In both cases the interaction between the two fed antennas and the DUT is taken into account and modeled in terms of mutual

impedances. The novelty of the proposed technique, based on the source stirring method, is the capability of using the reverberation chamber environment for effective immunity tests in the low frequency range, where usually mechanically stirred chambers exhibit important limitations.

II. IMMUNITY TEST SCENARIO

The geometry taken into consideration, shown in Fig. 1, is a rectangular cavity having dimensions $a=6\text{m}$, $b=4\text{m}$ and $c=2.5\text{m}$; 62 monopoles are placed in the chamber's wall and each couple of monopoles, and they can be fed varying their relative phase for a total of 1891 combinations. The (DUT) is placed in the working volume of the chamber. The analytical expressions of the fields inside the chamber allow us to evaluate all physical quantities in a closed form, including self and mutual impedances of the antennas, disturbances induced in the DUT.

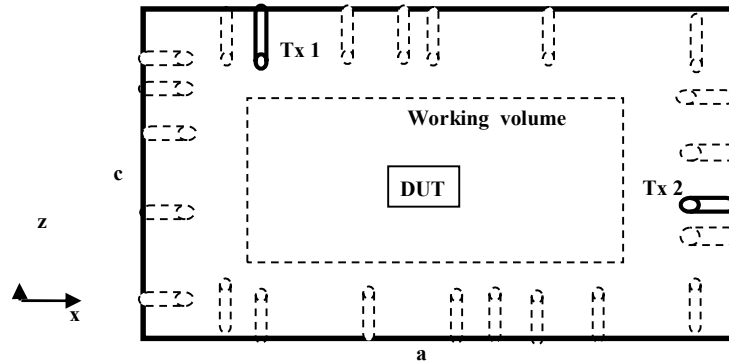


FIG. 1. SCENARIO OF AN IMMUNITY TEST IN A SOURCE STIRRED RC

III. COMMON MODE NOISE PREDICTION

A communication cable of length $h=1\text{m}$ connected to the DUT, having a metallic chassis, is placed inside the cavity onto a dielectric table. Using the image theorem the cable can be modeled as a dipole with length $2h$. The common mode impedance of the cable is $Z_L=300\Omega$.

Fig.2 reports the Cumulative Distribution Function (CDF) of the noise voltage calculated at 137 MHz: it can be observed that the simulated CDF curve matches well the expected CHI-2DOF distribution.

Fig.3 reports the Polar Plot of the V_L : it can be observed that the induced voltages are well centered in both cases and well distributed around the axis origin as expected for a well-stirred chamber.

Data reported reveal that making an immunity test inside a reverberation chamber at lower frequency can give some interesting results, in particular in terms of the maximum value of the induced voltage. This behavior can be related to the presence of strong reactive

fields, which exhibit a maximum coupling when polarized in the cable direction.

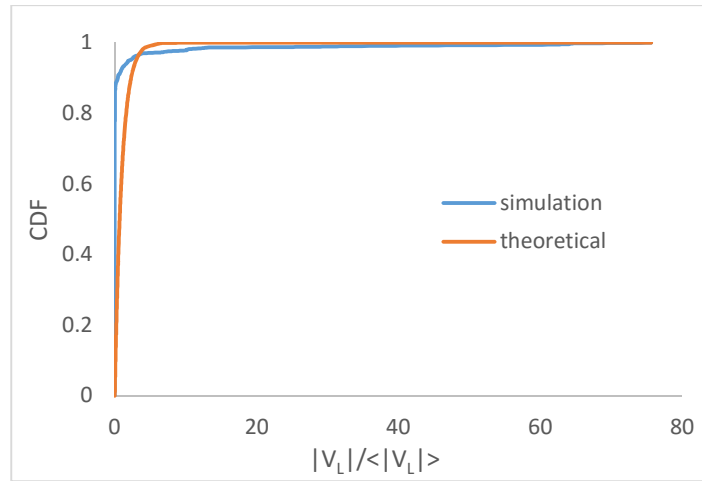


FIG.2. CDF OF THE OUTPUT VOLTAGE AT THE FREQUENCY F=137 MHz

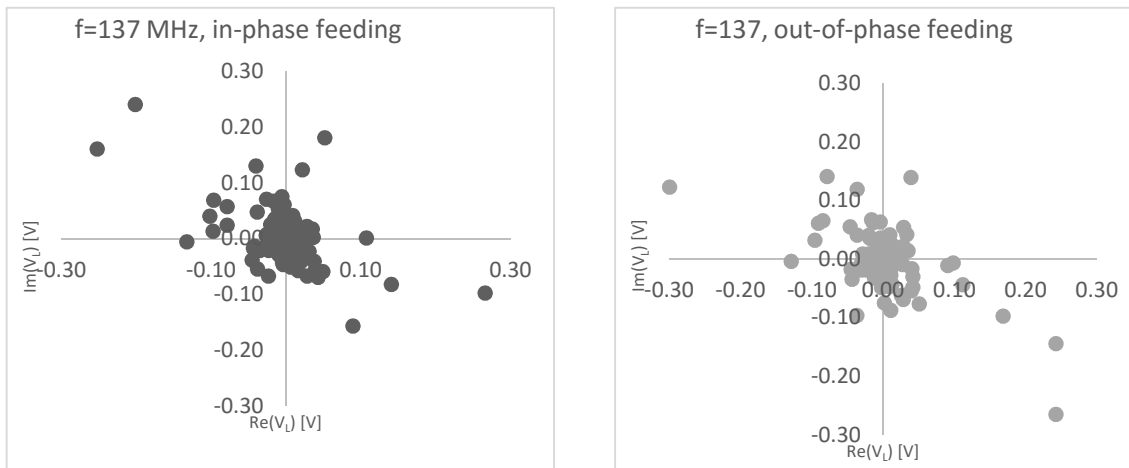


FIG. 3. POLAR PLOT OF THE OUTPUT VOLTAGE AT THE FREQUENCY F=137 MHz

IV. DIFFERENTIAL MODE NOISE PREDICTION

The insertion of a receiving loop, within the chamber working volume, has the scope to simulate a common mode induced noise.

A loop could represent a differential mode structure, like a PCB closed circuit, and the voltage induced by the chamber field could represent the quantity responsible for the circuit failure during an immunity test.

Fig. 4 shows the Polar Plot of the output voltage; values are normalized to the square root of the incident power (P_{inc}) and to the square root of the net power into the chamber (P_{ch}).

The output voltage was also measured using a traditional reverberation chamber based on mechanical stirring. Compared to a mechanical stirring technique, the output voltage to the square root of the incident power is higher using the presented source stirring technique and also the statistics of the output voltage is better.

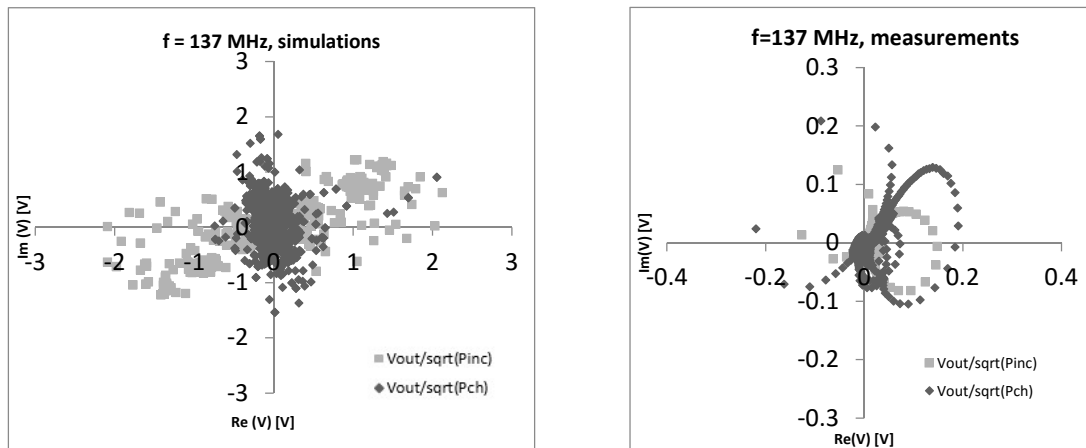


FIG.4 POLAR PLOT OF THE OUTPUT VOLTAGE FOR A LOOP.

V. CONCLUSION

A source stirring technique, based on the placement of 62 dipoles fed two a time for a total of 1891 combinations, was analyzed in the low frequency range. The field computation is based on the well known formulation of the interior problem for resonant cavities, and the presented results, in particular the simulated common and differential mode induced voltage represent examples of simulated immunity tests.

REFERENCES

- [1] Electromagnetic compatibility (EMC) - Part 4-21: "Testing and measurement techniques - Reverberation chamber test methods", 1st ed., International Standards- IEC 61000-4-21, GENEVA, Switzerland, Aug. 2003.
- [2] J. Clegg, A.C. Marvin, J.F. Dawson, S.J. Porter, "Optimization of stirrer designs in a reverberation chamber," *IEEE Trans. on Electromagnetic Compatibility*, , vol.47, no.4, pp. 824- 832, Nov. 2005
- [3] F. Moglie, V. Mariani Primiani, "Analysis of the Independent Positions of Reverberation Chamber Stirrers as a Function of Their Operating Conditions," *IEEE Trans. on Electromagn. Compatibility*, vol.53, no.2, pp.288-295, May 2011
- [4] F. Leferink, J. C. Boudenot, W. Van Etten, "Experimental results obtained in the vibrating intrinsic reverberation chamber," *Proc. IEEE Int. Symp. Electromagnetic Compatibility*, 639-644, Washington, 21-25 Aug. 2000.
- [5] Van Bladel, *Electromagnetic Fields*, Second Edition, John Wiley & Sons, 2007, pp. 509-562.
- [6] G. Cerri, V. Mariani Primiani, C. Monteverde, P. Russo "A Theoretical Feasibility Study of a Source Stirring Reverberation Chamber" *IEEE Trans. on Electromagnetic Compatibility*, vol.51, n.1, pp. 3-11, Feb. 2009.
- [7] Russo, P.; Primiani, V.M.; Cerri, G., "An efficient model for the field analysis in source stirred reverberation chambers," *Electromagnetic Compatibility (EMC EUROPE)*, 2013 International Symposium on , vol., no., pp.420-424, 2-6 Sept. 2013 *Proceedings of the EMC Europe 2012*, Rome.

BROADBAND TEST-SOURCE FOR ANTENNA MEASUREMENTS WITH UNMANNED AERIAL VEHICLES

F. Paonessa

Istituto di Elettronica e di Ingegneria dell'Informazione e delle
Telecomunicazioni (IEIIT), Consiglio Nazionale delle Ricerche (CNR)
C.so Duca degli Abruzzi 24, 10129 Torino, Italy
fabio.paonessa@ieiit.cnr.it

Abstract

In the last years, an innovative system to measure the radiation pattern of VHF and UHF antennas for radio astronomy has been presented [1]. The system exploits a small Unmanned Aerial Vehicle as a radio frequency test-source to characterize receiving antennas and arrays on the ground. In this work, a broadband (50 MHz - 650 MHz) test-source antenna has been designed in order to both improve the measurement accuracy at the lowest operating frequencies and enable multi-frequency measurements.

Index Terms – UAV, antenna measurements, radiation pattern.

I. INTRODUCTION

In the last years, an innovative strategy for antenna measurements in the VHF and UHF bands has been developed [1]. Such a novel technique exploits an Unmanned Aerial Vehicle (UAV) as a radio-frequency (RF) test source in order to measure the radiation pattern of a receiving antenna placed on the ground. Several experiments to radio astronomical antennas provided outstanding results, both with single elements [2] and arrays [3] [4].

In order to operate as a test source, the drone was originally equipped with a RF transmitter and a thin cylindrical dipole, whose length was selected according to the frequency to be measured. An example is shown in Fig. 1, where a 2-m long dipole was used for measurements at 50 MHz. This solution, which is already large as far as the UAV flight stability is concerned, does not exhibit a good matching at 50 MHz (the resonance is at about 70 MHz, see Fig. 2 dotted line). Therefore, the receiving measurement system on the ground is required to have a sufficient dynamic range to compensate for the antenna mismatch loss.

Moreover, it should be pointed out that reference antennas to calibrate the measurement system are not easily available at these low-frequencies. Therefore, the AUT gain measurement is carried out by means of an accurate characterization of all the system components of the RF chain (RF generator, balun, source antenna, cables, LNA). In this



FIG. 1 – The UAV equipped with the 2-m long dipole and the RF transmitter (white box below the arms).

framework, a mismatched source antenna would have a significant effect on the overall error budget.

In order to both improve the measurement accuracy at low frequencies and provide a larger operating bandwidth to perform measurements at multiple frequencies, a broadband antenna has been designed. It should be pointed out that the UAV is a battery-powered multicopter of about 80 cm width. Such a low-cost craft is versatile, as it requires little time-to-fly and few personnel on the measurement field. On the other hand, its maximum payload is limited to 1.5 kg. For these reasons, and to limit the wind resistance, a wire antenna is still the most appropriate choice.

The required operating frequency range is from 50 MHz to 650 MHz. Inside such a large band (13:1), a -3 dB matching would be an acceptable result in order not to give rise to a large error on the estimated radiated power. In addition, the maximum output power of the RF transmitter is 8 dBm, which is a small enough value to accept a fraction of power being reflected.

It should be noted that the test source radiation pattern will be removed from the measured power pattern in order to extract the AUT pattern [5]. Therefore, it should be as smooth as possible within $\pm 70^\circ$ from the nadir direction. Indeed, a source pattern with a complex behavior will be more difficult to model and characterize. Finally, the test-source should have a linear polarization and a low cross-polarization level (-30 dB or less) on the principal planes.

II. THE ANTENNA DESIGN

A wire bow-tie structure has been chosen for the application owing to its limited volume and weight [6]. The aperture angle of the bow-tie has been chosen equal to 90° in order to lower the first resonance frequency. The effect of the other shape parameters has been analyzed with full-wave approach in order to determine the best compromise between performance, weight and dimensions. The resulting antenna is shown in Fig. 3: the total length and the width are 1.5 m and 1 m, respectively, whereas the wire diameter is 5 mm. This kite-shaped bow-tie has been also simulated onboard the UAV to verify the influence of the drone metal frame.

The reflection coefficient of the antenna mounted on the UAV is shown in Fig. 2 (solid line). Since the antenna input impedance tends to concentrate around 150Ω , a balun with impedance transformation has been adopted. Such a balun is required since the output stage of the transmitter is unbalanced with 50Ω output impedance. With a 1:3 impedance transformer, a -6 dB matching level can be satisfied in most of the large band of interest. The matching improvement with respect to the 2-m long dipole (dotted curve) is clearly visible. Indeed, the dipole is matched in a narrow band centered at approximately 70 MHz and highly mismatched at other frequencies (except for the higher order resonances).

The radiation pattern will be shown at the conference. Owing to the two-fold symmetry of the whole test-source (the antenna mounted on the UAV), the polarization is linear and the cross polarization level is very low on the principal planes.

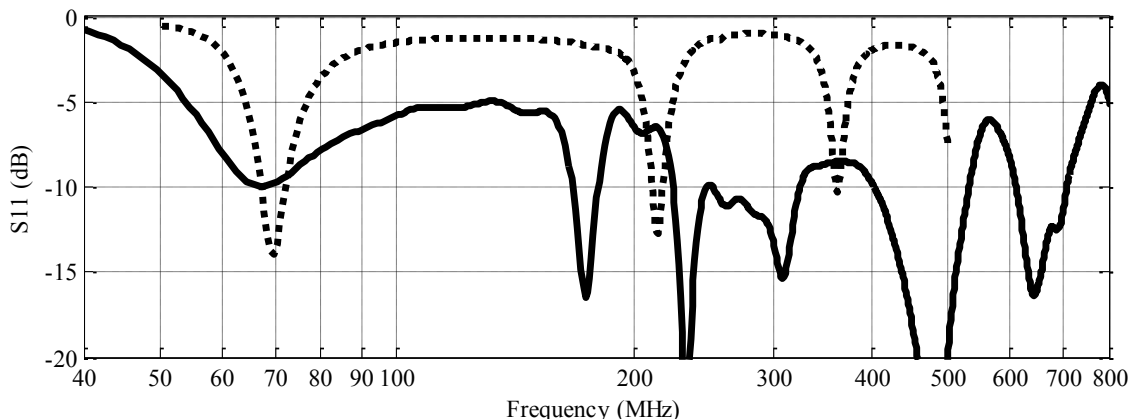


FIG. 2 – Reflection coefficient of the bow-tie mounted on the UAV (solid curve). Reflection coefficient of the 2-m long dipole mounted on the UAV (dotted curve).

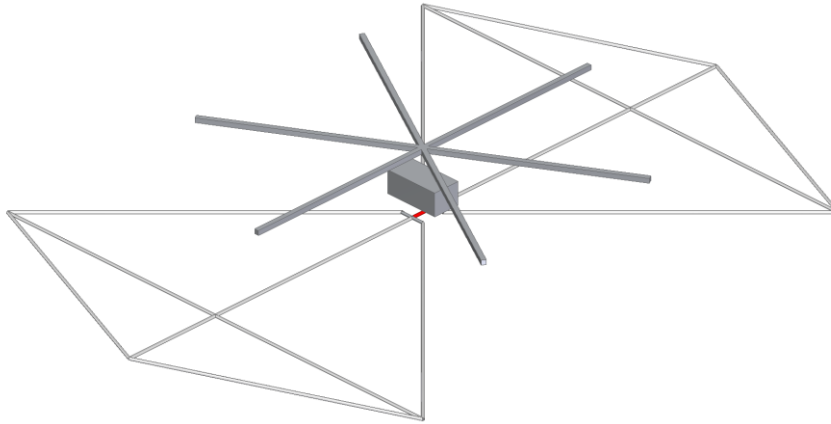


FIG. 3 – EM model of the designed bow-tie mounted on the UAV. Feed port in red. The metal box beneath the UAV hexagonal frame is the RF transmitter. Other dielectric parts not modeled (e.g. skids and propellers).

III. CONCLUSION

A broadband (50 MHz - 650 MHz) bow-tie radiator for antenna measurements with micro UAVs has been designed. The weight is about 290 g, whereas the length is 1.5 m and the width is 1 m. It satisfies -6 dB matching inside most of the band of interest, improving the measurement accuracy at low frequencies and enabling for multi-frequency measurements. Such an evolution would significantly enhance the time effectiveness of the system.

REFERENCES

- [1] G. Virone, et al., "Antenna Pattern Verification System Based on a Micro Unmanned Aerial Vehicle (UAV)," *IEEE Antennas and Wireless Propagation Letters*, vol. 13, pp. 169-172, Jan 2014.
- [2] F. Paonessa, et al., "UAV-based pattern measurement of the SKALA," *IEEE Antennas and Propagation Society International Symposium (APSURSI)*, July 19-25 2015, Vancouver, Canada.
- [3] G. Pupillo, et al., "Medicina Array Demonstrator: calibration and radiation pattern characterization using a UAV-mounted radio-frequency source," *Experimental Astronomy*, vol. 39, pp. 405-421, Apr. 2015.
- [4] P. Bolli, et al., "From MAD to SAD: the Italian experience for the Low Frequency Aperture Array of SKA1-LOW", *Radio Science*, 2016.
- [5] G. Virone, et al., "Antenna pattern measurements with a flying far-field source (hexacopter)," *IEEE International Conference on Antenna Measurements and Applications*, Nov. 16-19 2014, Antibes Juan-les-Pins, France.
- [6] Z. Zhang, H. Xie, L. Zheng, "V-shape wire-structured HF bowtie antenna," *8th International Symposium on Antennas, Propagation and EM Theory*, Kunming, 2008.

A SINGLE-LAYER PENTAGONAL ARRAY BASED ON THE SEQUENTIAL ROTATION ARRANGEMENT OF FIVE ELEMENTS

S. Maddio, G. Pelosi, M. Righini, S. Selleri

Department of Information Engineering, University of Florence.
Via S.Marta 3, Florence, Italy

[stefano.maddio, giuseppe.pelosi, monica.righini, stefano.selleri]@unifi.it

Abstract

A pentagonal circular polarized array composed of five elements is proposed for operation at 2.45 GHz. The system is based on the sequential rotation architecture of five elements, carried out with a sequential phase distribution network characterized by a progression of 72° .

Since a usable closed-form solution for the synthesis of a sequential phase network based on 5 elements is not available in the open literature, in this work the 5-SPN is studied and designed with an optimization procedure. In the proposed array, the five elements are arranged on the points of a five-pointed star, with the SPN at its center. In order to evaluate the array performance, a single-layer via-less prototype has been fabricated on a common FR4 substrate. The experimental results show a realized gain of 6.15 dB with a polarization purity greater than 20 dB at the center frequency.

Index Terms – Antenna Array, Circular Polarization

I. INTRODUCTION

Antennas operating in circular polarization (CP) are advantageous for both indoor and outdoor applications thanks to their ability to successfully operate regardless of orientation mismatch of target and source, and for their capability to reject oppositely polarized components. Sequential rotation arrangement (SRA) proves to be an effective technique to increase the pattern symmetry and the polarization ratio, [1]. On the basis of the above considerations, the aim of this paper is to deal with the problem of a CP array composed of five elements, which are arranged in a single-layer via-less pentagonal printed board of area $0.56 \lambda_0^2$ at 2.45 GHz. The feeding network, synthesized with a numeric optimization, is based on a 5-SPN composed of five 72° -out-of-phase outputs and inter-ports. The goal being that of using a pentagonal plate, suitable to be used as a sub-array in a bucky-ball or icosahedral set-up, attaining the best filling of the available area.

This paper is organized as follows: the first section is an introduction, while the second one shows the network design synthesized via numerical optimization. The third and fourth sections present the array configuration and the experimental results respectively. Finally, some conclusions are drawn.

II. NETWORK DESIGN AND OPTIMIZATION

The designed feeding network is composed of five junctions in order to split the power to each element. In fig. 1 the equivalent circuit of the proposed SPN is shown: it is formed by a combination of parallel and series transmission lines (TLs). In order to guarantee the correct feed on each element, the available input power is split at the first junction between the first output section and the rest of the network with 1:4 ratio. Re-iterating, the ratio must be 1:3 at the second junction, 1:2 at the fourth and 1:1 at the last one.

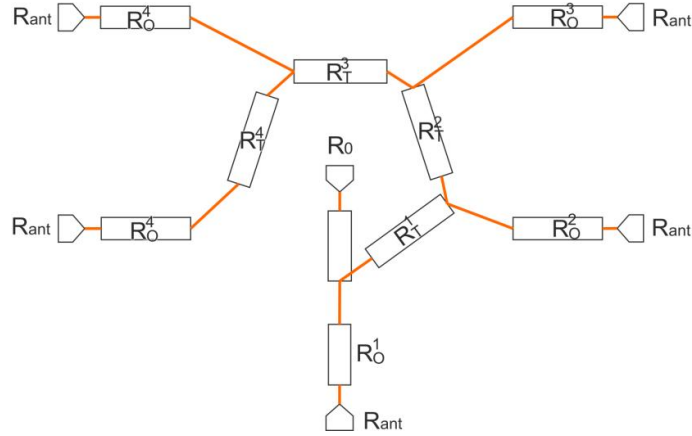


Fig 1 Equivalent circuit of the 5-SPN.

The progressive sequential phase of 72° is instead realized using series lines. In order to find the best location for each element, a Taguchi approach has been used [2]. In fact, since the unavoidable element coupling may deteriorate the network performance, the numerical optimization is then refined via hand-tuning over full wave simulations.

III. ARRAY DESIGN

The single antenna element is a circular patch centrally slitted by an elliptical cut, The ellipse behaves as a degeneration driver, splitting the fundamental TM_{11} mode of the disc into two detuned ones, TM_x and TM_y , due to the different current paths forced by the elliptical cut [3]. The three degree of freedom – i.e, radius and ellipse axes – permit to excite the modes in phase quadrature with the same magnitude, resulting in a far-field which is in a nominally CP in broadside, with a relatively compact disc dimension.

To successfully assemble the set of five disc elements, the SPN is arranged with a five-point star distribution, as shown in fig. 2. The coaxial-fed input line is located at the center of the pentagonal substrate. The network is connected to the cascade of T-section TLs, arranged as the arcs of a circle, as in [4,5].

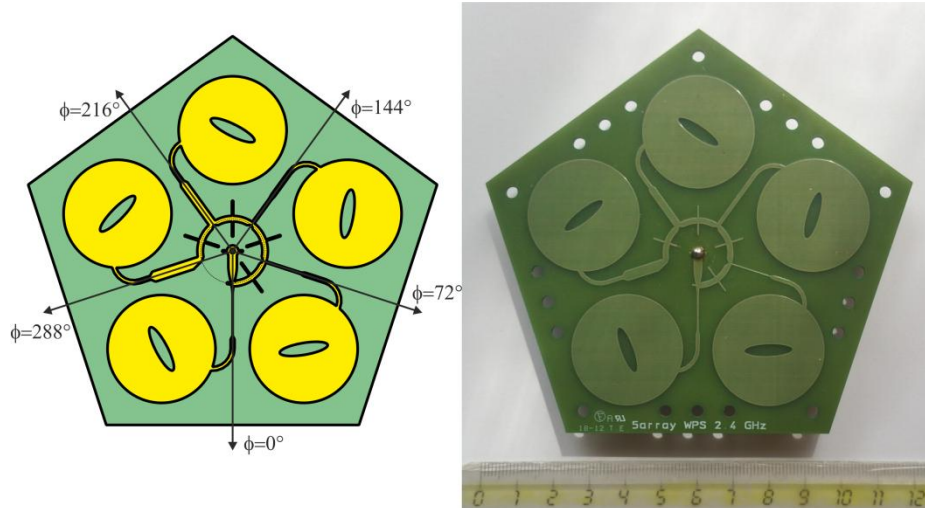


Fig. 2 Array arrangement: on the left a schematic of the array is presented, on the right the realized prototype is shown.

Each cascading section implements the corresponding sequential TL (Fig. 1) as a stub loaded line. The major advantages of this structure are smaller dimensions, a narrower line width and lesser spurious radiation. Furthermore, to improve the central symmetry, the four T-structures are implemented with the same line width. The five parallel output lines in Fig. 1 are implemented as five radial TLs, as is shown in Fig. 2. In order to avoid abrupt discontinuity, they are connected with the five antennas by using a short tapered section.

These design considerations allowed to minimize the size of the proposed array, permitting a pentagon side of only 7 cm. It is worth noting that, to achieve this small dimension, the distance between the elements is about $0.3\lambda_0$, which is much less than $0.7\lambda_0$, the optimal distance between the elements for SRA architectures.

IV. EXPERIMENTAL RESULTS

Based on the design in fig. 2a, a prototype has been manufactured on a standard FR4 dielectric substrate ($\epsilon_r = 4.5$, $\tan\delta = 0.02$), fig. 2b. Fig. 3 shows both the measured gain pattern at the center frequency of 2.45 GHz and the reflection coefficient. Considering the system symmetry, five ϕ -cuts are plotted, with $\phi = 0, 72^\circ, 144^\circ, 216^\circ, 288^\circ$ on θ in $[-180^\circ; 180^\circ]$. As pointed out, the pattern is almost center-symmetric, with a maximum just slightly off the bore-sight direction. The RH co-polar component presented its maximum of about 6.15 dB, for each ϕ -cut in $\theta=0$, while the LH cross-polar component, in the same condition, reaches a minimum below -14 dB. As far as the impedance matching is concerned, a 10 dB return loss is kept over a 300 MHz bandwidth. The antenna aperture at the central frequency of 2.45 GHz can be estimated as 58%, an above average performance, considering the dielectric loss.

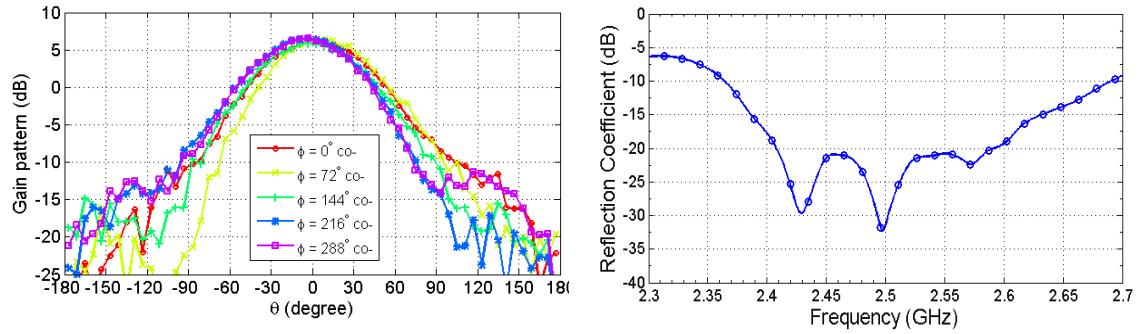


Fig. 3 Pattern (left) and reflection coefficient (right) of the proposed pentagonal array.

V. CONCLUSION

A circular polarized sequential rotated array composed of five disc elements is proposed. The array design, arranged in a pentagonal board of $0.56\lambda_0^2$ area at 2.45 GHz, is based on a sequential phase network with five outputs. Despite the compact dimension and the resulting strong coupling between the elements, the radiation pattern at central frequency is quite symmetric, with a maximum realized gain of 6.15 dB and 20 dB of cross polarization rejection. Furthermore, a return loss better than 10 dB is presented over a bandwidth of about 300 MHz, with an aperture efficiency of about 58 %.

REFERENCES

- [1] J. Huang, "A technique for an array to generate circular polarization with linearly polarized elements," *IEEE Transactions on Antennas and Propagation*, vol. 34(9), pp. 1113–1124, 1986.
- [2] E. Agastra, G. Pelosi, R. Taddei, S. Selleri, "Taguchi's method for multi-objective optimization problems," *International Journal of RF and Microwave Computer-Aided Engineering*, vol. 23(3), pp. 357-366, 2013.
- [3] S. Maddio, A. Cidronali, and G. Manes, "A New Design Method for Single-Feed Circular Polarization Microstrip Antenna with an Arbitrary Impedance Matching Condition," *IEEE Transactions on Antennas and Propagation*, vol. 59(2), pp. 379–389, 2011.
- [4] S. Maddio, "A Compact Wideband Circularly Polarized Antenna Array for C-band Applications," *IEEE Antennas and Wireless Propagation Letters*, vol. 14, pp. 1081–1084, 2015.
- [5] S. Maddio, "A circularly polarized antenna array with a convenient bandwidth/size ratio based on non-identical disc elements," *Progress In Electromagnetics Research Letters*, Vol. 57, 47–54, 2015.

TAPERED EBG SUPERSTRATES FOR HIGH-GAIN EBG RESONATOR ANTENNAS

C. Ponti⁽¹⁾, S. Ceccuzzi⁽¹⁾, P. Baccarelli⁽²⁾, G. Schettini⁽¹⁾

⁽¹⁾ Dept. of Engineering, Roma Tre University
Via Vito Volterra 62, 00146, Rome, Italy

cristina.ponti@uniroma3.it, silvio.ceccuzzi@enea.it,
giuseppe.schettini@uniroma3.it

⁽²⁾ Dept. of Inf. Eng., Electr. and Telecomm., Sapienza Univ. of Rome
Via Eudossiana 18, 00184, Rome, Italy

baccarelli@diet.uniroma1.it

Abstract

In this paper, a non-uniform Electromagnetic Band-Gap (EBG) structure to be used in antenna applications is presented. The EBG is a layered structure assembling a grid of rods with tapered spacing obeying a sinusoidal law. The structure is employed as superstrate of a planar antenna, at a resonating distance. Beyond the typical effects of gain enhancement achievable with this class of antennas, the tapering in the EBG allows for a reduction in the side-lobe level.

Index Terms – Electromagnetic Band Gap (EBG), high-gain antennas.

I. INTRODUCTION

Electromagnetic Band-Gap (EBG) materials are periodic structures used to filter radiation both in frequency and in space [1]. An application of EBG materials is their use as superstrates of planar antennas to achieve high-gain radiators [2]-[5]. A low-gain antenna, as a microstrip patch or a slot antenna, backed by or etched in a PEC ground plane, is adopted as a primary source, and a cavity is formed between the antenna ground plane and the EBG superstrate, placed above the ground plane at a resonating distance. Advantages of such an antenna architecture are in terms of ease of fabrication, simple feeding network, and low cost, compared to antenna arrays.

In this paper, an EBG structure with non-uniform arrangement of the periodic cell is proposed, with the aim of reducing the level of the lateral lobes. In particular, the EBG is a stack of three layers, and each layer is a grid derived by the crossing of two sets of perpendicular rectangular cross-section rods, with non-uniform spacing, i.e., with a sinusoidal tapering law for the rod-to-rod distances. The final structure, compared to EBG structures with in-plane periodicity, exhibits a non-uniform reflectivity, evaluated from the in-plane center towards the edges. Used as a superstrate of a planar antenna, at a resonating distance from the antenna ground plane, the tapered EBG allows for both a directivity

enhancement and a lower level of the side lobes, due to the gradual decreasing reflectivity from the center towards the edges.

II. THE EBG RESONATOR ANTENNA

An EBG resonator antenna is considered in this work. The primary radiator is a microstrip patch, covered by an EBG at the resonating distance $\lambda/2$, at $f = 10.3$ GHz (Fig. 1(a)). The EBG is composed by three layers with two-dimensional in-plane periodicity. Each layer is obtained by the crossing of two perpendicular arrangements of square cross-section rods with rod-to-rod distance modulated by a sinusoidal tapering law in both the x and y directions (Fig. 1 (b)):

$$p_{ni} = a_i \sin\left(\frac{\pi n_i}{2N_i}\right) \quad (1)$$

with $i = x, y$. In Eq. (1), p_{ni} is the distance between the edges of two adjacent rods with indexes n_i and n_i+1 , N_i is half the number of rods along each layer around the central one, in each direction. a_i is a parameter modulating the distances, being $a_i = p_{N_i}$, the maximum distance between the rods, satisfied at the edges of the structure.

With a view to the fabrication of the antenna, the EBG layers have been simulated with the permittivity of the PLA filament used in low-cost 3D printers, i.e., with $\epsilon_r = 2.76$ and $\tan \delta = 0.014$. Results are reported for an antenna with an EBG grid cover with $2N_x+1 = 2N_y+1 = 15$ rods along each layer and direction, as in Fig. 1(b). In the optimized layout, rods are 3.2 mm large, $a_i = 8$ mm, $P_z = 12.2$ mm, and $w_z = 5$ mm, and the permittivity of a plastic material is simulated, i.e., the permittivity of the PLA filament of low-cost 3D printers. Size of the EBG structure in xy -plane is $5.6 \lambda_0 \times 5.6 \lambda_0$. The radiation patterns of the antenna in the H and E planes at $f = 10.3$ GHz are compared to those from a 2D EBG with a periodic arrangement of rectangular cross-section rods, with vertical period $P_z = 12.2$ mm, and horizontal one $P_x = 8$ mm. The tapered EBG superstrate allows for an improvement in the side-lobe level in both planes: SLL is -21.6 dB (H plane) and -12.6 dB (E plane) for the periodic EBG, whereas it is -24.8 dB (H plane) and -15.7 dB (E plane) with the non-uniform grid, with a reduction of the SLL of almost 3 dB in both planes. As concerns the gain of the antenna, a maximum gain $G_M = 21.1$ dB is achieved with the non-uniform layout, whereas $G_M = 18.3$ dB is obtained with the periodic one. A good improvement in the SLL is achieved in the E plane, where, due to the linear polarization of the source field, the interaction of the incident field with the proposed EBG is lower.

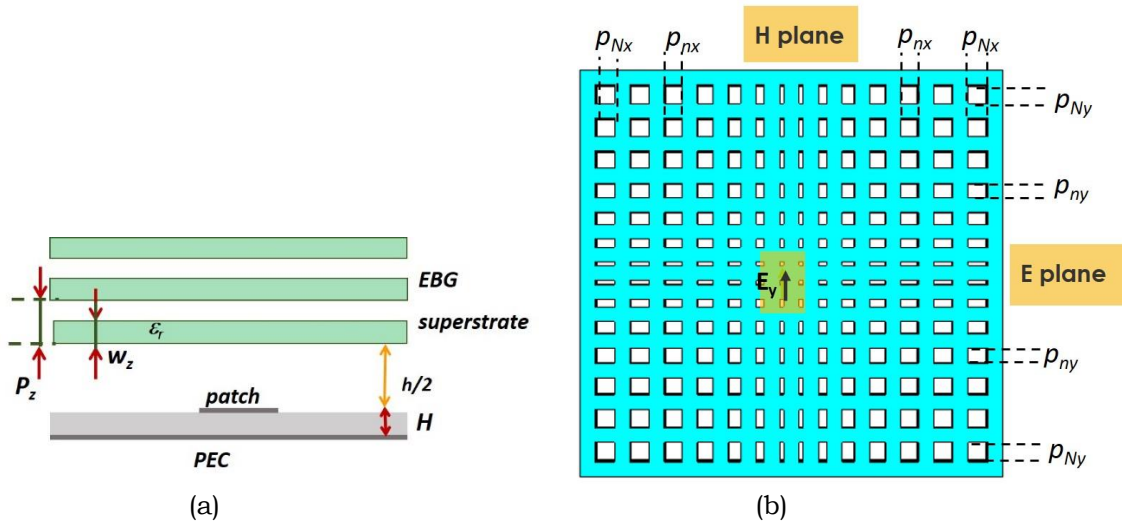


FIG. 1 – Layout of the EBG resonator antenna (a); detail of the geometrical parameters of each layer of the EBG (b).

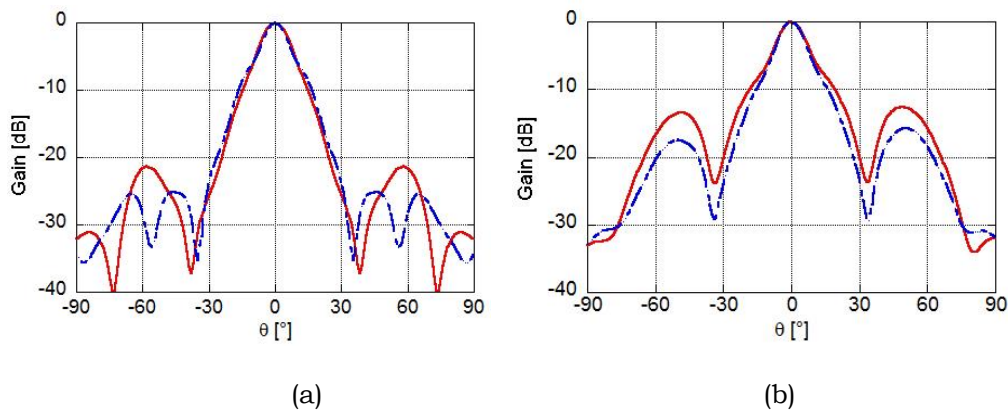


FIG. 2 – Far-field patterns of the antenna with uniform 2D superstrate of rectangular bars (continuous line) and grid tapered EBG (dotted line) as in Fig. 2: a) *H* plane; b) *E* plane.

III. CONCLUSION

A non-uniform tapering in EBG structures used as superstrates in planar cavity antennas is shown to be effective in the reduction of the side-lobe levels both in the *E*- and *H*-plane patterns. The proposed EBG resonator antenna has evident advantages of gain enhancement achieved with a simple antenna architecture. The main drawback is in the narrow-band response due to the resonant behaviour of the radiating structure. Further extension of this work will regard the use of a tapered EBG to obtain a wide-band high-gain radiator.

REFERENCES

- [1] F. Yang and Y. Rahmat Samii, *Electromagnetic Band Gap Structures in Antenna Engineering*. Cambridge, U.K.: Cambridge University.
- [2] A. Weily, L. Horvath, K. Esselle, B. Sanders, and T. Bird, "A planar resonator antenna based on a woodpile EBG material," *IEEE Trans. Antennas Propag.*, vol. 53, no. 1, pp. 216–223, Jan. 2005.
- [3] Y. J. Lee, J. Yeo, R. Mittra, and W. S. Park, "Application of Electromagnetic Band Gap (EBG) superstrates with controllable defects for a class of patch antennas as spatial angular filters," *IEEE Trans. Antennas Propag.*, vol. 53, no. 1, pp. 224–235, Jan. 2005.
- [4] Y. Ge, K. Esselle, and T. Bird, "Wideband high-gain EBG resonator antennas with small footprints and all-dielectric superstructures," *IEEE Trans. Antennas Propag.*, vol. 62, no. 6, pp. 2970–2977, 2014.
- [5] F. Frezza, L. Pajewski, E. Piuzzi, C. Ponti, and G. Schettini, "Radiation-enhancement properties of an X-band woodpile EBG and its application to a planar antenna," *Int. J. Antennas Propag.*, vol. 2014, no. 5, 2014.
- [6] Y. Lee, X. Lu, Y. Hao, S. Yang, J. R. G. Evans, and C. G. Parini, "Low-profile directive millimeter-wave antennas using free-formed three-dimensional (3-D) electromagnetic bandgap structures," *IEEE Trans. Antennas Propag.*, vol. 57, no. 10, pp. 2893–2903, 2009.

UWB-UHF RFID TAG ON PAPER FOR SIMULTANEOUS COMMUNICATION AND RF ENERGY HARVESTING

M. Fantuzzi⁽¹⁾, D. Masotti⁽¹⁾, A. Costanzo⁽²⁾

⁽¹⁾ DEI, University of Bologna
Viale del Risorgimento 2, 40136 Bologna, Italy

⁽²⁾ DEI, Cesena Campus, University of Bologna
Via Venezia 52, 47521 Cesena, Italy
marco.fantuzzi3@unibo.it

Abstract

This paper presents the design of a compact integrated UWB-UHF RFID solution enabling simultaneous wireless data and power transfer. The described integrated dual-band antenna is designed to cover the lower European UWB 3.1 to 4.8 GHz band for communication and localization functions and the European UHF RFID 868 MHz band for RF Energy Harvesting. Simultaneous operations are guaranteed by means of a proper feeding and matching network, a three-port diplexer, in a compact, low-profile solution. In order to fulfil eco-compatibility requirements, both the radiating system and the matching network are designed on paper substrate.

Index Terms – Ultra wideband antennas, UHF antennas, Radiofrequency Energy Harvesting, RFID.

I. INTRODUCTION

The evolution of microwave technology is leading toward the introduction of systems more and more distributed in the environment. In this context, the need for autonomy and maintenance-free functions is more than ever fundamental, together with the urgency for new solutions exploiting eco-friendly materials. Moreover, an important role in next fifth generation (5G) cellular networks is expected for a technology able to manage a Simultaneous Wireless Information and Power Transfer (SWIPT) [1].

RF Energy Harvesting and Wireless Power Transfer technologies are able to provide maintenance-free operations for Wireless Sensor Networks, while UWB technology has the advantage of extremely low power consumption, as well as robustness versus fast fading, and thus enabling sub-meter precision indoor localization [2]. Given this background, we developed an original solution, which combines these two technologies and at the same time fulfils the requirements of the national GRETA project [3] (GREen TAGs and sensors with ultra-wideband identification and localization capabilities). The RFID tag here described provides the operations highlighted in Fig. 1, showing the complete GRETA tag architecture.

With this work we present a novel dual-mode antenna, able to efficiently exploit both the European low UWB band (from 3.1 GHz up to 4.8 GHz) for communication and localization purposes and the RFID-UHF band (868 MHz) for Energy Harvesting. The main novelty consists in the compactness and eco-compatibility of the proposed solution, together with its single-port architecture, directly connected to a planar network for matching, filtering and decoupling operations.

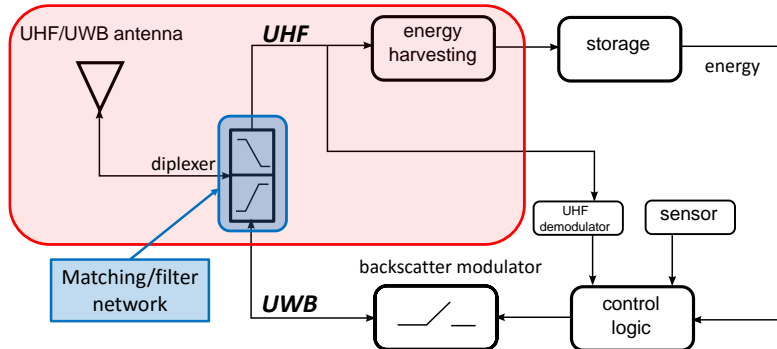


FIG. 1 – Block diagram of the GRETA tag architecture; the presented tag describes the compact implementation of the highlighted parts.

II. TAG ANTENNA

As tag radiating element a new, compact, one-port antenna has been designed. The UWB 3.1 to 4.8 GHz frequency band is covered by means of an Archimedean spiral, while the 868 MHz RFID band is covered by the meandered planar dipole obtained from the extension of the spiral outer arms. Common paper has been adopted for the design, having $\epsilon_r=2.85$, $\tan(\delta)=0.053$ @ 4 GHz and thickness 0.69 mm.

Such co-localization of the two radiating elements leads to a single-port antenna architecture, which has the twofold advantage of reducing antenna area and simplifying direct connection to a future UWB-UHF integrated chip. Fig. 2(a) reports antenna layout with the relative dimensions, while Fig. 2(b) shows antenna radiation patterns in the UHF band and at three different frequencies of the UWB band. Dipole length is selected to provide a 1.5λ resonance at 868 MHz, where a non-standard behavior is obtained: since the entire spiral path contributes to the total length, no secondary lobes are present. As regards the polarization properties of the antenna, standard dipole and spiral behaviors are achieved: vertical polarization (along the y-axis) in the UHF band and circular polarization (right-handed in the $z>0$ half space, left-handed in the $z<0$ half space) in the UWB band. It is worth noting the satisfying gain performance of the dual-mode antenna, despite of the high losses of the paper substrate: the antenna gain (taking into

account the matching conditions at the antenna port) are 0, 3.4, 3.2, 4.2 dBi, at 868, 3100, 4000, and 4800 MHz, respectively.

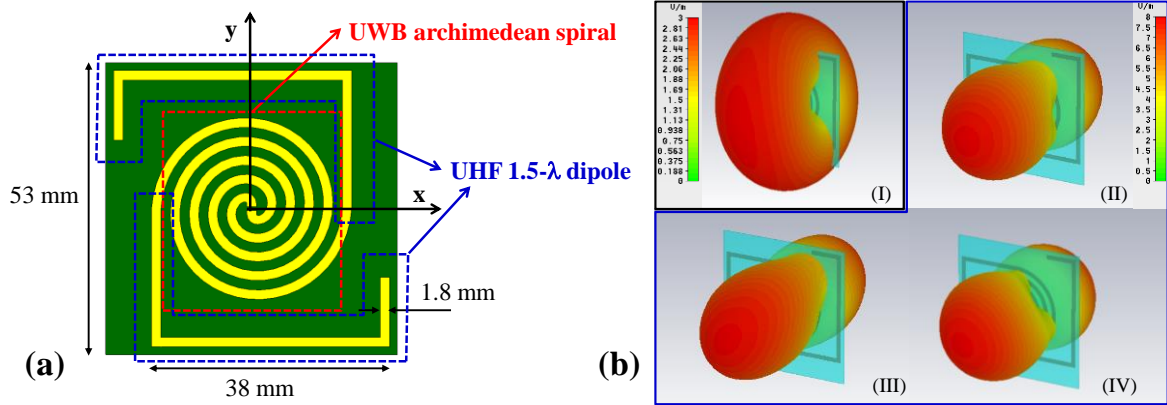


FIG. 2 – Tag antenna layout (a) and electric field radiation pattern in linear scale (b) at the operating frequencies of 868 MHz (I), 3.1 GHz (II), 4 GHz (III) and 4.8 GHz (IV).

III. DIPLEXER AND TAG ARCHITECTURE

The dual, simultaneous functionalities of the tag can be guaranteed only if a proper matching/filter network is implemented. This diplexing network separates the signal coming from the antenna by means of UHF and UWB filters. The first one, implemented with lumped components, is loaded by the rectifying section for Energy Harvesting purposes, while the second one is realized with distributed elements and will be loaded by the UWB backscatter modulator.

Due to the ungrounded nature of the antenna, the diplexer should have the smallest possible dimensions, especially for not influencing the highest operating frequencies, which are covered by the inner part of the Archimedean spiral. Besides diplexer miniaturization, developed by microstrip meandering and adoption of small size (0402 case) SMDs, the balanced antenna to the unbalanced diplexer microstrip connection has to be taken into account, while guaranteeing low tag profile. Fig. 3 depicts different views of the balun-free [4] connection adopted between the antenna and the diplexer. A volume of only 53x53x6 mm³ is needed for the whole tag.

Despite the lossy paper substrate, the final diplexer shows promising performance: reflection coefficient for both filters is less than -10 dB at the respective frequencies of interest, whereas the insertion loss is about -1 dB and -2 dB in the UHF and UWB bands, respectively. The fundamental strong decoupling between the two paths is always guaranteed higher than 35 dB: this way simultaneous communication and power transmission activities can be effectively implemented.

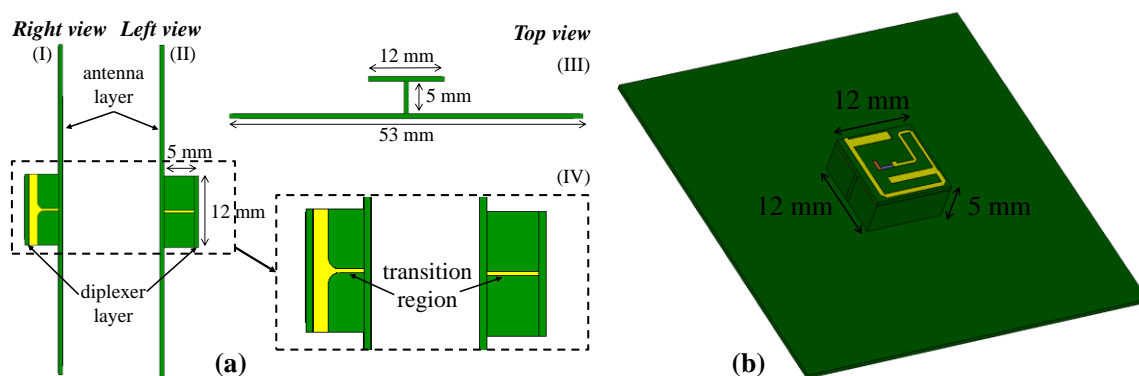


FIG. 3 – Side (I-II), top (III) and zoomed (IV) views of the antenna-diplexer connection (a); brick side supports are removed for ease of visualization. Back perspective tag view (b).

The rectifying section is realized by means of a voltage-doubler topology, employing two Skyworks SMS7630 Schottky diodes. For the nonlinear optimization of the RF-to-DC conversion efficiency, low power levels have been considered for the incoming UHF signal, typical of RF harvesting scenarios. The simulated results are promising: efficiencies around $50 \div 60\%$ are obtained in the range of input available power $[-15 \text{ dBm} \div -10 \text{ dBm}]$.

ACKNOWLEDGEMENT

This work was partly funded by the Italian Ministry of the Instruction, University and Research (MIUR), within the framework of the national project GRETA ("GREen TAGs and sensors with ultra-wideband identification and localization capabilities").

REFERENCES

- [1] E. Hossain, M. Rasti, H. Tabassum, and A. Abdelnasser, "Evolution toward 5G multi-tier cellular wireless networks: An interference management perspective," *IEEE Wireless Communications*, vol.21, no.3, pp.118-127, June 2014.
- [2] D. Dardari, R. D'Errico, C. Roblin, A. Sibille, and M. Win, "Ultrawide Bandwidth RFID: The next Generation?," *Proceedings of the IEEE*, vol. 98, no. 9, pp. 1570-1582, Aug. 2010.
- [3] National Italian project PRIN-GRETA ("GREen TAGs and sensors with ultra-wideband identification and localization capabilities"), 2012-2015, <http://www.greentags.eu/>.
- [4] M. Del Prete, D. Masotti, N. Arbizzani, and A. Costanzo, "Remotely Identify and Detect by a Compact Reader With Mono-Pulse Scanning Capabilities", *IEEE Transaction on Microwave Theory and Techniques*, Vol. 61, No. 1, Part II, Jan. 2013, pp. 641-650.

PASSIVE RFID SENSOR NETWORK FOR INDUSTRIAL INTERNET OF THINGS

C. Occhiuzzi⁽¹⁾, S. Amendola⁽¹⁻²⁾, S. Manzari⁽¹⁾, G. Marrocco⁽¹⁻²⁾

⁽¹⁾ RADIO6ENSE, ⁽²⁾ Pervasive Electromagnetics Lab,
University of Tor Vergata, Via del Politecnico, 1, 00133, Roma

Abstract

RFID technology is here applied to the low-level monitoring of critical infrastructures to detect early attempts of physical and cyber attacks. The proposed RFID sensor network provides the detection of complex events ranging from the un-authorized access to a critical area, the human interaction and tampering of electric equipment up to the occurrence of critical environmental events.

Index Terms – RFID sensor, industrial monitoring, IoT.

I. INTRODUCTION

After home automation, leisure and communication, the revolution of the Internet of Things (IoT) paradigms promises to produce changes also in many different industrial scenarios [1]. A key role in such perspective is played by the wireless sensor networks, and in particular to autonomous and reconfigurable monitoring infrastructures capable to sensibly increase the possibility to control systems and predict events, thus optimizing production, security and efficiency.

This contribution introduces for the first time the complete design and implementation of an *RFID industrial sensor network* (RFID-SN). More particularly, the proposed solution is applied to the empowering of SCADA (*Supervisory Control And Data Acquisition*) system in critical infrastructures by proper integrating on machinery and environment analogue and digital RFID autonomous sensors. The aim is to improve the defense against cyber-attacks and threats [2].

The work presents the design of both hardware and software components, up to deployment and test in a real environment.

II. RFID SENSOR NETWORK ARCHITECTURE

The proposed RFID-SN inside an industrial area (Fig.1) comprises *i)* one or more fixed multi-channel reader unit connected to the communication network hub; *ii)* for each reader unit, one or more surveillance antennas connected to the reader and properly distributed to achieve a uniform radio coverage of the environment or, more in general, a spatial selectivity of the interrogation; *iii)* a set of standard analog RFID tags to be used as wireless markers, *iv)* a set of digital sensing boards, hereafter denoted as *radio-boards*, equipped with

different sensors according to the monitoring to be performed and, *v*) a Control & Command software living into the reader module and able to dynamically modulate the functions of the network in term of active area, parameters to be measured, power and interrogation frequency.

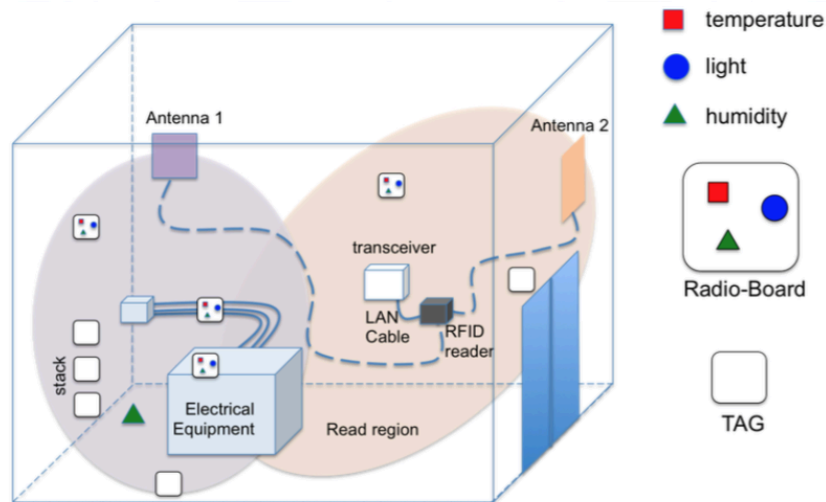


FIG. 1 – Possible implementation of the RFID-SN inside an industrial room.

The two types of RFID devices have complementary capabilities and roles. The multi-parameter wireless boards provide specific and quantitative sensing data while conventional RFID tag produces environmental backscattering modulation as a response to a variation of the electromagnetic fingerprint of the environment, produced by shadowing and scattering effects of humans and moving machinery parts (*ambient electromagnetic intelligence* [3]).

III. RADIO-BOARD

The Radio-boards are based on a new family of RFID transponders (SL900A by AMS) that, beside the pure identification features, provide a native integrated electronics for sensing activities. In particular the selected IC includes an Analog-to-Digital Converter (ADC) capable to control up to two analog external sensors and an integrated temperature with a programmable dynamic range and resolution in the interval $-40/150^{\circ}\text{C}$. This IC can be used in a fully passive mode or in battery-assisted mode. The design of the Radio-board was oriented to pursue the maximum flexibility in measurement and installation in complex environments. Beside the antenna, the matching element and the traces for battery and sensors (Fig.2), the board is equipped with several tuning elements (trimming points, solderable elements and lumped impedances) properly located onto the conductive traces. By acting on such elements the performance of the radio-board can be customized for the specific application. The read distance ranges from 2m to 7m in battery-less and battery-assisted mode respectively.

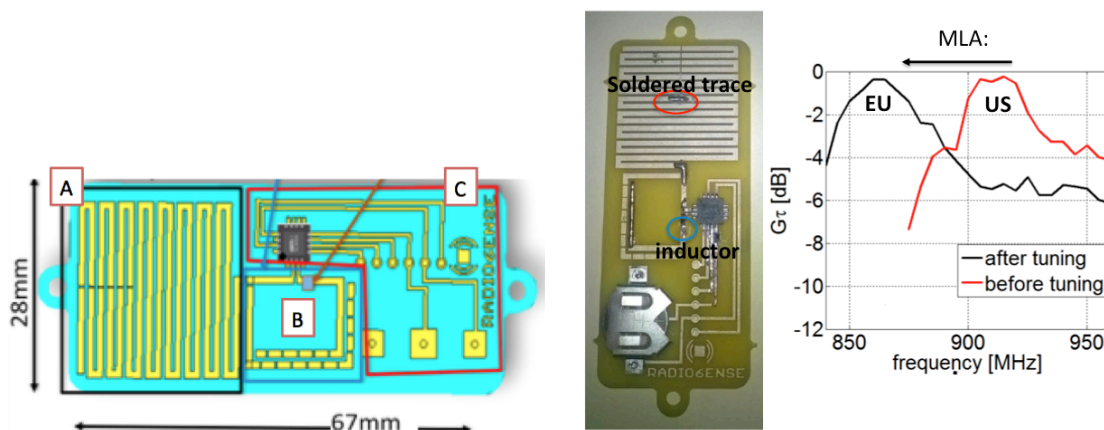


FIG. 2 – The configurable multi-sensor S-board. Left) (A) Antenna with tuning elements, (B) Matching loop with tuning elements, (C) Chip, sensors and battery (optional) traces. Right) Prototype with measured tuning features.

IV. A FIRST TEST-BED

An early version of the complete RFID-SN was deployed and tested within the Electrical transformer secondary substation of the University of Rome “Tor Vergata”. The configuration of the RFID-SN is sketched in Fig.3. A 3.2W long range RFID reader connected to four surveillance antennas was used to monitor four different zones in the cabin: Cabinets and meters (Antenna 1); Access (Antenna 2); Flooding sensitive area (Antenna 3); Cable harness (Antenna 4). The joint use of radio-boards and conventional tags enables to monitor both authorized and un-authorized access, tampering actions, flooding and humidity changes and, finally, power overloads of wire harness.

Fig.3 shows a subset of the signals recorded by the sensors network when an authorized access to the cabin for ordinary maintenance occurred. In the initial reference condition, the light in the room is off (Radio-board 44 with photo-diode) and the sensors for the access control (Tag F1) and cabinet opening (tag F3) show stable RSSI values. No people are detected inside the ambient (null signal from badge F5). The visible drop in the value of the RSSI collected from sensor F1 reveals the opening of access door. Immediately after, the person entering the room is automatically recognized by the system as authorized personnel through his badge identification (F5). The maintenance technician turns on the light (sensor 44 switches to ON state) and opens the electrical cabinet (sensor on the door F3 is no longer read in the open position) to perform ordinary operations. Finally, he approaches the exit door and turns-off the light; the system detects again his badge and records the exit.

V. CONCLUSION

Early considerations and tests seem to corroborate the feasibility of using RFID technology for multi-parameters monitoring of critical

infrastructures and, more in general, of industrial plants. The proposed sensing network was successfully experimented in a real electric cabin and, as better shown at the symposium, it enabled the detection of a great variety of events by means of a unique and scalable infrastructure, borrowed from logistics.

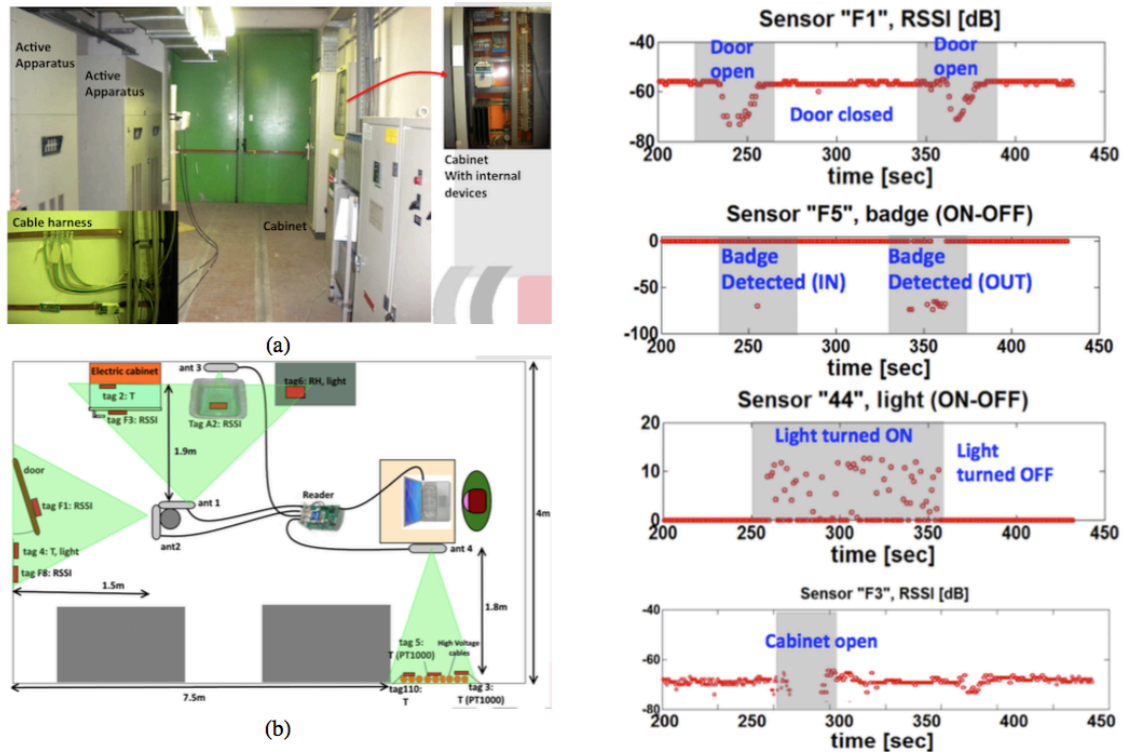


FIG. 3 – Electrical transformer secondary substation of the University of Rome “Tor Vergata”. b) Schematic representation of the RFID-SN. c) RFID-SN measurements in case of authorized access to the electric cabin.

ACKNOWLEDGEMENT

The work was supported by the Horizon 2020 SCISSOR ICT project no. 644425. The authors would like to thank Stefano Milici for his valuable support to the experimental preparation and exploitation.

REFERENCES

- [1] “Industrial internet of things: Unleashing the potential of connected products and services,” World Economic Forum, Tech. Rep., 2015.
- [2] Michael B. Kelley. The stuxnet attack on Iran’s nuclear plant was ‘far more dangerous’ than previously thought. <http://www.businessinsider.com/stuxnet-was-far-more-dangerous-than-previous-thought-2013-11?IR=T>. S.
- [3] Amendola, R. Lodato, S. Manzari, C. Occhiuzzi, and G. Marrocco, “Rfid technology for iot-based personal healthcare in smart spaces,” *IEEE Internet of Things Journal*, vol. 1, no. 2, pp. 144–152, April 2014.

MODULAR ANTENNAS FOR NEAR-FIELD UHF-RFID SYSTEMS

A. Michel, P. Nepa, and G. Manara
Dept. of Information Engineering, University of Pisa
via Caruso 16, 56122, Pisa, Italy

e-mails: a.michel@iet.unipi.it, p.nepa@iet.unipi.it, g.manara@iet.unipi.it

Abstract

Several ad-hoc antennas for Near-Field (NF) UHF-RFID applications have been proposed in the last decade. In particular, the authors recently proposed novel antenna configurations, the so-called Modular Antennas. In these layouts, a travelling wave antenna is combined with a low-gain resonating antenna, which share the surface of the desktop reader antenna. Specifically, a spiral Travelling Wave Antenna (TWA) is used to generate a strong and uniform field in proximity of the antenna surface. Then, such a microstrip transmission line is used to feed the resonating antenna in order to extend the reading range up to few decimeters. Also, to make the antenna almost scalable, several antenna solutions have been proposed, so spreading the generated field in a large and arbitrarily shaped area.

Index Terms– Near-field antennas, Radio Frequency Identification, UHF.

I. INTRODUCTION

Radio Frequency Identification (RFID) systems have been widely used in supply chain and logistics applications for wireless identification and tracking of goods, with excellent performance for long-range (up to 4-6m, with passive tags) interrogation of tagged pallets and cases. In particular, Item level tagging (ILT) has also received a lot of attention. In this contexts, Near-Field (NF) Ultra-High Frequency (UHF) RFID systems are largely used in retail and pharmaceutical industry, as for example for desktop readers [1]-[4], smart shelves [5],[6], smart point readers [7]-[9] and printer encoders [10].

Differently from High Frequency (HF) systems, which are largely used for near-field applications, Near-Field (NF) UHF RFID systems represent a valuable solution to implement a reliable short-range (up to a few tens of cm) wireless identification for ILT applications, which can steadily operate with small tags and in scenarios with closely spaced tagged items. However, the NF UHF-RFID system performance is affected by the presence of different materials and closeby tags - the item material the tag is attached to and the mutual coupling among tags in a stacked configuration can compromise the tags readability and reduce the read range [11].

Thus, reader antennas that can exhibit in unloaded conditions a read range larger than that required in operational conditions have been recently proposed [3],[4],[8],[9],[11]. Furthermore, reconfigurable antennas have been considered, which allow for a shaping of the interrogation field in the antenna near-field region, when a simple control of the reader output power is not enough to guarantee high successful reading percentages on the whole antenna surface and for any tagged item and tag topology/orientation.

In other words, *antenna reconfigurability* is becoming an interesting antenna feature which makes the entire near-field UHF RFID system more flexible to the specific operative scenario. For instance, reconfigurability can be used to change the electric and magnetic field distribution within a confined volume,

also extending the read range up to a specific distance. In this framework, the authors recently introduced the *Modular Antenna* concept [3]. In particular, to maximize the electromagnetic field in a confined volume within the antenna near-field region (namely, in both the reactive and radiative near-field regions), a travelling wave antenna is combined with a low-gain resonating antenna, which share the surface of the desktop reader antenna. The travelling wave antenna allows for covering the reactive near-field region, with almost uniform electric and magnetic fields up to a few cm from the antenna surface. The low-gain resonating antenna is used to cover the radiative near-field region, up to a few tens of cm from the antenna surface, yet radiating a relatively low field in the antenna far-field region as required by antennas for desktop readers. In this paper, an overview of the recently proposed Modular Antenna configurations is presented, highlighting the advantages of each antenna layout.

II. MODULAR ANTENNAS: A REVIEW

The Modular Antenna concept has been firstly presented in [3]. Then, in [4] a specific design is described. Specifically, in [4] a $50\text{-}\Omega$ coaxial cable feeds a spiral shaped TWA at the surface center, which in turn series-feeds a coplanar array of two miniaturized square patches (Fig. 1). Besides, by simply adding a switch, the spiral microstrip line can be either connected to the array (*Modular Antenna Configuration*) or ended on a matched load to implement a conventional TWA (*Spiral TWA Configuration*). The latter configuration ensures a strong and uniform field distribution in a small volume just above the antenna surface, which is high desirable for tag writing operations or single-tag readings. On the other hand, the modular combination of radiating elements is effective in improving the tag detection up to few decimeter from the antenna surface, even in presence of stacks of tags (where the mutual coupling effect is not negligible). As described [4], both the *Modular Antenna Configuration* and the *Spiral TWA Configuration* have been tested to measure the reader antenna read range. Tests have been carried out by moving the tag away from the antenna surface, with a step of 5 cm. At each distance, the RSSI value has been averaged in an interval of 10 s, for two orthogonal tag orientations. The read ranges (Fig. 1) are around 60 cm and 10 cm for the *Modular Antenna Configuration* and the *Spiral TWA Configuration*, respectively, regardless of the tag orientation.

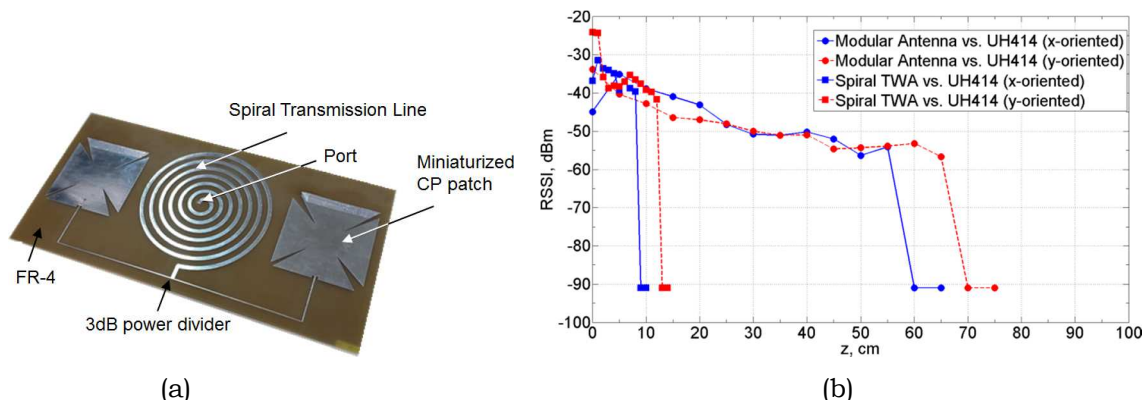


Fig. 1 – *Modular Antenna* prototype consisting in a 2×1 array of miniaturized CP patches serially-fed by a spiral-shaped transmission line [4]. RSSI distribution by varying the tag (LABID UH414) distance from the antenna center (along a direction perpendicular to the reader surface), with an input power of 23 dBm, for two orthogonal tag orientations and for both antenna configurations.

The transmission line antenna and the resonating antenna can be also arranged in order to share the same surface in the smart point reader or desktop reader (aperture-shared antennas). In [8], [9], the *Modular antenna* consists of two main elements, that is a spiral-shaped microstrip transmission line which serially-feeds a circularly polarized ring slot resonant antenna (Fig. 2a). However, such a configuration is not a fully-scalable solution, since the resonant ring slot size is strictly dependent on the operating frequency. To make the antenna layout more flexible and scalable, in [8],[9] the spiral transmission line is extended beyond the slot antenna, so covering a larger area and shaping the antenna according to the shape of the reader case.

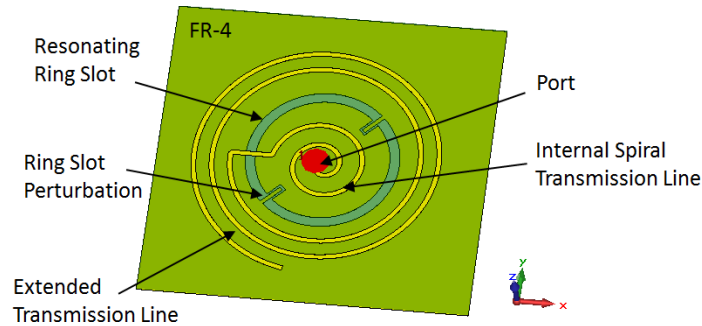


Fig. 2 – Two-elements Modular Antenna composed by a spiral transmission line which serially feeds an embedded ring slot antenna.

As an alternative, the circular ring slot has been replaced by four separated curved slot antennas, placed around the spiral TWA and 90-degree rotated with respect to the antenna center (Fig. 2b). In detail, to achieve a circularly polarized radiated field in the radiative near-field region, the four resonating slot antennas are series-fed by the spiral TWA with the same current amplitude but with a 90-degree phase shift (sequential rotation feeding technique). Sequential rotation feeding is effective to improve cross polarization (circular polarization purity) and radiation pattern symmetry.

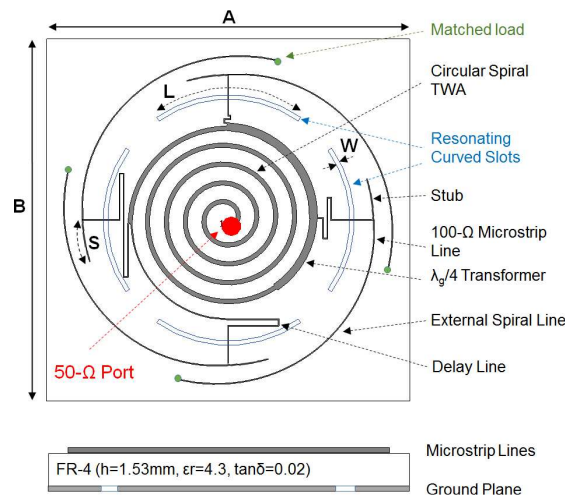


Fig. 3 – Two-elements Modular Antenna composed by a spiral transmission line which serially feeds four curved resonating slot antennas.

III. CONCLUSION

In this paper, an overview on the *Modular Antenna* configurations proposed for near-field UHF-RFID systems is presented. The advantage given by a similar modular combination is twofold. Firstly, a strong field is generated on the antenna surface thanks to the presence of the spiral TWA, which is especially suitable for writing operations. On the other hand, with respect to a TWA antenna alone, a significant field intensity is observed beyond a few decimeters from the antenna surface thanks to the presence of the resonating antennas, which allow tag detection in case of stacked tagged items too. However, since the input power is partially radiated by the spiral TWA, each slot antenna is fed by a smaller power level, so guaranteeing a relatively low radiation into the far-field region and reducing the cross-readings (false positives) out of the read zone required or the NF UHF RFID reader. The presence of switches is also useful to make the antenna reconfigurable and adaptable to the specific application scenarios.

REFERENCES

- [1] A. Michel, R. Caso, A. Buffi, P. Nepa, G. Isola, H.-T. Chou, "Design and Performance Analysis of a Planar Antenna for Near-Field UHF RFID Desktop Readers", *Asia-Pacific Microwave Conference (APMC)*, 2012.
- [2] A. Michel, R. Caso, A. Buffi, P. Nepa, G. Isola, "Meandered TWAS array for near-field UHF RFID applications", *Electronics Letters*, vol. 50, no. 1, pp.17-18, January 2014.
- [3] A. Michel, R. Caso, A. Buffi, P. Nepa, and G. Isola, "Modular antenna for reactive and radiative near-field regions of UHF-RFID desktop readers", *URSI General Assembly and Scientific Symposium (GASS)*, Beijing, China, August 2014.
- [4] R. Caso, A. Michel, A. Buffi, and P. Nepa, "A modular antenna for UHF RFID near-field desktop reader," *IEEE RFID Technology and Applications Conference (RFID-TA)*, Tampere, Finland, 11-13 September 2014.
- [5] A.S. Andrenko, "Optimized near-field antenna for UHF RFID smart shelf applications," *IEEE International Symposium on Antennas and Propagation & USNC/URSI National Radio Science Meeting*, pp.1576-1577, 19-24 July 2015
- [6] C.R Medeiros, J. R. Costa, and C. A. Fernandes, "RFID Reader Antennas for Tag Detection in Self-Confined Volumes at UHF," *IEEE Antennas and Propagation Magazine*, vol.53, no.2, pp.39-50, April 2011
- [7] J. Shi, X. Qing, and Z. N. Chen, "Electrically Large Zero-Phase-Shift Line Grid-Array UHF Near-Field RFID Reader Antenna," *IEEE Transactions on Antennas and Propagation*, vol.62, no.4, pp.2201-2208, April 2014
- [8] A. Michel, A. Buffi, R. Caso, and P. Nepa, "A two-element modular antenna for near-field UHF RFID applications," *1st URSI Atlantic Radio Science Conference (URSI AT-RASC)*, 2015, pp.1-1, 16-24 May 2015
- [9] A. Michel, A. Buffi, R. Caso, and P. Nepa, "A scalable modular antenna configuration to extend the detection volume of a near-field UHF-RFID desktop reader," *IEEE International Symposium on Antennas and Propagation & USNC/URSI National Radio Science Meeting*, pp.1766-1767, 19-24 July 2015
- [10] A. Michel, A. Buffi, P. Nepa and G. Manara, "Antennas for UHF-RFID printer-encoders," *IEEE 15th Mediterranean Microwave Symposium (MMS)*, Lecce, 2015, pp. 1-4.
- [11] A. Michel, and P. Nepa, "UHF-RFID Desktop Reader Antennas: Performance Analysis in the Near-Field Region", accepted on *IEEE Antennas and Wireless Propagation Letters*

ENHANCED BATTERY-FREE AUGMENTED RFID TAG

R. Colella, L. Catarinucci, L. Tarricone

Department of Innovation Engineering, University of Salento
Via Monteroni, Lecce, Italy
riccardo.colella@unisalento.it

Abstract

In this work an improved version of a recently published battery-less augmented RFID device enabling a tag-reader cooperative approach is presented. Based on a specifically designed physical layer implementing a logical communication procedure over LLRP, the device is now capable to react to the reader solicitations by reasoning, asking for extra info, taking autonomous decisions, piloting actuators and generating alerts. Tests performed in the building automation context demonstrate the capability of the proposed device of reasoning jointly with the reader and changing its behavior according to logical and physical events occurring in the surrounding environment.

Index Terms – RFID, augmented tags, sensing.

I. INTRODUCTION

RFID-based devices with augmented capabilities have appeared in recent years in the literature [1, 5]. Some of them, including the one recently published and named SPARTACUS (Self-Powered Augmented RFID Tag for Autonomous Computing and Ubiquitous Sensing) [4], conjugate RFID identification with extra functionalities such as sensing, computation, data storing, and actuation. As deeply clarified in [4], SPARTACUS (see prototype in Fig. 1) embeds an RF energy harvesting block which exploits the electromagnetic energy emitted by the RFID reader to power up a microcontroller (MCU), a memory bank, sensors, actuators and alert devices. In this paper, a new version of SPARTACUS provided with a new physical layer implementing a logical communication procedure over Low Level Reader Protocol (LLRP) is presented.

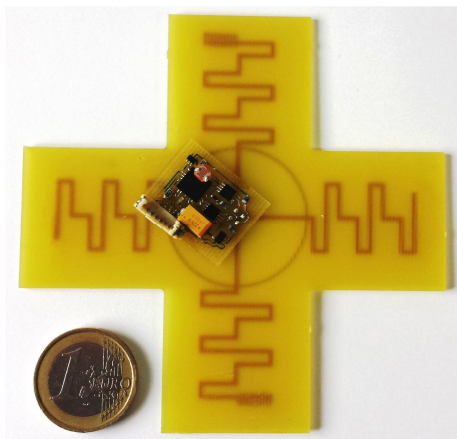


FIG. 1 – SPARTACUS Prototype.

In particular, the novel communication procedure makes tag and reader collaborate to solve a common problem based on the local knowledge of the tag and the global knowledge of the reader. Thus, the tag is not seen as a simple “decentralized static memory” accessible only by the reader. Indeed, the tag memory is now thought as mean of communication shared between reader and tag and it is continuously and dynamically updated by both of them.

II. IMPROVED BATTERY-LESS AUGMENTED RFID TAG

The implemented communication procedure supporting the SPARTACUS-reader cooperative interaction is shown in Fig. 2. Once energized and interrogated by the reader, the tag continuously sends the EPC by performing a bidirectional low-level communication according to gen2 standard timing. Thus, the tag is identified as long as it is located in the reader antenna radiation area. In the meanwhile SPARTACUS performs two different cyclical and asynchronous operations whose timing depends on both the level of available RF energy and the storage capacitor value: 1) it starts charging the capacitor, and 2) it computes, manages memory, senses the environment and updates its status by exploiting the harvested energy [6]. In particular, let's suppose that SPARTACUS needs data from the reader in order to perform a certain computation. With reference to the path highlighted in Fig. 1, when its MCU is energized, the tag changes certain memory bits to specify the required data. Then, the reader reads the memory through gen2 commands and, on the basis of data availability, updates the memory accordingly. Once these data are accessed by SPARTACUS, its MCU retrieves them from the memory at the next energization step, performs the computation, and writes the result into the memory. The reader can now use this information for further elaborations or interactions.

Finally, a crucial aspect related to this kind of communication is the timing regulating the SPARTACUS-reader interaction. On the one hand, being SPARTACUS gen2 compliant, the interaction with the reader occurs with the standardized timing specifications, as in the case of a canonical RFID tag. Consequently, when SPARTACUS is in the reader area, it is recognized and can also exchange LLRP commands. On the other hand, the updating of the tag memory done by the device itself is governed by a different timing depending on many factors: amount of available RF energy, computational load, working distance, reader antennas planning, specific application and, finally, on-board storage capacitor. In particular, this last must be set to minimize the computational latency case by case.

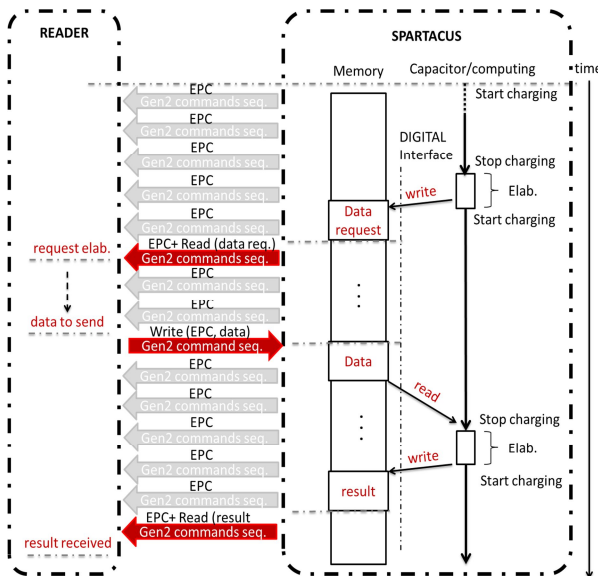


FIG. 2 – Example of SPARTACUS-Reader interaction

the other hand, the updating of the tag memory done by the device itself is governed by a different timing depending on many factors: amount of available RF energy, computational load, working distance, reader antennas planning, specific application and, finally, on-board storage capacitor. In particular, this last must be set to minimize the computational latency case by case.

III. RESULTS

In this Section a validation use case concerning the

implementation of a SPARTACUS-based system capable to control a fan located in an office room when certain conditions are verified is presented. In particular, it is required to switch on the fan only when the following conditions occur: (a) somebody is in the office room, (b) it is daytime, and (c) the external temperature exceeds 28.8 °C.

In order to detect conditions (a) and (b), an infrared sensor (PIR) and a light sensor are mounted on SPARTACUS. As for condition (c), a weather station mounted on the roof of our building is periodically interrogated through a computer. The same computer interfaces an RFID reader. Finally, the GPIO of the reader is connected to the fan through an appropriate hardware driver supporting higher power than GPIO. The reader receives temperature values from the laptop and compares them with the 28.8 °C threshold. Any threshold crossing is communicated to SPARTACUS, when requested. Vice versa, according to the algorithm sketched in Fig. 3, SPARTACUS is programmed to: 1) sense the light level and compare it with a threshold of 2500 Lux (daylight threshold); 2) verify the presence of people in the office room through a PIR sensor; 3) ask the reader about the fan status (ON/OFF); 4) ask the reader whether or not the temperature threshold is exceeded; 5) verify the true/false status of conditions (a), (b), and (c); 6) send to the reader, if needed, a trigger command to switch ON/OFF the fan. The test was performed leaving SPARTACUS in a standard office room for 24

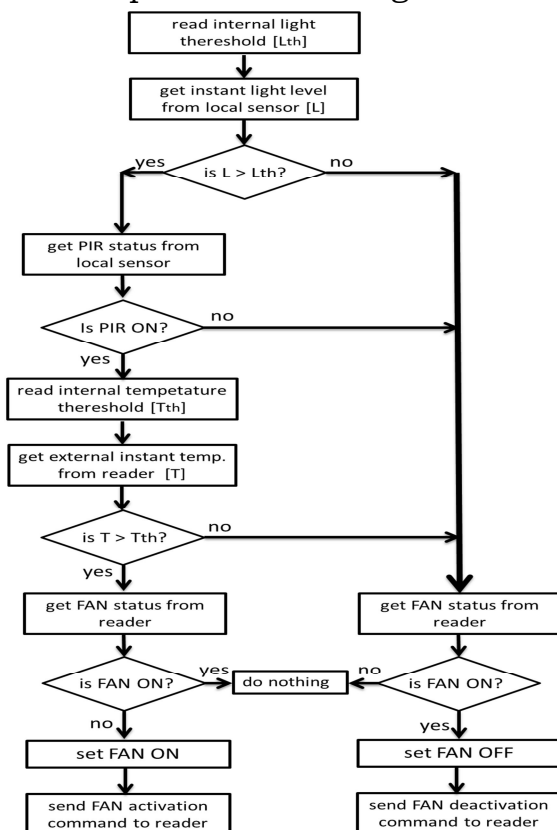


FIG. 3 – Algorithm performed by SPARTACUS.

hours, 2-meter away from the reader antenna, and rather close to a window to monitor the light conditions over the course of a day. Fig. 4 shows how sensor measurements performed by the tag are consistent with events occurred over the 24-hour observation period, with light rising around 6:00 and dropping around 19:30. This clearly demonstrates the ability of SPARTACUS to perform RFID-sensing. Also people presence in the office room, revealed by the PIR sensor and known only by the tag, is visible in Fig. 4, along with external temperature and related threshold, known at the reader stage. It can be observed that the fan is correctly activated or deactivated by SPARTACUS according to the occurrence of the mentioned conditions.

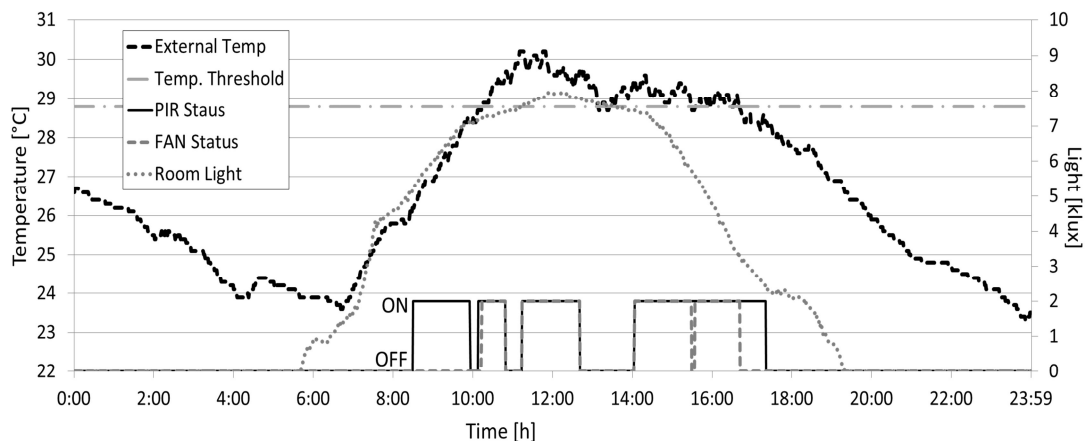


FIG. 4 – RFID-based ambient control on the basis of local and context data.

IV. CONCLUSION

In this paper, an improved augmented RFID tag enabling a tag-reader cooperative approach has been presented and validated in some application contexts which take advantage from several features of the renovated device: the capability of asking for and receiving context data, of sensing a physical value, of reasoning, and of taking decisions, have been exploited at the same time. These functionalities are enabled by the implemented communication procedure.

REFERENCES

- [1] J. R. Smith et al., "ID Modulation: Embedding Sensor Data in an RFID Timeseries," *Information Hiding, LNCS*, vol. 3727, pp. 234–246, 2005.
- [2] L. Catarinucci, R. Colella, and L. Tarricone, "Sensor data transmission through passive RFID tags to feed wireless sensor networks," *2010 IEEE MTT-S International Microwave Symposium*, Anaheim, CA, pp. 1772-1775, 2010.
- [3] T. Ussmueller, D. Brenk, J. Essel, J. Heidrich, G. Fischer, and R. Weigel, "A Multistandard HF/UHF-RFID-tag with Integrated Sensor Interface and Localization Capability," *2012 IEEE International Conference on RFID*, pp. 66–73, April 2012.
- [4] R. Colella, L. Tarricone, L. Catarinucci, "SPARTACUS: Self-Powered Augmented RFID Tag for Autonomous Computing and Ubiquitous Sensing," *IEEE Transactions on Antennas and Propagation*, vol. 63, no. 5, pp. 2272-2281, May 2015.
- [6] S. Amendola, L. Bianchi, G. Marrocco, "Movement Detection of Human Body Segments: Passive Radio-Frequency Identification and Machine-Learning Technologies.," *IEEE Antennas and Propagation Magazine*, vol.57, no.3, pp. 23-37, June 2015.
- [7] Yejun He; Xudong Cheng; Wei Peng; Stuber, G.L. "A Survey of Energy Harvesting Communications: Models and Offline Optimal Policies," *IEEE Communications Magazine*, vol.53, no.6, pp. 79-85, June. 2015.

CHIPLESS RFID TAGS AND SENSORS FOR WIRELESS SENSOR NETWORKS

F. Costa,^(1,2) S. Genovesi^(1,2), M. Borgese^(1,2), F. A. Dicandia^(1,2), A. Monorchio^(1,2), G. Manara^(1,2)

⁽¹⁾ Department of Information Engineering, Pisa University
Via G. Caruso 16, Pisa, Italy

⁽²⁾ Consorzio Nazionale Interuniversitario per le Telecomunicazioni
Via G. Usberti, Parma, Italy
simone.genovesi@unipi.it

Abstract

Chipless Radio Frequency Identification relies on the modulation of the backscattered signal produced by the tag. Several designs of tags are possible by exploiting the properties of periodic surfaces. An alteration of the physical properties of the chipless RFID tags under variable environment conditions suggest the use of this technology as a sensor. The challenge in designing chipless RFID sensors is how to perform data encoding without the presence of a chip and adding the sensing capability. These new class of low-cost sensors can be advantageously employed in wireless sensor networks and Internet of Things paradigm.

Index Terms – chipless RFID, chipless RFID sensor, wireless sensor network, Internet of Things (IoT).

I. INTRODUCTION

The Internet-of-Things paradigm requires the development of novel, reliable and low-cost wireless solutions. A promising research area regarding this topic deals with Radio Frequency Identification (RFID) systems that employ chip-based RFID tags with sensing capabilities. However, despite the great interest of conventional RFID, the need for an entirely-passive sensing solution is highly desirable in order to fulfill important practical requirements such as: real-time sensing, potentially infinite lifetime, green technology compliant and last but not least low-cost to allow a massive use of tags for environmental monitoring. It is therefore a challenging and necessary task to investigate on chipless RFID technology to reduce the unit cost and provide innovative solutions for realizing a ubiquitous wireless sensor network.

Chipless technology is based on the modulation of the backscattered signal and it has recently gained great attention in the logistic field for tracking objects. The challenge in designing chipless RFID tags is how to perform data encoding without the presence of a chip and a great research effort is ongoing to propose more and more clever encoding, both in frequency and in time domain. In addition to this, the sensing capability has to be added and the chipless RFID tag has to provide an estimate of an environmental entity. Numerous state-of-the-art designs of chipless sensors can be found in the open literature although the

reliability and reproducibility of most of them is critical. Several challenges still wait to be faced and efficiently solved, such as the choice of the materials able to sense an environmental change and the modeling of the relation between the sensed parameter and the change in the sensor response. In this sense, some promising designs of chipless RFID tags have been investigated in order to provide a tag that can also perform sensing operation

II. CHIPLESS RFID TAG DESIGN

Chipless tags synthesized with metasurfaces are a promising solution which allows different bit-encoding methods. Metasurfaces are a class of two-dimensional metamaterials comprising a periodic arrangement of resonators. To synthesize the chipless RFID tag, the periodic surface is printed on top of an ultra-thin grounded dielectric slab to form a so-called High-Impedance Surface (HIS) [1]. The layout of the structure is represented in Fig.1. Properties of Frequency Selective Surfaces (FSSs) and HIS can be advantageously modelled through simple yet accurate circuital approach [2].

There are three main reasons for using HIS-based tags:

- the structure can be easily analyzed by using a Periodic Method of Moments (PMM);
- the RCS average value is controlled by increasing or decreasing the number of unit cells;
- the presence of the ground plane allows isolating the response of the tag from the one of the surrounding objects.

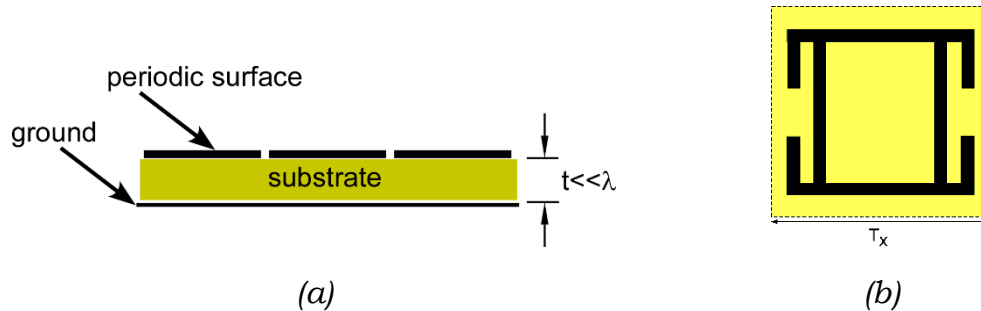


FIG. 1 – Stackup of the employed configuration *a)* and top view of the unit cell of the periodic surface *b)*.

By exploiting the peculiar properties of HIS surfaces various encoding mechanisms are possible. The first method is to synthesize a multi-frequency narrowband absorber [1]. The second approach consists in exploiting the polarization conversion capability of metasurfaces [3], [4]. The third approach relies on the phase encoding [5] whereas another one is based on a differential encoding exploiting a dual-polarized reader [6]. The last approach is more robust with respect to the environment and it

has been proved a viable solution for performing a reading procedure without any type of background subtraction [7].

III. TRANSFORMING A CHIPLESS RFID TAG INTO A SENSOR

A chipless RFID sensor can be realized by exploiting the permittivity variation of a Chemical Interactive Material (CIM) placed on a frequency-based chipless RFID. The changing permittivity of the superstrate material determines a variation of the frequency response of the chipless RFID tag. For example, a chipless RFID tag can be transformed in a humidity sensor if the permittivity of the CIM is a function of the relative humidity of the environment. The CIM can be placed on top of the periodic printed surface. It has to be underlined the CIM has to be in the direct contact of the resonator in order to maximize the frequency shift and therefore air gaps have to be accurately avoided. In this case, a sheet of paper has been adopted as the CIM superstrate. The permittivity of the dry paper has been considered equal to 3.5. A progressive increment of the 10% of the initial permittivity has been estimated because of humidity absorption. The increasing water content of the paper layer determines a shift of the absorption peak of the chipless RFID tag (Fig.2). In this case, the information is encoded in the frequency shift with respect to the reference values of the dry paper and it is not related to the peak deepness. Clearly, the most challenging part of this research is to demonstrate the phenomenon in practice and analyze its reliability and reproducibility. The current work is focused on linking the change in permittivity to the relative humidity (RH) by using a controlled climatic chamber developed by the authors. The ongoing experimental research and the most promising results will be presented at the conference.

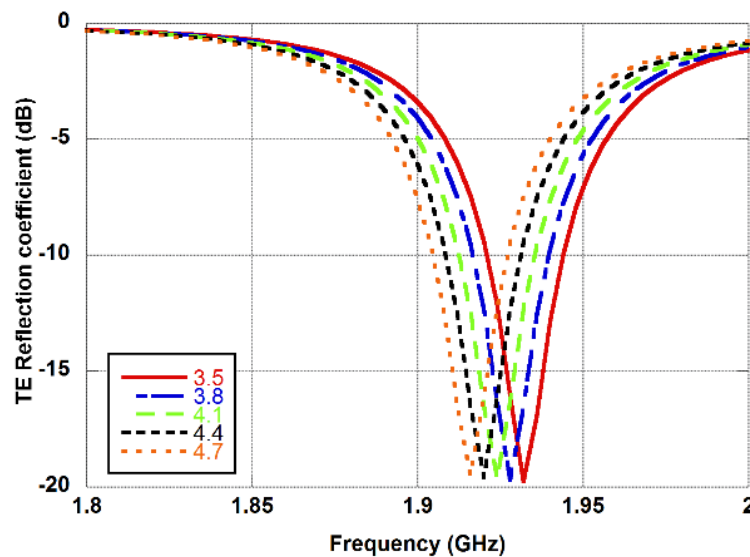


FIG. 2 – Shift of the absorption of the chipless tag peak as a function of the dielectric permittivity of the superstrate.

ACKNOWLEDGEMENT

Financed by the European Commission under the Call H2020-MSCA-RISE-2014, Project EMERGENT - GA n. 645771.

REFERENCES

- [1] F. Costa, S. Genovesi, and A. Monorchio, "A Chipless RFID Based on Multiresonant High-Impedance Surfaces," *IEEE Transactions on Microwave Theory and Techniques*, vol. 61, no. 1, pp. 146–153, Jan. 2013.
- [2] F. Costa, A. Monorchio, and G. Manara, "An Overview of Equivalent Circuit Modeling Techniques of Frequency Selective Surfaces and Metasurfaces.," *Applied Computational Electromagnetics Society Journal*, vol. 29, no. 12, 2014.
- [3] F. Costa, S. Genovesi, and A. Monorchio, "Chipless RFIDs for Metallic Objects by Using Cross Polarization Encoding," *IEEE Transactions on Antennas and Propagation*, vol. 62, no. 8, pp. 4402–4407, Aug. 2014.
- [4] F. Costa, S. Genovesi, and A. Monorchio, "Reading chipless RFID located on metallic platforms by using cross-polar scattering," in *General Assembly and Scientific Symposium (URSI GASS), 2014 XXXIth URSI*, 2014, pp. 1–4.
- [5] S. Genovesi, F. Costa, A. Monorchio, and G. Manara, "Chipless RFID Tag Exploiting Multifrequency Delta-Phase Quantization Encoding," *IEEE Antennas and Wireless Propagation Letters*, vol. PP, no. 99, pp. 1–1, 2015.
- [6] F. Costa, S. Genovesi, A. Monorchio, and G. Manara, "A Robust Differential-Amplitude Codification for Chipless RFID," *IEEE Microwave and Wireless Components Letters*, vol. 25, no. 12, pp. 832–834, Dec. 2015.
- [7] F. Costa, S. Genovesi, and A. Monorchio, "Normalization-Free Chipless RFIDs by Using Dual-Polarized Interrogation," *IEEE Transactions on Microwave Theory and Techniques*, vol. 64, no. 1, pp. 310–318, Jan. 2016.
- [8] A. Vena, E. Perret, and S. Tedjni, "A Depolarizing Chipless RFID Tag for Robust Detection and Its FCC Compliant UWB Reading System," *IEEE Transactions on Microwave Theory and Techniques*, vol. 61, no. 8, pp. 2982–2994, Aug. 2013.

EXPERIMENTAL TOOL FOR RFID TAG ELECTROMAGNETIC ANALYSIS

R. Colella

Department of Innovation Engineering, University of Salento
Via Monteroni, Lecce, Italy
riccardo.colella@unisalento.it

Abstract

Performance of RFID tags is strongly dependent on the context, so that the selection of the most suitable tag for the specific application becomes a key point. In this work, a cost-effective but accurate system for the electromagnetic characterization of UHF RFID tags is firstly presented and then validated in the challenging case of label-type tag antennas bent around cylindrical structures.

Index Terms – RFID antenna, electromagnetic performance, radiation pattern

I. INTRODUCTION

Thanks to the proliferation of scientific works related to novel layouts and strategies for designing compact and high-performance RFID tag antennas [1], [2], the development of novel kinds of test environments, tools, and methods suitable for UHF RFID tag characterization is becoming a topic of interest for the Electromagnetic (EM) Community. Indeed, at the state of the art, different kinds of methods have been proposed. Some of them are based on direct measurements of some important RFID tag parameters, such as chip or tag antenna impedance. Some others characterize the assembled tags through over-the-air methods by analyzing the backscattered signal [3],[4].

In this work, based on the author's PhD activity carried out at the EM Fields Group of the University of Salento under the supervision of Professors Tarricone and Catarinucci, an accurate, flexible, and low-cost tool for the UHF RFID tag EM characterization and performance evaluation is presented. Lying on a specific theoretical formulation of the EM problem, the novel system allows for the calculation of a set of metrics characterizing an RFID tag as a function of the tag activation power threshold when varying both tag orientation and interrogation frequency in the 865-928 MHz band. The system has been optimized to estimate radiation pattern (RP) and sensitivity of RFID tags through an over-the-air analysis when chip and antenna are assembled together. Hence, antenna gain, quality of antenna-chip conjugate matching, and substrate are contemporarily taken into account.

Once implemented the novel characterization tool has been validated through comparison with a reference measurement platform. Moreover, an experimental campaign has been carried out aimed at assessing the electromagnetic performance of flexible label-type RFID tag antennas bent around cylindrical structures with different diameters.

II. THEORETICAL FORMULATION AND METRICS DERIVATION

Let us consider the RFID communication system of Fig. 1.a where tag and reader antennas are placed along a straight horizontal line, with reader antenna kept fixed and tag antenna free to rotate around its axes. By using the Friis formula and naming d the tag-reader distance, η_{plf} the polarization loss factor, A_{cable} the cable attenuation and τ the power transmission coefficient between tag antenna and RFID chip, the minimum power activating the RFID chip, i.e. the chip sensitivity S_{chip} is:

$$S_{chip} = P_{tx,ON}(\theta, \varphi) \cdot G_{tx} \cdot G_{tag}(\theta, \varphi) \cdot \tau \left(\frac{\lambda}{4\pi d} \right)^2 \cdot \eta_{plf} \cdot A_{cable} \quad (1)$$

where the gain of the reader antenna G_{tx} is assumed to be fixed and the gain of the tag antenna G_{tag} is assumed to be an angular function of (θ, φ) . Consequently, since the chip sensitivity is a constant, the power emitted by the reader in correspondence of the chip activation event, denoted as $P_{tx,ON}(\theta, \varphi)$, must be necessarily an angle-dependent parameter. It is worth highlighting that the only chip sensitivity S_{chip} is not sufficient to quantify the goodness of the assembled tag, which definitely depends also on the quality of the tag antenna and on the quality of the conjugate matching between antenna and chip. In its place, a novel and more significant metric can be the “sensitivity of the whole tag” S_{tag} which as desired accounts chip, antenna gain, and conjugate matching. Starting from (1), the tag sensitivity can be defined as a function of the tag activation power threshold $P_{tx,ON}(\theta, \varphi)$:

$$S_{tag}(\theta, \varphi) \triangleq S_{chip} / \tau \cdot G_{tag}(\theta, \varphi) = P_{tx,ON}(\theta, \varphi) \cdot G_{tx} \cdot (\lambda/4\pi d)^2 \eta_{plf} \cdot A_{cable} \quad (2)$$

The tag sensitivity evaluated in (2) is an angle-dependent parameter. Nevertheless, by keeping constant the angles, the frequency-dependent version of the tag sensitivity can be obtained as follow:

$$S_{tag}(f) = S_{chip} / \tau(f) \cdot G_{tag}(f) = P_{tx,ON}(f) \cdot G_{tx} \cdot (c/4\pi df)^2 \eta_{plf} \cdot A_{cable} \quad (3)$$

Finally, another important tag characterization can be done in terms of radiation pattern of the tag antenna. Starting from (2) and after some simple steps, the tag antenna radiation pattern can be obtained as:

$$\frac{G_{tag}(\theta, \varphi)}{G_{tag,max}} = \frac{S_{tag,min}}{S_{tag}(\theta, \varphi)} = \frac{P_{tx,ON,min}}{P_{tx,ON}(\theta, \varphi)}. \quad (4)$$

It is important to observe that the three metrics (2)-(4), which would allow a complete characterization of any UHF RFID tag both by varying angle and frequency, are directly or indirectly depending on the activation power threshold $P_{tx,ON}$, once all the other static parameters of Fig. 1 (G_{tx} , d , η_{plf} , A_{cable}) are set. On such basis it is possible to define a novel system that experimentally determines the tag activation power threshold $P_{tx,ON}$ and then all the proposed metrics, as described below.

III. RFID TAG CHARACTERIZATION TOOL IMPLEMENTATION

The proposed system for UHF RFID Tag electromagnetic characterization is reported in Fig. 1.b. It is mainly composed of a fully-controllable UHF RFID reader board having its RF interface connected to a patch antenna with known electromagnetic characteristics and its digital output connected to an automatized rotating system. The selected reader board is the ThingMagic Mercury 6e (M6e) which is equipped with four GPIO (General Purpose Input Output) ports and which allows to modify both the emitted power (in the range 5 – 31.5 dBm in steps of 0.5 dB) and the working frequency in the whole RFID band. It is worth highlighting that the wide power excursion along with the good power resolution of this reader allow for the implementation of a measurement procedure based on the iterative research of the tag activation power threshold $P_{tx,ON}$. Besides the M6e, in order to implement the tag rotation with respect to the reader antenna, a stepper motor with minimum angular step of 1.8° has been selected. The stepper motor is controlled by the M6e GPIO ports through driver board. In order to carry out the performance evaluation of a tag, the main task to be performed by the proposed measurement tool is the individuation of the tag activation power threshold by gradually increasing via software, from zero to the maximum allowed value, the reader emitted power P_{tx} and, contextually, by verifying whether or not the tag is energized and answers to the reader.

IV. RESULTS

In this Section, the capability of the proposed system of performing the EM characterization of RFID tags is verified. First of all, both sensitivity and RP of some UHF RFID tags have been measured in the whole RFID band by using both the proposed tool and the Voyantic platform as described in [5]. The very good agreement of the results demonstrates the suitability of the proposed platform to characterize UHF RFID tags with a high level of accuracy. Moreover, a measurement campaign aimed at creating a taxonomy of label-type RFID tags bent around cylindrical structures has been performed. As observed in Fig. 2.a and 2.b both vertical RP and sensitivity of the tag Alien ALN-9640 for bending diameters of 7.5cm, 5.5cm, and 3.5cm have been preliminarily measured. Performance degradation up to 7 dB can be appreciated as

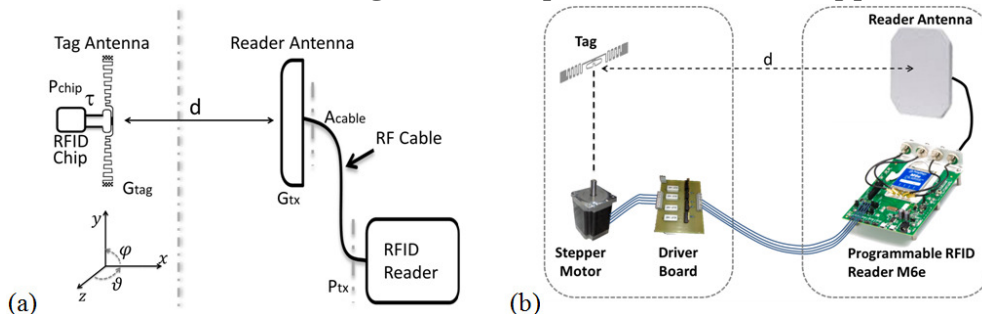


FIG. 1 – (a) Model and (b) architecture of the RFID tag characterization system.

the diameter is gradually reduced and the dipolar structure of the antenna is consequently modified. On such basis, a performance comparison in terms of measured tag sensitivity of a selection of RFID tags equipped with Higgs 3 chip ($S_{chip} = -20\text{dBm}$) in both standard position and when placed on a cylindrical structure with diameter of 3.5cm has been carried out. For instance, as shown in the case of in Fig. 2.c. the ALN-9654 exhibits greater robustness in the case of strong curvature with a sensitivity peak of -16dBm and a degradation of about 5dB with respect to the flat case. On the contrary, the ALN-9640 is less efficient than the previous one and, moreover, it is also more influenced by the curvature effect with a sensitivity peak of -11dBm when bent. Presented results jointly to others omitted for brevity confirm once again reliability and robustness of the proposed tool along with its real support in studying and selecting suitable tags for specific applications.

V. CONCLUSION

In this paper an accurate and cost-effective measurement tool for electromagnetic analysis of passive UHF RFID tags has been presented. It is optimized to estimate antenna radiation pattern and sensitivity of tags in different operating environments. Once realized, the system has been successfully validated through a comparison with a reference instrument and through a measurement campaign on label-type tag antennas bent around cylindrical structures. The novel tool guarantees high versatility, robustness and accuracy in characterizing RFID tags.

REFERENCES

- [1] G. Marrocco, "The art of UHF RFID antenna design: Impedance Matching and size reduction techniques," *IEEE Antennas and Propagation Magazine*, Vol. 50, No. 1, 66-79, 2008.
- [2] D.M. Dobkin, *The RF in RFID*, Elsevier, New York, 2007.
- [3] P. V. Nikitin, K. V. S. Rao and S. Lam "UHF RFID Tag Characterization: Overview and State-of-the-Art," *Proceedings of AMTA 2012*, Seattle, WA, October 2012.
- [4] S.-K. Kuo, S.-L. Chen, and C.-T. Lin, "An accurate method for impedance measurement of RFID tag antenna," *Progress In Electromagnetics Research*, Vol. 83, 93-106, 2008.
- [5] L. Ukkonen, L. Sydänheimo, "Threshold Power-based Radiation Pattern Measurement of Passive UHF RFID Tags," *PIER Symposium*, Vol. 6 No. 6, pp. 523-526, 2010.

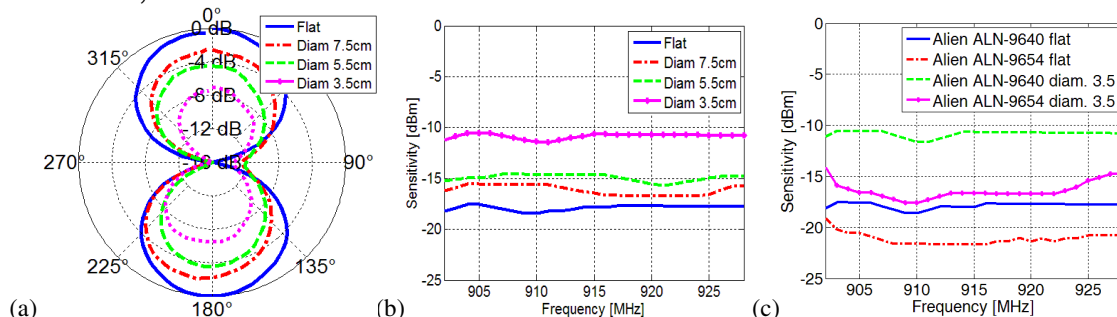


FIG. 2 – (a) Radiation pattern, and (b) sensitivity of ALN-9640. (c) Tag sensitivity test.

ANALYSIS OF THE ROBUSTNESS OF WEARABLE PIFAS TO THE HUMAN BODY COUPLING

G. A. Casula⁽¹⁾, A. Michel⁽²⁾, G. Montisci⁽¹⁾, P. Nepa⁽²⁾, G. Mazzarella⁽¹⁾

⁽¹⁾ Dipartimento di Ingegneria Elettrica ed Elettronica , Università degli Studi di Cagliari, 09123 Cagliari, Italy

⁽²⁾ Dept. of Information Engineering, University of Pisa, Pisa, Italy
e-mails: a.casula@diee.unica.it, andrea.michel@iet.unipi.it,
giorgio.montisci@unica.it, p.nepa@iet.unipi.it, mazzarella@diee.unica.it

Abstract

The robustness of wearable UHF-band grounded antennas with respect to body-coupling effects is addressed through numerical investigations, relating its performance to the distribution of the electric and magnetic energy densities in the antenna near-field region close to the ground plane border. A criterion for choosing a proper shape of the antenna ground plane is specified, which can increase the antenna robustness with respect to the body-coupling effects, but with a minimal impact on the antenna size.

Index Terms—Wearable Antennas, PIFA Antennas, Human Body Coupling

I. INTRODUCTION

In the last few decades, hundreds of scientific papers on wearable antennas have been published in the literature for a large variety of applications [1]-[2]. One of the challenges in the antenna design is making the antenna as robust as possible with respect to the random changes of the body-antenna coupling scenario (antenna-body distance changes randomly due to the wearer natural movements [3]-[4], and the dielectric and geometrical parameters of the human body tissues vary from person to person [5]-[6]). A typical solution considered to minimize the antenna-body coupling effects is designing antennas with a large metallic ground plane. However, for applications in the UHF band (such as in Radio Frequency Identification systems), the wearable antenna size could result uncomfortable. Thus, a criterion is desirable to choose the ground plane shape and size in order to make the antenna performance more robust to the antenna-body distance variation, without significantly increasing the antenna extent. In this paper, a design criterion is introduced to reduce the coupling with the human body, which consists in elongating the antenna ground plane at the section corresponding to an electric energy density peak. In order to demonstrate the proposed design criterion, two Planar Inverted-F Antennas (PIFAs) [7]-[8] with different ground plane configurations have been numerically investigated using CST Microwave Studio.

II. NUMERICAL RESULTS

The relation between PIFAs performance and their near-field energy distribution has been numerically examined to analyze the antenna

performance robustness with respect to the antenna-body coupling. In this paper, two PIFAs have been considered: a RFID tag antenna operating at 900 MHz [7] and a folded PIFA for on-body communications working at 2.4 GHz [8]. To account for the presence of the human body, a simplified three-layer model has been considered in the simulated environment, as shown in Fig. 1a, composed of a skin layer ($\epsilon_r=41.32$, $\sigma=0.855$ S/m) with a thickness of 1.5mm, a fat layer ($\epsilon_r=5.46$, $\sigma=0.05$ S/m) with a thickness of 20mm, and a muscle layer ($\epsilon_r=54.97$, $\sigma=0.934$ S/m) with a thickness of 30mm. Two key parameters have been computed to investigate the antenna performance when varying the antenna distance from the human body phantom, d , the radiation efficiency η , and the power transmission coefficient τ , expressed as:

$$\tau = 1 - \left| \frac{Z_{IN} - Z_0}{Z_{IN} + Z_0} \right|^2 \quad (1)$$

wherein Z_{IN} is the antenna input impedance, and Z_0 is a reference impedance. To evaluate the robustness of the different layouts by varying the body-antenna distance d , the reference impedance Z_0 has been chosen equal to the antenna input impedance at the resonance frequency ($\text{Im}\{Z_{IN}\}=0 \Omega$) and when the antenna is adherent to the human body model ($d=0\text{mm}$). The robustness of the proposed configurations has been studied separately for τ and $\tau \times \eta$, and the best ground plane configuration is considered to be the one exhibiting a reasonable value of $\tau \times \eta$, with a τ as great as possible, with both stable with respect to the antenna-body distance, d . For both the considered antennas [7] and [8], three ground plane configurations have been investigated: ANT (the reference layout), with a ground plane size equal to the size of the antenna radiating element; ANT-E, in which the ground plane is extended toward the regions close to an electric energy density peak; ANT-H, in which the ground plane is extended toward the regions close to a magnetic energy density peak.

A. Wearable Planar Inverted-F Antenna at 900MHz

In [7], a PIFA is proposed for RFID applications at 900MHz. In the reference antenna configuration, ANT, the ground plane size exactly fits the radiating patch dimension. The 3D layout is shown in Fig.1b. By means of CST Microwave Studio, the energy densities have been numerically computed and the results are shown in Fig.2a and 2b. As expected, the maximum of the electric energy density (Fig.2a) is close to the antenna open end, whereas the maximum of the magnetic energy density (Fig.2b) is close to the antenna shorting edge. Two modified versions of the above antenna have also been considered, where an extension of the ground plane has been added close to the electric energy density peak and the magnetic energy density peak, respectively. The percentage variation against d of both τ and the product $\tau \times \eta$, evaluated with respect to the corresponding value for the antenna with

$d=0$ mm, is shown in Fig. 2e and Fig.2f. The robustness of the antenna with respect to the presence of the human body can be significantly increased if the ground plane is extended towards the antenna section corresponding to the location of the maximum of the electric energy density.

B. PIFA antenna at 2.4 GHz

In Fig.1c, the 3D view of the folded PIFA [8] for on-body communications at 2.4 GHz is shown. Moreover, the electric and magnetic energy densities are shown in Fig.2c and Fig.2d, respectively. As described in the previous section, two modified layouts have been considered, obtained by adding an extension of the ground plane toward the peaks of the electric and magnetic energy density, respectively. In Fig. 2, the variation of τ (Fig. 2g) and $\tau \times \eta$ (Fig. 2h) is shown for ANT, ANT-E, and ANT-H configurations. Also in this case, the ANT-E configuration results significantly more robust to the body-antenna separation than the other configurations (i.e, ANT and ANT-H).

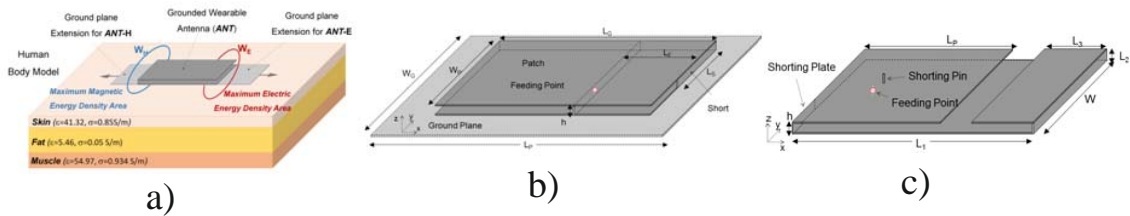


FIG. 1–(a) A PIFA on the phantom model used to perform the numerical investigation of the antenna robustness to the body proximity. (b) Layout of the antenna in [7] (c) Three-dimensional view of the PIFA presented in [8].

III. CONCLUSION

The robustness of the performance of two different PIFA antennas with respect to the human body coupling has been numerically investigated, by relating it to the electric and magnetic energy density distributions in the antenna near-field region around the ground plane border. The extension of the ground plane is more effective at those sections of the antenna border corresponding to a maximum of the electric energy density, rather than at those where the magnetic energy density exhibits a maximum. The proposed guideline can be considered a physics-based criterion to be used in the design of wearable antennas ground plane size and shape. This is the first time that the analysis of the distribution of the electric and magnetic energy densities nearby the antenna border is used to choose the shape of the antenna ground plane, for a resonant, non-electrically small, antenna.

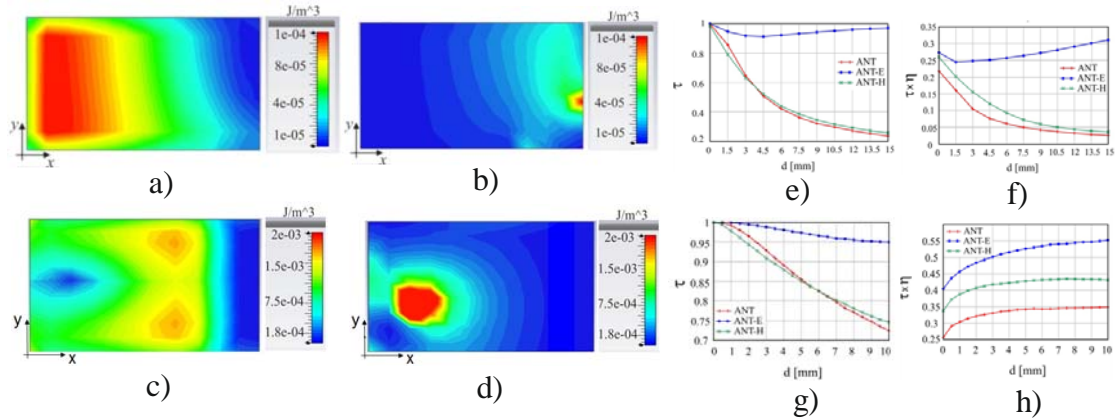


FIG. 2–(a) Electric and (b) magnetic energy densities close to the ground plane, at the resonant frequency for PIFA in [7]. (c) Electric and (d) magnetic energy densities close to the ground plane, at the resonant frequency for PIFA in [8]. (e) Variation of τ , and (f) of the product $\tau \times \eta$, for the ANT, ANT-E, ANT-H configurations analyzed to test the robustness of the PIFA in [7]. (g) Variation of τ , and (h) of the product $\tau \times \eta$, for the ANT, ANT-E, ANT-H configurations analyzed to test the robustness of the PIFA in [8].

REFERENCES

- [1] P. Nepa and H. Rogier, "Wearable antennas for off-body radio links at VHF and UHF bands (below 1 GHz): challenges, state-of-the-art and future trends," *IEEE Antennas and Prop. Magazine*, vol. 57, n. 5, pp. 1-23, 2015.
- [2] P.S. Hall, Y. Hao, V.I. Nechayev, A. Alomainy, C.C. Constantinou, C. Parini, M.R. Kamarudin, T.Z. Salim, D.T.M. Heel, R. Dubrovka, A.S. Owadall, W. Song, A.A. Serra, P. Nepa, M. Gallo and M. Bozzetti, "Antennas and Propagation for On-Body Communication Systems", *IEEE Antennas and Propagation Magazine*, vol. 49(3), pp. 41–58, 2007.
- [3] A. Serra, P. Nepa, and G. Manara, "A wearable two-antenna system on a life jacket for Cospas-Sarsat Personal Locator Beacons," *IEEE Trans. on Antennas and Propagation*, 60 (2), part II, pp. 1035-1042, 2012.
- [4] A. Baroni, P. Nepa and H. Rogier, "Wearable self-tuning antenna for emergency rescue operations", *IET Microwaves, Antennas & Propagation*, vol. 10, n. 10, pp. 173-183, 2016.
- [5] A. Michel, K. Karathanasis, P. Nepa and J.L. Volakis, "Accuracy of a Multi-probe Conformal Sensor in Estimating the Dielectric Constant in Deep Biological Tissues," *IEEE Sensor Journal*, vol. 15, n.9, pp. 5217-5221, 2015.
- [6] M. A. Islam, A. Kiourti and J. L. Volakis, "A Novel Method of Deep Tissue Biomedical Imaging Using a Wearable Sensor," in *IEEE Sensors Journal*, vol. 16, no. 1, pp. 265-270, Jan.1, 2016.
- [7] M.-H. Lin and C.-W. Chiu "Human-body effects on the design of card-type UHF RFID tag antennas", *Proc. IEEEAP-S Int. Symp.*, pp.521 -524 2011
- [8] C.-H. Lin, K. Saito, M. Takahashi, and K. Ito, "A compact planar inverted-F antenna for 2.45 GHz on-body communications," *IEEE Trans. on Antennas and Propagation*, vol. 60, no. 9, pp. 4422-4426, 2012
- [9] G. A. Casula, A. Michel, P. Nepa, G. Montisci, G. Mazzarella, "Robustness of Wearable UHF-band PIFAs to Human-Body Proximity", *IEEE Trans. on Antennas and Propagation*, in press.

A CENTRALISED ADS-B SYSTEM FOR EN-ROUTE AND LOW LEVEL COVERAGE

M. Arpaio ⁽¹⁾, S. Selleri ⁽²⁾

⁽¹⁾ Thales Italia Spa, Air Traffic Management Domain
Via Enrico Mattei 1, 20064 - Gorgonzola (MI), Italy
maximilian.arpaio@thalesgroup.com

⁽²⁾ Università degli Studi di Parma,
Dipartimento di Ingegneria dell'Informazione
Viale Parco Area delle Scienze 181/A, 43124 – Parma (PR), Italy
stefano.selleri@unipr.it

Abstract

Automatic Dependant Surveillance - Broadcast (ADS-B) is becoming of widespread use in modern Air Traffic Management system. Due to its small footprint, easiness of installation and reduced maintenance costs, it is nowadays a proven technology for air traffic surveillance with hundreds of site installations worldwide. Nevertheless, the design and setting-up of an ADS-B system for professional use and within an operational environment is a different matter, where the demand for reliable operation and excellent performances as well as high data rate and quality is mandatory for civil aviation surveillance needs.

Extending the capacity of a stand-alone ADS-B receiver system into a centralised ADS-B one, with multiple remote receivers, and a centralised processor that merges data, might be one of key factors in the future of next generation surveillance systems. This paper reports the successful implementation of an operational Centralised ADS-B system in one of the most congested airspaces of the APAC region. Methods and strategies to design, deploy it and minimise RF propagation issues to achieve required performances are presented.

Index Terms – ADS-B, Space Diversity, Siting Concept, Probability of Detection

I. INTRODUCTION

Automatic Dependent Surveillance -Broadcast (ADS-B) is a system in which electronic equipment on-board an aircraft automatically calculates and broadcasts the precise location of the aircraft via a digital data link on 1090 MHz. The system involves an aircraft with ADS-B determining its position using GPS. A suitable transponder then broadcasts that position at high rates, along with Mode S, identity, altitude, velocity and other data. ADS-B has the capability to cover an

area of nearly 250 NM under suitable RF power budget conditions and free Line-Of-Sight (LOS). Dedicated ADS-B ground stations then receive the broadcasts and relay the information to air traffic control (ATC) for precise tracking and surveillance of the aircraft, even without the need for radars [1].

ADS-B has many advantages when compared with conventional radar surveillance: accuracy does not degrade with range, atmospheric conditions or target altitude and update intervals do not depend on the rotation movement of mechanical antennas.

Nevertheless, to reach such efficient performances ADS-B receivers must be anyway placed correctly with regards to the targeted reception coverage and the air route to be surveilled.

II. A CENTRALISED ADS-B SYSTEM

Although the new generation of ADS-B ground station hardware is well responding to increased need for performance in terms of processing capacity, fruit handling, sensitivity, reduced communication network capacity, as well as improved maintenance and handling [3], nothing can be done if a preliminary site assessment is not carried out and the remote site network is not properly designed, considering many RF propagation scenarios, electromagnetic compatibility issues and redundancy needs.

The ability of a ground station to receive and properly decode an ADS-B signal depends on altitude, distance from the target and terrain orography. Although en-route surveillance is the main purpose of an ADS-B system, by means of proper antenna and installation site selection, surveillance coverage can be even extended down to near ground level. This is desirable when low level coverage is required, like for surveillance of search and rescue flights. When a single ADS-B site – either for en-route surveillance purposes, or for low level ones - is then joined to a network so that the coverage of all the involved ground stations is summed, mostly overlapped from certain flight level onwards, and its Asterix (All Purpose Structured Eurocontrol Surveillance Information Exchange) data is merged with all the others, it is then possible to define a Centralised ADS-B system.

III. IMPLEMENTATION OF THE SYSTEM

A signal that is transmitted over different distances to a receiver may be received at very different signal strengths, if not received at all. In a true multipath environment, the airplane is constantly in motion, so the nulls and the peaks would occur at different times on each receiver. Although there may be circumstances in which the signals at both receiver locations are at around the same level, when it doesn't matter

which receiver output is chosen, like in a centralised ADS-B system, most of the time one signal will be stronger than the other.

To increase even more the probability of getting a higher average output, more receivers are thus used in a centralised system. Often, especially close to urban environments, when approaching an airport for example, there is no clear line-of-sight (LOS) between the airplane transmitter and receiver. Instead the signal is reflected along multiple paths before finally being received. Each of these bounces can introduce phase shifts, time delays, attenuations, and distortions that can destructively interfere with one another at the aperture of the receiving ADS-B antennas [4].

As a consequence, the related ADS-B antenna must be installed on the very top of a structure in a way to reduce LOS obstruction and RF reflections by nearby obstacles as well as to prevent the neighbouring tower or structure from disrupting the natural antenna pattern. Common practice will inevitably lead to the installation of the omnidirectional antennas in a position of the structure where interaction between the tower structure and the antenna is inevitable, so countermeasures to mitigate this must be taken.

Furthermore, the use of specific configurations, like omnidirectional antennas in the receiving station may lead to the overlap in time of many Mode S signals on 1090 MHz band from different directions thus resulting in reduced detection and/or decoding performance [2].

As seen during the deployment of the ADS-B system, antenna diversity – or better, space diversity among the ground stations – together with careful positioning with regards to the holding structure, has been especially effective at mitigating these multipath situations. This is because multiple antennas offer several observations of the same signal to centralised ADS-B system. As a matter of fact, each antenna will experience a different interference environment and a slightly modified radiation diagram. Thus, if one ground station is experiencing a deep fade for a specific airplane in a specific position, it is very likely that another has a sufficient signal to feed the centralised processor with a suitable Mode S report.

IV. RESULTS AND PERFORMANCES

The more ground stations were installed, the more were joined to the centralised system network and the more the qualitative performances of the system were improved. The number of plots on the situational display were constant with barely no gaps, regardless of the route or flight level of the airplanes. From a quantitative perspective, performances of ADS-B systems are often evaluated based on their compliance with the guidance document of performance specifications as summarised within the test procedures for civil aviation equipment. One of the key performance parameters is Probability of Detection (PD) which is commonly used as a test parameter in surveillance systems.

For ADS-B, PD refers to the parameter of Update Probability which measures the probability of position report, i.e. the successful detection rate for each scan or update interval in general, would be calculated by examining, for a particular coverage area, the detections presented to the controller and dividing by the number of possible screen updates [5].

The key results from this operational deployment in the APAC region show an average PD of 98.6% over 5 seconds when calculated on a single ground station basis, while it boosts up to 99.9% over 5 seconds (99.2% over 2 seconds) when calculated as a centralised ADS-B system made of a total number of 9 ground stations. This should be of no particular surprise due to the broadening and overlapping of airspace coverage in different areas that lead to an increased detection probability.

In reality the off-line test results of PD performance are inevitably subject to the impact of test objects' geographic position and movement status in all surveillance systems. Special care must be taken during the data processing phase so as to minimize the variation in the data sample. As a matter of fact, data outside the coverage volume, both horizontal and vertical, were deleted. At the same time data from unstable transponders within the target of opportunity population, were deleted as well.

V. CONCLUSION

In this paper, it was proposed a new approach on the design of an ADS-B system in which ground stations are not treated anymore as standalone systems but as part of a centralised network, achieving amazing PD results based on some installation precautions that are able to mitigate RF interferences and achieve a suitable distributed system design. Results show an improved communication capability and situational awareness that would allow ADS-B to operate more safely inside the radar and non-radar airspace by significantly improving the overall quality and rate of the information for the controllers from en-route, down to very low flight levels.

ACKNOWLEDGEMENT

The author wishes to express his gratitude to customers in the APAC region for providing different ADS-B recordings and to Thales colleagues - both in Italy and Germany - for the great support received during the post-processing of the ADS-B data as well as during the execution of the main contractual phases. Appreciation must be shown as well to the Department of Information Engineering of the University of Parma for the many technical advices in the implementation of the solution.

REFERENCES

- [1] M. Strohmeier, M. Schafer, V. Lenders and I. Martinovic, "*Realities and Challenges of NextGen Air Traffic Management: The Case of ADS-B,*" IEEE Communications Magazine, May 2014, pp. 111-118.
- [2] Safety, Performance and Interoperability Requirements Document for ADS-B-NRA Application, ED-126, EUROCAE, December 2005.
- [3] J. Johnson, J. Beyer and H. Neufeldt, "*Wide Area Multilateration and ADS-B Proves Resilient in Afghanistan,*" 2012 Integrated Communications Navigation and Surveillance (ICNS) Conference, April 24-26, 2012.
- [4] M. Sopata, P. Kejik "*Enhanced techniques for improved ADS-B Messages Reception,*" 34th Digital Avionics Systems Conference September 13-17, 2015
- [5] Ning Xu, Chun-Hung Chen, Scott Hauswald "*Influence factors of probability of detection test on surveillance systems,*" 2011 Integrated Communications Navigation and Surveillance (ICNS) Conference May 10-12, 2011

CHARACTERIZATION OF LOCALIZED AND STATIONARY DYNAMIC BRILLOUIN GRATINGS

F. Chiarello, L. Palmieri, M. Santagiustina

Department of Information Engineering, University of Padova
Via G. Gradenigo 6/B, Padova, Italy
fabrizio.chiarello@dei.unipd.it

Abstract

We experimentally generate localized and stationary dynamic Brillouin gratings (DBGs) in a 5m long polarization maintaining fiber (PMF) by phase modulation with a pseudo-random bit sequence (PRBS). The DBGs are characterized in terms of length, bandwidth, reflectivity and optical signal-to-noise ratio (OSNR) by measuring the distribution of the complex reflected signal along the fiber through swept-wavelength interferometry (SWI). The performance of optimal noise-less modulation formats are estimated and compared to the PRBS case.

Index Terms – Dynamic Brillouin gratings, Nonlinear optical processing.

I. INTRODUCTION

Recently, DBGs [1], generated through stimulated Brillouin scattering (SBS), have been envisaged as an efficient architecture to realize wide and fast dynamic tunable microwave photonics filters [2], optical filters [3], optical delay lines [4], all-optical signal processing [5], radio signal processing [6] and high resolution sensing [7]. In PMFs, two counter-propagating pump waves, polarized along one of the principal axes of the fiber generate an acoustic wave that actually modulates the refractive index in the longitudinal direction. A probe signal launched on the orthogonal axis is back-reflected by the isotropic acoustic wave that actually constitute a dynamic grating. Similarly to fiber Bragg gratings (FBGs) [8], DBGs properties can be designed by properly imposing specific refractive index variations along the fiber. The main difference between FBGs and DBGs is that, once realized, FBGs can be weakly and slowly tuned only mechanically, while the DBGs can be dynamical reconfigured by a proper design of the acoustic wave, that essentially depends on the correlation between the pump waves [5]. For example the acoustic wave, and hence the DBG, can be spatially localized, with a prescribed apodization function, in a short portion of the fiber by properly modulating the phase of the pumps [9,10], realizing DBGs that are both localized and stationary [9,10]. Such DBGs have been experimentally demonstrated by Antman et al. [9] using the PRBS modulation, that is not optimal owing to the generation of spurious off-peak correlation points along the fiber [11]. Here, we experimentally generate localized and stationary DBGs in a PMF by PRBS modulation, and different configurations of DBGs are demonstrated. Heterodyne SWI is used to measure the complex transfer function of the DBGs, obtaining the distributed characterization in modulus and phase. From the complex transfer function the length, the

bandwidth, the reflectivity and the OSNR are determined, the transfer function under optimal conditions is also estimated and quantitative insight on the correlation noise is obtained.

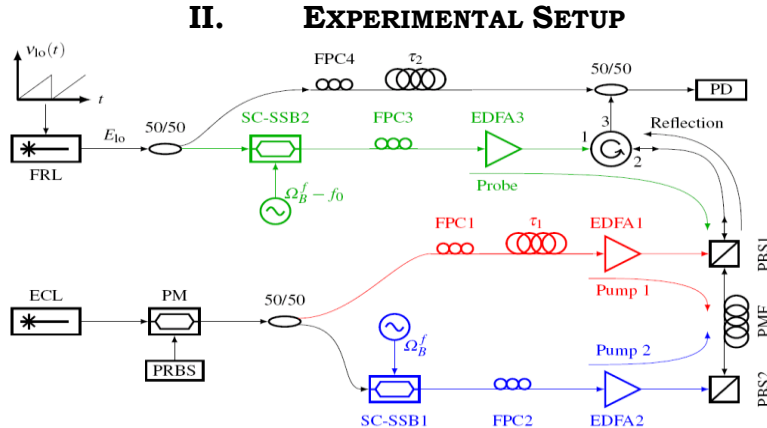


FIG. 1 – Experimental setup.

The experimental setup is shown in Fig. 1. The fiber used is a PMF of length 5m with a measured Brillouin shift $\Omega_B \approx 10.864\text{GHz}$. The pump wave P1 at frequency ν_1 is generated by an external cavity laser (ECL) while pump P2 at frequency $\nu_2 = \nu_1 - \Omega_B$ is obtained from P1 through a suppressed-carrier single sideband (SC-SSB1) modulator. The pump powers are controlled by Erbium-doped fiber amplifiers (EDFAs) and fiber polarization controllers (FPCs) are used to align their polarization to the PMF fast axis. Polarization beam splitters (PBSs) are used to couple all waves to the PMF. A phase modulator (PM) is used to modulate both pumps with the same PRBS signal, that actually controls the DBG apodization. The DBGs are interrogated by injecting a probe wave S, polarized along the slow axis, at frequency $\nu_s = \nu_1 - \Delta\nu$ (the shift $\Delta\nu \approx 45\text{GHz}$ is due to the phase matching conditions and depends on the PMF birefringence [1]). The probe S is partially reflected by the DBGs at frequency $\nu_r = \nu_s - \Omega_B$. The DBGs characterization is performed by SWI through a local oscillator (LO) whose frequency $\nu_{lo}(t)$ is linearly swept with rate $\gamma \approx 350\text{GHz/s}$. The signal S is obtained from the LO by a frequency downshift to $\Omega_B - f_0$ ($f_0 = 5\text{MHz}$) through SC-SSB2; the offset f_0 is used to spectrally separate the DBG reflection from the Rayleigh scattering. At the photodiode (PD), the beat between the reflected signal R and the LO is detected as $I(t) \propto |H(\nu)| \cos[2\pi(f_0 + \gamma t)t + \phi_H(\nu)]$, where $\nu = \nu_{lo}(t)$, $H(\nu) = |H(\nu)|e^{i\phi_H(\nu)}$ is the transfer function of the DBG and τ is the propagation delay difference between S and R. The delay τ_1 is selected so to place the DBGs at a distance $z_0 = 3\text{m}$ from the fiber end. The DBG apodization function $h(z)$ can be obtained by applying a Fourier transform to measured data.

III. RESULTS AND DISCUSSION

We present [14] four different configurations of pump and probe powers (A, B, C and D).

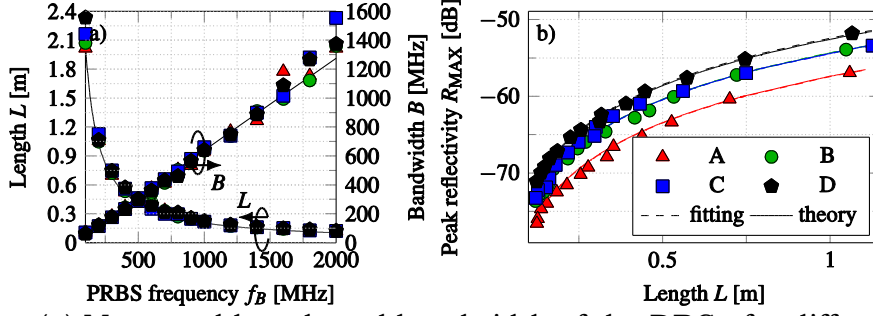


FIG. 2 – (a) Measured length and bandwidth of the DBGs for different PRBS frequencies. (b) Peak reflectivity as a function of the DBGs length L .

Figure 2(a) shows the DBG measured length L and bandwidth B as a function of the PRBS frequency f_B . The solid black curves are the theoretical values given by $L = v_g/f_B$ and $B = B_s f_B$, where B_s is the bandwidth of the sinc² function. Theory and the measured data are in remarkable agreement. By tuning the PRBS rate f_B , L and B can be modified. The measured reflectivity of the DBGs is reported in Fig.2(b) and is in remarkable agreement with the reflectivity theoretical values (solid curves) given by $R = P_1 P_2 (e^{\kappa L (P_1 + P_2)} - 1)^2 / (P_1 + P_2)^2$ [12], where $\kappa \approx 0.1 \text{ W}^{-1} \text{ m}^{-1}$ is a fiber parameter determined by fitting the data; its value agrees with previous measurements on the same fiber using a different setup [13].

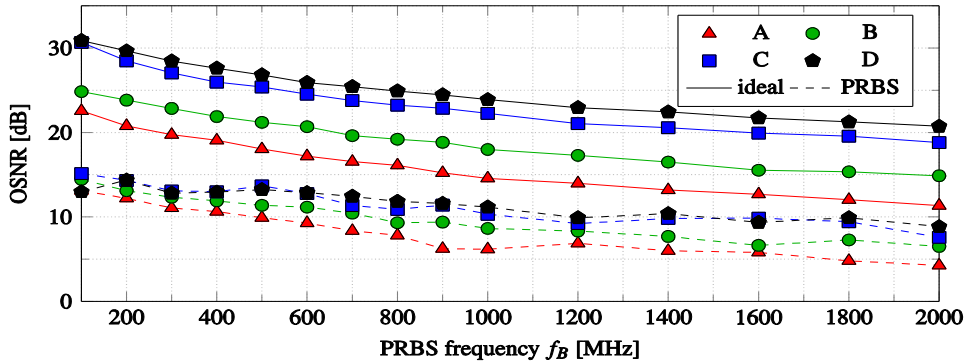


FIG. 3 – Fig. 7. Estimated OSNR for different PRBS frequencies f_B .

The OSNR for different f_B is quantified in Fig. 3; for the PRBS (dashed curves) it is calculated as $OSNR = \int_D |h(z)|^2 dz / \int_{Z-D} |h(z)|^2 dz$, where Z and D represent the fiber and the DBG integration domains. The OSNR decreases for increasing f_B (decreasing length). Shorter gratings have lower reflectivity and so the weight of off-peak reflections becomes larger [9]. The measured OSNR is higher than the prediction of [9], but also the power levels used here are higher than those in [9]. The OSNR penalty spans from about 7 to 18dB, decreases for increasing f_B and it depends on the power levels involved. In particular, higher power levels determine higher penalty. By filtering measured data [14] to eliminate noise, the OSNR of low correlation sequences [11] can be estimated (solid curves).

IV. CONCLUSIONS

We experimentally generated and characterized localized and stationary DBGs in a PMF through PRBS phase modulation of the pumps. The characterization of DBGs has been performed through SWI. From the complex transfer function of the DBGs, the length, the bandwidth, the reflectivity and the OSNR have been determined. All features depend on the PRBS frequency. The reflectivity depends mainly on the pumps powers, while the OSNR depends also on the probe power. The performance of reduced noise gratings generated in ideal conditions have been compared to those generated by PRBS that are affected by off-peak correlation noise.

ACKNOWLEDGEMENT

This research was supported by the Italian Ministry of University (project ROAD-NGN, PRIN 20102KAZKN_005), by the University of Padova (project "Signal processing and sensing based on dynamic Brillouin gratings in optical fibers", CPDA119030) and was held within the agreement with ISCTI.

REFERENCES

- [1] K.Y. Song, W. Zou, Z. He, and K. Hotate, "All-optical dynamic grating generation based on Brillouin scattering in polarization-maintaining fiber," *Opt. Lett.* 33(9), 926-928 (2008).
- [2] J. Sancho, N. Primerov, S. Chin, Y. Antman, A. Zadok, S. Sales, and L. Thévenaz, "Tunable and reconfigurable multi-tap microwave photonic filter based on dynamic Brillouin gratings in fibers," *Opt. Express* 20(6), 6157-6162 (2012).
- [3] F. Chiarello, D. Sengupta, L. Palmieri, and M. Santagiustina, "Characterization of reconfigurable ultranarrowband optical filters realized by localized dynamic Brillouin gratings," *ECOC 2015, Spain*, P.1.10 (2015).
- [4] S. Chin and L. Thévenaz, "Tunable photonic delay lines in optical fibers," *Laser Photon. Rev.* 6, 724-738 (2012).
- [5] M. Santagiustina, S. Chin, N. Primerov, L. Ursini, and L. Thévenaz, "All-optical signal processing using dynamic Brillouin gratings," *Sci. Rep.* 3, 1594 (2013).
- [6] L. Ursini and M. Santagiustina, "Applications of the dynamic Brillouin gratings to ultrawideband communications," *Photon. Technol. Lett.* 25(14), 1347-1349 (2013).
- [7] K.Y. Song, S. Chin, N. Primerov, and L. Thévenaz, "Time-domain distributed fiber sensor with 1cm spatial resolution based on Brillouin dynamic grating," *J. Lightwave Technol.* 28(14), 2062-2067 (2010).
- [8] T. Erdogan, "Fiber grating spectra," *J. Lightwave Technol.* 15(8), 1277-1294 (1997).
- [9] Y. Antman, N. Primerov, J. Sancho, L. Thévenaz, and A. Zadok, "Localized and stationary dynamic gratings via stimulated Brillouin scattering with phase modulated pumps," *Opt. Express* 20(7), 7807-7821 (2012).
- [10] M. Santagiustina and L. Ursini, "Dynamic Brillouin gratings permanently sustained by chaotic lasers," *Opt. Lett.* 37(5), 893-895 (2012).
- [11] Y. Antman, N. Levanon, and A. Zadok, "Low-noise delays from dynamic Brillouin gratings based on perfect Golomb coding of pump waves," *Opt. Lett.* 37(24), 5259-5261 (2012).
- [12] D.-P. Zhou, Y. Dong, L. Chen, and X. Bao, "Four-wave mixing analysis of Brillouin dynamic grating in a polarization-maintaining fiber: theory and experiment," *Opt. Express* 19(21), 20785-20798 (2011).
- [13] D. Sengupta, M. Santagiustina, F. Chiarello, and L. Palmieri, "Generation of dynamic Brillouin grating in polarization maintaining fiber," *Proc. SPIE* 92021Q (2014).
- [14] F. Chiarello, D. Sengupta, L. Palmieri, and M. Santagiustina, "Distributed characterization of localized and stationary dynamic Brillouin gratings in polarization maintaining optical fibers," *Opt. Express* 24, 5866-5875 (2016)

EXPLOITING FREQUENCY DIVERSITY IN PROPAGATION-BASED WIRELESS LOCALIZATION OF MOBILE DEVICES

A. Polo⁽¹⁾

⁽¹⁾ ELEDIA Research Center (ELEDIA@UniTN, University of Trento),
Via Sommarive 5, 38123, Trento, Italy
alessandro.polo@eledia.org

Abstract

The localization of users in indoor environments is an hot research topic and it is particularly interesting for the industry as it is required for enabling next-generation location based services. While methodologies proposed in literature exhibit different tradeoffs between location accuracy and system scalability, the opportunistic approach of exploiting existing infrastructure (e.g., Wi-Fi) and commodity devices such as smart-phone plays a key role for real-world application of these systems. In this paper, a train-less wireless localization method based on propagation modeling is proposed. The problem is addressed by evolutionary optimization exploiting received signal strength and wireless signal frequency information. Preliminary results proven an improvement of system accuracy in terms of localization error mean and variance.

Index Terms – evolutionary optimization, indoor positioning, propagation modeling, wireless localization.

I. INTRODUCTION

In last decade, the spread of Wireless Local Area Networks (WLAN) based on IEEE 802.11 standard, designed for data communication between wireless devices such as personal computers and mobile devices, has boosted the research field on indoor localization of users. In fact, assuming that the user carries a wireless device, WLAN infrastructure can be used not only for communication, but also for positioning. Many different techniques exploiting radio-frequency (RF) characteristics of signals received by target device such as time of arrival (TOA), angle of arrival (AOA), and received signal strength (RSS) have been widely explored. Although, state-of-the-art methodologies are still inadequate for matching industry and real applications requirements in terms of accuracy and scalability both [1]. Most accurate approaches often require dedicated and expensive hardware (e.g., measuring the phase of received signals), on the contrary RSS indicator is available on all wireless transceivers and can be obtained with low effort and no impacts on the system even on commercial and low-cost devices. There are two families of RSS-based positioning techniques: fingerprinting and propagation-based. The former is proven to provide a good accuracy, but lacks of scalability as it requires long

offline training and recalibration maintenance. Instead, the propagation-based approach requires minimal a-priori information as it relies on the estimation of the distances between wireless anchors and target device by applying an analytical propagation model. The main challenge related to the exploitation of RSS-based train-less localization comes from the complex electromagnetic propagation in indoor environments which exhibits phenomena like absorption, reflection, scattering and diffraction, that usually cannot be taken into account by the numerical model [2]. In this work, we propose an RSS propagation-based localization method based on evolutionary optimization that exploits multi-band wireless signals (e.g. provided by Access points of Wi-Fi networks) for improving estimation accuracy.

I. MATHEMATICAL FORMULATION

The RF-related information available at the receiver in the selected scenario (i.e., mobile devices and WLAN) is limited to the received signal strength (RSS) and the channel-carrier frequency of the periodic wireless beaconing signal transmitted by the anchor (i.e. Access point). Therefore propagation models that take into account information such as the phase or the channel state information cannot be applied. For the sake of simplicity and in order to experimentally validate the proposed approach, we selected the very simple log-distance path loss model with log-normal shadowing. Let us consider a receiver located at the unknown position $(x, y) \in D$ and a transmitter anchor located at the known position $(\hat{x}, \hat{y}) \in D$ in the bi-dimensional domain D . According to the selected model, the RSS can be formulated as follows:

$$RSS(x, y, \gamma) = P_0 - 10\alpha \log \left(\frac{\sqrt{(x - \hat{x})^2 + (y - \hat{y})^2}}{\hat{d}_0} \right) - \sigma \quad (1)$$

where $\gamma = [\alpha, P_0]$ is the channel parameter vector, in particular α is the path-loss exponent and depends on current channel conditions including transmitter frequency and P_0 is the reference signal power received at the reference distance $\hat{d}_0 = 1m$ far from the anchor. σ is a normal random variable with zero mean, reflecting the attenuation caused by flat fading. The proposed wireless localization method recasts the positioning problem as an inverse problem [3] and exploits Particle Swarm evolutionary Optimization (PSO) in order to reduce the effect of noisy inputs and the high number of suboptimal solutions [4]. Let us a set of N wireless signals transmitted by $K \leq N$ well-known anchors. In fact, modern Access point devices provide multiple wireless network interfaces in terms of connectivity service (i.e., many Wi-Fi networks) and operative band (i.e., 2.4GHz and 5-6GHz band).

The single-objective function to be minimized takes into account the measured RSS vector with respect to the one analytically calculated by the propagation model and is formulated as follows:

$$\Phi(x, y, \bar{\gamma}) = \frac{\sum_{n=1}^N \left\{ \left[\text{RSS}_n(\zeta(x, y)) - \text{RSS}_n(x, y, \gamma_n) \right]^2 \right\}}{\sum_{n=1}^N \left\{ \left[\text{RSS}_n(\zeta(x, y)) \right]^2 \right\}} \quad (2)$$

where $\text{RSS}_n(\zeta(x, y))$ is the RSS measurement of the n -th wireless signal, $\text{RSS}_n(x, y, \gamma_n)$ is the RSS numerically estimated for the corresponding k -th anchor position by applying the propagation model calibrated with the estimated channel parameter vector γ_n . Finally, $\bar{\gamma}$ is the ordered set of all optimized vectors $\gamma_n, n = 1, \dots, N$. It is worth noticing that the number of variables $V = 2N + 2$ depends on the number of input signals and typically change for each problem instance. The variables domain range of channel parameters is set accordingly to the n -th signal frequency.

II. PRELIMINARY RESULTS

The proposed system has been experimentally validated in a real office facility (i.e., one floor of about $3000m^2$) equipped with a standard WLAN infrastructure by means of 8 multi-band Access points supporting the standards IEEE802.11b-1999 and IEEE802.11a-1999, that work at 2.4GHz band and 5-6GHz band respectively. It is worth noticing that modern commodity mobile devices support both standards. For the performance assessment, a set of 30 test position were uniformly selected, in each position about one minute of RSS measurements of the Wi-Fi beaconing signals were acquired, the whole dataset includes more than 16 thousands of scan results which can be processed as independent problem instances. The domains of optimized wireless channel parameters were experimentally estimated from measurements and set to $\alpha \in [2.0, 4.8]$, $P_0 \in [-48dBm, -44dBm]$ and $\alpha \in [1.8, 2.8]$, $P_0 \in [-49dBm, -44dBm]$ for the 2.4GHz band and 5-6GHz band respectively. In Fig. 1 the distribution of RSS measurements clustered by the distance between transceivers for the two bands of interest is shown. As it can be noticed, the range of measured RSS at a given distance depends also on the considered transmission band. In fact, the RSS of received signals is affected by frequency-dependent phenomena, such as multi-path. In particular, as pointed out by the two shown path-loss model configurations ($\alpha = 2.0, \alpha = 3.0$), the distance estimated by the standard path-loss model is very sensitive to small variations of the input RSS and the considered channel parameters. Finally, the models using the channel parameters

optimized at run-time by the PSO for each band of interest are shown. The average difference between the two models is 6 dBm and in the considered scenario it can lead to an high estimation error for each distance estimation.

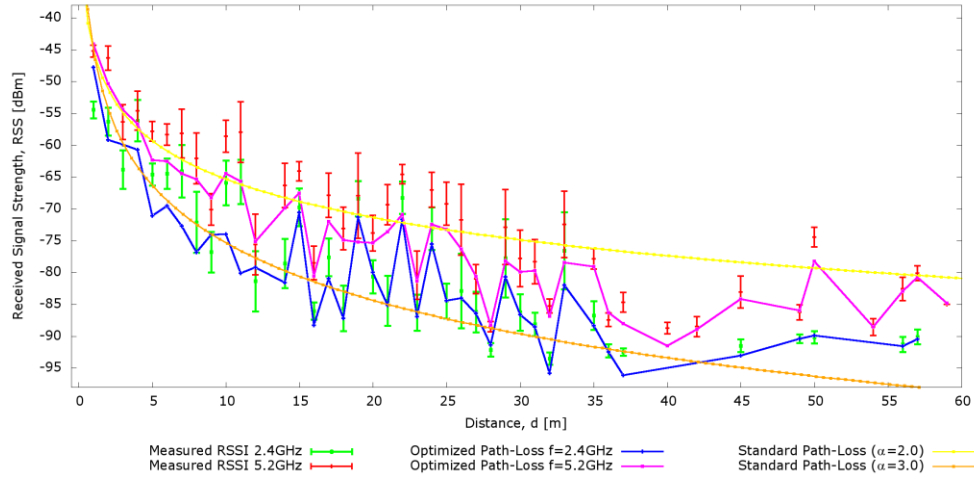


FIG. 1 – The distribution of measured RSS, two fixed configuration of path-loss model ($\alpha = 2.0, \alpha = 3.0$) and the models with optimized channel parameters at the two bands of interest.

III. CONCLUSION

The preliminary validation confirmed relevant statistical differences with respect to the two considered bands. The application of the two models optimized for each band improved the overall average method accuracy of 15% leading to an average localization error $\Delta\tilde{L} = 5.34m$, even using a very simple propagation modelling.

REFERENCES

- [1] F. Viani, F. Robol, A. Polo, P. Rocca, G. Oliveri, and A. Massa, “Wireless architectures for heterogeneous sensing in smart home applications – Concepts and real implementations,” *Proceedings of the IEEE – Special Issue on ‘The Smart Home,’* Invited Paper, vol. 101, no. 11, pp. 2381-2396, November 2013.
- [2] A. Goldsmith, *Wireless Communications*, 1st ed., Cambridge University Press, 2005.
- [3] P. Rocca, M. Benedetti, M. Donelli, D. Franceschini, and A. Massa, “Evolutionary optimization as applied to inverse problems,” *Inverse Problems - 25th Year Special Issue of Inverse Problems*, Invited Topical Review, vol. 25, pp. 1-41, Dec. 2009.
- [4] T. Moriyama, A. Polo, F. Viani, and A. Massa, “Improved wireless localization of mobile devices in smart indoor scenarios,” *Proc. 2015 IEEE Mediterranean Microwave Symposium (MMS’2015)*, Lecce, Italy, November 30 – December 2, 2015.

WIRELESS SENSOR NETWORK AND DOPPLER RADAR TECHNOLOGIES FOR WILDLIFE ROAD CROSSING MONITORING

F. Robol⁽¹⁾

⁽¹⁾ ELEDIA Research Center (ELEDIA@UniTN, University of Trento)
Via Sommarive, 5, 38123 Trento, Italy
fabrizio.robol@eledia.org

Abstract

A wireless sensor network (WSN) for addressing the wildlife road crossing problem is presented in this paper. In particular, the designed solution tries to overcome the so-called habit effect, which may arise with the standard alert road signs (e.g., static or flashing road signs). To this end, the wireless sensor network devices are spread over the stretch of road to be monitored, collecting information about the wildlife presence by integrating Doppler radar technology. The radar signal is therefore pre-processed by the wireless devices on-board, in order to identify the presence of the target at the roadsides. In the case, the collected data are transmitted to the control unit for further analysis and data storage, thus enabling a real-time and event-based driver alert. The prototype of the designed system has been deployed in a real test-site in the Alps region thus assessing the actual system performance on the mid-long term. Preliminary results are also discussed towards the end to demonstrate the performance of the proposed solution.

Index Terms – wireless sensor network, pervasive computing, doppler radar, wildlife road crossing.

I. INTRODUCTION

Wildlife road-crossing represents a challenging problem, with actual no effective solution nowadays. Several approaches have been investigated, exploiting a large variety of technologies, such as infrared sensors or thermal cameras [1], wearable devices or dedicated sensing technologies for specific application [2]. In addition, WSN-based architectures have been largely exploited in the last decades for several real-world problems, from environmental monitoring [3], up to advanced wireless localization services [4].

In this paper, a low cost and scalable wireless system for the prevention of wildlife-to-vehicles collisions is proposed. In particular, the wireless devices are equipped with Doppler radars for the real-time detection of wildlife presence on the roadsides. The radar signal, processed by the WSN node, triggers the adaptive alert notification to the incoming drivers, thus avoiding the so-called habit-effect.

The proposed system has been developed and deployed in a real test-site in the Alps region. Long-term testing has been performed to verify the robustness of the system in different environmental conditions. The

number of detected events has been statistically analyzed and compared with the ground truth acquired by means of a surveillance video recording system.

II. SYSTEM ARCHITECTURE

The proposed system is composed by a set of N wireless devices, which are deployed along the monitored road-sides. In particular, each WSN node is equipped with two Doppler radar sensors, properly oriented in order to widen the actual horizontal aperture. Therefore, the radar signals are multiplexed in time, thus processing a single data stream $x_n(t_k)$, with $n = 1, \dots, N$ being the node index and $t_k = t_0 + k\Delta t$ the sampling time instant, where t_0 is the boot time of the n -th device, k is the time sampling index and Δt is the constant time interval (defined according to the internal clock performance). The radar data are successively processed in order to filter undesired movements and to improve the detection of the desired target, thanks to signal amplification and rectification stages.

A calibrated hardware thresholder that provides in output the following binary behavior then analyzes the filtered signal $\hat{x}_n(t_k)$: $\delta(t_k) = 1$ if $\hat{x}_n(t_k) \geq X_{th}$ and $\delta(t_k) = 0$ if $\hat{x}_n(t_k) < X_{th}$, where X_{th} is the calibrated threshold computed as a percentage of Ω_n , being the maximum variability of the radar filtered signal $\hat{x}_n(t_k)$. When $\delta(t_k) = 1$ the sampling period Δt is reduced and the wireless transceiver is activated in order to transmit the scaled version of the filtered signal

$$\tilde{x}_n(t_k) = \frac{\hat{x}_n(t_k) - \min_k [\hat{x}_n(t_k)]}{\Omega_n} \times 100, \quad k = 1, \dots, K \quad (1)$$

The transmission continues till $\delta(t_k) = 0$, thus the transceiver is shut down and Δt is restored to default value.

The transmitted data are received by the gateway node and forwarded to the remote control unit for additional real-time processing. In particular, temporal and spatial correlations of the received data are performed in order to estimate additional features of the wildlife movement and to evaluate offline statistics about the road risk-level.

In addition, infrared video-surveillance system has been installed at the test-site, thus recording the monitored road and accurately assessing the system performance. In particular, the verification system output is a bi-static information directly related to the absence/presence of a target along the road-sides, namely $\xi(t) = 1$ if a wildlife occupies the security area, or $\xi(t) = 0$ otherwise. The comparison between the binary function $\delta(t)$ and the output of the

verification system $\xi(t)$ allows the system performance evaluation in terms of false positive and false negative detections.

III. EXPERIMENTAL VALIDATION

The proposed wildlife monitoring system has been deployed along a real stretch of road, in the Alps region near Trento, in the north of Italy. The monitored test-site is 300m long [Fig. 1(a)], thus $N = 21$ sensor nodes have been deployed along the two sides of the road as shown in Fig. 1(b) (the devices have been installed directly on the road delimiters, which are placed 20m far from each other - as stated by the Italian regulation).

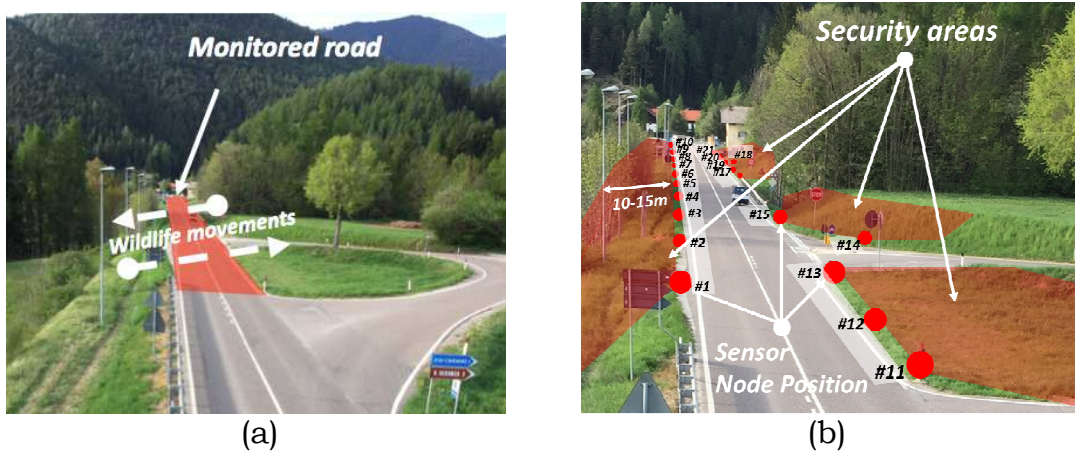


FIG. 1 – Experimental test-site: (a) wildlife movements, (b) security areas.

Each wireless devices has been equipped with two Doppler radar sensors operating at 24GHz, thus describing a security area with an horizontal aperture of about 160° and depth of about 10-15m.

The data-sampling rate is set to the default value of $\Delta t = 250\text{ ms}$ [when $\delta(t)=0$], reduced to $\Delta t = 30\text{ ms}$ when $\delta(t)=1$. The triggering threshold has been set to $X_{th} = 30\%$.

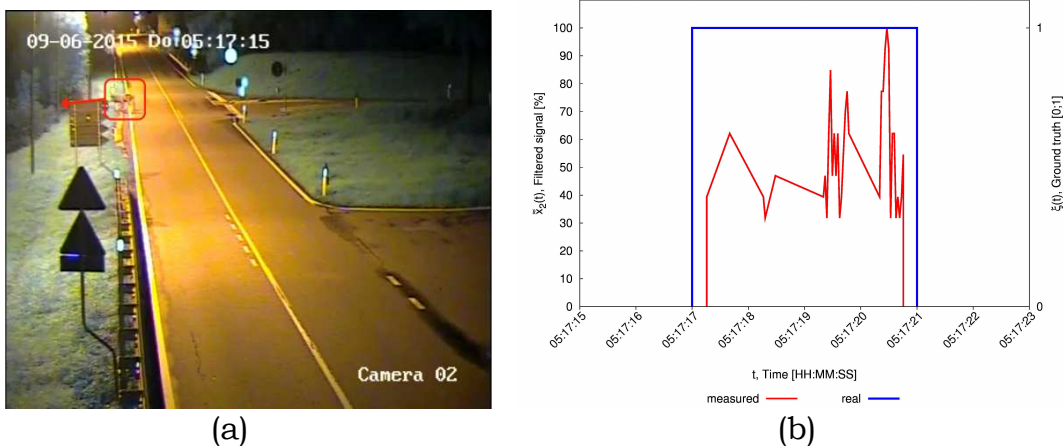


Fig. 2 - Event detection at the experimental test-site: (a) wildlife road-crossing, (b) acquired data.

Solar panels have also been integrated on the lateral sides of the wireless node prototype, thus extending the battery lifetime.

As an example of the system detection capability, a real event detected by the monitoring system is reported in Fig. 2. In detail, Fig. 2(a) shows a snapshot of the verification system acquisition and the actual position of the wildlife in the security area of node $n = 2$. Fig. 2(b), instead, reports the plot of the scaled signal $\tilde{\tilde{x}}_2(t)$ in comparison to the ground truth $\xi(t)$. A good matching can be observed between the two traces, thus confirming the good capability of the system in detecting the moving target.

IV. CONCLUSION

An innovative monitoring system for the real-time detection of wildlife road-crossing events has been presented. The integration of Doppler radar technology and WSN platform has allowed the definition of a low cost and scalable solution to the problem. In addition, by considering the mid-long term, during which the experimental validation has been carried out, good detection performance have been obtained. In particular, the percentage of correct detection rate has been confirmed above the 80%.

ACKNOWLEDGEMENT

This work has been partially supported by the Project “Study and Development of a Wildlife Road-crossing Monitoring System for the Prevention of Road Collisions” funded by the *Autonomous Province of Trento* (PAT), Italy.

REFERENCES

- [1] Z. He, “Energy-efficient integrated camera and sensor system design for wildlife activity monitoring,” *IEEE International Conference on Multimedia and Expo*, ICME 2009, pp.1580-1581, June 28 2009-July 3 2009.
- [2] P. Mathur, R.H. Nielsen, N.R. Prasad, R. Prasad, “Wildlife conservation and rail track monitoring using wireless sensor networks,” *4th International Conference on Wireless Communications, Vehicular Technology, Information Theory and Aerospace & Electronic Systems (VITAE)*, pp.1-4, 11-14 May 2014.
- [3] F. Viani, M. Salucci, P. Rocca, G. Oliveri, and A. Massa “A multi-sensor WSN backbone for museum monitoring and surveillance,” *2012 European Conference on Antennas and Propagation (EUCAP 2012)*, Prague, Czech Republic, pp. 51-52, March 26-30, 2012.
- [4] F. Viani, P. Rocca, M. Benedetti, G. Oliveri, and A. Massa, “Electromagnetic passive localization and tracking of moving targets in a WSN-structured environment”, *Inverse Problems*, vol. 26, no. 074003, pp. 1-15, 2010.

INVERSE SCATTERING METHODOLOGIES AND APPLICATIONS @ ELEDIA RESEARCH CENTER

N. Anselmi⁽¹⁾, M. Donelli⁽¹⁾, M. A. Hannan⁽¹⁾, G. Oliveri⁽¹⁾⁽²⁾, L. Poli⁽¹⁾, P. Rocca⁽¹⁾, M. Salucci⁽¹⁾⁽²⁾, L. Tenuti⁽¹⁾, and A. Massa⁽¹⁾⁽²⁾

⁽¹⁾ELEDIA Research Center (ELEDIA@UniTN, University of Trento)
via Sommarive 5, 38123 Trento, Italy

⁽²⁾ELEDIA Research Center (ELEDIA@L2S, UMR8506 [CNRS-CS-UPS])
3 rue Joliot Curie, 91192 Gif-sur-Yvette, France
andrea.massa@eledia.org

Abstract

This paper is aimed at reviewing the inverse scattering techniques and solution methodologies recently introduced and developed at the ELEDIA Research Center, as well as at discussing their adoption and customization in selected applicative scenarios. Towards this end, a set of numerical examples belonging to several different domains is discussed in order to illustrate the features, potentialities, and limitations of the presented techniques.

Index Terms – Microwave Imaging, Ground Penetrating Radar Imaging, Inverse Scattering, Evolutionary Algorithms, Compressive Sensing, Multi-Focusing Methods, Non-Destructive Testing/Non-Destructive Evaluation.

I. INTRODUCTION AND RATIONALE

The development of numerical methods able to address inverse scattering problems in a effective and numerically efficient way is a very challenging task both from the theoretical and the practical viewpoint, because of the issues (non-linearity, ill-posedness, ill-conditioning) which usually affect the associated mathematical formulations [1][2]. Nevertheless, the wide range of application of such algorithms (that comprises non-destructive testing and evaluation, biomedical imaging, remote sensing, localization, structural monitoring, and geophysical inspection) has motivated an increased academic and industrial interest for inverse scattering techniques. Consequently, several algorithms have been proposed in the last few years in order to address the above theoretical and practical challenges.

In this scenario, several different inverse scattering techniques have been proposed within the ELEDIA Research Center in the last few years, including (but not limited to) (i) sparse reconstruction methodologies based on generalized Compressive Sensing (CS) paradigms [3]-[7], (ii) multi-focusing techniques for ground-penetrating radar (GPR) imaging [8][9], and (iii) full-3D retrieval strategies [5][10].

Accordingly, this paper is aimed at reviewing the most recent advances in inverse scattering methods developed at the ELEDIA Research Center (with a specific focus on advanced CS techniques and multi-resolution strategies applied to GPR problems), as well as at illustrating a selected set of numerical experiments in different applicative scenarios.

II. INVERSE SCATTERING @ ELEDIA - METHODOLOGIES AND APPLICATIONS

The ELEDIA Research Center has developed several innovative methodological approaches in the last years for the solution of complex inverse scattering problems [1]-[10].

A first challenge addressed by ELEDIA has been the development of algorithms able to exploit (within the inversion process) *a-priori* information on the class of targets/profiles to be retrieved [3]-[7]. Such problems have been addressed by demonstrating that the prior knowledge can be used to formulate many imaging problems as *sparse* (i.e., the unknown quantities can be discretized as vectors with few non-zero coefficients [3]) whatever is the class of targets at hand. This observation has enabled the adoption, generalization, and customization of effective Compressive Sensing retrieval strategies which enforce the sparseness in several different conditions (i.e., a standard [5] or transformed [4] domains, with single [4][5] or multi-frequency data [6]). Such a theoretical advancement has enabled to overcome one of the main drawbacks of early CS imaging techniques, whose application was limited to very specific classes of targets (i.e., comprising few isolated pixels).

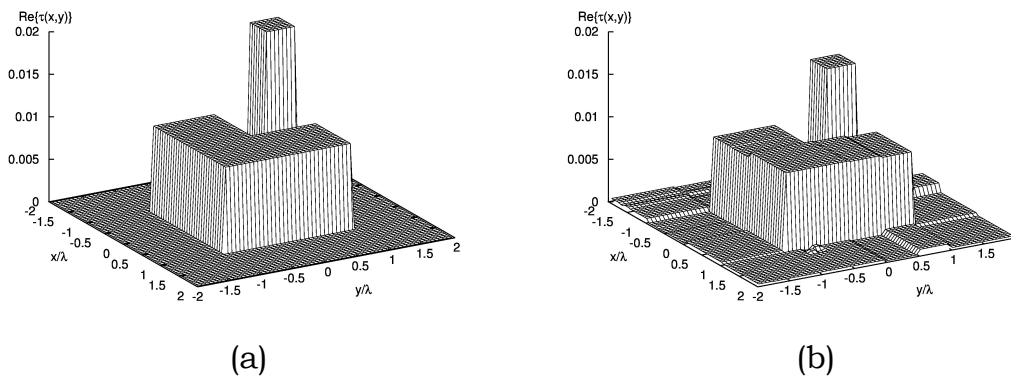


FIG. 1 – [Haar-Wavelet Object, $\tau_{MAX} = 0.02$, $SNR = 20$ [dB], $L_D = 4\lambda$] – Actual target profile (a) and Wavelet-CS retrieved profile (b).

To illustrate the flexibility of CS methods recently developed at the ELEDIA Research Center, a numerical example is presented next which is concerned with the application of the Wavelet CS methodology [7]. In this case, a square investigation domain D of side $L_D = 4\lambda$ is assumed. The target [Fig. 1(a)] is composed by two disjoint objects: an “L-shaped” object with contrast $\tau = 0.01$ and a second object of squared-cylindrical

shape, with contrast $\tau = 0.02$. The domain is discretized into $c_D = 4096$ cells and illuminated by $V = 36$ incident impinging plane wave (sources are equally spaced along a circumference of radius $\rho = 4\lambda$). On the same circumference $M = 36$ probes measure the field scattered by the target. Figure 1(b) shows the reconstruction obtained through the Wavelet-CS inversion when SNR=20 [dB]. Although the original object is not at all sparse with respect to standard “pixel” basis, the target has been retrieved with a very good accuracy.

As concerns the solution of inverse scattering problems arising in Ground Penetrating Radar imaging, the ELEDIA Research Center has proposed several innovative techniques which are based on “iterative information acquisition” procedures. More in detail, the development of iterative algorithms that combine efficient inversion procedures and multi-focusing techniques has been considered [8][9], and the arising integrated tools have been validated considering both synthetic [8][9] and experimental data [8].

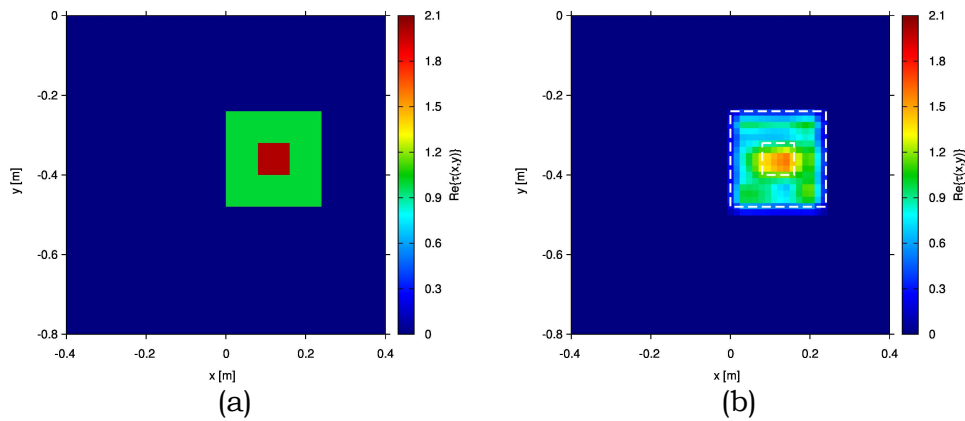


FIG. 2 – [Inhomogeneous square profile, $\varepsilon_{rb} = 4$, $\sigma_b = 10^{-3}$ S/m, $\varepsilon_{r,obj}^{in} = 6$, $\varepsilon_{r,obj}^{ext} = 5$, SNR=30 dB] - Dielectric profile of the (a) actual and (b) retrieved object by the FH-IMSA-CG [8].

The features of multi-focusing GPR imaging methods recently developed at the ELEDIA Research Center are illustrated next through a numerical example [8]. In this case, the inhomogeneous profile in Fig. 2(a) is imaged through the frequency-hopping iterative multi-scaling scheme presented in [8] (considering a background with $\varepsilon_{rb} = 4$, $\sigma_b = 10^{-3}$ S/m, $V=20$ views, $M=19$ probes, a Gaussian monocycle with central frequency $f=300$ MHz in transmission, and $Q=5$ frequency samples for the processing). The retrieved contrast when SNR=30 dB shows that the proposed technique is able to correctly identify the position, size, shape, and contrast of the unknown object and to avoid any artifacts (even if the target is buried in a lossy ground).

III. CONCLUSION

A concise overview of selected inverse scattering techniques and applications recently developed/addressed at the ELEDIA Research Center has been presented. A set of applications of such methodologies has been discussed in order to illustrate the advantages and features of the methodologies currently developed in ELEDIA.

ACKNOWLEDGEMENT

This work benefited from the networking activities carried out within the SIRENA Project (2004-2017), supported by the DIGITEO (France) under the "Call for Chairs 2014".

REFERENCES

- [1] P. Rocca, M. Benedetti, M. Donelli, D. Franceschini, and A. Massa, "Evolutionary optimization as applied to inverse problems," *Inverse Problems*, vol. 25, 123003, pp. 1-41, Dec. 2009.
- [2] P. Rocca, G. Oliveri, and A. Massa, "Differential Evolution as applied to electromagnetics," *IEEE Antennas Propag. Mag.*, vol. 53, no. 1, pp. 38-49, Feb. 2011.
- [3] Massa, P. Rocca, and G. Oliveri, "Compressive Sensing in Electromagnetics - A Review," *IEEE Antennas and Propagation Magazine*, pp. 224-238, vol. 57, no. 1, Feb. 2015.
- [4] G. Oliveri, N. Anselmi, and A. Massa, "Compressive sensing imaging of non-sparse 2D scatterers by a total-variation approach within the Born approximation," *IEEE Trans. Antennas Propag.*, vol. 62, no. 10, pp. 5157-5170, Oct. 2014.
- [5] G. Oliveri, P.-P. Ding, and L. Poli "3D crack detection in anisotropic layered media through a sparseness-regularized solver," *IEEE Antennas Wireless Propag. Lett.*, vol. 14, pp. 1031-1034, 2015.
- [6] L. Poli, G. Oliveri, P.-P. Ding, T. Moriyama, and A. Massa, "Multi-frequency Bayesian CS methods for microwave imaging," *J. Opt. Soc. America A*, vol. 31, no. 11, pp. 2415-2428, 2014
- [7] N. Anselmi, M. Salucci, G. Oliveri, and A. Massa, "Wavelet-based compressive imaging of sparse targets," *IEEE Trans. Antennas Propag.*, vol. 63, no. 11, pp. 4889-4900, Nov. 2015.
- [8] M. Salucci, G. Oliveri, and A. Massa, "GPR prospecting through an inverse scattering frequency-hopping multi-focusing approach," *IEEE Trans. Geosci. Remote Sens.*, vol. 53, no. 12, pp. 6573-6592, Dec. 2015.
- [9] M. Salucci, G. Oliveri, A. Randazzo, M. Pastorino, and A. Massa, "Electromagnetic subsurface prospecting by a multifocusing inexact Newton method within the second-order Born approximation," *J. Opt. Soc. Am. A*, vol. 31, no. 6, pp. 1167-1179, Jun. 2014.
- [10] X. Ye, L. Poli, G. Oliveri, Y. Zhong, K. Agarwal, A. Massa, and X. Chen, "Multi-resolution subspace-based optimization method for solving three-dimensional inverse scattering problems," *J. Opt. Soc. America A*, vol. 32, no. 11, pp. 2218-2226, Nov. 2015.

**DISTRIBUTED WIRELESS SENSING, MONITORING,
AND DECISION SUPPORT:
CURRENT ACTIVITIES @ ELEDIA RESEARCH CENTER**

H. Ahmadi⁽¹⁾, M. S. Dao⁽²⁾, E. Giarola⁽³⁾, A. Polo⁽³⁾, F. Robol⁽³⁾,
F. Viani⁽³⁾, and A. Massa⁽³⁾⁽⁴⁾

- (1) ELEDIA Research Center (ELEDIA@Innov'COM, Sup'Com Tunis)
Route de Raoued, km 3.5, 2083 El Ghazala, Ariana, Tunis, Tunisia
- (2) ELEDIA Research Center (ELEDIA@UTB, Universiti Teknologi Brunei)
Jalan Tungku Link, Gadong BE1410, Brunei Darussalam
- (3) ELEDIA Research Center (ELEDIA@UniTN, University of Trento)
Via Sommarive 5, 38123 Trento, Italy
- (4) ELEDIA Research Center (ELEDIA@L2S, UMR 8506 [CNRS-CS-UPS])
3 rue Joliot Curie, 91192 Gif-sur-Yvette, France
andrea.massa@eledia.org

Abstract

Low-power and compact wireless devices, including smart sensors, wireless tags, smartphones, are becoming everyday life tools not only bringing advantages to the mobile communications but also enabling additional wireless services where an improved context awareness is required. The potentialities of such wireless technologies are enriched by the integration of dedicated real-time processing techniques which enable not only the distributed sensing of heterogeneous parameters, but also the improved management, understanding, and forecasting of complex processes. In this framework, the ELEDIA Research Center has studied, designed, and developed heterogeneous solutions in the field of smart cities and communities, where distributed wireless sensors and mobile devices are largely applied both in indoor and outdoor scenarios. A selected set of applicative examples are presented in this paper to review the current ELEDIA activities.

Index Terms – Decision support systems, distributed wireless monitoring, wireless sensor network.

I. INTRODUCTION

In the last years, the widespread diffusion of the Internet of Things (IoT) technologies has been motivated by the key-challenge to increase the efficiency of smart cities and communities in the use of resources and the increase the city life quality. The advantages of low-cost and low-power wireless technologies have been largely exploited to develop new devices and services for innovative monitoring and control solutions at different scales, from the smart home to the smart building, up to the smart grid. Thousands of wireless sensors and custom devices for data collection and automation have been deployed turning into reality the so-called smart cities revolution [1]. However, such a rapid development

has also caused an uncontrolled spread of demonstrative and often useless IoT features, which risk to negatively impact on the proper integration of such technologies into society. As an example, the acquisition of tens of environmental parameters throughout house rooms, which are simply presented through bar-graphs and gauges, make the user feel overwhelmed by the amount of information without a clear objective or interpretation. In this sense, one of the key-challenge of such a revolution is to properly design the services starting from the real user needs and benefits.

In this framework, the ELEDIA Research Center has studied, designed, and developed different wireless solutions, which integrate innovative methodologies on top of the wireless platforms dedicated to the sensing and monitoring tasks. The proposed systems aim at supporting the decisions of end-users providing simple and clear indications, trying to reduce the intrinsic complexity of the monitored processes by applying advanced data processing techniques and algorithms.

In this work, the recent applications of such wireless solutions are presented pointing out the results of the experimental validations in real test fields.

II. WIRELESS SOLUTIONS FOR SMART BUILDINGS

The smart monitoring of indoor areas with wireless sensors has been widely investigated by ELEDIA in different applicative fields. Particular attention has been given to the monitoring of museums as well as smart buildings such as smart campus and residential homes. An overview of the proposed solutions is reported in the following.

Smart Museums. The wireless sensor network technology has been adopted to enable the IoT principle within museum areas. More in detail, besides the acquisition of environmental parameters for artworks conservation purposes [2], the same data have been processed to estimate additional information about the museum occupancy and visitors flow throughout the museum rooms [3][4]. An indicator based on the vertical trends of environmental temperature and humidity measured at different heights has been defined. Such an indicator has a strong relation with the indoor occupancy level and a customized learning-by-example strategy based on a support vector machine (SVM) has been implemented to learn how the visitor presence and movements impact on the indoor environment. Such a system has been deployed within the “Sala dei 500”, Palazzo Vecchio, Florence, Italy, and is currently monitoring the museum room.

Energy-efficient Buildings. The management of heating, ventilation, and air conditioning (HVAC) systems strongly impact on the energy consumptions of buildings. The accurate monitoring of indoor environmental parameters has been performed by means of simple wireless sensors in order to estimate the thermal comfort of users and

to predict the optimal trade-off between the desired comfort and the energy consumptions [5]. Toward this end, prediction methods based on the weather forecasts have been adopted in order to suggest to the energy manager how to control the set points of HVAC plants toward energy saving. The system is now active at the ELEDIA Research Center at the University of Trento, monitoring 24 rooms of the “Polo F. Ferrari”.

III. SMART ENVIRONMENT IN SMART CITIES

The concept of smart environment has been applied to different outdoor applicative scenarios, including the road security and the precision farming. The recent advances in such contexts are reported in the following.

Road Security. The monitoring of road sides for the real-time detection of wildlife road-crossing events has been realized using wireless sensors equipped with low-cost Doppler radars. Such a solution aims at alerting the approaching drivers to prevent the risk of wildlife-vehicle collisions. The main challenge of the system is to process the acquired radar signals in real-time in order to activate the road signs adaptively and only when actual events occur, thus reducing the users habit-forming to fixed signs. The system is currently installed in a real test field along a 300 m road section for experimental validation. In the last months, more than 80% of the road-crossing events have been correctly detected [6].

Precision Farming. The precision agriculture is growing rapidly due to the need to increase the efficiency and the quality of the productions. The IoT technologies have been adopted by ELEDIA to introduce smartness in the management of farming processes, such as the irrigation and the phytosanitary treatments. The soil and plants parameters are measured by distributed sensors and then processed by fuzzy logic methods to support the decisions of the farmers. The provided outputs are simple indications adaptively estimated according to the real-time acquisition of the plant status. Such outputs are the results of the complex evaluation of multiple empirical rules and best practices given by the expert farmers. The proposed integrated solution has been validated in a apple orchard, and is currently under installation in a vineyard. Concerning the smart irrigation, the preliminary results point out a reduction of water usage higher than 10% and an improvement in the quality of the soil water content, as well [7].

IV. CONCLUSION

The recent activities of the ELEDIA Research Center on wireless distributed monitoring by means of IoT technologies have been reviewed

in this paper. Each solution has been developed starting from the combination of wireless platforms with dedicated data analysis methods to enable not only the data acquisition but also the adaptive decision support according to the real end-users needs in different applicative scenarios. The selected examples have been experimentally validated in real test-sites to point out the real-world applicability of the proposed wireless solutions.

ACKNOWLEDGEMENT

The activities about energy-efficient buildings have been partially supported by the Project “Zero Energy Buildings in Smart Urban Districts” (CTN01_00034_594053) within the National Technological Cluster on Smart Communities, funded by the Italian Ministry of Education, University, and Research (MIUR).

REFERENCES

- [1] P. Valerio, “Is the IoT a tech bubble for cities?,” *IEEE Consum. Electron. Mag.*, vol. 5, no. 1, pp. 61-62, Jan. 2016.
- [2] F. Viani, F. Robol, E. Giarola, A. Polo, A. Toscano, and A. Massa, “Wireless monitoring of heterogeneous parameters in complex museum scenario,” *Proc. 2014 IEEE Antenna Conference on Antenna Measurements and Applications* (IEEE CAMA 2014), Antibes Juan-les-Pins, France, pp. 1-3, November 16-19, 2014.
- [3] F. Viani, E. Giarola, A. Polo, G. Vannuccini, L. Longo, and A. Massa, “Decision support system for museum management through distributed wireless sensing,” *Museum and the Web* (MWF 2014), Florence, Italy, February 19-21, 2014.
- [4] F. Viani, “Opportunistic occupancy estimation in museums through wireless sensor networks,” *Microwave and Optical Technology Letters*, vol. 57, no. 8, pp. 1975-1977, Aug. 2015.
- [5] F. Robol, F. Viani, E. Giarola, and A. Massa, “Wireless sensors for distributed monitoring of energy-efficient smart buildings,” *Proc. 2015 IEEE Mediterranean Microwave Symposium* (MMS’2015), Lecce, Italy, November 30 – December 2, 2015.
- [6] F. Viani, F. Robol, A. Polo, and E. Giarola, “Wildlife road-crossing monitoring system: Advances and test site validation,” *10th European Conference on Antennas and Propagation* (EUCAP 2016), Davos, Switzerland, April 11-15, 2016.
- [7] L. Paucar, A. Diaz, F. Viani, F. Robol, A. Polo, and A. Massa, “Decision support for smart irrigation by means of wireless distributed sensors,” *Proc. 2015 IEEE Mediterranean Microwave Symposium* (MMS’2015), Lecce, Italy, November 30 – December 2, 2015.

WIRELESS-BASED DECISION SUPPORT SYSTEMS AND FLEET MANAGEMENT @ ELEDIA RESEARCH CENTER

A. Polo ⁽¹⁾, A. Massa ⁽²⁾

⁽¹⁾ ELEDIA Research Center (ELEDIA@UniTN, University of Trento),
Via Sommarive 5, 38123, Trento, Italy

⁽²⁾ ELEDIA Research Center (ELEDIA@L2S, UMR 8506 [CNRS-CentraleSupélec-Univ. Paris Sud])
3 rue Joliot Curie, 91192 Gif-sur-Yvette, France
andrea.massa@eledia.org

Abstract

The diffusion of wireless technologies and the increasing number of interconnected devices are offering new opportunities for the introduction of location-based methodologies in the field of fleet and emergency management. In this paper, research activities related to wireless-based decision support systems and carried out at the ELEDIA Research Center are presented. In particular, we focus on the following topics: (a) the smart management of TETRA network and its mobile terminals together with software technologies enabling the interoperability between heterogeneous wireless systems; (b) decision support systems for real-time distributed monitoring of the environment and for the mission control; (c) decision support systems for the search and rescue of missing people; and finally (d) methodologies for the early detection of crises through the analysis of mobile social networks.

Index Terms – decision support systems, emergency and fleet management, TETRA, wireless technologies and interoperability.

I. INTRODUCTION

The research field and the interest related to fleet and emergency management is rapidly growing along with the spread of interconnected devices and the societal need of increasing efficiency and reducing costs. Modern organizations such as goods transportation industry and crisis management agencies share the need of tracking, dispatching and coordinating in real-time many heterogeneous resources distributed on the field (e.g., trucks, ambulances, fire-engines, helicopters, drones) for the accomplishment of simple tasks as well as critical missions.

In this context, the ELEDIA Research Center is involved with the design, the development and the experimental validation of innovative strategies and wireless-based tools supporting the control room decision makers and the operators on the field.

II. TETRA NETWORK AND TERMINALS MANAGEMENT

The terrestrial trunked radio (TETRA) is a worldwide telecommunication standard designed for military and civil defense domains. TETRA

provides modern mobile network services, such as voice and packet data, and defines extendible protocols for critical applications. Within the framework of fleet management and situation room support systems, the ELEDIA Research Center works on a scalable software system [1] that enables real-time wireless interaction between the fleet (e.g., handheld, vehicular radios, drones) and control rooms (headquarter, emergency agencies, mobile stations). In particular, the proposed system implements the full stack of on-air TETRA protocol and allows operators as well as external automated systems to consume services such as: (a) text messaging; (b) automated resource status notification for mission control; (c) terminal positioning and tracking (based on GPS embedded on terminals); (d) remote reconfiguration, such as enabling and tuning the automatic position beaconing; (e) network maintenance, the system builds and maintains a network coverage map estimated from distributed channel measurements for real-time troubleshooting and performance assessment. The prototype has been installed and connected to the TETRA network of the Autonomous Province of Trento (Trentino, Italy), made up of 63 base stations covering more than 87% of the outdoor territory and interconnecting about three thousands handheld wireless terminals, four hundreds civil defense vehicles, and three helicopters.

III. INTEROPERABILITY OF HETEROGENEOUS WIRELESS NETWORKS

Modern fleet and emergency management network architectures interconnect many heterogeneous systems and devices by means of wired and wireless communication technologies. At high level, different network devices often share similar end-user features and they can be abstracted in logical classes related to their capabilities. For example, TETRA handheld terminals and commodity smart-phones can provide similar services (i.e., voice, messaging, data, positioning) even if the network supports different levels of accuracy and reliability. In this field, the ELEDIA Research Center designed a distributed modular software system that enables the interoperability of a generic wireless smart device within the central network architecture by means of a secure and reliable bi-directional real-time communication protocol based on web and cloud technologies [1], [2]. In particular, the system prototype has been experimentally validated on Android devices equipped with an App and connected with the core architecture through the Internet (i.e., any wireless technology).

IV. FLEET AND EMERGENCY DECISION SUPPORT SYSTEM

Modern decision support systems (DSS) are able to rapidly gain the situation awareness in control rooms thanks to the massive amount of data acquired by systems distributed on the territory, such as wireless sensors, communication and tracking devices. The reference problem of interest is the selection of assets to be deployed for a given mission and

it requires the simultaneous optimization of different objectives [2]. The former, is to maximize the utility of candidate assets for the considered mission in terms of personnel, vehicle features, equipment. Secondly, the dispatch time and cost shall be minimized. Finally, the proposed plan shall be coherent with best practices and real-time constraints. In this framework, the ELEDIA Research Center exploits multi-objective evolutionary optimization techniques for offering to the user a set of candidate solutions (i.e., the Pareto front). An interactive web-based tool [3], shown in Fig. 1, has been implemented and experimentally validated for over one year at the fire-fighter station of Autonomous Province of Trento (Trentino, Italy), that coordinates many hundreds of TETRA fleet assets. The system acquires, integrates and displays real-time information from heterogeneous data-sources including traffic events, weather conditions and environmental wireless sensors (e.g., monitoring floods, landslides). This information is exploited in real-time by the decision engine for the selection and the routing of assets.

V. SEARCH AND RESCUE OPERATIONS MANAGEMENT

A very important and challenging role of emergency management agencies is the search of missing people and is particularly complex in rural and mountain areas. In this scenario, a DSS for the planning of search mission has been proposed. The system requires minimal information about the missing person (i.e., last seen information, physical conditions). The system provides three key functionalities: *(a)* estimate the area to search: the search algorithm considers the morphology of the nearby area, the presence of lakes and rivers, roads and trails, as well as weather conditions for estimating the probability map of his presence with respect to elapsed time; *(b)* the kind of rescue teams that shall be deployed accordingly to the territory and weather conditions, such as fire-fighters, mountain and medical rescue; *(c)* the combination of resources (i.e. personnel) to be dispatched: the system takes into account contradictory objectives including the travel time, the deployment cost and the utility of each resource to be selected [3]. The proposed system includes an interactive 3D globe interface and is actually under experimental validation at the emergency management headquarter (CUE) of Trentino, Italy.

VI. SOCIAL NETWORKS AS EMERGENCY SENSORS

In last years, the pervasive diffusion of social networks and their usage combined with the spread of wireless mobile devices has enabled many innovative applications based on crowdsourcing. Social media like Twitter have already been proven to provide real-time information about occurring emergencies and disasters. In this field, the ELEDIA Research Center works on unsupervised methodologies for the identification, the classification and the localization of small and medium-scale crises. The proposed early detection system processes real-time textual

streams and wireless metadata from social networks users. In order to deal with the massive amount of input messages and to discard non-emergency related messages (i.e., more than 99%), a multi-resolution analysis has been designed. Text expressions such as abbreviations and common saying are normalized and then content (decomposed in N-grams) is pre-classified against closed dictionaries and training sets defined with the support of domain experts. Messages related to possible emergencies are latter processed by a slower but more accurate pipeline that takes into account different key features such as writer's sentiment, temporal and place information. Finally, the classified information is correlated and eventually aggregated with previously discovered threats that are updated, ranked and presented to the user in real-time.



FIG. 1 – Two screenshots of the Fleet and Emergency Management DSS: (a) real-time profile of flood level; (b) the route of a TETRA vehicle.

VII. CONCLUSION

Modern decision support systems for fleet and emergency management can efficiently exploit distributed wireless sensors and communication technologies for providing situation awareness to decision makers.

REFERENCES

- [1] A. Polo, F. Robol, C. Nardin, S. Marchesi, A. Zorer, L. Zappini, F. Viani, and A. Massa, "Decision support system for fleet management based on TETRA terminals geolocation", *8th European Conference on Antennas and Propagation (EUCAP 2014)*, The Hague, The Netherlands, pp. 1195-1198, Apr. 2014.
- [2] A. Polo, F. Viani, L. Zappini, S. Marchesi, A. Zorer, and A. Massa, "Advances in decision-making support tools for fleet management in emergency and security applications," *Proc. 2014 IEEE Antenna Conference on Antenna Measurements and Applications (IEEE CAMA 2014)*, Antibes Juan-les-Pins, France, pp. 1-3, Nov. 2014.
- [3] L. Zappini, S. Marchesi, A. Polo, F. Viani, and A. Massa, "Evolutionary optimization strategies applied to wireless fleet management in emergency scenarios," *Proc. 2015 IEEE Mediterranean Microwave Symposium (MMS'2015)*, Lecce, Italy, November 30 – December 2, 2015.

**DESIGN AND OPTIMIZATION OF ADVANCED RADAR AND
COMMUNICATIONS SYSTEMS AND ARCHITECTURES
@ ELEDIA RESEARCH CENTER**

N. Anselmi⁽¹⁾, M. Donelli⁽¹⁾, M. A. Gelmini⁽¹⁾, G. Gottardi⁽¹⁾,
G. Oliveri⁽¹⁾⁽²⁾, L. Poli⁽¹⁾, P. Rocca⁽¹⁾, L. Tenuti⁽¹⁾, and A. Massa⁽¹⁾⁽²⁾

⁽¹⁾ELEDIA Research Center (ELEDIA@UniTN, University of Trento)
via Sommarive 5, 38123 Trento, Italy

⁽²⁾ELEDIA Research Center (ELEDIA@L2S, UMR8506 [CNRS-CS-UPS])
3 rue Joliot Curie, 91192 Gif-sur-Yvette, France
andrea.massa@eledia.org

Abstract

An overview of the recent optimization-based methodologies developed at the ELEDIA Research Center for the design of advanced radiating systems and architectures for radar and communications applications is presented. Selected representative numerical examples are reported and briefly discussed in order to highlight the characteristics of the proposed solutions.

Index Terms – Unconventional Array Architectures, Phased Array Antenna, Reflectarray, Metamaterials, System-by-Design, Evolutionary Algorithms, Compressive Sensing, Learning-by-Example Techniques.

I. INTRODUCTION AND MOTIVATIONS

Nowadays radar and communications applications require high-performance antenna systems able to satisfy challenging and conflicting requirements from both the hardware and software point of view, including for example the need of multiple functionality, large bandwidth, high reconfigurability, small dimensions, and low weight. Conventional array antenna solutions, based on fully-populated architectures with elements uniformly spaced and having one transceiver module (TRM) for each element, can not accomplish all these requirements. Therefore, irregular/unconventional array solutions [1], including sparse or thinned arrays for reducing the number of active elements, sub-arrayed arrays for adding extra functionalities at the sub-array level, or time-modulated arrays for the quick reconfiguration the radiation pattern or the generation of multiple beams, can be profitably exploited. Recently, the use of innovative electromagnetic (EM) materials, called metamaterials, and devices has also received a great boost for improving the radiation performance of antennas thanks to their EM field manipulation properties [2].

In these frameworks, several innovative design paradigms and synthesis methodologies [3]-[5] based on Compressive Sensing (CS), Evolutionary Algorithms (EAs), and Learning-by-Example (LBE) methods have been developed at ELEDIA and applied in several contexts including, but not limited to, communications, radars, power transmission, and remote sensing. Accordingly, this paper is aimed at reviewing the most recent advances about the design and optimization of radiating system carried out at the ELEDIA Research Center with main focus on radar and communications applications.

II. UNCONVENTIONAL ARRAY DESIGN

As compared to regular array architectures, unconventional arrays are characterized by an irregular distribution of the radiating elements for thinned and sparse arrays [6], and/or unconventional beam-forming networks for clustered [7] and time-modulated arrays [8]. In order to design sparse array solutions, several methodologies based on the Compressive Sensing have been proposed at ELEDIA to deal with the design of linear, planar, and conformal array arrangements characterized by real (amplitude-only), complex (amplitude-and-phase), and isophoric (uniform) excitation weights. Differently, the synthesis of clustered and time-modulated arrays has been addressed by means of customized approaches based on global optimization (e.g., Evolutionary Algorithms) [7, 8].

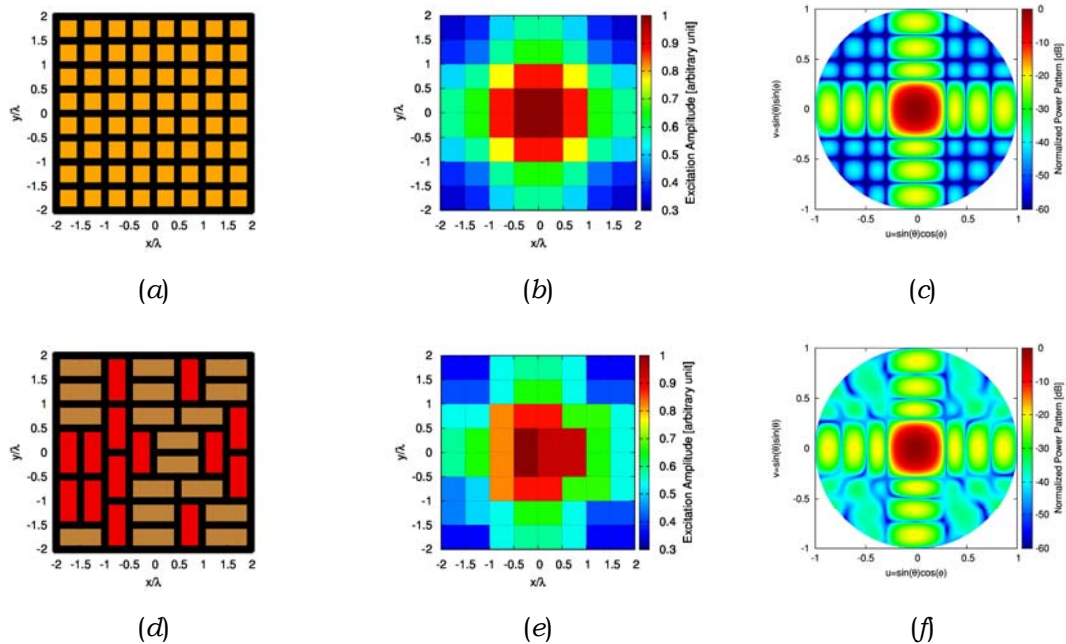


FIG. 1 – [Clustered Array - $N = 64$, $d = \lambda/2$, $SLL = -20dB$] – Array layout (a),(d), element excitations (b),(e), and power pattern (c),(f) of the reference (a)-(c) and tiled (d)-(f) phased array solution.

As a representative example, Fig. 1 shows the result of a novel methodology recently developed for the design of clustered arrays. The objective is the design of an optimized array architecture with a limited number of TRMs maintaining some pattern features, in this case the sidelobe level (SLL), close to that obtained by a reference fully-populated array. It is possible to observed that the clustered array [Figs. 1(d) and 1(e)] has half the number of elements of the reference solution [Figs. 1(a) and 1(b)] since sub-arrays of two elements are used. Although the array simplification, the SLL of the clustered solution is only 0.4dB above the one achieved by the reference solution, that is equal to -20dB.

III. THE SYSTEM-BY-DESIGN PARADIGM FOR TASK-ORIENTED OPTIMIZATION OF COMPLEX MATERIALS, DEVICES, AND SYSTEMS

A novel computational paradigm, called System-by-Design (SbD), has been recently proposed by the ELEDIA Research Center for enabling the task-oriented optimization-based design of complex electromagnetic systems and devices [9], unfeasible if using full-wave solvers. The SbD formulates the design as the integration of suitable blocks, comprising problem-dependent and efficient analysis techniques (e.g., based on LBE methods) and optimization strategies. The SbD has been effectively applied to the synthesis of multilayer wide-angle impedance-matching (WAIM) structures for phased arrays and radomes [9, 10].

As a representative example, Fig. 2 shows the results of the optimization of an electrically large radome where the exploitation of an EAs for the optimization of the radome profile has been enabled by an LBE-defined surrogate model used for the prediction of the cost function values. In particular, Fig. 2(a) shows that a 95% of time reduction can be obtained (using an exponential correlation for the LBE model) as compared to the use of a full-wave solver at the cost of a 5% error in the prediction of the cost function. Fig. 2(b) confirms the effectiveness of the SbD since the predicted cost function values are very close to the actual ones in case of a representative optimization for the radome design aimed at minimizing the beam-pointing error.

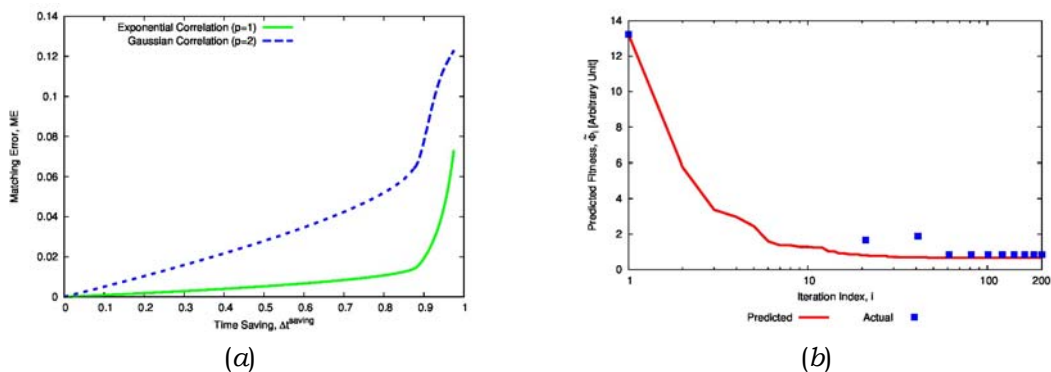


FIG. 2 – [Radome Design] – Plot of the time saving vs. prediction error (a) and of the predicted vs. true fitness value (b).

IV. CONCLUSION

A concise overview of the novel methodologies developed at the ELEDIA Research Center for the design and optimization of advanced radar and communications systems and architectures has been presented. The reported numerical solutions have shown the effectiveness of the proposed solutions.

ACKNOWLEDGEMENT

This work benefited from the networking activities carried out within the SIRENA Project (2004-2017), supported by the DIGITEO (France) under the “Call for Chairs 2014”.

REFERENCES

- [1] P. Rocca, G. Oliveri, R. J. Mailloux, and A. Massa, “Unconventional phased array architectures and design methodologies - A review,” *Proc. IEEE – Special Issue on ‘Phased Array Technologies,’ Invited Review Paper*, vol. 104, no. 3, pp. 544–560, Mar. 2016.
- [2] G. Oliveri, D. H. Werner, and A. Massa, “Reconfigurable electromagnetics through metamaterials - A review,” *Proc. IEEE – Special Issue on ‘Reconfigurable Systems – Theory, Analysis, and Applications,’ Invited Review Paper*, vol. 103, no. 7, pp. 1034–1056, Jul. 2015.
- [3] P. Rocca, M. Benedetti, M. Donelli, D. Franceschini, and A. Massa, “Evolutionary optimization as applied to inverse problems,” *Inverse Problems*, vol. 25, 123003, pp. 1–41, Dec. 2009.
- [4] P. Rocca, G. Oliveri, and A. Massa, “Differential Evolution as applied to electromagnetics,” *IEEE Antennas Propag. Mag.*, vol. 53, no. 1, pp. 38–49, Feb. 2011.
- [5] A. Massa, P. Rocca, and G. Oliveri, “Compressive Sensing in Electromagnetics - A Review,” *IEEE Antennas and Propagation Magazine*, pp. 224–238, vol. 57, no. 1, Feb. 2015.
- [6] M. Carlin, G. Oliveri, and A. Massa, “Hybrid BCS-deterministic approach for sparse concentric ring isophoric arrays,” *IEEE Trans. Antennas Propag.*, vol. 63, no. 1, pp. 378–383, Jan. 2015.
- [7] P. Rocca, R. J. Mailloux, and G. Toso, “GA-based optimization of irregular sub-array layouts for wideband phased arrays design,” *IEEE Antennas Wireless Propag. Lett.*, vol. 14, pp. 131–134, 2015.
- [8] P. Rocca, Q. Zhu, E. Bekele, S. Yang, and A. Massa, “4-D arrays as enabling technology for cognitive radio systems,” *IEEE Trans. Antennas Propag.*, vol. 62, no. 3, pp. 1102–1116, Mar. 2014.
- [9] A. Massa, G. Oliveri, P. Rocca, and F. Viani, “System-by-design: a new paradigm for handling design complexity,” 8th European Conf. Antennas Propag. (EUCAP 2014), The Hague, The Netherlands, pp. 1180–1183, Apr. 6–11, 2014.
- [10] G. Oliveri, F. Viani, N. Anselmi, and A. Massa, “Synthesis of multi-layer WAIM coatings for planar phased arrays within the system-by-design framework,” *IEEE Trans. Antennas Propag.*, vol. 63, no. 6, pp. 2482–2496, Jun. 2015.

JOINT EFFECTS OF CLOUDS AND RAIN ON EHF SATELLITE COMMUNICATION SYSTEMS

L. Luini⁽¹⁾, C. Capsoni⁽¹⁾

⁽¹⁾ Dipartimento di Elettronica, Informazione e Bioingegneria (DEIB),
Politecnico di Milano, Piazza L. Da Vinci 32, Milano, Italy
lorenzo.luini@polimi.it

Abstract

This contribution addresses the evaluation of the simultaneous impact of clouds and rain on electromagnetic waves in the EHF band. To this aim, MultiEXCELL and SMOC, two physically-based models recently developed to synthesize realistic rain and cloud fields, are employed. Taking advantage of their physical soundness, the two models are combined to derive, as an example, the simultaneous attenuation due to rain and clouds on a geostationary link operating at 39.6 GHz, as well as the gain that a two-site diversity system would achieve.

Index Terms – Atmospheric effects, Electromagnetic wave propagation, Remote sensing, Satellite communications.

I. INTRODUCTION

Modern satellite communication (SatCom) systems are gradually shifting to operational frequencies above the traditional Ku band, mainly to take advantage of the larger bandwidths available [1]. Research activities aimed at predicting propagation impairments, which strongly increase with frequency, are paramount, especially when scarce or no experimental data are available (e.g. link to Geostationary Earth Orbit – GEO – satellites working beyond 30 GHz): indeed, in this case, the design and performance assessment of the system would better be achieved by using physically-based prediction models, whose reliability, accuracy and global applicability is much higher than that of empirical models.

This contribution addresses the assessment of the simultaneous impact of clouds and rain on electromagnetic waves in the EHF band. To this aim, we exploit the combination of MultiEXCELL (Multi EXponential CELL) [2] and SMOC (Stochastic Models of Clouds) [3], two physically-based models recently developed to evaluate the impact of rain fields and cloud fields on Earth-space systems.

II. THE METEOROLOGICAL ENVIRONMENT: MODELING RAIN AND CLOUDS

MultiEXCELL is a model for the generation of synthetic rain rate fields (1 km×1 km spatial resolution, lateral dimension 200 km, constant rain rate from the ground up to the 0 °C isotherm height), developed with

the main aim of predicting the impact of precipitation on terrestrial and Earth-space millimeter-wave systems [2]. Synthetic rain fields, whose ensemble preserves the local rainfall statistics (i.e. the Complementary Cumulative Distribution Function – CCDF – of the rain rate, the sole input to the model) and reproduces the correct rainfall spatial correlation, originate from combining multiple synthetic exponential cells according to their natural aggregative process around (400/500 maps are typically sufficient to reliably represent the local rainfall process).

Recently presented in [3], SMOC is a model for the synthesis of the three-dimensional distribution of the liquid water content w (resolution: 1 km×1 km horizontal, 100 m vertical; extent: 200 km×200 km horizontal, 10 km vertical). This is achieved by exploiting features observed in real cloud fields (MODIS and CloudSat data) and from the knowledge of the fractional cloud cover (f_w) and the average integrated cloud liquid water content (E_w), both extracted for NWP pixels of dimension 2°×2° (latitude×longitude). The cloud base height h_0 is constant across the whole area but, and its value changes from field to field in accordance to MODIS data.

Taking advantage of the models' physical soundness, synthetic rain and cloud fields were combined so as to correctly reflect the correlation existing between these two quantities. Specifically, this goal is achieved on one side by assuring that the fractional cloud cover f_w is larger than the fractional rainy area f_R (all rainy pixels are covered by clouds), and, in addition, by changing the relative position of the two fields such that precipitation originates from denser clouds. Finally, as for the vertical profile, the rain rate is kept constant from the ground up to the 0° C isotherm height, where the cloud base height is assumed to lie.

III. THE SATELLITE COMMUNICATION SYSTEM

The combination of MultiEXCELL and SMOC allows a realistic simulation of the interaction between electromagnetic waves and the meteorological environment in several scenarios. As an example, in this work, we have considered uplinks to a GEO satellite operating at frequencies f in the Q band (of great interest for near future SatCom systems [1]), for which scarce experimental data exist.

The impairment caused by precipitation was calculated as follows: given a rain map, every voxel in the synthetic volume was associated to its specific attenuation $\gamma_R = kR^\alpha$, where R is the rain rate in the voxel (mm/h), while k and α are the specific attenuation power law coefficients extracted from ITU-R recommendation P.838-3 [4]. Afterwards the path rain attenuation A_R was obtained by numerically integrating γ_R along the link. A similar approach was employed for cloud attenuation by relying on the methodology recently proposed in [5],

which calculates the path attenuation due to clouds A_C from the sole knowledge of the liquid water content integrated along the link W , i.e.:

$$A_C(f) = 0.819 \left(0.016 f^{1.67} + 14.85 f^{0.39} - 27.49 \right) / \varepsilon'' (1 + \eta^2) W \quad (1)$$

In (1), $20 \text{ GHz} \leq f \leq 200 \text{ GHz}$, ε' and ε'' are the real and imaginary parts of the dielectric permittivity of water [5], while $\eta = (2 + \varepsilon') / \varepsilon''$. As a final step, the total path attenuation A was calculated as $A = A_R + A_C$.

Fig. 2 (a) shows the CCDF of the attenuation due to clouds and rain (curve labelled as “Single-site”) as predicted for a GEO system operating with $f = 39.6 \text{ GHz}$, elevation angle $\theta = 37.7^\circ$, circular polarization, ground station in Spino d’Adda (45.4° N , 9.5° E). The system characteristics have been chosen to allow the comparison between the predicted CCDF of A and the one originating from the long-term propagation measurements collected at Spino d’Adda during the ITALSAT campaign between 1994 and 2000 (red dashed line). Besides showing a very good agreement between the predicted and measured curves (discrepancies for $A > 20 \text{ dB}$ are likely ascribable to the limited dynamics of the experimental receiver), Fig. 2 (a) also reports the attenuation statistics that would be associated to a two-site diversity systems, at different distances, taking advantage of the spatial uneven distribution of clouds and rain: as expected, by selecting always the best signal between the two stations, the outage probability reduces considerably even with a relatively short separation distance between the stations. This is even clearer from Fig. 2 (b), which depicts the site diversity gain G as a function of the site separation distance D and the single-site outage probability P :

$$G(D, A_S) = A_S(P) - A_T(D, P) \quad (2)$$

In (2), A_S and A_T are the attenuation values of the single- and two-site CCDFs, respectively, both for the same P value.

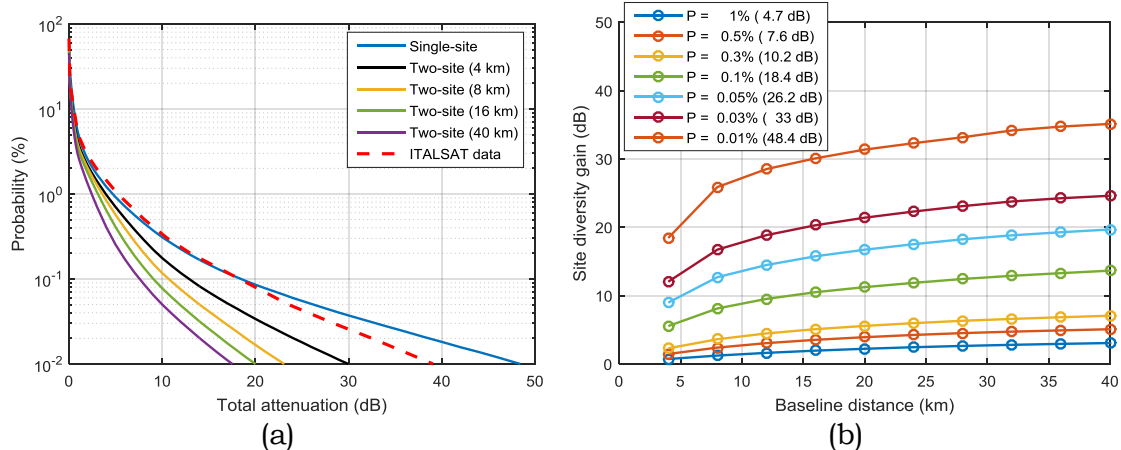


Fig. 2 – Predicted (single- and two-site) and measured (ITALSAT campaign) CCDFs of attenuation (a) and predicted site-diversity gain (b)

IV. CONCLUSION

This paper presents a new methodology to assess the simultaneous impact of rain and clouds on EHF satellite communication systems. The proposed modeling approach, which relies on MultiEXCELL and SMOC, is corroborated by the results obtained for a geostationary link operating at 39.6 GHz, which agree very well with the data collected during the ITALSAT propagation experiment. Besides allowing the accurate simulation of several complex scenarios that cannot be easily addressed using simple models (e.g. links from/to a Low Earth Orbit - LEO - satellite for which ray bending at very low elevation angles and spatial distribution of the atmospheric constituents need to be duly considered), the proposed modeling approach offers a “real-time” combination (instead of statistical as recommended by ITU-R [6]) of the effects of clouds and rain. Future work foresees the inclusion of the effects due to gases for an even more realistic simulation of the interaction of the troposphere with millimeter waves.

ACKNOWLEDGEMENT

Work supported by the Air Force Office of Scientific Research, Air Force Material Command, USAF, under Grant FA8655-13-1-3081. Thanks are addressed to the European Centre for Medium-range Weather Forecast (ECMWF) for producing and making available NWP data.

REFERENCES

- [1] A. Kyrgiazos, B. Evans, P. Thompson, N. Jeannin, “Gateway diversity scheme for a future broadband satellite system,” *Advanced Satellite Multimedia Systems Conference and 12th Signal Processing for Space Communications*, pp. 363 – 370, 2012.
- [2] L. Luini, C. Capsoni, “MultiEXCELL: a new rain field model for propagation applications,” *IEEE Trans. Ant. Prop.*, vol. 59 (11), pp. 4286 - 4300, 2011.
- [3] L. Luini, C. Capsoni, “Modeling High Resolution 3-D Cloud Fields for Earth-space Communication Systems,” *IEEE Trans. Ant. Prop.*, vol. 62 (10), pp. 5190 - 5199, 2014.
- [4] ITU-R recommendation P.838-3, “Specific attenuation model for rain for use in prediction methods,” Geneva, 2005.
- [5] L. Luini, C. Capsoni, “Efficient Calculation of Cloud Attenuation for Earth-space Applications,” *IEEE Antennas and Wireless Propagation Letters*, vol. 13, Page(s): 1136 - 1139, 2014.
- [6] ITU-R recommendation P.618-12, “Propagation data and prediction methods required for the design of Earth-space telecommunication systems,” Geneva, 2015.

RFIDRONES: PRELIMINARY EXPERIMENTS AND ELECTROMAGNETIC MODELS

G. Casati, M. Longhi, D. Latini, F. Carbone, F. Del Frate, A. Perrone,
G. Schiavon, and G. Marrocco

Civil Engineering and Computer Science, University of Rome Tor Vergata
Via del Politecnico 1, Roma, Italy

Abstract

The paper introduces the paradigm of radiofrequency identification (RFID) merged with the technology of Unmanned Aerial Vehicles (UAV) giving rise to RFIDrone devices. This family comprises the READER-Drone, which is a suitable UAV integrated with an autonomous RFID reader to act as mobile scanner of the environment, and the TAG-Drone, a UAV equipped only with an RFID sensor tag that hence becomes a mobile and automatically re-positioned sensor. Some handy electromagnetic models are shown at the purpose to identify the upper-bound communication performance of RFIDrones in close proximity of a scattering surface. Results of some preliminary open-air experimentation finally corroborate the theoretical analysis.

Index Terms – UAV, RFID, electromagnetic model, two-ray model.

I. INTRODUCTION

RFID technology is now currently orienting from logistic only applications toward higher-value sensing systems, hence becoming one of the enabling technologies of the Internet of Things. Unmanned Aerial Vehicles (UAV) are experiencing a huge growth in both amateur and professional contexts. RFID and UAV technologies are now mature to be merged together and stimulate a set of completely new application fields. It is conceived that an UAV could be equipped with an RFID scanner in the UHF band [1] and this moving agent could collect identification and sensing information from RFID tags displaced in harsh environments [2] like bridges [3], trees and open air warehouses [4], [5]. There are two possible architectures of RFID-UAV systems (hereafter denoted as *RFIDrones*) that differ for the specific integration of the UAV with either the reader or the tag devices. We show some preliminary electromagnetic models allowing to understand the upper bounds of the achievable electromagnetic performance in terms of communication and identification. We also summarize some real-life measurements with a professional airframe interacting with several RFID sensors in an open field.

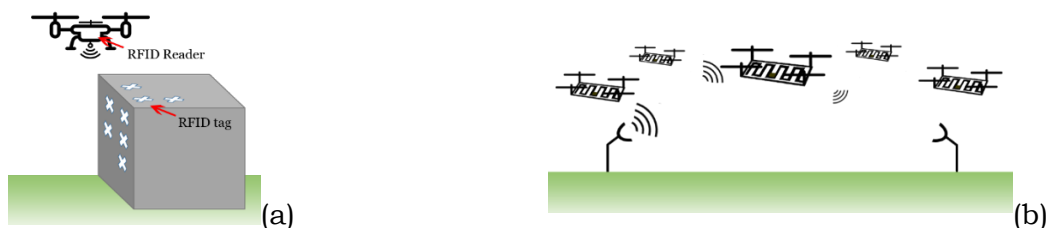


FIG. 1 – Topologies of RFIDrones: (a) Reader-Drone and (b) Tag-Drone.

II. RFIDRONES TOPOLOGIES AND POSSIBLE APPLICATIONS

The RFIDrone concept can be discussed by considering the two complementary paradigms:

A. R-drone: a suitable UAV is integrated with an autonomous RFID reader to act as mobile scanner of the environment (Fig. 1a). The drone can be remotely driven to approach tags displaced onto a surface and equipped with sensors. Alternatively, the R-drone may be programmed to autonomously and periodically approach sensors and retrieve sensed data.

B. T-drone: the UAV only equipped with an RFID sensor can be interpreted as a sensor with flying capability (Fig. 1b). The T-drone may be used in standalone mode or according to the more fascinating swarm configuration (like bees) cooperatively collecting information within a same environment. R-drones and T-drones may mutually interact, the R-drone could act as a mother drone moving and mastering a swarm of T-drones. Promising applications are the volumetric scanning of environments. A swarm of T-drones with environmental-oriented sensor capabilities will methodically fly within a large volume at the purpose to provide a 3D map of those parameters.

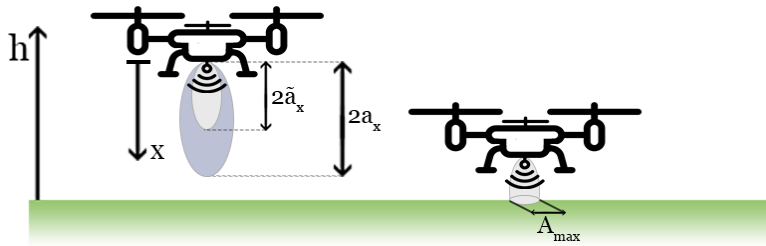


FIG. 2 – A schematic ellipsoidal representation of the reading zone of an R-drone: the free space hypothesis (major axis a_x) and the real model (major axis \tilde{a}_x).

III. PARAMETRIC ELECTROMAGNETIC MODELING

In the free-space, the read region of a reader placed at position $x = 0$ and radiating toward $x > 0$, e.g. the space where a tag with effective microchip sensitivity

$$\tilde{p}_c = \frac{P_c}{\tilde{G}_T} \quad (1)$$

collects enough power to be energized and send back its ID, can be roughly approximated by an ellipsoid (Fig. 2) whose axis a_ξ (with $\xi = \{x, y, z\}$) are related [6] to the electrical parameter of the link. The maximum read distance corresponds therefore to twice the major axis $r_{FS} = 2a_x$. For the RFIDrone scenario (Fig. 2) instead, the presence of a strongly reflecting infrastructure (ground, building walls) at a close distance to the reader forbids the use of the free-space equations. The read distance can be nevertheless corrected by means of a simple two-ray propagation model so that the ellipsoid maximum axis is a solution of the equation

$$\tilde{a}_x^2 - \left[\frac{h}{2} + (1 + \Gamma)a_x \right] \tilde{a}_x + h \cdot a_x = 0 \quad (2)$$

where Γ is the amplitude of the Fresnel reflection coefficient of the surface. The footprint of the R-drone over the surface is hence an ellipse given by the intersection of the above ellipsoid with the plane $x = h$. The diameter of the footprint is given by:

$$A_{\max} = 2 \sqrt{\frac{a_{\max}^2}{2} \left[1 - \frac{(h - a_x)^2}{\tilde{a}_x^2} \right]} \quad (3)$$

where $a_{\max} = \max\{a_y, a_z\}$.

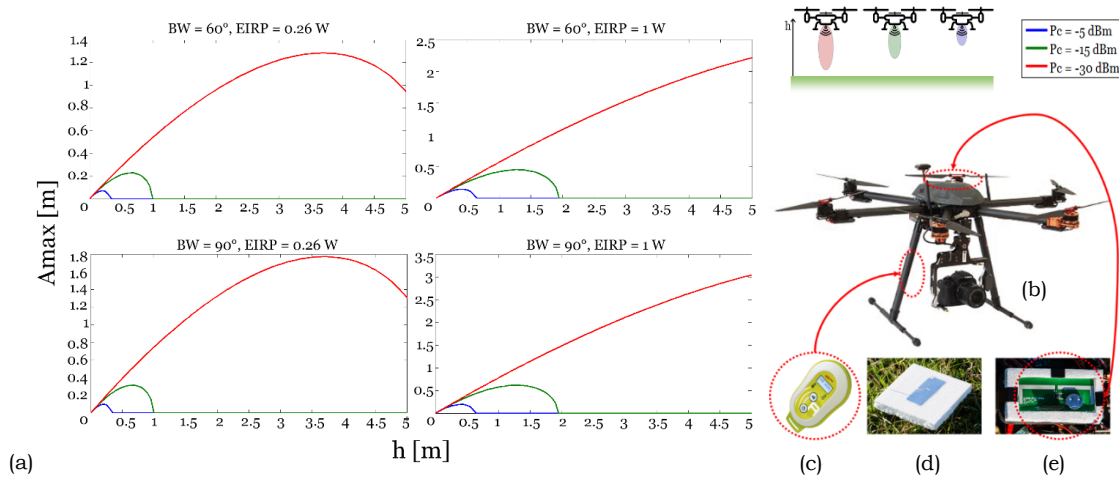


FIG. 3 – (a) Maximum size of the footprint of the R-drone over a surface for several combinations of reader’s EIRP and beam width and chip sensitivity, (b) Drone FlyTop FlyNovex, (c) on-board reader, (d) dipole-tag, (e) RFID data-logger .

Fig.3 (a) shows the major axis of the reader footprint, versus the distance h corresponding to some realistic values of the reader’s EIRP, the beam-width of the reader’s antenna resembling a dipole-like ($BW=90^\circ$) and a patch-like ($BW=60^\circ$) configuration, and finally the effective microchip sensitivity $\tilde{P}_c = \{-5dBmW, -15dBmW, -30dBmW\}$.

IV. OPEN-AIR EXPERIMENTATION

A first experiments with the R-drone and the T-Drone architectures involved a FlyTop FlyNovex drone (Fig.3b).

A. Scanning an array of tags: The R-drone scheme was implemented by installing on-board the portable battery-assisted low-power reader CAENRFID qIDmini (Fig. 3c) with declared EIRP=0.26W. The reader was remotely controlled in real time via a Bluetooth interface by the RADIO6ENSE RadioSCAN Software running over a notebook. The tags for on-ground deployment were Avery Dennison AD-843 dipoles (Fig. 3d) with chip sensitivity $P_c = 15dBmW$. Tags were placed at 8.5 cm distance from the soil and forming a 6 by 5 array with 0.5 m spacing (Fig. 4a). From ellipsoidal models, the optimal height of the R-drone over the soil is about 75 cm and the footprint is a circle of diameter

35 cm. In particular, flying in between two rows, the reader-drone was able to collect the response of two tags at a same time (Fig. 4b).

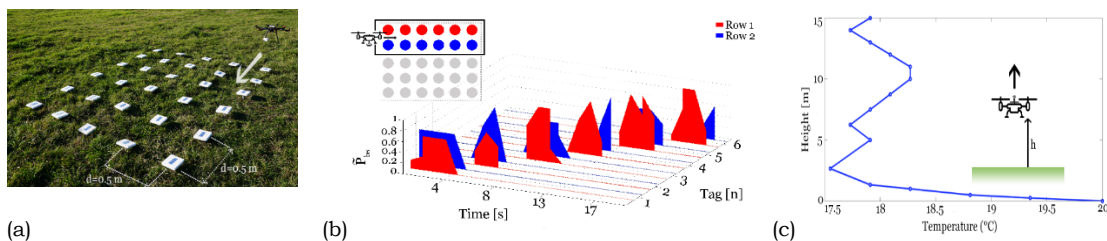


FIG. 4 – (a) R-drone: 5 by 6 array of dipole-like tags over meadow; (b) time-variant backscattered power signals collected when the drone flew, (c) T-drone: Temperature profile measured by the on-board RFID data logger when the T-drone took-off vertically.

B. Temperature profile measurement by a T-drone: The T-drone modality was implemented by installing aboard the same drone (Fig. 3e) the sensor board SL900A-DK-STQFN16 embedding the SL900A microchip. Once the board was activated by a Thing-Magic M6E reader, the drone slowly moved vertically from the soil up to a height $h=15m$ and the temperature was recorded. At the end of the experiment, the reader downloaded the collected data and an example of profile is shown in Fig. 4 (c).

V. CONCLUSIONS

In this work we have presented some electromagnetic bounds and preliminary experimentation of the RFIDrone architecture. The propagation model revealed that using low-sensitivity battery-less tags may yield a great challenge in establishing a robust link between a moving READER-drone and the sensor-tag, especially when the drone has to find the sensor and approach it. Battery-assisted sensor tags, or even solar-cell powered tags, may instead enable a much easier interrogation procedure. The preliminary experimental tests considering the reader-drone configuration have given a first corroboration of the theoretical analysis.

REFERENCES

- [1] J. Wang, E. Schlutz, B. Otis, T. Deyle, "A New Vision for Smart Objects and the Internet of Things: Mobile Robots and Long-Range UHF RFID Sensor Tags," *arXiv preprint whitepaper*, no. 1507.02373, Jul. 2015.
- [2] G. Greco, C. Lucianaz, S. Bertoldo, and M. Allegretti, "A solution for monitoring operations in harsh environment: a RFID reader for small UAV", *In Electromagnetics in Advanced Applications (ICEAA)*, 2015 International Conference on, pp. 859-862, Sept. 2015.
- [3] "Futuristic Inspections for Bridge Safety", *TuftsNow*, Tufts University, May 2014.
- [4] "The flying inventory assistant", Fraunhofer Institute for Material Flow and Logistics IML, Dec. 2014.
- [5] C. Swedberg, "RFID-Reading Drone Tracks Structural Steel Products in Storage Yard", *RFID Journal*, Sept. 2014.
- [6] G. Marrocco, E. Di Giampaolo, R. Aliberti, "Estimation of UHF RFID Reading Regions in Real Environments," *Antennas and Propagation Magazine*, IEEE, Vol. 51, pp. 44-57, Dec. 2009

LOW-COST WIRELESS SENSING BY MEANS OF RECONFIGURABLE RFID SYSTEMS

M.C. Caccami⁽¹⁾, G. Marrocco⁽¹⁾

⁽¹⁾ Department of Civil and Information Engineering
University of Rome Tor Vergata
Viale del Politecnico, 1, 00133, Rome, Italy
caccami@ing.uniroma.it, gaetano.marrocco@uniroma.it

Abstract

Recently introduced self-tuning UHF RFID microchips offer interesting potentials for low-cost sensing. We have investigated the response of such a chip embedded into a meandered-dipole tag versus variable boundary conditions. An electromagnetic model of the tag is set-up and hence calibrated by means of measurements to predict the sensor response over a broad range of permittivity and conductivity.

Index Terms – Internet of Things, RFID sensing, Self-tuning tags, Wireless sensor.

I. INTRODUCTION

In recent years the massive adoption of the UHF Radiofrequency Identification (RFID) technology has been encouraging the multi-face evolution of the Internet of Things. In addition to the more traditional logistic purposes, sensing potentialities of passive RFID tags have been widely investigated [1, 2]. However, sensing capabilities are often achieved at the expenses of communication features (read distance) and the measured signal is strongly affected by the propagation noise, by the specific arrangement of the measurement set up and by the environment variability. A new family of RFID microchips, very recently introduced [3], exhibits the unconventional capability to automatically modify their internal impedance at the purpose to balance the variation of the admittance of the antenna due to change of the boundary conditions. Therefore, such self-tuning chips may provide a useful mean to digitize, just at the chip level, the change of the antenna input admittance as a reaction to the variation of some external stimuli. The sensing information is hence transmitted in a digital form that is much more immune to the propagation uncertainties. At this purpose, the physical relationship between the change of the antenna admittance and the retuning capability of the chip has to be fully investigated and hence modelled to control the sensor response. This contribution analyses, by the help of experimentations and preliminary numerical models, the behavior of such chips and their potentialities for RFID sensing application.

II. FORMULATION OF RFID SENSING BY SELF-TUNING CHIPS

Let's denote with $Y_A(\Psi) = g_A(\Psi) + jB_A(\Psi)$ the input admittance of a tag antenna, where $\Psi(t)$ is a physical, chemical or geometrical parameter of the environment surrounding the tag to be monitored. The considered RFID microchip includes a self-configuring internal network (Fig.1a) of capacitors whose overall capacitance is $C_T(n) = C_{\min} + nC_0$. The equivalent admittance of the chip is finally denoted as $Y_C(n) = g_C + jB_C(n)$ where $B_C(n) = \omega C_T(n)$ is referred to the instantaneous value of the tuning capacitor network so that $|B_C(n) + B_A(\Psi)| \rightarrow 0$. The integer n is the *sensor code* and is an indirect measure of the degree of mismatching between the antenna and the chip and accordingly can be used as a digital sensing metric for the phenomenon under test where the antenna response plays the role of a transducer between Ψ and n .

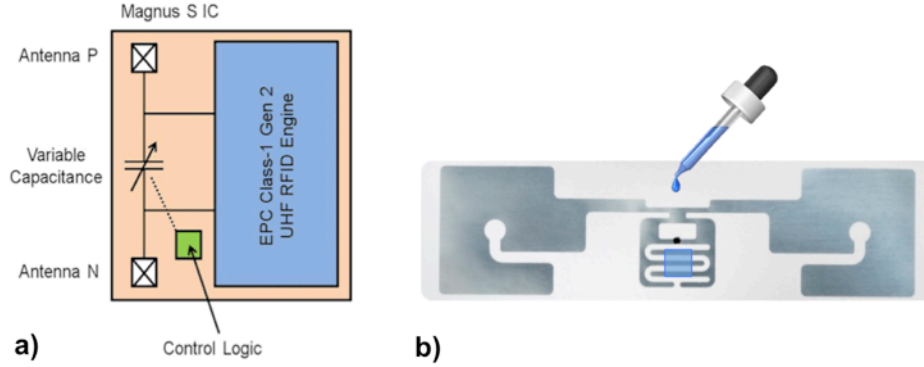


FIG. 1– a) Scheme of a reconfigurable RFID chip; b) RFID tag implementing the reconfigurable chip: coating with absorbing paper permits to interact with liquids.

The self-tuning chip generally does not preserve the communication performance of the chip during the change of the phenomenon under test. A useful metrics able to qualify the maximum read range of a tag, is the turn-on power $P_{in}^{to}(\Psi)$, e.g. the lowest power to provide the reader's antenna with in order to activate the tag's microchip. By assuming a perfect compensation $B_C = -B_A(\Psi)$, the turn-on power can be written as:

$$P_{in}^{to}(\Psi) = \left(\frac{4\pi d}{\lambda} \right)^2 \frac{P_C}{\eta_p G_R G_A(\Psi)} \frac{(g_A(\Psi) + g_C)^2}{4g_A(\Psi)g_C} \quad (1)$$

where $G_A(\Psi)$ and G_R are the gain of tag and reader antennas, d is the reader-tag distance, η_p is the polarization mismatch between the reader and the tag, and P_C is the ICs sensitivity. The loss in the communication performance is hence due to the sensitivity of both the gain and the admittance of the antenna to the physical stimulus Ψ . In

particular, when the antenna conductance is insensitive to the external environment, the degradation of the read distance is accordingly only related to an eventual change of the antenna gain $G_A(\Psi)$. Design conditions can be established in order to minimize the variation of the read distance of the tag when lumped-circuits sensors are used.

III. EXPERIMENTATIONS

The potentialities of self-tuning RFID tags are here discussed by means of a combined numerical and experimental campaign involving a set of liquid materials of different permittivity (Tab. I) that modify the input admittance of the tag antenna. The considered tag is a SMARTRAC Sensor Dogbone (Fig.1b) including the RFMicron Magnus chip and a printed interdigital capacitor to amplify the sensitivity of the antenna impedance to the variation of nearby permittivity. The measurement set-up comprises a ThingMagic M6e reader connected to a 5dB gain linear polarized patch antenna, placed 50cm apart from the sensor. The set-up is capable to measure the sensor code as well as the turn-on power by using an in-house software. Two kinds of interrogation modalities of the sensor are experimented: i) turn-on condition, such that the power collected by the chip (and hence affecting the chip impedance) is the same in all the measurements and equals to the ICs sensitivity; and ii) the power emitted by the reader is kept fixed to $P_{in} = 30dBm$. The digital and analog responses of the sensor were predicted by using a numerical model of the tag antenna (Method of Moment - FEKO).

TABLE I - DIELECTRIC PROPERTIES OF THE LIQUID DROPS IN THE UHF RFID BAND

Liquid drops	ϵ_r	σ [S/m]
Glycerol	~10	0.35
Ethyl alcohol	24.3	1.35×10^{-7}
Head phantom	41.2	0.95
Body phantom	54.1	1.05
NaCl solution	75.6	1.7
Distilled water	78.4	5.5×10^{-6}

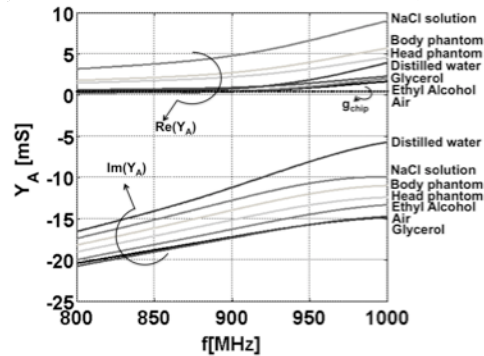


FIG. 2 – Simulated antenna input admittance versus frequency.

The liquids drops are placed right over the interdigital capacitor of the antenna by means of an absorbing paper sheet. The simulated profiles of the input admittance versus frequency for each liquid are shown in Fig 2. The self-tuning parameters $\{C_0, C_{min}\}$ of the chip are preliminary identified by minimizing the error between the numerically estimated sensor codes and the measured ones over reference different materials. An example of comparison between the estimated sensor code and turn-

on power by using the calibrated model and the measurement are shown in Fig.3a for the case of a liquid material with low electrical conductivity, (e.g, the ethyl alcohol), and the liquid head phantom which has instead a high value of conductivity. For the sake of corroboration, Fig.3b shows also the comparison among the simulated and measured turn-on powers that are in reasonable agreement especially for higher-permittivity fluids.

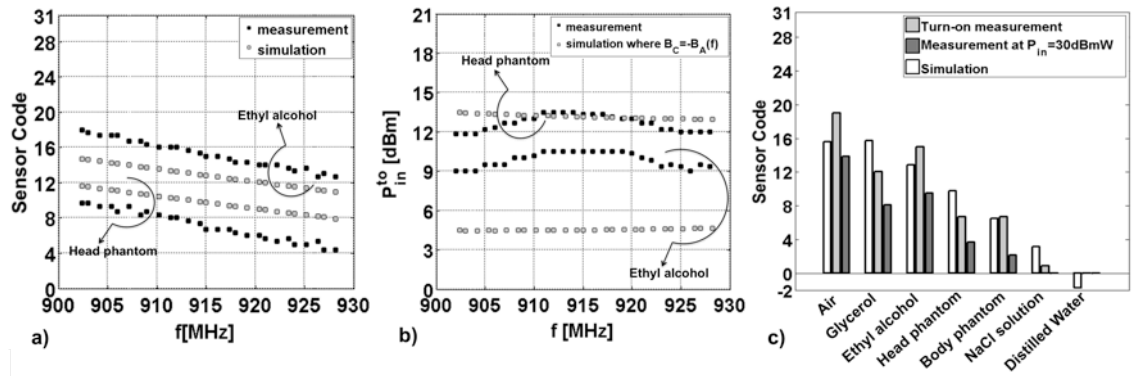


FIG. 3– Measured and simulated (after calibration) a) sensor code and b) turn-on power both for ethyl alcohol and head phantom drops. c) A comparison at 915MHz between the sensor code measured with two interrogation modes.

Finally, Fig.3c shows the sensor responses as measured in case of fixed-power interrogation superimposed to those obtained with the turn-on power mode. Measured data are different as the permittivity of the materials increases up to completely drop out the sensor code, that means the chip is not able to enforce impedance compensations anymore (e.g., in the case of distilled water).

IV. CONCLUSION

Self-tuning RFID microchips offer new possibilities in low-cost RFID sensing. In particular, the potential to merge the digital sensing (the sensor code) with analog sensing metrics (turn-on power) can generate multiple independent physical information from a single tag and suitable examples of humidity and temperature sensing will be provided at the conference.

REFERENCES

- [1] S. Amendola, M. C. Caccami, A. Caponi, L. Catarinucci, V. Cardellini, E. Di Giampaolo, S. Manzari, F. Martinelli, S. Milici, C. Occhiuzzi, and G. Marrocco, “RFID & IoT: a Synergic Pair”, IEEE RFID Virtual Journal, N.8, March 2015.
- [2] Occhiuzzi C., Caizzone S., Marrocco G., “Passive UHF RFID Antennas for Sensing Applications: Principles, Methods and Classifications”, IEEE Antennas and Propagation Magazine, Feb. 2014.
- [3] Magnus™ UHF RFID Tag IC, RFID tag chip antenna design guideline, Application Note [Online]. Available: www.rfmicron.com.

COPRIME SYNTHETIC ARRAYS

G. Di Martino, A. Iodice

Department of Electrical Engineering and Information Technology,
University of Naples “Federico II”
Via Claudio 21, Naples, Italy
gerardo.dimartino@unina.it, iodice@unina.it

Abstract

In this paper we present a comprehensive discussion regarding the application to Synthetic Aperture Radar (SAR) of the new concepts of coprime arrays. The proposed coprime SAR configurations, which we name CopSAR and OrthoCopSAR depending on the used waveforms, can be used to decrease the amount of data to be stored and processed and to increase the range swath, in case of bright targets at sea. The only costs are the reduction of the target-to-background ratio and the presence of a (non-stringent) limit on maximum ship size. Performance indicators and impulse response functions of all the implementations are reported.

Index Terms – Coprime arrays, sparse arrays, synthetic aperture radar.

I. INTRODUCTION

The requirements of high resolution and coverage of Synthetic Aperture Radar (SAR) systems for maritime applications dictate the need to manage storing and processing of a huge amount of data. In this paper, for the first time, we present a comprehensive discussion regarding the different ways of applying to SAR the new techniques based on coprime sensing concepts [1]. The proposed approaches are able, in the case of bright targets over a dark (not necessarily homogeneous) background to reduce the amount of data and, in specific cases, to increase the range swath, with no geometric resolution loss [2]-[3]. The general approach consists in the transmission of two interlaced sequences of pulses, with sub-Nyquist pulse repetition frequencies (PRFs), where the PRFs or the signal frequencies are related via coprime numbers. Each sequence is separately processed via standard SAR processing, and the two final aliased images are combined in a very simple way to cancel out aliasing. When the two sequences are made up of pulses of the same kind we name the technique CopSAR [2], conversely, when use is made of orthogonal pulses we name it OrthoCopSAR [3].

More specifically, three different CopSAR implementations are discussed, aimed at achieving data reduction and/or range swath extension. As for the OrthoCopSAR [3] technique, it can be seen as an enhancement of the CopSAR basic implementation based on the transmission of (quasi) orthogonal waveforms, i.e., up- and down-chirps. This implementation is able to achieve both data reduction and range swath extension with no appearance of ghosts and no resolution loss.

All the above-described coprime implementations only imply a reduction of the target-to-background ratio (TBR) and the presence of a (non-stringent) limit on maximum ship size [2]-[3]. In the following, the proposed coprime configurations performances are discussed.

II. COPRIME SAR CONFIGURATIONS

The basic CopSAR is based on the transmission of two interlaced sequences of pulses, one at $\text{PRF}_1 = \text{PRF}_0/N_1$, and the other at $\text{PRF}_2 = \text{PRF}_0/N_2$, where PRF_0 satisfies the Nyquist condition (i.e. $\text{PRF}_0 \geq 2\nu/L$, with ν the uniform sensor velocity and L the real azimuth antenna length) and N_1 and N_2 are coprime integers. The two sequences can be separately processed to obtain two SAR images, i.e., $s_1(x, r)$ and $s_2(x, r)$, with x and r standing for azimuth and range coordinates, respectively. If the entire SAR system bandwidth is processed, the geometric resolution of these images will not change with respect to the standard SAR case, but, of course, the images will be severely aliased. However, if the scene consists of bright targets on a dark background, only the true targets will be present on both aliased images at the same location, whereas aliased targets will be at different locations on the two images. The azimuth displacement of replicas for $s_1(x, r)$ and $s_2(x, r)$ are

$$\Delta x_{i_1} = i_1 \frac{\text{PRF}_0 \lambda r_0}{N_1 2\nu} \quad \Delta x_{i_2} = i_2 \frac{\text{PRF}_0 \lambda r_0}{N_2 2\nu} \quad , \quad (1)$$

where λ is the wavelength, and i_1 and i_2 are integers, so that replicas on the two images will not be at the same location unless $i_1/i_2 = N_1/N_2$. Since N_1 and N_2 are coprime, this only happens if $i_1 = iN_1$ and $i_2 = iN_2$, i.e. only at the positions of the replicas in the image that would be obtained in the standard acquisition mode. These replicas will be strongly attenuated by the azimuth antenna pattern and will not be considered in the following discussion [3]. Therefore, using the simple combination rule

$$s(x, r) = \begin{cases} s_1(x, r) & \text{if } |s_1(x, r)| < |s_2(x, r)| \\ s_2(x, r) & \text{otherwise} \end{cases} \quad , \quad (2)$$

the obtained $s(x, r)$ image is not affected by aliasing. However, since the minimum time separation between the pulses of the two sequences is $1/\text{PRF}_0$, the range swath cannot be increased with respect to standard SAR without the appearance of significant range ambiguities. A doubling of the range swath can be obtained via the missing pulse implementation avoiding to transmit in the sequence of pulses transmitted at rate PRF_0/N_1 , those pulses that would be separated by just $1/\text{PRF}_0$ from a pulse of the other sequence. In this case, in the image $s_1(x, r)$ each bright target will have not only replicas displaced according to (1), but also replicas at distances

$$\Delta x_{i_{12}} = i_{12} \frac{\text{PRF}_0 \lambda r_0}{N_1 N_2 2v} , \quad (3)$$

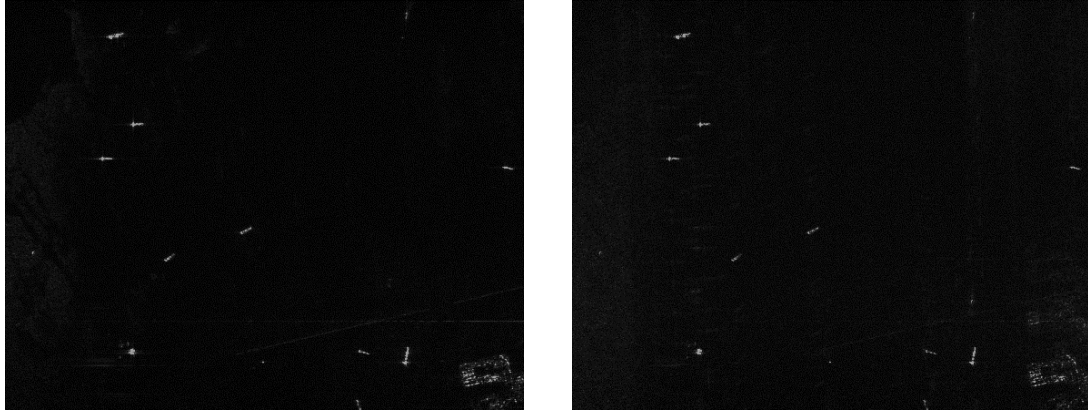
and these replicas will overlap with a replica of the second image for $i_{12}=i_2 N_1$, so that several “ghosts” will appear on the final image $s(x,r)$. However, these ghosts will be attenuated with respect to the true target by a factor N_2 due to the reduced number of pulses that contribute to focus them and to the attenuation due to the slight replica defocusing [2]. A more significant extension of the range swath, with no appearance of any ghost, can be obtained via the dual frequency implementation. In this case, the two sequences of pulses are both transmitted at rate $\text{PRF}_1=\text{PRF}_0/N_1$, but the first is transmitted at frequency f_1 and the second at frequency $f_2=(N_2/N_1)f_1$, so that wavelengths for the two sequences are related by $\lambda_2=(N_1/N_2)\lambda_1$. According to (1), replicas’ locations will be the same of the CopSAR basic implementation. Pulses at the two frequencies can be transmitted at the same times, if two different antennas are employed or they can be interlaced if a single antenna is used [2].

Until now, we considered the case in which the waveforms used in the two sequences are of the same kind. In the OrthoCopSAR technique, the pulses of the two interlaced subsampled sequences are mutually (quasi) orthogonal: the first sequence up-chirp waveforms are transmitted, whereas in the second one down-chirp waveforms are used. Since up-chirp and down-chirp waveforms are quasi orthogonal [3], non-aliased images can be obtained processing each sequence via the appropriate up- or down-chirp matched filtering during range compression. The energy of the unfocused target contribution due to the presence of the mismatched chirp will be spread over a pulse duration interval in the final focused image [3]. The proposed technique can be implemented on single-antenna SAR sensors: in this case, “blind ranges”, arising since the sensor cannot receive during the transmission interval, are present in the raw signal: however, when doubling the range swath, this only happens for pulses at distance $1/\text{PRF}_0$ (i.e., two out of $N_1 N_2$). Therefore, on the final image this implies no blind range, but only the possible appearance of strongly attenuated azimuth replicas, similar to those of the CopSAR missing-pulse implementation, over a specific slant range interval.

In Table I meaningful performance indicators are reported: the data rate reduction, i.e. the ratio between the number of pulses transmitted in coprime mode and in standard SAR mode, the potential range swath extension, i.e. the ratio between the CopSAR range swath size and the standard SAR one, and the maximum azimuth target size needed to avoid replicas. Finally, a discussion on TBR reduction can be found in [2].

III. EXPERIMENTAL RESULTS

We present just one sample result. Images in Fig. 1 are obtained by processing actual ERS raw data of the Long Beach harbor, via standard SAR (a) and CopSAR basic implementation for $N_1=5$ and $N_2=6$ (b).



(a)

(b)

FIG. 1 – ERS case study: (a) standard SAR; (b) CopSAR.**TABLE I - TECHNIQUE PERFORMANCE INDICATORS**

Configuration	Data rate reduction	Maximum range swath extension	Maximum azimuth target size
CopSAR basic	$\frac{N_1 + N_2 - 1}{N_1 N_2}$	1	$\frac{\text{PRF}_0 \lambda r_0}{N_1 N_2 2v}$
CopSAR missing pulse	$\frac{N_1 + N_2 - 3}{N_1 N_2}$	2	$\frac{\text{PRF}_0 \lambda r_0}{N_1 N_2 2v}$
CopSAR dual frequency	$\frac{2}{N_1}$	N_1 (single antenna: $N_1/2$)	$\frac{\text{PRF}_0 \lambda r_0}{N_1 N_2 2v}$
OrthoCopSAR	$\frac{N_1 + N_2}{N_1 N_2}$	N_1	$\frac{\text{PRF}_0 \lambda r_0}{N_1 N_2 2v}$

IV. CONCLUSION

The implementations of coprime synthetic arrays discussed in the paper allow for data rate reduction and increase of the range swath in case of bright targets at sea. This work can guide the choice of the best configuration, in terms of a trade-off between user needs, system complexity, and desired performances.

REFERENCES

- [1] P. P. Vaidyanathan and P. Pal, "Sparse Sensing With Co-Prime Samplers and Arrays," *IEEE Trans. Signal Process.*, vol. 59, no. 2, pp. 573–586, 2011.
- [2] G. Di Martino and A. Iodice, "Coprime Synthetic Aperture Radar (CopSAR): A New Acquisition Mode for Maritime Surveillance," *IEEE Trans. Geosci. Remote Sens.*, vol. 53, no. 6, pp. 3110–3123, June 2015.
- [3] G. Di Martino, A. Iodice and S. Medagli, "Orthogonal Coprime SAR", *Proceedings of IGARSS 2015*, pp. 3758–3761, July 2015.

MICROWAVE CHARACTERIZATION OF A DILUTED WATER-BASED FERROFLUID IN PRESENCE OF AN EXTERNAL POLARIZING MAGNETIC FIELD FOR BIOMEDICAL APPLICATIONS

G. Bellizzi^(1,2), G.G. Bellizzi^(2,3), O.M. Bucci^(3,4)

(1) DIETI, Università di Napoli Federico II Via Claudio 21, Napoli, Italy, gbellizz@unina.it

(2) IREA, Consiglio Nazionale delle Ricerche Via Diocleziano 324, Napoli Italy.

(3) DIIES, Università Mediterranea della Calabria, Via Reggio Calabria, Italy

(4) CNIT, viale G.P. Usberti 181/A, 43124 Parma, Italy.

Abstract

This paper presents the results of a broadband characterization, in the microwave frequency range, of the magnetic properties of a diluted suspension of magnetic nanoparticles in aqueous solution, in presence of an applied polarizing magnetic field of different intensities. This characterization has been performed by means of an ad hoc measurement strategy and apparatus specifically designed to allow the accurate measurement of the magnetic properties of such suspensions. A physical interpretation of the obtained results is also discussed.

These results are very important in prospective of the future implementation of some emerging biomedical applications of microwaves and magnetic nanoparticles, such as the microwave detection and imaging of breast cancer.

Index Terms – Biomedical applications, broadband microwave characterization, magnetic nanoparticles, magnetic permeability.

I. INTRODUCTION

In the recent years, magnetic nanoparticles (MNP) have gained an increasing interest as “contrast agent” in the microwave imaging (MWI) of breast cancer [1]-[2]. Indeed, MNP are already allowed for clinical use and can be functionalized with specific antibodies which enable their selective accumulation into the cancerous cells. Moreover, they are characterized by a remarkable microwave magnetic response, which can be modulated by applying a polarizing magnetic field (PMF) of proper intensity. These features have led to the definition of a new MWI technique [1] which exploits MNPs in order to selectively induce a tunable magnetic contrast in the tumor and a PMF modulation in order to discriminate its response from that of the background electric scenario. In such a way, by adopting a proper filtering, one can extract the contribution to the scattered field due to the MNPs in the tumor from the total scattered field and use it for detecting or imaging the tumor. Compared to standard MWI approaches, the approach in [1]

allows to reduce the occurrence of false negatives due to the low electric contrast between cancerous and fibro-glandular tissues, in that, if a signal is detected, it is unambiguously associated to the presence of a malignant lesion. Moreover, due to weak nature of the induced magnetic contrast (due to the low amount of MNPs deliverable to the tumor through the biochemical targeting), the imaging can be successfully addressed by exploiting a linear inversion procedure.

One of the main steps toward the implementation of such MWI technique is the accurate experimental characterization of the microwave magnetic response of the MNPs when subjected to an applied PMF of different intensities. Of course, such a characterization must be carried out under conditions as close as possible to those of the practical application, namely MNP suspended in a biocompatible liquid (water-based ferrofluid), at concentration comparable to those actually reachable in the tumor with the available targeting techniques. The aim of this communication is to present the preliminary results of such characterization performed on a commercially available water-based ferrofluid.

II. MATERIAL AND METHOD

The investigated ferrofluid is a suspension of magnetite nanoparticles with a core size of 10 nm, in aqueous solution. The original sample was diluted in phosphate buffer saline (PBS) up to a concentration of magnetite of about 25 mg per milliliter of solution. The measurements has been carried out by means of the Nicolson-Ross-Weir technique properly modified in order to enable the accurate estimation of the magnetic properties of a medium strongly dielectric and weakly magnetic, like the investigated ferrofluid. In particular, the magnetic permeability of the ferrofluid, in presence of a PMF of intensity H , say $\mu(H)$, is estimated by inserting the sample in a coaxial cell and measuring the scattering parameters in two different configurations: a) in presence of the PMF of the desired intensity H ; b) in presence of a PMF of intensity large enough to turn off the magnetic response of the MNP over the investigated frequency range. In such a way, two datasets are collected: the dataset (a) which depends on both $\mu(H)$ and the electric permittivity of the carrier liquid, say ϵ_r ; the dataset (b) which only depends on ϵ_r . Therefore, one can estimate $\mu(H)$ by properly processing together these two datasets. The implementation of this technique has required an *ad hoc* measurement apparatus made of coaxial cells and of an electromagnet for the generation of the PMF. We have considered coaxial cells in order to allow the characterization over the range 0.1-8 GHz, which is the band of interest in MWI of breast cancer. The cells are made of non-magnetic metal in order to allow the penetration of the applied PMF. More details on the used measurement technique and apparatus can be found in [3].

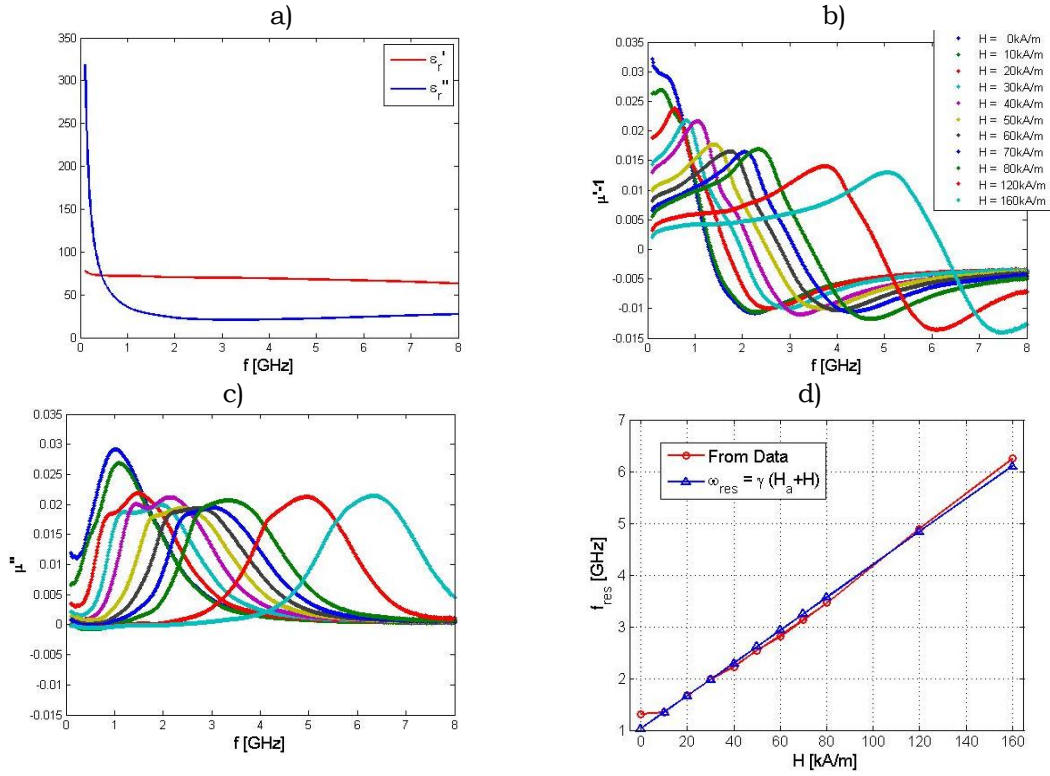


FIG. 1 – electromagnetic properties of the investigated ferrofluid: relative permittivity (a); real part (b) and the opposite of the imaginary (c) part of magnetic susceptibility; resonance frequency behavior vs PMF amplitude.

III. MEASUREMENT RESULTS

Fig. 1(a) shows the real part (ϵ_r') and the opposite of the imaginary part (ϵ_r'') of relative permittivity measured for the investigated ferrofluid; Fig. 1(b)-(c) shows the real and the opposite of the imaginary of the magnetic susceptibility $\chi(H)=\mu(H)-1$, for different intensity of the applied PMF (see legend in Fig. 1). From the results, it is confirmed that in the microwave frequency range the electric properties of a diluted water-based ferrofluid are prevalently entailed by carrier liquid (PBS in our case); moreover, it is confirmed that the adopted measurement technique enables the accurate estimation of the magnetic permeability despite an electric response several order of magnitude larger.

Concerning the magnetic susceptibility, it exhibits a resonant behavior with a resonance frequency moving toward the higher frequencies of the analyzed band as H increases. This shift is consistent with the fact that the observed resonance behavior is related to the phenomenon of the ferromagnetic resonance of the magnetic dipole moment characterizing each MNP, whose resonance frequency increases as H increases. This is confirmed by the result in Fig. 1(d) where we show the behavior of the resonance frequency vs H . As it can be seen,

there is a linear trend of the resonance frequency vs H , with a slope which is very close to the value of the electron gyromagnetic ratio characterizing the precession of the electron spin around the magnetic field direction in the ferromagnetic resonance phenomenon. Moreover, for $H=0, 10, 20, 30, 40$ kA/m we note a splitting of the resonance peak into two distinct peaks. The physics of this phenomenon will be the subject of future investigation.

Leaving aside the physical interpretation, the observed shift confirms the possibility of modulating the magnetic response of the suspended MNP by applying a PMF of proper intensity. Moreover, the accuracy of the obtained estimates allows an accurate quantitative prediction of the level of the field scattered by the MNPs in correspondence of the concentrations reachable in the tumor with the available targeting techniques and so of the limits of detectability of a MWI system for the breast cancer diagnosis exploiting MNPs as contrast agent.

IV. CONCLUSION

The results of a broadband characterization of the magnetic properties of a diluted water-based ferrofluid, in presence of an applied PMF, have been presented. The results confirm the possibility of modulating the magnetic response of the suspended MNP by applying a PMF of proper intensity. Moreover, the accuracy of the obtained estimates allows an accurate quantitative prediction of the level of the field scattered by the MNPs in correspondence of the concentrations reachable in the tumor with the available targeting techniques and so of the limits of detectability of a MWI system for the breast cancer diagnosis exploiting MNPs as contrast agent.

REFERENCES

- [1] G. Bellizzi, O.M. Bucci and I. Catapano, "Microwave cancer Imaging exploiting magnetic nanoparticles as contrast agent," *IEEE Transactions on Biomedical Engineering*, vol. 58(9), pp. 2528-2536, Jun. 2011.
- [2] M. Helbig, J. Sachs, F. Tansi and I. Hilger, "Experimental feasibility study of contrast agent enhanced UWB breast imaging by means of M-sequence sensor systems", *Proc. European Conference on Antennas and Propagation*, The Hague, Netherlands, pp. 311-315, 2014.
- [3] G. Bellizzi and O.M. Bucci, "A Novel measurement technique for the broadband characterization of diluted water ferrofluids for biomedical applications", *IEEE Transactions on Magnetics*, vol.49(6), pp. 2903-2912, Dec. 2012.

EXPERIMENTAL VALIDATION OF MAGNETIC NANOPARTICLE ENHANCED MICROWAVE IMAGING OF BREAST CANCER

O. M. Bucci^{(1),(4)}, G. Bellizzi^{(2),(4)}, A. Borgia⁽³⁾, S. Costanzo⁽³⁾, L. Crocco⁽¹⁾,
G. Di Massa⁽³⁾, R. Scapaticci⁽²⁾

⁽¹⁾ IREA, Consiglio Nazionale delle Ricerche, Via Diocleziano 324,
Napoli, Italy

⁽²⁾ DIETI, Università di Napoli Federico II, Via Claudio 21, Napoli,
Italy

⁽³⁾ DIMES, Università della Calabria, Via P. Bucci Edificio 42C,
Rende, Italy

⁽⁴⁾ Consorzio Nazionale Interuniversitario sulle Telecomunicazioni,
Viale G.P. Usberti 181/A, Parma, Italy
bucci@unina.it

Abstract

Magnetic nanoparticles enhanced microwave imaging is a novel technique for the breast cancer diagnostic which exploits magnetic nanoparticles as contrast agent. In this communication we present a laboratory set-up, made of optimized antennas and a simplified, but realistic, phantom of the breast, specifically designed to allow the experimental feasibility assessment of the technique under realistic conditions. The first experimental results of such feasibility assessment are also reported and their validity and meaning discussed.

Index Terms – Breast cancer, magnetic nanoparticles, microwave imaging.

I. INTRODUCTION

Magnetic nanoparticle (MNP)-enhanced microwave imaging (MWI) is an emerging tool for the breast cancer diagnostics that promises to overcome the limitations of the standard MWI approach [1]. This technique exploits MNPs as contrast agent, in order to selectively induce a tunable magnetic contrast in the tumor, and a polarizing magnetic field (PMF) modulation in order to discriminate the MNP response from that of the surrounding tissue, which, being non-magnetic it is not affected by the applied PMF. In such a way, by adopting a proper filtering, one can extract the contribution to the scattered field due to the MNPs in the tumor from the overall measured field.

The numerical assessment of the feasibility of this technique, carried out in realistic conditions [2], has shown that the noise level and dynamic range required to detect the signal due to a concentration of MNP in the tumor comparable to those actually reachable with biochemical targeting, are fully consistent with the performance of today MWI devices. However, an experimental proof-of-concept in realistic conditions, i.e. by dealing with real antennas radiating in the presence of a strong inhomogeneous medium, like the human breast, is

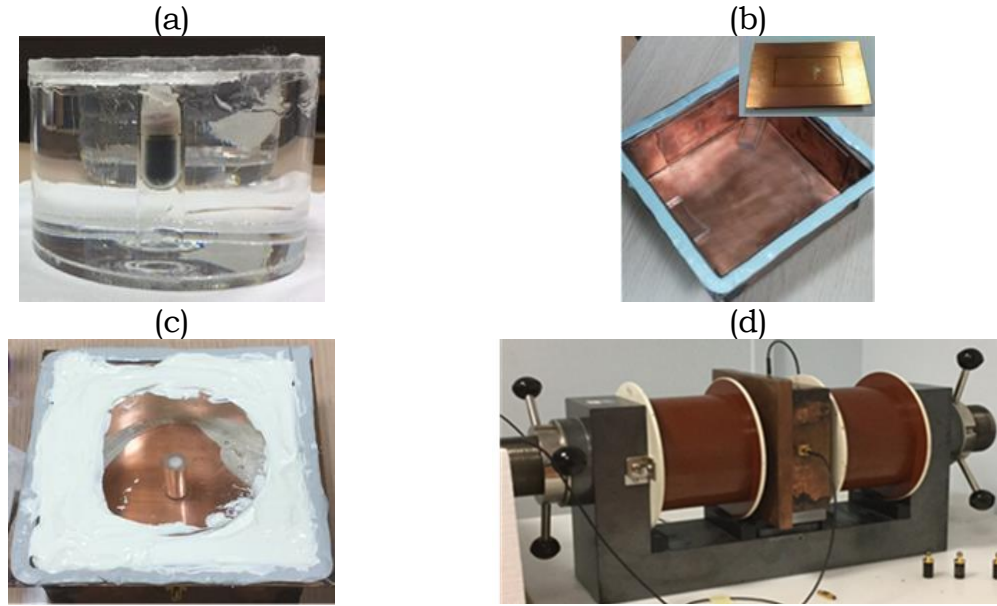


FIG. 1 – Pictures of the laboratory set-up: (a) breast phantom; (b) MWI system; (c) MWI system with matching liquid and phantom; (d) laboratory set-up between the poles of the electromagnet.

mandatory in view of a future clinical assessment of the approach. To this end, we have designed, realized and characterized [3] a first laboratory set-up.

In this communication we present such laboratory setup and report the first experimental results on the feasibility of the proposed MNP-enhanced MWI obtained with the developed system. A discussion of their validity and meaning is also reported.

II. LABORATORY SET UP

The laboratory set up is made of: a MWI system, a phantom mimicking the breast and an electromagnet generating the PMF. The MWI system and phantom only reproduce a “slice” of a realistic device, in order to fit the air gap of the used electromagnet. However, this is accurate enough (from the electromagnetic standpoint) to allow a reliable experimental validation of the approach.

Fig. 1(a) shows the phantom, consisting of two concentric cylinders of plexiglass having radii equal to 10 mm and 60 mm, and high 6.4 mm. The inner cylinder is filled with a mixture of 30% of triton in water, having relative permittivity $\epsilon_r=48$ and conductivity $\sigma=1.5$ S/m, over the band 2 –3 GHz, reproducing the fibroglandular tissue. Inside it, a 1 mL cuvette is positioned, filled with a diluted water suspension of magnetite nanoparticle of 10 nm in size, simulating the targeted tumor. The outer cylinder is filled with pure triton, having $\epsilon_r=5$ and σ between 0.07 and 0.01 S/m, over the range 2–3 GHz, mimicking the adipose tissue.

Fig. 1(b) shows the MWI system consists of a copper box, $16 \times 16 \times 7$ cm in size, allowing the allocation of four antennas on its lateral walls. However, due to the involved symmetry, only two antennas, located on two adjacent sides, have been mounted. The copper box acts as shield from the external interference, thus increasing the system sensitivity, but without impairing the penetration of the PMF (copper is diamagnetic). The antennas are cavity-backed micro-strip slots, specifically designed to exhibit the best radiating behavior over the range 2–3 GHz, in the presence of the adopted matching medium. The laboratory set-up is assembled by fixing the phantom at the center of the copper box and using a sun cream (Coppertone 50+ having $\epsilon_r = 32$ and $\sigma = 0.68$ S/m) as matching medium (Fig. 1(c)). Finally, the box is closed and put between the poles of the electromagnet (Fig. 1(d)).

I. MEASUREMENT SET UP

The measured quantity is the S_{21} parameter, by means of a vector network analyzer (VNA). The operative frequency is 2.32 GHz, i.e. the frequency to which the antennas coupling is maximum ($|S_{21}| = -47$ dB). As PMF modulation, we adopted an “on-off” law, between 160 and 0 kA/m. To switch between these values, the electromagnet requires about 30 s, in order to ensure a smooth, linear, variation of the field during the transition. Assuming the duration of the “on” and “off” states to be equal to the transition time, this leads to the modulation law depicted in Fig. 2(a), with an overall measurement time of 120 s. To minimize the noise, the set IF bandwidth of the VNA is 10 Hz (the narrowest), which allows collecting 1001 point over the measurement time span. In such a way, we get a SNR of -137 dB, which is well below the level of the differential signal, expected to be about -118 dB for a concentration of 15 mg/ML of MNP. As a matter of fact, the main limit of a such on-off modulation is not the noise, but the drift which for a measurement time of 120 s is well below the noise and comparable to the useful signal. In the light of this, in order to assure reliable quantitative results, in this preliminary experiment we adopted a MNP concentration of 40 mg/mL.

II. RESULTS AND DISCUSSION

Fig. 2(b) shows the average of the measured S_{21} parameters, resulting from the on-off PMF modulation, depurated by the linear component of the drift. From the data the following outcomes can be outlined. The minimum detectable concentration depends on the amplitude of the S_{21} fluctuations, whose overall standard deviation is six times smaller than the amplitude of the S_{21} variation. Accordingly, it can be foreseen that MNP concentrations as low as 6 – 7 mg/mL should be detectable.

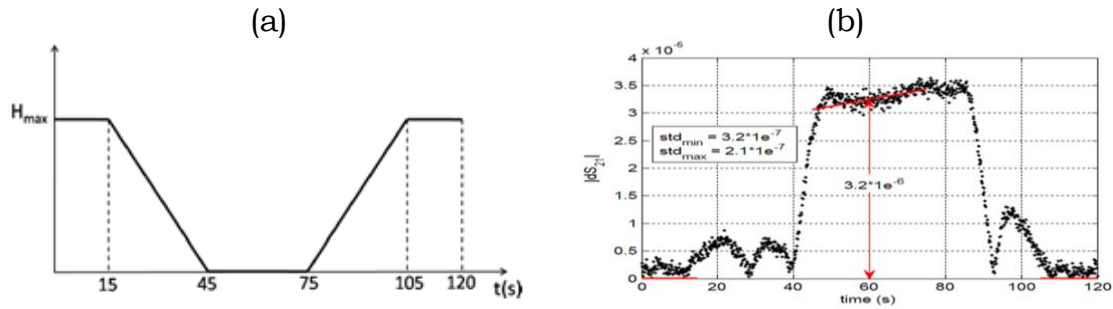


FIG. 2 – (a) On-off PMF modulation; (b) mean differential $|S_{21}|$.

The observed fluctuation of S_{21} are mainly due to the residual drift, which is well above the noise level (up to about ten times above). Hence, it is confirmed that for the adopted PMF modulation the main limitation to the detection capability of the system is the drift. As the drift increases with the measurement time, it can be remarkably reduced by reducing the measurement time or equivalently by adopting a proper PMF modulation, e.g. sinusoidal, with a period much shorter than characteristic time of the drift variation. In such a way, the limit becomes the noise level, which for the designed MWI system is such to allow detecting MNP concentrations as low as 1 mg/mL, well above those achievable with the targeting of the MNP.

The experimental assessment in the case of a sinusoidal PMF modulation is under way. Surprisingly, the first results have highlighted that there is a modulation of the S_{21} also in absence of MNP. This is likely due to the formation of a film of copper oxide in the box, which exhibits ferrimagnetic properties. This inconvenience has been overcome by replacing the copper box with an aluminum box. The results with the new box and a sinusoidal PMF modulation, presented at the conference, show the possibility of effectively detecting MNP concentrations lower than 1 mg/mL.

REFERENCES

- [1] G. Bellizzi, O.M. Bucci, I. Catapano, “Microwave cancer imaging exploiting magnetic nanoparticles as contrast agent”, *IEEE Transactions. On Biomedical Engineering*, vol. 58(9), pp. 2528-2536, 2011
- [2] O. M. Bucci, G. Bellizzi, I. Catapano, L. Crocco and R. Scapaticci, “MNP Enhanced Microwave Breast Cancer Imaging: Measurement Constraints and Achievable Performances”, *IEEE Antennas and Wireless Propagation Letters*, vol.11, pp.1630-1633, 2012
- [3] O. M. Bucci, G. Bellizzi, L. Crocco, R. Scapaticci, G. Di Massa, S. Costanzo, A. Borgia, “Characterization of a Laboratory Set-up for Magnetic Nanoparticle Enhanced Microwave Imaging”, *10th IEEE European Conference on Antennas and Propagation*, Davos, Switzerland, April 2016

A SPECTRAL-DOMAIN METHOD FOR THE ELECTROMAGNETIC SCATTERING FROM A MULTILAYERED SPHERE BURIED IN A STRATIFIED LOSSY MEDIUM

F. Mangini

Enrico Fermi Research Center, Piazza del Viminale 1, 00184, Roma, Italy. Department of Information Engineering, Electronics and Telecommunications, “La Sapienza” University of Rome, Via Eudossiana 18, 00184 Roma, Italy. fabio.mangini@uniroma1.it

Abstract

In this work we present a rigorous method to analyze the electromagnetic scattering of an elliptically polarized plane wave by a multilayered sphere buried in a stratified lossy medium. The interaction of the electromagnetic radiation with the stratified lossy material is assessed by the transfer-matrix approach. The electromagnetic fields are expanded in series of spherical vector harmonics. The transmitted field is scattered by the multi-concentric spheres, and the scattered field interacts again with the stratified material. The scattered-reflected and scattered-transmitted fields by the layered medium are computed by exploiting the plane-wave spectrum of the scattered field, considering the reflection and transmission of each elementary plane wave by the effective interface. The boundary-conditions imposition on the spheres' surfaces leads to a linear system that returns the unknown coefficients.

Index Terms – Electromagnetic scattering, lossy medium, multilayered sphere, spectral-domain method.

I. INTRODUCTION

The problem of the electromagnetic scattering by a sphere placed near a plane interface has been the subject of several studies in the last decades because of its important applications. The solution of the electromagnetic scattering of a plane wave by a sphere on or below a surface has been rigorously obtained in the literature with different methods: by the expansion in spherical vector functions and their plane-wave spectrum to take into account reflection and transmission by the interface [1], by the image theory [2], by a coupled-dipole method [3], or by the Green function approach [4]. In the present work we present a spectral-domain method in order to solve this scenario.

In section 2, the theoretical formulation of the problem is presented in detail. Finally, in Section 3, the conclusions are drawn.

II. THEORETICAL APPROACH

The geometry of the problem is depicted in Fig. 1a. A multilayered sphere is buried in a stratified lossy medium, each layer is characterized by ϵ_j , μ_j , σ_j , and ϵ_{sj} , μ_{sj} , σ_{sj} , i.e. the relative permittivity, relative permeability and the conductivity for the stratified medium and for the spheres, respectively. The impinging monochromatic radiation is an elliptical

plane wave traveling forming an angle ϑ with the z -axis, and the wave-vector projection on the $z = 0$ plane forms an angle φ with the x -axis.

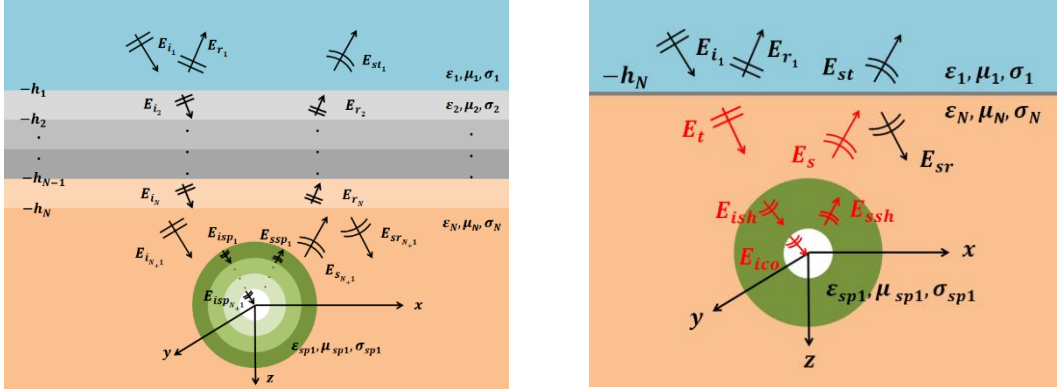


FIG. 1 – a) Geometry of the problem. b) Simplified geometry of the problem.

The incident field can be written as: $E_i(\underline{r}) = (E_{\vartheta_i} \underline{\varrho}_{0i} + E_{\varphi_i} \underline{\varphi}_{0i}) e^{i\mathbf{k}_i \cdot \underline{r}}$ with $\underline{\varrho}_{0i}$, $\underline{\varphi}_{0i}$ and \mathbf{k}_{0i} , are the unit vectors of the reference system. The focus of the problem is to obtain a simplified model of the scenario. The best way is to simplify the geometry model. Using the Transfer Matrix method on the stratified medium, we can simplify the problem as an effective single complex interface; to do that, we can write the transmitted and reflected field through the complex medium, as [4]:

$$\begin{aligned} \underline{E}_r &= (R_H^{1N} E_{\theta_i} \underline{\theta}_{0r} + R_E^{1N} E_{\varphi_i} \underline{\varphi}_{0r}) e^{i\mathbf{k}_r \cdot \underline{r}} e^{-2ih_N k_1 \cos \theta_i} \\ \underline{E}_t &= (T_H^{1N} E_{\theta_i} \underline{\theta}_{0t} + T_E^{1N} E_{\varphi_i} \underline{\varphi}_{0t}) e^{i\mathbf{k}_t \cdot \underline{r}} e^{ih_N (k_N \cos \theta_t - k_1 \cos \theta_i)} \end{aligned} \quad (1)$$

with R_E^{1N} , T_E^{1N} and R_H^{1N} , T_H^{1N} the Fresnel reflection and refraction coefficients for parallel and perpendicular polarizations, respectively, referring to the interface between medium 1 and medium N . The Fresnel coefficients can be obtained from the following formulas [5]:

$$R_E^{1N} = -\frac{M_{21}}{M_{22}}; \quad R_H^{1N} = -\frac{N_{21}}{N_{22}}; \quad T_E^{1N} = -\frac{1}{M_{22}}; \quad T_H^{1N} = -\frac{1}{N_{22}}$$

with M_{ij} and N_{ij} the transfer-matrix elements, defined as follows:

$$\begin{aligned} \begin{pmatrix} E_{\phi_{i_{N+1}}} \\ 0 \end{pmatrix} &= \prod_{j=N}^1 \frac{1}{T_{j,j+1}^E} \begin{bmatrix} e^{i\phi_{j+1}} & -R_{j,j+1}^E e^{i\phi_{j+1}} \\ -R_{j,j+1}^E e^{-i\phi_{j+1}} & e^{-i\phi_{j+1}} \end{bmatrix} \begin{pmatrix} E_{\phi_{i_1}} \\ E_{\phi_{r_1}} \end{pmatrix} = [M]_j \begin{pmatrix} E_{\phi_{i_1}} \\ E_{\phi_{r_1}} \end{pmatrix} \\ \begin{pmatrix} E_{\theta_{i_{N+1}}} \\ 0 \end{pmatrix} &= \prod_{j=N}^1 \frac{1}{T_{j,j+1}^H} \begin{bmatrix} e^{i\phi_{j+1}} & -R_{j,j+1}^H e^{i\phi_{j+1}} \\ -R_{j,j+1}^H e^{-i\phi_{j+1}} & e^{-i\phi_{j+1}} \end{bmatrix} \begin{pmatrix} E_{\theta_{i_1}} \\ E_{\theta_{r_1}} \end{pmatrix} = [N]_j \begin{pmatrix} E_{\theta_{i_1}} \\ E_{\theta_{r_1}} \end{pmatrix} \end{aligned}$$

where $R_{j,j+1}^E$, $R_{j,j+1}^H$, $T_{j,j+1}^E$, $T_{j,j+1}^H$ are the Fresnel coefficients between the j -th layer and the next one. We have to remember that, being in the presence of losses, our incident angle ϑ_i is complex: $\vartheta_i = \vartheta_R + i\vartheta_I$, and we can prove that the angle assumes the following form [6]:

$$\cos \vartheta_R = \frac{k_{R_{N+1}} \beta_{N+1} \cos \xi_{N+1} + k_{I_{N+1}} \alpha_{N+1} \cos \eta_{N+1}}{\sqrt{k_{R_{N+1}}^2 \beta_{N+1}^2 - k_{I_{N+1}}^2 \alpha_{N+1}^2 + 2(k_{R_{N+1}} k_{I_{N+1}})^2}} \quad \text{tg } 2\vartheta_I = \frac{2\beta_{N+1} \alpha_{N+1}}{k_{N+1}^2}$$

The general case of the scattering from a sphere behind an interface, can be treated by the representation of the incident field as a series of regular spherical vector wave functions, as [4]-[6]:

$$\underline{E}_t = \sum_{n=1}^{+\infty} \sum_{m=-n}^n \left[a_{mn} \underline{M}_{mn}^{(1)}(k_N \underline{r}) + b_{mn} \underline{N}_{mn}^{(1)}(k_N \underline{r}) \right]$$

The orthogonality of the vector spherical harmonics implies that the coefficients in the expansion may assume the following form [4]:

$$a_{mn} = (-1)^m i^n \frac{2n+1}{n(n+1)} \frac{(n-m)!}{(n+m)!} e^{ih(k_{N+1} \cos \theta_t - k_i \cos \theta_i)} \left(T_H^{1N} E_{\theta_i} \underline{\theta}_{0t} + T_E^{1N} E_{\phi_i} \underline{\phi}_{0t} \right) \cdot \underline{m}_{mn}^* (\theta_t, \phi_t)$$

$$b_{mn} = (-1)^m i^n \frac{2n+1}{n(n+1)} \frac{(n-m)!}{(n+m)!} e^{ih(k_{N+1} \cos \theta_t - k_i \cos \theta_i)} \left(T_H^{1N} E_{\theta_i} \underline{\theta}_{0t} + T_E^{1N} E_{\phi_i} \underline{\phi}_{0t} \right) \cdot \underline{n}_{mn}^* (\theta_t, \phi_t)$$

Now, before passing to assess the scattered electric field, it turns out to be convenient, similarly to the previous case, to simplify the spherical scenario. To do that it is convenient to use again the Transfer Matrix Approach but in spherical frame. In this case the electric fields inside and outside the sphere can be written as [1]:

$$\underline{E}_s(\underline{r}) = \sum_{n=1}^{+\infty} \sum_{m=-n}^n \left[e_{mn} \underline{M}_{mn}^{(3)}(k_2 \underline{r}) + f_{mn} \underline{N}_{mn}^{(3)}(k_2 \underline{r}) \right]$$

$$\underline{E}_{sp_j}(\underline{r}) = \sum_{n=1}^{+\infty} \sum_{m=-n}^n r_{mn}^i \underline{M}_{mn}^{(1)}(k_j \underline{r}) + s_{mn}^i \underline{N}_{mn}^{(1)}(k_j \underline{r}) + u_{mn}^i \underline{M}_{mn}^{(2)}(k_j \underline{r}) + v_{mn}^i \underline{N}_{mn}^{(2)}(k_j \underline{r})$$

In these expressions the radial functions are the spherical Hankel functions of the first kind. So, applying the transfer spherical matrix [6], we obtain:

$$\begin{pmatrix} r_{mn}^{N+1} \\ 0 \end{pmatrix} = \prod_{j=N}^1 \frac{1}{\zeta_j A_{j,j+1}} \begin{bmatrix} \zeta_j j_n(k_j) y_n'(k_{j+1}) - j_n'(k_j) y_n(k_{j+1}) & \zeta_j y_n(k_j) y_n'(k_{j+1}) - y_n'(k_j) y_n(k_{j+1}) \\ -\zeta_j j_n(k_j) j_n'(k_{j+1}) - j_n'(k_j) j_n(k_{j+1}) & -\zeta_j y_n(k_j) j_n'(k_{j+1}) - y_n'(k_j) j_n(k_{j+1}) \end{bmatrix} \begin{pmatrix} r_{mn}^1 \\ u_{mn}^1 \end{pmatrix}$$

$$\begin{pmatrix} s_{mn}^{N+1} \\ 0 \end{pmatrix} = \prod_{j=N}^1 \frac{1}{\zeta_j A_{j,j+1}} \begin{bmatrix} -\zeta_j j_n'(k_j) y_n(k_{j+1}) - j_n(k_j) y_n'(k_{j+1}) & -\zeta_j y_n'(k_j) y_n(k_{j+1}) - y_n(k_j) y_n'(k_{j+1}) \\ \zeta_j j_n'(k_j) j_n(k_{j+1}) - j_n(k_j) j_n'(k_{j+1}) & \zeta_j y_n'(k_j) j_n(k_{j+1}) - y_n(k_j) j_n'(k_{j+1}) \end{bmatrix} \begin{pmatrix} s_{mn}^1 \\ v_{mn}^1 \end{pmatrix}$$

Now that the scenario is simplified (Fig. 1b) we can apply the Spectral-Domain method to solve the problem. How we can see, in the medium containing the spherical scatterer, we have three fields, the third field is the result of the scattered field reflecting on the surface and striking the particle. It can be described through an expansion of the scattered field in infinite plane waves traveling in various directions (α_i, β_i) , each multiplied by the appropriate Fresnel coefficient [4]:

$$\underline{E}_{sr} = \sum_{n=1}^{+\infty} \sum_{m=-n}^n \frac{i^{-n}}{2\pi} \left\{ e_{mn} \int_0^{2\pi} \int_0^{\pi/2-i\infty} \left[iR_H^{N1} m \frac{P_n^m(\alpha_i)}{\sin \alpha_i} \underline{\alpha}_{0r} - R_E^{N1} \frac{dP_n^m(\alpha_i)}{d\alpha_i} \underline{\beta}_{0r} \right] e^{i(2k_N h \cos \alpha_i + k_r \cdot \underline{r} + m\beta_i)} \sin \alpha_i d\alpha_i d\beta_i + f_{mn} \int_0^{2\pi} \int_0^{\pi/2-i\infty} \left[iR_H^{N1} \frac{dP_n^m(\alpha_i)}{d\alpha_i} \underline{\alpha}_{0r} - R_E^{N1} m \frac{P_n^m(\alpha_i)}{\sin \alpha_i} \underline{\beta}_{0r} \right] e^{i(2k_N h \cos \alpha_i + k_r \cdot \underline{r} + m\beta_i)} \sin \alpha_i d\alpha_i d\beta_i \right\}$$

In particular, the coefficients \underline{E}_{Re}^{mn} and \underline{E}_{Rh}^{mn} are related to the reflection from the $N+1$ -th layer to the first one, obtained again with the transfer-matrix formalism. To determine the coefficients of the superposition, one must

apply the boundary conditions. It is useful to expand each plane wave in spherical harmonics [4]. Finally, an infinite linear system of equations is obtained:

$$\left\{ \begin{array}{l} a_{pq} j_n(k_{n+1}b) + e_{mn} h_n^{(1)}(k_{n+1}b) + g_{mn}^{pq} j_n(k_{n+1}b) - r_{mn} j_n(k_{sh}b) - u_{mn} y_n(k_{sh}b) = 0 \\ b_{pq} j_n'(k_{n+1}b) + f_{mn} h_n^{(1)'}(k_{n+1}b) + h_{mn}^{pq} j_n'(k_{n+1}b) - s_{mn} j_n'(k_{sh}b) - v_{mn} y_n'(k_{sh}b) = 0 \\ a_{pq} k_{n+1} j_n'(k_{n+1}b) + k_{n+1} e_{mn} h_n^{(1)'}(k_{n+1}b) + k_{n+1} g_{mn}^{pq} j_n'(k_{n+1}b) - k_{sh} r_{mn} j_n'(k_{sh}b) - k_{sh} u_{mn} y_n'(k_{sh}b) = 0 \\ b_{pq} k_{n+1} j_n'(k_{n+1}b) + k_{n+1} f_{mn} h_n^{(1)'}(k_{n+1}b) + k_{n+1} h_{mn}^{pq} j_n'(k_{n+1}b) - k_{sh} s_{mn} j_n'(k_{sh}b) - k_{sh} v_{mn} y_n'(k_{sh}b) = 0 \\ \left(\begin{array}{c} r_{mn}^{N+1} \\ 0 \end{array} \right) = \prod_{i=N}^1 [M]_i \left(\begin{array}{c} r_{mn}^1 \\ s_{mn}^1 \end{array} \right); \quad \left(\begin{array}{c} s_{mn}^{N+1} \\ 0 \end{array} \right) = \prod_{i=N}^1 [N]_i \left(\begin{array}{c} s_{mn}^1 \\ v_{mn}^1 \end{array} \right) \end{array} \right.$$

Solving the linear system, we obtain the unknown coefficients of all electric fields.

III. CONCLUSION

A rigorous method to solve the electromagnetic scattering of an elliptically polarized plane wave by a multilayered sphere buried in a lossy stratified medium, is presented. To solve the reflection and transmission problem through the stratified medium and the scattering from the sphere, we have developed the transition-matrix method in a lossy environment. The boundary conditions have been imposed on the surface of the spheres in order to obtain a linear system for the calculation of the unknowns. The generality of the presented method allows its application to several fields of engineering, as detection of buried objects, biomedical sensing problems, metamaterial analysis, and microscopy.

REFERENCES

- [1] G. Videen, "Light scattering from a sphere on or near a surface," *J. Opt. Soc. Am. A*, 8, 483–489 (1991).
- [2] M. A. Taubenblatt and T. K. Tran, "Calculation of light scattering from particles and structures on a surface by the coupled-dipole method," *J. Opt. Soc. Am. A*, 10, 912–919 (1993).
- [3] G. L. Wang and W. C. Chew, "Formal solution to the electromagnetic scattering by buried dielectric and metallic spheres," *Radio Sci.* 39, RS5004 (2004).
- [4] F. Frezza, F. Mangini, L. Pajewski, G. Schettini, and N. Tedeschi, "A spectral-domain method for the electromagnetic scattering by a buried sphere," *J. Opt. Soc. Am. A*, 30, 783–790 (2013).
- [5] F. Frezza, F. Mangini, L. Pajewski, G. Schettini, and N. Tedeschi, "Electromagnetic scattering by two concentric spheres buried in a stratified material," *J. Opt. Soc. Am. A*, 32, 277–286 (2015).
- [6] F. Frezza and F. Mangini, "Electromagnetic scattering of an inhomogeneous elliptically polarized plane wave by a multilayered sphere," *Journal of Electromagnetic Waves and Applications*, DOI: 10.1080/09205071.2015.1121842, (2016).

ANALYSIS OF DB UNIT CELL AND EXTRACTION OF ITS EFFECTIVE CONSTITUTIVE PARAMETERS

M. Khalid, N. Tedeschi and F. Frezza

Department of Information Engineering, Electronics and
Telecommunications, “La Sapienza” University of Rome, Rome, Italy
khwattoo@yahoo.com

Abstract

In the present paper, we numerically analyze the three-dimensional unit-cell structure proposed for the practical realization of the metamaterial, satisfying the DB boundary conditions. Taking into account the anisotropy of the structure, we extract all components of its effective permittivity and permeability both in the axial and orthogonal directions to the metamaterial surface. Numerically calculated reflection and transmission data are used to retrieve the effective constitutive parameters by applying the S-parameters inversion technique recently introduced for a plane wave obliquely incident on a metamaterial slab.

Index Terms – DB boundary conditions, metamaterials, effective parameters, S-parameters inversion method.

I. INTRODUCTION

The DB boundary conditions which enforce cancellation of normal components of the electromagnetic flux densities on the boundary surface ($\hat{n} \cdot \mathbf{D} = 0, \hat{n} \cdot \mathbf{B} = 0$; \hat{n} being the normal unit vector) were introduced in the previous decade and their realization was proposed in terms of a particular anisotropic material with its optic axis perpendicular to the interface [1]. An anisotropic medium, with its principal axes aligned with the Cartesian coordinate system, can be represented by the following permittivity and permeability tensors:

$$\underline{\underline{\varepsilon}} = \varepsilon_x \hat{x}\hat{x} + \varepsilon_y \hat{y}\hat{y} + \varepsilon_z \hat{z}\hat{z} \quad \text{and} \quad \underline{\underline{\mu}} = \mu_x \hat{x}\hat{x} + \mu_y \hat{y}\hat{y} + \mu_z \hat{z}\hat{z} \quad (1)$$

Assuming that the normal direction to the interface is along the z -axis, the DB boundary conditions ($\hat{n} \cdot \mathbf{D} = 0, \hat{n} \cdot \mathbf{B} = 0$) are satisfied when $\varepsilon_z \rightarrow 0$ and $\mu_z \rightarrow 0$. In this situation the components with subscripts x and y are tangential to the interface and it was proposed in [1] that they may have arbitrary values as they do not affect the DB behavior.

Most of the works reported in the literature use a theoretical approach by treating the DB boundary conditions as ideal conditions. However, the first attempt towards their practical realization was presented in [2],[3]. The structure proposed for the realization of DB metamaterial was composed of two split-ring resonators (SRRs) connected by a metallic wire immersed in a dielectric medium, as shown in Fig. 1(a). The authors presented in [2] the numerical results for the components of effective permittivity and permeability but only in one

direction, perpendicular to the plane of SRRs, whereas, as proposed in [1] the other components were supposed as unity, i.e., $\varepsilon_x = \varepsilon_y = \mu_x = \mu_y = 1$.

The DB boundary interface as an angular selective filter shows total reflection to all incident waves with an exception of normal incidence where the interface is totally transparent. It has been shown by Tedeschi *et al.* [4] that the DB behavior does depend on the tangential components of the constitutive parameters of the metamaterial emulating the DB boundary and if the tangential components are properly chosen, the DB medium can behave as an electromagnetic absorbing medium for all incidence angles. Therefore, knowledge of explicit values of all components of the effective permittivity and permeability is necessary for a better characterization of the DB metamaterial.

In this paper, a free-space numerical simulation analysis of the three-dimensional unit-cell structure is presented. All components of the effective permittivity and permeability tensors of the unit inclusion are extracted by using the S-parameter inversion method.

II. PROBLEM FORMULATION

S-parameters extraction method, initially introduced in [9] for normal incidence, has become the most commonly used parameters extraction technique. This method has been very recently extended for oblique incidence case which enables extraction of all components of the effective constitutive parameters from the reflection and transmission coefficients for an anisotropic metamaterial slab [5].

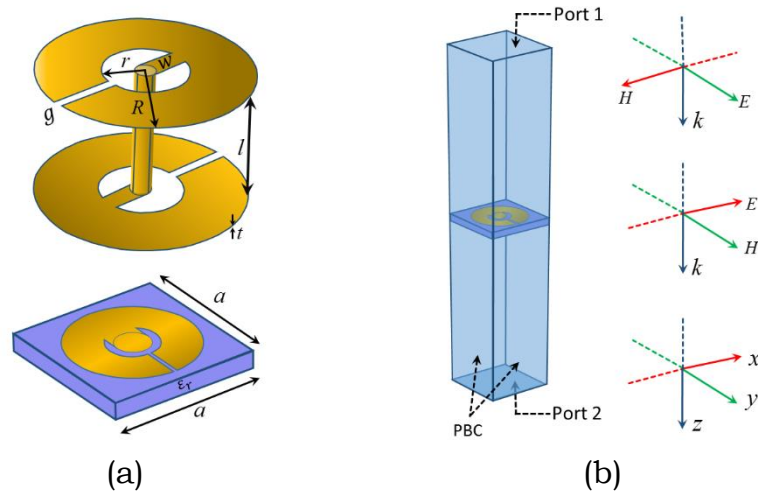


FIG. 1 – (a) DB unit-cell immersed in a dielectric medium (b) simulation setup.

We have used a commercial software Comsol Multiphysics to evaluate the reflection and transmission data used in parameter retrieval process. The unit-cell structure immersed in a dielectric medium with $\varepsilon_r = 2.6$ is placed in a rectangular parallelepiped, as shown in Fig. 1. The dimensions of the unit cell are (in mm): $R = 2.5, r = 1, l = d = 0.7, w = 1.4, g = 0.15, a = 6$ and $t = 0.017$. Periodic boundary conditions (PBC) are applied on the side walls of the parallelepiped which emulate the case as

the space in the x - and y -directions was infinitely extended. The wave is incident from the Port 1 and propagates in the positive z -direction. By considering the xz -plane as the plane of incidence, four complex value measurements at Port 1 for reflection coefficients and four complex values measurements at Port 2 for transmission coefficients at one normal and one oblique incidence for two orthogonal polarizations were taken to calculate the effective constitutive parameters.

III. NUMERICAL RESULTS

The effective constitutive parameters evaluated from the reflection and

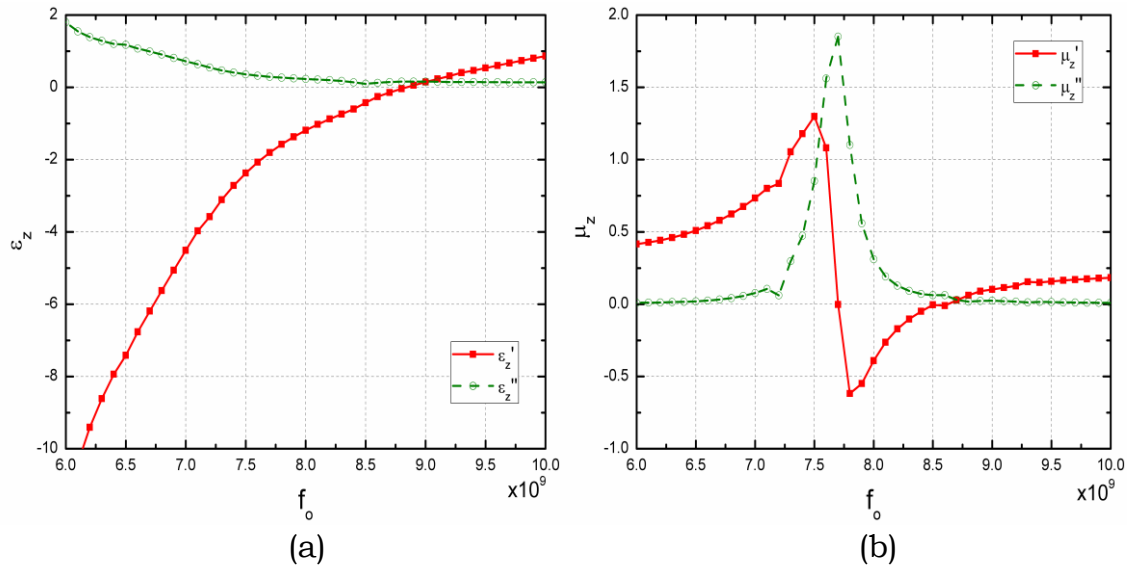


FIG. 2 – Components of effective (a) permittivity and (b) permeability in the normal direction to the metamaterial interface.

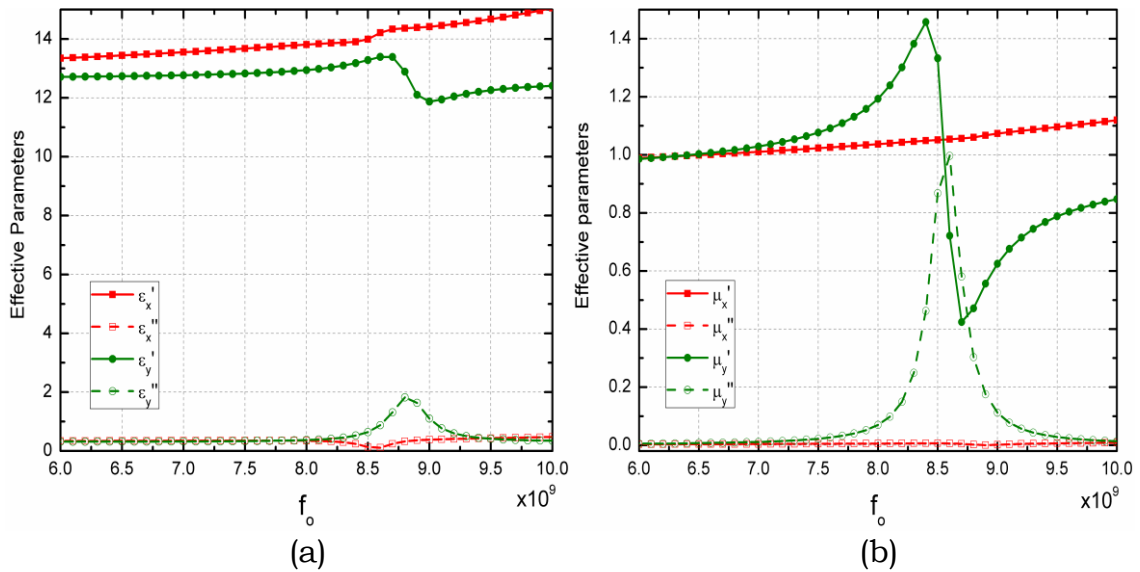


FIG. 3 – Components of effective (a) permittivity and (b) permeability in the tangential directions to the metamaterial interface.

transmission coefficients are shown in Figs. 2 and 3. The components perpendicular to the metamaterial interface, depicted in Fig. 2, simultaneously approach zero around the frequency of 8.86 GHz. It can be seen from Fig. 3 that the tangential components are different from unity. Further, we noticed that the normal components in Fig. 2 do not correspond to those presented in [2]. This discrepancy was resolved after several simulation iterations by taking different directions of excitation. We found that results similar to those presented in [2] for the permittivity and permeability curves can be achieved when the unit-cell structure is excited in such a way that the propagation vector lies along the x -axis, see Fig. 1.

IV. CONCLUSION

Simulation results for the effective parameters of the metamaterial unit cell proposed for the realization of DB boundary conditions are presented. All components of the effective permittivity and permeability tensors of the structure are extracted by using the S-parameters inversion method for obliquely incident wave. The results show that for the proposed structure the tangential components of the effective parameters cannot be simply assumed as unity. Moreover, depending upon the direction of the wave vector, the structure shows different behaviors. It means that the proposed DB unit-cell is not truly a biaxial material but can also be spatially dispersive. Further research must be carried out on the metamaterial inclusion to analyze the effects of spatial dispersion and bi-anisotropy in order to effectively mimic the DB behavior.

REFERENCES

- [1] I. V. Lindell and A. H. Sihvola, "Electromagnetic boundary and its realization with anisotropic metamaterial," *Phys. Rev. E*, vol. 79(026604), pp. 1-7, 2009.
- [2] D. Zaluski, D. Muha, and S. Hrabar, "Experimental verification of metamaterial-based DB unit cell," *Proc. ELMAR-2012, Zadar, Croatia, 2012*, pp. 321-324.
- [3] D. Zaluski, S. Hrabar, and D. Muha, "Practical realization of DB metasurface," *Appl. Phys. Lett.*, vol. 104(234106), pp. 1-5, 2014.
- [4] N. Tedeschi, F. Frezza, and A. Sihvola, "On the perfectly matched layer and the DB boundary conditions," *J. Opt. Soc. Am. A*, vol. 30(10), pp. 1941-1946, 2013.
- [5] D. R. Smith, S. Schultz, P. Markos, and C. M. Soukoulis, "Determination of effective permittivity and permeability of metamaterials from reflection and transmission coefficients," *Phys. Rev. B*, vol. 65(195104), pp. 1-5, 2002.
- [6] D. Cohen and R. Shavit, "Bi-anisotropic metamaterials effective constitutive parameters extraction using oblique incidence S-parameters method," *IEEE Trans. Antennas and Propag.*, vol. 63(5), pp. 2071-2078, May 2015.

ELECTROMAGNETIC INTERACTION WITH A MISALIGNED BROKEN PIPE

P.P. Di Gregorio⁽¹⁾, V. Ferrara⁽¹⁾, F. Frezza⁽¹⁾ F. Mangini^(1,2) and M. Muzi⁽¹⁾

⁽¹⁾ Department of Information Engineering, Electronics and Telecommunications, “La Sapienza” University of Rome, Via Eudossiana 18, 00184 Roma, Italy

⁽²⁾ Enrico Fermi Research Center, Piazza Viminale 1, 00184, Roma, Italy

pietropaolo.digregorio@uniroma1.it

Abstract

In this work a numerical study on the effects that can be observed in the electromagnetic scattering on a plane wave due to the presence of a misaligned broken pipe buried in a half-space occupied by cement, is presented. We consider a circularly polarized plane wave impinging normally to the air-cement interface. To perform the study, a commercially available simulator based on the Finite Element Method, is adopted. The three components of the scattered electric field along a line just above the interface between the two media, are monitored. The model, by considering different distances between the longitudinal axis of the tubes in two cases (PVC and metallic material), is studied.

Index Terms – Electromagnetic interaction, broken buried pipe, GPR.

I. INTRODUCTION

In this work we present a numerical study of the effects that can be observed in the electromagnetic scattering of a plane wave due to the presence of a misaligned broken pipe buried in a half-space occupied by cement in the civil-engineering field.

The pipe, supposed to be used for water conveyance, is modeled as a cylindrical shell made of metallic or poly-vinyl chloride (PVC) material. We consider the longitudinal axis of the pipe running parallel to the air-cement interface. We suppose, after the break of the pipe, that the longitudinal axes of the two pipes shift on a parallel plane with respect to the separation interface, moving away in opposite directions.

We consider that a circularly polarized plane wave impinging normally to the interface between air and the previously mentioned medium excites the structure, in order to determine the most useful in terms of scattered-field sensitivity. To perform the study, a commercially available simulator based on the Finite Element Method (FEM) was adopted. A preliminary frequency sweep allows us to choose the most suitable operating frequency depending on the dimensions of the commercial pipe cross-section. We monitor the three components of the scattered electric field along a line just above the interface between the two media. The electromagnetic properties of the materials employed in this study are present in the literature. We study the

model by considering different distances between the longitudinal axes of the tubes in two cases: PVC and metallic material. One of the practical applications of this study in the field of Civil Engineering may be the use of ground penetrating radar (GPR) techniques to monitor the status of a buried pipe without the need to intervene destructively in the structure [1]-[3].

In the second Section the statement of the problem is described. In the third Section the numerical simulations and some results are reported. Finally, the conclusions are drawn.

II. STATEMENT OF THE PROBLEM

As stated above, in Fig. 1, the geometry of the problem taken into consideration is depicted. The half-space on top is composed of air, the other one instead is occupied by a medium supposed to be cement. The relative dielectric permittivities are $\epsilon_{air}=1$, $\epsilon_{cem}=5.241$. The cylinder, of radius $R_{cyl}=12.5$ cm is buried at a distance $d=3R_{cyl}$, with respect to the interface between the two media. The study is performed considered tubes in two cases: PVC ($\epsilon_{pvc}=3.1$) and metallic material.

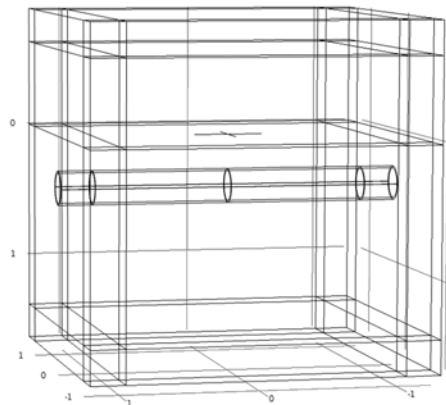


FIG. 1 – Geometry of the problem.

The impinging radiation is a plane wave circularly polarized along z , incoming from the air half-space. The field probe, instead, is positioned on the air-cement interface (see the cross in Fig. 1). The incident wave is considered for frequencies from 100 MHz to 1000 MHz and a sweep of the radius of the tubes in two cases, PVC and metallic material, is performed.

III. NUMERICAL SIMULATIONS AND RESULTS

For this study, the RF module of the commercially available simulation software COMSOL Multiphysics has been adopted. The software has proven to be very reliable for the solution of this kind of problems. A thorough investigation on the validity of the models constructed in COMSOL has been performed by our group in [4]. Plotting the sum of the scattered electric field components as a function of the distance

between the longitudinal axes of the tubes (see Fig. 2), the maximum variation of the scattered field occurs at 400 MHz in both cases: PVC and metallic pipe. The most important difference we note is the non-linearity in the PVC case, most likely due to the resonance phenomena of the PVC layers, while the metallic cylinder can be considered with good approximation, from an electromagnetic point of view, as a full PEC pipe.

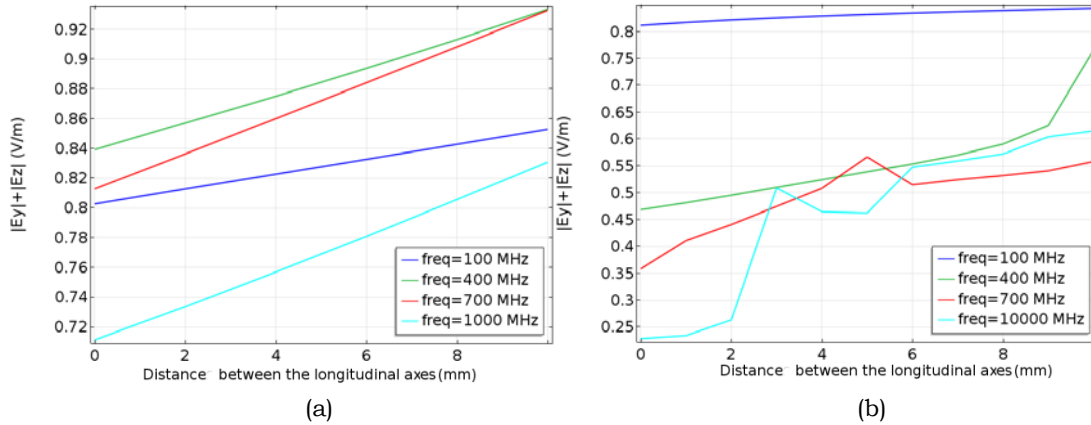


FIG. 2 – Sum of the absolute values of the scattered electric field components as a function of the distance between the longitudinal axes of the tubes in two cases: a) Metallic pipe; b) PVC pipe.

We have also studied the scattered electric field as a function of the radius pipe on a point on the air-cement interface centered in the origin of the reference system. As we can see from Fig. 3, changing the tube's radius, we note that the scattered field is still a good indicator of the breaking of a pipe: in particular, we note an increasing trend and monotone in the case of the metallic tube.

I. CONCLUSION

In this work, we show that the field scattered from a misaligned broken pipe depends of the distances between the longitudinal axes of the pipes. From the results we can affirm that it is possible to determine with the electromagnetic interaction the stage of separation of the two sub-pipes using the sum of the absolute values of the scattered electric field component. Future works will take into account the analytical relationship between the scattered field and the relative position of the two half pipes.

ACKNOWLEDGEMENT

This work is a contribution to COST Action TU1208 "Civil Engineering Applications of Ground Penetrating Radar".

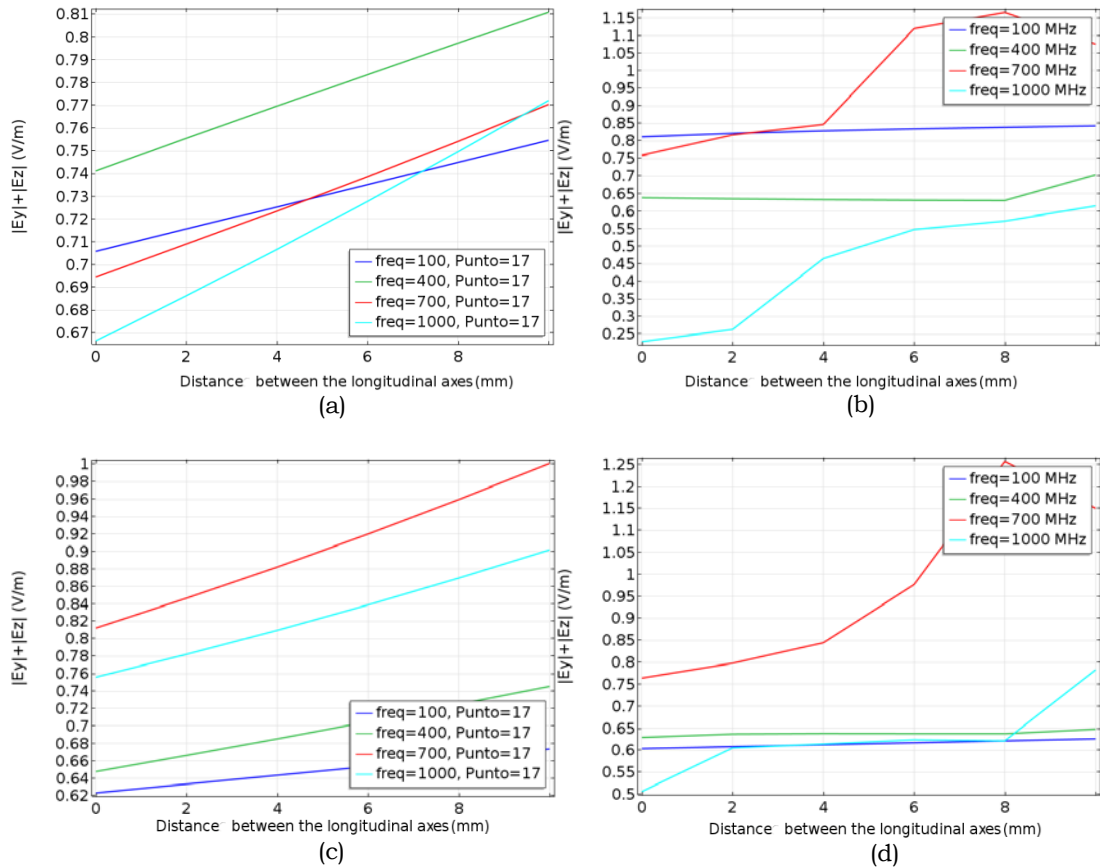


FIG. 3 – Sum of the absolute values of the scattered electric field components as a function of the distance between the longitudinal axes of the tubes in two cases: a) Metallic pipe with 10 cm of radius; b) PVC pipe with 10 cm of radius; c) Metallic pipe with 7.5 cm of radius; d) PVC pipe with 7.5 cm of radius.

REFERENCES

- [1] F. Frezza, F. Mangini, E. Stoja, and N. Tedeschi, “Effects on the Electromagnetic Scattering of a Plane Wave due to the Surface Roughness of a Buried Perfectly Conducting Pipeline”, *Geophysical Research Abstracts*, Vol. 15, EGU2013, Vienna, Austria, April 2013 (EGU2013-12059).
- [2] F. Frezza, F. Mangini, E. Stoja, and N. Tedeschi, “Fouling detection in buried water pipelines by observation of the scattered electromagnetic field,” *Geophysical Research Abstracts*, Vol. 16, EGU2014, Vienna, Austria, 2014 (EGU2014-13008-1).
- [3] P.P. Di Gregorio, F. Frezza, F. Mangini, M. Muzi, and N. Tedeschi, “Detection of Two Buried Cross Pipelines by Observation of the Scattered Electromagnetic Field,” *Geophysical Research Abstracts*, Vol. 17, EGU2015, Vienna, Austria, 2015. (EGU2015-13008-1).
- [4] F. Frezza, F. Mangini, M. Muzi, P. Nocito, E. Stoja, and N. Tedeschi, “Numerical Study of the Scattering of a Short-Pulse Plane Wave by a Buried Sphere in a Lossy Medium,” *Proceedings of the 2012 COMSOL Conference*, Milan, 2012.

RECONFIGURABLE FABRY-PEROT CAVITY LEAKY-WAVE ANTENNAS BASED ON NEMATIC LIQUID CRYSTALS FOR THz APPLICATIONS

W. Fuscaldo^{(1),(2)}, S. Tofani^{(1),(3)}, P. Burghignoli⁽¹⁾, P. Baccarelli⁽¹⁾,
D. C. Zografopoulos⁽³⁾, R. Beccherelli⁽³⁾, and A. Galli⁽¹⁾

⁽¹⁾ Department of Information Engineering, Electronics and
Telecommunications (DIET), “Sapienza” University of Rome,
Via Eudossiana 18, 00184, Rome, Italy
fuscaldo@diet.uniroma1.it

⁽²⁾ Institut d’Électronique et de Télécommunications de Rennes,
UMR CNRS 6164, Université de Rennes 1, 35700, Rennes, France

⁽³⁾ Institute for Microelectronics and Microsystems (CNR-IMM),
National Research Council, 00133, Rome, Italy

Abstract

In this work we analyze the tunable properties of a Fabry-Perot cavity leaky-wave antenna based on nematic liquid crystals (NLCs). The possibility of dynamically tuning the permittivity of an NLC layer through the application of a low driving voltage is exploited in order to affect the propagation constant of the TM fundamental leaky mode supported by the planar structure. A suitable configuration is analyzed in the low-THz range. Numerical results confirm the reconfigurability of the proposed devices, making them potentially very attractive for THz applications.

Index Terms – Liquid crystals, Fabry-Perot cavities, leaky waves, terahertz.

I. INTRODUCTION

It is well known that highly directive radiation patterns can easily be produced by a simple (e.g., dipole-like) source embedded in a grounded dielectric layer, when multiple layers of alternating thicknesses and materials (as in Fabry-Perot cavities) are stacked above a ground plane [1]. Such devices exhibit a frequency-scanning behavior (i.e., the steering of the main beam as the operating frequency is changing) due to the leaky-wave radiation mechanism that dominates the aperture field and, as a consequence, the far-field pattern. However, in most of microwave applications, it is of interest to achieve beam steering at fixed frequency. To this aim, different solutions have been proposed over the years (see, e.g., [2] and Refs. therein).

In this context, we present the analysis of a Fabry-Perot cavity leaky-wave antenna (FPC-LWA) based on *nematic liquid crystals* (NLCs). The well-known reconfigurable properties of NLCs [3] are exploited in order to efficiently affect the propagation constant of the fundamental leaky mode and, consequently, the radiation properties of the proposed device. In particular, our structure consists here of a multilayered stack of alternating dielectric layers, placed above a grounded dielectric slab. The

alternation of a tunable low-permittivity layer (here represented by the NLC layer) and a high-permittivity layer (HPL), with thicknesses fixed at odd multiples of a quarter wavelength in their respective media, produces a ‘resonance condition,’ which allows for obtaining a narrow radiated beam at broadside [1]. Then, the application of a common bias voltage to the NLC layer allows for changing the resonance condition and thus the propagation constant of the fundamental leaky modes, with consequent beam steering capability.

By developing a suitable circuit model for the dispersive analysis of planar structures in the presence of anisotropic layers, this work investigates the properties of such a reconfigurable antenna employing NLCs for THz applications. In Sec. II, a generalized transmission-line model of the structure is presented, which includes also the characterization of the anisotropy of the NLC permittivity. In Sec. III, basic numerical results are shown for a FPC-LWA operating around 1 THz, which emphasize the promising features of the proposed configuration. Conclusions are finally drawn in Sec. IV.

II. TRANSMISSION-LINE MODEL OF A FPC-LWA WITH NLC LAYERS

In this section, first we get a general expression for the dispersion equation of the layered structure depicted in Fig. 1. The dispersion equation can readily be obtained by imposing the resonance condition of the transverse equivalent network (TEN). As is known, this transverse resonance condition states that the sum of the input admittances looking upwards Y_{up} and downwards Y_{dw} at any cross section of yz plane (see Fig. 1) must equal zero. When N layers are placed above the grounded slab, Y_{up} and Y_{dw} at the section $x = h_0$, where h_0 is the thickness of the slab, assume the following expressions

$$Y_{\text{dw}} = -jY_0 \cot(k_{x,0}h_0) \quad (1)$$

$$Y_{\text{up}} = Y_{\text{in},1}, \quad Y_{\text{in},i} = Y_i \frac{Y_{\text{in},i+1} \cos(k_{x,i}h_i) + jY_i \sin(k_{x,i}h_i)}{Y_i \cos(k_{x,i}h_i) + jY_{\text{in},i+1} \sin(k_{x,i}h_i)}, \quad \text{for } i = 1, 2, \dots, N \quad (2)$$

where Y_i , $k_{x,i} = \sqrt{k_0^2 \varepsilon_{ri} - k_z^2}$, and h_i are the characteristic admittances, transverse wavenumbers, and thicknesses of the i -th layer ($i = 0$ indicates the slab), respectively, and $Y_{\text{in},i}$ are the input admittances looking upwards at the beginning of the i -th layer (note that $Y_{\text{in},i}$ are calculated recursively from $Y_{\text{in},N+1}$, that is equal to the characteristic admittance of air). In particular, the dispersion curves of the fundamental *TE* and *TM leaky modes* can be found by numerically searching for the *improper complex roots* of the dispersion equation.

In the following, we derive the expressions of the characteristic admittances of the NLC anisotropic layer for both *TM* and *TE* polarizations, in order to show that only the *TM* modes are affected by the application of a bias voltage to the NLC layer.

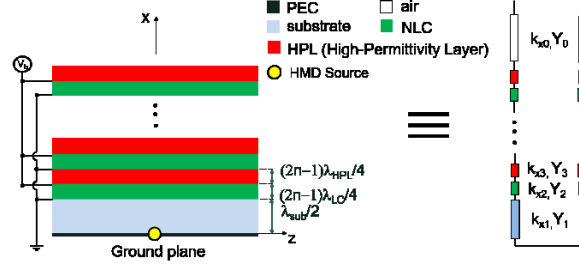


FIG. 1 – 2D-section view of the proposed FPC-LWA and its equivalent transmission-line representation. The NLC layers are polarized by means of a bias voltage applied to a pair of extremely thin conductive polymers.

The NLC material considered here is the high- Δn mixture 1825 [3], which is a uniaxial crystal described by a diagonal tensor permittivity, with ordinary and extraordinary relative permittivities equal to $\varepsilon_o = 2.42 - j0.05$ and $\varepsilon_e = 3.76 - j0.08$, respectively. As is shown in [3], in the absence of bias, the LC molecules are aligned along z -axis (Fig. 1), i.e., $\varepsilon_{xx} = \varepsilon_o$, $\varepsilon_{yy} = \varepsilon_o$, $\varepsilon_{zz} = \varepsilon_e$, whereas when a low driving voltage V_b (an electric field of about $0.7 \text{ V}/\mu\text{m}$) is applied, the LC molecules reorient along x -axis, i.e., $\varepsilon_{xx} = \varepsilon_e$, $\varepsilon_{yy} = \varepsilon_o$, $\varepsilon_{zz} = \varepsilon_o$. As a consequence, the characteristic admittances and the normal wavenumbers of the NLC layers in Eqs. (1) and (2) must take into account both the anisotropy of the material and its dependence on the bias voltage. To this aim, starting from Maxwell's equations, we have calculated the transmission-line secondary constants of a NLC for both TE and TM case (the structure is invariant with respect to the y -axis)

$$Y_0^{\text{TM}} = (\omega\varepsilon_0\varepsilon_{zz}) / k_x^{\text{TM}} \quad k_x^{\text{TM}} = \sqrt{(\varepsilon_{zz} / \varepsilon_{xx})(k_0^2\varepsilon_{xx} - k_z^2)} \quad (3)$$

$$Y_0^{\text{TE}} = k_x^{\text{TE}} / (\omega\mu_0) \quad k_x^{\text{TE}} = \sqrt{(k_0^2\varepsilon_{yy} - k_z^2)} \quad (4)$$

As is clear from Eqs. (3) and (4), the TE modes are not affected by the bias, since $\varepsilon_{yy} = \varepsilon_o$ regardless of V_b . Thus, in the following section, only the dispersion curve of the fundamental TM leaky mode will be reported for different values of V_b .

III. NUMERICAL RESULTS

The dispersion curves of the fundamental TM leaky mode have been calculated for the structure depicted in Fig. 1 considering an operating frequency $f = 1 \text{ THz}$. In the present design, $N = 7$ alternating layers of NLC and alumina ($\varepsilon_r = 9$) of thicknesses $h_1 = 48 \mu\text{m}$ and $h_2 = 125 \mu\text{m}$ have been considered. It is worth noting that these thicknesses are given by formulas in Fig. 1 for the choice of $n = 3$ in order to reduce the fabrication complexity of the multilayered stack.

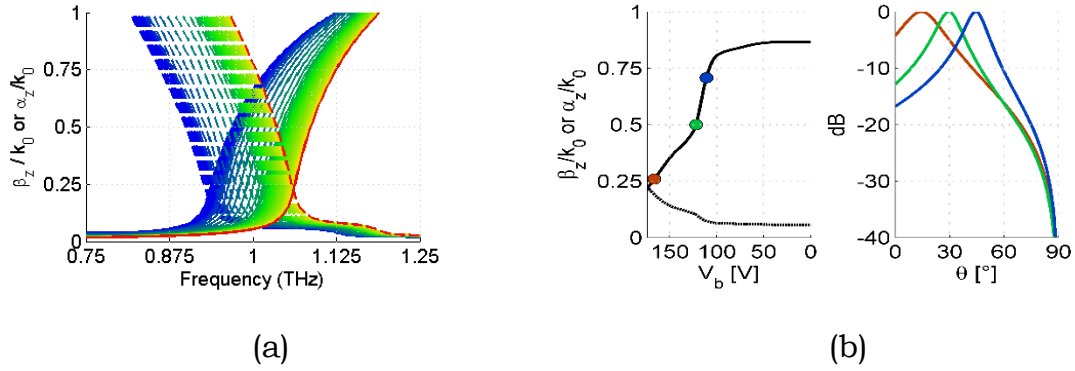


FIG. 2 – (a) Dispersion curves of the TM leaky mode β_z/k_0 vs. f (solid lines) and α_z/k_0 vs. f (dashed lines). Color shades from blue to red as V_b varies from 0 to 174 V. (b) Dispersion curves of the TM leaky mode β_z/k_0 vs. V_b and α_z/k_0 vs. V_b and related radiation patterns calculated for different pointing angles (colored dots indicate the corresponding points on the dispersion curves).

The substrate layer is made of Zeonor, a low-loss polymer ($\epsilon_r = 2.3$), of thickness $h_0 = 98 \mu\text{m}$. This dielectric slab is backmetallized with a 200 nm layer of gold, along which a slot is etched and backilluminated by a coherent THz source, such as a quantum cascade laser (QCL) beam.

In Fig. 2(a) the normalized complex propagation constant of the TM leaky mode is shown in the range 0.75-1.25 THz, for applied voltages V_b ranging from 0 V (blue lines) to 174 V (red lines). In Fig. 2(b), the variation of the propagation constant with the applied voltage is shown for the fixed frequency $f = 1.06$ THz (corresponding to the leaky-wave cutoff condition $\beta_z \cong \alpha_z$ for $V_b = 174$ V). The radiation patterns for pointing angles $\theta_p = 15^\circ, 30^\circ, 45^\circ$ are also calculated by means of LWA theory [1].

IV. CONCLUSION

A promising tunable THz FPC-LWA based on NLCs has been presented. Beam steering at fixed frequency has been shown as a function of a bias voltage, exhibiting radiation patterns with slowly-varying beamwidth.

REFERENCES

- [1] D. R. Jackson, A. A. Oliner, and A. Ip, "Leaky-wave propagation and radiation for a narrow-beam multiple-layer dielectric structure," *IEEE Trans. Antennas Propag.*, vol. 41(3), pp. 344-348, Mar. 1993.
- [2] G. Lovat, P. Burghignoli, and S. Celozzi, "A tunable ferroelectric antenna for fixed-frequency scanning applications," *IEEE Antennas Wireless Propag. Lett.*, vol. 5, pp. 353-356, Aug. 2005.
- [3] D. C. Zografopoulos and R. Beccherelli, "Tunable terahertz fishnet metamaterials based on thin nematic liquid crystal layers for fast switching," *Sci. Rep.*, vol. 5, 13137, Aug. 2015.

Cellular volume fraction estimation through complex dielectric permittivity measurement and Monte Carlo algorithm

F. Mangini⁽¹⁾, M. Muzi^(1,*), N. Tedeschi⁽¹⁾

⁽¹⁾ Dept. of Information Engineering, Electronics and Telecommunications, “La Sapienza” University of Rome, Via Eudossiana 18, 00184, Rome, Italy

^(1,*)marco.muzi@uniroma1.it

Abstract

In this paper a new method for the cellular volume fraction estimation is presented. It is based on the measurement of the complex dielectric permittivity of a cell suspension and the extrapolation of the cellular volume fraction through the interpolation of the parameters of the effective medium approximation model with a Monte Carlo algorithm. The method is tested both with simulations and with real data from different alumina and yeast cells in physiological solution suspensions with known volume fractions. The obtained results demonstrate a good capability to discriminate the alumina and yeast cell volume fraction also for high values of dilution.

Index Terms – cellular volume fraction, complex conductivity measurements, Monte Carlo methods.

I. INTRODUCTION

In this work is shown how is possible to estimate the cellular volume fraction (CVF) of a liquid culture making use of effective dielectric permittivity homogenization models and Monte Carlo algorithm.

Thanks to the effective medium approximation model of biological tissues [1], is possible to predict their dielectric behavior from the knowledge of the shape, dimensions, dielectric permittivity of the cell parts, CVF occupied by the cells and the working frequency.

It is possible to estimate the cellular CVF using dielectric spectroscopy as suggested in [2], especially in the monoculture cases. The weak point of this kind of techniques is the necessity of the dielectric permittivity pre-calibration with a sample of culture with known CVF [3].

Many authors [4-5] make use of simplified cellular dielectric behavior model where cells are assumed to be simple impedances characterized during the calibration procedure. A further achievement may be done in both geometric and dielectric behavior cellular characterization [6].

A first attempt to estimate CVF and other information from the measurement of the complex permittivity of a cell culture is reported in [7] where is presented an example of CVF and shell and core cell permittivity estimation by the algorithm presented in [8]. Such kind of approach presents the limit that it is supposed to know the complex

permittivity of the growth medium, cellular geometrical dimension and cellular membrane thickness.

In this paper we propose a Monte Carlo method able to overcome the mentioned limitation and produce an accurate estimation of the CVF.

II. METHODS

The purpose of the algorithm described in Fig.1 is to find the point of minimum of the following cost functional:

$$F(\Phi, \varepsilon_1^*, \varepsilon_2^*, \varepsilon_s^*, \nu, d, a, b, c)_0 = \min_{(\Phi, \varepsilon_1^*, \varepsilon_2^*, \varepsilon_s^*, \nu, d, a, b, c)} \|\hat{\varepsilon}_{meas}^* - \hat{\varepsilon}_{est}^*(\Phi, \varepsilon_1^*, \varepsilon_2^*, \varepsilon_s^*, \nu, d, a, b, c)\|_\infty \quad (1)$$

with $(\Phi, \varepsilon_1^*, \varepsilon_2^*, \varepsilon_s^*, \nu, d, a, b, c)_0$ to indicate the cost functional F minimum point and $\hat{\varepsilon}_{est}^*(\Phi, \varepsilon_1^*, \varepsilon_2^*, \varepsilon_s^*, \nu, d, a, b, c)$ is obtained from [1]:

$$\hat{\varepsilon}_{est}^*(\Phi, \varepsilon_1^*, \varepsilon_2^*, \varepsilon_s^*, \nu, d, a, b, c) = \hat{\varepsilon}^* = \varepsilon_1^* \left[1 + \frac{1}{3} \Phi \sum_{i=x,y,z} \frac{\hat{\varepsilon}_2^i - \varepsilon_1^*}{\varepsilon_1^* + (\hat{\varepsilon}_2^i - \varepsilon_1^*) L_{i,out}} \right] \quad (2)$$

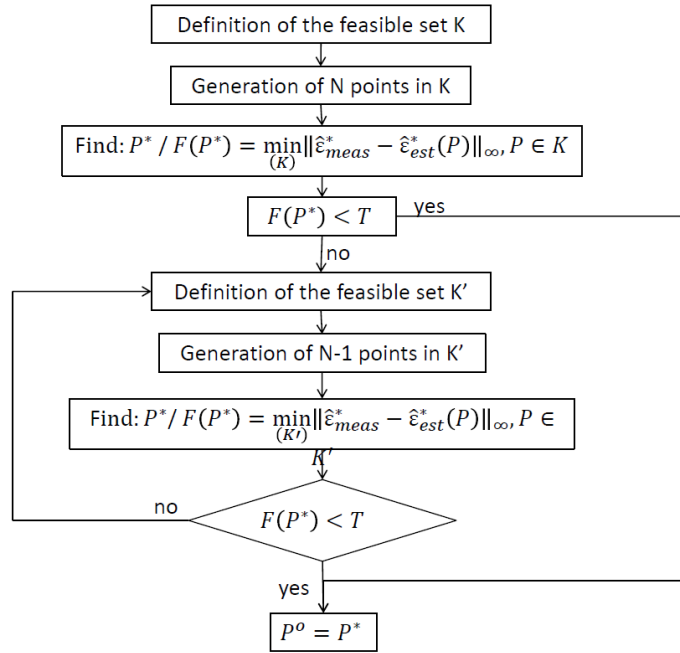


Fig.1. Flux diagram of the proposed algorithm.

The minimum point is obtained by the following steps:

- Definition of the admissibility range for the model parameters $(\Phi, \varepsilon_1^*, \varepsilon_2^*, \varepsilon_s^*, \nu, d, a, b, c)$;
- Generation of the set K containing N random admissible points;
- While the magnitude of the functional is greater than the threshold value:

- Locating the local minimum point such that the minimum value of (1) is obtained.
- Convergence check:
 - Convergence reached: the local minimum P^* point is the minimum point P° .
 - Stop iterations.
 - Convergence unreached: creation of the set K' of N elements such that one of them is the local minimum and the others lie on its neighborhood.
 - Passage to the next iteration.

Regarding the average performances of the algorithm, it converges in 0.02 s after 2 iterations considering a frequency sampling of the spectrum of 50 points and a dimension of K and K' of 700 elements.

III. RESULTS

The proposed algorithm is tested by simulations (results shown in Tab. I) and verified by measurements of alumina and yeast cells suspended in standard physiological solution with different volume fractions (results shown in Tabs. II-III)

TABLE I – DISTRIBUTION OF THE RELATIVE ESTIMATION ERROR OF THE CVF BY SIMULATIONS

Lower limit	First quartile	Second quartile	Third quartile	Upper limit
$2.5e^{-7}$	$6e^{-3}$	$1.4e^{-2}$	$3.2e^{-2}$	$7e^{-2}$

TABLE II – ESTIMATION OF THE CVF OF ALUMINA SUSPENSIONS

CVF Nominal Value	CVF Estimated Value
0.04 ± 0.01	0.03 ± 0.01
0.08 ± 0.02	0.09 ± 0.01
0.20 ± 0.04	0.22 ± 0.01

TABLE III – ESTIMATION OF THE CVF OF YEAST CELL SUSPENSIONS

CVF Nominal Value	CVF Estimated Value
0.01 ± 0.01	0.01 ± 0.01
0.04 ± 0.01	0.04 ± 0.01

IV. CONCLUSION

In this paper the CVF of a cell suspension is obtained from the complex permittivity measurement and a Monte Carlo algorithm. As shown by the results presented in Tabs. I-III, there is a very good accordance between the expected accuracy obtained by the simulations and the actual accuracy found in the CVF estimation of real suspension.

ACKNOWLEDGEMENT

This work is part of the research project: Assessment techniques of three-dimensional (3D) cell growth and morphology in microgravity using electromagnetic diffraction, realized through the Italian Space Agency (ASI) co-financing.

REFERENCES

- [1] K. Asami, "Characterization of heterogeneous systems by dielectric spectroscopy," *Progress in Polymer Science*, vol. 27(8), 1617-1659, 2002.
- [2] C. M. Harris, R. W. Todd, S. J. Bungard, R. W. Lovitt, J.G. Morris and D.B. Keli, "Dielectric permittivity of microbial suspensions at radio frequencies: a novel method for the real-time estimation of microbial biomass," *Enzyme Microb. Technol*, vol. 9, pp. 181-186, 1987.
- [3] P. Ducommun, I. Bolzonella, M. Rhiel, P. Pugeaud, U. Von Stockar and I. W. Marison, "On-line determination of animal cell concentration," *Biotechnology and bioengineering*, vol. 72(5), pp. 515-522, 2001.
- [4] R. M. Matanguihan, K. B. Konstantinov and T. Yoshida, "Dielectric measurement to monitor the growth and the physiological states of biological cells," *Bioprocess Engineering*, vol. 11(6), pp. 213-222, 1994.
- [5] J. Suehiro, R. Yatsunami, R. Hamada and M. Hara, "Quantitative estimation of biological cell concentration suspended in aqueous medium by using dielectrophoretic impedance measurement method," *Journal of Physics D: Applied Physics*, vol. 32(21), pp. 2814-2820, 1999.
- [6] J. P. Carvell and J. E. Dowd, "On-line measurements and control of viable cell density in cell culture manufacturing processes using radio-frequency impedance," *Cytotechnology*, vol. 50(1-3), pp. 35-48, 2006.
- [7] F. Frezza, F. Mangini, M. Muzi and E. Stoja, "In silico validation procedure for cell volume fraction estimation through dielectric spectroscopy," *Journal of biological physics*, vol. 41(3), 223-234, 2015.

EARTHQUAKE DAMAGE DETECTION IN URBAN AREAS FROM VHR SAR IMAGERY

R. Anniballe⁽¹⁾, M.Chini⁽²⁾, N.Pierdicca⁽¹⁾

⁽¹⁾ Department of Information Engineering, Electronics and Telecommunications, Sapienza University of Rome, Via Eudossiana 18, 00184 Rome, Italy, roberta.anniballe@diet.uniroma.it

⁽²⁾ Luxembourg Institute of Science and Technology, 41, rue du Brill, L-4422 Belvaux, Luxembourg.

Abstract

Considering the earthquake that hit L'Aquila city on April 6, 2009, the present study assess the feasibility of producing damage maps at the scale of single building from Very High Resolution (VHR) Synthetic Aperture Radar (SAR) imagery. The proposed approach relies on the theoretical model of building SAR response and its expected changes because of a collapse. We perform the change analysis at object-level implementing image segmentation techniques followed by a supervised classification. Experimental results achieved using a pair of Spotlight COSMO-SkyMed images are compared with ground truth data provided by the Istituto Nazionale di Geofisica e Vulcanologia (INGV).

Index Terms – Damage Detection, Earthquake, Urban Areas, Very High Resolution (VHR) Synthetic Aperture Radar (SAR)

I. INTRODUCTION

The latest generation of space-borne Synthetic Aperture Radar (SAR) provides images with metric resolution allowing the identification of individual buildings. However, the complexity of the image forming mechanisms within urban settlements makes the automatic detection of damaged buildings from VHR SAR data still a challenging task. While a wide literature exists on the use of SAR data for assessing the damage level of an area, few works address the problem of detecting earthquake damage at single building level exploiting only SAR data. In a medium resolution image, build-up areas appear almost uniformly bright due to the predominance of the double reflections from the ground to the buildings wall facing the radar. Thus, the decrease of the backscattering is a key feature for detecting severely damaged urban settlement from a pair of SAR images with a resolution in the order of tens of meters. In metric resolution imagery, different scattering effects generated by individual buildings can be detected separately. Moving from the near range to the far range the following main contributions can be identified: a) a bright area corresponding to the backscatter from ground, building walls and roof, which are integrated mostly in the same resolution cell (i.e., the layover area); b) a very bright stripe due to the double reflection from the ground to the wall facing the radar; c) a

dark area corresponding to the SAR building shadow. When a building collapses the double bounce and the layover areas drastically decrease their brightness. At the same time, an increase of backscattering can be observed due to the scattering from debris laying within the building footprint and to the return coming from the ground previously occluded by the shadow [1].

Based on these considerations we developed an object-oriented change detection approach for mapping earthquake damage at single building level.

II. MATERIALS AND METHODS

The present study has been conducted using a pair of Spotlight COSMO- SkyMed (CSK) images collected before and after the L'Aquila earthquake. Both observations were performed along ascending orbit with a right-side looking and 50.57° of incidence angle. The spatial resolution is about 1 m in both range and azimuth. Ancillary data were also exploited to gather information about buildings height. For testing our approach we used a ground based damage map resulting from the macro-seismic survey performed by INGV (Istituto Nazionale di Geofisica e Vulcanologia). It consist of a layer of polygons reporting the damage grade associated to each building according to European Macroseismic Scale 1998 (EMS 98), which defines five levels of damage ranging from grade 1, for negligible or slight damage, to grade 5 for collapsed buildings.

We implemented a procedure for identifying collapsed buildings going through several steps. The first step consists of the segmentation of the pre-event image, to extract layover areas and bright stripes due to double bounce (DB/LO objects), that are the regions where a decrease of the backscattering in the post-event SAR image is expected because of the building collapse. This step is carried out according to the procedure proposed in [2]. Fig. 1(b) shows the results for a neighbor of L'Aquila city. The second stage aims at identifying changes occurred within the building footprint and in the shadow area, generally characterized by an increase of backscattering in case of collapse (INC objects). For this purpose a thresholding and region growing based approach exploiting the Kullback-Leibler Divergence [3] (KLD) computed between pre- and post- event SAR image is used, after masking DB/LO regions. The result is shown in Fig. 1(c). Once extracted from the image, DB/LO and INC objects are associated to polygons representing individual buildings in a vectorial urban map. The association of DB/LO objects to a building is performed after correction of range displacement of the building itself to compensate for layover which depends on building height and radar incidence angle. At the end of this step, a building may be associated to only one or both types of objects. Finally, exploiting change features extracted using only pixel belonging to the DB/LO and INC objects, a classification step based on the Bayesian

Maximum A Posteriori Probability (MAP) criterion is performed. Besides the ratio between the pre- and post-event backscatter images, others change detection features are considered, such as the KLD, the intensity correlation, and the interferometric coherence [2].

Two independent classifications are performed: the one based on features extracted from DB/LO objects, the other based on features evaluated on the INC objects. For those building having associated both DB/LO and INC objects, a fusion of INC and DB/LO MAP classifications are performed by assigning the building to the class with greater posterior probability. We considered two classes, discriminating between collapses (Damage Grade, or DG, equal to 5 in the EMS98) and less severe damages (DG < 5 in the EMS98). The non-parametric approach, known as Parzen window method [4], is used to retrieve the class conditioned probability density functions from the training set. The performances are assessed using a leave one out cross validation approach. In order to evaluate the usefulness of the investigated features and assess their contributions to the classification performances, we varied the number and the combination of features used as input space of the classification algorithm.

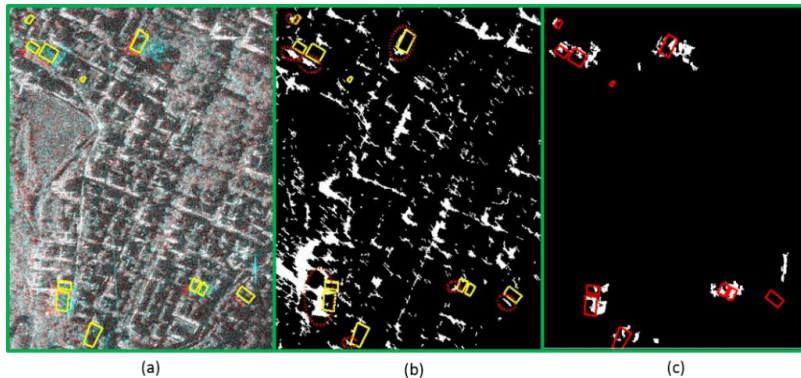


FIG. 1 – (a) RGB color composite of pre-event (Red and Green) and post-event (Blue) CSK intensity images. Red and cyan areas single out respectively the decrease and the increase of backscattering in the post-seismic image. (b) DB/LO objects extracted from the pre-event image. Polygons delineate buildings that have sustained a damage of grade 5. Red dashed circles highlight the associated DB/LO object. (c) INC objects extracted from the KLD.

III. RESULTS

Among the considered features, KLD and intensity ratio turned out to be the most significant features for discriminating between collapsed and not collapsed buildings from changes in DB/LO regions. As for the INC objects the most effective features were the interferometric coherence and the intensity ratio. When the classification was performed based on features extracted only from DB/LO objects, the 29.3% of the building with damage grade 5 were correctly identify. An increase of the sensitivity (44 %) to the damage grade 5 was observed

when also the INC objects were considered. All the results are summarized in the confusion matrices reported in Table I and II. The high rate of misdetection can be ascribed to the fact that some buildings classified as DG 5 by the ground survey are not easily detectable even by visual inspection of optical imagery; indeed, the complexity of the L'Aquila urban fabric represents a challenge for damage detection from space. Most of the buildings not recognized as damaged are located in the city historical center. Instead, considering the new build-up area shown in Fig.1, better classification performances in terms of sensitivity to the damage were achieved. Being this area less densely settled with respect to the historical center, the SAR response of the buildings is more similar to the canonical one, so that we are able to detect all the damaged buildings except for one, probably due to its small size.

TABLE I - CLASSIFICATION CONFUSION MATRIX (FEATURES FROM DB/LO OBJECTS)

		Classifier		
		DG < 5	DG = 5	Total
Ground Truth	DG < 5	1515	84	1599
	DG = 5	53	22	75
	Total	1568	106	1674
Cohen's Kappa				0.201
Overall Accuracy				91.8%

TABLE II - CLASSIFICATION CONFUSION MATRIX (FEATURES FROM DB/LO AND INC OBJECTS)

		Classifier		
		DG < 5	DG = 5	Total
Ground Truth	DG < 5	1498	101	1599
	DG = 5	42	33	75
	Total	1541	134	1674
Cohen's Kappa				0.274
Overall Accuracy				91.5%

IV. CONCLUSION

In this work building damage detection from VHR SAR image of the L'Aquila earthquake was carried out. Classification performances are not excellent when tested using the available ground truth, but a similar uncertainty has been observed comparing the INGV ground truth with that provided by the Italian Department of Civil Protection demonstrating the challenge of an accurate damage assessment even when performed on ground.

REFERENCES

- [1] R. Anniballe, M. Chini, N. Pierdicca, C. Bignami, S. Stramondo, F. Noto, T. Scalia, A. Martinelli and A. Mannella, "Detecting earthquake damage in urban area: application to Cosmo-SkyMed imagery of L'Aquila earthquake", *Proc. SPIE 9642, SAR Image Analysis, Modelling, and Techniques XV*, 2015.
- [2] M. Chini, R. Anniballe, C. Bignami, N. Pierdicca, S. Mori and S. Stramondo, "Identification of building double-bounces feature in Very High Resolution SAR data for earthquake damage mapping", *Proc. of International Geoscience and Remote Sensing Symposium (IGARSS) 2015*, pp.1144-1147.
- [3] S. Kullback, and R. A. Leibler, "On information and sufficiency", *The annals of mathematical statistics*, 22(1), pp. 79-86, 1951.
- [4] E. Parzen, "On estimation of a probability density function and mode". *The annals of mathematical statistics*, 33(3), pp. 1065-1076, 1962.

HTS FILTERS FOR THE SARDINIA RADIO TELESCOPE

P. Bolli⁽¹⁾, L. Cresci⁽¹⁾, F. Huang⁽²⁾, S. Mariotti⁽³⁾, D. Panella⁽¹⁾

⁽¹⁾ Arcetri Astrophysical Observatory, INAF
Largo E. Fermi 5, Florence, Italy
pbolli@arcetri.inaf.it

⁽²⁾ School of EESE, University of Birmingham
Edgbaston, Birmingham, B15 2TT, UK

⁽³⁾ Institute of Radio Astronomy, INAF
Via P. Gobetti 101, Bologna, Italy

Abstract

For the Sardinia Radio Telescope two designs of band-pass filters, centered at 355 MHz and 6.7 GHz, based on High Temperature Superconductor have been recently developed. We describe here the main steps in the production: from the electromagnetic design, the assembly and finally the cryo-characterization. Experimental results at 20 Kelvin shows for both filters scattering parameters in good agreement with the expected results: a reflection coefficient better than -15 dB and an insertion loss of about 0.2 dB.

Index Terms – Microwave filters, Radio Astronomy, High Temperature Superconductor, cryo-cooled measurements.

I. INTRODUCTION

Planar microwave components based on High Temperature Superconductor (HTS) have been intensively studied in recent years thanks to their excellent electrical conductivity [1]. For instance, Yttrium Barium Copper Oxide (YBCO) shows a significant drop of the electrical conductivity below its critical temperature of 89 K, reaching at 20 K a value several orders of magnitude higher than that of copper. However, the usage of such devices has been limited to very few applications, due to the impracticality of the cooling process for many telecommunication systems. In contrast, radio astronomy is amenable to this kind of technology since the front-ends of the receivers are already cooled to 20 K to reduce the receiver noise temperature. At the same time, with the large usage of the radio spectrum nowadays, a filter in front of the Low Noise Amplifier (LNA) for attenuating artificial radio frequency signals can be mandatory to prevent the non-linearity of LNA and mixer.

In the last five years, some HTS microwave filters have been designed and fabricated for two radio astronomical receivers of the 64-m Sardinia Radio Telescope (SRT). SRT is a new radio astronomical facility managed by the Italian National Institute for Astrophysics located 40 km North of Cagliari. This paper describes the main steps for producing these filters and their final performance.

Section 2 of this paper gives an overview of the filters fabricated. Sections 3 and 4 briefly show some steps of the production process: electromagnetic design and assembly respectively. The experimental results are described in Section 5. Finally, in the last Section the conclusions and the future related activities are given.

II. HTS FILTERS FOR SRT

The SRT has been recently technically commissioned in four different frequency bands ranging between 300 MHz up to 26 GHz [2]. Two sets of band-pass filters have been designed for operating in the frequency bands: 305 – 410 MHz (P-band) and 5.7 – 7.7 GHz (C-band), both with 30% fractional bandwidth and described respectively in [3] and [4]. Both series are based on a YBCO film laid on a Magnesium Oxide (MgO) substrate with thickness of 0.5 mm and dielectric constant 9.65.

For the P-band filters, two identical filters have operated, since 2013, in the two chains of the receiver (one for each linear polarization). They have been designed to attenuate by at least 30 dB the FM radio broadcasts and a 426 MHz carrier whose transmitter is in the line of sight of SRT. This filter includes also a low-pass circuit to avoid filter harmonic responses.

During the design of the C-band filters, besides the standard approach we focused also on testing alternative technical solutions, for example different carrier materials / plating / connectors. Out of the seven filters realized, only four survived to the experimental tests. However, since the nominal band of the C-band receiver turned out to be so far relatively free from strong interference, it was decided to not make use of them yet.

III. ELECTROMAGNETIC DESIGN

The filter circuits are based on a classical microstrip design using the electromagnetic coupling between different resonators. From the filter specifications, the order of the filter is defined and the coupling coefficients between resonators are given by tables available in the literature. Then by using the commercial electromagnetic simulator SONNET, adjacent pairs of resonators were simulated to estimate suitable resonator spacings (and for the spiral resonators, suitable shapes and number of turns) to create these coupling coefficients (and resonant frequencies). Finally, with a trial-and-error procedure, the circuit geometry is optimized in order to reach the desired responses. The losses in the substrate and in the HTS are not included in the electromagnetic models owing to their negligible values.

The layout of the band-pass filter operating in P-band is based on a fourth order filter with interdigitated and capacitively loaded spirals, for assuring such a large bandwidth. The low-pass filter consists of three capacitors (rectangular pads) and two inductors (meander lines).

The C-band filter has a more standard layout with four resonators labelled 1-4: 1 and 2 are coupled through the gaps between the microstrip lines, as are resonators 3 and 4, while capacitive pads couple the input to resonator 1, resonator 4 to the output line, and resonator 2 to 3.

IV. ASSEMBLY AND CHARACTERIZATION

When the filter layout is complete, the final chips are manufactured, through an ion-beam milling process, arranged by the substrate supplier CERACO. The chips are then glued to the gold or silver plated titanium alloy carriers using “Ablestik” adhesive conducting film. The titanium alloy is selected because it shows a thermal expansion coefficient quite close to that of the MgO substrate, avoiding stresses during cooling. Titanium alloy carriers require gold and/or silver plating because of their poor electrical conductivity. In the C-band filter, we tested copper carriers, whose advantages would have been: cheaper material and no need for plating. This test turned out to be unsuccessful due to micro-fractures in the substrate. As far as the connectors are concerned, we use either SMA connectors with separate non-captive pin contacts or sparkplug K connectors. The central pins of the connectors are glued to microstrip line by using “Epo-Tek” conducting silver epoxy glue.

The characterization of the devices is performed at cryo-temperature, around 20 K, with a Vector Network Analyzer (VNA). One of the main issues of this measurement is the VNA calibration, which is done by placing accurate standards at the end of the input and output cables, inside the cryostat. To avoid several cooling cycles for several terminating standards, this is done at room temperature, with a correction made for the lower losses of the cables when they are cooled.

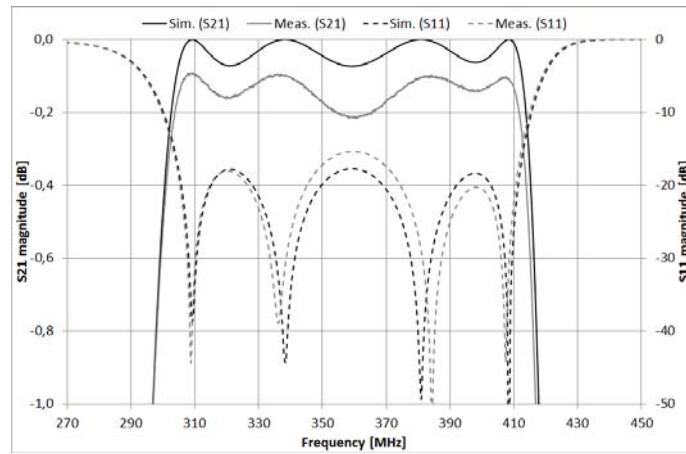
V. RESULTS

Both filters are designed with the goal of -20 dB of reflection coefficient in simulation, corresponding to about -17 dB in the measurements due to inaccuracies in the model and discontinuities in the transitions between microstrip and connector. The ohmic losses are not computed in the simulations being dominated by the connectors and the glue. Fig. 1 shows the experimental scattering parameters (transmission and reflection) for one prototype of each design in the respective pass band together with the simulated results.

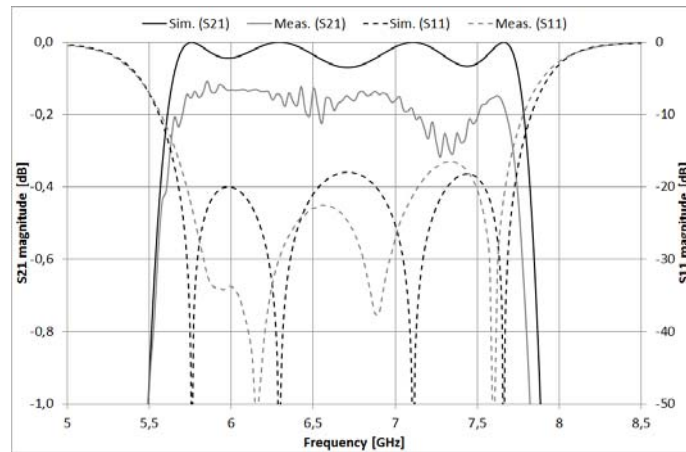
VI. CONCLUSION

HTS technology finds a proper environment in the front-end of the radio astronomical receivers. For SRT, we designed, fabricated and characterized band-pass filters centered at 355 MHz and 6.7 GHz. New projects are now under way for producing other filters working around

2.3 and 4.9 GHz respectively, characterized by a low-loss pass band plus a strong rejection quite close to the nominal band of the receivers.



(a)



(b)

FIG. 1 – Scattering parameters for the: (a) P-band and (b) C-band filter. Dashed curves refer to reflection coefficient and scale is on the right side; continuous curves refer to transmission coefficient and scale is on the left side.

REFERENCES

- [1] M.J. Lancaster, *Passive Microwave Device Applications of High-Temperature Superconductors*, Cambridge University Press, December 2006, ISBN: 9780521034173.
- [2] P. Bolli, et al., “Sardinia Radio Telescope: General Description, Technical Commissioning and First Light,” *Journal of Astronomical Instrumentation*, vol. 4(3-4), Dec. 2015.
- [3] P. Bolli, F. Huang, “Superconducting Filter for Radio Astronomy Using Interdigitated Spirals,” *Experimental Astronomy*, vol. 33(1), pp. 225-236, 2012.
- [4] P. Bolli, L. Cresci, F. Huang, S. Mariotti, D. Panella, “A high temperature superconductor microwave filter working in C-band for the Sardinia Radio Telescope,” *Journal of Astronomical Instrumentation*, vol. 3(1), Mar. 2014.

ORTHO-MODE TRANSDUCERS FOR MULTI-FEED RECEIVERS

G. Addamo, G. Virone, O. A. Peverini, M. Lumia, R. Tascone
CNR-IEIIT, c/o Politecnico di Torino
Corso Duca degli Abruzzi 24, 10129, Torino, Italy
giuseppe.addamo@ieiit.cnr.it

Abstract

This paper presents a novel configuration of ortho-mode transducers that is suitable for multi-feed receivers to be used in correlation radiometers with very high sensitivity aimed at cosmological and earth observations. In particular, the design, manufacturing and testing of the 49 Q-band ortho-mode transducers of the Large Scale Polarization Explorer will be reported. The latter is a balloon-based experiment funded by the Italian Space Agency aimed at the measurement of the Cosmic Microwave Background polarization state at large angular scales. The ortho-mode transducers configuration has been conceived toward a high parallelization rate of the manufacturing process, while meeting the high electromagnetic specifications set by the application (i.e., cross-coupling < -50 dB, isolation > 50 dB).

Index Terms – Multi-feed receivers, ortho-mode transducers, waveguide components, platelet technique.

I. INTRODUCTION

Ortho-mode transducers (OMTs) are key elements in dual-polarization antenna-feed systems employed in communication payloads, remote sensing applications, radio-astronomy, and astrophysical observations. In the framework of the latter application domain, the Large Scale Polarization Explorer (LSPE) will embark two instruments: the STRatospheric Italian Polarimeter (STRIP) [1] consisting of an array of 49 coherent receivers operating in the Q-band, and the Short Wavelength Instrument for the Polarization Explorer (SWIPE) [2] that is based on bolometric detectors operating from W to G bands. Because of the very faint signals to be detected, the LSPE-STRIP instrument is based on the simultaneous detection of the Q and U Stokes parameters of the incoming radiation through an array of 49 correlation receivers operating in the [39, 48] GHz band (20 % bandwidth).

Since the OMTs are used to separate/combine the two orthogonal linearly-polarized components that are present at the common waveguides, their cross-coupling and isolation levels define the polarization purity of the receivers. Several OMT configurations are already available in the technical literature. Asymmetric side-coupling structures minimize mechanical complexity at the expense of moderate RF performance, in terms of bandwidth and isolation. Symmetrical structures, based on Bøifot junction or the turnstile junction, exhibit wide-band capability but greater mechanical complexity owing to the

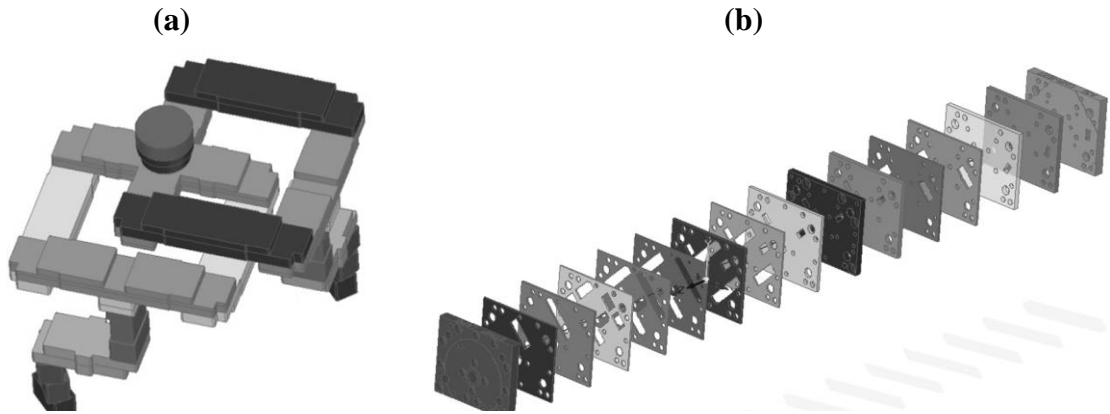


Fig. 1. Q-band platelet OMT architecture. (a) Internal waveguide geometry. (b) Exploded view of the mechanical assembly.

presence of the recombination networks. This issue can prevent the use of wide-band symmetrical configurations in multi-feed receivers with tens/hundreds of feeding networks. In order to overcome this drawback, this paper describes a multi-layer platelet OMT architecture based on the turnstile junction, in which all the building blocks have been designed in order to be machined out of standard-thickness metal plates via wire electrical-discharge machining (EDM). On the basis of the configuration described in Section II, the 49 OMT flight units of the LSPE-STRIP instrument have been successfully manufactured and tested (Section III).

II. DESIGN AND MANUFACTURING

The inner waveguide geometry of the Q-band OMT is shown in Fig. 1(a). It consists of a two-section circular waveguide adapter connected to a turnstile junction. The two pairs of opposite rectangular arms of the turnstile junction are recombined by means of two L-shaped junctions and two E-plane T-junctions [3]. The two L-shaped junctions extend through different layer levels, in order to avoid mechanical interference while guaranteeing phase-matching of the two channels. Finally, an S-junction and a compact twist are connected to each T-junction output port, in order to match the port flange of the correlation unit to be connected to the OMTs.

Figure 1(b) shows the exploded view of the corresponding mechanical assembly. The overall architecture has been conceived so that all the metal layers only exhibit through holes (as shown in Fig. 2). In particular, the matching pin of the turnstile junction is a cylinder that is press fitted into a mating hole. In this way, tens of identical layers can be manufactured at the same time via EDM. In order to identify the best material, the electrical resistivity of different standard-thickness metal layers has preliminary been measured both at room- and at cryogenic temperature.



Fig. 2. Al-alloy layers of the Q-band platelet OMTs for the LSPE-STRIP instrument.

III. TESTING

On the basis of the select Al-alloy, five OMT prototypes have been preliminarily manufactured and tested. In particular, the prototypes have undergone thermal cycles down to 15 K in order to assess their compliance to operation in cryogenic environment. Subsequently, all the 49 OMT flight units have been developed and accurately measured. The measured return loss and isolation are higher than 22 dB and 50 dB, while the measured insertion loss and cross-polarization are lower than 0.6 dB and -50 dB, respectively. Figure 1(a) and (b) show the measured reflection coefficient and cross-coupling of the 49 units as a function of frequency.

IV. CONCLUSION

The multi-layer platelet OMT architecture described in this paper has been successfully developed for the Q-band multi-feed receiver of the LSPE-STRIP. The authors have already demonstrated that the configuration is scalable to higher frequency bands, e.g. 30% bandwidth centered at 94 GHz.

ACKNOWLEDGEMENT

This work was supported by the Agenzia Spaziale Italiana (ASI) in the framework of Contract I/022/11/0 entitled “Large Scale Polarization Explorer (LSPE).

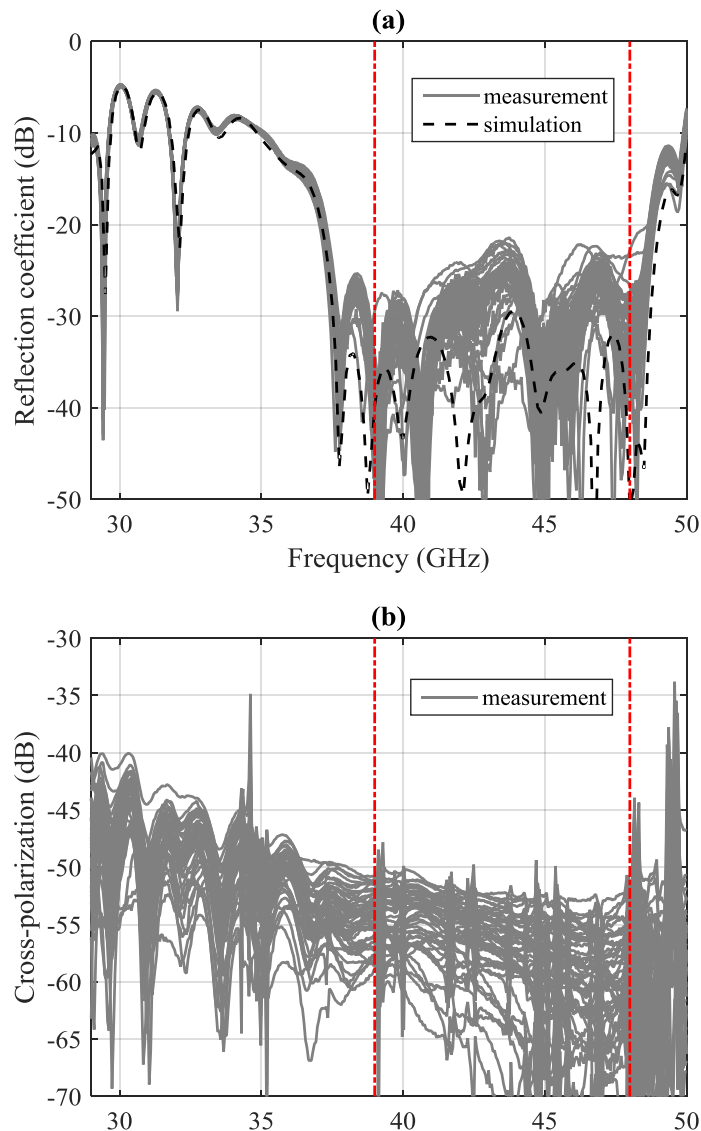


Fig. 3. Frequency response of the 49 OMT flight units of the LSPE-STRIP instrument. (a) Reflection coefficient. (b) Cross-polar transmission.

REFERENCES

- [1] M. Bersanelli, *et al.*, "A coherent polarimeter array for the Large Scale Polarization Explorer (LSPE) balloon experiment", in *Proc. of the SPIE Conference Astronomical Telescopes + Instrumentation 2012*, Amsterdam, The Netherlands, July 2012.
- [2] P. De Bernardis, *et al.*, "SWIPE: a bolometric polarimeter for the Large-Scale Polarization Explorer", in *Proc. of the SPIE Conference Astronomical Telescopes + Instrumentation 2012*, Amsterdam, The Netherlands, July 2012.
- [3] G. Virone, O. A. Peverini, M. Lumia, G. Addamo, R. Tascone, "Platelet Orthomode Transducer for Q-Band Correlation Polarimeter Clusters," *IEEE Transactions on Microwave Theory and Techniques*, vol. 62(7), pp. 1487-1494, July 2014.

DESIGN OF ERBIUM DOPED CHALCOGENIDE MICRODISK EMITTING AT 4.5 μm Wavelength

G. Palma ⁽¹⁾, M. C. Falconi ⁽¹⁾, F. Starecki ⁽²⁾, V. Nazabal ⁽²⁾, L. Bodiou ⁽³⁾,
Y. Dumeige ⁽³⁾, J. Lemaitre ⁽³⁾, J. Charrier ⁽³⁾, F. Prudenzano ⁽¹⁾

⁽¹⁾ Politecnico di Bari, DEI - Dipartimento di Ingegneria Elettrica e dell'Informazione, Via E. Orabona 4, Bari, 70125, Italy

⁽²⁾ ISCR, UMR UR1-CNRS 6226, Université de RENNES 1, 35042
Rennes Cedex, France

⁽³⁾ FOTON -UMR-CNRS 6082, ENSSAT BP80518, F-22305 Lannion
Cedex, France

francesco.prudenzano@poliba.it

Abstract

The electromagnetic design of a novel chalcogenide glass microdisk coupled to a ridge waveguide is performed. The microdisk is rare-earth doped in order to obtain emission useful for biological application. A home-made computer code is developed by taking into account the active behavior of the Erbium ions interacting with the resonating Whispering Gallery Modes. The simulation shows that, by using Erbium-doped chalcogenide microdisk, lasing at 4.5 μm can be obtained.

Index Terms – Chalcogenide Glass, Microdisk, Mid-Infrared emission, Rare-earth.

I. INTRODUCTION

Mid-Infrared (Mid-IR) wavelength range is very promising for different applications in biology, molecular spectroscopy, environmental monitoring. It includes a lot of strong vibrational transitions, acting as “fingerprints” for many organic species and bio molecules. This allows innovative spectroscopic applications and novel bio-molecular sensing solutions. In addition, there are two atmospheric transmission windows at 3–5 μm and 8–13 μm , in which the earth atmosphere is transparent enough to allow applications such as remote explosive detection, e.g. in airports and for border control, and covert communication systems [1].

Silica glass becomes an opaque medium beyond 2 μm wavelength. The wide transparent window of chalcogenide glasses in mid-infrared makes possible to overcome this limitation [1-3]. Chalcogenide glasses exhibit other interesting properties that make them suitable as host materials for efficient emission, e.g. high rare-earth solubility, low phonon energy, high refractive index enabling suitable absorption and emission cross sections. Moreover, they have good mechanical robustness and chemically durability in water and atmosphere.

A home-made computer code is developed in order to simulate rare-earth doped chalcogenide microresonators, such as: a) microdisks, b) microrings and c) microspheres coupled to a d) ridge waveguides or e) fibers. It is possible to simulate different kinds of chalcogenide glasses

doped with different rare-earths among which: f) Erbium (Er³⁺), g), Dysprosium (Dy³⁺) and h) Praseodymium (Pr³⁺). Moreover, the results concerning the design of an Erbium-doped chalcogenide microdisk lasing at 4.5 micron are reported.

II. ELECTROMAGNETIC DESIGN

Cylindrical microresonators, bounding resonant Whispering Gallery Modes [4], exhibit very interesting properties, such as narrow spectral linewidth, high-quality factors Q , small mode volume, and high power density [5]. Fig. 1 shows a microring made of a core in chalcogenide glass on a silicon substrate. It is fabricated by photolithography process at FOTON laboratory in Lannion. The simulations are performed realistically by considering spectroscopic parameters measured on glass chalcogenide samples and feasible geometries, thus allowing a complete feasibility investigation.

Each $WGM_{m,p,n}$ is characterized by the azimuthal parameter m (which defines the number of field maxima in the azimuthal direction), the longitudinal parameter p (number of field maxima in the longitudinal direction) and the radial parameter n (number of field maxima along the radial direction).

The design is performed in two steps. In the first one a full-vectorial Finite Element Method (FEM) is used for the electromagnetic analysis of both the resonating WGMs and ridge waveguide propagation modes. In the second one, the home-made numerical code solves the coupled mode equations (modeling the coupling between the ridge waveguide propagation modes and WGMs) and the ion population rate equations [7]. The model include the absorption rates, the stimulated emission rate, the amplified spontaneous emission noise, the lifetimes and branching ratios of the energy levels, the ion-ion energy transfers and the excited state absorption in order to simulate the light amplification due to different rare-earths.

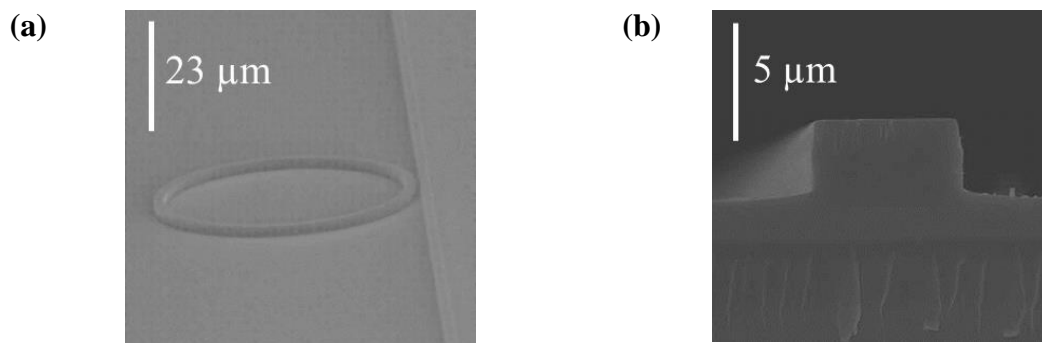


FIG. 1 – SEM images of (a) top view of a chalcogenide microring coupled to a ridge waveguide on a silicon substrate and (b) transversal view of the ridge waveguide fabricated at FOTON Laboratory in Lannion.

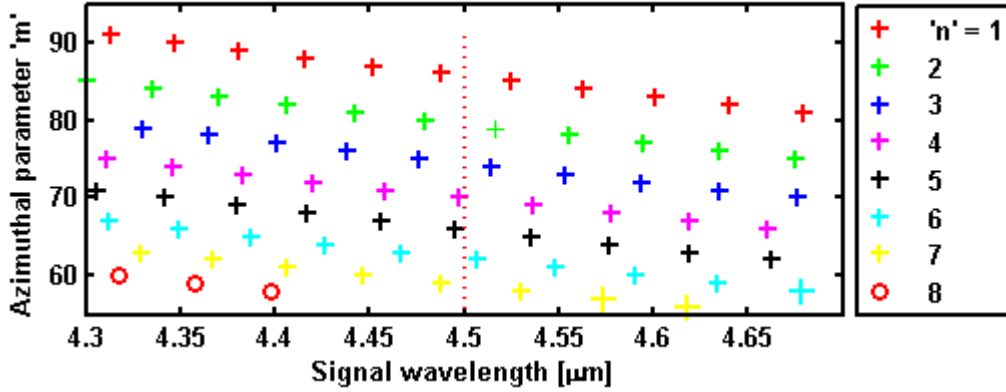


FIG. 2 – WGMs resonances in the chalcogenide microdisk with radius $R=40\mu\text{m}$ and height $h=600\text{nm}$.

A chalcogenide microdisk with radius $R = 40 \mu\text{m}$ and height $H = 600 \text{ nm}$ is simulated. It is coupled to two ridge waveguides (one for signal at $\lambda_S = 4.5 \mu\text{m}$ and one for pump at $\lambda_P = 0.8 \mu\text{m}$) having height $h_W = 1.0 \mu\text{m}$ and width $w_W = 2.5 \mu\text{m}$. The refractive index at $\lambda_S = 4.5 \mu\text{m}$ is $n=2.35$ and $\lambda_P = 0.8 \mu\text{m}$ is $n=2.42$. Erbium is uniformly distributed in glass with a concentration $C=2.8 \times 10^{20} \text{ cm}^{-3}$. All these parameters are optimized by an ad-hoc design or taken by literature [6]. Fig. 2 shows the WGMs resonating in the disk within a wavelength range of 400 nm around the nominal signal wavelength $\lambda_S = 4.5 \mu\text{m}$. The simulation is carried out by imposing $p = m$. WGMs with $p \neq m$ can be neglected because they exhibit low electromagnetic overlapping with uniform rare-earth profile. $N = 73$ WGM resonances with n parameter varying from 1 to 8 and m parameter varying from 56 to 91 are calculated. The obtained mean Free Spectral Range (FSR) is about $\text{FSR} = 37 \text{ nm}$. Among these solutions, one exhibits a strong interaction with rare-earth ions. It is the fundamental $\text{WGM}_{86,86,1}$ having resonant wavelength close to the nominal wavelength $\lambda_S = 4.5 \mu\text{m}$, where the ($^4I_{9/2} \rightarrow ^4I_{11/2}$) Erbium emission occurs. In the case of the pump, $N = 2008$ different WGMs, in a range of 200 nm centered on the nominal pump wavelength $\lambda_P = 0.8 \mu\text{m}$, with n parameter varying from 1 to 8 and m parameter varying from 506 to 761, are identified. The mean $\text{FSR} = 1.1 \text{ nm}$ is calculated. The first seven radial order pump modes $\text{WGM}_{723,723,1}$, $\text{WGM}_{711,711,2}$, $\text{WGM}_{700,700,3}$, $\text{WGM}_{691,691,4}$, $\text{WGM}_{683,683,5}$, $\text{WGM}_{675,675,6}$, $\text{WGM}_{668,668,7}$, strongly interact with the signal via the rare earth. Fig. 3 shows the signal power P_S at the end section of the output waveguide as a function of the input pump power P_P and the gap g_S between the ridge waveguide and the disk. The maximum output signal power is $P_S = 10.21 \mu\text{W}$; it is obtained for the input pump power $P_P = 0.5 \text{ W}$ and the gap $g_S = 2.1 \mu\text{m}$.

The simulation shows that an erbium-doped chalcogenide microdisk can be optimized for lasing at $\lambda_S = 4.5 \mu\text{m}$. These results are in agreement with those reported in [6] for a similar glass.

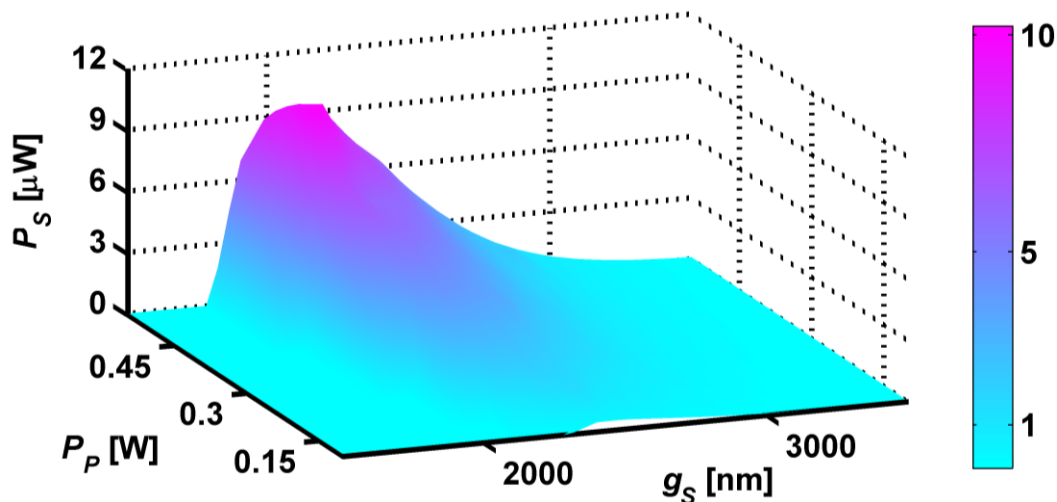


FIG. 3 – Output signal power P_S versus the gap g_s and input pump power P_P for the Erbium doped chalcogenide microdisk.

III. CONCLUSION

A home-made code is employed to perform the design and the feasibility investigation of an Erbium-doped chalcogenide disk coupled to two ridge waveguides. Lasing at $\lambda=4.5 \mu\text{m}$ pumped at $\lambda=800\text{nm}$ is simulated, the feasibility of different chalcogenide microdisks doped with Praseodymium and Dysprosium will be investigated.

ACKNOWLEDGEMENT: This research is performed within COST Action MP1401.

REFERENCES

- [1] J.L. Adam, L. Calvez, J. Trolès, V. Nazabal, “Chalcogenide Glasses for Infrared Photonics,” *International Journal of Applied Glass Science*, vol. 6, no.3, pp. 287-294, 2015.
- [2] F. Prudenzano, L. Mescia, L. Allegretti, V. Moizan, V. Nazabal, F. Smektala, “Theoretical Study of Cascade Laser in Erbium-Doped Chalcogenide Glass Fibers,” *Optical Materials*, vol. 33, no. 2, pp. 241–245, 2010.
- [3] A. B Seddon, Z. Tang, D.d Furniss, S. Sujecki, T. M Benson, “Progress in rare-earth-doped mid-infrared fiber lasers,” *Optics Express*, Vol. 18, No. 25, pp. 26704 – 26719, 2010.
- [4] L. Mescia, P. Bia, O. Losito, F. Prudenzano, “Design of Mid-IR Er³⁺ - Doped Microsphere Laser,” *IEEE Photonics Journal*, vol. 5, no.4 , 2013.
- [5] G. Righini, Y. Dumeige, P. Féron, M. Ferrari, G. Nunzi Conti, D. Ristic, S. Soria, “Whispering gallery mode microresonators : Fundamentals and applications,” *Rivista del Nuovo Cimento, Società Italiana di Fisica*, vol. 34, no. 7, pp.435-488, 2011.
- [6] F. A. Tal, C. Dimas, J. Hu, A. Agarwal, L. C. Kimerling, “Simulation of an erbium-doped chalcogenide micro-disk mid-infrared laser source,” *Optics Express*, vol. 19, no. 13, pp. 11951-11962, 2011.
- [7] G. Palma, C. Falconi, V. Nazabal, T. Yano, T. Kishi, T. Kumagai, M. Ferrari, F. Prudenzano, “Modeling of Whispering Gallery Modes for Rare Earth Spectroscopic Characterization,” *IEEE Photonics Technology Letters*, vol. 27, no. 17, pp. 1861 – 1863, 2015.

MONTE CARLO MODEL OF CLOUD SCATTERING OF SOLAR RADIATION FOR VLC AIRCRAFT SYSTEMS

D.Tagliaferri¹, R.Nebuloni², L.Luini^{1,2}, C.Capsoni¹

¹Dipartimento di Elettronica, Informazione e Bioingegneria, Politecnico di Milano

Piazza L. Da Vinci 32, 20133 Milano, {dario.tagliaferri, lorenzo.luini, carlo.capsoni}@polimi.it

²IEIIT-CNR, Via Ponzio 34/5, 20133 Milano, roberto.nebuloni@ieiit.cnr.it

Abstract

With the raising interest in aircraft-based visible light communication (VLC) systems, characterizing the amount of sunlight scattered by clouds becomes important for modelling the incoming solar radiation. In fact, sunlight comes through the aircraft windows and affects the receivers as a form of disturbance. In this regard, this paper proposes a Monte Carlo photon transport simulator that provides the spatial scattering function of a water cloud with an arbitrary liquid water content, when it is illuminated by the sunlight coming from a given direction.

Index Terms – Clouds, scattering, Monte Carlo, aircraft VLC systems

INTRODUCTION

Visible light communications are becoming a promising alternative to classical radio communications in many difficult environments, thanks to their intrinsic advantages, such as unlicensed and virtually unlimited communication bandwidth, insensitivity to E.M. interference, high capacity per unit area and many others. Among the various applications, aircraft-based VLC systems have gained much attention in recent years, for the possibility to provide low-cost, green communication links in E.M. sensitive spaces. For guaranteeing the robustness of the links, a detailed noise model is desirable. Solar noise (both direct and diffuse) is detrimental for this kind of application, given that it comes through the aircraft windows and affects the receivers. The most part of the analytic solar radiation models nowadays present in literature do not consider the presence of clouds, which is by contrast very important in order to estimate the irradiance at a given location, height and time.

This paper provides the description of a Monte Carlo based simulation tool able to compute the spatial phase function of a water cloud volume with fixed, homogeneous water content, given the incidence direction of the sunlight and the microphysical characterization of the medium. At the end, we will show some results regarding the difference in the transmittance of the whole cloud with respect to the Lambert-Beer prediction in few meaningful cases, together with a graphical representation of selected outputs. The tool can be useful in other research areas where the characterization of the cloud scattering phenomena involving solar radiation is important, for instance climatology (radiative heat transfer to the ground) and solar panels engineering (to estimate the reduction of the available solar energy in cloud conditions). Finally, the code can be used with few modifications to model the interaction between radiation at optical wavelengths and other types of atmospheric particles (fog, rain, snow, etc.).

NUMERICAL TECHNIQUE

The simulator is based on the Monte Carlo photon transport method, a well-known technique to simulate the behaviour of complex systems [1]. The underlying principle is to “sample” the system by injecting a number of photons of a given wavelength in the volume according to a random initial position and fixed direction (sunlight) and study the propagation inside the random medium by properly simulating scattering and absorption events. For the specific purpose of clouds scattering, it is important to count how many photons come out from the volume (with respect to the number of incident photons) and their outgoing direction (in order to build up the spatial phase function).

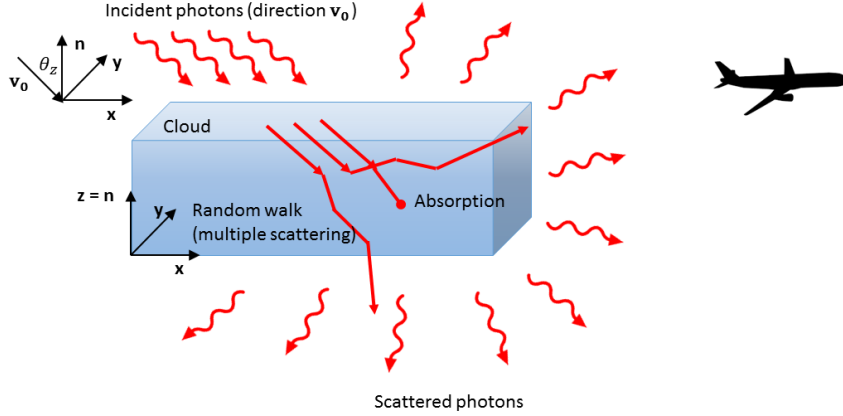


Figure 1: Graphical illustration of the problem, with relative geometry. Sunlight strikes the volume and then it is either absorbed or scattered by cloud droplets: scattered light affects the receivers inside the airplane.

To model the propagation medium (water clouds) we use, for simplicity, a monodispersion of spherical water particles with a fixed, equivalent radius r_{eq} , that preserves the extinction coefficient $\gamma_{ext}(\lambda)[m^{-1}]$ resulting from a refined model of cloud microphysics, i.e. a modified gamma Particle Size Distribution (PSD) [2]. Given the Liquid Water Content (LWC) of the volume, $L [mm]$, taken for example from the model in [3], the extinction coefficient $\gamma_{ext}(\lambda)$ is obtained by multiplying the volumetric concentration of particles for the extinction cross-section at the wavelength of interest $C_{ext}(\lambda)$. The latter, together with the absorption and scattering cross-sections $C_{abs}(\lambda)$ and $C_{sca}(\lambda)$, single scattering albedo $\omega(\lambda)$ and single scattering angular phase function $P(\lambda, \theta, \phi)$ (normalized to have unit integral over 4π steradians), is obtained from the application of the rigorous Mie theory to a water sphere with radius r_{eq} . Moreover, $P(\lambda, \theta, \phi)$ can be obtained in analytical form by means of the Henyey-Greenstein approximation, that in most cases leads to a substantial reduction of the simulation time [4].

Once having the extinction coefficient at each wavelength of interest, the program propagates a photon through the cloudy layer, going through the following steps:

1. Randomly choose the initial position \mathbf{p}_0 and the wavelength λ_k of the photon. The former is chosen on the surface of the volume, according to the direction of arrival of the sunrays (unit vector $\mathbf{v}_0 = [-\sin(\theta_z) \sin(\psi_{az}), -\sin(\theta_z) \cos(\psi_{az}), -\cos(\psi_{az})]$, where θ_z and ψ_{az} are the zenith and azimuth angles of the Sun, respectively).
2. Until the photon comes out from the cloud volume or it is absorbed:
 - a. Find the path travelled by the photon before hitting a particle, as: $s = -\ln(\eta)/(\gamma_{ext}(\lambda_k))$, where η is a uniform random variable between 0 and 1, hence s is exponentially distributed with mean value equal to $1/\gamma_{ext}(\lambda_k)$ (mean free path)

- b. propagate the photon: $\mathbf{p} = \mathbf{p}_0 + s \mathbf{v}_0$. If the new position is out of the volume, mark the photon as “scattered” and exit the loop, otherwise:
 - c. generate a random number between 0 and 1: if the result is less than the single scattering albedo $\omega(\lambda_k)$, the photon is scattered by the particle, otherwise it is flagged as “absorbed” (in this case, simply consider it as “lost” and go to step 1)
 - d. If the photon is scattered:
 - e. generate a pair of scattering angles $(\hat{\theta}, \hat{\phi})$ according to the inversion method, applied to the cumulative distribution of $P(\lambda_k, \theta, \phi)$
 - f. adjust the initial direction of the photon \mathbf{v}_0 according to the generated angles and obtain the new direction \mathbf{v} .
 - g. go to step 2a with the new direction \mathbf{v} .
3. If the photon is marked as “scattered”, the exit direction \mathbf{v}_{out} is used to compute the co-elevation and azimuth exit angles $(\theta_{out}, \phi_{out})$. Then, the photon is counted in two different structures (arrays) for co-elevation and azimuth angles, named $S_{\vartheta}(\lambda_k, \theta)$ and $S_{\varphi}(\lambda_k, \phi)$
 4. Go to step 1. The procedure must be repeated for all the generated photons.

At the end of the procedure, the two resulting arrays are used to compute the matrix of the 3d spatial phase function, $S(\lambda, \theta, \phi)$, assuming that, for each co-elevation angle θ_{out} , the associated power $S_{\vartheta}(\theta_{out})$ follows the same trend as the function $S_{\varphi}(\phi)$ in azimuth. This is a simplifying assumption, justified by the need of limiting the overall simulation time. As last step, the matrix is normalized so that its integral over 4π steradians is equal to the fraction of scattered photons with respect to the total launched number.

RESULTS AND CONCLUSIONS

Table 1 reports some meaningful simulation outputs, for various cases. We compared the results of two different wavelengths and three different LWCs, at a given direction of the Sun and equivalent radius of the particles (computed from typical Stratus/Cumulus cloud parameters [2]). The volume was 1 km x 1 km x 100 m width. For each case, we used the rigorous single scatter phase function to simulate the interaction between photons and water particles. We show both the whole cloud (multiple scattering) transmittance and the Lambert-Beer (L-B) estimation, i.e. single scattering regime. As expected, the overall transmittance values are higher than L-B predictions for all the LWCs: there is an increasing amount of photons (for increasing values of LWC) that are redirected to the initial direction after having undergone one or more interactions (multiple scattering regime). These values of cloud transmittance also take into account the border effects of the parallelepiped cloud volume, where photons incur in less events. Analysing the dependence of the results from the wavelength, the main difference is in the average number of events per photon (both scattering and absorption): the different single scatter functions (more peaked in the forward direction at 0.3 μm with respect to 1 μm) lead to different average paths in the cloudy medium. Furthermore, Figure 2 shows graphically the resulting outputs of the code ($S_{\vartheta}(\lambda_k, \theta)$, $S_{\varphi}(\lambda_k, \phi)$ and $S(\lambda_k, \theta, \phi)$) for $\lambda_k = 0.3 \mu\text{m}$ and $L = 0.05 \text{ mm}$. In the plot of $S_{\vartheta}(\lambda_k, \theta)$, photons in the $[0-\pi/2]$ range are backscattered, while the others are scattered forward (thus, “below” the cloudy volume). The code is expected to be upgraded to include the realistic case of non-homogeneous cloudy volumes, composed of several 1 km x 1 km x 100 m pixels as in [3], and it will reasonably extended to the scattering of ice clouds (under some simplifying assumptions).

	$L = 0.005 [mm]$		$L = 0.05 [mm]$		$L = 0.5 [mm]$	
$\lambda = 0.3 [\mu m]$	T_{cloud}	T_{L-B}	T_{cloud}	T_{L-B}	T_{cloud}	T_{L-B}
	0.1013 (9.5 dB)	0.0998 (10.04 dB)	0.0084 (20.7 dB)	0.0075 (21.26 dB)	0.0013 (29.01 dB)	$9.15E - 4$ (30.38 dB)
	Number of events		Number of events		Number of events	
	3.6		40		404	
$\lambda = 1 [\mu m]$	T_{cloud}	T_{L-B}	T_{cloud}	T_{L-B}	T_{cloud}	T_{L-B}
	0.1090 (9.6 dB)	0.1052 (9.77 dB)	0.0084 (20.7 dB)	0.0077 (21.12 dB)	0.0011 (29.7 dB)	$7.45E - 4$ (31.27 dB)
	Number of events		Number of events		Number of events	
	3.5		39		283	
Simulation times [s]	40.2		232.2		1880	

Table 1: Comparison of selected cases results. For each case, the total number of launched photons is equal to 200000, the equivalent radius is $6.7 \mu m$, and the Sun angles are $\theta_z = 45^\circ$, $\psi_{az} = 150^\circ$. The simulation times are bounded to half an hour in the worst case (measured using a parallelized MATLAB® code run on an Intel Core2 Quad Q6600 @ 2.40 GHz).

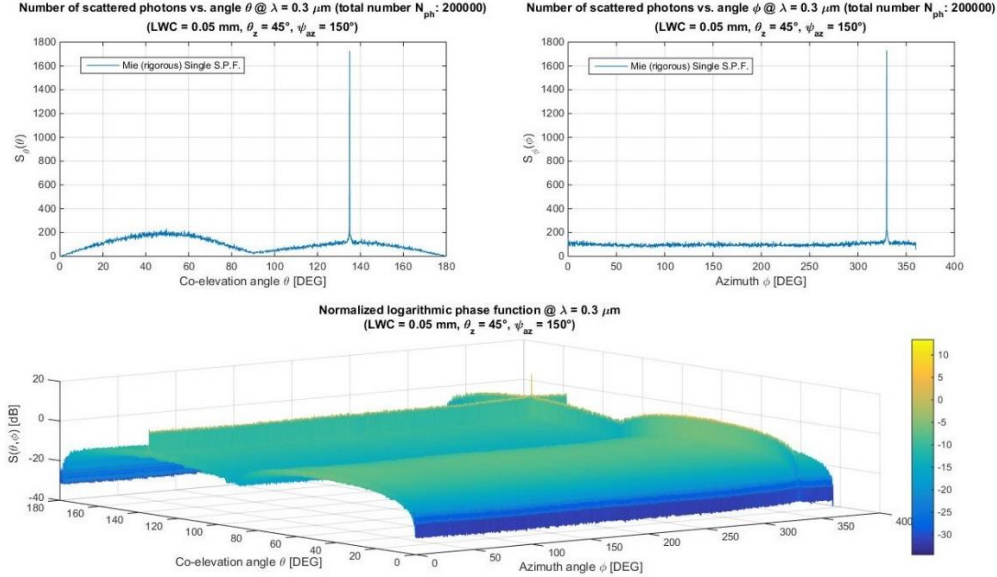


Figure 2: Plots of the results. The peaks in the upper two plots correspond exactly to the incident Sun direction, with a π -shift. The angles bin-widths for computation of the results are $\Delta\theta = \frac{\pi}{2000}$ and $\Delta\psi = \frac{2\pi}{2000}$.

REFERENCES

- [1] Arnon S. Sadot D. Kopeika N.S. (1994) "Simple Mathematical models for temporal, spatial, angular and attenuation characteristics of light propagating through the atmosphere for free space optical communications: Monte Carlo simulations" Journal of Modern Optics, vol 41, p 1955-1972
- [2] Tampieri F. and Tomasi C. (1976) "Size distribution models of fog and cloud droplets in terms of the modified gamma function", Tellus XXIII, p.333-347
- [3] L. Luini and C. Capsoni (2014) "Modeling High-Resolution 3-D Cloud Fields for Earth-Space Communication Systems", IEEE Transactions on Antennas and Propagation, vol. 62, no. 10, p. 5190-5199.
- [4] Henyey L.G. and Greenstein J.L. (1941) "Diffuse radiation in the galaxy", Astrophysical Journal, vol. 93, p.70-83.

PRELIMINARY RESULTS ON A MINIATURIZED QUADRATURE HYBRID COUPLER USING SLOW-WAVE TRANSMISSION LINES

G. Acri⁽¹⁾, P. Ferrari⁽²⁾, L. Boccia⁽¹⁾, D. Calzona⁽¹⁾, G. Amendola⁽¹⁾

⁽¹⁾ Department of Telecommunication Engineering, University of Calabria, Italy

luigi.boccia@unical.it

⁽²⁾ University Grenoble-Alpes, IMEP-LAHC, Campus Minatec, 3 Parvis Louis Neel, Grenoble, France

Abstract

In this paper, a compact quadrature branch-line hybrid coupler implemented using a standard 28 nm CMOS (FDSOI) process is introduced. The proposed component was designed for 77 GHz radar applications for a proof-of-concept. Size reduction is achieved by employing an innovative configuration based on monolithically integrated slow-wave microstrip lines which allow reducing the chip area of about 80% with respect to other solutions. Simulated full-wave results of the entire structure show an insertion loss of 4.2 dB at the nominal operation frequency of the coupler, a magnitude unbalance of 0.1 dB as well as a return loss and isolation below 22 dB. The phase difference between the output ports remains in the order of 89° within the entire bandwidth that is equal to 14%.

Index Terms – Quadrature hybrid, slow-wave transmission lines, CMOS

I. INTRODUCTION

In the last few years, there has been renewed interest in the implementation of traditional microwave passive circuits in monolithic silicon technologies. The need for composite analog and microwave circuit design techniques in CMOS in the radio-frequency (RF) and millimeter-wave frequency bands is one of the reasons for this resurgent interest [1]. Typically, RF building blocks tend to occupy a large chip area and, for this reason, there is a strong interest to develop miniaturization strategies. One of the functional blocks occupying the largest chip area is the hybrid coupler. A number of different implementations of hybrid couplers has been proposed in literature using different technologies. Branch-line couplers, in 90 nm CMOS technology, with modified CPWs were proposed in [2], leading to a size of 0,1 mm² and an insertion loss (IL) of 5.5 dB, for a 60 GHz working frequency. A simple SiGe BiCMOS branch-line coupler with meandered transmission lines was reported in [3], working at 77 GHz, achieving IL within 4.5 dB and occupying an area of 0,28 mm². In [4], an example of 3-dB directional coupler incorporating the edge-coupled meandered synthetic transmission line was presented. In this example, by applying the transmission line synthesis of complementary-conducting-strip coupled-lines, 3-dB directional coupler (with a bandwidth 14,2-36,9 GHz) was meandered in an area of 0,029 mm² and realized by using the standard 0.18- μ m 1P6M CMOS technology. Although this represents an interesting approach in terms of size reduction, its performance were not satisfactory as the prototyped chip showed insertion loss of about 3.6 dB, a coupling of 5.5 dB and a

phase imbalance of 5° . In [5], a wideband miniature branch line coupler was presented for 60 GHz phased array applications. In this case, insertion loss was in the order of 3.8 dB whereas the chip area was equal to 0.08 mm^2 .

In this work, a miniaturized 90° hybrid coupler based on a novel configuration of slow-wave microstrip line is proposed. The proposed arrangement is realized using meandered microstrip lines implemented on a substrate populated by a set of metallic micro-wires referred to as bed of nails. As it will be illustrated, results show a reduction of the chip area of more than 80% with respect to other on-chip microstrip couplers.

II. BRANCH LINE DESIGN

The branch-line coupler, also known as quadrature (90°) hybrid coupler, is a 4-port network whose circuital representation is shown in Fig.1 [6]. The coupler is composed of four transmission lines. Each transmission line is a quarter wavelength section and it has a characteristic impedance of either Z_0 or $Z_0/\sqrt{2}$.

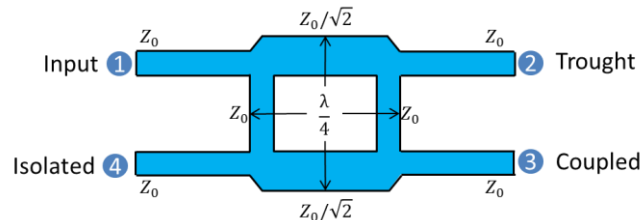


Fig.1 Branch-line quadrature hybrid coupler

In this work, a miniaturization approach for the quadrature hybrid coupler based on a novel slow-wave microstrip line is presented. Each section of the quadrature hybrid is implemented using meandered microstrip lines designed on a substrate populated by arrays of metallized via holes. The slow wave effect of microstrip lines on bed of nails has been already demonstrated in [7] for PCB technologies. In this work, a configuration similar to [7] is explored in CMOS technology and demonstrated for a hybrid coupler.

In particular, the $\lambda/4$ hybrid coupler branch having characteristic impedance $Z_0 = 50\Omega$ has been implemented using a standard meandered microstrip line loaded with open-ended stubs whose length has been reduced exploiting the slow wave effect of the bed of nails (Fig. 2-a). This structure ensures a significant increment of the equivalent capacitance and inductance, which in turn yields to an effective propagation constant equal to 31.6 achieved without affecting the characteristic impedance of the transmission line. The other two branches of the quadrature hybrid were implemented using a $35\text{-}\Omega$ meandered microstrip line entirely designed on a bed of nails (Fig. 2-b). These branches should geometrically match the previous ones. This effect is achieved tuning the width of the line and the meandering geometry. Each branch line was simulated individually using a FEM-based commercial tool [8].

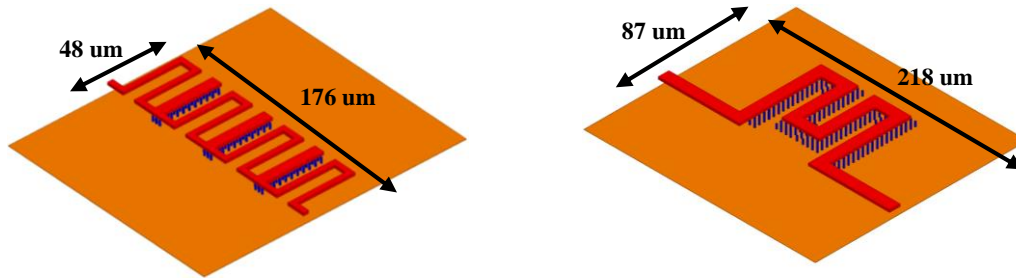


Fig.2 (a) 50-Ω Meandered-stub-vias structure (b) 35-Ω Meandered&Vias structure

III. HYBRID COUPLER DESIGN AND RESULTS

The final layout of the 90° hybrid coupler was generated integrating the sub-blocks presented in the previous section as shown in the Fig.3.

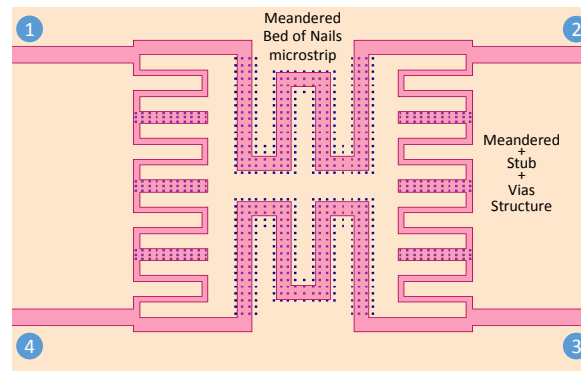


Fig.3 Final layout of the hybrid coupler

TABLE I - HYBRID COUPLER BRANCH LINES

TLine	Z _c (Ohm)	Φ (degree)	L (μm)
Conventional μs width=11μm (T-Junction)	50.8	N/A	N/A
<i>Meandered Bed of Nail</i>	35.7	90.2	218
<i>Meandered-Stub-Vias</i>	50.2	91.4	176

The resulting geometry was then entirely simulated using HFSS and fine-tuned to take into account mutual coupling effects. The final chip area is equal to 0,043 mm² thus achieving a miniaturization of 85% with respect to a conventional branch-line coupler implemented using microstrip lines on the same substrate. Furthermore, as it can be observed in Fig.4-a, the configuration proposed in this work shows an excellent input matching at 77 GHz and an insertion loss from the input to the two output ports (through and coupled) equal to 4.2 dB (against nominal intrinsic IL of 3 dB). In Fig.4-b is also shown the output phase

difference that is equal to about 89° at the operating frequency. The 15 dB return loss bandwidth exceeds 14% between 72-86 GHz.

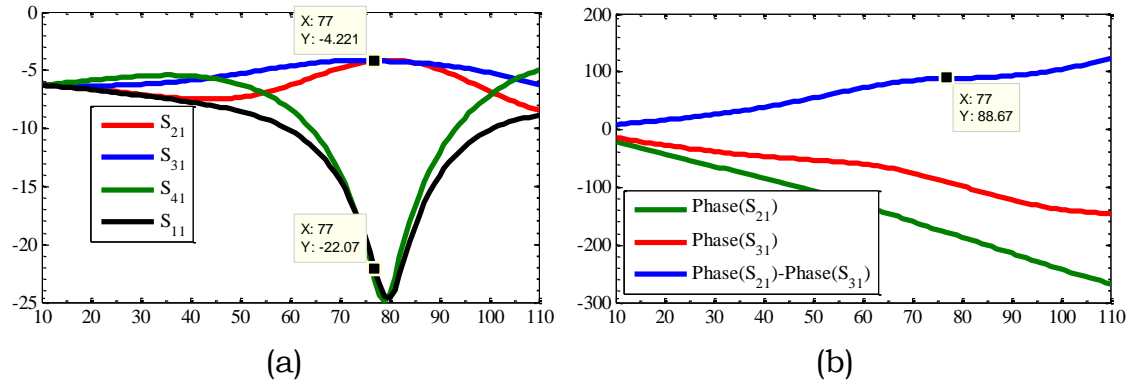


Fig.4 Simulation results of the quadrature hybrid coupler

IV. CONCLUSIONS

Preliminary results on a novel CMOS quadrature hybrid coupler operating at 77 GHz are presented in this work. The proposed configuration is the first on-chip demonstration of the so called bed of nail slow wave structures. Results show excellent electrical performance combined with a miniaturization factor, which exceeds 85% with respect to a conventional quarter wave coupler implemented in the same technology. Further results will be presented during the conference.

REFERENCES

- [1] S. Reynolds, B. Floyd, U. Pfeiffer, and T. Zwick, "60GHz transceiver circuits in SiGe bipolar technology," in *Solid-State Circuits Conference, 2004. Digest of Technical Papers. ISSCC. 2004 IEEE International*, 2004, pp. 442–538 Vol.1.
- [2] I. Haroun, J. Wight, C. Plett, A. Fathy, and D. C. Chang, "Experimental Analysis of a 60 GHz Compact EC-CPW Branch-Line Coupler for mm-Wave CMOS Radios," *IEEE Microw. Wirel. Compon. Lett.*, vol. 20, no. 4, pp. 211–213, Apr. 2010.
- [3] H. Ding, G. Wang, K. Lam, D. Jordan, A. Zeeb, A. Bavisi, E. Mina, and B. Gaucher, "Modeling and implementation of on-chip millimeter-wave compact branch line couplers in a BiCMOS technology," in *Microwave Conference, 2007. European*, 2007, pp. 458–461.
- [4] M.-J. Chiang, H.-S. Wu, and C. K. C. Tzuang, "A CMOS 3-dB directional coupler using edge-coupled meandered synthetic transmission lines," in *Microwave Symposium Digest, 2008 IEEE MTT-S International*, 2008, pp. 771–774.
- [5] D. Titz, F. Ferrero, R. Pilard, C. Laporte, S. Jan, H. Ezzeddine, F. Ganesello, D. Gloria, C. Luxey, and G. Jacquemod, "New wideband integrated miniature branchline coupler for beamforming applications," in *Microwave Symposium Digest (MTT), 2012 IEEE MTT-S International*, 2012, pp. 1–3.
- [6] D. M. Pozar, *Microwave Engineering*. New York: Wiley, 1998, ch. 7.
- [7] A. L. C. Serrano, A. L. Franc, D. P. Assis, F. Podevin, G. P. Rehder, N. Corrao, and P. Ferrari, "Modeling and Characterization of Slow-Wave Microstrip Lines on Metallic-Nanowire-Filled-Membrane Substrate," *IEEE Trans. Microw. Theory Tech.*, vol. 62, no. 12, pp. 3249–3254, Dec. 2014.
- [8] "ANSYS HFSS." [Online]. Available: Ansys, "Ansoft HFSS, Canonsburg, PA, ver. 14," 2012. [Accessed: 19-Feb-2014].

Analysis and design of in-package transmit-arrays

G. R. Chamba Romero, F. Greco, L. Boccia, G. Amendola, E. Arnieri

University of Calabria DIMES – Microwave laboratory Rende, Italy;
luigi.boccia@unical.it; f.greco@dimes.unical.it

Abstract

In this work is presented a novel configuration of transmit-array antenna integrated in a standard open cavity package. The proposed configuration is designed for 77 GHz automotive applications. Typically, in these applications, the integration between the core chip and the antenna is complex, costly and it can significantly reduce the overall system efficiency. In this work, we show how transmit-array antennas can be employed to efficiently bridge the integration gap between the on-chip antenna and a larger radiating surface which can be integrated in the package in place of standard package covers.

Index Terms – Transmit-array; radar sensors; automotive radars.

I. INTRODUCTION

In the next few years, millimeter wave radars are expected to play a key role in reducing traffic fatalities [1]. Indeed, the number of radar sensors embedded into cars is continuously increasing. Most commonly used active safety methods include collision warning systems often combined with automatic steering and braking intervention, adaptive cruise control and blind spot detectors. In this perspective, it will be crucial to decrease the fabrication costs of 77 GHz automotive radars [2]. One of the main cost drivers is related to the integration of the radiating boards and the radar core chips. Usually, radar core chips are implemented using a single SiGe CMOS Monolithic Microwave Integrated Circuit (MMIC) which includes both digital and RF blocks which have to be connected to the radiating elements. This transition is usually complex to implement. A possible solution is given by embedded wafer level packaging (eWLP) [3] which allows the 3D integration of the silicon dies which are encapsulated within a reconstitution wafer. This wafer hosts redistribution layers which can be used to integrate antenna elements with efficient RF performance. Although this solution represents the most viable technology to integrate MMIC and antenna elements for the frequency range at hand, it becomes ineffective when larger radiating surfaces have to be used. In this paper, it will be investigated the possibility to use transmit-array antennas as a possible solution to efficiently bridge the integration gap between 77 GHz radar core chips and antenna arrays suitable for short range sensing. In the proposed configuration, the transmit-array element will be embedded in the protective cover of standard QFN open-cavity packages. In order to

efficiently design this structure, an analytical model of the transmit-array antenna has been developed. Analytical results have been validated simulating the entire configuration with HFSS. Analytical and full-wave results are in good agreement thus confirming and the correctness of the analytical approach and the effectiveness of the proposed transmit-array architecture which demonstrates an efficiency of 70 % with the exclusion of the feed losses.

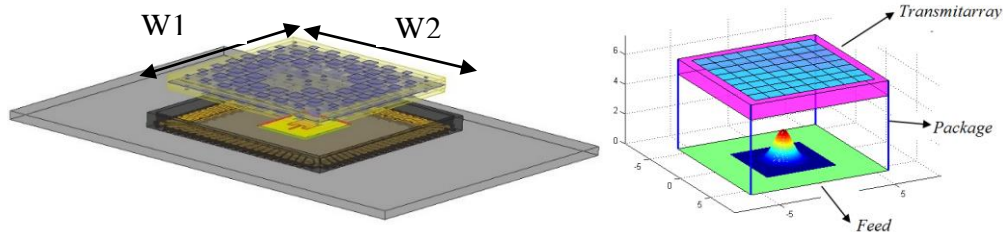


Fig.1 Transmit-array antenna integrated on a QFN package

II. TRANSMIT-ARRAY ANTENNA STRUCTURE

The complete structure of the proposed transmit-array is presented in Fig.1. The transmit-array is fed by a patch antenna which is directly integrated inside a standard QFN package having size 12x12mm. This antenna can be either monolithically integrated or simply printed on the package redistribution dielectric. The transmit-array is placed at a distance D from the feed and it has an aperture size of 10x10mm. The radiating efficiency of the transmit-array is given by $\eta = \eta_{FS} \cdot \eta_{IL} \cdot \eta_{SO}$ where η_{FS} is the efficiency of the focal source, η_{IL} is the illumination efficiency while η_{SO} is the spillover efficiency.

III. UNIT CELL DESIGN

The most important step in designing transmit-array antennas consists in obtaining a correct representation of the signal transmitted by each cell. To this end, it is necessary to evaluate the amplitude and the phase of the scattered field at the surface of a single transmit-array cell. For the

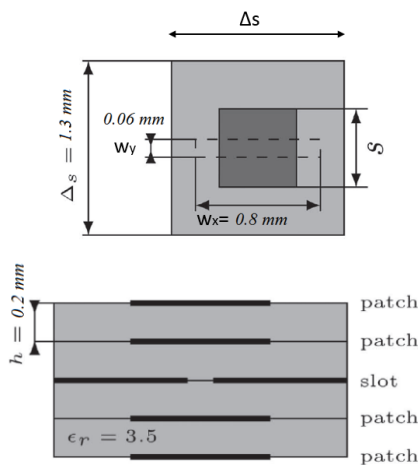


Fig. 2 Geometry of the unit cell.

case at hand, a unit cell based of four stacked patches coupled by a slot has been used [4]. The dimensions of all the patches are equal and the phase is controlled by jointly changing the side length s of all stacked patches that compose the cell. The cell size is $\Delta_s \times \Delta_s$, the aperture size is $w_x \times w_y$ as shown in Fig. 2. The structure is printed on Arlon AD350A ($\epsilon_r=3.55$) and its height is equal to 0.2mm, as shown in Fig. 2.

The behavior of the unit cell has been simulated using HFSS in an infinite array configuration. The phase of the transmission coefficient has been

evaluated for different sizes of the patch and at different angles of

incidence. As it can be observed in Fig. 3, a phase range variation higher than 320° can be achieved by varying the patch size from 0.3 to 0.95mm. The phase remains stable when the incident angle varies from 0 to 60° . However, at higher angles the transmission amplitude is subject to variations higher than 5dB. Variations of amplitude higher than 10 dB are found for $\theta=85^\circ$.

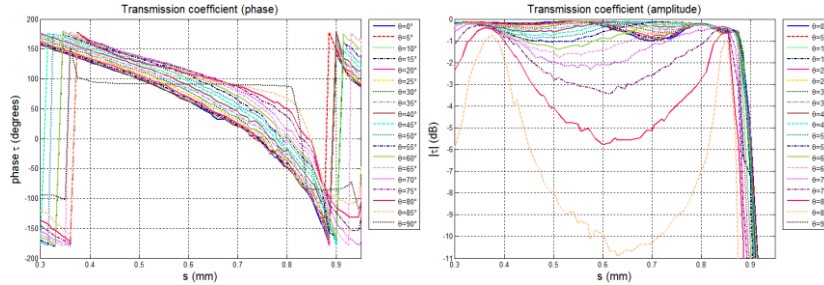


Fig. 3 Simulated transmission coefficient of a transmit-array unit cell as a function of patch size.

IV. ANALYTICAL MODEL

An analytical model of the transmit-array structure has been developed.

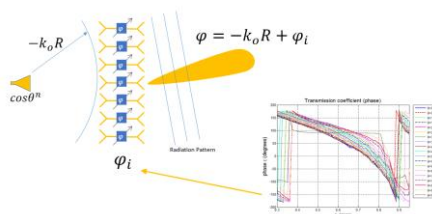


Fig. 4 Analytical model of the transmit-array

The transmit-array has been represented following the approach depicted in Fig. 4. As it can be observed, the feed has been firstly modeled using a $\cos^N \theta$ function for the amplitude and a point source model for the phase variations. Each unit cell, has been represented considering a $\cos \theta$ function for the radiated field along with the actual transmission coefficients (in amplitude and phase) shown in Fig. 3. In

Fig. 5 are shown the results in terms of gain, directivity and efficiency as

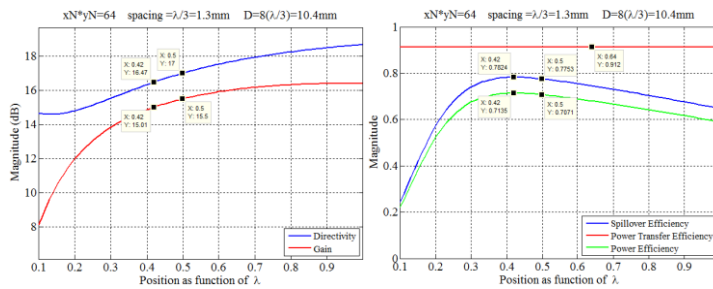


Fig.5 Directivity, gain and efficiency computed using the analytical model. $F=\lambda/2=1.95\text{mm}$

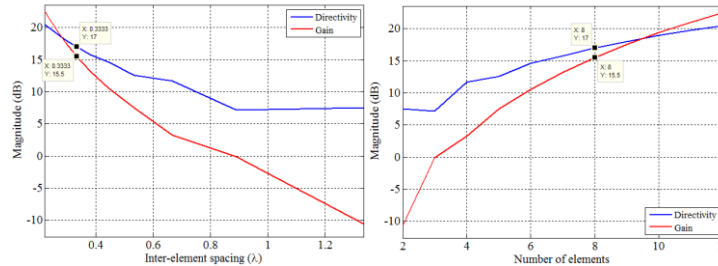


Fig.6 Directivity and gain as a function of inter-element spacing computed using the analytical model.

a function of F when $D=\lambda/2$ while in Fig. 6 are shown the results as a function of inter-element spacing taking into account the value of $F=0.5\lambda$. The value of the directivity decreases as the inter-element spacing increases reaching a maximum in terms of efficiency when the inter-element spacing is equal to 0.3λ .

V. VALIDATION OF THE STUDY WITH HFSS

The proposed configuration has been designed taking into account an 8×8 transmit-array with an inter-element spacing equal to $\lambda/3$ in both planes. The nominal operating frequency is equal to 77GHz while F is equal to 0.5λ . The entire structure has been simulated using the analytical model whose results have been then validated using HFSS. Analytical and full-wave radiation patterns are shown in Fig. 6. As it can be observed, thanks to the uniform response of the unit-cells with respect to the incidence angles, it is possible to achieve a gain of about 19 dBi even though F/D is equal to 0.2. Moreover, the analytical model is well matched with the full-wave simulations with limited differences in the side lobes. The efficiency of the overall structure is around 70%.

VI. CONCLUSION

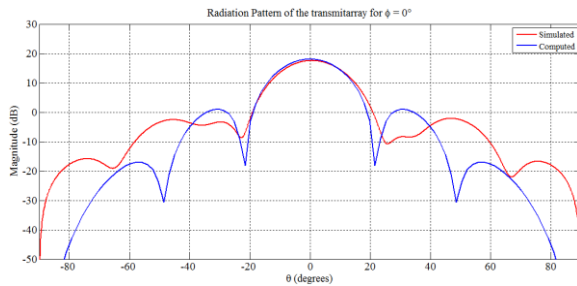


Fig.7 Radiation pattern at 77GHz

A transmit-array operating in the 77 GHz automotive band have been studied numerically and experimentally. The proposed configuration employs transmit arrays to bridge the gap between monolithically integrated antennas and the radiating elements which are integrated

as a cover of a standard open-cavity package. An analytical model has been developed to design the proposed structure and it has been validated through HFSS simulations.

REFERENCES

- [1] J. Wenger, "Automotive radar - status and perspectives," in *IEEE Compound Semiconductor Integrated Circuit Symposium, 2005. CSIC '05*, 2005, p. 4 pp.-.
- [2] J. Hasch, E. Topak, R. Schnabel, T. Zwick, R. Weigel, and C. Waldschmidt, "Millimeter-Wave Technology for Automotive Radar Sensors in the 77 GHz Frequency Band," *IEEE Trans. Microw. Theory Tech.*, vol. 60, no. 3, pp. 845–860, Mar. 2012.
- [3] C. Wagner, J. Böck, M. Wojnowski, H. Jäger, J. Platz, M. Treml, F. Dober, R. Lachner, J. Minichshofer, and L. Maurer, "A 77GHz automotive radar receiver in a wafer level package," in *2012 IEEE Radio Frequency Integrated Circuits Symposium*, 2012, pp. 511–514.
- [4] E. Plaza, G. Leon, S. Loredó, and F. Las-Heras, "A Simple Model for Analyzing Transmit-array Lenses," *IEEE Antennas Propag. Mag.*, vol. 57, no. 2, pp. 131–144, Apr. 2015.

LINEAR PROGRAMMING RELAXATION IN 3D ELECTROMAGNETIC CONSTRAINED POWER FOCUSING

Domenica A. M. Iero⁽¹⁾

⁽¹⁾ DIIES, Univ. Mediterranea di Reggio Calabria, Via Graziella, Loc.
Feo di Vito, 89100 Reggio Calabria
domenica.iero@unirc.it

Abstract

An innovative and computationally efficient power focusing approach is developed and assessed. It relies on the linear relaxation of the original NP-hard problem to find a suitable starting point for solving it by means of fast local search algorithms.

Index Terms – Energetic Applications of Microwaves, Optimal Focusing, Biomedical Applications of Microwaves, Hyperthermia, Antenna synthesis.

I. INTRODUCTION

The canonical problem of spatially focusing a field into a target point is relevant in many engineering areas [1,2]. It usually consists in defining the excitation set, the problem's actual degrees of freedom, of an array antenna, whose geometry is fixed a priori.

The vector nature of an electromagnetic field in a 3D scenario set important challenges in the array synthesis as the corresponding power focusing problem is a non-deterministic polynomial-time hard (NP-hard) [3,4]. A possible solution to this challenging problem is Optimal Constrained Power Focusing (OCPF) approach [5]. OCPF provides a flexible power shaping while guaranteeing the optimality of the solution found and it relies on the formulation of the focusing problem as several Convex Programming (CP) ones. By doing this the intrinsic computational burden of the original NP-hard Constrained Power Focusing (CPF) problem is counteracted achieving the globally optimal solution without global optimization techniques [6].

In this paper an innovative and computationally efficient CPF strategy is presented. It relies on a Linear Relaxation of the original NP-hard CPF problem. The Convex Relaxation is an important tool for tackling NP-hard problems that has already found application in several scientific areas [7], and which we want to apply in an original way to the CPF problem. Differently from OCPF, by exploiting the presented Linear Relaxation tool, the CPF problem can be tackled in a very efficient way, by just solving few (2^4) CP problems. However this simplification of the original NP-hard CPF problem leads to the loss of the optimality guarantee. Therefore the LRF solution is not the globally best solution

and, saying in other words, there may be an alternative excitation's set which outperforms the LRF one.

Anyway it is important to stress that when the LRF solution is not the globally optimal, it provides some important information about the optimal research space. Therefore it can be used as a starting point for CPF optimization which can be efficiently performed by means of local search algorithms.

II. LINEAR RELAXATION AND CONSTRAINED POWER FOCUSING

Let us consider an interest 3D domain Ω surrounded by an array of N elementary electric sources, in the frequency domain, the general focusing problem can be conveniently stated as a power focusing problem, i.e.

Find the complex excitations I_n ($n = 1, \dots, N$) of the given sources such to

$$\max |\mathbf{E}(\underline{\mathbf{r}}_T)|^2 \quad (1.a)$$

subject to

$$|\mathbf{E}(\underline{\mathbf{r}})|^2 < \mathcal{UB}(\underline{\mathbf{r}}) \quad \underline{\mathbf{r}} \in \Omega \setminus \Pi(\underline{\mathbf{r}}_T) \quad (1.b)$$

wherein $\underline{\mathbf{r}}_T$ denotes the target point location, $\mathbf{E}(\underline{\mathbf{r}}) = \sum_{n=1}^N I_n \Phi_n(\underline{\mathbf{r}})$, $\mathbf{E}(\underline{\mathbf{r}}) = E_x(\underline{\mathbf{r}})\mathbf{i}_x + E_y(\underline{\mathbf{r}})\mathbf{i}_y + E_z(\underline{\mathbf{r}})\mathbf{i}_z$, $\mathcal{UB}(\underline{\mathbf{r}})$ is a “mask” (non-negative arbitrary) function that enforces upper bound constraints on the power deposition everywhere but in the neighborhood of the target point, that is the focal area $\Pi(\underline{\mathbf{r}}_T)$.

The optimization problem (1) is non-linear and belongs to the class of NP-hard problems [4,5]. The strategy developed to cope with this kind of problem relies on the observation that, fixing the phase of one component of the field as a reference in the direction $\underline{\mathbf{r}}_T$, the power focusing problem (1) can be conveniently formulated as

Find the complex excitations I_n ($n = 1, \dots, N$) of the given sources such to

$$\max [\Re[E_x(\underline{\mathbf{r}}_T)]^2 + \Re[E_y(\underline{\mathbf{r}}_T)]^2 + \Im[E_y(\underline{\mathbf{r}}_T)]^2 + \Re[E_z(\underline{\mathbf{r}}_T)]^2 + \Im[E_z(\underline{\mathbf{r}}_T)]^2] \quad (2.a)$$

subject to

$$\Im[E_x(\underline{\mathbf{r}}_T)]^2 = 0 \quad (2.b)$$

$$|\sum_{n=1}^N I_n \Phi_n(\underline{\mathbf{r}})|^2 < \mathcal{UB}(\underline{\mathbf{r}}) \quad \underline{\mathbf{r}} \in \Omega \setminus \Pi(\underline{\mathbf{r}}_T) \quad (2.c)$$

which allows to take advantage of the linear relaxation obtaining the following Linearly Relaxed Focusing (LRF) problem

Find the complex excitations I_n ($n = 1, \dots, N$) of the given sources such to

$$\max [|\Re[E_x(\underline{\mathbf{r}}_T)]| + |\Re[E_y(\underline{\mathbf{r}}_T)]| + |\Im[E_y(\underline{\mathbf{r}}_T)]| + |\Re[E_z(\underline{\mathbf{r}}_T)]| + |\Im[E_z(\underline{\mathbf{r}}_T)]|] \quad (3.a)$$

subject to

$$\Im[E_x(\underline{r}_T)]^2 = 0 \quad (3.b)$$

$$|\sum_{n=1}^N I_n \Phi_n(\underline{r})|^2 < \mathcal{UB}(\underline{r}) \quad \underline{r} \in \Omega \setminus \Pi(\underline{r}_T) \quad (3.c)$$

which can be explicitly written as

Find the complex excitations I_n ($n = 1, \dots, N$) of the given sources such to

$$\max[\Re[E_x(\underline{r}_T)] \mp \Re[E_y(\underline{r}_T)] \mp \Im[E_y(\underline{r}_T)] \mp \Re[E_z(\underline{r}_T)] \mp \Im[E_z(\underline{r}_T)]] \quad (4.a)$$

subject to

$$\Im[E_x(\underline{r}_T)]^2 = 0 \quad (4.b)$$

$$\Re[E_y(\underline{r}_T)] \geq 0 \text{ or } \Re[E_y(\underline{r}_T)] \leq 0 \quad (4.c)$$

$$\Im[E_y(\underline{r}_T)] \geq 0 \text{ or } \Im[E_y(\underline{r}_T)] \leq 0 \quad (4.d)$$

$$\Re[E_z(\underline{r}_T)] \geq 0 \text{ or } \Re[E_z(\underline{r}_T)] \leq 0 \quad (4.e)$$

$$\Im[E_z(\underline{r}_T)] \geq 0 \text{ or } \Im[E_z(\underline{r}_T)] \leq 0 \quad (4.f)$$

$$|\sum_{n=1}^N I_n \Phi_n(\underline{r})|^2 < \mathcal{UB}(\underline{r}) \quad \underline{r} \in \Omega \setminus \Pi(\underline{r}_T) \quad (4.g)$$

Then, LRF problem (4) corresponds to the solution of 2^4 Convex programming problems as in each of the hyper-quadrants, defined by (4.c)-(4.f), (4.a) is a linear function of the unknowns I_n and constraints (4.b-4.g) define a convex set in the space of the unknowns I_n .

Therefore the solution of the original NP-hard problem is reduced to the resolution of 2^4 Convex programming sub-problems, which can be efficiently done by means of local search algorithms. Moreover those CP sub-problems are independent from each other and can be solved efficiently by taking advantage of the parallel programming toolboxes.

Then one can identify the best LRF solution selecting the sub-problems' solution which provides the highest $|\mathbf{E}(\underline{r}_T)|^2$ value. This solution cannot be considered as the globally optimal one of the original NP-hard problem (1) due to the relaxation process. Anyway it can be exploited as a starting point for solving NP-Hard CPF problem (1) by means of local search algorithms as if the starting point is in the attraction region of the globally best solution of the NP-Hard CPF problem a local search procedure will identify its globally best solution.

It is worth to note that this procedure allows a computationally efficient resolution of an NP-Hard problem without recurring to global search algorithms [7].

III. NUMERICAL ANALYSIS AND CONCLUDING REMARKS

A preliminary numerical analysis has been conducted in a simplified scenario represented in Fig.1a. It consists of an ellipsoidal lossless object ($\epsilon_{ellips} = 1.5$, $a = 0.75\lambda_b$, $b = 0.55\lambda_b$) embedding a sphere ($\epsilon_{sph} = 2$, $r_{sph} = \lambda_b/8$), whose center is the desired target point

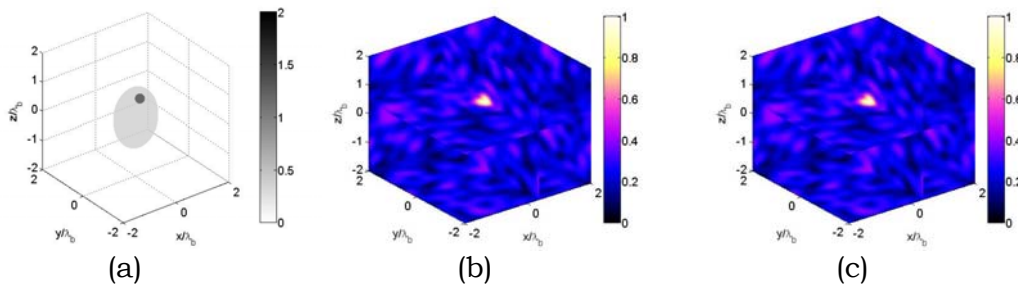


FIG. 1 – Focusing in an heterogeneous medium: (a) permittivity profile, (b) intensity of the focused CPF-LRF field $|E(\underline{r})|$, (c) intensity of the focused OCPF $|E(\underline{r})|$.

$\underline{r}_T = (0.35\lambda_b, 0.25\lambda_b, 0.4\lambda_b)$. λ_b is the wavelength in the background medium, which, in this case, is free space. The applicator to be synthesized is a spherical array of $N = 58$ half wavelength antennas polarized along the ϑ and φ directions.

Fig.1b reports the focused field's amplitude obtained using the LRF solution as a starting point for the CPF optimization (1). The CPF-LRF field shows to be well focused into the target point which corresponds to the globally optimal solution provided by OCPF (see Fig.1c). It is also worth to notice that LRF procedure allows to find the suitable starting point necessary to solve the overall CPF problem (1) efficiently by means of local search algorithms, while proving a solution which is equivalent to the globally best solution in terms of focusing performances.

A more detailed numerical analysis will be presented at the conference.

REFERENCES

- [1] A. J. Fenn, "Adaptive Phased Array Thermotherapy for Cancer," *Artech House, London, UK*, 2008.
- [2] T. W. Wong, "Use of microwave in processing of drug delivery systems," *Curr. Drug. Deliv.*, vol. 5(2), pp. 77–84, 2008.
- [3] D.A.M. Iero et al. "Constrained power focusing of vector fields: an innovative globally optimal strategy," *J. Electromagnet. Wave*, vol. 29 (13), pp. 1708–1719, 2015.
- [4] D. G. Luenberger and Y. Ye "Linear and Nonlinear Programming," *International Series in Operations Research & Management Science*, Springer, 3rd edition, 2008.
- [5] D. H. Wolpert, and W. G. Macready, "No free lunch theorems for optimization," *IEEE Trans. Evol. Comput*, vol. 1(1), pp. 67–82, 1997.
- [6] J. Robinson and Y. Rahmat-Samii. "Particle swarm optimization in electromagnetics," *IEEE Antennas Propagat. Trans.*, vol. 52 (2), pp. 397–407, 2004.
- [7] Z. Luo et al., "Semidefinite relaxation of quadratic optimization problems," *IEEE Signal Process. Mag.*, vol. 27 (3), pp. 20–34, 2010.

**A STEP-WISE MICROWAVE IMAGING STRATEGY
FOR LANDMINE DETECTION
MODELLING AND NUMERICAL ASSESSMENT**

A. Brancaccio^(1,7), G. Maiello^(1,7), M.D. Migliore^(2,7), D. Pinchera^(2,7),
F. Schettino^(2,7), T. Isernia^(3,7), M. Ambrosanio^(4,7), V. Pascazio^(4,7),
L. Di Donato^(5,7), L. Crocco^(6,7)

⁽¹⁾ DIII, Seconda Università di Napoli

⁽²⁾ DIEI, Univ. di Cassino e del Lazio Meridionale

⁽³⁾ DIIES, Univ. Mediterranea di Reggio Calabria

⁽⁴⁾ Dipartimento di Ingegneria, Univ. di Napoli Parthenope

⁽⁵⁾ DIEEI, Università di Catania, Catania

⁽⁶⁾ IREA-CNR, Napoli

⁽⁷⁾ CNIT

⁽⁸⁾ adriana.brancaccio@unina2.it

Abstract

The problem of mine detection by means of electromagnetic waves is dealt with. The paper summarizes the authors' contribution to the European project D-Box. Three complementary techniques for data processing in a short range detection configuration are presented and applied to a common numerical test-bed.

Index Terms – antenna, compressive sensing, electromagnetic inverse scattering, mine detection.

I. INTRODUCTION

A complete step-wise Microwave Imaging Strategy for landmine detection and characterization has been proposed and tested in both numerical and experimental scenarios. The proposed novel approach is based on a succession of three different steps, which increases the useful information on the unknown buried objects by means of step-wise refinements. More in detail, the different “levels” of the processing are: localization of the target in the scan plane; in-depth target localization and shape imaging; “quantitative” characterization of the unknown objects, defining their nature and classification (i.e., rock, mine, plastic objects, etc.).

The whole processing takes advantage of the useful independent information coming from frequency diversity.

Before moving towards the experimental case, the proposed methodology has been tested in a controlled, numerical environment in order to assess its retrieving performance. The numerical test-bed consisted of a multiview-multistatic configuration with a horn antenna (16.7 dBi gain) with both Anti Personal (AP) and Anti Tank (AT) like mine phantoms.

Such a validation has been carried out for dielectric as well as metallic mines.

II. NUMERICAL RESULTS

The soil is modelled by a $2.5\text{m} \times 2.5\text{m} \times 1\text{m}$ box having relative permittivity 4 and conductivity 0.01 S/m , embedded in a $3.3\text{m} \times 3.3\text{m} \times 1.3\text{m}$ box of absorbing material having the same relative permittivity 4 and conductivity 0.1 S/m . Source is a horn antenna (16.7 dBi gain), placed at two meters above and rotated by 30 degrees toward the soil as shown in Fig. 1. The three rectangular components of the field are evaluated at soil-air interface over a uniform grid along x and y having 50 mm step. Data are simulated at three frequencies: 0.9 GHz , 1.0 GHz and 1.17 GHz , and for different positions of the transmitting antenna along the soil box perimeter. Mines are modelled by circular cylinders buried at 50 mm from the surface of the soil: metallic AT mine radius 100 mm , height 100 mm , material PEC (perfect electric conductor); dielectric AP mine radius 50 mm , height 50 mm , relative permittivity of the material equal to 2.7 . In order to obtain the scattered field, measurements in absence of mines have been simulated and subtracted to those calculated in presence of mines.

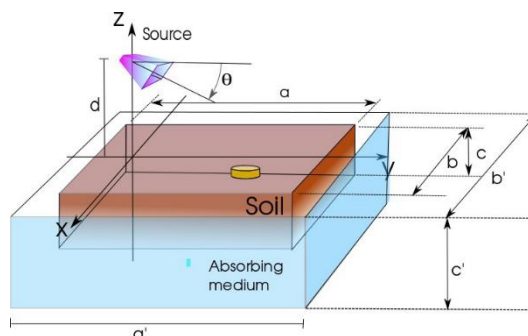


FIG. 1 – Numerical test-bed employed in the numerical assessment.

First step: localization of the target in the scan plane has been carried out by exploiting an equivalent-surface-current approach. The scattered field caused by an external single frequency electromagnetic source is seen as the field radiated by equivalent surface electric currents located over a plane at a depth smaller than the scatterers' one. The support of such equivalent currents is assumed as the unknown of the inverse problem. In this way the mathematical relationship between data (the scattered field) and unknown (the equivalent surface current) is linear where its kernel depends on either far or near field measurement conditions occur. It has to be stressed that the model does not require knowledge of the incident field, except for its frequency. The inversion result is a 2D image representing the reconstructed current, whose support indicates presence and position of scattering objects (mines). The output of the first

step is a two-dimensional map of the position of the support of the objects “projected” on the surface plane (Fig. 2).

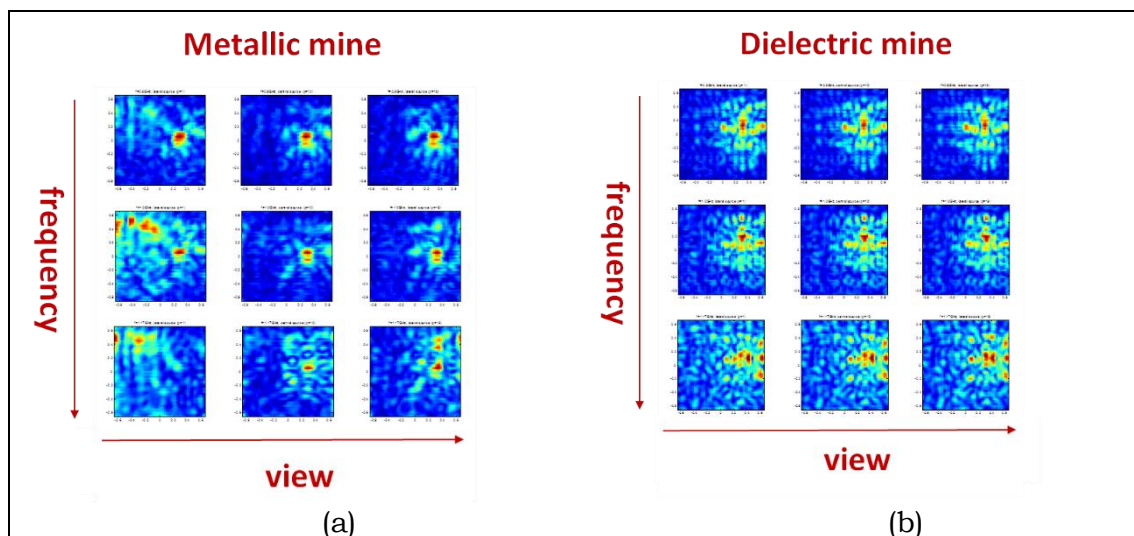


FIG. 2 – First-step recoveries for metallic (a) and dielectric (b) mines

Second step: in-depth target localization and shape imaging has the aim of improving the information on the detected objects providing approximately their shape and in-depth location. It performs single-frequency recoveries by exploiting the Linear Sampling Method (LSM), as shown in Fig. 3.

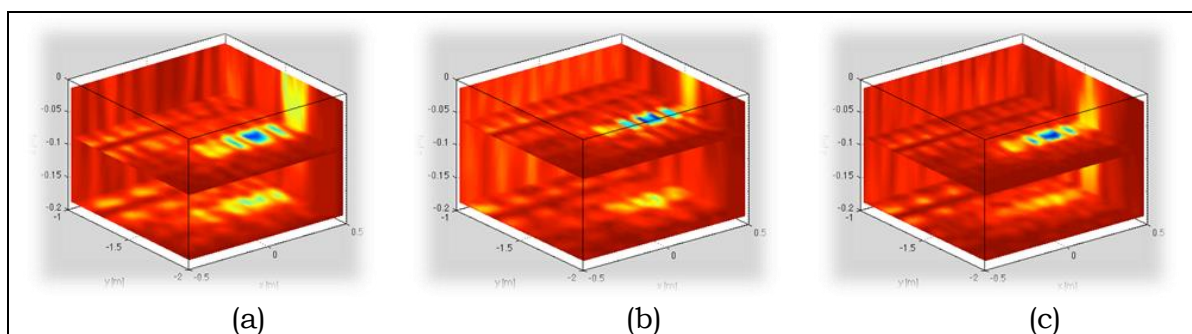


FIG. 3 – Second-step single-frequency recoveries by exploiting LSM:
 (a) 900 MHz, (b) 1 GHz and (c) 1.17 GHz.

Third step: quantitative characterization of buried targets thanks to the reduction of the imaging area, this last step uses a hybrid strategy which exploits the compressive sensing (CS) theory and the quantitative “virtual experiments” (VE) framework [3].

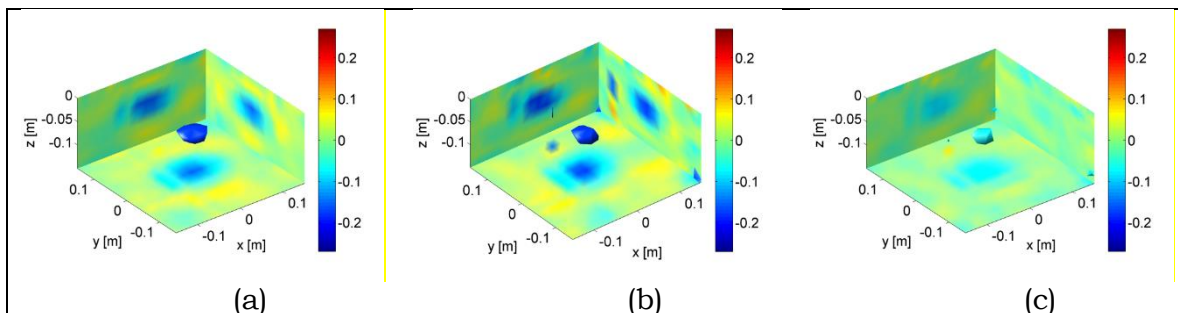


FIG. 4 – Third-step single-frequency single-component scattered field recoveries by exploiting CS: (a) x-component, (b) y-component and (c) z-component.

III. CONCLUSIONS

The proposed strategy manages in retrieving both the shape and locations of buried unknown objects quite well, as proved in the numerical analysis. Some advantages of the proposed methodologies are related to retrieving qualitative information on targets location (i.e., shape), reducing the number of measurements compared to standard tomographic approaches and no need of expert user to understand the retrieved maps. After the numerical validation, the processing has been tested preliminarily in a laboratory-controlled situation [1] and then directly on a sandy soil. During the experimental campaign, both horn antenna and a home-made ultra-wide-permittivity antennas (UWPA) have been tested [2]. Such experimental validation is in progress and will be shown at the Conference.

ACKNOWLEDGEMENT

This project has received funding from the European FP7 initiative under grant agreement no 284996.

REFERENCES

- [1] A. Brancaccio, A. Del Vecchio and G. Maiello, “An algorithm for mine detection and localization by single frequency near field measurements”, *ICEAA 2015*, September 2015, Torino, pp. 1512 - 1515.
- [2] D. Pinchera, M.D. Migliore, F. Schettino, “ An Ultra Wide Permittivity Antenna (UWPA) for Reliable Through-Wall Communications”, *IEEE Trans. on Ant. and Prop.*, vol. 61(2), 2013, pp. 957-960, DOI 10.1109/TAP.2012.2223439
- [3] Di Donato L., L. Crocco, R. Palmeri, T. Isernia “Exploiting Sparsity and Field Conditioning in Subsurface Microwave Imaging of Non-weak Buried Targets”, *Radio Science*, in print.

NEAR-FIELD WPT TO LOOSELY-COUPLED SMALL IMPLANTS

A. Pacini, F. Berra, A. Costanzo, F. Mastri, D. Masotti

DEI, University of Bologna, Viale Risorgimento 2, Bologna, Italy
alex.pacini2@unibo.it

Abstract

We present a new Resonant Wireless Power Transfer system based on a geometrically optimized coil and a double immittance inverter design. The receiver Tee immittance inverter is obtained by a coil identical to the receiver one, but orthogonally placed, whereas a discrete inductor is deployed on the transmitter side. The reference link consists of the receiving coil (implanted in bio-tissue/blood) and the external conformal transmitting coil at a distance of 50mm (20mm in blood, 30mm in free-space): the overall link design focuses on transmitting coil optimization for maximum coupling factor. The simulated link efficiency at 6.78 MHz reaches the promising value of 14.4%, with a load of 55 Ohm. The influence of coils copper thickness is also investigated: the replacement of the standard 35 μm -thick copper with a 0.5 mm-thick one allows to achieve a more than twice efficiency of 34%.

Index Terms – Conformal coil, Inductive Coupling, Near-Field WPT.

I. INTRODUCTION

Evolution pace of electronic devices is orders of magnitude faster than that of batteries, which still presents health issues and power density limitations, when powering of implantable devices is considered. The alternative is the Wireless Power Transfer (WPT) to biomedical micro-systems and this can be done by following multiple approaches [1]-[3]. An interesting solution is the Inductive Resonant WPT which takes advantage from the nonmagnetic structure of human tissues and makes the system less sensible to different use cases. Indeed, while the main resonant frequency [3] remains the same for different tissues and different distances, the optimal load depends on the coupling factor [4] and hence on the coils distance and alignment. The use of secondary resonances [3] or multiple coils [5] can help in reaching a flat coupling. In this paper we present a novel solution both from the transmitter and receiver sides viewpoint: a conformal TX coil allows superior coupling performance if compared to standard flat ones; the miniaturized RX coil is equipped with an orthogonal copy of itself acting as an immittance inverter for matching purposes. We focus on systems with standby consumption of few μW and rare peak consumption of some mW: hence, the optimal load condition should be a trade-off between these two states. The maximization of the overall link coupling factor is carried out by means of full-wave simulations.

II. LINK DESCRIPTION

A. Coupled Coils

The layout-wise description of the coils is fundamental to accurately calculate the link power transfer efficiency. Fig. 1 shows the final dimensions of the coils and the topological choices adopted in the link operating at 6.78 MHz: the rectangular Rx-coil is described in Fig. 1(a), whereas Fig. 1(c) shows the orthogonal placement of two identical coils for matching purposes on the RX side: common FR4 1.5 mm-thick, with 35 μm -thick copper is used for coils realization; finally in Fig. 1(b) the conformal shape (a sector of a cylinder surface) of the TX coil is reported: the TX coil support is a curved plexiglass 5 mm-thick.

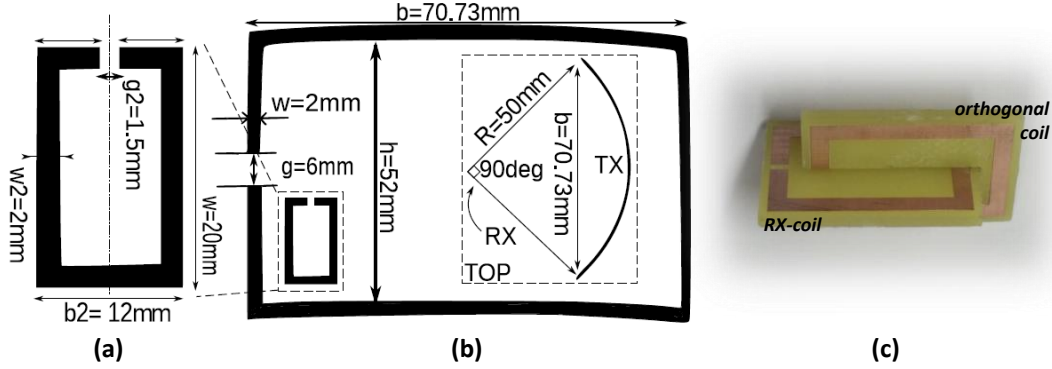


FIG. 1 (a) RX coil, and (b) conformal TX coil layouts (top view). The dashed box on right side of (b) is the schematic side view of the link: the circular sector shape of TX coil is 50 mm apart from RX coil. (c) picture of RX coil and its orthogonal copy, acting as immittance inverter.

In the following port 1, 2, and 3 corresponds to input TX-coil port, output RX-coil port, and orthogonal coil port, respectively. The coupling factor to be maximized is thus k_{12} :

$$k_{12} = \frac{\text{Im}(Z_{12})}{\sqrt{\text{Im}(Z_{11})\text{Im}(Z_{22})}} \quad (1)$$

where \mathbf{Z} represents the link impedance matrix. By referring to Fig.2, the link power transfer efficiency (η) is given by the fraction of the power transferred to the WPT link (P_{in}) that is then transferred to the load (P_{out})

$$\eta = \frac{P_{out}}{P_{in}} \quad (2)$$

To maximize the coupling factor, we focus on the external Tx coil (dimensions h and b in Fig.1), since the receiving one has to fulfill size constraints.

We start with a circular wire loop as TX coil shape: in this case the (quasi-static) magnetic field can be expressed as

$$B(z, R) = \frac{\mu_0 I}{2} \frac{R^2}{(R^2 + z^2)^{3/2}} \quad (3)$$

In Eq. 3, R is the loop radius while z is the distance from the loop centre. The derivative of $B(z;R)$ with respect to R indicates that the maximum of the field is located at $R = \sqrt{2}z$. Being z related to the fixed RX coil dimensions, this result is used as a starting point of the

electromagnetic optimization process. A significant improvement is achieved by resorting to a curved shape of the coil: for practical reasons, this suggests to pass to a rectangular conformal shape whose final layout is depicted in Fig.1(b). With respect to the starting flat and circular TX coil, a 30% improvement of the coupling factor is obtained.

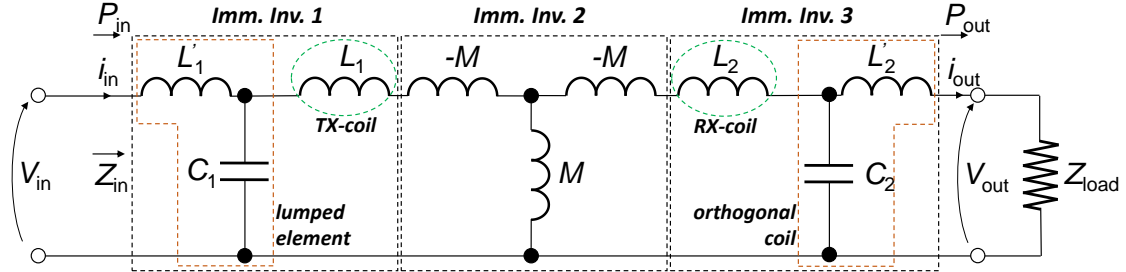


FIG. 2 – Complete schematic of the link using the Tee representation for the coupled inductors. The immittance inverters are indicated with boxes.

B. Entire Link

The whole link consists of 30 mm in free space and 20 mm in blood, and its schematic is given in Fig.2: the TX (in free-space) and RX (in blood) coupled inductors (L_1 and L_2) are sided by two immittance inverters [6]. In the ideal case of $L'_1 = L_1$ and $L'_2 = L_2$, the circuit provides a load transformation at the resonance frequency (6.78 MHz):

$$Z_{in} = \frac{\omega_r^2 L_1^2 L_2^2}{M^2 Z_{load}} \quad (4)$$

The design of the RX-immittance inverter (the orthogonal coil of Fig.2) must be done in such a way to minimize the coupling with both the RX and the TX coils. This is obtained by rotating of 90° a copy of the RX-coil and then by translating it of 4mm in order to avoid coils contact (see Fig.1(c)).

III. RESULTS

In Table I we report the simulated inductances of the coils and the coupling factors, along with the series parasitic resistances. From Tab. I, it can be evinced that the unwanted couplings of the orthogonal coil with the RX one (k_{23}) and with the transmitter (k_{13}) are small and can thus be neglected. The input inverter coil is easily obtained by using a remote lumped SMD inductor.

TABLE I – LUMPED ELEMENT SIMULATED VALUES

$L_1 = 200$ nH	$C_1 = 2.75$ nF	$M_{12} = -0.76$ nH	$k_{13} = -1.67 \times 10^{-5}$	$\text{Re}(Z_{11}) = 0.0718$ Ω
$L_2 = 27.9$ nH	$C_2 = 19.7$ nF	$k_{12} = -0.0103$	$k_{23} = 9.147 \times 10^{-6}$	$\text{Re}(Z_{22}) = 0.0187$ Ω

In Fig. 3, the efficiency plot is reported: a very promising maximum of 14.4% is achieved with $R_{load} = 55$ Ohm. It is worth noting that, by

increasing copper thickness up to 0.5mm, the efficiency is more than doubled ($\eta = 34\%$). Fig. 3 also outlines the effect of the output load on the the input impedance: the curve behaviour agrees with (4), and the high achieved values of $|Z_{in}|$ allow an easy matching with the needed input amplifier.

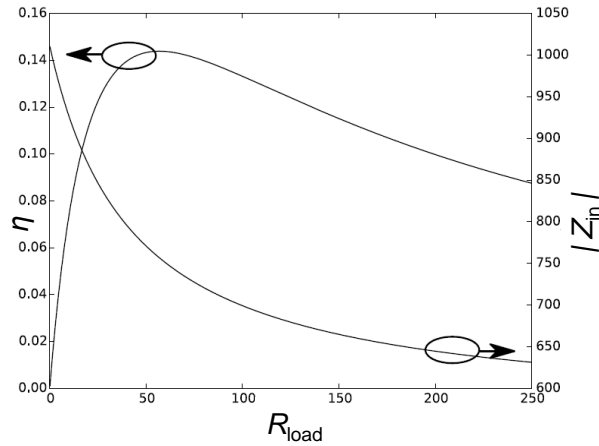


FIG. 3 – Efficiency and input impedance of the proposed link when loaded with R_{load} .

IV. CONCLUSIONS

We design an implantable Near-Field WPT system capable of an efficiency of 14.4% at a distance of 50mm. The transmitting coil size and shape are optimized, by making use of a conformal coil design. An input and output immittance inverters are used to rise the very low impedance values caused by the extremely small coupling factor.

REFERENCES

- [1] A. Costanzo, M. Dionigi, D. Masotti, M. Mongiardo, G. Monti, L. Tarricone, and R. Sorrentino, “Electromagnetic energy harvesting and wireless power transmission: A unified approach,” *Proceedings of the IEEE*, vol. 102, no. 11, pp. 1692–1711, nov 2014.
- [2] R. Bashirullah, “Wireless Implants,” *IEEE Microwave Magazine*, vol. 11, no. 7, pp. S14–S23, dec 2010.
- [3] F. Mastri, A. Costanzo, and M. Mongiardo, “Coupling-Independent Wireless Power Transfer,” *IEEE Microwave and Wireless Components Letters*, vol. 26, no. 3, pp. 222–224, 2016.
- [4] A. Costanzo, M. Dionigi, F. Mastri, M. Mongiardo, J. A. Russer, and P. Russer, “Design of magnetic-resonant wireless power transfer links realized with two coils: comparison of solutions,” *Int. J. Microw. Wireless Technol.*, vol. 7, no. 3-4, pp. 349–359, apr 2015.
- [5] A. Pacini, F. Mastri, R. Trevisan, A. Costanzo, and D. Masotti, “Theoretical and Experimental Characterization of Moving Wireless Power Transfer Systems,” *IEEE 10th European Conference on Antennas and Propagation*, Apr 2016, accepted for publication.
- [6] A. Costanzo, M. Dionigi, F. Mastri, M. Mongiardo, J. A. Russer, and P. Russer, “Rigorous network modeling of magnetic-resonant wireless power transfer,” *Wireless Power Transfer*, vol. 1, no. 1, pp. 27–34, mar 2014.

ALL-OPTICAL UNSCRAMBLING OF MIXED SPATIAL MODES ON A SILICON PHOTONIC CHIP

Francesco Morichetti¹, Andrea Annoni¹, Stefano Grillanda¹, Nicola Peserico¹, Marco Carminati¹, Pietro Ciccarella¹, Giorgio Ferrari¹, Emanuele Guglielmi¹, Marc Sorel², and Andrea Melloni¹

¹*Dipartimento di Elettronica, Informazione e Bioingegneria, Politecnico di Milano, via Ponzio 34/5, 20133 Milano, Italy*

²*School of Engineering, University of Glasgow, Glasgow, G12 8LT, UK*
francesco.morichetti@polimi.it

Abstract

We demonstrate all-optical unscrambling and reconstruction of four mixed spatial modes on a silicon photonic chip. Mode unscrambling is achieved by means of a cascaded Mach-Zehnder architecture that is sequentially reconfigured by individually monitoring each stage through integrated transparent detectors, namely Contact Less Integrated Photonic Probes (CLIPPs). Robust demultiplexing of 10 Gbit/s channels with less than -20 dB crosstalk is achieved over a bandwidth of several nanometers. Eye diagrams show that the quality of the unscrambled signals is not affected when four concurring mixed channels at the same wavelength are injected simultaneously in the device.

Index Terms – Integrated optics devices; Silicon; Multiplexing; Photodetectors

I. INTRODUCTION

Mode-division multiplexing (MDM) is now considered a promising approach to boost the capacity of optical fiber transmission [1]. However, such a new paradigm requires optical components capable to manipulate signals encoded on different orthogonal modes and mixed after propagation through a multimode link. Multiple-input multiple output (MIMO) photonic integrated architectures realizing reconfigurable mode (de)multiplexing and unscrambling have been recently proposed [2] and realized [3]. In these schemes the possibility to monitor individual channels multiplexed in the MDM signal is an essential feature to enable simple and robust tuning strategies. However, channel monitoring in MDM systems must be non invasive in order to preserve mode orthogonality. In this work we demonstrate all-optical unscrambling of four-mixed modes on a silicon photonic (SiP) chip. We exploit transparent photodetectors, realized through the non-invasive ContactLess Integrated Photonic Probe (CLIPPs) technology [4], to monitor the evolution of the modes intensity along a MIMO demultiplexer, without impairing mode orthogonality.

II. DESIGN AND FABRICATION

The scheme of the realized 4-channel all-optical MIMO unscrambler is shown in Fig. 1 (a). Four optical channels (Ch. A – Ch. D) are mixed by

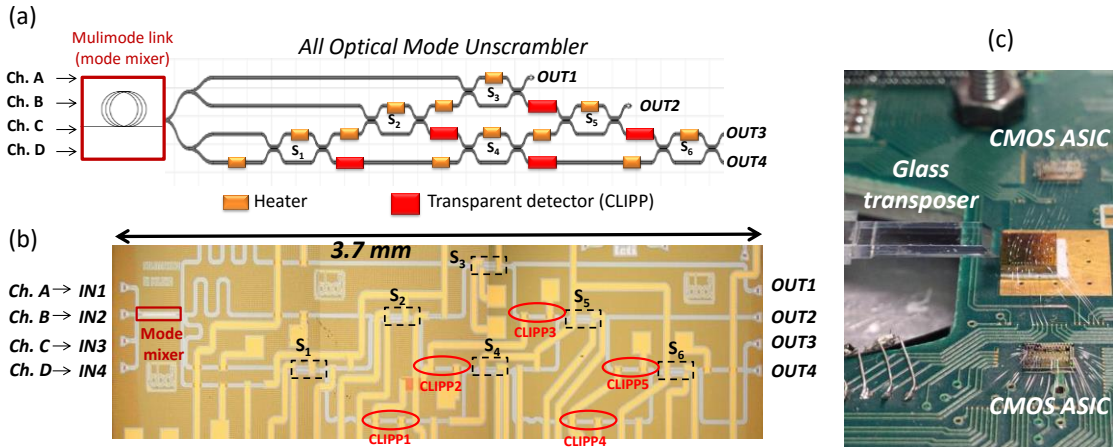


Fig. 1: (a) Schematic and (b) top-view microphotograph of the 4-channel MIMO demultiplexer realized on a SiP platform. A multimode waveguide is used to induce mode mixing of the input channels (A,B,C,D). (c) Photograph of the SiP chip wire-bonded to two readout CMOS electronic ASICs and integrated onto the same printed circuit board. A glass based transposer is used to couple the four channels into the SiP circuit.

means of an on-chip multimode link (a multimode waveguide section). The all-optical MIMO unscrambler is made using 6 integrated Mach-Zehnder Interferometers (S_i , $i = 1, 2, \dots, 6$), that can be sequentially tuned in order to reconstruct each channel at each output port (OUT1–OUT4). For instance, to reconstruct Ch. x ($x = A, B, C, D$) at port OUT1, stages S_1 , S_2 and S_3 need to be sequentially biased in order to minimize Ch. x power at the output lower branch of each stage. With such architecture, transparent detectors are needed to monitor the switching state of each stage without introducing optical loss that would impair mode orthogonality. The 4-channel MIMO demultiplexer was realized on a 220-nm SiP platform through LETI-ePIXfab multi-project-wafer run. A top-view photograph of the Si chip is shown in Fig. 1(b). Two thermal actuators are integrated in each switching stage S_i to control the relative phase of the optical field at the input ports and between the inner arms of each MZI. A CLIPP detector is integrated at one output port and used to monitor individually the switching state of each MZI. As shown in Fig. 1(c), the four channels are coupled to the SiP through a glass based transposer [5] enabling to inject the signals coming from four single-mode-fibers to four input grating couplers. The SiP chip is mounted on PCB and bridged to a CMOS electronic ASIC, enabling simultaneous read out of the integrated CLIPPs and providing the driving voltage for the thermal actuators [6].

III. EXPERIMENTAL RESULTS

Figure 2 show the crosstalk level, for an input channel Ch. x , when the demultiplexer is configured to reconstruct Ch. x at the output port 1. To measure the crosstalk we sequentially tuned the switching stages S_1 - S_3 by minimizing the light intensity of the Ch. x at the lower output branch

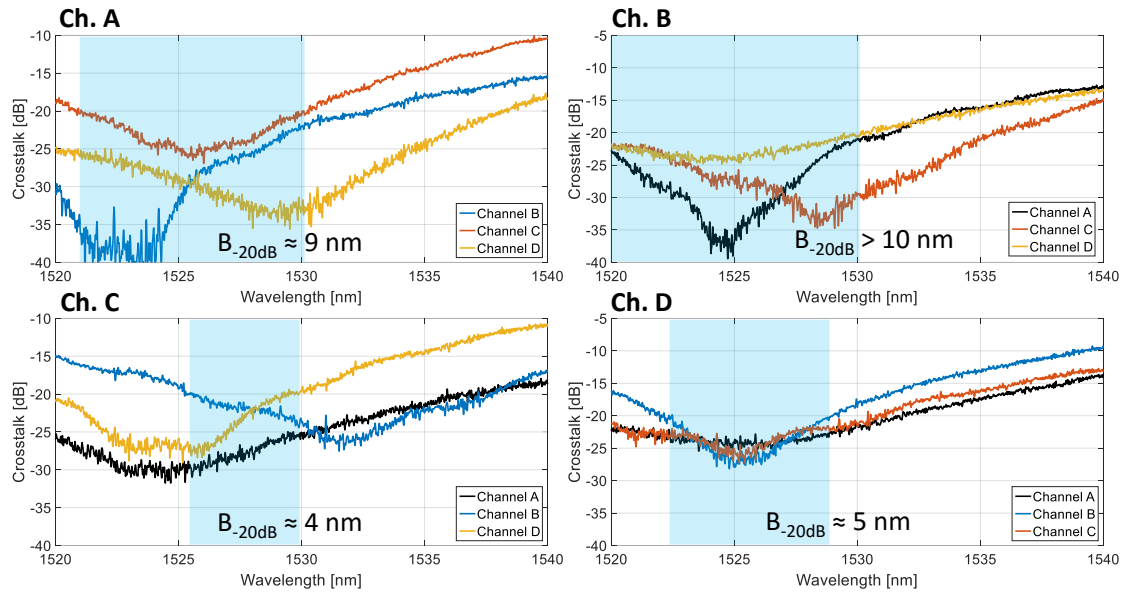


Figure 2: Crosstalk spectra for the four extracted channels (Ch. A - Ch. D) at port OUT1; the label at the top left corner of each graph identifies which channel is reconstructed at the output port 1; the curves show the crosstalk as a function of wavelength for the remaining “interfering” channels. Bandwidths with a crosstalk of -20dB are highlighted for each of the possible configuration.

of stages S1-S3 by using CLIPPs 1-3, respectively. The crosstalk over wavelength was obtained by measuring, with of a tunable laser source and an optical spectrum analyzer, the contribute to the output power of Out 1 for each of the four input channel. As visible in Fig. 2, the performances obtained vary between the different configuration of the demultiplexer; however, bandwidths with crosstalk lower than -20 dB and spanning over several nanometers were obtained for each of the four configurations.

Figure 3 shows the eye diagrams of two unscrambled channels (Ch. A and C) as in the two corresponding cases in Fig. 2. Four 10 Gbit/s OOK NRZ channels sharing the same carrier wavelength of 1528 nm are achieved by splitting and decorrelating through a few-km-long fiber coils the data stream generated from a LiNb Mach-Zehnder modulator. The modulator is driven with a pattern $2^{31}-1$ bit long generated by a PRBS; the power levels of the four data channels were equalized by means of variable optical attenuators and polarization controlled independently.

To prove the performances of the MIMO unscrambler we measured the eye diagrams of the reconstructed channel for an increasing number of concurrent channels. The panels in Fig. 2 show that the eye diagram remain unhindered as the concurring channels are turned on, demonstrating that the device is performing the unscrambling of the four mixed modes. To further prove the effect of the MIMO unscrambler, the rightmost panel show the eye diagram of the output signal when the device is not configured to reconstruct any input optical channels.

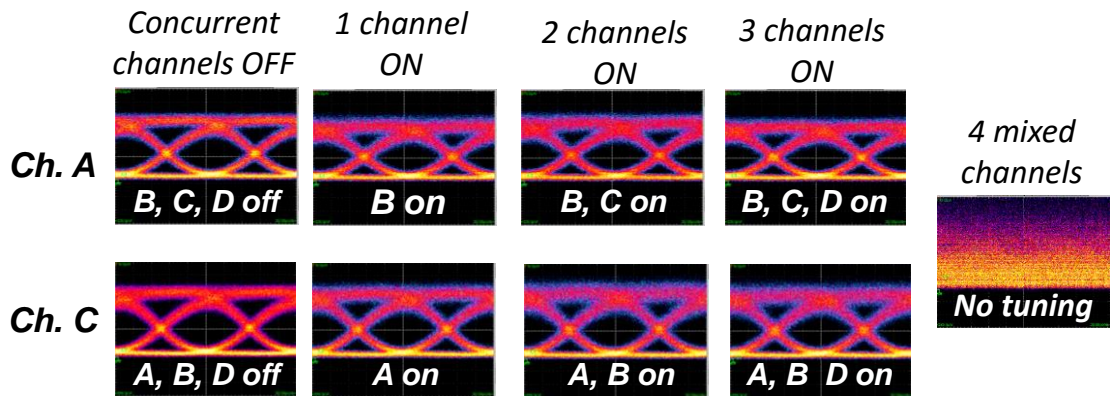


Fig. 3: Measured eye diagrams of the unscrambled 10 Gbit/s OOK NRZ modes. The upper row shows the eye diagrams of the input Ch.A as the concurring channels are turned ON; the lowest row shows instead the unscrambling operation on the input Ch.C. The eye diagrams with 3 concurring channels ON can be compared with the rightmost panel which show the output when the circuit is not tuned to unscramble the input channels.

IV. CONCLUSION

We demonstrated a 4-channel SiP photonic MIMO demultiplexer performing all-optical unscrambling of four mixed modes. On-chip light monitoring through transparent CLIPP detectors was exploited to achieve accurate and robust sequential tuning of the demultiplexer without affecting mode orthogonality, thus enabling demultiplexing of 10 Gbit/s channels with less than -20 dB crosstalk over bandwidths spanning from 4 nm to more than 10 nm. Eye diagrams show that the signals quality is well recovered by the unscrambling process.

REFERENCES

- [1] P. J. Winzer, "Making spatial multiplexing a reality," *Nat. Photon.* **8**, 345-348 (2014).
- [2] D. A. B. Miller, "Self-configuring universal linear optical component," *Photon. Res.* **1**, 1-15 (2013).
- [3] N. K. Fontaine, "Space division multiplexing and all-optical MIMO demultiplexing using a photonics integrated circuit," *Proceed. Optical Fiber Communication Conference (OFC 2012)*, Los Angeles (CA), 4-8 March 2012, paper PDP5B.1
- [4] F. Morichetti, *et al.*, "Non-invasive on-chip light observation by contactless waveguide conductivity monitoring," *IEEE J. Sel. Topics Quantum Electron.* **20**, 292-301 (2014).
- [5] For details on the glass transposer technology, refer to the website: <http://www.plconnections.com/documents/ICE%20R020815.pdf>
- [6] S. Grillanda *et al.* "Non-invasive monitoring and control in silicon photonics using CMOS integrated electronics," *Optica* **1**, 129-136 (2014).

INVESTIGATING THE USE OF A HYBRID PLASMONIC-PHOTONIC NANORESONATOR FOR OPTICAL TRAPPING USING FINITE-DIFFERENCE TIME-DOMAIN METHOD

M. Mossayebi⁽²⁾, G. Bellanca⁽¹⁾, A. J. Wright⁽²⁾, A. Parini⁽¹⁾,
M. G. Somekh⁽³⁾, E. C. Larkins⁽²⁾

⁽¹⁾ Department of Engineering, University of Ferrara, Ferrara, Italy

⁽²⁾ Department of Electrical and Electronic Engineering, University of Nottingham, Nottingham, NG7 2RD, UK

⁽³⁾ Department of Electrical and Information Technology, Hong Kong Polytechnic University, Kowloon, Hong Kong, China
gaetano.bellanca@unife.it

Abstract

We investigate the use of a hybrid photonic-plasmonic nanoresonator for optical trapping of nanoparticles. The device comprises a photonic crystal (PhC) cavity coupled to a plasmonic bow tie nanoantenna (BNA) with a silicon dioxide (SiO₂) layer separating the two. Using the Finite-Difference in the Time-Domain (FDTD) approach, we show that this structure can confine the light to an extremely small volume of $\sim 30 \text{ nm}^3$ in the BNA gap whilst maintaining a high quality factor (5,400 - 7,700). This device has potential applications in optical manipulation, enabling the creation of subwavelength optical traps with an intensity gradient over a distance much smaller than the diffraction limit, allowing trapping of nanoparticles with dimensions much smaller than the light wavelength.

Index Terms – Photonics, plasmonics, optical tweezers, nanoresonators

I. INTRODUCTION

In the past 30 years, optical trapping and manipulation has been a major tool for advances in biology, physics and chemistry. In general, optical tweezers take advantage of the radiation pressure of light to immobilize, move and rotate particles from tens of nanometers to tens of micrometres in size. Conventional optical tweezers are mostly used to trap particles with dimensions comparable to the wavelength of the light used for trapping. When the size of the particle is considerably smaller than the wavelength, trapping becomes more difficult. This is especially true for the transparent biological specimens. To enable trapping of nanoparticles, near field optical traps have been demonstrated (see references on [1]). In these devices, plasmonic substrates such as nanoantenna pairs and plasmonic nanocavities allow light confinement into subwavelength “hotspots” of the order of tens of nanometers. However, these near field plasmonic traps have relatively low quality factors ($Q < 100$), due to the high radiative and absorption losses in the metal, making them inefficient. PhC cavities and waveguides have also been demonstrated for use in optical trapping and manipulation. PhC devices have high quality factors ($Q \sim 500 - 100,000$) and enable

enhancement and control of the profile of light, but they have a low spatial confinement compared the near field plasmonic traps (PhC spatial confinement $\sim 0.5 - 1 \mu\text{m}$). Recently, there have been efforts to combine photonic and plasmonic devices to create hybrid structures for optical tweezing. In this paper, we propose the integration of an L3 PhC and a gold BNA, to take advantage of the high quality factor of the PhC cavity and the extreme light confinement of the BNA for the purpose of optically trapping of nanoparticles. To investigate the suitability of this device, we represent the particle in trap with a polystyrene nanosphere (PS bead) positioned above the BNA. We show that this hybrid device has a high quality factor also when immersed in water, and is capable of confine light into a small volume in the BNA gap.

II. DESCRIPTION OF THE STRUCTURE AND THE FDTD MODEL

The device proposed in this paper is illustrated in Fig.1. It consists of (i) an L3 PhC cavity based on a 275 nm thick GaAs membrane with a triangular lattice of holes (hole radius, $r = 125 \text{ nm}$, lattice constant $a = 410 \text{ nm}$), obtained by removing three adjacent and aligned holes of the PhC lattice; (ii) a 40 nm thick gold BNA made with two head-to-head isosceles triangles with a gap of 30 nm between the two faced vertices and a total length of 700 nm; (iii) a 175 nm thick SiO_2 interplay layer separating the two. A PS bead with a 50 nm radius, positioned 45 nm above the BNA gap, represents the specimen in the trap. To maximize the quality factor of this hybrid device, the holes of the PhC are extended through the SiO_2 layer and the external holes of the L3 cavity are shifted out along the x axis by a factor of 0.2 a .

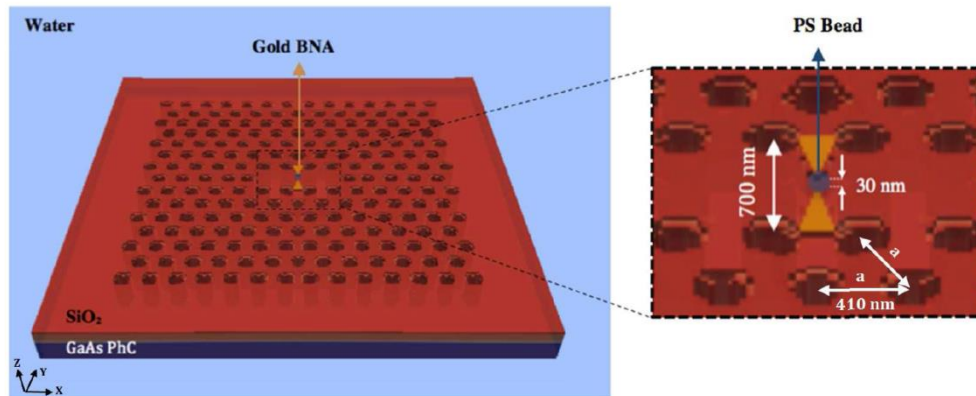


FIG. 1 – 3D schematic of the hybrid photonic-plasmonic nano cavity. The structure consists of an L3 PhC cavity based on a 275 nm thick GaAs slab, a 40 nm thick Au BNA and a 175 nm thick SiO_2 interplay layer.

Results presented in this paper were obtained through 3D-FDTD simulations with a conformal mesh in x , y and z directions and a 500 nm thick Perfectly Matched Layers (PML) placed at the borders of the computational domain, to prevent artificial reflections from the

boundaries. A Drude-Lorentz model with Palik parameters was used to represent the behaviour of gold at optical frequencies.

To excite the structure and investigate its resonances and quality factors, an H_z dipole was placed near the centre of the PhC cavity, to produce a TE polarized wave. The source was turned on for approximately 300 ps at the beginning of the simulation, which run for a total amount of 3,000 ps to ensure that the signal is fully decayed by the end and cavity modes have been well established inside the resonator. The time step of the simulation was chosen sufficiently small ($dt = 0.267$ ps) to ensure both accurate results and stability of the FDTD algorithm. Dipole probes randomly placed inside the PhC cavity were used to capture the resonances of the structure and their corresponding quality factors. Mode profiles were extracted by performing Discrete Fourier Transform (DFT) on the electromagnetic field components on selected planes of the computational domain at each resonance.

III. RESULTS

Table I presents the first three resonant modes and their corresponding quality factors of the structure at various design stages and when the device is supposed to be immersed in water. Note that the quality factor of the fundamental mode is always the highest and is high also when the BNA is introduced in the computation scenario. This is obtained by properly designing the thickness of the SiO_2 layer.

TABLE I – RESONANT WAVELENGTHS AND QUALITY FACTORS OF THE STRUCTURE AT VARIOUS DESIGN STAGES FOR THE STRUCTURE SUBMERGED IN WATER.

Structure	Fundamental resonant mode		Second resonant mode		Third resonant mode	
	λ (nm)	Q	λ (nm)	Q	λ (nm)	Q
PhC L3 + SiO_2	1,593	8,200	1,522	700	1,408	1,270
PhC L3 + SiO_2 + BNA	1,591	5,495	1,520	716	1,405	1,270
PhC L3 + SiO_2 + BNA + PS bead	1,591	7,726	1,520	709	1,405	1,255

The mode patterns of the E_y field component of the first three modes of the cavity at their resonances are reported in Fig. 2. As one can observe, the fundamental mode is the best suited to efficiently excite the BNA, as it provides the correct field polarization (along the axis of the antenna) and has the maximum in the position of the antenna gap, which is placed in the center of the resonator. Fig. 3 compares the intensity profiles on an YZ plane passing through the center of the structure, respectively when the BNA and the PS bead are removed and introduced in the structure. It is clearly observed that, when the BNA is introduced in the simulation scenario, the light is confined to a small volume in the BNA gap (volume ~ 30 nm³). Fig. 3 also shows the optical intensity

gradient in the structure. As it can be noticed, there is a strong increase in the intensity gradient of the light in the antenna region, and close to the antenna gap. This will in turn increase optical trapping forces.

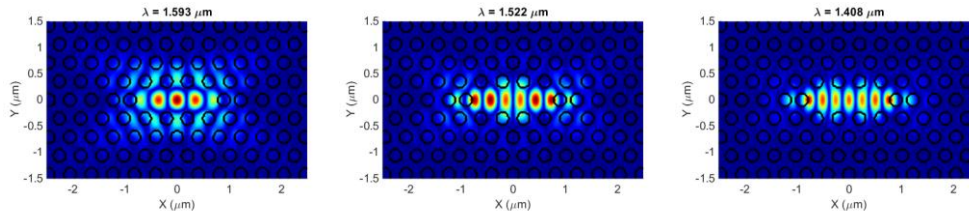


FIG. 2 – Mode pattern of the E_y field component of the first (on the left), second (in the center), and third (on the right) order modes of the PhC cavity at the resonance. The E_y field component of the fundamental mode, with the maximum in the center of the cavity and the matched polarization, is the best suited to excite the BNA.

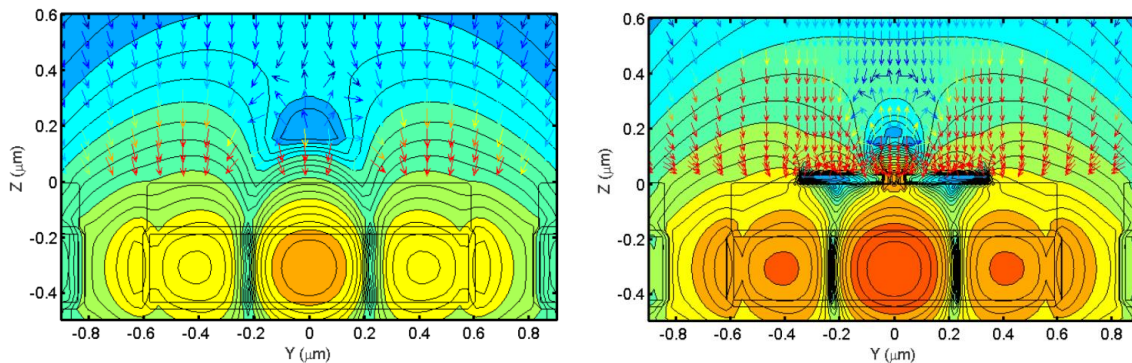


FIG. 3 – Optical intensity patterns (log scale) on an YZ slice passing through the centre of the structure without the BNA and the PS bead (on the left) and including the BNA and the PS bead (on the right). Each graph is independently normalized to its maximum, to ease comparisons among the field intensity profiles. The arrows show the optical intensity gradients with light blue representing the lowest and red showing the highest values.

IV. CONCLUSION

We present a hybrid photonic plasmonic nanocavity with applications in optical trapping of transparent nanoparticles. This device can significantly confine the electromagnetic field to a volume of $\sim 30 \text{ nm}^3$ while maintaining a high quality factor of $\sim 5,400\text{-}7,700$.

REFERENCES

- [1] M. Mossayebi, A. J. Wright, A. Parini, M. G. Somekh, G. Bellanca, E. C. Larkins, “Investigating the use of a hybrid plasmonic-photonic nanoresonator for optical trapping using finite-difference time-domain method”, OQE, 2015 (accepted).

OPTICAL KERR DARK-LUMP DYNAMICS OF HYDRODYNAMIC ORIGIN

F. Baronio⁽¹⁾, C. De Angelis⁽¹⁾, S. Wabnitz⁽¹⁾, Y. Kodama⁽²⁾

⁽¹⁾ INO CNR and Department of Information Engineering,
University of Brescia, Via Branze 38, Brescia, Italy

⁽²⁾ Department of Mathematics, Ohio State University,
Columbus, OH 43210, USA
fabio.baronio@unibs.it

Abstract

There is considerable fundamental and applicative interest in obtaining non-diffractive and non-dispersive spatio-temporal localized wave packets propagating in optical cubic nonlinear or Kerr media. Here, we analytically predict the existence of a novel family of spatio-temporal dark lump solitary wave solutions of the (2+1)D nonlinear Schrodinger equation. Dark lumps represent multi-dimensional holes of light on a continuous wave background. We analytically derive the dark lumps from the hydrodynamic exact soliton solutions of the (2+1)D shallow water Kadomtsev-Petviashvili model, inheriting their complex interaction properties. Our findings open a new avenue for research in spatio-temporal extreme nonlinear optics.

Index Terms – Optics, Nonlinear Optics, Light Fluids, Hydrodynamics.

I. INTRODUCTION

The propagation of intense, ultra-short pulses of electromagnetic radiation in a nonlinear medium is a multi-dimensional phenomenon, leading to complex spatio-temporal behavior. Pulse dynamics is influenced by the interplay of various physical mechanisms: the most important among them being diffraction, material dispersion and nonlinear response [1]. Since the 1990's, theoretical and experimental studies of the self-focusing behavior of intense ultra-short pulses have indicated that spatial and temporal degrees of freedom cannot be treated separately. When the three length scales naturally associated with diffraction, dispersion, and nonlinearity become comparable, the most intriguing consequence of space-time coupling is the possibility to form a non-diffractive and non-dispersive localized wave packet, namely, a spatiotemporal soliton or light bullet [2]. A strict constraint for the formation of light bullets is that the nonlinear phase changes counteract both the linear wave-front curvature and the dispersion-induced chirp, thus leading to space-time focusing. In the 2000's, theoretical and experimental studies have demonstrated that non-diffractive and non-dispersive localized wave packets also exist within the normal dispersion regime, in the form of the so-called nonlinear X waves, or X-wave solitons [3]. Here, we contribute to the field of non-diffractive and non-dispersive spatiotemporal localized wave packets in cubic nonlinear (or Kerr) optical media, by predicting the existence and the interactions of dark lump

solitary wave solutions of the (2+1)D nonlinear Schrodinger equation (NLSE). The key point of our approach consists in that we are able to derive the conditions for optical dark lump solitary waves existence, and analytically describe their shape and interactions, from the exact soliton solutions of the (2+1)D Kadomtsev-Petviashvili (KP) equation. In hydrodynamics, the KP equation describes weakly dispersive and small amplitude water wave propagation in a (2+1)D framework [4].

II. NLSE SOLITARY WAVES OF HYDRODYNAMIC KP ORIGIN

The dimensionless time-dependent paraxial wave equation in cubic Kerr media (NLSE), in the presence of group-velocity dispersion, and limiting diffraction to one dimension, reads as:

$$iu_z + \frac{\alpha}{2}u_{tt} + \frac{\beta}{2}u_{yy} + \gamma|u|^2u = 0,$$

where $u(t,y,z)$ represents the complex wave envelope; t, y represent temporal and spatial transverse coordinates, respectively, and z is the longitudinal propagation coordinate. Each subscripted variable stands for partial differentiation. $\alpha, \beta > 0, \gamma$ are real constants that represent the effect of dispersion, diffraction and Kerr nonlinearity, respectively. Writing $u = \sqrt{\rho} \exp(i\theta)$, $\rho = \rho_0 + \eta$, $\theta = \gamma\rho_0z + \phi$, $\tau = t - c_0z$, $u = y$, $\varsigma = z - \gamma\rho_0z$, we obtain

$$\left(-\eta_\varsigma + \frac{3\alpha\gamma}{2c_0}\eta\eta_\tau + \frac{\alpha^2}{8c_0}\eta_{\tau\tau\tau} \right)_\tau - \frac{c_0\beta}{2\alpha}\eta_{vv} = 0$$

which is a KP equation for η ; moreover $\phi_\tau = -(\gamma/c_0)\eta$. After some algebra, we can obtain the optical NLSE solutions $u(t,y,z)$ of hydrodynamic KP soliton origin [$\eta(\tau,u,\varsigma), \phi(\tau,u,\varsigma)$] with $\tau = t - c_0z$, $u = y$ and $\varsigma = z$:

$$u(t, y, z) = \sqrt{\rho_0 + \eta(\tau, u, \varsigma)} e^{i(\gamma\rho_0z + \phi(\tau, u, \varsigma))}.$$

In the following, we focus our attention on the anomalous dispersion and self-defocusing regime ($\alpha > 0, \beta > 0, \gamma < 0$). Moreover, we fix $\alpha = 4\sqrt{2}$, $\beta = 6\sqrt{2}$, $\gamma = -2\sqrt{2}$; $\rho_0 = 1$.

III. SINGLE NLSE DARK LUMP SOLUTION OF KPI ORIGIN

When considering the small amplitude regime ($\varepsilon \ll 1$), a form of KP lump-soliton solution can be expressed as $\eta(\tau, u, \varsigma) = -4[\varepsilon^{-1} - (\tau - 3\varepsilon\varsigma)^2 + \varepsilon u^2] / [\varepsilon^{-1} + (\tau - 3\varepsilon\varsigma)^2 + \varepsilon u^2]$. The parameter ε rules the amplitude/width and velocity properties of the KP lump soliton. The lump peak amplitude in the (ς, u) plane is -4ε ; the velocity in the τ -direction is 3ε . Figure 1 shows the numerical spatio-temporal envelope intensity profile $1 - |u|^2$ of a

NLSE dark lump solitary wave in the y - t' plane ($t' = t - c_0 z$), at the input $z = 0$ and after the propagation distance $z = 100$, for $\varepsilon = 0.05$. In the numerics, the initial dark NLSE profile, of KP lump origin, propagates stably in the z -direction, with virtually negligible emission of dispersive waves, with the predicted velocity $c_0 + 3\varepsilon$, and intensity dip of 4ε .

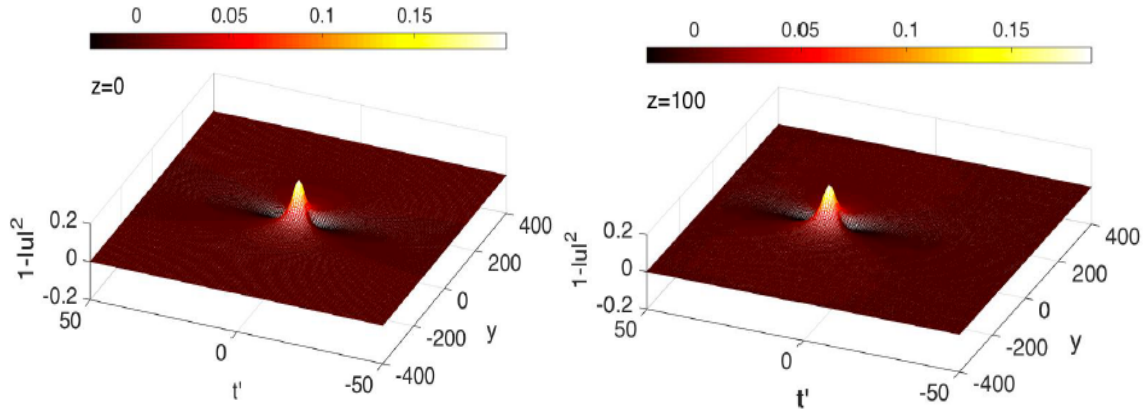


FIG. 1 – Numerical spatio-temporal dark-lump NLSE intensity $1 - |u|^2$, shown in the y - t' plane with $t' = t - c_0 z$, at $z=0$, and $z=100$. Here, $\varepsilon=0.05$.

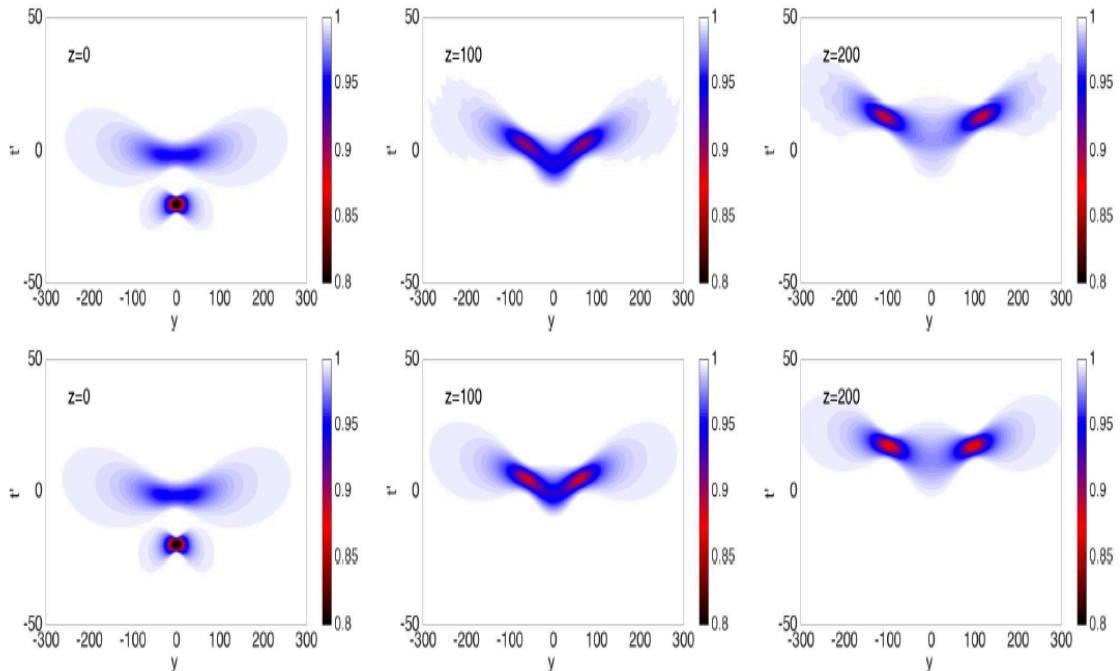


FIG. 2 – Spatio-temporal NLSE intensity distribution $|u|^2$, in the y - t' plane, showing anomalous scattering, at $z = 0$, at $z = 100$ and $z = 200$. Top, numerical simulations; bottom theoretical prediction.

IV. ABNORMAL SCATTERING OF NLSE DARK LUMP SOLUTION.

We then consider multi-pole lump solution with two peaks, which is expressed as: $\eta(\tau, u, \varsigma) = -2\partial_{\tau}^2 \log F$, where $F = |f_1|^2 + |f_2 + f_1/\varepsilon + 1/2\varepsilon^2|^2 + |f_1 + 1/\varepsilon|^2/2\varepsilon^2 + 1/4\varepsilon^4$, and $f_1 = \tau_1 + 2i\varepsilon u_1 - 12\varepsilon^2 \varsigma_1 + \delta_1$, $f_2 = -2u - 24i\varepsilon \varsigma + \delta_2$. $\tau_1 = \tau - \tau_0$, $u_1 = u - u_0$, $\varsigma_1 = \varsigma - \varsigma_0$ define the dislocation; δ_1 , δ_2 are arbitrary complex parameters. Figure 2 (top) shows the initial spatio-temporal envelope intensity profile $|u|^2$ of a two peaked NLSE dark lump in the $y - t'$ plane, along with the numerically computed profiles after propagation distances $z=100$, and $z=200$, for $\tau_0 = 0, u_0 = 0, \varsigma_0 = -50, \delta_1 = 0, \delta_2 = 0$ ($\tau_0 = 0, u_0 = 0, \varsigma_0 = -50, \delta_1 = 0, \delta_2 = 0$). In particular, Fig. 2 depicts the scattering interaction of the two-peaked waves: two dark lumps approach each other along the t' -axis, interact, and recede along the y -axis. These solutions exhibit anomalous (nonzero deflection angles) scattering due to multi-pole structure in the wave function of the inverse scattering problem. We remark that the numerical result of NLSE dynamics is in an excellent agreement with analytical dark solitary solution with KP multi-pole lump solution, as seen in Fig. 2 (bottom).

V. CONCLUSIONS

We have analytically predicted a new class of dark solitary wave solutions that describe non-diffractive and non-dispersive spatio-temporal localized wave packets propagating in optical Kerr media. We numerically confirmed the existence, stability, and peculiar anomalous scattering interactions of dark-lump solitary waves of the (2+1)D NLSE. The key novel property of these solutions is that their existence and interactions are inherited from the hydrodynamic soliton solutions of the well known KP equation. Our findings open a new avenue for research in spatio-temporal extreme nonlinear optics of hydrodynamic nature.

ACKNOWLEDGEMENT

The present research was supported by the Italian Ministry of University and Research (MIUR, Project No. 2012BFNWZ2).

REFERENCES

- [1] R. Boyd, *Nonlinear Optics*, 3rd ed. (Academic Press, London, 2008).
- [2] Y. Silberberg, "Collapse of optical pulses," *Opt. Lett.* 15, 1282 (1990).
- [3] C. Conti, S. Trillo, P. Di Trapani, G. Valiulis, A. Piskarskas, O. Jedrkiewicz, and J. Trull, "Nonlinear electromagnetic X waves," *Phys. Rev. Lett.* 90, 170406 (2003).
- [4] Y. Kodama, "KP solitons in shallow water," *J. Phys. A: Math. Theor.* 43, 434004 (2010).

DESIGN OF MESOSCOPIC PHOTONIC CRYSTAL MICROCAVITY BASED SENSORS DEVOTED TO OPTICAL TWEEZING APPLICATIONS

B. Ferrara⁽¹⁾, M. Grande^{(1)*}, G. Calò⁽¹⁾, A. D’Orazio⁽¹⁾, V. Petruzzelli⁽¹⁾,
G. Magno^{(2)*}, B. Dagens⁽²⁾,
A. Monmayrant⁽³⁾, O. Gauthier-Lafaye⁽³⁾

⁽¹⁾ Dipartimento di Ingegneria Elettrica e dell’Informazione, Politecnico di Bari, Viale Orabona 4, Bari, Italy

⁽²⁾ IEF,CNRS, Univ Paris-Sud, Univ Paris-Saclay, 91405 Orsay Cedex France

⁽³⁾ CNRS, LAAS, 7 avenue du colonel Roche, F-31400 Toulouse, France ; Univ. De Toulouse, LAAS, F-31400 Toulouse, France

*corresponding authors: giovanni.magno@u-psud.fr, vincenzo.petruzzelli@poliba.it

Abstract

In this paper we report on the design of a refractive index sensor based on a mesoscopic photonic crystal microcavity that exhibits good performance in terms of quality factor and sensitivity. This device paves the way for the integration of optical sensors and tweezers thanks to its translation invariance property.

Index Terms—refractive index sensor, mesoscopic photonic crystal.

I. INTRODUCTION

Refractive index sensing has become a powerful tool for different fields that include physical, chemical and biological parameter detection. The nanotechnology progress allows the fabrication of high performance resonant sensors based on different geometrical configurations such as ring resonators, microstructured optical fibers and plasmonic sensors [1-3] to mention a few. In the last years, Photonic Crystals (PhCs) have been largely exploited to realize high performance refractive index sensors in different configurations such as line defect, point cavity and Mach-Zehnder interferometer [4-6].

Recently, Mesoscopic Photonic Crystals (MPhCs) have attracted the interest of research as a possible alternative of the traditional PhCs since they exploit the self-collimation phenomenon to achieve ‘guideless’ waveguiding in linear media. A MPhC can be realized by cascading slabs of different materials (or metamaterials) showing opposite spatial dispersion, such as traditional PhCs and slabs of bulk materials. This 1D periodic superstructure supports the Mesoscopic Self-Collimation (MSC) phenomenon. For a given direction, MSC is obtained when the focusing properties of the PhC slabs compensate the natural defocusing of the bulk material slabs [7-8]. The MSC allows for defining guiding structures on the base of the spatial dispersion engineering without the need of any traditional guiding mechanism, such as engraving index guiding defects. This paves the way for the conception of structures showing discrete (vertical) translational invariance. Hence, MPhCs can be exploited to design a full novel class of MSC based devices, such as high sensitivity and Q-factor microcavities inheriting the translational

invariance property. As demonstrated in [8,9], the strong near field localized within the cavity and the translational invariance make this structure befitting for devices able to tweeze-and-sense micro- and nano-object systems. Furthermore, being its properties mainly topological (and less related to material properties), it can be easily adapted to be fabricated by means of well-established technological solutions (GaAs membranes, SOI, etc.) that can be integrated in microfluidic systems and labs-on-chip.

In this contribution, we report on the design of a refractive index sensor based on a mesoscopic photonic crystal microcavity that exhibits sensitivity as high as 112 nm/RIU.

II. DESIGN OF REFRACTIVE INDEX SENSOR BASED ON MESOSCOPIC PHOTONIC CRYSTAL MICROCAVITY

As a first step, the design process of MPhC-based microcavities requires the definition of reflectors. A mesoscopic mirror (MM) can be conceived by asking a MPhC to show, along its high symmetry direction and at the same time, both MSC and high reflectivity. These conditions can be both verified by solving the following algebraic system:

$$\begin{cases} \frac{d_c}{n_c(u)} + \frac{d_b}{n_b} = 0 \\ d_b n_b = m \frac{\lambda}{4} = m \frac{a}{4u} \\ d_c n_{eff}(u) = p \frac{\lambda}{4} = p \frac{a}{4u} \end{cases} \quad (1)$$

where d_c is the length of the PhC slabs, d_b is the length of the bulk slabs, n_c is the PhC curvature index, u is the normalized frequency [a/λ], n_b is the bulk medium (effective) refractive index, (m,p) are integers, λ is the wavelength, a is the lattice constant and n_{eff} is the PhC phase index.

As shown in Fig. 1, a Fabry-Pérot cavity is thus obtained by combining two 5-mesoperiod-long MMs [7]. We considered the whole device as etched on a 270 nm-thick membrane of GaAs ($n_{GaAs} = 3.4$), fully surrounded by a dielectric analyte having refractive index n in the range 1.1-1.5. The analysis of the structure has been performed by means of 2D-FDTD calculation (MEEP). At telecom wavelength (1.55 μm), the effective refractive index n_b of the fundamental mode supported by the membrane is equal to $n_b = 2.8853, 2.8898, 2.8949, 2.9005, 2.9067$ and 2.9136, when n is 1, 1.1, 1.2, 1.3, 1.4 and 1.5, respectively.

When air ($n=1$) is considered as surrounding medium, the device exhibits a high Q-factor equal to 7888.

Fig. 2 shows normalized transmission spectra as a function of n . The resonant peak within the bandgap, corresponding to the formation of a stable cavity mode, redshifts linearly as n increases.

Fig. 3 shows the position of the resonant wavelength as a function of the analyte index when a lattice constant a equal to 360 nm is considered to locate the resonance of the suspended membrane ($n=1$) at about 1550 nm. The corresponding sensitivities are 28 and 112 nm/RIU, respectively, when the MPhC holes are filled by air (blue curve) or by the analyte itself (red line).

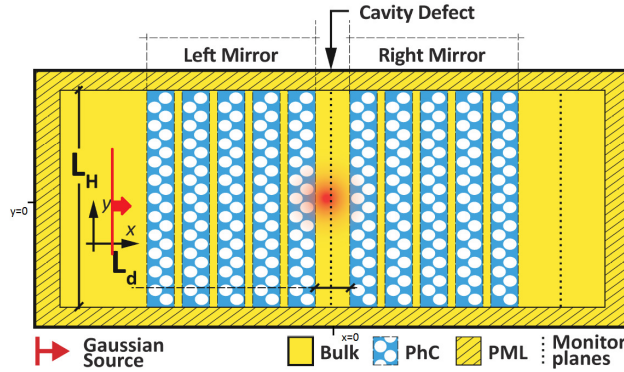


FIG. 1–Sketch of the mesoscopic photonic crystal microcavity. Each MM is obtained by interleaving focusing slabs constituted by 13 hole rows of a 45°-tilted hole-type square-lattice PhC (having hole radius $r = 0.28 \times a$ and an overall width $d_c = 9.192 \times a$, where a is the lattice constant), and defocusing slabs constituted by bulk material having a refractive index n_b and a width $d_b = 2.612 \times a$. The cavity defect has width $W = 7.065 \times a$.

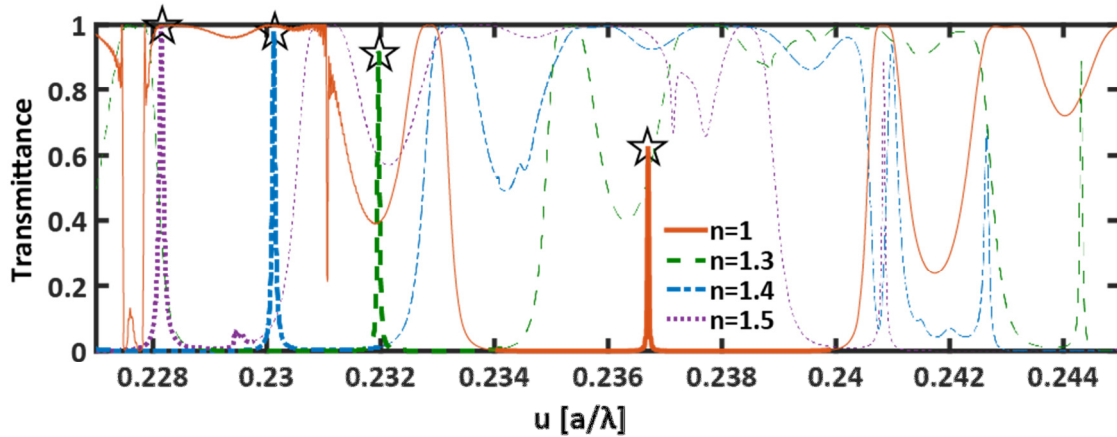


FIG. 2–Transmittance as a function of the reduced frequency for $n_{eff} = 2.8853$ (solid black line, λ_1), 2.9005 (dash blue line, λ_2), 2.9067 (dash dot red line, λ_3) and 2.9136 (dotted magenta line, λ_4), respectively.

III. CONCLUSION

The design of a refractive index sensor based on a mesoscopic photonic crystal microcavity has been reported. The proposed device exhibits a Q-factor and a sensitivity as high as 7888 and 112 nm/RIU, respectively. These results pave the way for a new class of highly compact index sensors showing translation invariance property for tweezing applications.

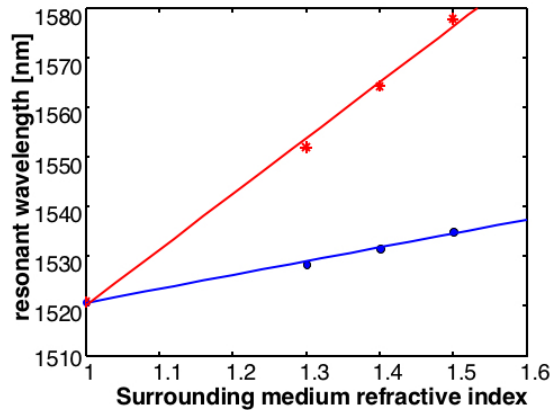


FIG. 3—Resonant wavelength as a function of the analyte refractive index: the blue and red lines correspond to a PhC holes filled by air and by the analyte, respectively.

ACKNOWLEDGEMENT

M. Grande thanks the Apulia Region program "FutureInResearch" (7K76VI3) for financial support.

REFERENCES

- [1] Jin Liu, Xi Zhou, Zhi Qiao, Jianhao Zhang, Chenzhao Zhang, Tuowen Xiang, Lingling Shui, Yaocheng Shi, Liu Liu: Integrated Optical Chemical Sensor Based on an SOI Ring Resonator Using Phase-Interrogation, *IEEE Photonics Journal*, Volume 6, Number 5, October 2014.
- [2] Scarcia, W., Palma, G., Falconi, M.C., de Leonardis, F., Passaro, V.M.N., Prudenzano, F.: Electromagnetic modelling of fiber sensors for low-cost and high sensitivity temperature monitoring, *Sensors (Switzerland)*, vol.15, no.12, pp. 29855-29870, 2015
- [3] M.Grande, R. Marani, F. Portincasa, G. Morea, V. Petruzzelli, A.D’Orazio, V. Marrocco, D. de Ceglia, M.A. Vincenti: Asymmetric plasmonic grating for optical sensing of thin layers of organic materials, *Sensors and Actuators B*, vol.160, pp.1056-1062, Dec 2011.
- [4] F. Bagci and B.Akaoglu, “Enhancement of refractive index sensitivity in photonic crystal waveguide-based sensors by selective infiltration,” *Acta Physica Polonica A*, vol. 124, No.1, pp. 50-55, Apr. 2013.
- [5] D. Zecca, A. Quattieri, G. Magno, M. Grande, V. Petruzzelli, B. Prieto-Simon, A. D’Orazio, M. De Vittorio, N.H. Voelcker and T. Stomeo, “Label-free Si_3N_4 photonic crystal based immunosensors for diagnostic applications,” *IEEE Photonics Journal*, vol. 6, No.6, Dec. 2014.
- [6] Y. Chen, T. Liu, W. Wang, Q. Zhu and W. Bi, “Refractive index sensing performance analysis of photonic crystal Mach-Zehnder interferometer based on BP neural network optimization,” *Modern Physics Letters B*, vol. 29, No.10, Apr. 2015.
- [7] G. Magno, M. Grande, A. Monmayrant and F. Lozes-Dupuy, “Controlled reflectivities in self-collimating mesoscopic photonic crystal,” *Journal of the Optical Society of America B*, vol. 31, No. 2, pp. 355-359, 2013.
- [8] G. Magno, A. Monmayrant, M. Grande, F. Lozes-Dupuy, O. Gauthier-Lafaye, G. Calò and V. Petruzzelli, “Stable planar mesoscopic photonic crystal cavities,” *Optics Letters*, vol. 39, pp. 4223-4226, Jul. 2014.
- [9] G. Magno, A. Monmayrant, M. Grande, F. Lozes-Dupuy, O. Gauthier-Lafaye, G. Calò, and V. Petruzzelli, “Stable planar microcavities based on mesoscopic photonic crystals,” in Proc. SPIE, Integrated Optics: Devices, Materials, and Technologies XVIII, vol. 8988, pp. 89881G-1-89881G-10, S. Francisco (US), Feb. 1-6, 2014.

A DESIGN TOOL FOR INTEGRATED OPTICAL SEGMENTED WAVEGUIDES

Ali Emre Kaplan⁽¹⁾, Gaetano Bellanca⁽²⁾, Paolo Bassi⁽¹⁾

⁽¹⁾Alma Mater Studiorum - University of Bologna
Department of Electrical, Electronic and Information Engineering
Viale del Risorgimento 2, I 40136 Bologna, Italy

⁽²⁾University of Ferrara, Engineering Department,
Via Saragat 1, I 44122 Ferrara, Italy
alিয়েmre.kaplan@studio.unibo.it,

Abstract

Simulation of 3D structures requires large memory and CPU time, which may then forbid realistic simulations of complex structures. Computational requirements can be dramatically reduced using the Transmission matrix \mathbf{T} of the structure elements. The \mathbf{T} matrix of the whole structure is in fact the product of the \mathbf{T} matrices of the constituting elements. The model is proposed and tested in 2D with some specific examples. Possible critical points, such as radiation modes effects and multimode guided propagation are commented.

Index Terms – Silicon Photonics, Segmented waveguides, Numerical methods.

I. INTRODUCTION

The design of Photonic Integrated Circuits has been strongly affected by the so-called Generic Foundry model [1,2]. Optical circuits are designed at functional high level (using, for example the Scattering matrix \mathbf{S} or the Transmission matrix \mathbf{T}) considering Design Kits, i.e. rules to assemble the basic Building Blocks, circuits, whose geometrical features result from a previous fabrication and characterization activity, to provide a fully known functional behavior. Such Design Kits provide also masks compatible with the technology of a specific foundry.

However, new component can be designed only with the classical approach: a loop of numerical design, fabrication and measurements until the realized device features correspond to the desired ones. A 3D modeling is then mandatory for an accurate study. Such an approach is however very demanding both in terms of CPU and memory needs.

There are anyway some devices that can be subdivided in smaller parts, each characterized separately. A typical example is given by the so-called Segmented Waveguides [3], periodic or almost periodic sequences of longitudinally varying smaller elements. They can realize gratings, acting as spectral filters, or tapers, optimizing coupling between different structures. For these devices one can get the overall \mathbf{T} matrix simply as the product of the \mathbf{T} matrices of the sub-elements, which can then be calculated separately, at a lower computational cost.

In this paper we prove the viability of this approach in 2D cases, where single elements and whole structures can be simulated and results compared. Possible issues will be introduced and discussed.

II. THE PROPOSED APPROACH

Segmented Waveguides have been intensively studied for linear [3,4] and non linear [5] applications and are known also as Photonic Wires [6] in Silicon Photonics. Their longitudinal changes make reflections unavoidable. This prevents using codes not including them, such as BPM. Only full wave approaches, such as FEM, FDTD, FVTD, etc., consider the whole structure at a time and can then manage this issue. Unfortunately, memory and CPU time constraints forbid their use for long structures.

Here, we propose to study these structures using the Transmission Matrix approach. The \mathbf{T} matrix of the whole structure can in fact be obtained as the cascaded multiplication of those of each constituting element. This approach, if viable, sets no limit to the longitudinal size of the considered structure and can then be applied also to 3D ones.

The approach will be preliminarily tested in 2D, where results can easily be compared to those of the calculation of the whole structure.

III. RESULTS

The first example is a waveguide grating with N periods. The structure is studied with COMSOL [7], which provides the values of \mathbf{S} matrix, from which \mathbf{T} can be easily derived. The matrix \mathbf{T}_N of the cascade of N periods equals $(\mathbf{T}_1)^N$, where \mathbf{T}_1 is the matrix of a single period. The schematic of the structure, made by elements with Duty Cycle $DC = 50\%$, is sketched in the left part of Fig. 1. The \mathbf{S} matrices of the single period and of the whole grating are computed considering each structure preceded and followed by a $2 \mu\text{m}$ long straight waveguide excited by the TE fundamental mode. The effects of these coupling sections are then removed multiplying the overall calculated \mathbf{T} by \mathbf{T}_L^{-1} , being \mathbf{T}_L the \mathbf{T} matrix of each straight piece of guide. This allows determining the \mathbf{S} matrix of the grating only. The initial waveguide is assumed monomode, which is not a limit, since real structures are so. N varies from 1 to 64. Radiation losses make \mathbf{S} never unitary for any N . Moreover, $|S_{11}| = |S_{22}|$ and $|S_{12}| = |S_{21}|$, because of structure symmetry and reciprocity. Fig. 2 shows ε_{ij} , the percent error of the reflection and transmission coefficients $|S_{ij}|$ and $|S_{ij}|$ computed composing the structure with respect to the exact solution at $\lambda = 1.52 \mu\text{m}$. Errors are negligible for $|S_{ii}|$ while those of $|S_{ij}|$ increase up to $\sim 3\%$ when $N=32$. So small errors also prove that no coupling back of radiation modes into the structure occurs, a phenomenon considered in the full structure simulation, but not in the composition process. Fig. 3 shows the spectral response in the spectral range $1.45\text{-}1.6 \mu\text{m}$.

Once the expected behavior has been shown in a periodic structure, a further test has been done. Since ripples in the spectral response are due to reflections, a 16 period grating of the studied type has been preceded by a taper formed by 4 periods with $DC = 10\%$, 20% , 30% , 40% (right part of Fig. 1). Such taper should flatten transmission and reflection spectra. Results shown in Fig. 4 confirm both this expectation and the viability of the approach, since good agreement is found again between the \mathbf{S} matrix of the whole structure and that resulting multiplying those of the constituting elements. One can then envisage to use this method to optimize the structure using a previously calculated library of known grating sub-elements with different DC and optimizing $|S_{ii}|$ and $|S_{ij}|$ of the tapered grating by multiple runs.

IV. FUTURE DEVELOPMENTS

The procedure illustrated so far will be extended to the 3D case, where it may be particularly useful for the analysis or the optimized design of Segmented Waveguide structures with desired transmission and reflection spectra. Calculation of the Scattering matrix of single grating periods is in fact possible and product of the calculated \mathbf{T} matrices can provide the \mathbf{T} matrix of any segmented waveguide, no matter its length.

V. CONCLUSIONS

A procedure to study 3D segmented integrated optical structures including also possible reflections at the various interfaces has been proposed and tested in 2D. The approach decomposes the complete structure in its sub-periods and determines numerically their Scattering and Transmission matrices. The Transmission matrix of the whole device is the product of the cascaded single period transmission matrices. Such matrices can be calculated in 3D with standard FEM codes, which do not suffer the memory or CPU constraints coming from the study of the complete device. The method could be used to design structures with specified transmission characteristics. The approach has been successfully tested with some 2D structure examples.

REFERENCES

- [1] M. K. Smit et al., "An introduction to InP-based generic integration technology", *Semicond. Sci. Technol.*, vol. 29, p.083001, 2014.
- [2] F. Morichetti et al., "The outcomes of SAPPHIRE, a generic foundry platform for silicon photonics", Proc. of *XX RiNEm*, Padova, 15-18 September 2014, pp. 113-116.
- [3] Z. Weissman, A. Hardy, "Modes of periodically segmented waveguides", *IEEE-JLT*, vol.11 (11), pp. 1831-1838, 1993.
- [4] D. Castaldini et al, "Soft-Proton-Exchange Tapers for Low Insertion-Loss LiNbO3 Devices", *IEEE-JLT*, vol. 25 (6), pp. 1588-1593, 2007.

[5] M. H. Chou et al., “Adiabatically tapered periodic segmentation of channel waveguides for mode-size transformation and fundamental mode excitation”, *Opt. Lett.*, vol. 21, pp. 794-796, 1996.

[6] M. Gnan et al., “Fabrication of low-loss photonic wires in silicon-on-insulator using hydrogen silsesquioxane electron-beam resist”, *El. Lett.*, vol. 4 (2), pp. 115-116, 2008.

[7] COMSOL Package, <http://www.comsol.com>



FIG. 1 – Studied structures schematic, without (left) and with (right) the taper, $L = 390$ nm, $R = 120$ nm, $W = 400$ nm.

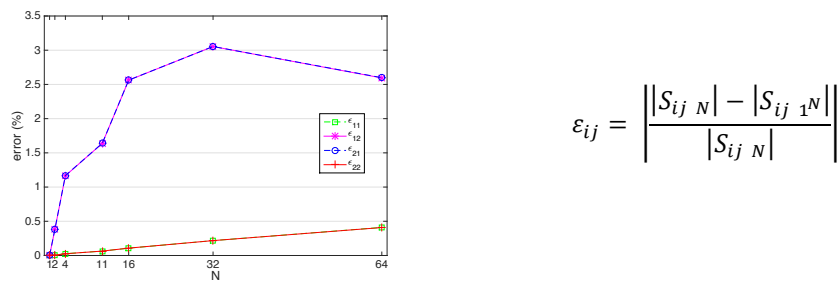


FIG. 2 – Percent error of $|S|$ parameters vs N at $\lambda=1.52$ μm .

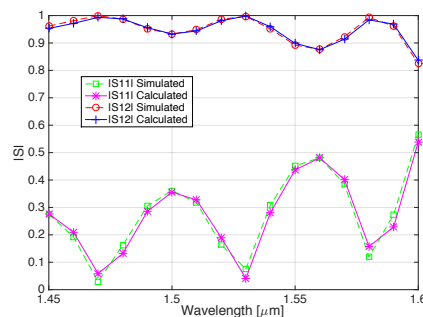


FIG. 3 – $|S|$ parameters vs wavelength for a 16 periods grating.

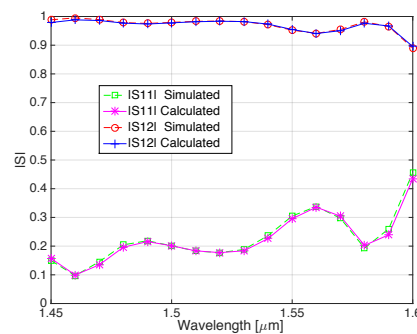


FIG. 4– $|S|$ parameters vs wavelength for a 16 periods grating preceded by a taper.

EFFECT OF ETCHING SLOPE IN HIGH Q-FACTOR OPTICAL NANOBEAMS

Danilo Panettieri ⁽¹⁾, Liam O'Faolain⁽²⁾, Marco Grande^{(1)*}

⁽¹⁾*Dipartimento di Ingegneria Elettrica e dell'Informazione (DEI), Politecnico di Bari, Italy*

⁽²⁾ *SUPA, School of Physics and Astronomy, University of St. Andrews, UK*
**marco.grande@poliba.it*

Abstract

We report on the design of silicon nitride nanobeam cavities fully encapsulated in silica operating at about 1 micron. The proposed configuration allows achieving high Q-factor and small mode volume in a low refractive index contrast configuration. Moreover, we investigate the effect of fabrication imperfections due to the hole etching slope, proving that the Q-factor experiences a 3-fold decrement when an etching angle of about 10° is taken into account.

Index Terms – optical nanobeams, photonic crystals, fabrication tolerances.

I. INTRODUCTION

In recent years Photonic Crystal (PhC) nanobeam cavities have been the subject of intense research due to their attractive characteristics offering great promises for different applications such as refractive index sensing [1], optomechanics [2], filters [3] and nonlinear optics [4]. Nanobeam cavities are the most natural geometry for integration with waveguides [5] and can achieve high Q-factor and low mode volume in a small footprint area. For this reason, they define a powerful alternative to the two-dimensional PhC (2D-PhC) cavities [3,6].

Another important advantage of optical nanobeams is related to the possibility to achieve high Q-factor modes in relative low refractive index materials such as diamond [7], Si₃N₄ [2] and SiC [8] to mention a few. Particularly, Si₃N₄ is an excellent material for photonic applications at visible wavelengths due to its relatively high refractive index and transparency over the visible and near infrared bands. Moreover, Si₃N₄ is standard CMOS compatible technology platform for dense photonic integrated circuits.

In this paper, we describe the optimised design of silicon nitrate ($n_{\text{Si}_3\text{N}_4} = 2$) nanobeam cavities embedded in a low refractive index medium ($n_{\text{SiO}_2} = 1.5$) to obtain high Q-factor of the order of 10^5 . Then, we investigate the effect of the fabrication imperfections due to the not perfect vertical hole sidewalls of the nanobeam affected by the etching slope.

II. HIGH Q-FACTOR CAVITY IN A LOW REFRACTIVE INDEX CONTRAST

Due to the low refractive index contrast between the ridge waveguide and the surrounding medium, the classic design of the nanobeam cavity [5] must be optimized to obtain high Q-factor. The nanobeam cavity consists of a waveguide perforated with elliptical gratings instead of circular holes, since elliptical gratings have larger bandgap and allow a better confinement of the localized mode [1]. Fig. 1(a) shows the sketch of the Si_3N_4 ridge waveguide. To obtain a cavity resonance wavelength of about $1 \mu\text{m}$, the periodic lattice constant was fixed equal to $p = 0.31 \mu\text{m}$ and the cross section width and thickness were set equal to $0.6 \mu\text{m}$ and $0.4 \mu\text{m}$, respectively.

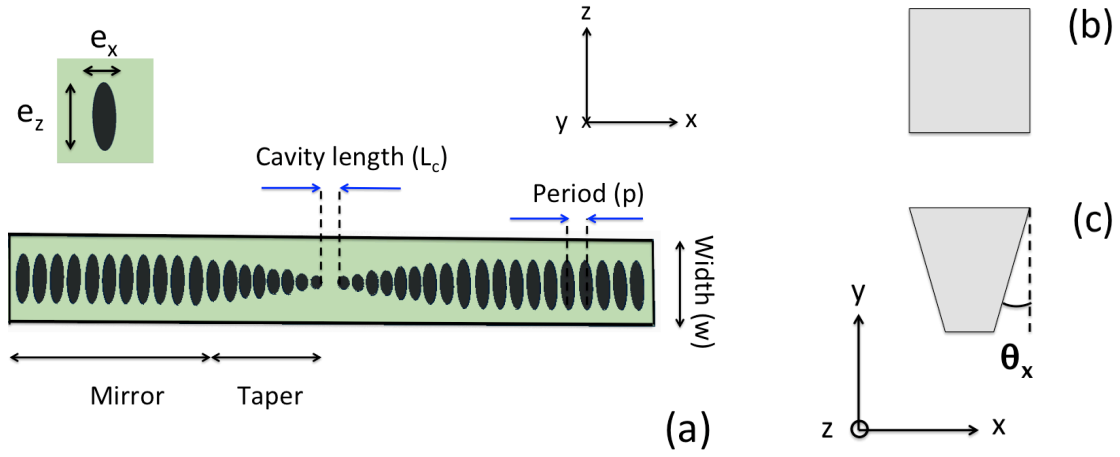


FIG. 1(a) – Top view of the Si_3N_4 nanobeam embedded in homogeneous silica; (inset) detail of the periodic hole; cross section of **(b)** the perfect straight and **(c)** not straight hole with etching angle due to the fabrication imperfection. The angles θ_x and θ_z are measured with respect to the y -axis.

To reduce the mismatch between the cavity and the mirror segments, and thus obtaining Q-factors in the order of about 10^5 , the number of holes of the taper and of the mirror are set equal to 10 and 40, respectively. A quadratic tapering law was used with the increment of the major diameter of the elliptical holes (e_z) between $e_{zmin} = 0.2 \mu\text{m}$ and $e_{zmax} = 0.4 \mu\text{m}$, maintaining the minor diameter $e_x = 0.2 \mu\text{m}$ unaffected. The same law was employed for the distance between the holes, that is varied between $p_{min} = 0.285 \mu\text{m}$ and $p = 0.31 \mu\text{m}$. Finally, the optimal cavity length (L_c), i.e. the spacing between the two central holes, was fixed equal to $0.082 \mu\text{m}$.

III. INFLUENCE OF ETCHING SLOPE

In this section, we analyse the effect of the fabrication imperfections due to the angle of the etching slope. In particular, when the ridge waveguide is perforated, the holes can result not perfectly straight, leading to conical air holes with a specific angle along x -axis and z -axis. The numerical analysis of these structures was performed by

commercial software Fullwave (Rsoft) implementing the FDTD method, and using a computational mesh of $p/32$ along each axis.

Figs. 1(b) and 1(c) show the perfect straight hole and the conical hole along the x -axis, respectively. Fig. 2(a) shows the Q-factor of the previously described nanobeam cavity configuration when the angle of the conical holes is varied between 0° and 10° along both axis ($\theta_x = \theta_z$) with a step equal to 2.5° . In particular, the Q-factor decreases of about a factor 3 and we observe a linear dependence of resonance wavelength on the etching angle, with a relevant red-shift of about $0.025 \mu\text{m}$. Furthermore, Fig. 2(b) reports the distinct influence of the etching angle along each single axis, considering the other one unaffected by the error ($\theta_x=0$ or $\theta_z=0$). These results reveal that the decrease of the Q-factor is dependent by the orientation on both directions. In particular, the fabrication imperfections due to etching slope along z -axis highly affect the one-dimensional nanobeam cavity performance, and this can be related to the fact that the major component (E_z) of the TE cavity mode is lined along the imperfection direction.

In 2D-PhC cavities, affected by an etching slope imperfection, the Q-factor degrades rapidly (about two orders of magnitude) because of the overlap between the TE cavity mode and the TM slab mode [9]. Conversely, our numerical results, show a decrease of about a factor 3 for 10° proving high fabrication tolerances over a wide range of etching angles.

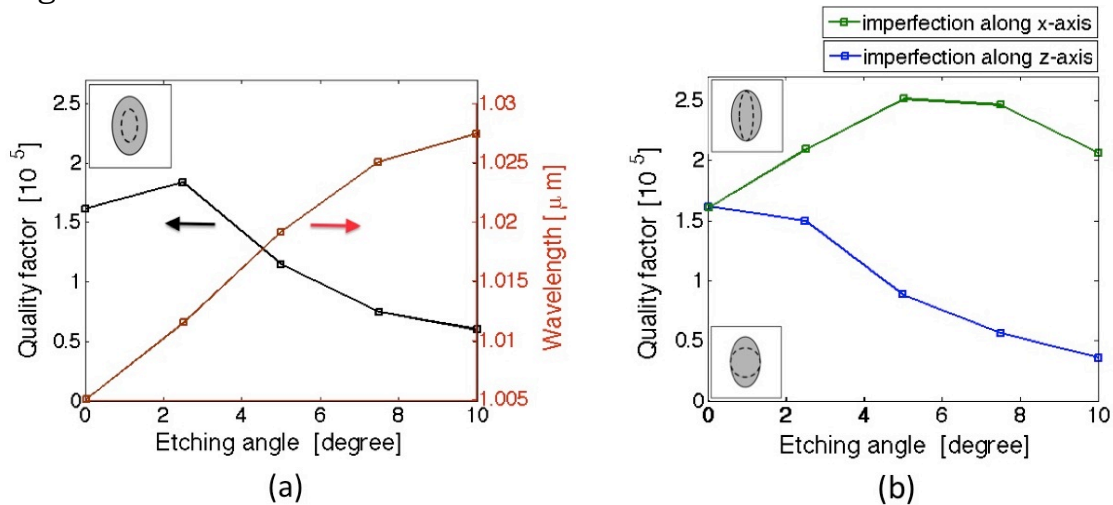


FIG. 2(a) – Q-factor (black curve) and wavelength of the resonant mode (red curve) as a function of the angle of the conical hole; (inset) top view of the conical hole (the dashed line refers to the nanobeam bottom face). **(b)** Q-factor as a function of the angle of the etching slope along x -axis (green line) and z -axis (blue line), respectively; top view hole with imperfection along x -axis (top inset) and along z -axis (bottom inset), respectively.

IV. CONCLUSION

In conclusion, we studied the influence of etching slope on optical nanobeam cavity performance in terms of Q-factor and resonant

wavelength. In particular, we have shown that a proper design can lead to high Q-factor avoiding the coupling between the TE and TM modes. At the same time, numerical results show that the etching angle can lead to modification of the Q-factor. Therefore, these results shed light on the effect of fabrication imperfections on optical nanobeams and give guidance in the reduction and improvement of their influence in integrated photonic circuits.

ACKNOWLEDGEMENT

D. Panettieri thanks the Politecnico di Bari for “Best Erasmus traineeship for jobs” grant. L. O’Faolain acknowledges support from a European Research Council Starting grant (no. 337508). M. Grande thanks the Apulia Region program "FutureInResearch" (7K76VI3) for financial support.

REFERENCES

- [1] Q. Quan, I. B. Burgess, S. K. Y. Tang, D. L. Floyd, and M. Loncar, “High-Q, low index-contrast polymeric photonic crystal nanobeam cavities,” *Opt. Express*, vol. 19, no. 22, pp. 22191–22197, (2011).
- [2] M. Davanço, S. Ates, Y. Liu, and K. Srinivasan, “Si₃N₄ optomechanical crystals in the resolved-sideband regime,” *Appl. Phys. Lett.*, vol. 104, no. 4, (2014).
- [3] Grande, M., L. O’Faolain, T. P. White, M. Spurny, A. D’Orazio, and T. Krauss, “Optical filter with very large stopband (≈ 300 nm) based on a photonic crystal vertical directional coupler,” *Optics Letters*, vol. 34, No. 21, 3292–3294, (2009).
- [4] S. Buckley, M. Radulaski, J. L. Zhang, J. Petykiewicz, K. Biermann, and J. Vuc̆ković, “Multimode nanobeam cavities for nonlinear optics: high quality resonances separated by an octave,” *Opt. Express*, vol. 22, no. 22, pp. 26498–509, (2014).
- [5] Q. Quan, and M. Loncar, “Deterministic design of high Q, small mode volume photonic crystal nanobeam cavities,” *Opt. Express* vol. 19, 18529–18542 (2011).
- [6] R. L. Savio, S. L. Portalupi, D. Gerace, A. Shakoor, T. F. Krauss, L. O’Faolain, L. C. Andreani & M. Galli "Room-temperature emission at telecom wavelengths from silicon photonic crystal nanocavities," *Appl. Phys. Lett.* Vol. 98, 201106 (2011).
- [7] T. M. Babinec, J. T. Choy, K. J. M. Smith, M. Khan, and M. Lončar, “Design and focused ion beam fabrication of single crystal diamond nanobeam cavities,” *J. Vac. Sci. Technol. B*, vol. 29, no. 010601, pp. 1–6, (2010).
- [8] S.Sergent, M. Arita, S.Kako, K.Tanabe, S.Iwamoto and Y. Arakawa, “High-Q AlN photonic crystal nanobeam cavities fabricated by layer transfer” *Appl. Phys. Lett.* vol. 101, 101106 (2012).
- [9] Kim, M.-K, Yang, J.-K, Lee, Y.-H and Hwang, I.-K, “Influence of etching slope on two-dimensional photonic crystal slab resonators,” *J. Korean Phys. Soc.* 50, 1027 (2007).

DESIGN AND ANALYSIS OF AN ULTRA-THIN DUAL-BAND METAMATERIAL ABSORBER FOR THZ APPLICATIONS

Maria Denise Astorino⁽¹⁾ and Nicola Tedeschi⁽¹⁾

⁽¹⁾ Department of Information Engineering, Electronics and Telecommunications, "La Sapienza" University of Rome
Via Eudossiana 18, 00184 Rome, Italy
mariadenise.astorino@uniroma1.it, nicola.tedeschi@uniroma1.it

Abstract

In this paper, we consider the design and analysis of an ultra-thin dual-band metamaterial absorber in the THz regime with a thickness of about $\lambda_0/16$ where λ_0 is the free-space wavelength, at the higher operating frequency. We have observed both a narrowing of the frequency response and a broadening of the angular response obtained through the insertion of a conducting ground plane. To retrieve the effective electromagnetic parameters of the structure, we have applied a homogenization technique to extract the relative electric permittivity, magnetic permeability and wave impedance.

Index Terms Absorber, homogenization, metamaterial, terahertz.

I. INTRODUCTION

Metamaterial absorbers find widespread and specific applications in the electromagnetic spectrum, ranging from the microwave to optical frequencies. In particular, in the THz regime, they are employed as photodetectors, microbolometers, phase modulators and they can be integrated into existing equipment to improve the performance (e.g. in reducing radar cross section to limit radar echo and in decreasing sidelobe radiation for antennas [1]).

In some cases, it is necessary to filter out multiple unwanted frequencies by means of selective multiple-band absorbers that reduce environmental disturbances and consequently increase the sensitivity and resolution of the images [2]. A characteristic model is represented by dual-band absorbers which are used in spectroscopic applications and development of terahertz detectors [3].

In this paper, exploiting the electric ring resonator (ERR) proposed in [4], we develop in Section II a model of ultra-thin dual-band metamaterial absorber with metallic ground plane thicker than the penetration depth, capable of providing a zero transmission of the wave at THz, for normal and oblique incidence for both TE and TM polarizations. In Section III, we present a homogenization technique for extracting the effective electromagnetic parameters and, finally, in Section IV we draw the conclusions.

II. ULTRA-THIN DUAL-BAND METAMATERIAL ABSORBER

The unit cell of the dual-band metamaterial absorber (Fig. 1), simulated with proper periodic boundary conditions, is composed of three gold metallizations (an upper ERR, a central cross and a lower metal plate) spaced by a 5 μm thick dielectric layer of benzocyclobutane BCB with relative permittivity $\epsilon_r = 2.5$ and loss tangent $\tan\delta = 0.005$, and a lower layer of silicon with a thickness of 6.5 μm .

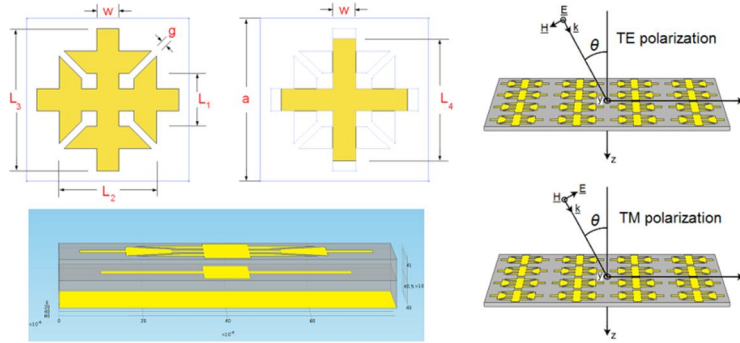


FIG. 1 Geometry of the ultra-thin dual-band metamaterial absorber with dimensions (in microns) $a=80$, $g=3.5$, $w=11$, $L_1=26$, $L_2=48$, $L_3=70$, $L_4=60$ and scheme of TE and TM polarizations.

The results obtained in Fig. 2 highlight two significant absorption peaks of 98.67% and 99.15%, respectively, at the frequencies of 0.75 THz and 1.15 THz at normal incidence. The relative full width at half-maximum (FWHM) absorption bandwidth is equal to 8.00% and 9.57% for the two absorption peaks, respectively. The TE-wave case was analysed with a parametric sweep on the angle of incidence θ (Fig. 2(a)) and it can be observed that, as the incidence angle increases, absorption levels decrease, the resonance frequencies remaining, however, unchanged. In Fig. 2(b), the dual-band metamaterial absorber was simulated in TM polarization and we observe with the increase of the incidence angle both a slight blueshift of the two resonance peaks and two additional absorption peaks at the frequencies of 0.93 THz and 1.38 THz.

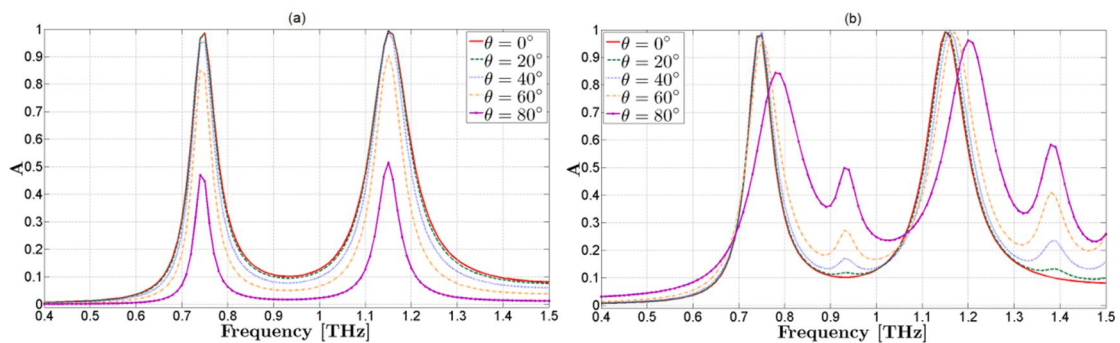


FIG. 2 Absorption spectra at normal incidence and at oblique incidence with (a) TE and (b) TM polarizations.

By performing a parametric sweep on the angle of incidence θ , the comparison between the absorptions relevant to the two resonance frequencies in both TE and TM polarizations shows wide angular responses typical of a polarization-insensitive absorber (see Fig. 3).

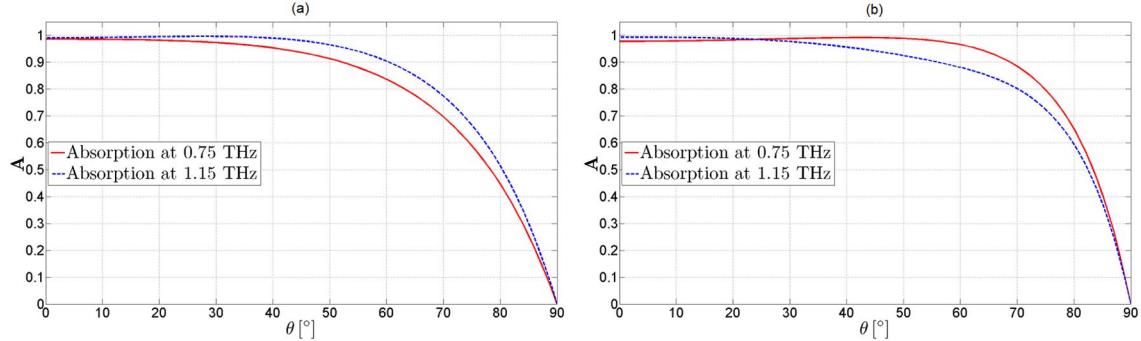


FIG. 3 Comparison between the absorptions at 0.75 THz and 1.15 THz in (a) TE and (b) TM polarizations.

Then, we study the influence of the loss tangent $\tan \delta$ of BCB on the absorption peaks, increasing gradually $\tan \delta$ from 0 (lossless dielectric) to 1 (Fig. 4(a)). The absorber shows a different behaviour for the two resonance frequencies and, in general, the absorption levels decrease with increasing $\tan \delta$ especially at 1.15 THz. We can also observe in Fig. 4(b) that at the resonance peaks, 98.54% and 99.73% energy are absorbed, respectively, with a lossless BCB. Therefore, the absorption is mainly due to the Ohmic losses of the metallizations and the dielectric losses of the highly resistive silicon layer.

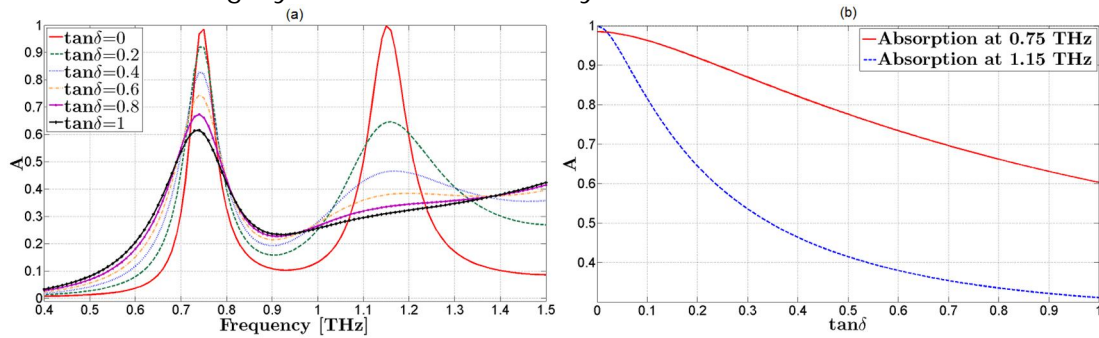


FIG. 4 (a) Absorption spectra and (b) comparison between absorptions at two resonance frequencies with increasing loss tangent.

III. HOMOGENIZATION TECHNIQUE

To retrieve the electromagnetic characteristics of the dual-band absorber, we have adopted the method of Nicolson, Ross and Weir (NRW) [5]. This algorithm has the advantage of a broadband characterization of materials and devices, but requires the translation of the scattering parameters from the reference planes to the surfaces of the material. The electromagnetic parameters extracted in normal

incidence through the implementation of the NRW algorithm in a Matlab code, show a resonant behavior characteristic of the Lorentz model. Figure 5 represents the real and imaginary parts of the permittivity, permeability and wave impedance of the dual-band metamaterial absorber which reaches a near-perfect impedance matching to free space at the absorptive peaks of 0.75 THz and 1.15 THz. In fact, the real part of the relative impedance close to the unity $Re(z) \cong 1$ and the minimized imaginary part $Im(z) \cong 0$ produce a reflection almost null at the resonance frequencies. Therefore, dielectric and magnetic losses in the system, characterized by the imaginary part of the refractive index, produce considerable attenuation of the wave.

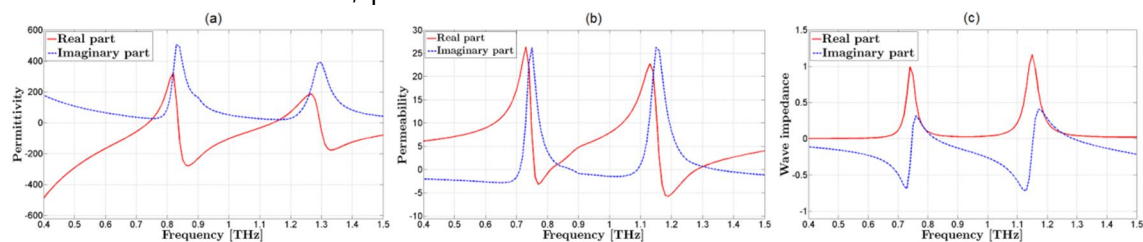


FIG. 5 Real and imaginary parts of the (a) permittivity, (b) permeability and (c) wave impedance of the ultra-thin dual-band metamaterial absorber.

IV. CONCLUSION

The proposed ultra-thin dual-band metamaterial absorber with remarkable absorption peaks at 0.75 THz and 1.15 THz, analysed at different incidence angles and polarizations, has shown a narrow frequency response and a wide angular response. The NRW algorithm has allowed to extract the effective electromagnetic parameters which have taken the typical form of the Lorentz oscillator response.

REFERENCES

- [1] C. M. Watts, X. Liu, and W. J. Padilla, "Metamaterial electromagnetic wave absorbers," *Advanced Optical Materials*, vol. 24, no. 23, pp. 98-120, Jun. 2012.
- [2] F. Hu, L. Wang, B. Quan, X. Xu, Z. Li, Z. Wu, and X. Pan, "Design of a polarization insensitive multiband terahertz metamaterial absorber," *Journal of Physics D: Applied Physics*, vol. 46, pp. 1-8, 2013.
- [3] Y. Ma, Q. Chen, J. Grant, S. C. Saha, A. Khalid, and D. R. S. Cumming, "A terahertz polarization insensitive dual band metamaterial absorber," *Optics Letters*, vol. 36, no. 6, pp. 945-947, Mar. 2011.
- [4] N. I. Landy, C. M. Bingham, T. Tyler, N. Jokerst, D. R. Smith, and W. J. Padilla, "Design, theory, and measurement of a polarization-insensitive absorber for terahertz imaging," *Phys. Rev. B*, vol. 79, no. 12, 2009.
- [5] A. M. Nicolson and G. F. Ross, "Measurements of the intrinsic properties of materials by time-domain techniques," *IEEE Transactions on Instrumentation and Measurement*, vol. 19, no. 4, pp. 377-382, Nov. 1970.

MATERIAL-BY-DESIGN PHASED ARRAYS SYNTHESIS

L. Tenuti⁽¹⁾

- (1) ELEDIA Research Center (ELEDIA@UniTN, University of Trento)
via Sommarive 5, 38123 Trento, Italy
lorenza.tenuti@eledia.org

Abstract

An innovative approach based on the Material-by-Design paradigm is proposed in this paper in order to synthesize metamaterial devices able to enhance the features (radiation, size, etc.) of advanced antenna arrays. Various blocks which integrate a search procedure based on the inertial-weight version of the particle-swarm (PS) approach and a Learning-by-Example (LBE) regression strategy will be exploited in the design process. The cost function, which will be a measure of the mismatch between desired and obtained radiation features, will be evaluated without requiring full-wave numerical simulations at each iteration of the iterative search procedure. The effectiveness of the introduced approach will be validated in the design of an inhomogeneous isotropic metamaterial lens exploited to miniaturize a linear array.

Index Terms – Learning-by-Example, Material-by-Design, Transformation-Optics.

I. INTRODUCTION

The problem of miniaturizing an array is a fundamental antenna engineering problem arising whenever the weight, size, or bulk of the radiating system is a requirement/constraint in the design process (e.g., in satellite or airborne applications) [1][2]. Toward this end, several methodologies have been proposed in the literature, usually based on non-uniform geometries [1]-[5]. Nevertheless, the reduction of the aperture width and of the number of TRM at the same time is an issue which has been seldomly addressed in scientific community.

Recently, suitably designed metamaterial covers have been proposed in the process of designing miniaturized arrays [10]. A generalization of the quasi-conformal-transformation-optics (QCTO) [6][9] is in this work presented in order to deduce the inhomogeneous radome profile properties as well as the new array configuration such that the field radiated by the new architecture matches the one of a wider array comprising more elements [10]. Unfortunately, very often the permittivity values of the designed lens turn out being extremely large, thus yielding to high costs/complexities for its fabrication.

In this work, the intrinsic degrees of freedom in the design procedure in [10] are exploited to reduce the final radome anisotropy. A virtual geometry (large array in free space, whose radiation features we want to reproduce) and a physical geometry (shorter and with less elements

array covered by the radome) must be defined [10]. If we are able to parametrize the virtual geometry by using for example a spline-shaped contour it is then possible to reformulate the design problem as an optimization one in which the degrees of freedom that have to be optimized are the spline control points. In the cost function it is then possible to include a term for the minimization of the radome permittivity and a term for the minimization of the mismatch between the fields radiated by the compact and the large arrays.

In the following the SbD paradigm, defined as “functional ecosystem to handle complexity in the design of large systems” [11][12], will be exploited in order to decompose the optimization problem described above into simpler functional blocks.

II. PROBLEM FORMULATION AND DESIGN METHODOLOGY

Let the large array in free space be constituted by N_v radiating elements located at position $\mathbf{r}_n = \left(x_n = 0, y_n = (n-1)d_v - \frac{L_v}{2} \right)$ where d_v is the inter-element spacing and L_v is the virtual array length. The physical array that has to be synthesized must comprise a reduced number of elements $N_p < N_v$, have a reduced aperture $L_p = (N_p - 1)d_p < L_v$ and radiate a field $E(\mathbf{r})$ as close as possible to the one radiated by the virtual geometry. As a further constraint, the relative permittivity of the synthesized lens should be as close as possible to the one of the empty space.

The SbD paradigm is customized by combining a transformation electromagnetic block [6]-[10], through which the virtual and physical geometries are defined, and a surrogate-enhanced cost function evaluation block [11]-[12]. The problem addressed by the first block can be stated as “finding the physical lens relative dielectric properties and the array excitations such that the field radiated by the array coated with the lens radiates a field $E(\mathbf{r})$ as close as possible to the reference one”; if the virtual geometry is discretized using a set of spline descriptors \mathbf{s} , the aim of the second block is the minimization of the following cost function

$$\Phi(\mathbf{s}) = \frac{\beta_1 \psi_{rad} + \beta_2 \psi_{\epsilon_{max}}}{\beta_1 + \beta_2} \quad (1)$$

where ψ_{rad} is the term which counts for the mismatch between physical and virtual geometry, $\psi_{\epsilon_{max}}$ is the term which counts for the permittivity values of the synthesized lens and β_1, β_2 are user defined weights. Because of the continuous nature of the design variables, and because of the high nonlinearity of the cost function, the search procedure is

based on the inertial-weight version of the particle-swarm (PS) approach [13].

The Learning-by-Example (LBE) regression strategy (belonging to the class of Gaussian Process (GP) [12]) is adopted to reduce the number of expensive full-wave simulations required to compute (1) without performing expensive full-wave simulations at each iteration of the optimization process.

III. RESULTS

In order to preliminarily assess the validity of the proposed method, let us consider an array which comprises $N_v = 16$ uniformly-excited elements with inter-element spacing equal to $d_v = \frac{\lambda}{2}$. The radiated pattern is represented in Fig.1 (red line).

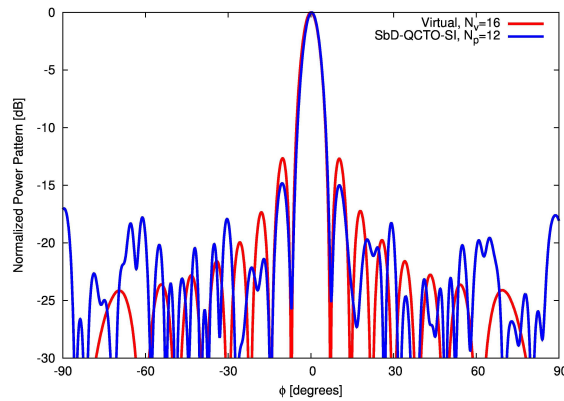


FIG. 1 – Power patterns radiated by the virtual and the miniaturized configurations.

The proposed synthesis methodology has been applied; as for the control parameters of the inertial-weight version of the particle-swarm approach, the swarm dimension has been set equal to $S = 8$, and the maximum number of iterations to $I = 200$. The plot of the final layout comprises only $N_p = 12$ non-uniformly excited elements. Moreover, the lens synthesized using the proposed approach yields a reliable control of the mainlobe width and of the envelope of the sidelobes, as can be noticed analyzing the far field pattern in Fig. 1 (blue line). Furthermore, the maximum permittivity value is only $\epsilon_{\max} = 3.0 \times 10^1$.

IV. CONCLUSION

An innovative approach which combines an Learning-by-Example-enhanced optimization loop has been presented for the synthesis of

advanced antenna systems comprising complex metamaterial lenses. The effectiveness of the proposed technique has been preliminarily assessed in the design of miniaturized arrays demonstrating its effectiveness and flexibility.

REFERENCES

- [1] D. H. Browne, M. Manteghi, M. P. Filtz, and Y. Rahmat-Samii, "Experiments with compact antenna arrays for MIMO radio communications," *IEEE Trans. Antennas Propag.*, vol. 54, no. 11, pp. 3239-3250, Nov. 2006.
- [2] Y. Fei, Y. Fan, B. K. Lau, and J. S. Thompson, "Optimal single-point matching impedance for capacity maximization in compact MIMO arrays," *IEEE Trans. Antennas Propag.*, vol. 56, no. 11, pp. 3566-3575.
- [3] G. Oliveri, F. Caramanica, C. Fontanari, and A. Massa, "Rectangular thinned arrays based on McFarland difference sets," *IEEE Trans. Antennas Propag.*, vol. 59, no. 5, pp. 1546-1552, May 2011.
- [4] G. Oliveri and A. Massa, "Bayesian compressive sampling for pattern synthesis with maximally sparse non-uniform linear arrays," *IEEE Trans. Antennas Propag.*, vol. 59, no. 2, pp. 467-481, Feb. 2011.
- [5] G. Oliveri, M. Carlin, and A. Massa, "Complex-weight sparse linear array synthesis by Bayesian Compressive Sampling," *IEEE Trans. Antennas Propag.*, vol. 60, no. 5, pp. 2309-2326, May 2012.
- [6] D. H. Werner and D.-H. Kwon Eds., *Transformation Electromagnetics and Metamaterials: Fundamental Principles, and Applications*, London: Springer, 2014.
- [7] G. Oliveri, D. H. Werner, and A. Massa, "Reconfigurable electromagnetics through metamaterials - A review", *Proc. IEEE*, vol. 103, no. 7, pp. 1034-1056, Jul. 2015.
- [8] D.-H. Kwon, "Quasi-conformal transformation optics lenses for conformal arrays," *IEEE Antennas Wireless Propag. Lett.*, vol. 11, Sep. 2012.
- [9] G. Oliveri, E. T. Bekele, D. H. Werner, J. P. Turpin, and A. Massa, "Generalized QCTO for metamaterial-lens-coated conformal arrays," *IEEE Trans. Antennas Propag.*, vol. 62, no. 8, pp. 4089-4095, Aug. 2014.
- [10] G. Oliveri, E. T. Bekele, M. Salucci, and A. Massa, "Array miniaturization through QCTO-SI metamaterial radomes," *IEEE Trans. Antennas Propag.*, vol. 63, no. 8, Aug. 2015.
- [11] A. Massa, G. Oliveri, P. Rocca, and F. Viani, "System-by-Design: a new paradigm for handling design complexity," in 8-th European Conf. Antennas Propag (EuCAP 2014), The Hague (NL), pp. 1423-1426, Apr. 6-11, 2014.
- [12] G. Oliveri, L. Tenuti, E. Bekele, M. Carlin, and A. Massa, "An SbD-QCTO approach to the synthesis of isotropic metamaterial lenses," *IEEE Antennas Wireless Propag. Lett.*, vol. 13, pp. 1783-1786, 2014.
- [13] P. Rocca, M. Benedetti, M. Donelli, D. Franceschini, and A. Massa, "Evolutionary Optimization as applied to inverse scattering problems," *Inverse Prob.*, vol. 25, no. 12, pp. 1-41, Dec. 2009.

EFFECT OF EXTREME ANISOTROPY ON THE REFLECTION FROM THE INTERFACE OF A MATCHED UNIAXIAL MEDIUM

M. Khalid

Department of Information Engineering, Electronics and Telecommunications, "La Sapienza" University of Rome, Rome, Italy
khwattoo@yahoo.com

Abstract

Electromagnetic plane-wave reflection from the interface of a general uniaxially anisotropic medium, characterized by extreme material parameters, very large transverse and very small axial components of the permittivity and permeability tensors, is investigated. The effect of the direction of the optic axis and the plane of incidence on the reflection behavior is analyzed. Reflection results show that the medium exhibits interesting properties of behaving like a perfect reflector, a perfect absorber and a polarization inverter.

Index Terms – Anisotropic media, extreme parameters, plane-wave reflection, metamaterials.

I. INTRODUCTION

Various classes of metamaterials with extreme parameters (very large or very small) have been proposed for the realization of well-known boundary conditions, for example: perfect electric conductor (PEC), perfect magnetic conductor (PMC) and perfect electric magnetic conductor (PEMC) boundary conditions [1]-[3]. Similarly, impedance boundary (IB) conditions can be approximated by an anisotropic medium having infinite components of both permittivity and permeability in the normal direction to the material interface [4]. On the other hand, the DB boundary introduced in [5] can be mimicked in terms of an anisotropic medium with null values of both permittivity and permeability in the normal direction to the interface. It was suggested that the components in the tangential directions may have arbitrary values as they do not influence the DB response [5].

DB boundary shows the behavior of an angular spatial filter. It presents total transmission for normally incident waves and total reflection for all other incidence angles. It has been shown in [6] that the DB-boundary medium can behave as an electromagnetic absorbing medium for all incidence angles if the permittivity and permeability components of the anisotropic metamaterial in the tangential direction to the interface are properly chosen. It is important to mention that the optic axis of the uniaxial metamaterial emulating the DB boundary conditions must be perpendicular to the interface.

The purpose of the present paper is to analyze the reflection from the interface of a peculiar anisotropic medium with arbitrarily oriented

optic axis and characterized by particular material parameters (very large transverse and very small axial components). The effect of direction of the optic axis and the plane of incidence on the reflection properties is investigated.

II. REFLECTION FROM THE INTERFACE

A general uniaxially anisotropic medium with arbitrarily directed optic axis can be expressed by the following permittivity and permeability dyadics:

$$\underline{\underline{\varepsilon}} = \varepsilon_t \underline{\underline{I}}_t + \varepsilon_c \hat{c} \hat{c} \quad \text{and} \quad \underline{\underline{\mu}} = \mu_t \underline{\underline{I}}_t + \mu_c \hat{c} \hat{c}, \quad (1)$$

where t and c represent the perpendicular and parallel directions with respect to the optic axis. $\underline{\underline{I}}_t$ is the two-dimensional unit dyadic such that $\underline{\underline{I}}_t = \underline{\underline{I}} - \hat{c} \hat{c}$. Let us consider a plane wave impinging from Medium 1 on an interface with the uniaxial medium (Medium 2) defined by Eq. (1). The wave vector k_i makes an angle θ_i with the z -axis and its projection on the interface makes an angle ϕ_i with the x -axis, as shown in Fig. 1. The optic axis represented by a vector c makes an angle ψ with the z -axis.

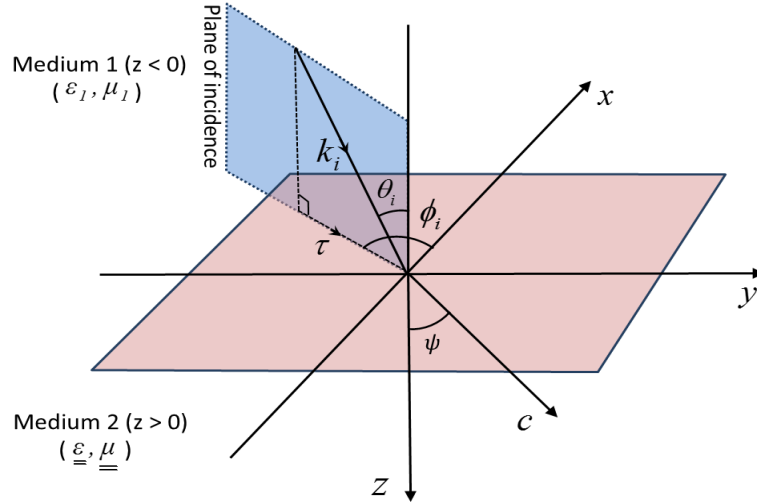


FIG. 1 – Geometry of the problem.

We assume that the impedance of the uniaxial medium is matched with the medium in front of the interface and the permittivity and permeability components in Eq. (1) fulfill the following conditions:

$$\varepsilon_t = M \varepsilon_1 - j \alpha_t \quad \text{and} \quad \varepsilon_c = \frac{\varepsilon_1}{M} - j \alpha_c, \quad (2)$$

where the parameter M defines the amplitude of the real parts of permittivity and permeability. α_t and α_c represent the material losses in the transverse and axial directions, respectively. It can be noted that when $M \rightarrow \infty$, $\text{Re}[\varepsilon_t] \rightarrow \infty$ and $\text{Re}[\varepsilon_c] \rightarrow 0$. Analytical expressions for the

reflection and transmission coefficients for a general electric-magnetic uniaxial medium are explicitly reported in [7].

III. NUMERICAL RESULTS AND DISCUSSION

The quantities α_t and α_c in Eq. (2), in general, may have different values but for simplicity we assume that they are equal, i.e., $\alpha_t = \alpha_c = \alpha$. To study the reflection first we consider that the plane of incidence and the plane of optic axis are co-planar, i.e., $\phi_i = \pi/2$. The reflection coefficient as a function of the angle ψ of the optic axis is shown in Fig. 2. We note that the reflection coefficient is zero when the optic axis is perpendicular to the interface ($\psi = 0$). However, for $\psi \neq 0$ the reflection coefficient suddenly

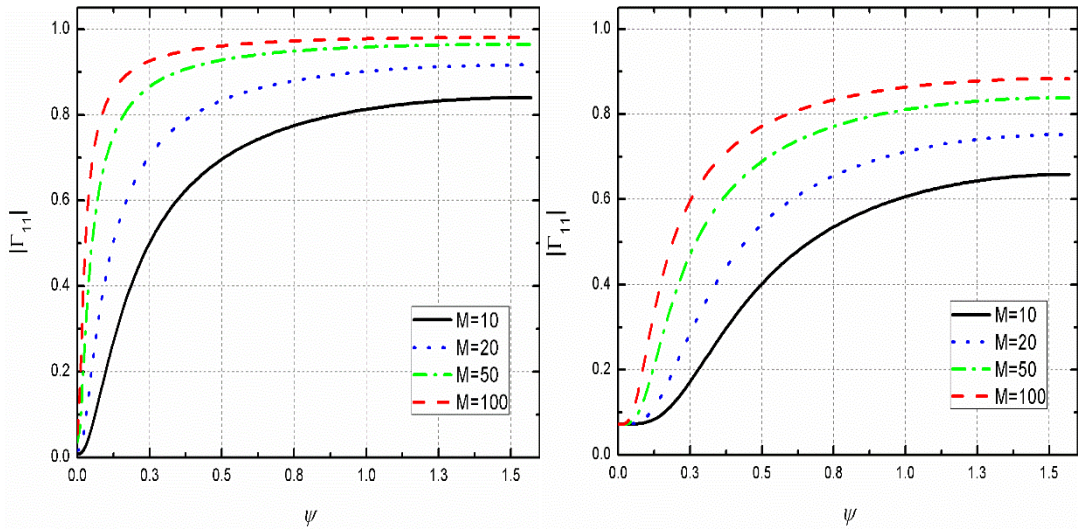


FIG. 2 – Magnitude of the reflection coefficient $|\Gamma_{11}|$ for (a) $\alpha = 0.01$ and (b) $\alpha = 1.0$ as a function of the angle ψ of the optic axis for different M values when $\varepsilon_1 = \mu_1 = 1$ and $\theta_i = \pi/6$.

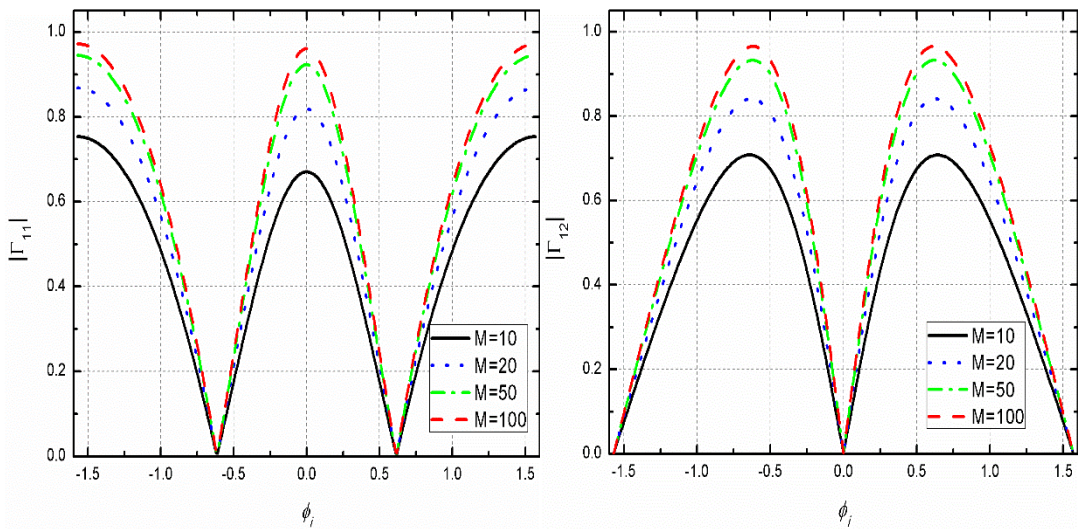


FIG. 3 – Magnitude of the reflection coefficient (a) $|\Gamma_{11}|$ and (b) $|\Gamma_{12}|$ as a function of the angle ϕ_i for different M values when $\varepsilon_1 = \mu_1 = 1$, $\theta_i = \pi/6$ and $\alpha = 0.01$.

approaches unity when $M \rightarrow \infty$ and $\alpha \ll 1$. In Fig. 3 the magnitudes of the reflection coefficients as a function of the angle ϕ_i defining the direction of the plane of incidence for different values of M are plotted. The results show that the cross components Γ_{12} are also present in the reflected field when the plane of incidence is neither parallel nor perpendicular to the plane containing the optic axis. Moreover, for sufficiently large M , there exists a direction of the plane of incidence at which the co-component of the reflection coefficient is totally transmitted whereas the cross-component is totally reflected.

IV. CONCLUSION

In this paper the reflection from the interface of a novel uniaxial medium characterized by peculiar material parameters (very large transverse and very small axial) and with optic axis in a generic direction is studied. It is noted that for large M the interface of the medium acts as a perfect transmitter or perfect reflector depending on the direction of the optic axis. Furthermore, we note that there exists a particular direction ϕ_i of the plane of incidence at which the interface shows total transmission to the co-component of the reflected field and total reflection to the cross-component. Due to this property, the medium can be used to invert the polarization of the incident wave. The future work can be focused to calculate an analytical relation for this Brewster-like angle.

REFERENCES

- [1] I. V. Lindell, *Methods of electromagnetic field analysis*, Oxford UK, Oxford Univ. Press, 1992.
- [2] I. V. Lindell and A. H. Sihvola, "Realization of the PEMC boundary," *IEEE Trans. Antennas and Propag.*, vol. 53(9), pp. 3012-3018, Sep. 2005.
- [3] A. H. Sihvola, S. Tretyakov, and A. de Baas, "Metamaterials with extreme material parameters," *J. Commun. Tech. Electronics*, vol. 52(9), pp. 986-990, Sep. 2007.
- [4] I. V. Lindell and A. H. Sihvola, "Realization of impedance boundary," *IEEE Trans. Antennas and Propag.*, vol. 54(12), pp. 3669-3676, Dec. 2006.
- [5] I. V. Lindell and A. H. Sihvola, "Electromagnetic boundary condition and its realization with anisotropic metamaterial," *Phys. Rev. E*, vol. 79(026604), pp. 1-7, Feb. 2009.
- [6] N. Tedeschi, F. Frezza, and A. Sihvola, "On the perfectly matched layer and the DB boundary conditions," *J. Opt. Soc. Am. A.*, vol. 30(10), pp. 1941-1946, 2013.
- [7] N. Tedeschi, F. Frezza, and A. Sihvola, "Reflection and transmission at the interface with an electric-magnetic uniaxial medium with applications to boundary conditions," *IEEE Trans. Antennas and Propag.*, vol. 61(11), pp. 5666-5675, Nov. 2013.

Influence of Disorder on Lasing Onset in Planar Media

C. Molardi⁽¹⁾, X. Yu⁽²⁾, H.K. Liang⁽²⁾, A. Cucinotta⁽¹⁾, S. Selleri⁽¹⁾.

⁽¹⁾ Department of Information Engineering, Parma University
Viale delle Scienze 181/A, Parma, Italy

⁽²⁾ Precision Measurement Group, Singapore Institute of
Manufacturing Technology,
71Nanyang Drive 638075, Singapore
email@unipr.it

Abstract

Lasing properties of a two dimensional active disordered structure with enhanced scattering have been investigated. The structure consists in a QCL substrate properly etched to obtain a random pattern of holes. The number of holes has been varied to achieve different intensities of scattering and to investigate the impact of the increasing disorder. The analysis has been attained with the help of a Monte Carlo numerical strategy, implemented in a custom software. The obtained results show the dependency of lasing onset on the growth of holes filling factor. In particular, it is possible to evidence a transition from a gaussian-like distribution to a negative exponential distribution, when the lasing threshold is reached.

Index Terms – Disordered media, Mid-IR laser, Monte Carlo method, Random laser.

I. INTRODUCTION

As the transport behavior of light in disordered media is growing interest, in particular due to the difficulty to find a complete theoretical description [1], the scientific community is actively searching for tangible applications to exploit the properties of such materials. Some examples can be retrieved in the field of imaging and sensing [2], or in the area of energy harvesting [3]. Such structures, which exhibit an intense degree of disorder, force photons transport to be influenced by multiple scattering. The interaction between photons and the scattering centers makes the light transport to become similar to a random walk.

The scattering intensity is a key factor to describe photon diffusion in the material [4], which can range from a ballistic behavior to a more complex localized regime, as the scattering increases its contribution. The idea of localization, originated from the work of Anderson [5], can be referred as a stop of light diffusion in the material. Nevertheless the issues, related to localization, are far more complicated and only with the help of a quantum mechanics description it can be fully understood. A simplified picture can be drawn claiming for simpler mechanism like back-scattering or whispering gallery modes onset [6], [7].

When the light transport, influenced by the disorder, is combined with the effect of amplification given by an active medium, the structure

can become a cradle of an uncommon lasing effect, usually referred as “random lasing”. A random laser is a laser without a cavity, where the feedback is given by multiple scattering. Light, forced to travel through longer paths, can reach lasing threshold, exhibiting an emission characterized by a spectrum composed by several narrow spikes with poor correlation with respect to each other. The comparison with a traditional laser evidences a complex scenario, where the lasing frequencies, i.e. the modes, are not only influenced by the disorder distribution, but also by the competition between the amplification resources.

In this contribution, a 2D slab emitting in the region of Mid-IR [8], [9], obtained by digging a random pattern of holes in a Quantum Cascade Laser (QCL) substrate, has been numerically investigated through the use of a custom software, based on Monte Carlo (MC) method. This software has been equipped with a complete pump and amplification model. Statistical information on photon travel distance and lasing onset have been retrieved varying the scattering intensity.

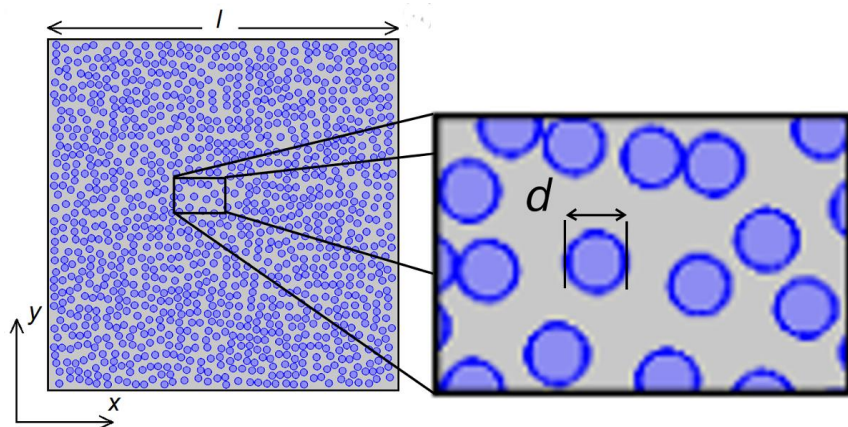


FIG. 1 – Example of a square slab with $FF = 0.4$. The side l is $150 \mu\text{m}$, while the random pattern is composed by holes with diameter d of $3 \mu\text{m}$.

II. 2D SLAB

The structure, analyzed in this contribution and shown in Fig.1, is a planar slab where a number of holes is carved in a QCL substrate compound of Indium-Gallium and Aluminum Arsenide. The refractive index of the compound is 3.35, at the emitting wavelength around $10 \mu\text{m}$, in the Mid-IR region. The pumping system is described by an electronic mechanism. The square slab is shaped with side of $150 \mu\text{m}$ and thickness of $2.2 \mu\text{m}$. The large ratio between square side and thickness is enough to justify a 2D approximation. The circular holes have diameter of $3 \mu\text{m}$. The random holes pattern has been varied, changing the Filling Factor (FF), defined as the area of the holes over the total area of the slab, in order to evaluate the different scattering impact given by the increase of disorder.

III. INVESTIGATION METHOD

To investigate the structure, putting on evidence the statistics of the emission properties with respect to the degree of disorder and to the impact, given by the scattering imposed by the holes, a Monte Carlo (MC) method, implemented with a custom software, has been chosen. Using this strategy it is possible to access to the properties of photons diffusion, which cannot be achieved using numerical method like Finite Element Method (FEM). The core of MC strategy is to consider packets of photons, which travel into the disordered structure, and interact with the scattering centers, according to the Mie theory. During their diffusion, photon packets locally absorb or lose energy, in agreement with lasing amplification and competition for pumping resources.

IV. RESULTS

The system has been analyzed in two different, but significant, situations: with pump turned off, i.e in the cold cavity case , and with pump turned on with a input current density of 9 kA cm^{-2} . In the lossy case, the emitted packets intensity statistic, considering a poor material attenuation, appears to be gaussian-like, with the tendency to concentrate the average emission intensity on values lower than the average intensity of the input packet, Fig. 2a, when the filling factor is raised. This can be explained by the fact that the increase of disorder, given by the higher value of filling factor, forces the photons to travel a larger distance with a consequent higher loss.

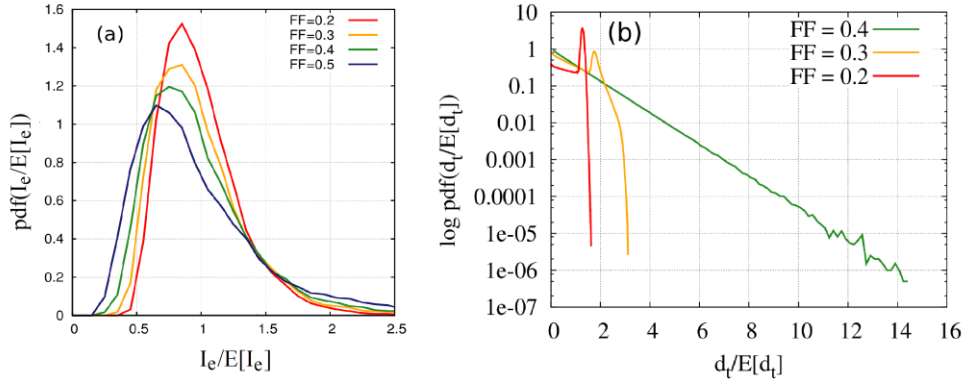


FIG. 2 – (a) Statistic of intensity emission pattern in the cold cavity. (b) Statistic of photon travel distance when the system is turned on and fed with a current density of 9 kA cm^{-2} .

When the pump is activated, the photon packets experience a gain induced by the mechanism of stimulated emission. The gain counteracts the attenuation of the material, permitting the photon packets to travel longer distance. Depending on the value of filling factor, some packets, typically a small fraction, can travel enough to contribute to the onset of laser emission. In such a case, Fig. 2b, it is

evident that the transition of the statistic, toward a negative exponential distribution, is representing the lasing threshold. Otherwise the statistics, dominated by the attenuation, maintain a gaussian-like profile.

V. CONCLUSION

In this work, the phenomenon of random lasing in a QCL slab, provided with a disordered pattern of holes, has been investigated. The impact of holes Filling Factor reduces the lasing onset. Through the use of a Monte Carlo strategy it has been possible to investigate the statistics of photons diffusion. The simulations show a clear transition to a negative exponential distribution of the photons travel distance at the lasing threshold.

ACKNOWLEDGEMENT

This work has been supported by the Agency for Science Technology and Research through the Advanced Optics in Engineering Program (Grant No. 122 360 0011) and A_STAR Research Attachment Program.

REFERENCES

- [1] J. Andreasen, A. Asatryan, L. Botten, M. Byrne, H. Cao, L. Ge, L. Labonté, P. Sebbah, A. Stone, H. Türeci, and C. Vanneste, “Modes of random lasers,” *Adv. Opt. Photon.* , vol. 3, pp. 88-127, 2011.
- [2] B. Redding, M. A. Choma, and H. Cao, “Speckle-free laser imaging using random laser illumination,” *Nature Photon.* , vol. 6, pp. 355–359, 2012.
- [3] F. Pratesi, M. Burresi, F. Riboli, K. Vynck, and D. S. Wiersma “Disordered photonic structures for light harvesting in solar cells,” *Opt. Express*, vol. 21, pp. A460–A468, 2013.
- [4] N. M. Lawandy, R. M. Balachandran, A. S. L. Gomes, and E. Sauvain, “Laser action in strongly scattering media,” *Nature*, vol. 368, pp. 436-438, 1994.
- [5] M. Segev, Y. Silberberg, and D. N. Christodoulides “Anderson localization of light,” *Nature Photon.* , vol. 7, pp. 197–204, 2013.
- [6] K. L. van der Molen, R. W. Tjerkstra, A. P. Mosk, and A. Lagendijk, “Spatial extent of random laser modes,” *Phys. Rev. Lett.* , vol. 98, pp. 143901-4, 2007.
- [7] D. S. Wiersma, “The physics and applications of random laser,” *Nature Phys.* , vol. 4, pp. 359–367, 2008.
- [8] H. K. Liang, B. Meng, G. Liang, J. Tao, Y. Chong, Q. J. Wang, and Y. Zhang, “Electrically Pumped Mid-Infrared Random Lasers,” *Adv. Mater.* , vol. 25, pp. 6859-6863, 2013.
- [9] C. Molardi, X. Yu, H. Liang, Y. Zhang, A. Cucinotta, and S. Selleri, “Modal analysis in 2D media with variable disorder,” *Opt. Express*, vol. 23, pp. 3681-3689, 2015.

A SIMPLE WIDE-ANGLE METAMATERIAL ABSORBER

E. Sassolini, N. Tedeschi, M. Khalid, E. Lia, M.D. Astorino, F.Frezza

Department of Information Engineering, Electronics and Telecommunications
(DIET), "La Sapienza" University of Rome
Via Eudossiana 18, 00184 Rome, Italy

Abstract

We present a metamaterial device with a simple structure, which efficiently absorbs electromagnetic radiation for a wide range of incidence angles. The metamaterial device consists of a square split-ring resonator and a metallic plate separated by a dielectric layer. We show that by optimizing the design and by properly tailoring the structure's dimensions, the metamaterial device allows us to obtain a good wide angular absorption in the microwave X-band.

Index Terms – Angular absorption, metamaterials, perfect absorber.

I. INTRODUCTION

Metamaterials were theorized by Veselago in 1968 [1]. The Russian scientist hypothesized that a material with negative refractive index might have some exotic properties: for example, negative refraction. In subsequent decades, knowledge of metamaterials grew and their possible fields of application became more numerous and varied [2]. In this paper, we examine the behavior of a particular kind of metamaterial device: perfect absorbers, originally introduced in [3]. The structure of this metamaterial device consists of two suitably shaped metallic inclusions placed on a dielectric slab. This paper presents a simple structure of a perfect metamaterial absorber. The preliminary layout has a classic configuration consisting of a square split-ring resonator and a metallic strip that works well as a perfect absorber at a fixed frequency in the microwave X-band, but only for the wave striking at normal incidence. Small alterations in the geometric structure of the device permitted us to obtain a new device, with very simple geometry but strongly enhanced angular absorption. The initial structure was made up of a square ring resonator and a metallic strip placed on the two sides of a dielectric layer with thickness 0.65 mm and complex relative dielectric constant $3-i0.06$, as shown in Fig. 1.

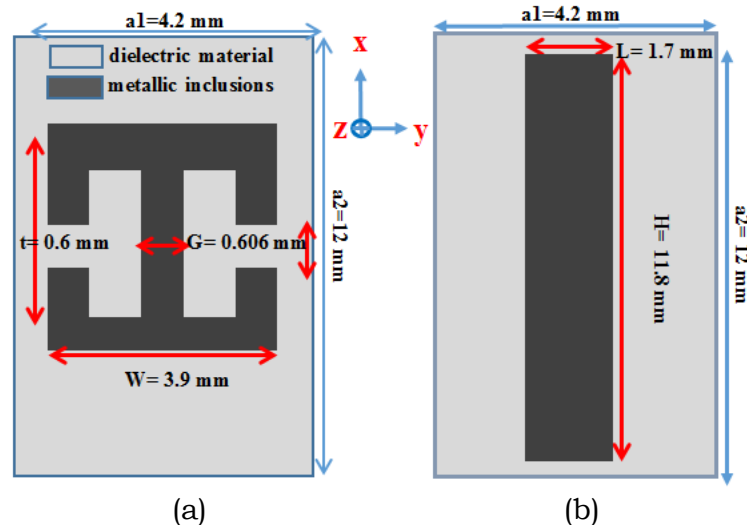


Fig. 1. Layout of the metamaterial device. The resonator and the metallic strip are located on the two sides of a dielectric layer. The electromagnetic radiation propagates along the z-axis. The complex relative permittivity of the dielectric medium is $3-i0.06$.

Fig. 1 shows the geometry of the metamaterial absorber introduced in [3]. The metallic inclusions are made of copper. The square resonator is located at the top layer, and the metallic strip is located at the bottom one (the electromagnetic radiation propagates along the positive z direction, impinging on the side with square resonator, see Fig.1). This metamaterial device behaves like an absorber in the microwave X-band, particularly at the frequency of 11.60 GHz for a normally incident plane wave. However, the absorption quickly decreases as the incidence angle of the electromagnetic radiation increases. The behavior of the metamaterial device as a function of the operating frequency and the angle of incidence is illustrated in Fig. 2.

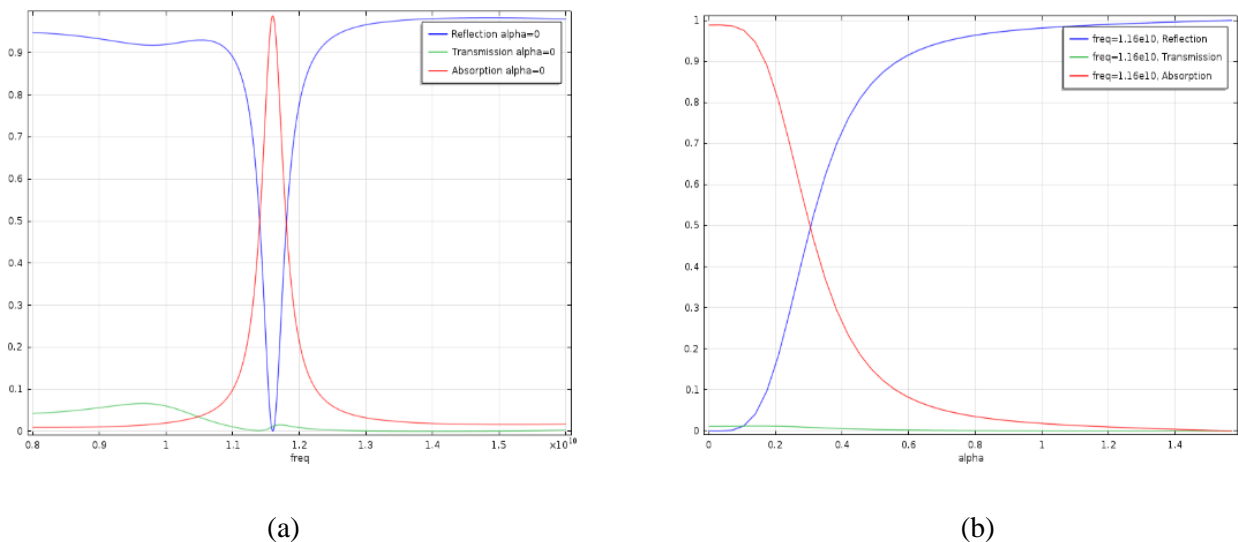


Fig. 2. Simulated reflection, transmission and absorption curves: (a) as a function of frequency (Hz) for normal incidence; (b) as a function of the incidence angle (radians) at the operating frequency of 11.60 GHz.

In the next section we describe the new device which enhances the angular absorption.

II. A SIMPLE WIDE-ANGULAR METAMATERIAL ABSORBER

The initial structure was modified to achieve an improved performance of the metamaterial absorber. The main factor which determines the properties of this kind of device is its geometry. In fact, since the size and shape of the metallic inclusions affect the value of the capacitance and inductance [4-6], it is possible to control the response of this device by tuning the geometry of the structure. In this section we present a simple perfect metamaterial device which efficiently absorbs electromagnetic radiation at 11.49 GHz for a wide range of incidence angles. The geometry of this metamaterial device and its behavior as a function of frequency and incidence angle are depicted in Fig. 3.

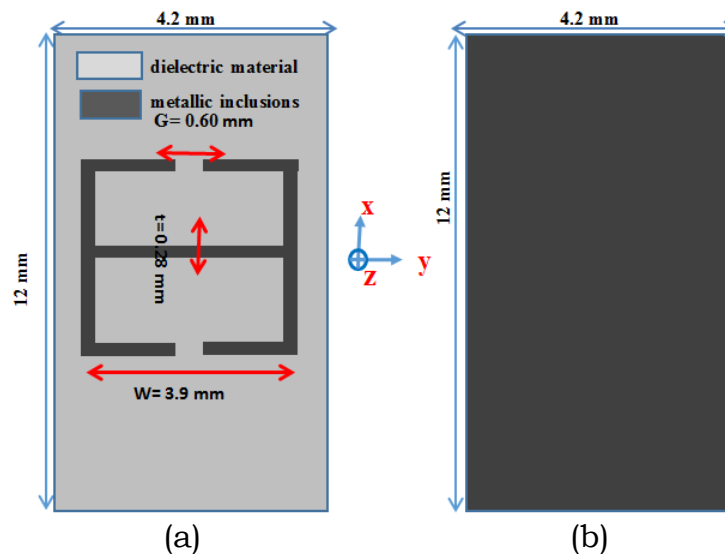


Fig. 3. Layout of the new metamaterial absorber. The resonator and metallic plate are located at the two sides of a dielectric layer. The electromagnetic radiation propagates along the z-axis positive direction. The complex relative permittivity of the dielectric medium is $4.50-i0.06$.

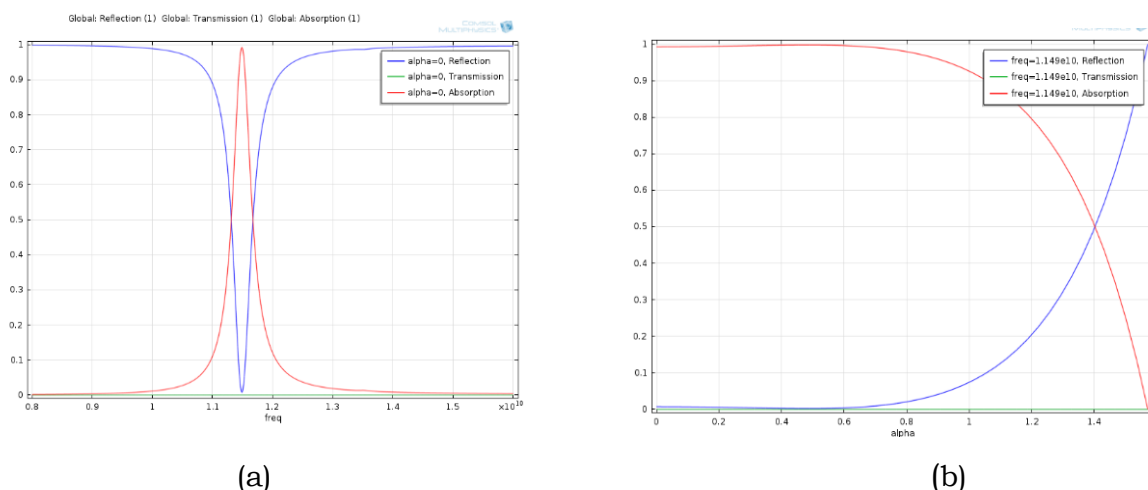


Fig. 4. Results of numerical simulations: (a) frequency sweep with resonance at 11.49 GHz; (b) angular sweep (radians). Clearly for wide angles a strong absorption occurs (indicated in red).

The figures show an apparent strong absorption for a wide range of incidence angles at a frequency of 11.49 GHz. The modifications with respect to the

preliminary structure are simple but decisive for this target: rotation of the square resonator of 90 degrees; the width of the metallic strips of the square resonator is modified from 0.60 mm to 0.28 mm, while the bottom layer is replaced with a metallic copper plate. The thickness of the dielectric slab is now 0.51 mm and the complex relative dielectric constant of the dielectric slab is 4.50-i0.06. These simple small changes lead to a major improvement in the angular absorbance.

III. CONCLUSIONS

This paper presents a metamaterial device which gives a perfect absorption for a wide range of incidence angles. We show that some simple modifications in the metamaterial structure and proper tailoring of its dimensions can lead to significantly better absorption.

REFERENCES

- [1] V. G. Veselago, "The electrodynamics of substances with simultaneously negative values of ϵ and μ ," *Sov. Phys. Usp.* 10, 509-514 (1968).
- [2] C. M. Watts, X. Liu, and W.J. Padilla "Metamaterial Electromagnetic Wave Absorbers," *Advanced Optical Materials*, 2012, 24, OP98-OP120.
- [3] N. I. Landy, S. Sajuyigbe, J. J. Mock, D. R. Smith, and W. J. Padilla, "Perfect Metamaterial Absorber", *Phys. Rev. Lett.* 100, 207402,1-4, (2008).
- [4] F. Bilotti, A. Toscano, L. Vegni, K. Aydin, K. B. Alici, and E. Ozbay, "Equivalent-Circuit Models for the Design of Metamaterials Based on Artificial Magnetic Inclusions," *IEEE Transactions on Microwave Theory and Techniques*, Vol. 55, No. 12, pp. 2865-2873, December 2007.
- [5] B. J. Arritt, D. R. Smith, and T. Khraishi, "Equivalent circuit analysis of metamaterial strain-dependent effective medium parameters," *Journal of Appl. Phys.* 109, 073512, 1-5, (2011).
- [6] O.G. Vendik, S.P. Zubko, and M.A. Nikol'skii, "Modeling and calculation of the capacitance of a planar capacitor containing a ferroelectric thin film," *Technical Physics*, Vol. 44, No. 4, pp. 349-355, April 1999.

SIW FILTERS BASED ON PERFORATED DIELECTRIC SUBSTRATE

L. Silvestri⁽¹⁾, E. Massoni⁽¹⁾, M. Bozzi⁽¹⁾, L. Perregrini⁽¹⁾,
C. Tomassoni⁽²⁾, A. Coves⁽³⁾

⁽¹⁾ Dept. of Electrical, Computer and Biomedical Engineering,
University of Pavia, Pavia, Italy

⁽²⁾ Dept. of Engineering, University of Perugia, Perugia, Italy

⁽³⁾ Dept. de Ingenieria de Comunicaciones,
Universidad Miguel Hernandez Elche, Spain

Abstract

A novel class of substrate integrated waveguide (SIW) filters based on perforations of the dielectric substrate is presented in this paper. The air-hole perforations allow the local modification of the characteristic impedance of the SIW as well as its cutoff frequency, thus permitting the easy design of filtering structures. Four-pole filters operating at 3.6 GHz, based on conventional (full-mode) and half-mode SIW, have been designed, experimentally validated, and discussed. The proposed approach provides high flexibility, low sensitivity to fabrication inaccuracy, and simple design rules.

Index Terms – Filter, periodic structure, Substrate Integrated Waveguide (SIW).

I. INTRODUCTION

The recent advances in the field of RF and microwave technologies are leading towards a growing interest for manufacturing techniques allowing for simple design and complete integration of microwave components and systems. Among the most relevant candidates, the substrate integrated waveguide (SIW) technology has gained a key position, due to its large popularity and widespread potentials [1,2]. The major advantages of SIW technology are the capability to integrate in planar form classical waveguide components, the complete shielding of the structure, the higher quality factor compared to microstrip circuits, and the large design flexibility. In the field of filter design, SIW structures have been adopted for a variety of different filter topologies, ranging from simple inductive-post filters and filters with iris windows to cavity filters with transmission zeros [3].

This paper presents a novel class of SIW filters, based on locally periodic perforations of the dielectric substrate with air holes. The use of air holes allows modifying the characteristic impedance of the SIW as well as its cutoff frequency, thus determining the filtering function. The operation principles of this structure are discussed, along with the design, manufacturing, and experimental characterization of two four-pole filters operating at 3.6 GHz, based on full-mode and half-mode SIW structures.

II. SIW STRUCTURES WITH PERIODIC PERFORATIONS

In the proposed class of filters, the filtering effect is obtained by periodically perforating some regions of the dielectric substrate with air holes (Fig. 1a). The primary effect of the air holes in the dielectric substrate is the local reduction of the effective dielectric permittivity (Fig. 1b). The reduction is larger when increasing the size and density of the air holes [4,5]. In turn, the reduction of the effective dielectric permittivity determines two major effects in the perforated section, namely the increase of the modal impedance of the SIW and the increase of the cutoff frequency of the SIW (Fig. 1c).

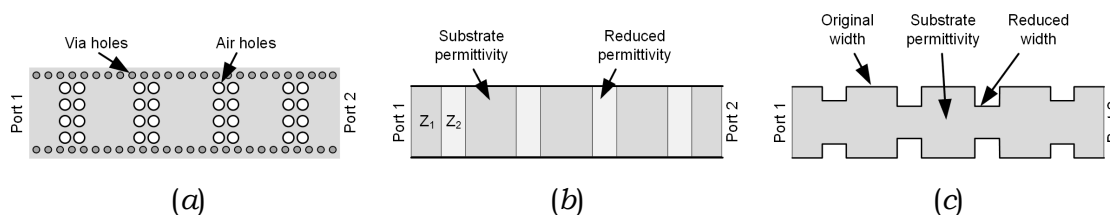


FIG. 1 – SIW filter obtained by air-hole perforations of the dielectric substrate: (a) geometry of the filter; (b) equivalent model as a step-impedance filter; (c) equivalent model as an iris-window filter.

III. FULL-MODE SIW FILTER

A four-pole filter operating at 3.6 GHz, based on a full-mode SIW structure with perforations in the dielectric substrate, was designed by using the dielectric substrate Taconic CER-10, with relative permittivity $\epsilon_r=10$, loss tangent $\tan\delta=0.0035$, and thickness $t=0.64$ mm. The design of the filter was performed by using the commercial FEM code Ansys HFSS. Complete details on this filter design can be found in [6].

A prototype of the filter was fabricated by milling technique, adopting a LPKF milling machine. The via holes of the sidewalls were metallized by using conductive paste, and the top and bottom apertures of the air holes were closed by applying a copper foil. A photograph of the prototype is shown in Fig. 2a. Fig. 2b shows the comparison between simulated and measured scattering parameters of the filter: the measured insertion loss is 1.9 dB (1.1 dB in the simulation), and the measured width of the pass band is 600 MHz (590 MHz in the simulation). The measured out-of-band rejection is better than 10 dB in the frequency band from 4.15 GHz to 5.20 GHz.

The footprint size of the filter is 80×18 mm², corresponding to $0.2\lambda^2$, where λ is the wavelength in vacuum at the central frequency of 3.6 GHz.

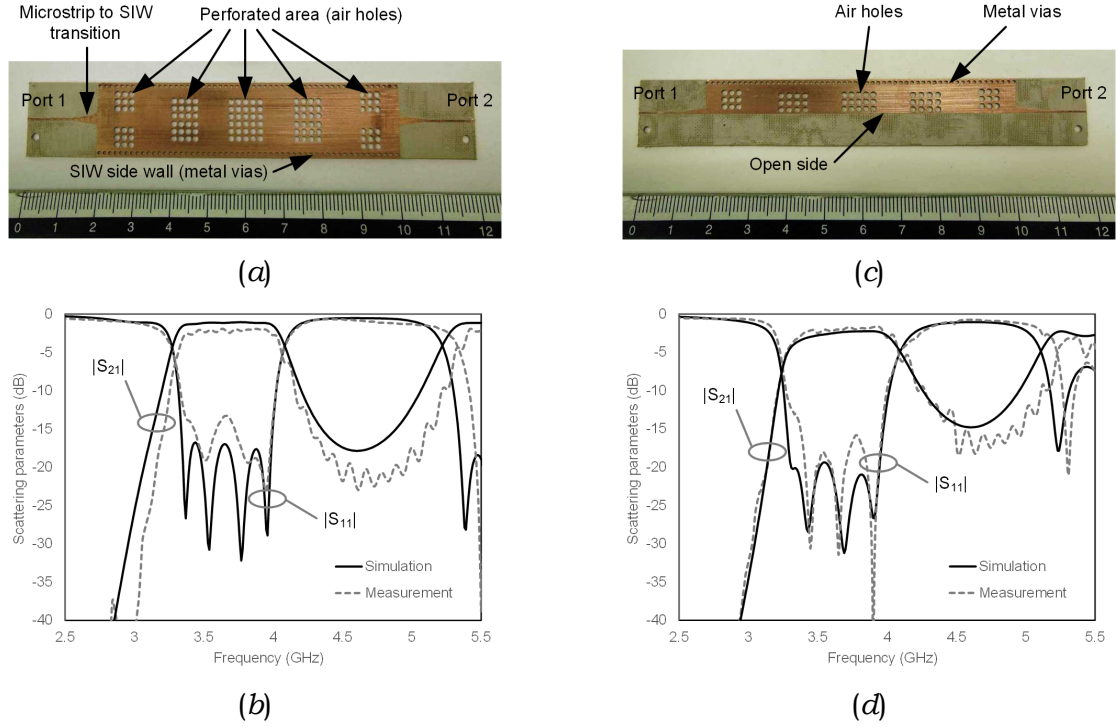


FIG. 2 – Four-pole filters operating at 3.6 GHz, based on SIW structures with perforations: (a) photograph of the prototype of the full-mode SIW filter; (b) simulated and measured frequency response of the full-mode SIW filter; (c) photograph of the prototype of the half-mode SIW filter; (d) simulated and measured frequency response of the half-mode SIW filter.

IV. HALF-MODE SIW FILTER

The size of the SIW filter can be reduced by adopting a half-mode SIW configuration, which provides comparable performance and a size reduction by a factor of two. The half-mode SIW filter with the frequency response similar to the filter presented in Sec. III was designed by using the same dielectric substrate. Complete details on this filter design can be found in [6].

A prototype of the half-mode SIW filter was fabricated by milling technique and the photograph of the structure is shown in Fig. 2c. Moreover, Fig. 2d shows the comparison between simulated and measured scattering parameters of the half-mode SIW filter: the measured insertion loss at 3.6 GHz is 2.25 dB (2.55 dB in the simulation), and the width of the pass band is practically identical to the one shown in Fig. 2b. The footprint size of the half-mode SIW filter, as expected, is reduced by a factor of two compared to the full-mode SIW filter.

The performance of the half-mode SIW filter is comparable to the standard SIW counterpart, except for a different value of the insertion loss in the pass band. The larger insertion loss is attributed to additional radiation leakage, which is not present in the standard SIW.

In particular, the insertion loss is larger at lower frequency (Fig. 2d). This effect is due to the field configuration in the filter: in fact, the lowest resonant mode of the filter (where losses are larger) exhibits in-phase field along the open side, thus resulting in large radiation leakage. Moreover, a poor out-of-band rejection is achieved.

Both out-of-band rejection and radiation issues can be significantly mitigated by adopting a folded filter topology, which allows introducing transmission zeros and reducing radiation leakage, as discussed in [6].

V. CONCLUSION

A novel SIW filter topology, based on the periodic perforation of some regions of the dielectric substrate, has been proposed in this paper. The major advantages of this filter are the simple design rules, the easy manufacturing process, and the low sensitivity to fabrication inaccuracy. Two examples of four-pole filters, based on conventional and half-mode SIW structures, have been designed and experimentally validated. Moreover, the preliminary idea of a folded filter topology has been outlined, which provides advanced performance in terms of out-of-band rejection and radiation leakage.

REFERENCES

- [1] R. Garg, I. Bahl, and M. Bozzi, *Microstrip Lines and Slotlines*, Third Edition, Artech House, 2013.
- [2] M. Bozzi, A. Georgiadis, and K. Wu, "Review of Substrate Integrated Waveguide (SIW) Circuits and Antennas," *IET Microwaves, Antennas and Propagation*, Vol. 5, No. 8, pp. 909-920, June 2011.
- [3] X.-P. Chen and K. Wu, "Substrate Integrated Waveguide Filter: Basic Design Rules and Fundamental Structure Features," *IEEE Microwave Magazine*, Vol. 15, No. 5, pp. 108-116, July-Aug. 2014.
- [4] M. Bozzi, D. Deslandes, P. Arcioni, L. Perregrini, K. Wu, and G. Conciauro, "Efficient Analysis and Experimental Verification of Substrate Integrated Slab Waveguides for Wideband Microwave Applications," *International Journal of RF and Microwave Computer-Aided Engineering*, Vol. 15, No. 3, pp. 296-306, May 2005.
- [5] A. Coves, E. Bronchalo, G. Torregrosa-Penalva, A.A. San-Blas, M.A. Sanchez-Soriano, A. Martellosio, and M. Bozzi, "A Novel Band-Pass Filter Based on a Periodically Drilled SIW Structure," *Radio Science*, Vol. 51, 2016.
- [6] L. Silvestri, E. Massoni, C. Tomassoni, A. Coves, M. Bozzi, and L. Perregrini, "A New Class of SIW Filters Based on Periodically Perforated Dielectric Substrate," *46th European Microwave Conference (EuMC2016)*, London, UK, Oct. 3-7, 2016.

SINGULARITY EXTRACTION FOR WEAKLY SINGULAR INTEGRALS ON HIGH ORDER ELEMENTS

G. Borzi⁽¹⁾

⁽¹⁾ Department of Engineering, Messina University
Via Panoramica dello Stretto, Messina, Italy
gborzi@ieee.org

Abstract

The singularity extraction technique for the numerical evaluation of weakly singular integrals is extended to high-order, linear elements. Unlike Duffy's method, this novel technique does not suffer from accuracy problems when the singularity point is near the element's border. Moreover, it relies on well established formulas for singular integral evaluations and its implementation is quite simple.

Index Terms – Singular integrals, Method of moments.

I. INTRODUCTION

The singularity extraction method is widely used to compute singular integrals on first order elements [1], and it has been extended to straight-high order elements in [2]. This paper presents an alternative extension for weakly singular integrals on straight-high order elements, which is simpler to implement than the technique presented in [2]. The method is compared with the Duffy method [3], which is the method of choice to deal with weakly singular integrals on high order elements.

II. LINEAR ELEMENTS

The integrals that must be computed to assemble an EFIE matrix for an object discretized by straight elements are

$$\int_{S_i} \varphi_l(\xi_1, \xi_2) \frac{\exp(-jk_0 \|\bar{r} - \bar{r}'\|)}{4\pi \|\bar{r} - \bar{r}'\|} d\xi_1 d\xi_2 \quad (1)$$

where φ_l is the l -th form function, ξ_1, ξ_2 are the local coordinates, k_0 is the wavenumber, \bar{r}' is a fixed point on the integration domain (the singularity) with local coordinates ξ_1^s, ξ_2^s and $\bar{r}(\xi_1, \xi_2)$ depends on the local coordinates. Defining

$R = \|\bar{r} - \bar{r}'\|$, integral (9) can be separated into a regular, complex valued part

$$\int_{S_i} \varphi_l(\xi_1, \xi_2) \frac{\exp(-jk_0 R) - 1}{4\pi R} d\xi_1 d\xi_2 \quad (2)$$

and a singular, real valued part

$$\int_{S_i} \varphi_l(\xi_1, \xi_2) \frac{1}{4\pi R} d\xi_1 d\xi_2 \quad (3)$$

that must be regularized in order to allow its numerical integration.

Subtracting $\varphi_l(\xi_1^s, \xi_2^s)(4\pi R)^{-1}$ from the integrand in (3) is not an effective way to regularize the integrand because the resulting function is limited but not continuous, as can be verified if one tries to compute the limits of the difference function when the local coordinates approach the coordinates of the singularity. However these limits also suggest a solution, that is to say to replace the constant that multiplies $1/4\pi R$ with a function that not only matches the value but also the partial derivatives of φ_l at the singularity. A first degree polynomial

$$q_l(\xi_1, \xi_2) = a_l \xi_1 + b_l \xi_2 + c_l \quad (4)$$

with

$$a_l = \frac{\partial \varphi_l}{\partial \xi_1}(\xi_1^s, \xi_2^s), b_l = \frac{\partial \varphi_l}{\partial \xi_2}(\xi_1^s, \xi_2^s), c_l = \varphi_l(\xi_1^s, \xi_2^s) - a_l \xi_1^s - b_l \xi_2^s \quad (5)$$

satisfies the conditions and can be exactly integrated with the formulas from [4]. The partial derivatives in (5) can be computed analytically, for example with Sylvester differentiation matrices [5].

Since $\varphi_l - q_l$ is differentiable on the entire domain and its differential vanishes at ξ_1^s, ξ_2^s it follows that

$$\lim_{(\xi_1, \xi_2) \rightarrow (\xi_1^s, \xi_2^s)} \frac{\varphi_l(\xi_1, \xi_2) - q_l(\xi_1, \xi_2)}{\|\Delta \bar{\xi}\|} = 0 \quad (6)$$

with $\Delta \bar{\xi} = (\xi_1 - \xi_1^s, \xi_2 - \xi_2^s)$. Noting that $R = O(\|\Delta \bar{\xi}\|)$ (6) implies

$$\lim_{(\xi_1, \xi_2) \rightarrow (\xi_1^s, \xi_2^s)} \frac{\varphi_l(\xi_1, \xi_2) - q_l(\xi_1, \xi_2)}{R} = 0 \quad (7)$$

which means that the regularized function is continuous.

Using the polynomial defined by (5), integral (1) is obtained as the sum of the integral

$$\int_{S_i} \left[\varphi_l(\xi_1, \xi_2) \frac{\exp(-jk_0 R)}{4\pi R} - \frac{q_l(\xi_1, \xi_2)}{4\pi R} \right] d\xi_1 d\xi_2 \quad (8)$$

that has a continuous integrand (with value $-jk_0$ at the singularity) and is numerically computed, with the integral

$$\int_{S_i} \left[\frac{q_l(\xi_1, \xi_2)}{4\pi R} \right] d\xi_1 d\xi_2 \quad (9)$$

which is computed analytically.

For points \bar{r}' outside the element but still close enough to hinder the effective numerical computation of (1) this singularity extraction method can be used as well. In this case ξ_1^s, ξ_2^s are the local coordinates of the projection of \bar{r}' onto the plane where the element lies.

III. NUMERICAL RESULTS

Integral (1) is computed with Gauss quadrature rules of increasing degree with Duffy's method and the singularity extraction method, on a straight second order triangle with vertex $v_0 = (0.1368, -0.0015, 0)$, $v_1 = (0.0266, 0.2498, 0)$, $v_2 = (-0.2513, -0.0073, 0)$. The singularity is placed at $\xi = (0.0915762, 0.0915762)$, and $k_0 = 2\pi$. Six integrals are computed, one for each nodal form function φ_l ,

with $l=1,\dots,6$.

Since the exact value of the integral is unknown, the exact integration error can not be computed. So, in order to compare the methods the relative error between two consecutive quadratures is used. It is defined as follows. Let I_d be the six-entries array containing the results from the quadrature with a rule of degree d and define the relative error for the degree d rule as $\delta_r(d) = \|I_d - I_{d-1}\| / \|I_d\|$.

An alternative way to check the error is to compute a reference integrals array I_{ref} obtained by means of Duffy's method and very high order integration rules, and check $\|I_d - I_{ref}\| / \|I_{ref}\|$. A reference I_{ref} for this element has been computed with a degree 99 Cartesian product rule, which involves 7500 integration points. The result are not dramatically different from those obtained with the previous method, which is more realistic because δ_r is the quantity that is checked for adaptive numerical quadrature.

In the comparison the quadrature rules from [6] are used for both methods. Since these are near-optimal rules, the number of quadrature points for the rule of degree d is close to $\lceil (d+1)(d+2)/6 \rceil$. The rules for the triangle, used for the extraction method, are available up to degree 50 and at the maximum degree there are 453 integration points. The rules for the square, used for Duffy's method, are available up to degree 30, with 167 integration points for the maximum degree. Hence, the maximum number of integration point for the two methods is roughly similar, 453 vs 501.

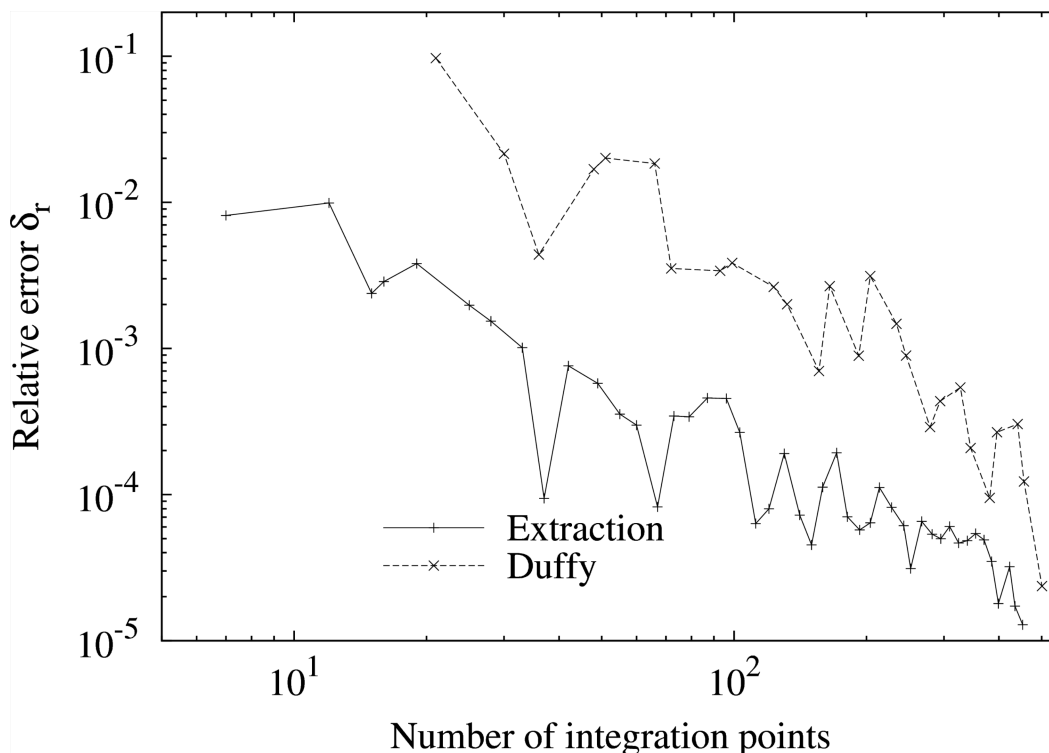


FIG. 1 – Relative error vs. Number of integration points, Xiao-Gimbutas rules.

From the results shown in Fig. 1 it is clear that for integration accuracies as small as 10^{-5} the extraction method outperforms Duffy's method. For smaller accuracies, which require more than a thousand integration points, Duffy's method

regains competitiveness. Numerical experiments show that the convergence of the singularity extraction method does not change dramatically with the singularity location. Unlike Duffy's method whose accuracy heavily depends on the deformation of the sub-triangles [2], hence on the singularity coordinates.

IV. CONCLUSION

The extension of the singularity extraction method to high-order straight elements presented in this paper is a valid alternative to Duffy's method for weakly singular integrals.

The method relies on well established formulas for singular integral evaluations and its implementation is straightforward. Moreover, the burden associated with the computation of the regularizing functions on quadrature points is limited because these functions only involve first degree polynomials.

REFERENCES

- [1] M. S. Tong and W. C. Chew, "A novel approach for evaluating hypersingular and strongly singular surface integrals in electromagnetics," *IEEE Transactions on Antennas and Propagation*, vol. 58(11), pp. 3593–3601, Nov. 2010.
- [2] S. Järvenpää, M. Taskinen, and P. Ylä-Oijala, "Singularity subtraction technique for high-order polynomial vector basis functions on planar triangles," *IEEE Transactions on Antennas and Propagation*, vol. 54(1), pp. 42–49, Jan. 2006.
- [3] M. G. Duffy, "Quadrature over a pyramid or cube of integrands with a singularity at a vertex," *SIAM Journal on Numerical Analysis*, vol. 19(6), pp. 1260–1262, Jul. 1982.
- [4] R. D. Graglia, "On the numerical integration of the linear shape functions times the 3-D Green's function or its gradient on a plane triangle," *IEEE Transactions on Antennas and Propagation*, vol. 41(10), pp. 1448–1455, Oct. 1993.
- [5] P. P. Silvester and R. L. Ferrari, *Finite Elements for Electrical Engineers*, 3rd ed. Cambridge, UK: Cambridge University Press, 1996.
- [6] H. Xiao and Z. Gimbutas, "A numerical algorithm for the construction of efficient quadrature rules in two and higher dimensions." *Computers and Mathematics with Applications*, vol. 59(2), pp. 663–676, 2010.

A FINITE-ELEMENT BASED FIELD ESTIMATION VIA A KALMAN FILTERING APPROACH

G. Battistelli, L. Chisci, N. Forti, G. Pelosi, S. Selleri

⁽¹⁾ Department of Information Engineering, University of Florence
Via di Santa Marta, 3 – 50139 – Florence, Italy.

[giorgio.battistelli, luigi.chisci, nicola.forti, giuseppe.pelosi, stefano.selleri]@unifi.it

Abstract

The contribution focuses on decentralized estimation of a generic field obeying to a given partial differential equation from discrete in-space-and-time noisy measurements provided by sensor nodes scattered over the spatial domain. Each node runs a local finite-dimensional Kalman filter which exploits the finite element approach for spatial discretization and the parallel Schwarz method to iteratively enforce boundary conditions on adjacent subdomains.

Index Terms – Distributed parameter systems; Finite element method; Kalman filtering; Networked state estimation.

I. INTRODUCTION

Wireless sensor networks constitute now a pervasive technology enabling many different applications, such as monitoring of a given spatially distributed field, which can be either a scalar field like the concentration of a polluting substance in a river or lake [1], temperature, humidity and atmospheric pressure on a region [2], or vector electromagnetic fields for human safety monitoring, via deployment of multiple inexpensive sensors over the area of interest.

Such a monitoring can be accomplished either in a centralized way, when there is a single fusion center collecting data from all sensors, or in a distributed, decentralized, fashion with multiple inter-communicating fusion centers (nodes) each of which can access, and hence needs to handle, only part of the data. The decentralized approach is of course preferable in terms of system scalability and will be considered here.

The problems at hand are modeled as infinite-dimensional systems, governed by partial differential equations (PDEs) with given boundary conditions (BCs). Many papers in the open literature address the estimation problem for finite-dimensional systems, both linear and nonlinear ([3] and references therein), while considerably less attention has been devoted to the more difficult case of infinite-dimensional distributed-parameter systems.

Recent work [4] has addressed the design of distributed estimation for large-scale systems and, in the specific case of distributed-parameter systems, interesting contributions have been provided in [5]. The present contribution differs from [5] inasmuch a different strategy is adopted: each node is only responsible for estimating the field over a sub-domain of the overall domain, exploiting the Schwarz domain decomposition

method [6], in conjunction with the finite element (FE) method [7] in order to approximate the original infinite dimensional problem, and a Kalman filter for performing the real-time estimation, as preliminarily discussed in [8].

II. FORMULATION

Let us assume the field $x(\mathbf{p}, t)$ to be estimated, function of position \mathbf{p} and time t , scalar for the sake of simplicity, as obeying to the following equation and boundary conditions:

$$\frac{\partial x}{\partial t} + \mathcal{H}(x) = u \quad \text{in } \Omega; \quad \mathcal{B}(x) = 0 \quad \text{on } \partial\Omega; \quad (1)$$

$\mathcal{H}(\cdot)$ and $\mathcal{B}(\cdot)$ being space differential operator, which can either be the differential equation governing temperature, or a pressure field, or an electric potential field. The forcing term is assumed to be composed of one or more unknown point sources in the form $u(\mathbf{p}, t) = u(t)\delta(\mathbf{p} - \mathbf{p}_0)$, $u(t)$ being a scalar time function and $\delta(\cdot)$ the Dirac delta function. The idea is to estimate both the field x and the source u over the domain given a finite set of measurements $y_{k,i}$ spatially distributed on points \mathbf{p}_i and sampled at times t_k . It can be proven that problem (1) can be recast via FEM [7] in a marching-in-time matrix form: $\mathbf{x}_{k+1} = \mathbf{A}\mathbf{x}_k + \mathbf{B}\mathbf{u}_k + \mathbf{w}_k$, where \mathbf{A} and \mathbf{B} are FEM matrices and \mathbf{x} and \mathbf{u} vectors containing the samples on FEM discretization of Ω of the field and of the sources and \mathbf{w} an additive process noise. This is indeed a finite-dimensional discrete time filtering problem, to which the Kalman filter, or extended Kalman filter when sensor nonlinearities are considered, can be readily applied to the whole domain [9].

In order to develop a scalable distributed filter for monitoring the target field, the idea is to decompose the original problem on Ω into estimation subproblems concerning smaller subdomains assigned to different nodes which can locally process and exchange data (Fig. 1). Subdomains are partially overlapping and neighboring estimators iteratively exchange data concerning nodes on overlapping regions, searching for a consensus.

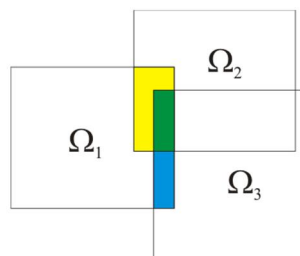


FIG. 1 – Subdivision in overlapping subdomains with different colors showing overlapping regions between two or more subdomains.

III. NUMERICAL EXAMPLES

To illustrate the performance of the proposed distributed finite element Kalman (dFE-KF) filter technique, as opposed to its centralized version (cFE-KF), we present here a transient heat conduction problem on a thin L-shaped metal plate (Fig. 2) with constant, homogeneous, and isotropic properties. In this case the problem reduces to 2D, since temperature can be assumed constant along the thickness direction.

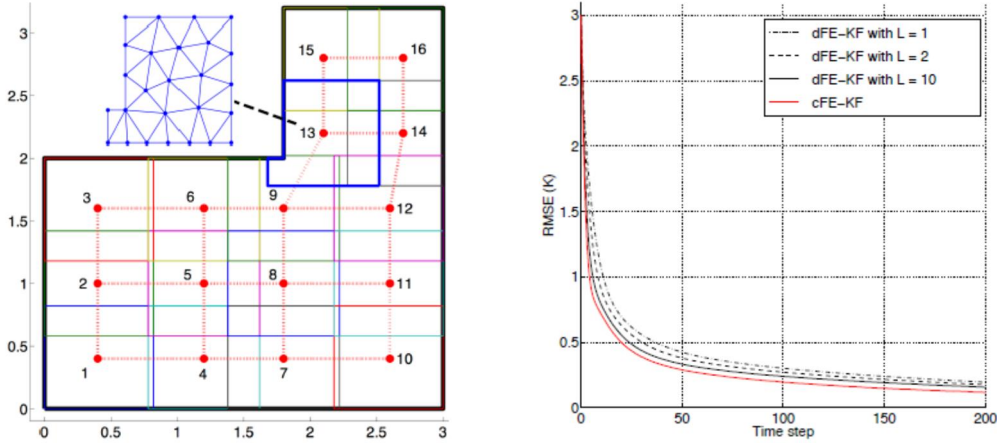


FIG. 2 – Right: L-shaped plate example, decomposed into 16 subdomains, shown in solid line, and graph interconnecting sensor nodes, shown in dashed lines. FE mesh of subdomain number 13 is also shown. Left: convergence in terms of RMSE for cFE-KF and dFE-KF for various L values.

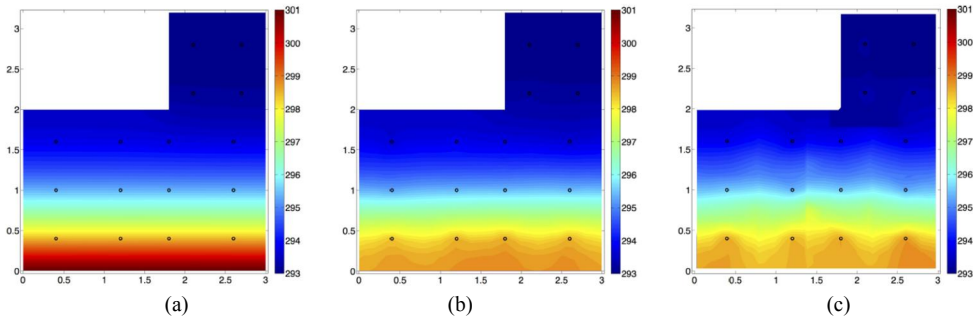


FIG. 3 – (a) reference solution (b) cFE-KF field estimation and (c) dFE-KF field estimation with $L=10$.

The plate is supposed to be adiabatic, its initial temperature is 293 K and the bottom edge is set at a fixed 298 K. As shown in Fig. 2 the domain is subdivided into 16 subdomains in the middle of which, in a known position, there is a sensor node, collecting temperature every 100 s. Measurements are generated on a separate, accurate, FE model in a fully deterministic setup, providing also the reference solution. Sensors operates on a coarse, subdivided, mesh unaware not only of sources, but also of boundary conditions and only rely on sampled, noisy, data. The performance of the proposed dFE-KF filter has been evaluated in terms

of Root Mean Square Error (RMSE) of the estimated temperature field, averaged over a set of sampling points evenly spread within Ω , and 100 Monte Carlo trials. The duration of each simulation experiment is fixed to 20.000s (200 samples). As a reference, the cFE-KF filter is also applied to the same problem but on the whole domain. Fig. 2 reports convergence for dFE-KF for different values of the number of iterations L in the Schwarz technique taking place between any sample pair, and Fig. 3 reports field maps for the reference solution, for the cFE-KF and for the dFE-KF, this latter for $L=10$.

IV. CONCLUSIONS

The contribution has dealt with the decentralised estimation of a time-evolving and space-dependent field governed by a linear partial differential equation, given point-in space measurements of multiple sensors deployed over the area of interest, exploiting the finite element method and a consensus approach inspired by the parallel Schwarz method for domain decomposition and the Kalman filter technique to solve in a decentralized and scalable fashion filtering problems involving distributed parameter systems.

REFERENCES

- [1] M. Ortner, A. Nehorai and A. Jeremic, "Biochemical transport modeling and Bayesian source estimation in realistic environments," *IEEE Transactions on Signal Processing*, vol. 55(6), pp. 2520-2532, 2007.
- [2] M. Fisher, J. Nocedal, Y. Tremolet and S.J. Wright, "Data assimilation in weather forecasting: A case study in PDE-constrained optimization," *Optimization and Engineering*, vol. 10(3), pp. 409-426, 2009.
- [3] G. Battistelli and L. Chisci, "Kullback-Leibler average, consensus on probability densities, and distributed state estimation with guaranteed stability", *Automatica*, vol. 5(3), pp. 707-718, 2014.
- [4] H. Zhang, J. Moura and B. Krogh, "Dynamic field estimation using wireless sensor networks: Tradeoffs between estimation error and communication cost," *IEEE Transactions on Signal Processing*, vol. 57, no. 6, pp. 2383-2395, 2009.
- [5] M.A. Demetriou, "Design of consensus and adaptive consensus filters for distributed parameter systems," *Automatica*, vol. 46(2), pp. 300-311, 2010.
- [6] A. Toselli and O.Widlund, *Domain decomposition methods – Algorithms and theory*, Springer-Verlag, Berlin, Germany, 2005.
- [7] G. Pelosi, R. Coccioli and S. Selleri, *Quick finite elements for electromagnetic waves*, Artech House, Norwood, MA, 2009.
- [8] G. Battistelli, L. Chisci, N. Forti, G. Pelosi and S. Selleri, "Distributed finite element Kalman filter", *Proceedings of the European Control Conference 2015*, Linz, Austria, 2015, pp. 3700-3705.
- [9] R. Suga and M. Kawahara, "Estimation of tidal current using Kalman filter finite-element method", *Computers & Mathematics with Applications*, vol. 52, pp. 1289-1298, 2006.

ELECTROMAGNETIC IMAGING IN L^p BANACH SPACES: 3D FREE SPACE RECONSTRUCTIONS

A. Fedeli, M. Pastorino, A. Randazzo, and E. Tavanti

Department of Electrical, Electronic, Telecommunications
Engineering, and Naval Architecture, University of Genoa
Via Opera Pia 11A, 16145 Genoa, Italy

alessandro.fedeli@edu.unige.it; matteo.pastorino@unige.it; andrea.randazzo@unige.it;
emanuele.tavanti@edu.unige.it

Abstract

A method for solving electromagnetic imaging problems involving dielectric structures is presented in this paper. The developed approach is based on a two-step inexact Newton scheme, performing a regularization in the framework of the L^p Banach spaces. Some recent developments are discussed and numerical results, aimed at validating the proposed inversion method, are reported.

Index Terms – Electromagnetic imaging, inverse problems, regularization, Banach spaces.

I. INTRODUCTION

In the last years, there has been an ever growing interest in the development of efficient approaches for solving electromagnetic imaging problems [1]–[4]. As it is well known, such problems turn out to be quite complicated, since they involve the “inversion” of non-linear and strongly ill-posed equations. Consequently, novel solving strategies are continuously proposed by the national and international research community in order to improve imaging capabilities.

This paper reports some recent results obtained by the SIEM Unit of Genoa in this framework. In particular, a two-step inexact Newton scheme has been developed for addressing the nonlinearity and ill-posedness of the considered inverse problem. The approach, initially proposed for inspecting cylindrical targets by means of a 2D tomographic arrangement [5], is based on a Newton scheme in which the full non-linear scattering model is iteratively linearized and the resulting equations are solved in a regularized sense by using the truncated Landweber method. The novelty of the approach is the use of nonconventional spaces, and in particular, the functional Banach L^p spaces. Moreover, a new extension to 3D imaging is presented and validated by means of numerical simulations. Some further advances aimed at reducing the computational complexity (based on the so-called “frozen” and “Broyden” strategies) are also introduced.

The paper is organized as follows. Section II provides a brief description of the mathematical formulation of the approaches. Some

numerical results are reported in Section III. Finally, conclusions are drawn in Section IV.

II. OUTLINE OF THE MATHEMATICAL FORMULATION

Let us consider an unknown target characterized by a complex dielectric permittivity $\epsilon_r(\mathbf{r})$ and located in a known investigation area V_{inv} . The inspected scene is “illuminated” by means of a known incident electric field \mathbf{E}_{inc} (for the sake of simplicity, a single-view case is considered here) and the total field is collected in a measurement domain D_{meas} . As it is well known, the total electric field is related to the dielectric properties of the inspected scene by the following relationship (data equation) [1]

$$\mathbf{E}_{tot}(\mathbf{r}) = \mathbf{E}_{inc}(\mathbf{r}) - k_0^2 \int_{V_{inv}} c(\mathbf{r}') \mathbf{E}_{tot}(\mathbf{r}') \cdot \bar{\mathbf{G}}_0(\mathbf{r}, \mathbf{r}') d\mathbf{r}', \quad \mathbf{r} \in D_{meas} \quad (1)$$

where $c = \epsilon_r - 1$ is the contrast function, k_0 is the free-space wavenumber, and $\bar{\mathbf{G}}_0$ is the free-space dyadic Green’s function (a $e^{j\omega t}$ time dependence is assumed and omitted). A similar equation holds for the total field inside the investigation domain (state equation). If the target has a cylindrical shape (with dielectric properties independent from the axial coordinate) and the incident field is transverse-magnetic, the data and state equations can be simplified and become two dimensional and scalar [1]. On the contrary, for 3D problems, the full three-dimensional vector quantities must be considered.

The scattering problem can be written in compact form as

$$y(\mathbf{r}) = F(c)(\mathbf{r}), \quad \mathbf{r} \in D_{meas} \quad (2)$$

where F is a nonlinear operator [1] (depending on the considered configuration) and y is the known term, which is the axial component of the scattered electric field in the 2D case and the full field vector in the 3D case. The inverse problem of finding c starting from the knowledge of y is solved by means of the following iterative procedure performing a regularization in the framework of the L^p Banach spaces:

1. Initialize the solution with an initial guess c_0 .
2. Linearize (2) around the current estimate of the solution by means of the Fréchet derivative F'_n of the operator F [5].
3. Find a regularized solution h_n of the obtained linear equation by using a truncated Landweber method in Banach spaces [5].
4. Update the current solution with $c_{n+1} = c_n + h_n$.
5. Repeat steps 2-4 until a proper stopping criterion is satisfied.

When dealing with 3D problems, the computation of the Fréchet derivative is quite expensive. Consequently, two specific strategies have been developed for reducing the computational burden. In the first one, the Fréchet derivative is kept constant for a given number of Newton

iterations (frozen approach). The second one is a Broyden-like strategy, in which the Fréchet derivative is approximated as

$$F'_n \cong F'_{n-1} + \frac{(r_n - F'_{n-1}s_n) \otimes s_n}{\|s_n\|_H^2} \quad (3)$$

where $r_n = F(c_n) - F(c_{n-1})$, $s_n = c_n - c_{n-1}$, H denotes the completion of the considered Banach space, and \otimes is the outer product. In both cases, after a maximum number T of Newton iterations, the Fréchet derivative is calculated with the exact formula to avoid divergence behaviors.

III. NUMERICAL RESULTS

Some results concerning a 3D configuration are reported in the following. The investigation area is a cubic domain of side $L = 1.5\lambda_0$ and partitioned into $N = 8000$ voxels. The target is a circular cylinder with radius $r_c = 0.25\lambda_0$ (λ_0 being the free-space wavelength), height $l_c = \lambda_0$, center $\mathbf{r}_c = (0.1\lambda_0, 0.1\lambda_0, 0)$, and relative dielectric permittivity $\epsilon_c = 2\epsilon_0$. The scattered field data are collected in $M = 82$ measurement points, uniformly located on a sphere of radius $R = 2\lambda_0$. $V = 6$ plane waves with uniformly spaced directions of propagation are used to sequentially illuminate the inspected scene. A zero-mean value white Gaussian noise with SNR equal to 25 dB has been added to the computed field data for emulating real operating conditions. In the inversion procedure, the maximum numbers of outer and inner iterations are equal to $N_{IN} = 20$ and $K_{LW} = 10$, respectively. The inner loop is stopped when the relative difference in the residual between two consecutive iterations is below the threshold value $d_{th} = 0.01$. The recalculation period for the frozen and Broyden strategies has been fixed equal to $T = 4$. Table I reports the optimal mean relative reconstruction errors (on the whole investigation domain, the target and the background). In all cases, they have been obtained with norm parameters $p_{opt} < 2.0$. The errors on the reconstruction provided by the standard Hilbert-space approach are also reported. As can be seen, the two approximated strategies provide errors comparable to those of the complete approach. An example of the reconstructed distribution of the dielectric properties is shown in Fig. 1(a) (for $p = 1.3$ and by using the complete strategy). For comparison purposes, the corresponding reconstruction obtained with a standard Hilbert-space approach (i.e., for

TABLE I – MEAN RELATIVE RECONSTRUCTION ERRORS AND BEST L^p NORM PARAMETERS.

	Banach approach			Standard approach
	Complete	Frozen	Broyden	
p_{opt}	1.3	1.2	1.3	-
e_{inv}	0.05	0.04	0.06	0.10
e_{obj}	0.19	0.18	0.19	0.22
e_{bg}	0.04	0.04	0.06	0.09

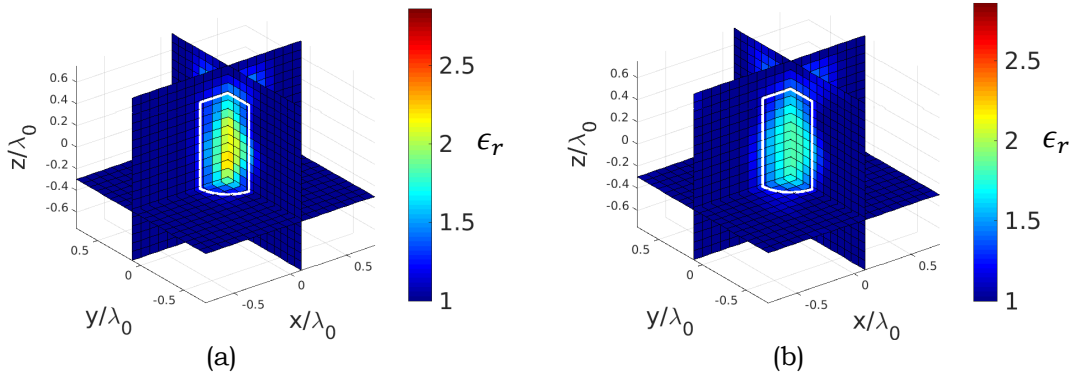


FIG. 1 – Reconstructed distributions of the dielectric permittivity obtained with (a) $p = 1.3$ (complete strategy) and (b) the standard Hilbert-space procedure.

$p = 2$) is also reported in Fig. 1(b). As can be seen, the Banach-space procedure allows a better shaping of the target (as also confirmed by the errors in Table I).

IV. CONCLUSION

An approach for electromagnetic imaging of dielectric targets, performing a regularization in the framework of the L^p Banach spaces, has been presented in this paper. The method, initially developed for two-dimensional scalar problems, has been extended for dealing with full three-dimensional problems. Specific strategies have also been developed for reducing the computational burden. The approach has been validated by means of several numerical simulations and the obtained results confirm that it is able to efficiently reconstruct the considered targets.

REFERENCES

- [1] M. Pastorino, *Microwave imaging*. Hoboken, N.J.: Wiley, 2010.
- [2] L. Di Donato, M. T. Bevacqua, L. Crocco, and T. Isernia, “Inverse Scattering Via Virtual Experiments and Contrast Source Regularization,” *IEEE Transactions on Antennas and Propagation*, vol. 63, no. 4, pp. 1669–1677, Apr. 2015.
- [3] L. Poli, G. Oliveri, F. Viani, and A. Massa, “MT-BCS-Based Microwave Imaging Approach Through Minimum-Norm Current Expansion,” *IEEE Transactions on Antennas and Propagation*, vol. 61, no. 9, pp. 4722–4732, Sep. 2013.
- [4] G. Gennarelli, I. Catapano, F. Soldovieri, and R. Persico, “On the Achievable Imaging Performance in Full 3-D Linear Inverse Scattering,” *IEEE Transactions on Antennas and Propagation*, vol. 63, no. 3, pp. 1150–1155, Mar. 2015.
- [5] C. Estatico, M. Pastorino, and A. Randazzo, “A novel microwave imaging approach based on regularization in L^p Banach spaces,” *IEEE Transactions on Antennas and Propagation*, vol. 60, no. 7, pp. 3373–3381, Jul. 2012.

THE BI-RME METHOD COMBINED WITH THE SEGMENTATION TECHNIQUE APPLIED TO THE MODELING OF 3D COMPONENTS

Simone Battistutta, Maurizio Bozzi, Marco Bressan,
Marco Pasian, Luca Perregrini

Department of Electrical, Computer and Biomedical Engineering
University of Pavia, Pavia, Italy

Abstract

This paper presents a novel technique for the numerical modeling of three-dimensional waveguide components. The segmentation technique is adopted to divide the component into homogeneous boxed building blocks. The generalized admittance matrix of each building block is determined by the Boundary Integral-Resonant Mode Expansion (BI-RME) method, using the Green's function of the box, calculated by the Ewald technique. The frequency response of the whole component is obtained by cascading the admittance matrices of the building blocks. Two examples demonstrate the capabilities of the proposed algorithm.

Index Terms – Boundary Integral-Resonant Mode Expansion method, Ewald technique, Segmentation technique.

I. INTRODUCTION

In the analysis of waveguide components, the segmentation technique can be adopted to reduce the computational burden, by analyzing simple building blocks and cascading their frequency responses [1,2]. In general, the electromagnetic field on the interconnecting surfaces is expanded using a set of waveguide modes, and a mode-matching technique is adopted to cascade frequency-by-frequency the building blocks. Though more efficient than general-purpose methods, this technique does not permit to handle components where a clear waveguide section cannot be identified between two building blocks. Moreover, if the discontinuities are very close, a large number of modes is needed to carefully represent the spatial field variation over the surface.

The numerical algorithm proposed in this paper adopts an approach similar to [1], but overcoming these problems. In particular, Rao Wilton Glisson (RWG) basis functions [3], are used to expand the electromagnetic field on the interface surfaces, thus avoiding any limitation on the surface shape and being applicable also to non-planar surfaces. Moreover, the generalized admittance matrix of the building blocks is efficiently calculated by the BI-RME method in conjunction with the Ewald technique. The analysis of two complex waveguide components including non-homogeneous and lossy materials demonstrates the effectiveness of the proposed algorithm.

II. OUTLINE OF THE ALGORITHM

The waveguide component (Fig. 1a) is segmented into elementary building blocks (Fig. 1b). Each block is filled with a homogeneous and

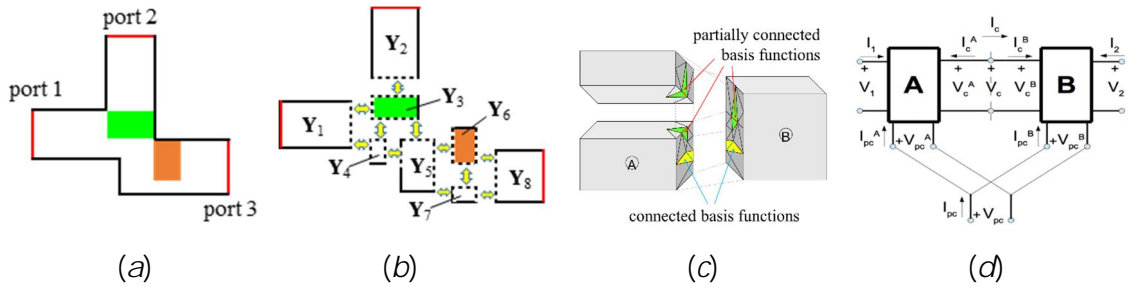


FIG. 1 - The segmentation/recombination technique: (a) the component including different materials; (b) the component segmented into homogeneous building blocks; (c) example of connected and partially connected basis functions; (d) schematic of the electrical condition imposed to connected (subscript “c”) and partially connected (subscript “pc”) basis functions.

possibly lossy dielectric medium (relative dielectric constant ϵ' , and loss tangent $\tan\delta$), and represented through a generalized admittance matrix (Fig. 1b). The unknown current on the surface of a building block is defined over a triangular mesh by means of the RWG basis functions [3], and each entry of the admittance matrix of a block relates two basis functions. In this way, the interconnection surfaces may have an arbitrary shape and eventually be curved. In this paper, however, to keep the theory simple, only boxed building blocks are considered (Fig. 1c).

Each block is modeled by using the BI-RME method [4] in conjunction with the Ewald representation of the Green's function of the metallic box [5], obtaining a pole-expansion representation of the admittance matrix. Only the surfaces interconnecting two blocks and the terminal ports (dashed and red lines in Fig. 1b, respectively) need to be meshed, since the perfect electric wall condition on the metallic walls (solid black lines in Fig. 1b) is naturally taken into account by the Green's function of the box.

Finally, the Y-matrices of the building blocks are cascaded to determine the frequency response of the whole component. A frequency-by-frequency procedure can be followed, but in the case of lossless media a frequency-independent cascading technique [6] can be adopted. Special care must be paid to combine the basis functions defined on edges shared by more than two blocks (partially connected basis functions), marked in green in Fig. 1c, where the recombination shown in Fig. 1d is adopted.

More details on the theory and implementation of the method can be found in [7].

III. VALIDATION EXAMPLES

Example 1 - The dual-band orthomode transducer (OMT) presented in [8] is analyzed to validate the proposed algorithm (Fig. 2a). The micromachining process adopted for manufacturing the OMT leads to a structure with sharp edges that can be segmented into boxed building blocks without any loss of accuracy in the geometry representation. The

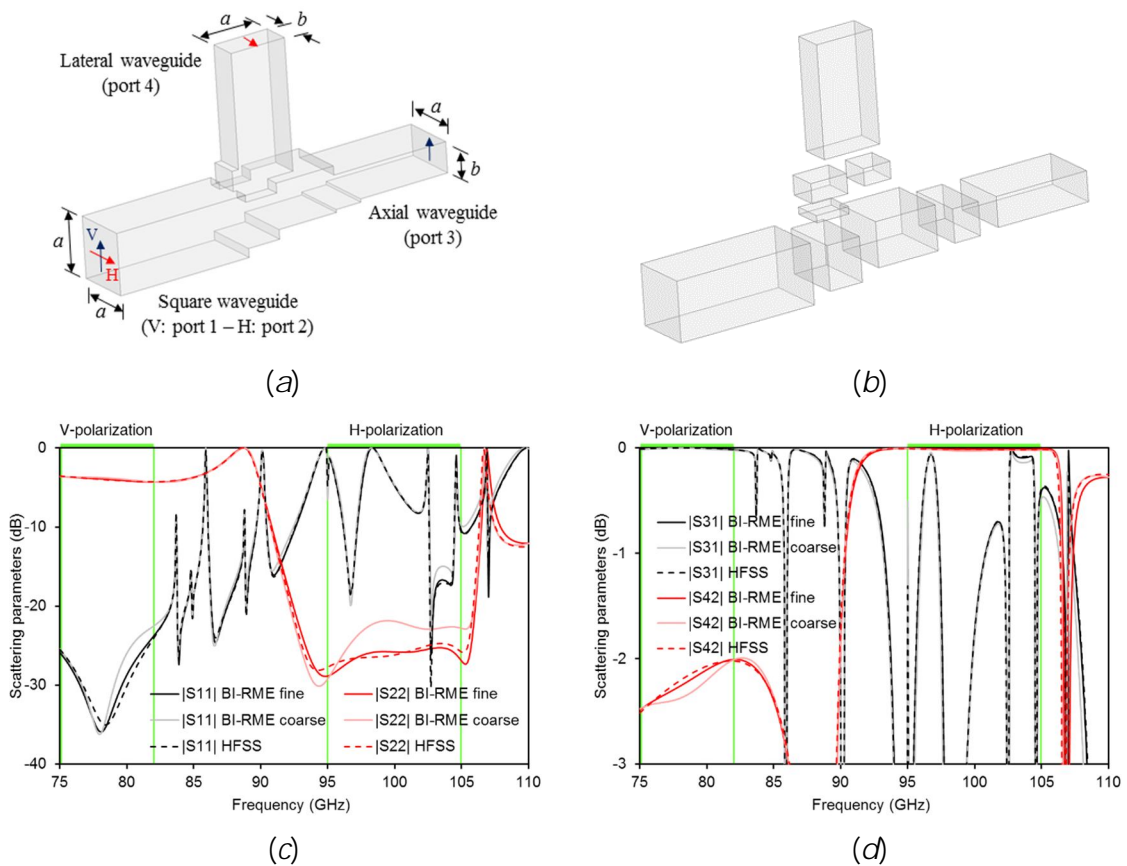


FIG. 2 - The W-band OMT proposed in [8]: (a) geometry of the whole structure with the TE₁₀ port definition; (b) the component segmented into boxed building blocks; (c,d) the frequency response of the OMT.

OMT transmits the vertical polarized signal from port 1 to port 3 in the frequency band 75-82 GHz, and the horizontally polarized signal from port 2 to port 4 in the frequency band 95-105 GHz, in both cases with a return loss better than 25 dB. The rectangular waveguides are WR-10 and all the dimensions are given in [9]. The structure has been analyzed by the proposed algorithm, adopting a coarse and fine mesh (average triangle edge size $\lambda/8$ and $\lambda/12$, respectively). Figs. 2c,d show the very good agreement between the simulation results obtained with the proposed algorithm and ANSYS HFSS.

Example 2 – The waveguide filter proposed in [9] is considered, which is based on two dielectric slabs coupled via below cutoff waveguide sections (Fig. 3a). The resonator are realized using a material with relative dielectric constant $\epsilon' = 2.2$ and loss tangent $\tan\delta = 0.001$ (all the dimensions are given in [10]). The mesh adopted for the analysis is shown in Fig. 3b. Fig. 3c shows the comparison between the simulation results obtained with the proposed algorithm and ANSYS HFSS. A very good agreement is observed over a very large frequency band. It is noted that the effect of the losses of the material on the insertion loss of the filter is accurately modeled, as shown in the close-up of the two passbands (Fig. 3d).

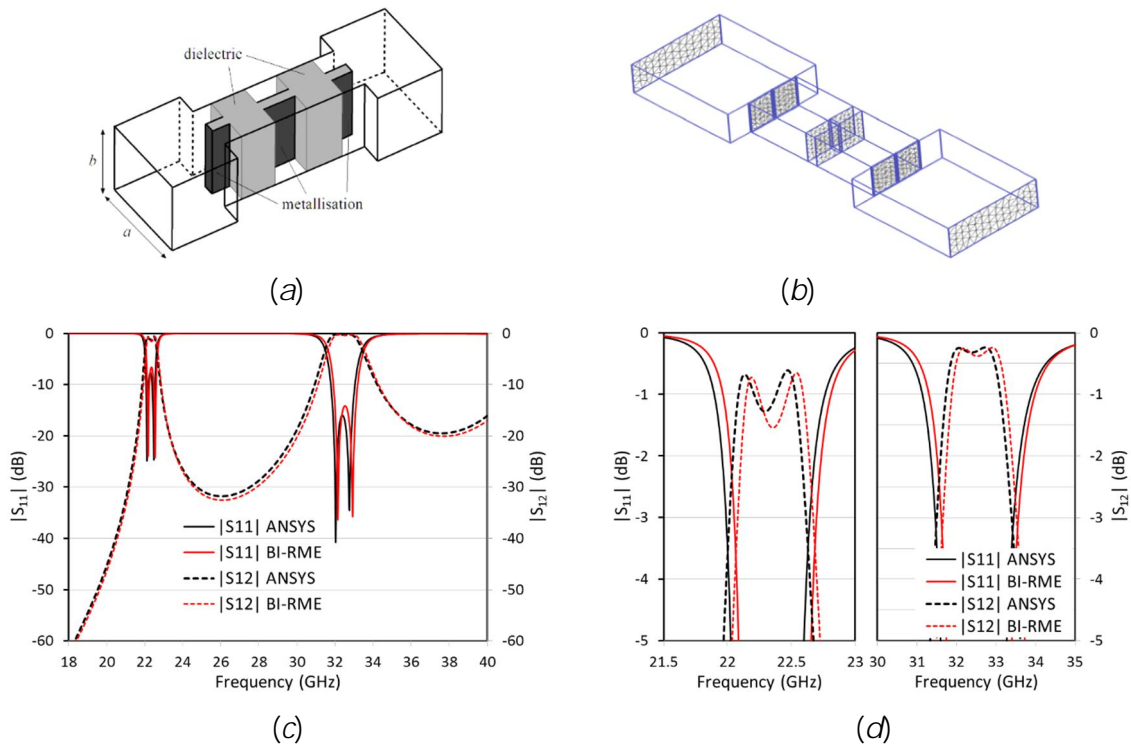


FIG. 3 - The dual-band filter proposed in [10]: (a) the geometry of the filter; (b) the mesh adopted in the interconnecting surfaces; (c) comparison between the simulated frequency response calculated by the proposed technique and by HFSS; (d) close-up of the scattering parameters in the two passbands.

REFERENCES

- [1] F. Alessandri, M. Mongiardo, R. Sorrentino, "A technique for the fullwave automatic synthesis of waveguide components: application to fixed phase shifters," *IEEE Trans. Microw. Theory Techn.*, Vol. 40, No. 7, pp. 1484-1495, Jul. 1992.
- [2] M. Ludovico et al., "CAD and optimization of compact ortho-mode transducers," *IEEE Trans. Microw. Theory Techn.*, Vol. 47, No. 12, pp. 2479-2486, Dec. 1999.
- [3] S.M. Rao, D. Wilton, A.W. Glisson, "Electromagnetic scattering by surfaces of arbitrary shape," *IEEE Trans. Antennas Propag.*, Vol. 30, No. 3, pp. 409-418, May 1982.
- [4] G. Conciauro, M. Guglielmi, and R. Sorrentino, *Advanced Modal Analysis. CAD Techniques for Waveguide Components and Filters*, Wiley, 1999.
- [5] M. Bressan, L. Perregrini, E. Regini, "BI-RME modeling of 3D waveguide components enhanced by the Ewald technique," *IEEE MTT-S 2000*, June 11-16, 2000.
- [6] P. Arcioni, G. Conciauro, "Combination of Generalized Admittance Matrices in the Form of Pole Expansions," *IEEE Trans. Microw. Theory Techn.*, Vol. 47, No. 10, pp. 1990-1996, Oct. 1999.
- [7] S. Battistutta, M. Bozzi, M. Bressan, M. Pasian, and L. Perregrini, "Modeling of Inhomogeneous and Lossy Components by the BI-RME Method and the Segmentation Technique," *46th European Microwave Conference*, London, UK, Oct. 3-7, 2016.
- [8] C.A. Leal-Sevillano et al., "A Micromachined Dual-Band Orthomode Transducer," *IEEE Trans. Microw. Theory Techn.*, Vol. 62, No. 1, pp. 55-63, Jan. 2014.
- [9] R. Vahldieck, W. Hofer, "Computer-aided design of dielectric resonator filters in waveguide sections below cutoff," *IEE Electronics Letters*, Vol. 21, No. 19, pp. 843-844, Sept. 12, 1985.
- [10] S. Battistutta, M. Bozzi, M. Bressan, M. Pasian, and L. Perregrini, "Modeling of Waveguide Components by the BI-RME Method with the Ewald Green's Function and the Segmentation Technique," *2016 IEEE MTT-S International Microwave Symposium (IMS2016)*, San Francisco, CA, USA, May 22 - 27, 2016.

THE SYSTEM-BY-DESIGN APPROACH FOR SOLVING HIGH-COMPLEXITY EM DESIGN PROBLEMS

M. Salucci⁽¹⁾⁽²⁾

⁽¹⁾ELEDIA Research Center (ELEDIA@UniTN, University of Trento)
via Sommarive 5, 38123 Trento, Italy

⁽²⁾ELEDIA Research Center (ELEDIA@L2S, UMR8506 [CNRS-CS-UPS])
3 rue Joliot Curie, 91192 Gif-sur-Yvette, France
marco.salucci@eledia.org

Abstract

In this work, the System-by-Design (SbD) paradigm is introduced to solve high-complexity electromagnetic (EM) design problems in an effective and computationally efficient way. The SbD is an integrated design framework where several functional blocks are suitably interconnected and the overall system functionality is considered as the synthesis target. An illustrative example is shown in order to assess the potentialities of the SbD approach when dealing with the design of a large-scale radome for airborne applications.

Index Terms – System-by-Design; Evolutionary Optimization; Learning-by-Examples; Radome Design.

I. INTRODUCTION

The impressive growth of the computational capabilities of commercial computers during the last years could lead to the erroneous assumption that any electromagnetic (EM) design problem can nowadays be effectively dealt with and solved in reasonable time. However, the need for hundreds (even thousands) accurate full-wave simulations to exhaustively explore the solution space makes some high-complexity EM designs still numerically intractable using standard optimization approaches as "magic black-boxes". Within this context, the System-by-Design (SbD) paradigm [1] has been recently introduced to reformulate the design process as a task-oriented *ecosystem* of interconnected and interchangeable *functional blocks*, each of which deals in an efficient way with a small and simple task. Indeed, the main idea of SbD is to realize an integrated design procedure where the overall system functionality is the actual target of the synthesis, rather than considering the functionality of each constituent part separately [1]. Such an approach allows to meet specific end-user constraints and objectives with a significant reduction of the overall computational requirements. The SbD has been successfully applied to many EM problems, such as for example the design of innovative meta-material coatings for phased arrays [2],[3], fractal antennas [4] and radomes [5]-[7].

II. THE SBD SOLUTION APPROACH

The *SbD* is based on the interconnection of basic *functional blocks* (Fig. 1). A first block is devoted to the definition of the user requirements and design constraints, while a second block is aimed at the mathematical formulation of the problem. This latter defines a suitable cost function able to model the problem, and identifies the smallest number of degrees-of-freedom (*DoFs*) able to balance design flexibility and complexity. A third block is then devoted to the evaluation of each candidate solution. Towards this end, a *physical response emulator* based on Learning-by-Examples (LBE) techniques [8],[9] can be exploited as a fast surrogate of accurate but time-consuming full-wave solvers. Finally, a last block is aimed at exploring the solution space, by suitably exploiting both deterministic and stochastic approaches [10].

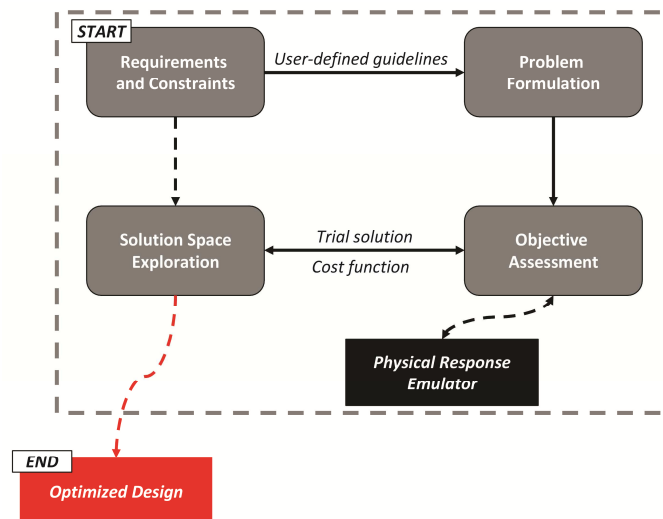


FIG. 1 – Functional blocks of the *SbD* design approach.

III. AN ILLUSTRATIVE EXAMPLE

In order to show the potentialities of *SbD* approach in designing high-complexity *EM* structures, let us consider the synthesis of a radome for airborne applications (Fig. 2). The electrical dimensions of the structure are very large, being its height and diameter (supposed to be fixed by mechanical/aero-dynamical constraints) equal to $H \approx 17 \lambda_0$ and $D \approx 30.7 \lambda_0$, respectively, where λ_0 is the free-space wavelength at the central frequency $f_0 = 9.35$ GHz. The radome is made of teflon ($\epsilon_r = 2.1$ and $\tan \delta = 3 \times 10^{-4}$ @ 10 GHz) and it encloses a uniform linear array of dipoles. To reduce the number of *DoFs*, the internal profile is defined by means of a spline curve, whose shape is governed by $P = 5$ control points (x_p, z_p) , $p = 1, \dots, P$ [$z_p = p \times H / (P + 1)$ - Fig. 2]. Since the radome should not affect the radiated field by the

array while protecting it from the external environment [7], the cost function has been defined as the antenna boresight error (BSE)

$$\Phi(\underline{x}) = \frac{1}{Q \times S} \sum_{q=1}^Q \sum_{s=1}^S \left| \vartheta_s - \vartheta_s(\underline{x}, f_q) \right|^2. \quad (1)$$

In Eq. (1), $\underline{x} = (x_p, p = 1, \dots, P)$ is the vector of optimized variables, while $\vartheta_s \in [0, 45] \text{deg}$ and $\vartheta_s(\underline{x}, f_q)$ are the s -th desired and resulting steering direction of the array ($s = 1, \dots, S = 4$) at frequency f_q ($q = 1, \dots, Q = 10$), respectively.

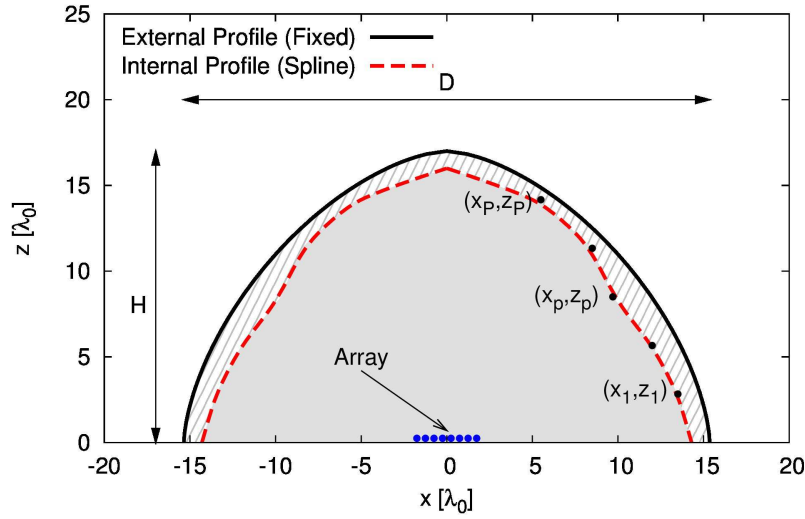


FIG. 2 – Geometry of the spline-shaped radome.

Given that real-valued *DoFs* are at hand, a Particle Swarm Optimizer (PSO) [10] has been used to identify the optimal design as

$$\underline{x}^{opt} = \arg \left\{ \min_{\underline{x}} [\Phi(\underline{x})] \right\}. \quad (2)$$

It is worth remarking that an average time of $\Delta t \approx 56$ hour is required to exactly compute $\Phi(\underline{x})$ and that the time required by a standard optimization using a swarm size of L and I iterations would be equal to $\Delta t^{std} = L \times I \times \Delta t$ (i.e., almost 13 years when $L = 10$ and $I = 200$). Accordingly, a Kriging predictor [9] has been exploited in order to avoid the need for time-consuming full-wave simulations during the optimization. More precisely, a set of $N = 250$ input/output (I/O) pairs $\{(\underline{x}_n; \Phi(\underline{x}_n)), n = 1, \dots, N\}$ have been generated by sampling the input space (P -dimensional) via a Latin hypercube sampling (*LHS*) strategy and has been used to train an efficient emulator of the cost function. After being optimized, the field radiated outside the radome shows a good matching with the free-space scenario, as confirmed by the resulting average steering error, that turns out to be less than 0.6 deg. Moreover, the time saving of the *SbD* approach with respect to the standard one turns out to be $\Delta t^{sav} = (\Delta t^{SbD} - \Delta t^{std}) / \Delta t^{std} > 90\%$.

IV. CONCLUSION

The solution of high-complexity EM synthesis problems through the *SbD* paradigm has been presented. The proposed approach allows to significantly increase the computational efficiency and the effectiveness of the design process. An illustrative example has been presented to show the potentialities of the *SbD* in designing a large-scale radome.

REFERENCES

- [1] A. Massa, G. Oliveri, P. Rocca, and F. Viani, "System-by-Design: a new paradigm for handling design complexity," 8th European Conference on Antennas Propag. (EuCAP 2014), The Hague, The Netherlands, pp. 1180-1183, Apr. 6-11, 2014.
- [2] G. Oliveri, L. Tenuti, E. Bekele, M. Carlin, and A. Massa, "An *SbD*-QCTO approach to the synthesis of isotropic metamaterial lenses," *IEEE Antennas Wireless Propag. Lett.*, vol. 13, pp. 1783-1786, 2014.
- [3] G. Oliveri, F. Viani, N. Anselmi, and A. Massa, "Synthesis of multi-layer WAIM coatings for planar phased arrays within the system-by-design framework," *IEEE Trans. Antennas Propag.*, vol. 63, no. 6, pp. 2482-2496, Jun. 2015.
- [4] G. Oliveri, P. Rocca, M. Salucci, and A. Massa, "Efficient synthesis of complex antenna devices through system-by-design," Proc. 2014 IEEE Symposium Series on Computational Intelligence (IEEE SSCI 2014), Orlando, Florida, USA, pp. 1-6, December 9-12, 2014.
- [5] M. Carlin, M. Salucci, L. Tenuti, P. Rocca, and A. Massa, "Efficient radome optimization through the system-by-design methodology," 9th European Conf. Antennas Propag. (EuCAP 2015), Lisbon, Portugal, pp. 1-3, Apr. 12-17, 2015.
- [6] M. Carlin, M. Salucci, L. Tenuti, P. Rocca, F. Viani, and A. Massa, "Complex radome design through the system-by-design approach," Proc. 2015 IEEE AP-S Int. Symp. USNC-URSI Radio Science Meeting, Vancouver, BC, Canada, pp. 1324-1325, Jul. 19-25, 2015.
- [7] D. J. Kozakoff, *Analysis of Radome-Enclosed Antennas*. Norwood, MA: Artech House, 1997.
- [8] G. Oliveri, P. Rocca, and A. Massa, "SVMs for electromagnetics: State-of-the-art, potentialities, and trends," Proc. 2012 IEEE AP-S International Symposium, Chicago, Illinois, USA, July 8-14, 2012.
- [9] D. R. Jones, M. Schonlau and W. J. Welch, "Efficient global optimization of expensive black-box functions," *J. Global Optim.*, vol. 13, pp. 455-492, 1998.
- [10] P. Rocca, M. Benedetti, M. Donelli, D. Franceschini, and A. Massa, "Evolutionary optimization as applied to inverse scattering problems," *Inv. Probl.*, vol. 25, no. 12, pp. 1-41, Dec. 2009.

ε -ENTROPY OF SCATTERED FIELD

M. A. Maisto⁽¹⁾, R. Solimene⁽¹⁾, R. Pierri⁽¹⁾

⁽¹⁾ Dipartimento di Ingegneria Industriale e dell'Informazione

Via Roma 29, Aversa (Ce), Italy

mariaantonio.maisto@unina2.it

Abstract

The role of multiple views and/or multiple frequencies on "the information" that can be conveyed back from data to the unknown in linear inverse scattering problems is addressed. In order to establish such a role, the analysis can be pursued within the framework of the topological information theory in terms of the ε -entropy.

Index Terms – Inverse scattering, Kolmogorov information, ε -entropy, inverse problems.

I. INTRODUCTION

Linear inverse electromagnetic scattering problems amount to inverting a Fredholm integral equation of the first kind for an object function which is related to the scatterer's features. By interpreting the scattering operator as a *propagator* of information, the role of multiple views and/or multiple frequencies on the performance can be studied in terms of their impact on the maximum number of ε -distinguishable "messages" \mathfrak{M}_ε that can be conveyed back on the unknown space. In [1] a lower bound for \mathfrak{M}_ε is given and the following estimates have been derived

$$\mathcal{H}_\varepsilon \geq \sum_{n=0}^{N_\varepsilon} \log_2 \sigma_n(\mathcal{A}) / \varepsilon \text{ and } \mathfrak{M}_\varepsilon \geq 2^{\mathcal{H}_\varepsilon} \quad (1)$$

where \mathcal{H}_ε is the ε -entropy, $\sigma_n(\mathcal{A})$'s are the singular values of the scattering operator \mathcal{A} and N_ε is the number of significant singular values whose values is greater than ε .

Here, based on analytical arguments reported in [2], a lower bound for \mathcal{H}_ε in terms the parameter of the configuration is estimated. This allows to say what is the "optimal" configuration when the parameters have been fixed.

II. VIEW DIVERSITY

Consider the two-dimensional scalar configuration sketched in Fig.1. Let be $I = [-a, a]$ the scatterer domain which is assumed to lay along the x-axis (see Fig. 1) and $\Omega_o = [-u_{\max}, u_{\max}]$ the observation angular corner so that $u_o = \sin \theta_o \in \Omega_o$. Moreover, thanks to view diversity the scattered field is collected for different incidence directions $u_i = \sin \theta_i \in \Omega_i$ with

$\Omega_i = \Omega_o$ and at the angular frequency k_0 . The pertinent scattered operator is \mathcal{A}_i , its expression is given in [2].

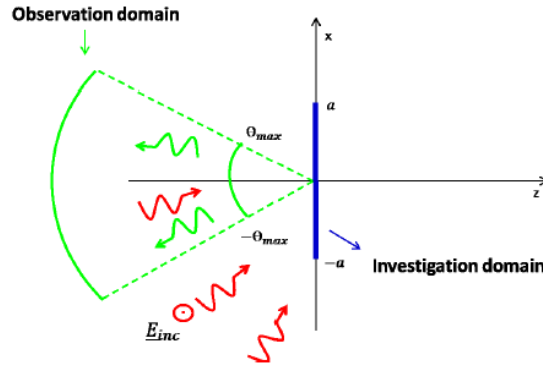


FIG. 1 – Pictorial view of the scattering configuration considered in this paper.

In [2] a procedure that allows to estimate an upper and lower bound for the singular values of \mathcal{A}_i in terms of the singular values of two auxiliary operator is introduced. All analytical arguments related to this procedure are reported in [2]. Here the lower bound is exploited to give an estimate of ε -entropy. Let be $A_v(w)$ the Fourier transform of the kernel of the operator $\mathcal{A}_i^\dagger \mathcal{A}_i$ where \mathcal{A}_i^\dagger represents the adjoint operator of \mathcal{A}_i [2]. Let us divide the frequency interval $[-2k_0 u_{\max}, 2k_0 u_{\max}]$ in $2M$ disjoint subintervals Ω_m , with $m \in (1, 2, \dots, 2M)$, whose width is Δw and define the sequence $\{\hat{A}_{vm}\}$ as $\hat{A}_{vm} = \min_{\Omega_m} \{A_v(w)\}$. Let be $\mathcal{H}_\varepsilon(\mathcal{A}_i)$ the ε -entropy when the field is collected by varying the incidence angle. The following inequality can be proved

$$\mathcal{H}_\varepsilon(\mathcal{A}_i) \geq \frac{2a\Delta w}{\pi} \sum_{m=1}^{M_\varepsilon} \log_2 \frac{\sqrt{A_v(m\Delta w)}}{\varepsilon} \quad (2)$$

where $M_\varepsilon = \max\{m : \hat{A}_{vm} \geq \varepsilon^2\}$. Equation (2) allows to obtain an estimate of ε -entropy in terms of the parameters of the scattering configurations. As expected, to collect the data for different angles of illumination entails an increasing on "the information" that can be conveyed back from data to the unknown respect to the case of a one view and this improving if $\varepsilon^2 \leq \lambda_0$ (with λ_0 the wavelength at the frequency k_0), can be quantified by the following expression

$$\frac{\mathcal{H}_\varepsilon(\mathcal{A}_i)}{\mathcal{H}_\varepsilon(\mathcal{A})} \geq \frac{\int_{\Omega(\varepsilon)} \log_2 \sqrt{A_v(w)} / \varepsilon dw}{ku_{\max} \log_2 \sqrt{\lambda_0} / \varepsilon} \quad (3)$$

where $\mathcal{H}_\varepsilon(\mathcal{A})$ represents the ε -entropy for the one view case and $\Omega(\varepsilon) = \{w \geq 0 : A_v(w) \geq \varepsilon^2\}$. As can be seen this improvement is related to

a ratio between the area subtended by $\log_2 \sqrt{A_v(w)} / \epsilon$ and the rectangular window whose base is $k_0 u_{\max}$ and height is $\log_2 \sqrt{\lambda_0} / \epsilon$.

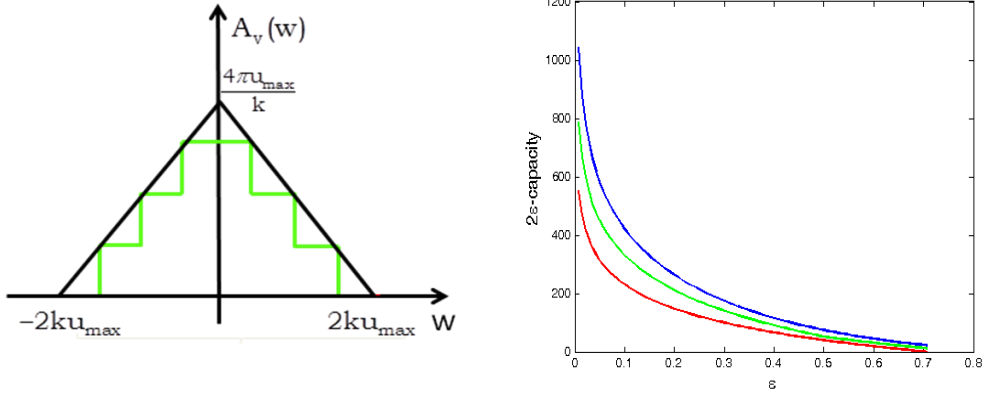


FIG. 2 – On the left column the black line represents $A_v(w)$, while the green line the sequence $\{\hat{A}_{vm}\}$. On the right column, the blue and green line represent the estimate for the ϵ -entropy $\mathcal{H}_\epsilon(\mathcal{A}_i)$ obtained by Eq. (1) and Eq. (2) while the red line is the estimate for $\mathcal{C}_{2\epsilon}(\mathcal{A})$. The parameters are $I = [-20\lambda_0, 20\lambda_0]$, $\Omega_i = \Omega_o = [-1, 1]$.

III. FREQUENCY DIVERSITY

In this section the the role of frequency diversity is considered. Therefore, let us assume that the frequency of the incident waves varies within the interval $\Omega_k = [k_{\min}, k_{\max}]$. In this case the scattering operator is \mathcal{A}_f and its particularization is given in [2]

The analysis follows the same steps as above. Let be $A_f(w)$ the Fourier transform of the kernel of the operator $\mathcal{A}_f^\dagger \mathcal{A}_f$ whose expression is given in [2]. As before, divide the frequency interval $[-k_{\max} u_{\max}, k_{\max} u_{\max}]$ in $2M$ disjoint subintervals Ω_m , with $m \in (1, 2, \dots, 2M)$, whose width is Δw and define the sequences $\{\hat{A}_{fm}\}$ as $\hat{A}_{fm} = \min_{\Omega_m} \{A_f(w)\}$. The following inequality for ϵ -entropy $\mathcal{H}_\epsilon(\mathcal{A}_f)$ when the field is collected by varying the frequency can be proved

$$\mathcal{H}_\epsilon(\mathcal{A}_f) \geq \frac{2a\Delta w}{\pi} \sum_{m=1}^{M_\epsilon} \log_2 \frac{\sqrt{A_f(m\Delta w)}}{\epsilon} \tag{4}$$

where $M_\epsilon = \max\{m : \hat{A}_{vm} \geq \epsilon^2\}$. As expected to collect the data for different frequency entails an increasing on "the information" that can be conveyed back from data to the unknown respect to one frequency

(k_0) configuration and this improving if $\epsilon^2 \leq \lambda_0$, can be quantified by the following area ratio

$$\frac{\mathcal{H}_\epsilon(\mathcal{A}_f)}{\mathcal{H}_\epsilon(\mathcal{A})} \geq \frac{\int_{\Omega(\epsilon)} \log_2 \sqrt{A_f(w)} / \epsilon dw}{k_0 u_{\max} \log_2 \sqrt{\lambda_0} / \epsilon} \quad (5)$$

As can be seen, this improvement depends by k_0 , in fact, if $k_0 < k_{\max}$ to introduce frequencies greater than the current entails increasing both the number of significant singular values and their magnitude. Instead, if $k_0 = k_{\max}$ an improvement in ϵ -entropy is observed but it is lower than the previous situation.

As concern the comparison between the view and frequency diversity, it requires dealing with several parameters related to the frequency band and the illumination as well as the observation directions. For some parameters the multiview configuration can be better than the multifrequency one and for other parameters the opposite is true. Therefore, we cannot say what is the optimal configuration. However, the presented analytical analysis allows to get the answer when the parameters have been fixed according to some constraints.

IV. VIEW PLUS FREQUENCY DIVERSITY

In this section we study the role of view and frequency diversity when both are simultaneously employed. The corresponding scattering operator is \mathcal{A}_{if} and its expression is reported in [2].

Let be $A_{\text{vf}}(w)$ the Fourier transform of the kernel of the operator $\mathcal{A}_{\text{if}}^\dagger \mathcal{A}_{\text{if}}$ whose expression is given in [2].

The following inequality for ϵ -entropy $\mathcal{H}_\epsilon(\mathcal{A}_{\text{if}})$ can be proved

$$\mathcal{H}_\epsilon(\mathcal{A}_{\text{if}}) \geq \frac{2a\Delta w}{\pi} \sum_{m=1}^{M_\epsilon} \log_2 \frac{\sqrt{A_{\text{vf}}(m\Delta w)}}{\epsilon} \quad (6)$$

where $M_\epsilon = \max\{m : \hat{A}_{\text{vf}m} \geq \epsilon^2\}$.

REFERENCES

- [1] R. Solimene, M. A. Maisto, R. Pierri, "Inverse scattering in presence of a reflecting plane," *Journal of Optics* 18, 2, 025603
- [2] R. Solimene, M. A. Maisto, R. Pierri, "The role of diversity on the singular values of linear scattering operators: the case of strip objects," *J. Opt. Soc. A* 30, 2266-2272 (2013).

ANTENNA NEAR FIELD PHASE RECOVERY BY IMPROVED INDIRECT HOLOGRAPHIC METHOD

G. Di Massa, S. Costanzo

Dipartimento di Ingegneria Informatica, Modellistica, Elettronica e Sistemistica
Università della Calabria
dimassa@unical.it

Abstract

A new approach is proposed for the phase recovery in Near Field measurement of the antenna characteristics. A novel indirect holographic technique is developed in this paper which combines all the best features of phaseless methods. A basically interferometric approach is adopted, but avoiding the use of a reference antenna as in standard interferometry. The problem of overlapping between the spectral components of hologram is avoided through the direct combination of the signals in the space domain. The effectiveness of the modified technique is confirmed by numerical results obtained for a 45 elements array antennas at 9.6 GHz frequency.

Index Terms – Near Field, Phase recovery, Holographic Methods.

I. INTRODUCTION

Far Field determination from near zone measurements is a powerful tool for antenna testing and diagnostics. Standard approaches require the knowledge of complex near field distribution on a prescribed scanning surface, which is collected by a vector receiver and numerically processed to efficiently evaluate far field patterns. Near-field to far field (NF-FF) transformation performances essentially rely on the precision of the measurement setup and positioning system, with increasing complexity and cost when dealing with electrically large antennas.

In recent years, phaseless planar near field measurements have gained a considerable amount of interest among antenna measurement researchers [1] - [3]. Their promising cost effectiveness allows operating at higher frequencies with non-vector instruments.

Interferometric techniques are based on the algorithm first proposed by Gabor in microscopy [4], and require a reference antenna to be used for transmitting the phase reference to the receiving antenna, wherein the reference signal interferes with that transmitted by the Antenna Under Test (AUT). Simple and fast algorithms are required to evaluate the phase of the AUT signal. Furthermore, the accuracy of standard interferometric techniques is limited by the overlapping between the spectrum of the AUT and that of the reference antenna [5].

Microwave indirect holographic techniques [6] provide a simple and low cost method for antenna measurements and imaging of metallic and dielectric objects. Whilst traditional scalar measurement techniques only provide information regarding the magnitude of the signals

scattered from the object, indirect holographic techniques can provide both magnitude and phase information over selected measurement planes. This additional information can be used to reconstruct the complex fields, which in turns is adopted to determine the antenna aperture fields as well as the far field radiation characteristics, or it can be helpful to provide good quality images for a range of passive objects. A novel indirect holographic procedure is developed in this paper which combines all the best features of the recalled phaseless methods. A basically interferometric approach is adopted, but avoiding the use of a reference antenna as in standard interferometry. The problem of overlapping between the spectral components of hologram is avoided through the direct combination of the signals directly in the space domain.

II. Theory of Modified Indirect Holography

Let us assume the AUT radiating an electromagnetic field E_0 , (Fig. 1), and the sum of reference channel with the field radiated from the AUT:

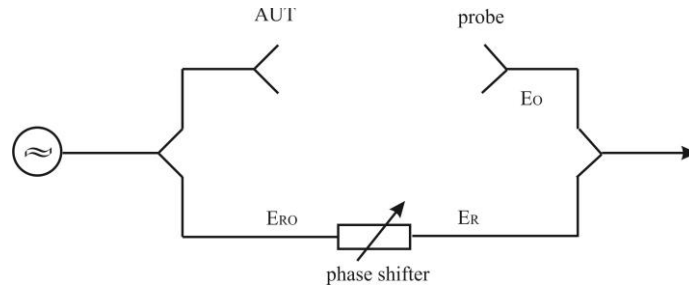


Fig. 1. Near Field acquisition scheme

$$I_0 = |E_0 + E_R|^2 = |E_0|^2 + |E_R|^2 + E_0^* E_R + E_0 E_R^* \quad (1)$$

where:

$$E_R = E_{R0} e^{-j\alpha} \quad (2)$$

Through the phase shifter of Fig.1 is possible to set $\alpha = \frac{\pi}{2}$. Consequently, we have:

$$E_R = E_{R0} e^{-j\frac{\pi}{2}} = -jE_{R0} \quad (3)$$

From (1) we obtain:

$$I_1 = |E_0|^2 + |E_{R0}|^2 - jE_0^* E_{R0} + jE_0 E_{R0}^* \quad (4)$$

Setting $\alpha = -\frac{\pi}{2}$, we have:

$$E_R = E_{R0} e^{j\frac{\pi}{2}} = jE_{R0} \quad (5)$$

Again, from (1) we obtain:

$$I_2 = |E_0|^2 + |E_{R0}|^2 + jE_0^*E_{R0} - jE_0E_{R0}^* \quad (6)$$

Considering the sum and difference between expressions (1), for $\alpha=0$, and (4) or (6), we obtain:

$$A = I_0 - I_1 = E_0^*E_{R0}(1 - j) + E_0E_{R0}^*(1 + j) \quad (7)$$

$$B = I_0 - I_2 = E_0^*E_{R0}(1 + j) + E_0E_{R0}^*(1 - j) \quad (8)$$

By adjusting the length of the cable from splitter to phase shifter, we have:

$$\frac{A + B}{E_{R0}} = 4Re\{E_0\} \quad (9)$$

Under the same conditions, we obtain:

$$\frac{B - A}{E_{R0}} = 2j(E_0^* - E_0) = 4Im\{E_0\} \quad (10)$$

From eqs. (9) and (10), we obtain the phase of signal E_0 :

$$\varphi = \arctan \left\{ \frac{B - A}{B + A} \right\} \quad (11)$$

From eq. (11) we see that the determination of AUT phase occurs through the knowledge of quantities (A+B) and (A-B). To verify the proposed algorithm, a 45 elements array of elementary dipoles is considered. The Near Field is simulated on a planar surface 5λ away from the antenna.

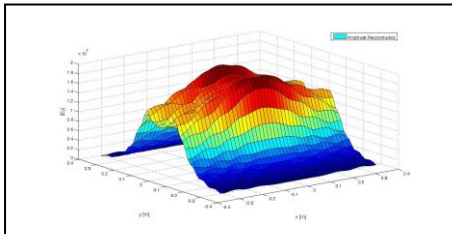


Fig. 2. Near Field amplitude

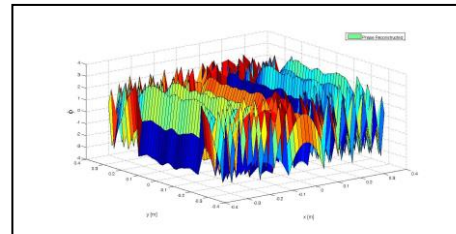


Fig. 3. Near Field phase

In Figs. (2), (3) the amplitude and phase reconstructed with the proposed method are reported, while in Figs. (4),(5) a comparison between the direct phase computation and the reconstructed one is reported for the central cuts of the near field diagram.

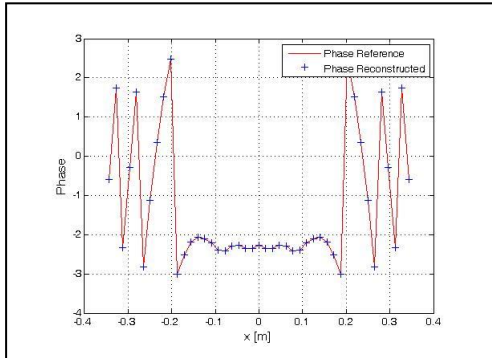


Fig. 4. Reconstructed near-field phase in the plane $y=0$

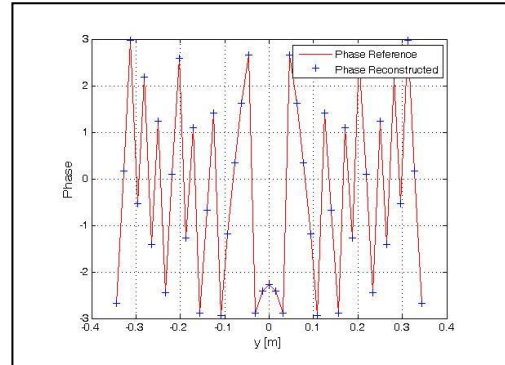


Fig. 5. Reconstructed near-field phase in the plane $x=0$

III. CONCLUSION

An indirect holographic technique for the determination of the antenna radiation characteristics has been described. A major feature of this technique is to avoid the problem of overlapping between the spectral components of hologram, by combining the signals directly in the space domain. The technique can be practically implemented through a circuit to the scheme of Fig. 1. The authors are applying the proposed theory to measured data with the proposed set up in order to have realistic reconstruction for the near-field phase.

REFERENCES

- [1] S. Costanzo, G. Di Massa, M. D. Migliore, Integrated Microstrip Probe for Phaseless Near-Field Measurements on Plane- Polar Geometry, *Electronic Letters*, vol. 37, No. 16, pp. 1018- 1020, August 2001. 1018-1020.
- [2] S. Costanzo, G. Di Massa, M. D. Migliore, A novel hybrid approach for Far-Field characterization from Near-Field amplitude-only measurements on arbitrary scanning surfaces, *IEEE Trans. Antennas Propag.*, vol. 53, No. 6, pp. 1866-1974, 2005.
- [3] S. Costanzo, G. Di Massa, Wideband Phase Retrieval Technique from Amplitude-Only Near-Field Data, *RADIOENGINEERING*, vol. 17, pp. 8-12, 2008.
- [4] D. Gabor, A New Microscopic Principle, *Nature*, vol. 161, pp. 777-778, May 1948.
- [5] M. D. Migliore, G. Panariello, A comparison among interferometric methods applied to array diagnosis from near-field data, *Proc. Inst. Elect. Eng.*, vol. 148, pp. 261267, 2001.
- [6] D. Smith, M. Leach, M. Elsdon, J. Foti, Indirect Holographic Techniques for Determining Antenna Radiation Characteristics and Imaging Aperture Field, *IEEE Ant. and Propagat. Magazine*, vol 49, No. 1, pp. 54-67, Feb. 2007.

SYNTHESIS OF DIELECTRIC CLOAKS VIA INVERSE SCATTERING DESIGN WITHOUT METAMATERIAL COATINGS

G. Labate⁽¹⁾ and L. Di Donato⁽²⁾

(1) Dipartimento di Elettronica e Telecomunicazioni, Politecnico di Torino, Corso Duca degli Abruzzi 29, Torino, Italy

giuseppe.labate@polito.it

(2) Dipartimento di Ingegneria Elettrica, Elettronica e Informatica, Università di Catania, Viale Andrea Doria 6, Catania, Italy

loreto.didonato@dieei.unict.it

Abstract

In this paper, we discuss the possibility of inducing a cloaking effect without using metamaterials. Starting from the inverse scattering problem (ISP), an ideal cloaking effect (i.e., zero scattered fields) is analytically synthesized in quasi-static regime: it is shown how object and cloak regions need positive-negative contrast values at subwavelength scale. However, reasoning on the role of contrast and source functions, both unknowns of the ISP, we intentionally pilot the ISP, solved via numerical optimizations, towards a cloak made up of only common dielectric permittivity. Interestingly, this is possible beyond quasi-static regime, where common cloaking methods (Scattering Cancellation) are no longer valid or need metamaterials (Transformation Optics).

Index Terms – Cloaking, Contrast Source, Inverse Scattering Problem, Metamaterials.

I. INVERSE SCATTERING: FROM PROBLEM TO DESIGN

The scattering data, naturally carried by electromagnetic fields during measurements, can be processed in order to know location, shape and even physical properties of unknown radiating systems embedded in a background scenario [1]. However, scattering data can be also postulated (and not sensed) to synthesize electromagnetic device with desired properties. In this paper, we apply this concept to the cloaking problem in order to facilitate the design of coatings able to sustain (ideally) zeros in the radar cross section (RCS) when they are put around an object to be hidden. To this aim, the scattering equation is first analyzed in the quasi-static regime, i.e. when the bare object is small with respect to the probing wavelength. In this case, it is found that a necessary and sufficient condition to achieve transparency is a positive-negative oscillating contrast values of the entire cloaking system. However, beyond quasi-static regime, the non-linearity of the ISP [2] is properly exploited to design coatings made of common dielectrics, without recurring to materials with negative constitutive parameters, i.e. metamaterials. This result implies an extraordinarily simplification in the design of the cloaking device. At the author's best knowledge, existing cloaking methods are not able to achieve such a goal, because they are not

applicable beyond quasi-static regime (Scattering Cancellation [3]) or they need metamaterials in the cloak region (Transformation Optics [4]).

II. ANALYTICAL METHOD: QUASI-STATIC REGIME

We assume a cylindrical coordinate reference system and a volumetric distribution of dielectric materials, the physical cause of the scattering event is the induced currents [1]

$$\vec{J}_v(\rho', \varphi') = j\omega\epsilon_b\chi(\rho', \varphi')\vec{E}_t(\rho', \varphi') \quad (1)$$

where volumetric (polarization) sources $\vec{J}_v(\cdot)$ show a dependence on the total field configuration $\vec{E}_t(\cdot)$ and the contrast function $\chi(\cdot)$ as well, the latter defined as

$$\chi(\rho', \varphi') = \frac{\epsilon(\rho', \varphi') - \epsilon_b}{\epsilon_b}, \quad (2)$$

representing the normalized difference between constitutive parameters of the scattering system and background region. As a result, by definition, if the vacuum is assumed as background medium, positive/negative sign of the contrast indicates common dielectric objects (+) or metamaterials (-), respectively. The mathematical relation between scattered field and source is given by:

$$-j\omega\mu_b \int_{\Omega} \vec{J}(\rho', \varphi') G(\rho, \varphi, \rho', \varphi') d\Omega = \vec{E}_s(\rho, \varphi) \quad (3)$$

where a general observer, located at (ρ, φ) , is looking at the scattering event $\vec{E}_s(\cdot)$ radiated by volumetric sources distributed in the scenario Ω . Moreover, the Green's function $G(\cdot)$, taking into account the mutual interactions of the scattering phenomenon, is the kernel of the radiation operator which maps sources into scattered fields. Considering the ideal scattering output of the cloaking problem (i.e., $\vec{E}_s = 0$), the ISP can be solved in a straightforward manner in quasi-static condition. In this respect, it is worthwhile mentioning that Eq. (3) can be restricted to a domain Σ where the induced sources are localized, supporting the cloaking system. For quasi-static regime, the Green's function can be assumed to be constant over Σ , as well as the total field. As a result, turning to zero the scattered fields, Eq. (3) becomes a compact relation only between contrast values of the overall cloaking system, i.e.,

$$\int_{\Sigma} \chi(\rho', \varphi') d\Sigma = 0. \quad (4)$$

Splitting eq. (4) in two subdomains (cloak and object areas), a positive/negative nature of the contrast function comes out as *necessary and sufficient* condition: it is interesting to note that Eq. (4) generalizes *plasmonic cloaking* [3] for scatterers of arbitrary shape. In quasi-static condition, cloaking a common material is possible only inserting metamaterials in the cloak region. In fact, the designer can turn-off the effect of the volumetric sources only by locally compensating the positive induced polarization associated to a positive contrast (i.e. the object) with

the negative one associated to a negative contrast (i.e. the metamaterial cloak). An example for a non-canonical shape cloaking system at subwavelength is shown in Fig. 1.

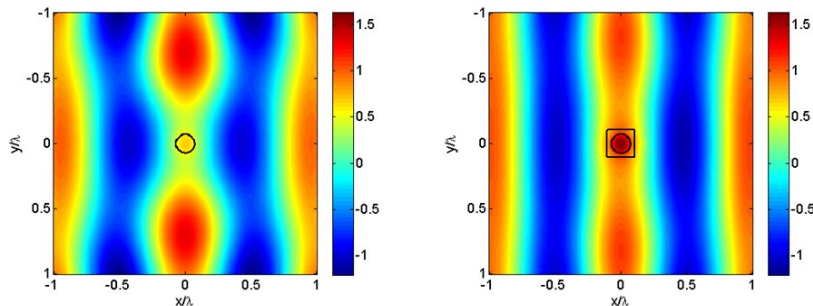


Fig. 1. Real part of the total field for the bare object (left) and the cloaked object (right) synthesized by using Eq. (4). The bare object is a circle with $\epsilon=6\epsilon_0$ and radius $r=4.2\text{mm}$, while the cover is a square of $\epsilon_c=-3.13\epsilon_0$ and width $3r$. The frequency is 5 GHz.

III. NUMERICAL METHOD: BEYOND QUASI-STATIC REGIME

Beyond quasi-static condition, the main consideration to derive condition (4) from Eq. (3) is no longer valid. However, inspired by critique and alternatives about metamaterials [5], we ask if there is still the need of making use of negative contrast within the cloak region. In fact, if we look at Eq. (3), in this case, the ISP ‘reduces’ to the problem of finding proper contrast distributions which account for a cancellation, or at least a considerable reduction, of the scattered field through the source function in Eq. (1). Indeed, when the size of the cloaking system become larger and larger with respect to the wavelength, non-scattering behaviour can be pursued even if the contrast shows a positive value. As a matter of fact, being the effects of total field configuration no more lumped in the cloaking domain, but distributed, the cloaking mechanism can be achieved through proper distribution of contrast taking into account the non-linear effects on the source configuration. Inspired by the reasoning above, we exploit the numerical solution of the ISP solving the following optimization problem:

$$\phi(\chi, J) = \sum_{v=1}^N \left\{ \frac{\|J^v - \chi E_i^v + \chi A_i[J^v]\|^2}{\|E_i^v\|^2} \Big|_{\Omega} + \frac{\|A_e[J^v]\|^2}{\|E_i^v\|^2} \Big|_{\Gamma} \right\}. \quad (5)$$

In Eq. (5), the first addendum enforces, for a given set of incident field views N , the solution (in the least square sense) of the scattering equation in Ω (the state equation in the common ISP [1-2]), while the second addendum is nothing but the minimization of the RCS over an observation domain Γ at a given distance from Ω . Moreover, A_i and A_e are short notations of the integral operators which relate the contrast source to the scattered field in Ω and Γ , respectively. Finally, it is worth noting that both the contrast function and the source are unknowns of the problem. In particular, in order to look for real contrast function

exhibiting positive values, we enforce that the relative permittivity is everywhere greater than one and conductivity is zero (i.e., lossless).

IV. NUMERICAL RESULTS: CLOAKING WITHOUT ARTIFICIAL MATERIALS

In order to demonstrate the validity of our considerations, we address the solution of Eq. (5) considering the same object discussed in the quasi-static condition (i.e., $\varepsilon=6\varepsilon_0$), but at higher frequency (e.g., 25 GHz). We choose the cloak region to be a circular annulus of radius 2λ and we require the RCS to be zero in the near-field all around the cloaking system, for two antiparallel direction of the incident (plane waves) fields (i.e. $-x$ and x). The synthesized permittivity distribution is shown in Fig. 2. As it can be seen, this leads to a cloak with a specific arrangement of dielectric materials with $\varepsilon_c=1.6\varepsilon_0$ around the object. The effect of the cloaking is also shown in Fig. 2.

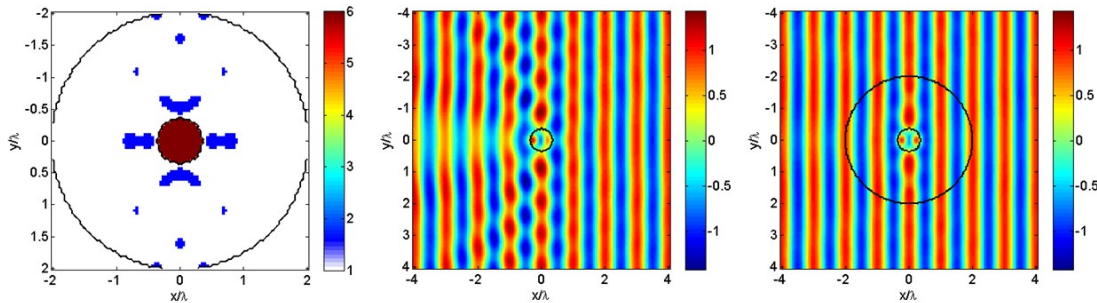


Fig.2 Results of the synthesis of natural dielectric cloak via Eq. (5). From left to right: permittivity values of the cloaking system, real part of the total field in the case of bare and cloaked object.

CONCLUSIONS

The synthesis of a cloak has been suggested with analytical and numerical approach based on the inverse scattering problem. Interestingly, the possibility to achieve transparency (with respect to the direction of the incoming wave) has been demonstrated well beyond quasi-static condition, re-evaluating standard dielectrics instead of metamaterials in the cloak region. More details and results will be shown at the conference.

ACKNOWLEDGEMENT

The authors would like to thank Prof. L. Matekovits and Prof. T. Isernia for their valuable comments and suggestions.

REFERENCES

- [1] D. Colton and R. Kress, *Inverse Acoustic and Electromagnetic Scattering Theory*, Springer-Verlag, 1992
- [2] O. M. Bucci and T. Isernia, “Electromagnetic Inverse Scattering: Retrievable information and measurement strategies”, *Radio Science*, Vol. 32 (6), 1997.
- [3] A. Alù and N. Engheta, “Achieving transparency with plasmonic and metamaterial coatings”, *Physical Review E*, Vol. 72 (016623), 2005.
- [4] J. Pendry, D. Schurig, D. R. Smith, “Controlling Electromagnetic Fields”, *Science*, Vol. 312, no. 5781, pp. 1780-1782, 2006.
- [5] B. A. Munk, *Metamaterials: Critique and alternatives*, Wiley and Sons, 2009.

DEEP PENETRATION PROPERTIES OF INHOMOGENEOUS WAVES

P. Baccarelli, F. Frezza, P. Simeoni, and N. Tedeschi

Department of Information Engineering, Electronics and
Telecommunications (DIET), “La Sapienza” University of Rome,
Via Eudossiana 18, 00184 Rome, Italy.
patrizio.simeoni@uniroma1.it

Abstract

This article demonstrates that high penetration on lossy media can be achieved by using inhomogeneous waves. Penetration properties of inhomogeneous waves are initially presented studying a plane wave impinging on the separation surface between two media, where at least the medium in which the wave is transmitted is assumed lossy. The theory presented in the first part of the article is then explored by considering more realistic scenarios based on leaky waves generated by uniform microstrip antennas in the X band. Finally, practical limits and potentialities of the shown approach are discussed.

Index Terms – Deep penetration, inhomogeneous waves, leaky-wave antennas, lossy media.

I. INTRODUCTION

Homogeneous waves always turn into attenuated waves when entering into a lossy medium. In particular, the attenuation vector is always orthogonal to the separation surface between lossy and lossless media, thus strongly affecting the penetration. Recent studies highlighted that this limit can be overcome by inhomogeneous waves [1]. We will explore here the penetration properties of inhomogeneous waves verifying whether deep penetration may be practically achieved.

II. PROPERTIES OF INHOMOGENEOUS PLANE WAVES

Let us define a plane wave incoming from a lossless medium and impinging on the separation surface with a lossy medium and let us call $\underline{k}' = \underline{\beta}' - j\underline{\alpha}'$ and $\underline{k}'' = \underline{\beta}'' - j\underline{\alpha}''$ the wave vectors of incident and transmitted waves, respectively, where $\underline{\beta}'$, $\underline{\beta}''$ are the phase vectors and $\underline{\alpha}'$, $\underline{\alpha}''$ are the attenuation vectors. Let us define angles according to Fig. 1. It is well known [2] that $\underline{\alpha}' = 0$ (homogeneous wave) causes $\chi'' = 0$, while $\underline{\alpha}' \perp \underline{\beta}'$ (inhomogeneous wave) causes $\chi'' \neq 0$ [2]; in both cases $\theta'' < \pi/2$. It was already demonstrated in [1] that, for an inhomogeneous wave, a particular value ξ'_c for ξ' may exist for which $\chi'' = \pi/2$, allowing deep penetration:

$$\xi'_c \geq \frac{1}{2} \arcsin \left[\frac{\text{Im}[k''^2]}{\beta' \alpha'} \right] \Leftrightarrow \beta' \geq \frac{k'}{\sqrt{2}} \sqrt{1 + \sqrt{1 + \frac{4 \text{Im}[k''^2]^2}{k'^2}}}. \quad (1)$$

As a consequence of (1) it follows:

$$\alpha' \geq \frac{k'}{\sqrt{2}} \sqrt{\sqrt{1 + \frac{4 \text{Im}[k''^2]^2}{k'^2}} - 1}. \quad (2)$$

Equations (1) and (2) determine β' and α' values which allow deep penetration and, in particular, their minimal values, β'_{MIN} and α'_{MIN} , are obtained for $\xi'_c = \pi/4$. It can be further demonstrated that the components of $\underline{\alpha}'$ and $\underline{\beta}'$ orthogonal to the separation surface between the two media need to have opposite signs.

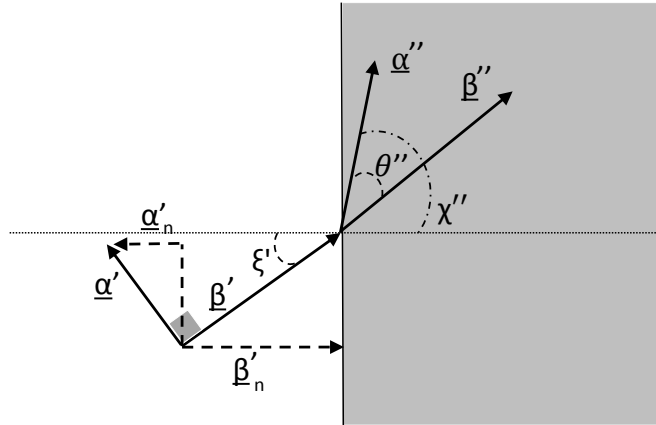


FIG. 1 – Incident and transmitted waves

III. APPLICATION

Leaky-Wave Antennas (LWAs) can generate improper leaky waves in a limited angular region of the near field that well approximate the inhomogeneous waves described in the previous section [3]. Hence, two microstrip LWAs [4] based on the Menzel antenna [5] and operating in the X-band were used to prove the deep-penetration properties of inhomogeneous waves. In both cases, a lossy medium having unitary relative permittivity and permeability was chosen, in order to minimize unwanted reflection effects. The LWAs were designed using a procedure based on the Method of Moments [6] in order to radiate improper leaky waves (through the EH_1 leaky mode) at an angle of $\pi/4$ in free space, which is also the angle of incidence on the separation surface with the

lossy medium, and at an operating frequency of 12 GHz. Once the conductivity of the lossy medium was chosen, the relevant values of $\underline{\alpha}'$ and $\underline{\beta}'$ were imposed according to (1) and (2), thus also fixing the leaky-mode normalized phase and attenuation constants β'_z/k_0 and α'_z/k_0 , respectively. The first antenna was designed to allow deep penetration for $\sigma'' \leq 0.015$ S/m, resulting in $\beta'_z/k_0|_{12\text{GHz}} = 0.7074$ and $\alpha'_z/k_0|_{12\text{GHz}} = 0.0523$ (see Fig. 2 for the physical and geometrical parameters of the microstrip antenna). The second antenna was designed for $\sigma'' \leq 0.05$ S/m, with $\beta'_z/k_0|_{12\text{GHz}} = 0.7088$ and $\alpha'_z/k_0|_{12\text{GHz}} = 0.0523$ (see Fig. 3 for the physical and geometrical parameters of the microstrip antenna).

A rectangular parallelepiped of dimension equal to the length L of the LWA on both z and y directions and slightly wider than W on the x direction was chosen as lossy medium and posed above the antenna at a distance $y_0 = 1.5\lambda_0$. A full-wave analysis was performed through the commercial tool CST and the antenna was fed by a waveguide port at $z = z_0$. The estimation of deep penetration was achieved evaluating the amplitude of the electric field $E_x = E_x(0, y, z_i)$ normalized by its value at the interface between lossy and lossless media $E_{0x} = E_{0x}(0, \lambda_0, z_i)$ for $z_i > z_0$.

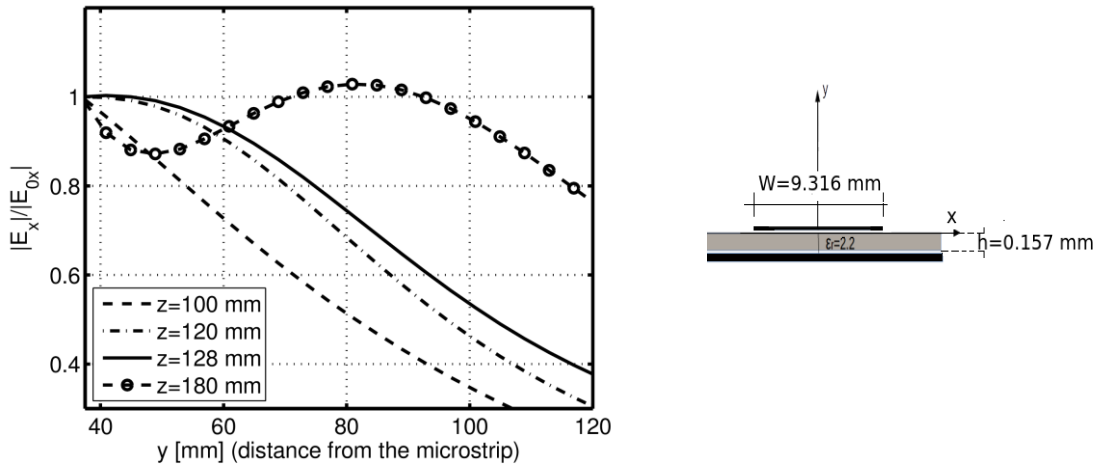


FIG. 2 – First antenna layout and its $|E_x|/|E_{0x}|$ ratio for $\sigma'' = 0.015$ S/m

The penetration results for the two antennas are shown in Figs. 2 and 3, respectively. Deep penetration is achieved in both scenarios. The first antenna sustains the penetration for a long distance being $L \approx 10\lambda_0$ (see the curve for $z = 180$ mm), while a critical issue is observed on the second antenna, where the deep penetration is limited toward the

termination at $L \approx 5\lambda_0$ and the field starts decaying at $y_{MAX} \approx y_0 + 0.5\lambda_0$. These results indicate that such a LWA cannot be easily designed to provide deep penetration in lossy media with higher σ'' values.

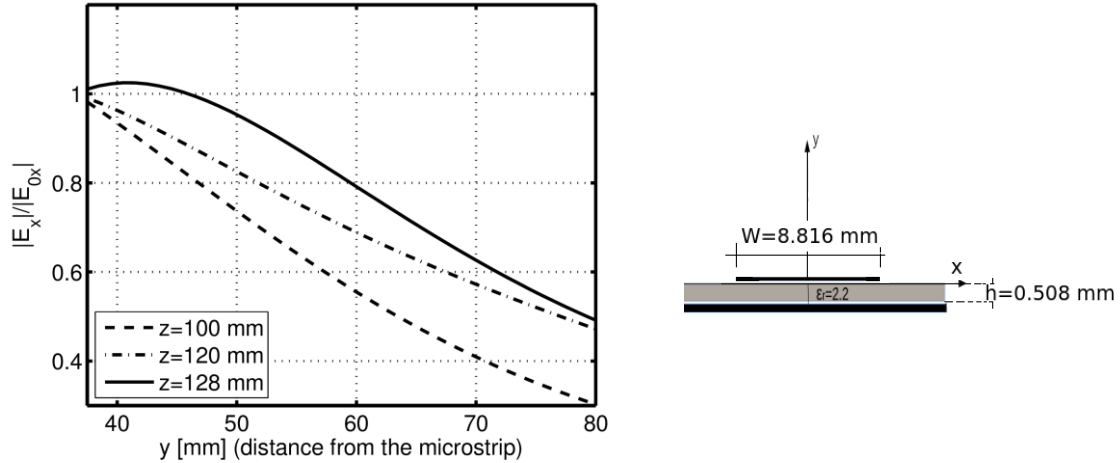


FIG. 3 – Second antenna layout and its $|E_x|/|E_{0x}|$ ratio for $\sigma'' = 0.05$ S/m

IV. CONCLUSION

The deep-penetration property of inhomogeneous plane waves and the possible deep-penetration achievement by means of LWAs have been studied and discussed. The practical limits of this approach were also highlighted. Different radiating structures will be considered in future studies in order to overcome the limits shown by the proposed microstrip LWAs.

REFERENCES

- [1] F. Frezza and N. Tedeschi, "Deeply penetrating waves in lossy media," *Optics Letters*, vol. 37, pp. 2616-2618, July 2012.
- [2] F. Frezza, *A Primer on Electromagnetic Fields*, Springer, Switzerland, 2015.
- [3] A. A. Oliner and D. R. Jackson, "Leaky-Wave Antennas," in *Antenna Engineering Handbook*, 4th Edition, Chap. 11, John Volakis Editor, McGraw Hill Professional, 2007.
- [4] A. A. Oliner and K.S. Lee, "Microstrip leaky wave strip antennas," *Proc. of IEEE International Symposium on Antennas and Propagation*, pp. 443-446, June 1986.
- [5] W. Menzel, "A new travelling-wave antenna in microstrip," *Proc. 8th European Microwave Conference*, Paris, 1978.
- [6] P. Baccarelli, C. Di Nallo, S. Paulotto, and D. R. Jackson, "A full-wave numerical approach for modal analysis of 1D periodic microstrip structures," *IEEE Trans. Microwave Theory Tech.*, vol. 54, pp. 1350-1362, Apr. 2006.

ANALYSIS OF LEAKY-WAVE THz ANTENNAS BASED ON GRAPHENE

W. Fuscaldo^{(1),(2)}, P. Burghignoli⁽¹⁾, P. Baccarelli⁽¹⁾, and A. Galli⁽¹⁾

⁽¹⁾ Department of Information Engineering, Electronics and Telecommunications (DIET), “Sapienza” University of Rome, Via Eudossiana 18, 00184 Rome, Italy.

fuscaldo@diet.uniroma1.it

⁽²⁾ Institut d’Électronique et de Télécommunications de Rennes, UMR CNRS 6164, Université de Rennes 1, 263 Avenue du Général Leclerc, 35700 Rennes, France.

Abstract

In this work we analyze different configurations of graphene-based leaky-wave antennas (LWAs) operating in the low THz range. The performance of a grounded dielectric slab covered with a monolayer graphene sheet and of a grounded substrate-superstrate antenna in which the sheet is placed inside the substrate are discussed in details. Our analysis emphasizes that such leaky-wave-based structures are considerably more efficient than graphene antennas based on the propagation of surface plasmon polaritons (SPPs). Quantitative results, derived by both ad hoc numerical codes and commercial CAD implementations, reveal us that this increased efficiency is partly paid at the expenses of a reduced reconfigurability of the device. Thus, a trade-off should be established between directivity, efficiency and reconfigurability of such graphene LWAs.

Index Terms – Graphene, leaky-wave antennas, plasmonics, terahertz.

I. INTRODUCTION

Since its discovery in 2004 by the Nobel Prizes A. K. Geim and K. S. Novoselov [1], graphene has attracted a lot of interest in physics as well as in engineering communities thanks to its unique physical, electrical, mechanical, and thermal properties. From an engineering point of view, the most attractive feature is represented by the possibility of tuning the graphene surface conductivity by changing its chemical potential through the application of an electrostatic bias [1]. Specifically, in the low-THz range, graphene surface conductivity becomes mostly reactive and hence can support plasmonic propagation. As a consequence, graphene can be employed as a tunable element for modulating the conductivity patterns of various THz devices based on plasmonics, such as transformation-optics devices [2] or reconfigurable antennas [3]. However, the theoretical efficiency of THz antennas based on the propagation of surface plasmon polaritons (SPPs) along graphene looks still rather poor [3].

In this context, we propose here *two different reconfigurable graphene antennas* (see Fig. 1) whose radiation mechanism is not based on SPPs but instead on *ordinary leaky waves* (LWs): the Graphene-based Planar Substrate (GPS) antenna [4] and the Graphene-based Substrate-Superstrate (GSS) antenna.

A rigorous numerical analysis will establish that *our proposed LW* configurations have comparable performance in terms of directivity with their *plasmonic* counterpart reported in [3], whereas the achieved efficiency is considerably higher. This significant improvement is just partly paid at the expense of a reduced reconfigurability of the devices.

In Sec. II, we describe the modal and radiating features of the proposed LW devices. In Sec. III, the achievable efficiencies of such antennas are compared with those available in the literature for solutions based on SPPs. Conclusions are drawn in Sec. IV.

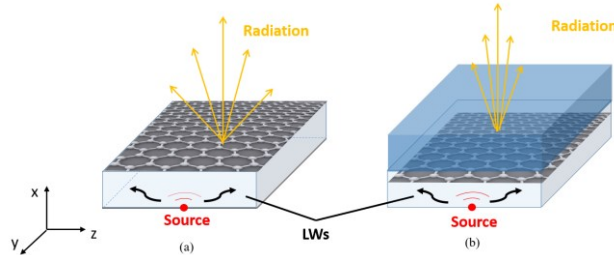


FIG. 1 – 3D sketches of the proposed graphene-based LWAs. a) The Graphene-based Planar Substrate (GPS) antenna and b) the Graphene-based Substrate-Superstrate (GSS) antenna.

II. STRUCTURES AND RADIATION OF GRAPHENE LWAS

Our *GPS antenna* [4] is a grounded dielectric slab (e.g., a silica layer of relative permittivity $\epsilon_{r1} = 3.8$ and thickness $h_1 = 0.5\lambda / \sqrt{\epsilon_{r1}}$ at the operating frequency $f_{op} = 1$ THz are considered in all results), covered with a high-quality monolayer graphene sheet (relaxation time $\tau = 3$ ps), possibly biased through the application of a DC voltage between the sheet and a conducting polymer layer placed just underneath. As shown in our previous work by means of a rigorous modal analysis [4], a GPS antenna supports leaky modes in the low-THz range for suitable values of the chemical potential μ_c . In particular, for values of μ_c in the range 0.25-1 eV, the fundamental TM and TE leaky-mode pair exhibits relatively low leakage rates α_z , thus opening very interesting perspectives for the design of tunable graphene-based LWAs in the low-THz range. Moreover, numerical results [4] have shown that the tunability of graphene conductivity allows for achieving beam scanning at the fixed frequency $f_{op} = 1$ THz over a considerable angular range. However, the directivity of the GPS antenna looks rather low, being the typical beamwidths relatively large (see *dashed lines* in the radiation patterns of Fig. 2). In order to improve the directivity, we therefore propose here the different multilayered configuration of a *GSS antenna*.

Our *GSS antenna* is a standard substrate-superstrate (low-high permittivity) antenna [5], in which a graphene sheet is introduced at a suitable position within the substrate. In short, starting from the design of the GPS described in [4], we have fixed a superstrate layer of higher

relative permittivity ε_{r2} (in all results we have considered a Hafnium Oxide layer, $\varepsilon_{r2} = 25$), and thickness $h_2 = 0.25\lambda / \sqrt{\varepsilon_{r2}}$, as suggested in [5] to increase directivity at broadside. Then, we have considered different positions for the graphene sheet within the substrate in order to find an ‘optimum’ location where the leakage rate of the dominant TM-TE leaky mode pair is minimum at the cutoff frequency f_c (i.e., the frequency where $\beta_z(f_c) \cong \alpha_z(f_c)$ [5]), and the radiated power is maximum at broadside. Numerical results, derived by ad hoc transverse-resonance formulations [4] and validated also by a CAD tool, revealed us that this optimum condition is achieved when the graphene sheet is located at $x = 0.8h_1$.

The relevant radiation patterns in Fig. 2 (*solid lines*) confirm that the optimized GSS shows essentially improved directivities with respect to the GPS solution for all the considered pointing angles ($\theta_p = 0^\circ, 15^\circ, 30^\circ, 45^\circ$). Moreover, the directivities of both GPS and GSS are comparable with those obtained in [3] with antennas based on plasmonic propagation. In the following section, the different performance in terms of efficiency and reconfigurability between *ordinary* and *plasmonic* leaky-wave solutions are qualitatively and quantitatively discussed.

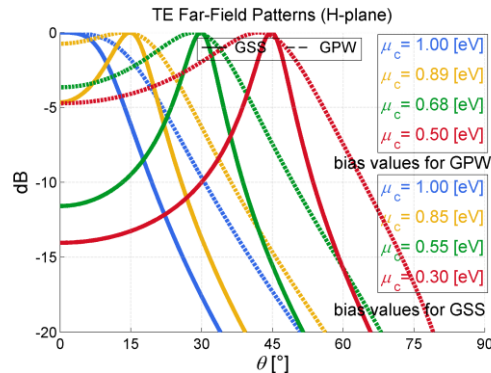


FIG. 2 – Normalized radiation patterns vs. elevation angle θ on the H-plane for a GPS (*dashed lines*) and for a GSS (*solid lines*) antenna. The beam-scanning behavior at a fixed frequency is shown for pointing angles $\theta_p = 0^\circ, 15^\circ, 30^\circ, 45^\circ$. The values of μ_c for the GPS and the GSS are reported in the legend. Similar results are obtained on the E-plane for both structures.

III. EFFICIENCY AND RECONFIGURABILITY OF GRAPHENE LWAS

The radiation efficiencies of both the GPS and the GSS have been evaluated in terms of the ratio $\eta = P_{\text{rad}} / (P_{\text{rad}} + P_g)$ where P_{rad} is the power radiated in space and P_g is the power dissipated along the graphene sheet. The quantities P_{rad} and P_g have been calculated using the ABCD-matrix approach with the relevant transverse equivalent network. The calculation showed that for a GPS it is $\eta = 70\%$, whereas for a GSS η varies from 40% to 90% depending on the graphene position. As expected, the efficiency of the GSS sensitively depends on the position of the

graphene sheet within the substrate. On one hand, if graphene is placed in a position where it strongly interacts with the electric field (towards the middle plane), the efficiency attains its minimum. On the other hand, if graphene is placed in a position where it weakly interacts with the electric field (towards the substrate-superstrate interface), the efficiency attains its maximum. In particular, when graphene is placed at its ‘optimum’ position ($x = 0.8h_1$), i.e., when the GSS shows its maximum directivity, the efficiency is about $\eta = 60\%$, that is an intermediate condition. Hence, the graphene position that leads to the maximum directivity at broadside does not generally coincide with the maximum efficiency condition.

It is worth stressing that, when graphene weakly interacts with the electric field, the reconfigurability of the device substantially decreases, hence the beam scanning is restricted to a narrower angular range. However, even in the worst condition, the ordinary leaky-wave solutions allow for achieving higher radiation efficiencies than their plasmonic counterparts, that are in fact limited to values of the order of 20% in the best case [3]. Moreover, the possibility to choose the graphene position in a GSS, according to the requirements in terms of reconfigurability, directivity and efficiency, provides designers a further degree of freedom with respect to all other structures.

IV. CONCLUSION

We have proposed two different graphene THz antennas based on leaky waves. Numerical results have shown that these structures have comparable directivities but much improved efficiencies with respect to previous solutions based on SPPs. In general, a trade-off exists among the available directivity, efficiency, and reconfigurability features. Thanks to its additional degrees of freedom, the GSS looks particularly promising for flexible design under typical performance constraints.

REFERENCES

- [1] A. K. Geim, and K. S. Novoselov, “The rise of graphene,” *Nature Mat.*, vol. 6(3), pp. 183–191, 2007.
- [2] A. Vakil and N. Engheta, “Transformation optics using graphene,” *Science*, vol. 332(6035), pp. 1291–1294, Jun. 2011.
- [3] M. Esquiús-Morote, J. S. Gómez-Díaz, and J. Perruisseau-Carrier, “Sinusoidally modulated graphene leaky-wave antenna for electronic beamscanning at THz,” *IEEE Trans. THz Science Tech.*, vol. 4(1), pp. 116–122, Jan. 2014.
- [4] W. Fuscaldo, P. Burghignoli, P. Baccarelli, and A. Galli, “Complex mode spectra of graphene-based planar structures for THz applications,” *J. Infrared Milli. Terahz Waves*, vol. 36(8), pp. 720–733, Aug. 2015.
- [5] D. R. Jackson and A. A. Oliner, “A leaky-wave analysis of the high-gain printed antenna configuration,” *IEEE Trans. Antennas Propag.*, vol. 36(7), pp. 905–910, Jul. 1988.

WIRE-MEDIUM LOADED FABRY-PEROT CAVITY ANTENNAS

D. Comite, P. Burghignoli, P. Baccarelli, A. Galli

Department of Information Engineering, Electronic and
Telecommunications, Sapienza University of Rome
00184 Rome, Italy
comite@diet.uniroma1.it

Abstract

The radiation features of a wire-medium loaded Fabry-Perot cavity antenna (WM-FPCA) are investigated by means of an ad hoc transmission-line model. The network formalism allows for an effective determination of the relevant spectral Green's functions and of the far-field radiation pattern produced by simple sources, as opposed to a more cumbersome field-matching approach. The capability to suppress the undesired contribution of the quasi-TEM mode propagating inside the structure is demonstrated and the radiation efficiency is evaluated for scannable conical beams with improved performance.

Index Terms – Fabry-Perot cavity, leaky waves, wire medium.

I. INTRODUCTION

Since the discovery of its rather unique spatially-dispersive nature, wire media (WM) have received considerable attention. Several planar structures including layers with different wire orientations have been studied in the last decade by various authors [1], [2]. In particular, Fabry-Perot cavity antennas (FPCAs), derived by a parallel-plate waveguide (PPW) whose upper plate is a partially reflecting surface (PRS) and internally loaded by a layer of vertically-aligned wires (see Fig. 1(a)), were recently analyzed in [3], where a convenient transmission-line formulation was introduced to study the relevant modal properties. In addition, the capability of the WM to minimize undesired radiation from the quasi-TEM mode, propagating at any frequency, has been demonstrated. In this contribution, the main radiative features of the structure are summarized and the relevant spectral-domain Green's function is derived by a straightforward application of the developed transmission-line formalism. The radiated and the surface-wave powers produced by an elementary source are also evaluated, allowing for the analysis of the improved radiation efficiency of the proposed antenna.

II. EQUIVALENT NETWORK MODEL OF WM-LOADED STRUCTURES

A transmission line model (TLM) has been proposed for the first time in [3] for closed and open layered structures loaded by WM (Fig. 1(b)), which in the large-wavelength limit can be represented as a homogeneous medium showing both anisotropic and spatially-dispersive behavior. Its spectral dyadic permittivity is expressed as [2], [3]

$$\underline{\underline{\varepsilon}} = \varepsilon_0 \varepsilon_{rh} \left[\underline{\underline{u}}_x \underline{\underline{u}}_x + \underline{\underline{u}}_y \underline{\underline{u}}_y + \left(1 - \frac{k_p^2}{\varepsilon_{rh} k_0^2 - k_z^2} \right) \underline{\underline{u}}_z \underline{\underline{u}}_z \right] \quad (1)$$

being ε_r the relative permittivity of the host medium and k_0 and k_p the free-space and plasma wavenumbers. By applying the standard boundary conditions (total voltages and currents be continuous at the interface) along with the additional boundary condition for the WM [3], the relations among currents and voltages are written in terms of the longitudinal wavenumber and plasma frequency of the WM. In [3] a three-port network representation of a dielectric/WM interface was derived, allowing us to evaluate both the input impedance and the ABCD matrix of a WM layer. Thus, the equivalent-network model for a planar structure comprising an arbitrary number of WM layers, possibly including loss effects, can be established. Thanks to the proposed formalism it is possible to derive the spectral dyadic Green's functions of the structure, which are needed, e.g., for the evaluation of the near field excited by elementary sources. A vertical electric dipole (VED), which excites an azimuthally-symmetric TM field, is considered here, placed on the metal ground plane of the WM-loaded FPCA.

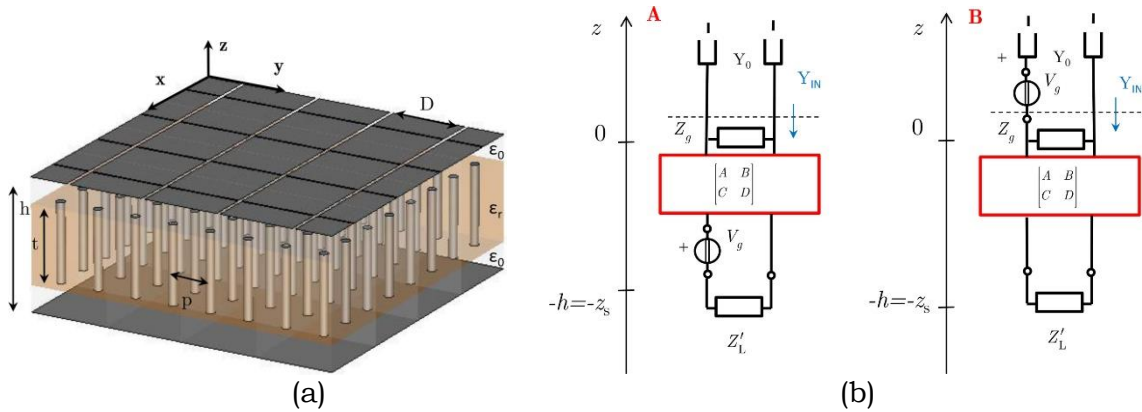


FIG. 1 – (a) Fabry-Perot cavity including a WM with vertical wires for the parallel-plate structure considered in this paper: $h = 14.27$ mm, $t = 8$ mm, $p = 1.5$ mm, $D = 3$ mm, $\varepsilon_r = 1.06$; (b) Equivalent networks for the calculation of the spectral Green's function of the azimuthal magnetic field produced by a VED.

III. RADIATIVE PROPERTIES

In the far-field region, the electric field is polarized along θ_0 and can be written as $E_\theta(r, \theta) = E^{ff}(\theta) e^{-jk_0 r} / r$. The far-field pattern can be calculated through reciprocity as $E^{ff}(\theta) = E^{pw}$, where E^{pw} is the z component of the electric field at the source location $r = (0, 0, z_s)$ due to an impinging plane wave. E^{pw} can in turn be evaluated exploiting the transverse equivalent network of the structure [3]. In Fig. 2(a) the normalized radiation patterns for a PPW-based FPCA are reported at two different frequencies: in addition to the main lobe due to the TM_1 leaky mode, a further lobe can

be observed due to leakage from the perturbed TEM mode that deteriorates the desired TM_1 -based single-beam scanning behavior. In Fig. 2(b), the normalized radiation patterns for a structure loaded with a WM slab are shown: the main lobe remains virtually unaltered, whereas the contribution from the ‘spurious’ quasi-TEM mode is completely suppressed by the WM.

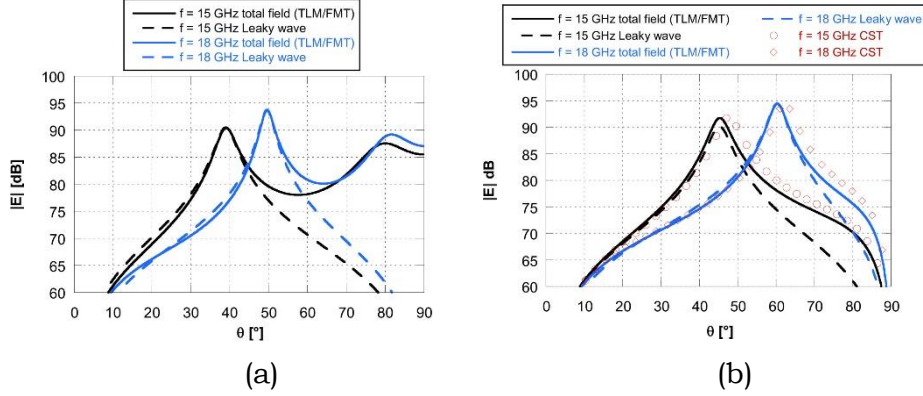


FIG. 2 – Far-field radiation patterns at two different frequencies for an open structure as in Fig. 1: (a) not loaded by a WM slab; (b) loaded by a WM slab.

The leaky-wave contribution is also reported for comparison. Numerical validation of our approach is obtained through CST Microwave Studio, by using a single unit cell in a periodic environment and applying reciprocity.

The total complex power delivered by the VED can be calculated by using Poynting’s theorem: by exploiting the integral representation of the azimuthal component of the magnetic field H_ϕ [4], it can be written as

$$P_{tot} = -\frac{\pi}{\omega^2 \epsilon^2} \int_0^{+\infty} k_\rho^3 \left| J_{S_z}^* (k_\rho) \right|^2 \hat{I}_V^{TM*} (-h, k_\rho) dk_\rho \quad (2)$$

where \hat{I}_V^{TM} is the current at z produced by a unit-amplitude voltage generator placed at $z=-h$ in the equivalent network of the structure, as shown in configuration A of Fig. 1(b). $J_{S_z} = P_0 \delta(\rho) / 2\pi\rho$ is the vertical surface current density and P_0 the current amplitude. The real (active) part of the total power is finite and for a VED of amplitude P_0 it is given by the sum of two contributions: the radiated power P_r given by the portion of the integral along the visible spectrum

$$P_r = -\frac{1}{4\pi\omega^2 \epsilon^2} |P_0|^2 \int_0^{+k_0} k_\rho^3 \hat{I}_V^{TM} (-h, k_\rho) dk_\rho \quad (3)$$

and the surface-wave power P_{sw} , given by the residue contribution of the surface-wave poles $k_\rho^{sw} > k_0$ (if any) on the real axis:

$$P_{sw} = -\frac{1}{2\omega^2 \epsilon^2} |P_0|^2 (k_\rho^{sw}) B_{sw}, \quad (4)$$

where $jB_{sw} = \text{Res}[\hat{I}_V^{TM}(-h, k_\rho); k_\rho^{sw}]$. The radiation efficiency η of the considered FPCA can be evaluated as $\eta = P_r / (P_{sw} + P_r)$. In Table I such radiation efficiency is reported for a structure as in Fig. 1(a). It can be noted that, by increasing frequency, the efficiency increases until it reaches the value of 100%. This can be explained considering that the modal field of the TEM surface wave is increasingly confined inside the WM layer at higher frequencies [3]. As a consequence, its coupling to the VED source placed on the bottom plate of the PPW decreases monotonically. In particular, the TEM surface wave ceases to exist above a specific asymptote frequency (see [3] for the relevant dispersion curve), beyond which, in the absence of ohmic and dielectric losses, the total active power delivered by the source is entirely radiated in free space.

TABLE I – RADIATION EFFICIENCY OF A WM-FPCA FOR DIFFERENT FREQUENCIES

Frequency [GHz]	Efficiency
16	46.23 %
17	79.40 %
18	99.24 %
19	100 %
20	100 %
21	100 %

IV. CONCLUSION

The radiation features of FPCAs excited by an azimuthally-symmetric VED source and loaded by a WM slab have been investigated through an ad hoc network formalism. The spectral-domain Green's function has been derived and the contribution of the desired TM_1 leaky pole to the aperture field has been calculated. The radiation efficiency of the considered antenna has been evaluated, showing that, when the TEM surface wave is properly suppressed by the WM slab, the power radiated approaches the total active power delivered by the source.

REFERENCES

- [1] P. Burghignoli, G. Lovat, F. Capolino, D. R. Jackson, and D. R. Wilton, "Directive leaky-wave radiation from a dipole source in a wire-medium slab," *IEEE Trans. Antennas Propag.*, vol. 56(5), pp 1329-1339, Dec. 2015.
- [2] M. G. Silveirinha and S. I. Maslovski, "Radiation from elementary sources in a uniaxial wire medium," *Phys. Rev. B*, vol. 85, 155125, 2012.
- [3] D. Comite, P. Burghignoli, P. Baccarelli, D. Di Ruscio, and A. Galli, "Equivalent-network analysis of propagation and radiation features in wire-medium loaded planar structures," *IEEE Trans. Antennas Propag.*, vol. 63(12), pp. 5573-5585, Dec. 2015.
- [4] K. A. Michalski and J. R. Mosig, "Multilayered media Green's functions in integral equation formulations," *IEEE Trans. Antennas Propag.*, vol. 45(3), pp. 508-519, Mar. 1997.

A HIGH GAIN DIELECTRIC RESONATOR ANTENNA FOR WIDEBAND WIRELESS APPLICATIONS

R. Cicchetti, E. Miozzi, O. Testa

Department of Information Engineering, Electronics and Telecommunications, University of Rome "La Sapienza", Rome 00184, Italy e-mail: cicchetti@diet.uniroma1.it

Abstract

A high-gain dielectric resonator antenna (DRA) for broadband wireless communications is proposed. The antenna is composed of a hollow cylindrical dielectric resonator (DR) inside which an assembly of two dielectric truncated cones of different permittivities are embedded. A suitably excitation system and an air cavity inserted close to the ground plane are used to further enhance the antenna bandwidth. The resulting antenna features a high fractional bandwidth (FWB=54%), gain (over 8 dBi) and polarization purity. CST Microwave Studio™ has been employed to analyze and design the proposed antenna.

Index Terms – Dielectric resonator antenna, broadband, high-gain, wireless communications.

I. INTRODUCTION

Dielectric resonator antennas (DRAs), which have been extensively investigated during the last two decades [1]-[12], are presently receiving a great attention to realize low-cost wideband wireless communication systems. In this contest, low dielectric permittivity materials or a suitable shaping of the radiating elements, useful to improve the DRAs bandwidth, can be adopted [3]. In fact, DRAs realized with low permittivity plastic materials allow to obtain low Q-value antennas avoiding the use of ceramic materials having high costs and weights. Both of these aspects are important issue in the realization of wireless communication systems. Moreover, also the antenna geometry plays a considerable role on the resulting antenna bandwidth. For this reason, hybrid resonators [4], [5], new feeding arrangements [6], [7], multi-level multi-permittivity (MLMP) dielectrics [8]-[9], lower Q-values DRAs [3], [10], and stacked DRAs [11], [12], have been proposed in literature. In particular in [3], a wideband supershaped dielectric resonator antenna realized with a low-permittivity plastic material has been introduced. This antenna exhibits a high fractional bandwidth and a stable radiation pattern.

In this paper, a novel wideband DRA antenna suitable to operate in the frequency band ranging from 2.95 GHz up to 5.15 GHz, satisfying the requirements of the most important communication standards, as well as those adopted for satellite communications, is presented. The proposed antenna, featuring a cylindrical symmetry, and exhibiting a FBW of about 54%, is equipped with a differential dual-feed excitation scheme to sustain a linear polarization.

The paper is organized in IV Sections. In Section II the antenna geometry and the related design solutions are presented. In Section III the full-wave analysis and the radiation characteristics of the antenna are presented and discussed, while some concluding remarks are provided in Section IV.

II. ANTENNA GEOMETRY AND DESIGN

The antenna, consisting of a cylindrical resonator having permittivity $\epsilon_r = 2$, inside which two truncated cones of dielectric constant $\epsilon_r = 4$ and $\epsilon_r = 6$, respectively, are embedded, is shown in Fig. 1. An air cavity, placed at the base of the first truncated cone, close to the ground plane, has been employed to further increase the antenna bandwidth (see Fig. 1).

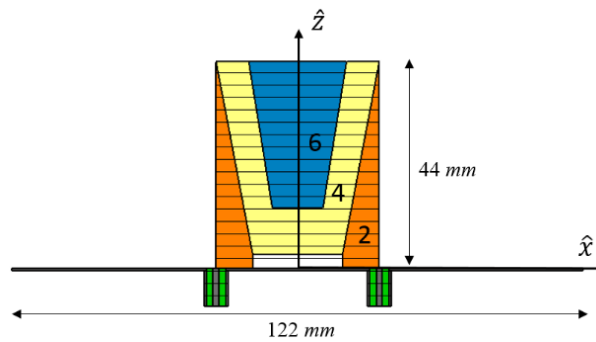


FIG. 1 – Geometry of the proposed DRA antenna.

The dielectric resonator, excited by two electric probes of length 16 mm, is lodged on the top of a flat circular ground plane below which two SMA connectors are located for feeding the antenna. An extensive full-wave parametric analysis has been performed to determine the optimal values of the geometrical and electrical parameters describing the antenna.

III. RESULTS AND DISCUSSIONS

In this section, a full-wave analysis of the proposed antenna, performed using *CST Microwave Studio*TM, is presented. Because the radiation characteristics of the antenna strongly depend on the geometry and the dielectric materials forming the cones, as well as the probes, a parametric analysis was performed to synthesize the antenna performance in terms of radiation patterns and impedance matching.

By way of example, in Fig. 2 the frequency behavior of the antenna equivalent input reflection coefficient Γ is shown.

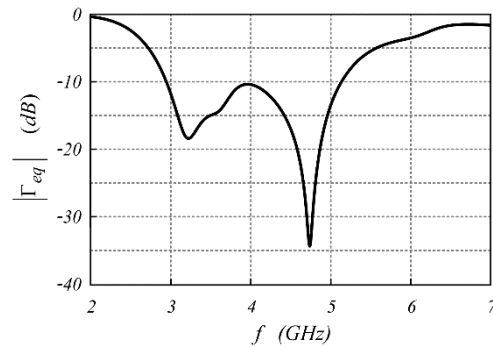


FIG. 2 – Magnitude of the antenna reflection coefficient Γ versus frequency.

Finally, in Fig. 3 the antenna radiation patterns at a frequency of 4 GHz and 5 GHz are reported. From the figures it appears that the radiation diagrams present a shape useful for indoor/outdoor wireless applications.

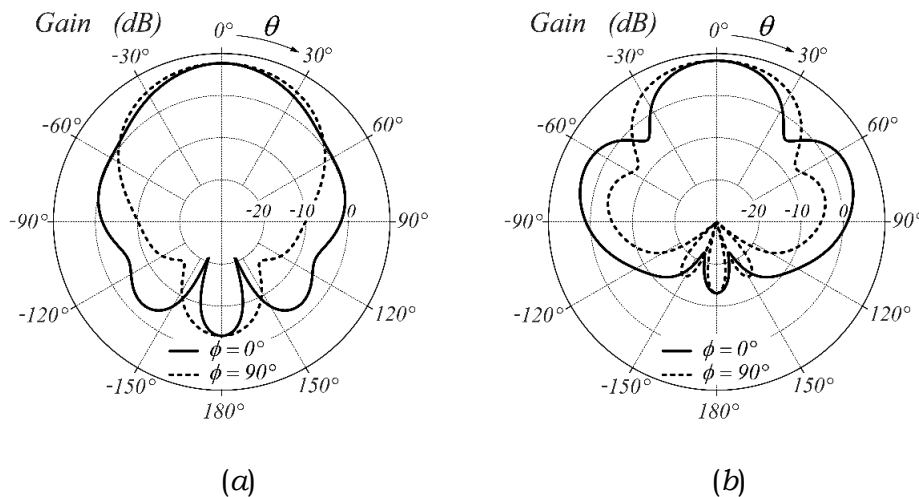


FIG. 3 – Radiation diagrams of the proposed DRA (a) $f=4$ GHz, (b) $f=5$ GHz.

IV. CONCLUSIONS

A novel high-gain dielectric resonator antenna for wideband wireless applications has been presented. The antenna, formed by concentric truncated cones and suitable excitation probes, ensures a field focusing process along the antenna axis in a wide frequency band. Moreover, the antenna symmetry ensures excellent polarization purity that makes the antenna suitable to be employed both in indoor and outdoor applications. Further, the antenna features a high gain (over 8 dBi) and high bandwidth (FBW=54%), useful to meet the requirements of several wireless communication standard. In addition, the adoption of low permittivity dielectric materials keeps down the DRA manufacturing costs and reduces the complexities of the fabrication processes, which are remarkable issues to realize wireless communication systems. In

conclusion, the antenna is a good candidate for the most common wireless communication standards, requiring high gain, wide bandwidth and high polarization purity.

V. REFERENCES

- [1] A. Petosa and A. Ittipiboon, "Dielectric resonator antennas: a historical review and the current state of the art," *IEEE Antennas Propag. Mag.*, Vol. 52, No.5, pp.91-116, Oct. 2010.
- [2] K. W. Leung, E. H. Lim, and X. S. Fang, "Dielectric resonator antennas: from the basic to the aesthetic," *Proc. IEEE*, Vol. 100, No. 7, pp. 2181-2193, July 2012.
- [3] M. Simeoni, R. Cicchetti, A. Yarovoy, and D. Caratelli, "Plastic-based supershaped dielectric resonator antennas for wide-band applications," *IEEE Trans. Antennas Propag.*, vol. 59, no. 12, pp. 4820-4825, Dec. 2011.
- [4] Y. Gao, B.-L. Ooi, W.-B. Ewe, and A. P. Popov, "A compact wideband hybrid dielectric resonator antenna," *IEEE Microw. Compon. Lett.*, Vol. 16, No. 4, pp. 227-229, Apr. 2006.
- [5] A. Perron, T. A. Denidni, and A.-R. Sebak, "High-gain hybrid dielectric resonator antenna for millimeter-wave applications: design and implementation," *IEEE Trans. Antennas Propag.*, vol. 57, no. 10, pp. 2882-2892, Oct. 2009.
- [6] Z.-B. Weng, X.-M. Wang, Y.-C. Jiao, and F.-S. Zhang, "Wideband rectangular dielectric resonator antenna (DRA) with slot-fed design," *Prog. Electromagnet. Res. Lett.*, Vol. 16, 181-190, 2010.
- [7] R. G. Madhuri and P. M. Hadalgi, "Rectangular ring-slot dielectric resonator antenna with metallic patch," *Prog. Electromagn. Res. M*, Vol. 20, 171-177, 2011.
- [8] T. Matsumuro, Y. Ishikawa, N. Shinohara, "Small-size large-aperture antenna using multilayered spherical dielectric resonators," *2013 7th European Conference on Antennas and Propagation (EuCAP)*, April 8-12, 2013, Gothenburg, pp. 3068 – 3072.
- [9] R. K. Chaudhary, K. V. Srivastava, and A. Biswas, "A concentric three-layer half-split cylindrical dielectric resonator antenna for wideband applications," *Proceedings of 2013 URSI International Symposium on Electromagnetic Theory (EMTS)*, May 20-24 2013, Hiroshima, Japan, pp. 664-667.
- [10] S. M. Shum and K. M. Luk, "Characteristics of dielectric ring resonator antenna with an air gap", *Electron. Lett.*, vol. 30, no. 4, pp. 277 - 278, Feb. 1994.
- [11] Y. Ge, K. P. Esselle and T. S. Bird, "A wideband probe-fed stacked dielectric resonator antenna," *Microw. Opt. Techn. Let.*, Vol. 48, No. 8, pp. 1630-1633, Aug. 2006.
- [12] G. D. Makwana, D. Ghodgaonkar, "Wideband stacked rectangular dielectric resonator antenna at 5.2 GHz," *International Journal of Electromagnetics and Applications*, vol. 2, no. 3, pp. 41-45, 2012.

COMPUTATIONAL MODELLING OF THE INDUCED FIELDS DURING CEREBELLAR AND SPINAL DIRECT CURRENT STIMULATION IN CHILDREN

S. Fiocchi⁽¹⁾, P. Ravazzani⁽¹⁾, A. Priori⁽²⁾, M. Parazzini⁽¹⁾

⁽¹⁾ CNR Consiglio Nazionale delle Ricerche, Istituto di Elettronica e di Ingegneria dell'Informazione e delle Telecomunicazioni IEIIT, Piazza Leonardo da Vinci 32, 20133, Milano, Italy
serena.fiocchi@ieiit.cnr.it; paolo.ravazzani@ieiit.cnr.it;
marta.parazzini@ieiit.cnr.it

⁽²⁾ Università degli studi di Milano, Dipartimento di Scienze della Salute, Ospedale San Paolo, Via Antonio di Rudini 8, 20142 Milano, Italy
alberto.priori@unimi.it

Abstract

In the last few years, cerebellar transcranial direct current stimulation (ctDCS) and transcutaneous spinal direct current stimulation (tsDCS), have been successfully applied to modulate and restore some cerebellar and spinal functions. Of particular interest is the possible use of these techniques in paediatric age, since many pathologies and injuries, which affect the cerebellar cortex as well as spinal cord circuits, are diffuse in adults as well as in children. To this purpose, there is still a lack of information about the safety issues as well as the appropriate dose to be used during the treatment. In order to fill these gap in knowledge, this work wants to estimate, through computational techniques, the electric field distributions induced in the target tissues during the application of ctDCS and tsDCS administered to differently aged and gender children models.

Index Terms – children, computational modelling, ctDCS, high-resolution human models, neuromodulation, tsDCS

I. INTRODUCTION

Recent studies (see i.e. the review studies [1]-[2]) showed that the specific application of transcranial Direct Current Stimulation (tDCS) over the cerebellum (ctDCS) can modify cerebello-brain networks, affect locomotive and motor learning skills, enhance cognitive functions and also improve the treatment of cerebellar disorders. In parallel, the need to find a noninvasive neuromodulatory tool to prevent neuronal dysfunction developing after spinal cord injuries, opened the use of transcutaneous spinal DC stimulation (tsDCS) to modulate conduction

along the spinal somatosensory pathways and alter spinal cord functions (for a review see [3]).

Of particular interest is the possible application of these techniques in paediatric age, since many pathologies and injuries, which affect the cerebellar cortex as well as spinal cord circuits, are diffuse in adults as well as in children. Up to now, experimental studies of cerebellar tDCS and transcutaneous spinal DCS on children are still missing and therefore there is lack of information about both the safety and the appropriate dose to be used during the treatment. This also in view of the recent finding of [4] that suggests a better electric current transmission effectiveness in the brain of children than of adults during tDCS. In order to fill this gaps, the knowledge of electric field and current distributions induced into the cerebellum and over the spinal cord during ctDCS and tsDCS, respectively, is required. Those can be valuably assessed by computational approaches, as recently performed on adults [5]-[6].

This work wants to better explore this issue, by estimating through computational techniques the electric field induced in the area of cerebellum and of the spinal cord during ctDCS and tsDCS applied to other models of children of different ages and gender.

II. MATERIALS AND METHODS

Simulations were conducted using the simulation platform SEMCAD X [7], solving the Laplace equation to determine the electric potential (φ) distribution inside the human tissues.

$$\nabla \cdot (\sigma \nabla \varphi) = 0 \quad (1)$$

where σ is the electrical conductivity of the human tissues. The electric field (\mathbf{E}) distributions were obtained by means of the following relation:

$$\mathbf{E} = -\nabla \varphi \quad (2)$$

We used two child models of the Virtual Population [8] (Thelonious, 6-years-old male; Dizzy, 8-years-old female). These models have been developed from high-resolution MRI of healthy volunteers and are based on the computer-aided design representation of the organ surfaces. The dielectric properties of each tissue were assigned on the basis of the literature data at low frequency [9]-[10] as described in literature [5]-[6]. The active electrode was placed on the scalp over the cerebellar area in ctDCS and over the spinal process of the tenth thoracic vertebra for tsDCS; the reference over the right arm in both montages. The electrodes were modelled as rectangular pads conductors ($\sigma = 5.9 \times 10^7$ S/m) placed above a rectangular sponge ($\sigma = 0.3$ S/m). According to the practical use of this technique, the potential difference between the electrodes was adjusted to inject a total current of 2 mA for ctDCS and 3 mA for tsDCS. Uniform rectilinear meshes were applied to easily discretize the computational domain with a grid discretization step ranging from 0.5 to 0.7 mm.

III. RESULTS

Fig.1 shows the descriptive statistic, in terms of minimum, maximum, 25th, 50th, and 75th percentiles of the \mathbf{E} distribution induced over the cerebellum and other brain tissues (1st row) and the over the spinal cord at different spine levels (2nd row), for the model Thelonious and Dizzy. The figure reveals that the general trend of the spatial distributions of the field amplitude remains similar across the different human models, with the stronger electric field occurred mainly near the active electrode on the cerebellum and on the thoracic level.

Within the cerebellum, the field distributions varies across the two subjects, with a widespread field amplitude distribution towards the more anterior area of the cerebellum and also to other brain structures, in particular the brainstem region, with a prevalence toward the medulla. Similarly in tsDCS, \mathbf{E} spreads also to the spinal nerves (results not shown) and at lumbar level.

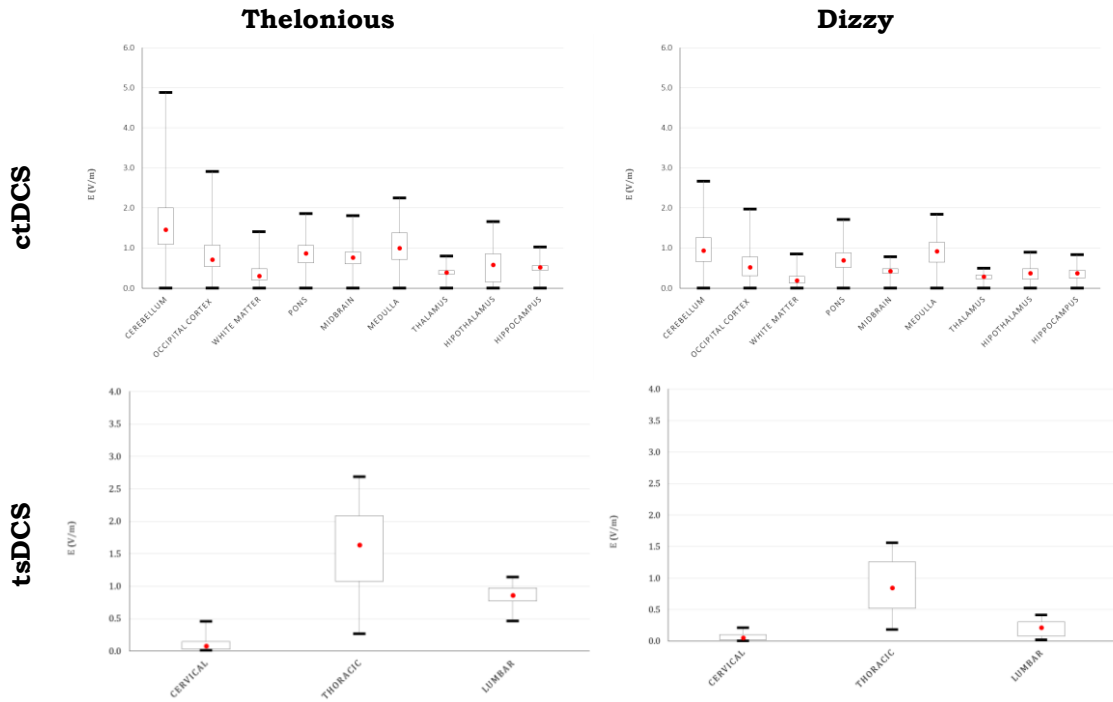


FIG. 1 – Descriptive statistic of \mathbf{E} amplitude distribution over cerebellum and close brain tissues (1st row) and over the spinal cord at different spine levels (2nd row), for the models Thelonious and Dizzy (left and right, respectively).

For both the techniques, one can observe a trend of the peak of the distribution with age: the younger is the children, the higher is the peak of the field values induced.

IV. CONCLUSIONS

Despite inter-individual differences, this study suggests that the cerebellum is the structure mainly affected by ctDCS, whereas the **E** generated by tsDCS can reach the spinal cord also in children. Moreover, it reveals also that for these subjects there is a noticeable spread also to the anterior area of the cerebellum and towards the brainstem region for ctDCS and over the spinal nerve for tsDCS. To sum up, our models predict that the electric field amplitude spreads in complex patterns that greatly depends on individual anatomy, thus giving further insight into safety issues and optimization of pediatric tDCS investigations.

V. ACKNOWLEDGMENTS

The authors wish to thank Schmid & Partner Engineering AG (www.speag.com) for having provided the simulation software SIM4Life/SEMCAD X.

REFERENCES

- [1] A. Priori, M. Ciocca, M. Parazzini, M. Vergari, and R. Ferrucci, "Transcranial cerebellar direct current stimulation and transcutaneous spinal cord direct current stimulation as innovative tools for neuroscientists," *J Physiol*, 592(Pt 16), pp. 3345–69, 2014.
- [2] R. Ferrucci, F. Cortese, and A. Priori, "Cerebellar tDCS: how to do it," *Cerebellum*, vol. 14(1), pp.:27–30, 2015.
- [3] F. Cogiamanian, G. Ardolino, M. Vergari, R. Ferrucci, M. Ciocca, E. Scelzo, S. Barbieri, and A. Priori, "Transcutaneous spinal direct current stimulation," *Front Psychiatry*, vol.3, 63 (5 pp), 2012.
- [4] S. Kessler S, P. Minhas, A. Woods, A: Rosen, C. Gorman, and M. Bikson M, "Dosage considerations for transcranial direct current stimulation in children: a computational modeling study," *PLoS ONE*, vol. 8(9), pp. e76112, 2013.
- [5] M. Parazzini, E. Rossi, R. Ferrucci, I. Liorni, A. Priori, and P. Ravazzani, "Modelling the electric field and the current density generated by cerebellar transcranial DC stimulation in humans," *Clin Neurophysiol*, vol. 125, pp. 577–584, 2014
- [6] M. Parazzini, S. Fiocchi, I. Liorni, E. Rossi, F. Cogiamanian, M. Vergari, A. Priori, and P. Ravazzani, "Modelling the current density generated by transcutaneous spinal direct current stimulation (tsDCS)," *Clin Neurophysiol*, vol. 125, pp. 2260–2270, 2014
- [7] SEMCAD X v14.8 by SPEAG, Schmid & Partner Engineering, AG, Zurich, Switzerland, www.speag.com.
- [8] A. Christ, W. Kainz, G.E. Hahn, K. Honegger, M. Zefferer, E. Neufeld, et al., „The Virtual Family-development of surface-based anatomical models of two adults and two children for dosimetric simulations," *Phys Med Biol*, vol. 55, pp. N23–38, 2010.
- [9] S. Gabriel, R.W. Lau, and C. Gabriel, "The dielectric properties of biological tissues: II. Measurements in the frequency range 10 Hz to 20 GHz," *Phys Med Biol*, vol. 41, pp. 2251–2269, 1996.
- [10] C. Gabriel, "Comments on dielectric properties of the skin," *Phys Med Biol*, vol. 42, pp. 1671–1674, 1997.

DESIGN OF PATTERN RECONFIGURABLE SPARSE ANTENNA ARRAYS

G. Buttazzoni⁽¹⁾

⁽¹⁾ Department of Engineering and Architecture, University of Trieste
Via A. Valerio 10, 34127, Trieste, Italy
gbuttazzoni@units.it

Abstract

This paper presents a fully deterministic approach for the design of phase-controlled, reconfigurable, sparse antenna arrays. The objective is that of synthesizing a sparse array which radiates, by phase-only control, a number of desired far-field co-polar patterns, simultaneously controlling the cross-polar patterns and the dynamic range ratio (DRR) of the excitations. The proposed procedure, which optimizes the number, the positions and the excitations of the array elements, is divided in two steps. First, the geometrical synthesis is performed in order to obtain the number and the positions of the array elements. Then, the excitations of these elements are determined with a suitable fixed-grid synthesis algorithm. The optimality of the solution is not guaranteed, but numerical examples provided satisfactory results.

Index Terms – Convex optimization, Pattern reconfiguration, Phase-only control, Sparse array synthesis.

I. INTRODUCTION

Nowadays, in an increasing variety of applications, antenna arrays involving a great number of elements are used, potentially leading to structures that require complex feeding networks. This explains the interest in synthesis techniques capable of minimizing the number of array elements, eventually employing non-regular structures, which have many advantages but also an increased complexity in the design. The problem addressed in this paper has additional complex requirements since it considers the design of sparse arrays with phase-only reconfigurable patterns of arbitrary shapes. Moreover, the cross-polar patterns and the DRR of the excitations (defined as the ratio between the maximum and the minimum excitation amplitude) are subject to constraints. This problem is cleverly solved by exploiting a sequential convex optimization technique for determining the array geometry [1], followed by a fixed-grid synthesis algorithm for the excitations of the array elements [2]. The final result is a sparse array capable of radiating a number of radiation patterns fulfilling some prescribed mask requirements and some upper bounds on the cross-polar components. Each of these patterns can be reconfigured into any of the others by phase-only control, so that the amplitude of the excitation of each array element keeps constant during the reconfiguration process, and only its phase is modified. Furthermore, excitation amplitudes of different array

elements may be different, but their DRR is kept below a given threshold. In the following section the synthesis procedure is outlined. Then, a numerical example is provided and some conclusions are summarized.

II. THE PROBLEM AND THE SYNTHESIS PROCEDURE

The problem considered in this paper consists of synthesizing an antenna array in such a way that:

- the number of array elements be as small as possible;
- the antenna be capable of radiating a given number S of far-field patterns satisfying S prescribed masks;
- the S cross-polar far-field patterns do not exceed a prescribed threshold;
- each of the S synthesized patterns can be reconfigured into any of the others by phase-only control of the array excitations;
- the DRR of the excitations does not exceed a given upper bound.

To this aim, the algorithm here proposed provides the number of elements, their locations and their excitations.

Firstly, the array geometry (number and locations of the array elements) is determined by separately solving the problem for each of the S radiation patterns. This is accomplished according to the procedure described in [3], which requires to define a very dense grid of *fictitious* array elements, and chooses their minimum number by iteratively solving a convex problem with constraints on the far-field patterns. The resulting S sets of element locations are denoted with $R^s = \{\vec{r}_n^s\}, s = 1, \dots, S, n = 1, \dots, N_s$, and the set $R = \cup_s R^s$ specifies the positions of the elements of the final array. The final number of elements is $N \leq \sum_s N_s$ (the inequality arises when one or more locations belong to more than one set R^s). So, the array (sparse) geometry is determined. Now, also S sets of element excitations are determined, which give far-field patterns satisfying the constraints. But, they do not comply with the phase-only requirement and with the constraint on the maximum allowed DRR.

Thus, as a second step, a further optimization is implemented in which the array geometry is known, being specified by the set R . So, any fixed-grid synthesis algorithm suitable for phase-only reconfigurable arrays of arbitrary geometry, taking into account both the co-polar and the cross-polar components of the far-field patterns and capable of controlling the DRR of the excitations can be used. Here the algorithm developed in [2] has been chosen, which is based on an alternating projection approach. With this choice, the entire design procedure is deterministic. Next section provides a numerical example to show the effectiveness of the above described procedure.

III. NUMERICAL RESULTS

Now, in order to show the improvement that the proposed method can provide in terms of reduction of the number of radiating elements, the first example in [2] was considered. There, the power synthesis of $S = 2$ far-field patterns was performed, with an array of $N' = 132$ Huygens radiators (black circles in Fig. 1), equally spaced on four arcs parallel to the xy -plane. The cross-polar components were imposed not to exceed -40 dB. A DRR of the excitations less than or equal to 5 was required.

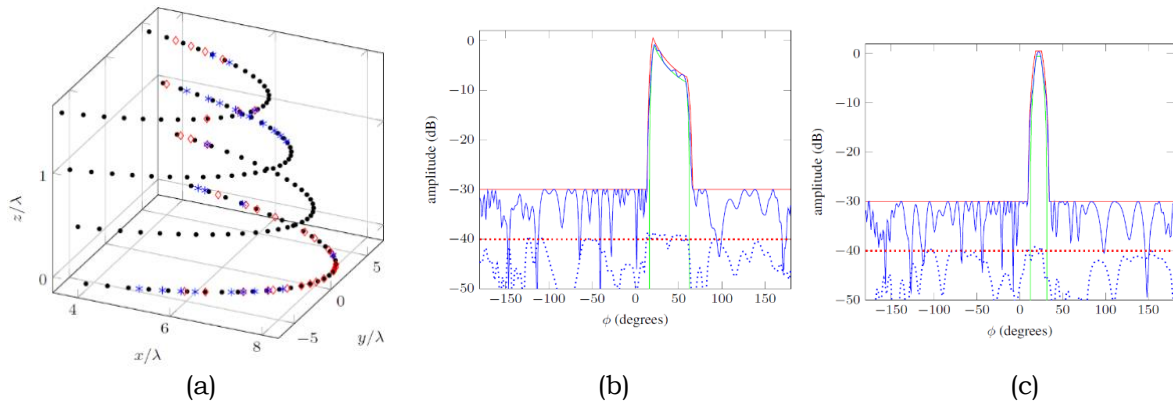


FIG. 1 – (a): Black circles ($N' = 132$): the regular array in [2]. Red diamonds ($N_1 = 32$): the element positions for the mask shown in (b). Blue stars ($N_2 = 27$): the element positions for the mask shown in (c). (b): cosecant pattern. (c): pencil-beam pattern. Solid lines: the synthesized patterns (blue), upper (red) and lower (green) bounds of the masks, as defined in [2]. Dashed lines: the cross-polar patterns (blue) and the upper bounds of -40 dB (red).

Here, the geometry of the array was left unmodified with respect to [2] and, as a first step, the inter-element spacing between adjacent elements on the four arcs was reduced in order to have a very dense mesh of *possible positions* for the sparse array elements. Then, the problem was solved for each of the two radiation patterns separately, with the method in [3]. Figure 1(a) shows the geometry of the synthesized array. The $N_1 = 32$ red diamonds represent the positions synthesized for the mask in Fig. 1(b), and the $N_2 = 27$ blue stars represent the positions synthesized for the mask in Fig. 1(c). According to the synthesis procedure described in the previous section, the positions of the final array elements are specified by the red diamonds together with the blue stars. Since four common positions were obtained, the total number of radiating elements was $N = 32 + 27 - 4 = 55$. Thus, a reduction of 58.33 % was obtained with respect to the reference array, consisting of 132 radiators. As the second step, the algorithm presented in [2] was used for the phase-only synthesis of the excitations, with maximum allowed DRR equal to 5 (so that the considered problem was exactly that of [2]). The patterns of Fig. 1(b) and Fig. 1(c) were obtained. As it can be seen, the co-polar patterns belong to the masks, and the cross-polar level of -40 dB was very slightly exceeded. In fact, a maximum cross-polar level of -38.5 dB was obtained. This step concluded the process of synthesis.

Finally, the approach proposed in this paper was also tested with the more stringent constraint of -50 dB for the cross-polar level. The geometrical synthesis step provided a sparse array with $N = 93$ elements ($N_1 = 54$, $N_2 = 49$, minus ten common positions, corresponding to a reduction of 29.5 %). The fixed grid synthesis gave very good co-polar and cross-polar patterns, but a high DRR of the excitations.

IV. CONCLUSION

In this paper a fully deterministic approach for the design of sparse arrays was presented. The procedure is easy to implement and does not require heavy computational resources (computer time and/or memory). The synthesis is divided in two steps. In the first step, a sequential convex optimization is used, which provides the (sparse) geometry of the array. In the second step, the power pattern synthesis is performed with an alternating projection approach, suitable for arrays of arbitrary (but fixed) geometry. The final result of the design is a sparse array capable of radiating, by phase-only control, a number of desired far-field co-polar patterns, keeping the far-field cross-polar patterns below a prescribed threshold and the DRR of the excitations below a given upper bound. Although the optimality of the solution is not guaranteed, the proposed approach allows to strongly reduce the number of radiators, keeping the same performance of a regular array.

ACKNOWLEDGEMENT

This work is partly supported by the European Space Agency (ESA Contract No. 4000108924/13/NL/FE: “Design Tool for SAR Instruments based on Aperiodic Phased Arrays”), and by the Italian Ministry of University and Research (project FRA 2015, Univ. of Trieste, Italy: “Peer-to-peer Millimeter-Wave Communications in 5G Networks: Theoretical Modeling and Algorithms for Massive MIMO Systems”).

REFERENCES

- [1] B. Fuchs, “Synthesis of sparse arrays with focused or shaped beampattern via sequential convex optimizations,” *IEEE Transactions on Antennas and Propagation*, vol. 60(7), Jul. 2012, pp. 3499-3503.
- [2] G. Buttazzoni, and R. Vescovo, “Synthesis of co-polar and cross-polar patterns with dynamic range ratio reduction for phase-only reconfigurable arrays,” EuCAP 2012, Prague, March 2012, pp. 2623-2627.
- [3] G. Buttazzoni, and R. Vescovo, “Far-field synthesis of sparse arrays with cross-polar pattern reduction,” Submitted to *ACES Express Journal*.

POLARIMETRIC SAR RAW SIGNAL SIMULATION

G. Di Martino, A. Iodice, D. Poreh, D. Riccio

Department of Electric Engineering and Information Technology,
University of Naples “Federico II”
Via Claudio 21, Naples, Italy
gerardo.dimartino@unina.it

Abstract

We present an updated version of the Synthetic Aperture Radar (SAR) raw signal simulator (SARAS), developed at the University of Naples, which is able to simultaneously simulate the raw signals of the different polarimetric channels of a polarimetric SAR system in such a way that the correct covariance matrix is obtained for the final images. Presentation of theory is supplemented by meaningful experimental results.

Index Terms – Polarimetry, Simulation, Synthetic Aperture Radar.

I. INTRODUCTION

In recent years, Synthetic Aperture Radar (SAR) Polarimetry has been successfully applied to soil moisture retrieval, forest monitoring, change detection and marine applications [1]. Therefore, a polarimetric SAR raw signal simulator, based on a sound physical electromagnetic scattering model, would be certainly useful for mission planning, algorithm development and testing, and prediction of suitability of the system to different applications. An efficient simulator with many of the above cited features, called SARAS [2]-[5], is actually available in literature: in fact, it is a model-based raw signal simulator that, among other system characteristics, also accounts for the transmitting and receiving polarizations. However, it can only simulate one polarimetric channel at a time, with the result that data of different channels turn out to be independent. Accordingly, although the correct relations between channels' powers are obtained, the covariance (or coherence) matrix of the final images is not realistic.

Here we present an updated version of that simulator that is able to simultaneously produce the raw signals of the different polarimetric channels in such a way to obtain the correct covariance or coherence matrixes on the final images. In the following we will refer to the simulator for the classical stripmap acquisition mode [2], but the same modifications also apply to simulators for spotlight [3] and hybrid [4] acquisition modes, as well as to the one accounting for platform trajectory deviations [5]. In addition, we here only consider surface scattering, but, due to the modular structure of the simulator, also other scattering mechanisms (volumetric, double bounce) can be included, if reliable models are available.

II. THEORY

The SARAS simulator of [2]-[6] employs a procedure that consists of two main stages. In the first stage, given the orbit and system data and the scene geometric and electromagnetic parameters, the scene reflectivity map is evaluated. In the second stage, the SAR raw signal is computed via a superposition integral in which the reflectivity map is weighted by the SAR system two-dimensional (2D) pulse response. This superposition integral is efficiently evaluated in the Fourier domain via FFT codes. When we move to the polarimetric case, the second stage remains conceptually unchanged, whereas the first one, i.e., reflectivity map evaluation, must be properly changed, as detailed in the following. As in the usual SARAS simulator, the surface macroscopic profile, provided by an external Digital Elevation Model (DEM), is approximated by rectangular rough facets, large with respect to wavelength but smaller than SAR system resolution. However, at variance with the available SARAS, zero-mean random deviations of the facets' azimuth and range slopes, with respect to those prescribed by the external DEM, are added; their standard deviations can be selected by the user to model the large-scale roughness (in addition to the facet small-scale roughness). The reflectivity γ of each facet can be computed by using the small perturbation method (SPM) or the Physical Optics (PO), according to the facet roughness [6], and it can be expressed as

$$\gamma_{pq}(x, r; \vartheta_l, \beta) = \chi_{pq}(x, r; \vartheta_l, \beta) w(x, r; \vartheta_l) \quad , \quad (1)$$

where, see also Fig.1, p and q are the polarizations of the incident and scattered field, respectively, and can each stand for H (horizontal) or V (vertical), x and r are the azimuth and range coordinates of the facet's center, ϑ_l is the local incidence angle (i.e., the angle formed by the look direction and the direction perpendicular to the facet), β is the angle between global and local incidence planes (i.e., between the vertical plane including the look direction, and the plane perpendicular to the facet and including the look direction), χ_{pq} are the elements of the matrix

$$\underline{\underline{\chi}}(\vartheta_l, \beta) = \underline{\underline{R}}_2(\beta) \cdot \begin{pmatrix} F_H(\vartheta_l) & 0 \\ 0 & F_V(\vartheta_l) \end{pmatrix} \cdot \underline{\underline{R}}_2^{-1}(\beta) \quad , \quad (2)$$

$$\underline{\underline{R}}_2(\beta) = \begin{pmatrix} \cos \beta & \sin \beta \\ -\sin \beta & \cos \beta \end{pmatrix} \quad (3)$$

is the 2x2 unitary rotation matrix, and F_H and F_V are either the Bragg (if SPM is used) or the Fresnel (if PO is used) coefficients for H and V

polarization, respectively. Finally, $w(\mathcal{G}_l)$ is a polarization-independent circular Gaussian random variable with zero mean, and variance to be computed according to the employed scattering model [6]: in the SPM case, it is proportional to the power spectral density $W(\cdot)$ of the facet's roughness:

$$\langle |w(\mathcal{G}_l)|^2 \rangle = k^4 \cos^4 \mathcal{G}_l W(2k \sin \mathcal{G}_l) \quad , \quad (4)$$

where k is the wavenumber; for the PO case, see [6] and references therein. At variance with the already available simulator, in this updated version the three polarimetric channels HH , VV and $HV=VH$ (HV and VH coincide, due to reciprocity) are simulated at the same time, and the same realization of the random variable $w(\mathcal{G}_l)$ is used for the three channels. This ensures that the polarimetric channels are not independent; on the other hand, the randomness of the facet slopes (which causes the randomness of local incidence and β angles) introduces a decorrelation among the different channels. The corresponding computed coherency matrix is in agreement with theoretical predictions, when they are available, as shown in the next Section.

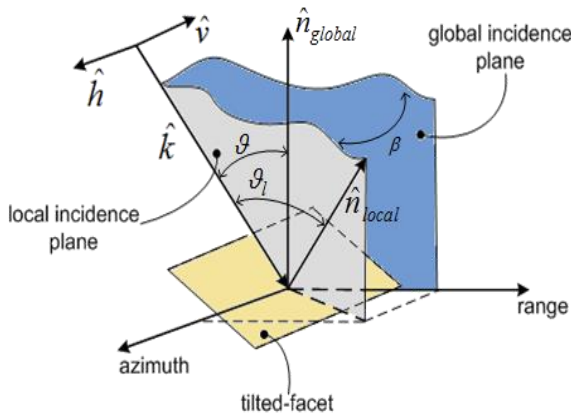


Fig. 1: Facet's \mathcal{G}_l and β angles.

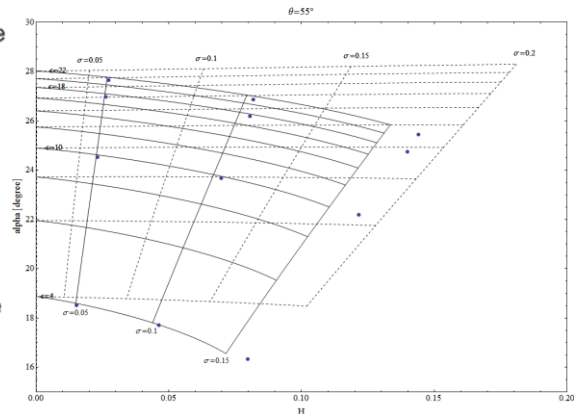


Fig.2: H - α graphs comparison.

III. SIMULATION RESULTS

We here report some of the results obtained using the proposed simulator by setting system parameters similar to those of the L-band PALSAR sensor. In Fig. 2 we show the coherency matrix entropy-alpha graphs [1] obtained from simulated images (dots) of a flat scene with random facets slopes, whose standard deviations (equal for range and azimuth) vary from 0 to 0.2, and compare them with theoretical ones obtained by using the PTSM [6] (solid line) and X-Bragg [1], [6] (dashed line) approximated theoretical models. This comparison shows that obtained coherency matrix behavior is in agreement with what expected from theory, and in particular from PTSM.

Finally, in Fig.3 we show the entropy and alpha images obtained from simulated polarimetric data of a scene with significant topography, namely the area of Mt. Vesuvius, near Naples, Italy.

IV. CONCLUSION

Presented polarimetric simulator has been shown to provide coherency matrixes in agreement with theoretically expected ones. It will allow us checking the effects on polarimetric data of scene features also when they are not easy to be theoretically modeled, such as anisotropy of large-scale roughness, often present in ploughed agricultural fields.

REFERENCES

- [1] J. S. Lee and E. Pottier, *Polarimetric Radar Imaging: From Basics to Applications*, CRC Press, Boca Raton (FL), 2009.
- [2] G. Franceschetti, M. Migliaccio, D. Riccio, and G. Schirinzi, "SARAS: a SAR raw signal simulator", *IEEE Trans. Geosc. Remote Sensing*, vol.30, pp.110-123, 1992.
- [3] S. Cimmino, G. Franceschetti, A. Iodice, D. Riccio, and G. Ruello, "Efficient Spotlight SAR Raw Signal Simulation of Extended Scenes", *IEEE Trans. Geosc. Remote Sensing*, vol.41, pp. 2329- 2337, 2003.
- [4] G. Franceschetti, R. Guida, A. Iodice, D. Riccio, and G. Ruello, "Efficient Simulation of Hybrid Stripmap/Spotlight SAR Raw Signal From Extended Scenes", *IEEE Transactions on Geoscience and Remote Sensing*, vol.42, no.11, pp. 2385-2396, 2004.
- [5] G. Franceschetti, A. Iodice, S. Perna, and D. Riccio, "SAR Sensor Trajectory Deviations: Fourier Domain Formulation and Extended Scene Simulation of Raw Signal", *IEEE Transactions on Geoscience and Remote Sensing*, vol.44, no.9, pp. 2323-2334, 2006.
- [6] A. Iodice, A. Natale, D. Riccio, "Polarimetric Two-Scale Model for Soil Moisture Retrieval via Dual-Pol HH-VV SAR Data", *IEEE Journal of Selected Topics in Applied Earth Observations and Remote Sensing*, vol.6, no.3, pp. 1163-1171, 2013.

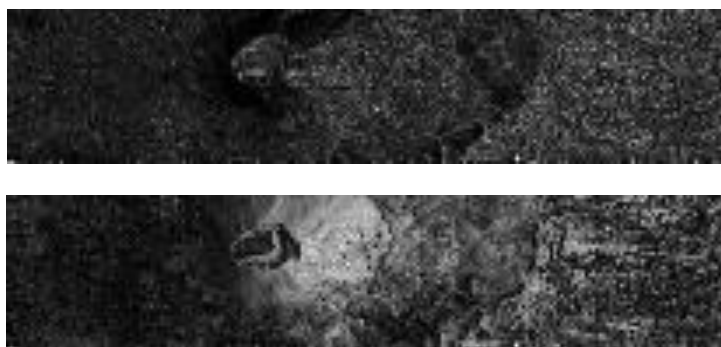


Fig. 3: Entropy (top) and alpha angle (bottom) maps for the Vesuvius scene. Near range is on the left.

TWO-PORT WPT LINK USING THREE COUPLED INDUCTORS

Giuseppina Monti⁽¹⁾, Alessandra Costanzo⁽²⁾, Franco Mastri⁽²⁾, Mauro Mongiardo⁽³⁾, Luciano Tarricone ⁽¹⁾

⁽¹⁾ DII, University of Salento, Lecce, Italy, ⁽²⁾ DEI, University of Bologna, Bologna, Italy, ⁽³⁾ DE, University of Perugia, Perugia, Italy
giuseppina.monti@unisalento.it

Abstract

A two-port network realizing a Wireless Power Transmission (WPT) link is analyzed. The case of a magnetic coupling between three inductors is considered and solved in the case where two of the three inductors are connected in series or parallel. It is demonstrated that the power delivered by the generator to the network can be maximized by adding appropriate series compensating reactances. Additionally, for the compensated two-port network, analytical formulas for the load maximizing the power delivered to the load are derived.

Index Terms – Wireless power transfer, network theory, resonant coupling, conjugate matching, efficiency.

I. INTRODUCTION

Non-radiative WPT is gaining a growing interest among researchers [1]. In particular, configurations using magnetically coupled inductors appear as the best choice for implementing robust and efficient WPT links. In this regard, in the literature extensive studies are available demonstrating that appropriate compensating reactances are necessary in order to maximize both the power delivered to the load and the efficiency of the link, thus resulting in a so called Resonant Inductive Coupling (RIC). The basic configuration of a WPT link based on RIC, consists of two coupled inductors loaded by appropriate capacitances for realizing the resonance condition at the desired operating frequency. For this configuration, closed form formulas for the loads maximizing either the power on the load or the efficiency of the link have been derived [2]. However, in applications with a mobile receiver and or transmitter, configurations using a receiving and/or a transmitting inductor consisting of two or more inductances are of interest for guaranteeing a nearly constant power on the load.

Accordingly, in this paper a system consisting of three coupled inductors is considered and solved assuming that two of them are connected so to realize a two-port WPT link.

II. ANALYTICAL FORMULATION

The problem analyzed in this paper is illustrated in Fig. 1; a WPT link consisting of three coupled inductors, with inductances L_i , $i=1,2,3$

and coupling coefficients k_{ij} , $(i,j)=1,2,3$, is considered. By using an impedance matrix representation, the network is described by the equation: $\mathbf{V} = \bar{\mathbf{Z}}\mathbf{I}$, where \mathbf{V} and \mathbf{I} are the vectors of port voltages and currents of the three-port network, and $\bar{\mathbf{Z}}$ is its impedance matrix:

$$\bar{\mathbf{Z}} = \begin{bmatrix} r_1 + j\omega L_1 & j\omega M_{12} & j\omega M_{13} \\ j\omega M_{12} & r_2 + j\omega L_2 & j\omega M_{23} \\ j\omega M_{13} & j\omega M_{23} & r_3 + j\omega L_3 \end{bmatrix} \quad (1)$$

the terms M_{ij} , $(i,j)=1,2$, are the mutual inductances between the inductors L_i and L_j : $M_{ij} = k_{ij}\sqrt{L_i L_j}$. Assuming a series (Case A of Fig. 1) or a shunt (Case B of Fig. 1) connection between the second and the third inductor, the link can be modeled as a two-port network. The general case where either port 1 or port 2 can be connected to a voltage generator and either port 2 or port 1 can be terminated on a load Z_L is analytically solved for realizing the maximum power transfer condition.

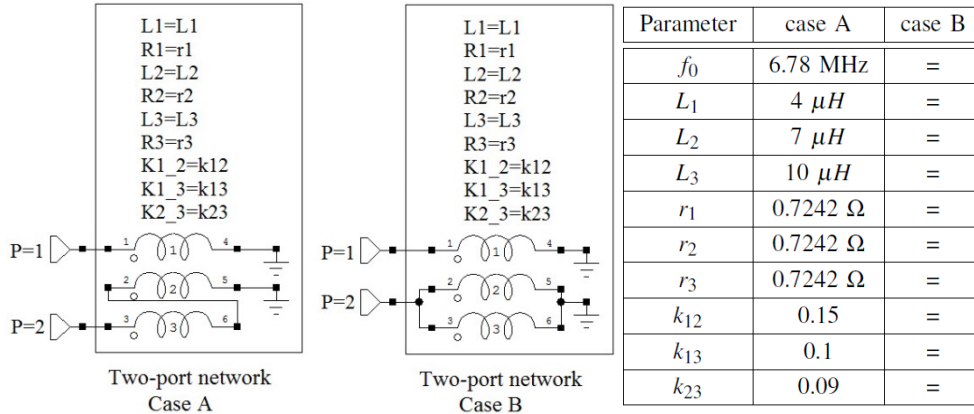


FIG. 1 – Schematic representation and parameters of the analyzed problem. Case A corresponds to the case of a series connection between inductors 2 and 3, while Case B corresponds to the case of a shunt connection.

- *Series connection*

When the inductances L_2 and L_3 are connected in series/anti-series (see case A of Fig. 1), the following impedance matrix can be recovered for the two-port network:

$$\bar{\mathbf{Z}}^s = \begin{bmatrix} r_1 + j\omega L_1 & j\omega(M_{12} \pm M_{13}) \\ j\omega(M_{12} \pm M_{13}) & (r_2 + r_3) + j\omega(L_2 + L_3 \pm M_{23}) \end{bmatrix}, \quad (2)$$

where the prime 's' denotes the case of inductors L_2 and L_3 connected in series. The \pm signs that appear in (2) refer to the series connection ($I_2 = I_3$) and the anti-series ($I_2 = -I_3$): the positive sign has to be taken in the case of a series connection; while, the negative sign has to be taken in the case of an anti-series connection. According to the theory developed in [2], the power delivered to the network by a generator on port i , $(i=1,2)$, can be maximized by adding appropriate series reactances compensating the imaginary part of the terms Z_{ii} . From (2), it

can be derived that, at a given frequency $f_0 = \omega_0/2\pi$, the compensating reactances that allow nullifying the imaginary part of Z_{11} and Z_{22} , are:

$$C_1^s = \frac{1}{L_1\omega_0^2}, C_2^s = \frac{1}{L_2+L_3 \pm 2M_{23}\omega_0^2} \quad (3)$$

By adding to the two-port network the compensating reactances C_1^s and C_2^s , the power delivered by a voltage generator on port 1 (port 2) to a load on port 2 (port 1) is maximized when the load Z_{L2}^s (Z_{L1}^s) is the complex conjugate of the input impedance seen at port 2 (port 1) when the generator is short-circuited. Accordingly, the expression of Z_{L1}^s and Z_{L2}^s that maximizes the power on the load are:

$$Z_{L1}^s = r_1 + \frac{\omega^2(M_{12} \pm M_{13})^2}{(r_2+r_3)}, Z_{L2}^s = (r_2 + r_3) + \frac{\omega^2(M_{12} \pm M_{13})^2}{r_1} \quad (4)$$

- Shunt connection

The case of a shunt connection between L_2 and L_3 leads to very long expressions for the terms of the impedance matrix of the two-port network, as a consequence, for the sake of brevity, but without loss of generality for the calculation of the compensating reactances, results corresponding to loss-less inductors are here reported. By imposing $V_2 = V_3$ in (1), for the elements Z_{ii}^p of the impedance matrix of the two-port network it can be derived:

$$Z_{11}^p = \frac{j\omega[2L_1M_{23}+(M_{13}-M_{12})^2-L_1L_3-L_1L_2]}{2M_{23}-L_3-L_2}, Z_{22}^p = \frac{j\omega(M_{23}^2-L_2L_3)[-M_{13}-M_{12}]}{2M_{23}-L_3-L_2} \quad (5)$$

where the prime 'p' denotes the case of inductors L_2 and L_3 connected in parallel. From the latter it is seen that, in order to nullify the reactive parts of Z_{11}^p and Z_{22}^p , at the desired operative angular frequency ω_0 we need to insert the following series capacitances:

$$C_1^p = \frac{2M_{23}-L_3-L_2}{[2L_1M_{23}+(M_{13}-M_{12})^2-L_1L_3-L_1L_2]\omega_0^2}, C_2^p = \frac{2M_{23}-L_3-L_2}{(M_{23}^2-L_2L_3)\omega_0^2} \quad (3)$$

Once the compensating capacitors have been added, the impedance matrix of the two-port network including losses can be numerically evaluated, and the formulas reported in Table I of [2] can be used for calculating the values of the optimum loads Z_{L1}^p and Z_{L2}^p realizing the maximum power transfer condition.

III. NUMERICAL VERIFICATION

The analytical formulas reported in the previous section have been verified by circuit simulations. The parameters of the three coupled inductors that have been analyzed are summarized in Fig. 1. Both the cases of a series connection, case A, and a shunt connection, case B, between the inductors L_2 and L_3 have been considered. The values of the compensating reactances and the optimum loads calculated according to the theory presented in the previous section are given in

Fig. 2a. First of all, the correctness of the compensating capacitances was verified by calculating the impedance matrix of the compensated network. The values calculated by circuit simulations for the elements $Z_{11}^{s/p}$ and $Z_{22}^{s/p}$ in the case of a series/parallel connection between inductors L_2 and L_3 and by using the capacitances reported in Fig. 2 are: $Z_{11}^s = 0.7242 \Omega$, $Z_{22}^s = 1.4484 \Omega$, $Z_{11}^p = 0.7243 \Omega$, $Z_{22}^p = 0.37568 \Omega$. As for the power delivered to the load, results obtained by circuit simulations for the two-port network with compensating reactances are summarized in Figs.~2b-2c. Figure 2b refers to the case of a series connection between inductors L_2 and L_3 , while Fig. 2c refers to the case where these inductances are connected in parallel. In both cases, the black (red) curve illustrates the results obtained by assuming that the load is on port 1 (port 2) and that a voltage generator is on port 2 (port 1). From these figures, it is evident that circuit simulations confirm the theoretical values given in Fig. 2a.

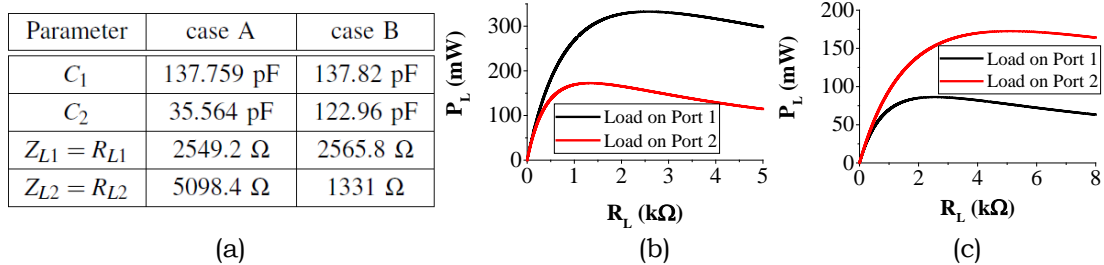


FIG. 2 – (a) Compensating capacitances and optimal loads calculated according to the analytical formulas presented in section II. (b)-(c) Powers behavior for Case A, (b), and Case B, (c).

IV. CONCLUSION

A system of three coupled inductors with two of them connected in series or parallel in order to realize a two-port WPT link has been considered. The general case where all the inductances and the mutual couplings are different has been solved.

Analytical formulas for the compensating reactances and the loads maximizing the power delivered to the load are derived and validated by circuit simulations.

REFERENCES

- [1] A. Costanzo, M. Dionigi, D. Masotti, M. Mongiardo, G. Monti, L. Tarricone, R. Sorrentino, “Electromagnetic Energy Harvesting and Wireless Power Transmission: A Unified Approach,” Proceedings of the IEEE, Vol. 102 , Issue 11, pp. 1692-1711, Oct. 2014.
- [2] M. Dionigi, M. Mongiardo, R. Perfetti, “Rigorous network and full-wave electromagnetic modeling of wireless power transfer links,” IEEE Transactions on Microwave Theory and Techniques, Vol. 63, no. 1, pp. 65–75, 2015.

MONOPOLE ARRAY WITH PARASITIC ELEMENTS AND CORPORATE-FEED NETWORK

M. Farran⁽¹⁾, S. Boscolo⁽²⁾, A. Locatelli⁽¹⁾, A.D. Capobianco⁽³⁾,
M. Midrio⁽²⁾, V. Ferrari⁽¹⁾, D. Modotto⁽¹⁾

⁽¹⁾ Dipartimento di Ingegneria dell'Informazione,
Università di Brescia, via Branze 38, 25123 Brescia, Italy
daniele.modotto@unibs.it

⁽²⁾ Dipartimento di Ingegneria Elettrica, Gestionale e Meccanica,
Università di Udine, via delle Scienze 208, 33100 Udine, Italy

⁽³⁾ Dipartimento di Ingegneria dell'Informazione,
Università di Padova, via Gradenigo 6/b, 35131 Padova, Italy

Abstract

A printed 1×5 monopole array is designed and experimentally characterized. Only two monopoles are active and fed by means of a corporate network, whereas the remaining three monopoles are parasitic and fed by currents from the ground plane. In presence of an additional metallic plane acting as a reflector, the measured 10 dB gain and the 700 MHz bandwidth make the proposed antenna suitable for point-to-point links and for radar sensors.

Index Terms – Corporate-feed network, monopole array, printed antenna.

I. INTRODUCTION

A printed monopole can be fed by an input microstrip line and it is easily integrated on a circuit board [1]. In order to obtain the desired working frequency and a good impedance matching, the length of the metallic strip forming the monopole and the dimensions of the ground plane must be carefully chosen [1,2]. If a directivity larger than 5 dB is sought, an array made of several printed monopoles appears as a good solution, but the need of a complex corporate-feed or series-feed network [3] has hampered the adoption of this solution. We will show that the design of the feeding network of a $2N+1$ strip monopole array is considerably simplified if N monopoles are directly fed by the network and $N+1$ monopoles are connected to the ground plane and indirectly fed by currents on the edge of the ground plane. The following Sections explain the details of our design and comment the experimental results for the case of a 5-element array (i.e. with $N=2$).

II. CORPORATE-FEED ARRAY DESIGN

A sketch of the designed 1×5 monopole array is shown in Fig. 1(a): the substrate is FR4 ($\epsilon_r=4,3$, $\tan\delta=0.025$, thickness=1.58 mm), the input

microstrip has a characteristic impedance of 50Ω and the working frequency is 2.44 GHz ($\lambda_0=12.3 \text{ cm}$). Two microstrip monopoles (on the substrate top face) are fed by a corporate network composed of a power splitter and two half-wavelength transformers and these two active monopoles are separated by $0.5 \lambda_0$. Three parasitic monopoles (on the substrate bottom face and connected to the ground plane) are placed on both sides of each active element at a distance of $0.25 \lambda_0$, which is small enough to prevent the onset of grating lobes [3]. Since a broadside radiation pattern is required, the currents flowing in all the five strip monopoles must oscillate in phase and this is achieved by inserting a meander line (see Fig. 1(a)) between each active monopole and the feeding network. These meanders work as delay lines and can be used to select the phase of the current flowing inside the active elements [4]. The geometrical parameters of the array were tuned by means of numerical simulations done by the time domain solver of CST. The length of each metallic strip monopole is 2.5 cm and the board sizes are $13.9 \times 7.6 \text{ cm}^2$.

A snapshot of the calculated current density vectors is reported in Fig. 1(b): the current vectors in the five monopoles have the same orientation and their magnitudes are comparable both in active and parasitic metallic strips. Moreover, the input impedance matching condition is fulfilled, as it is proved by the presence of a travelling wave from the input port to the feeding network (see Fig. 1(b)). It must be underlined that without the meanders the currents in the five strips would not be in phase.

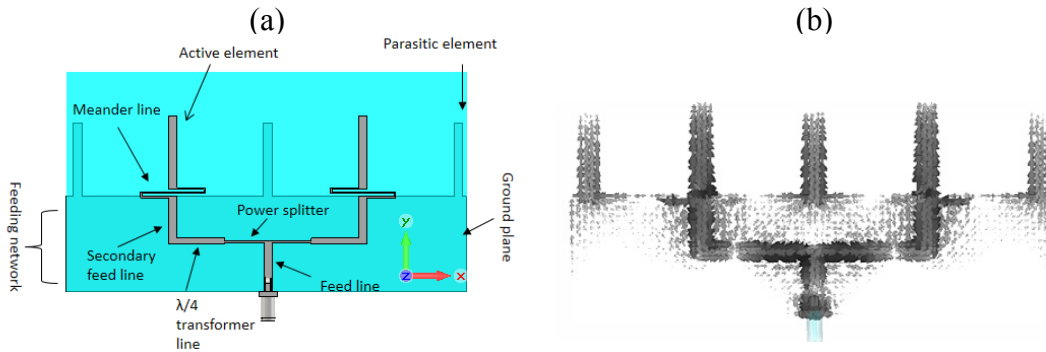


FIG. 1 – (a) Drawing of the 1×5 strip monopole array with the corporate-fed network; (b) computed current density vectors (whose magnitude is given in a logarithmic scale) at 2.44 GHz .

Simulations confirm the predicted broadside radiation pattern (as reported in Fig. 2(a)). The calculated directivity is about 7 dB (and gain is 6.5 dB), but it can be readily increased by 3 dB by placing a reflecting metallic sheet at a distance of $0.25 \lambda_0$ from the array board: in such a case there is only one single main lobe, as it can be recognized in Fig. 2(b).

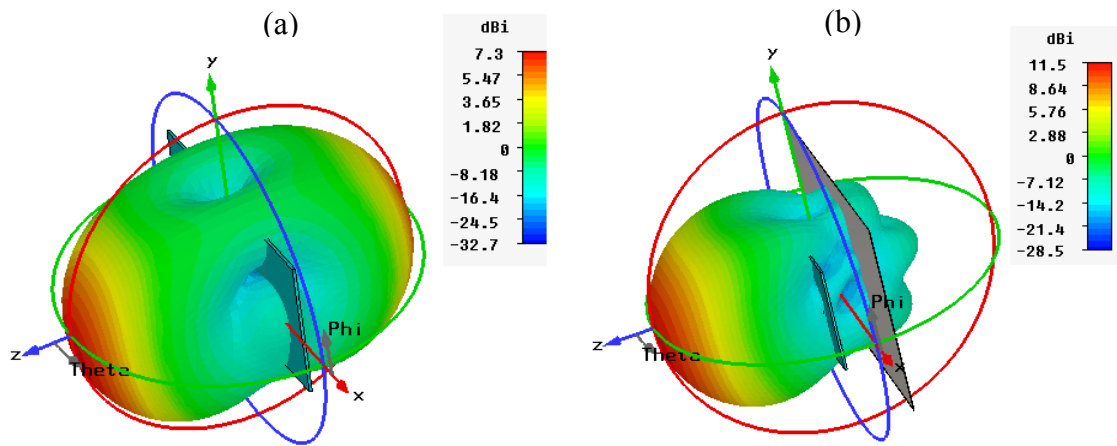


FIG. 2 – (a) Simulated 3D radiation pattern of the 1×5 array (at 2.44 GHz); (b) simulated 3D radiation pattern of the 1×5 array in presence of a reflecting metallic plane at a distance of $0.25 \lambda_0$ from the board (at 2.44 GHz).

III. EXPERIMENTAL RESULTS

Figure 3(a) shows a photo of the fabricated 1×5 array prototype. Simulated and measured reflection coefficients, both with and without the reflecting metallic sheet, are plotted in Fig. 3(b): the experiments confirm a -10 dB band which spans from about 2.23 GHz up to 3 GHz.

The radiation patterns measured in anechoic chamber reasonably agree with the calculated ones. The array with reflecting plane exhibits a large main lobe whose gain is almost constant over about 700 MHz (the gain is 9.6 dB at 2.44 GHz and 9.8 dB at 2.75 GHz). Figure 4 presents the radiation patterns in the E-plane and both numerical and experimental results show that the main lobe is slightly tilted with respect to the normal (z axis) to the board.

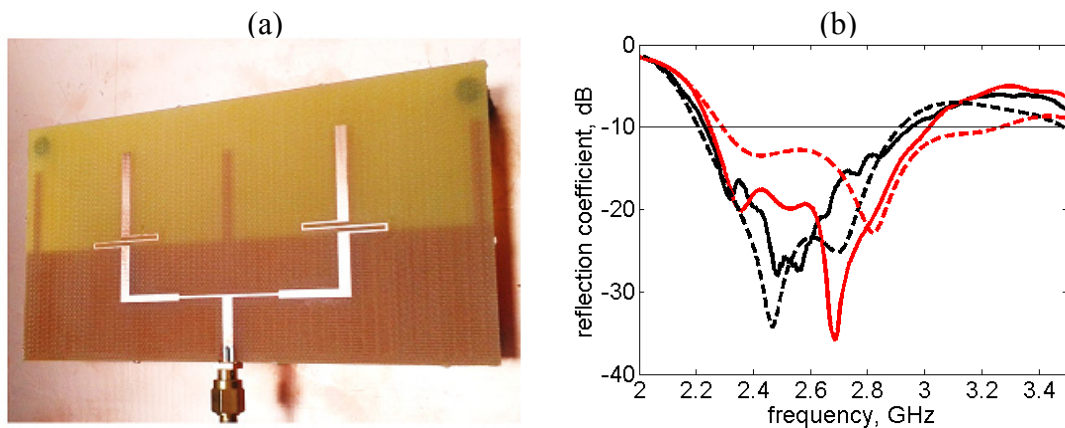


FIG. 3 – (a) Photo of the 1×5 array prototype with the reflecting metallic plane; (b) calculated (dashed lines) and measured (solid lines) reflection coefficients of the 1×5 array without reflector (black lines) and with reflector (red lines).

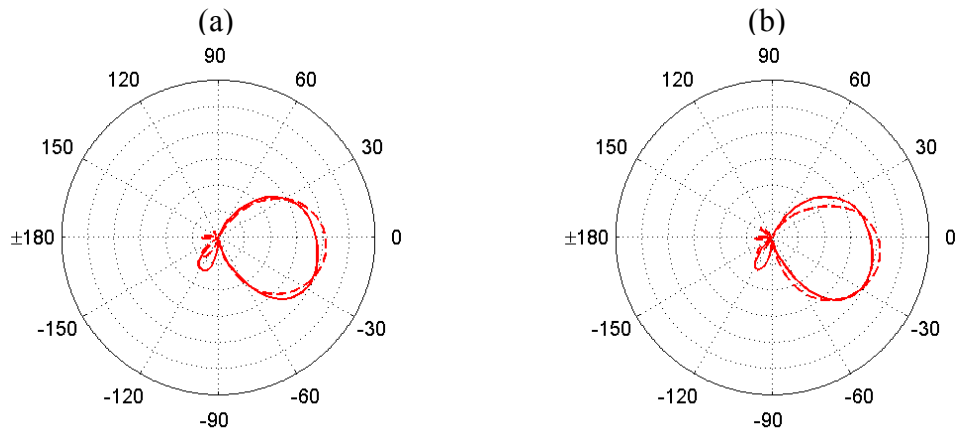


FIG. 4 – Calculated (dashed lines) and measured (solid lines) radiation patterns in the E-plane at (a) 2.44 GHz and (b) 2.75 GHz. Angles are measured starting from the z axis towards the y axis. The scale is from -10 to 20 dB.

IV. CONCLUSION

This work shows evidence that a printed $2N+1$ element array composed of N active strip monopoles and $N+1$ parasitic strip monopoles can give almost the same gain of an array composed of $2N+1$ half-wavelength dipoles. Thanks to the good gain (9.6 dB for $N=2$), the fractional bandwidth of about 30% and the compactness of the corporate-feed network, these printed antennas could find application in point-to-point links and in radar sensors, that cannot work with the small fractional bandwidth of a standard printed patch array.

REFERENCES

- [1] M. J. Ammann and M. John, "Optimum design of the printed strip monopole," *IEEE Antennas and Propagation Magazine*, vol. 47(6), pp. 59-61, Sept. 2005.
- [2] M. John and M. J. Ammann, "Optimization of impedance bandwidth for the printed rectangular monopole antenna," *Microwave and Optical Technology Letters*, vol. 47(2), pp. 153-154, Oct. 2005.
- [3] C. A. Balanis, *Antenna Theory: Analysis and Design*, 3rd Edition, Wiley, 2005.
- [4] M. Farran, D. Modotto, S. Boscolo, A. Locatelli, A.D. Capobianco, M. Midrio, V. Ferrari, "Compact printed parasitic arrays for WLAN applications," *IEEE Antennas and Wireless Propagation Letters*, vol. 15, pp. 918-921, 2016.

PATH-LOSS STATISTICAL MODEL FOR URBAN MOBILE BACKHAULING AT MM-FREQUENCIES

F. Fuschini⁽¹⁾, M. Barbiroli⁽¹⁾, M. Zoli⁽¹⁾, A. Perikleous⁽²⁾, V. Petrini⁽³⁾,
C. Carciofi⁽³⁾

⁽¹⁾ DEI, Alma Mater Studiorum University of Bologna
Viale Risorgimento 2, 40136 Bologna, Italy.
{franco.fuschini, marina.barbiroli, marco.zoli5}@unibo.it

⁽²⁾ Consorzio Elettra2000
Villa Griffone, via Celestini 1, 40037 Pontecchio Marconi (BO) Italy.

⁽³⁾ Fondazione Ugo Bordoni
Villa Griffone, via Celestini 1, 40037 Pontecchio Marconi (BO) Italy.
{vpetrini, ccarciofi}@fub.it

Abstract

In order to meet the unceasing demand for greater data-rates, future cellular network will be deployed according to heterogeneous layouts, with traditional macro-cellular sites acting as umbrella for a multitude of underlain micro-cells. Backhauling communications will likely rely on point-to-point wireless links not always in clear line of sight. A path loss model for urban backhauling at mm-frequencies is presented in this work, based on a Monte Carlo approach applied to a proper statistical description of the environment.

Index Terms – wireless propagation, path-loss, backhauling, 5G radio networks.

I. INTRODUCTION

Future mobile broadband systems should provide very high data-rate for a high number of users at the same time. Today existing cellular systems layout can't fulfil this demanding requirements, thus low power micro Base Stations (BS) will be deployed to increase capacity and bitrate and existing small/macro BS sites should act as umbrella cells, achieving an heterogeneous network. Traditional wired Back-Hauling (BH) solutions (also optical) are not envisaged due to the high cost in installation and deployment and existing small/macro BS sites can be used as HUBs for wireless, less expensive BH [1], [2]. For this wireless BH links the underutilized millimetre frequency bands seem to be very promising as they can support significantly higher data rate than traditional centimetre bands. In urban environment, the μ BSs will be likely placed well below rooftop levels and often a clear Line-of-Sight (LoS) between the micro BS and the HUBs may be prevented.

In this paper wireless BH propagation is investigated by means of a narrow-band statistical model, based on a Monte Carlo approach applied to a proper statistical description of the profile between the transmitter and the receiver.

II. MODEL DESCRIPTION

Since the HUBs involved in the BH wireless communication will likely stand out over the urban layout (Fig. 1), propagation can be assumed to

mainly occur through multiple diffractions over the rooftops of the buildings in between the antennas [3], [4].

Over Roof Top (ORT) propagation in BH links is here fundamentally modeled according to the 2D statistical approach presented in [3]. In [3] the analysis was limited to a frequency range around 1 GHz, whereas it is here extended to the millimeter wave band, and in particular to the frequency values so far mainly considered for the forth-coming, multi-gigabit 5G wireless networks (28, 38, 60 and 73 GHz).

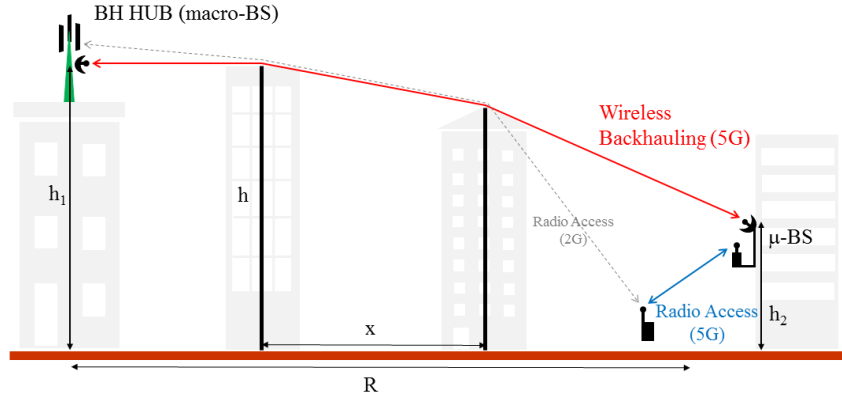


FIG. 1 – Geometrical representation of the back-hauling link.

As sketched in Fig. 1, the HUB and the μ BS are placed at distance R with heights h_1 and h_2 , respectively. For the sake of simplicity, the buildings between the antennas are represented as a middle-placed Knife Edge (KE) (thick black lines in Fig. 1). Of course, they may prevent the LoS depending on the KE heights (h) and the distance between contiguous KEs (x). Both h and x are considered as random variables modeled according to a Gaussian and to a Gamma distribution, respectively [3]. The environment is therefore taken into account through the KEs mean height (h_m), the KEs heights std. deviation (σ_H) and the mean distance between KEs (x_m).

The model mainly aims at estimating the mean attenuation (path-loss – PL) and the attenuation std. dev. σ at different link distances when non-LoS (NLoS) conditions occur. This is accomplished by means of a Monte Carlo approach: for each value of R , several ORT profiles are first generated according to the statistical description of the link; then the ORT loss is computed for the only NLoS extracted cases by means of the Epstein-Peterson model. Finally, the $PL_{NLoS}(R)$ and $\sigma_{NLoS}(R)$ are computed according to the collected samples of ORT attenuation.

The overall PL and its std. deviation can be also immediately achieved as follows:

$$PL(R) = PL_{NLoS}(R) \cdot [1 - P_{LoS}(R)] + PL_{LoS}(R) \cdot P_{LoS}(R) \quad (1)$$

$$\sigma(R) = \sqrt{P_{LoS}(R) \cdot [PL(R) - PL_{LoS}(R)]^2 + [1 - P_{LoS}(R)] \cdot [(PL(R) - PL_{NLoS}(R))^2 + \sigma_{NLoS}^2]} \quad (2)$$

being P_{LoS} the LoS probability (also computed by the Monte Carlo simulation) and PL_{LoS} the attenuation in LoS condition (e.g. computed through the Friis equation).

III. RESULTS AND COMMENTS

For the sake of brevity, results presented in this section are limited to the following case study: $\Delta^+=h_1-h_m=6\text{m}$, $\Delta^-=h_m-h_2=3\text{m}$, $\sigma_H=4\text{m}$ and $x_m=100\text{m}$. The corresponding PL values are represented vs. the link distance in Fig. 2a at the frequency of 73 GHz. PL plus/minus σ are also included to somehow account for possible deviation from the average due to shadowing effects. The grey and black lines refer to the NLoS and to the overall attenuation, respectively.

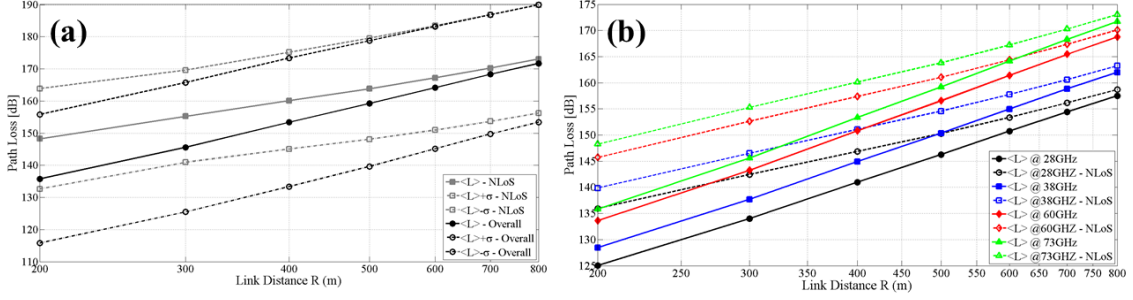


FIG. 2 – PL vs link distance, case study: (a) $f = 73$ GHz – (b) comparison at different frequencies

The difference between the NLoS and the overall PL values is of course due to the LoS probability, not negligible at short distances but quickly approaching zero as R increases. Since PL clearly exhibits an almost linear dependence on R (in logarithmic scale), then it may be expressed as $PL \approx 10 \cdot \alpha \cdot \log(R) + \beta$, where α is often indicated as Path Loss Exponent (PLE). In Fig. 2a, $PLE_{NLoS} \approx 4.3$, but it has turned out to range from 2.3 to 8.3 in most cases depending on the values of the model parameters. The value of σ_{NLoS} is equal to about 15.5 dB and it seems almost unaffected by the distance. The overall std. dev. is of course larger, since accounting also for the LoS occurrence extends the variability of the PL values with respect to the only NLoS cases.

The dependence of PL on frequency is investigated in Fig. 2b: stronger attenuation are clearly experienced at higher frequencies, with an average PL_{NLoS} difference equal to 13.5 dB between 28 and 73 GHz. PLE values also slightly increase with frequency ($PLE_{NLoS} \approx 3.9/4.3 @ 28/73$ GHz). This seems consistent with the multiple diffraction approach: a larger number of diffraction is of course involved (on the average) at larger distance, and each diffraction is less effective as the frequency increases. Therefore, the higher the frequency, the steeper the PL vs. distance rate. A similar behavior is achieved for σ_{NLoS} , which ranges from 14 dB @ 28 GHz to about 15.5 dB @ 73 GHz.

Results in Fig. 2 clearly show that attenuation is much stronger at mm-frequency than at frequencies below 6 GHz up to now mainly considered for wireless personal communications. The difference, rather remarkable in LoS condition, becomes even greater when NLoS occurs. If compared to radio access in traditional macro-cellular network (grey, dashed link in Fig. 3), wireless BH at mm-frequency will benefit by the increased μ BS height with respect to the street level (from the grey,

continuous line to the the grey dashed line in Fig. 3). The situation is then reversed by the frequency difference, which worsen the propagation conditions to a much greater extent (black lines in Fig. 3).

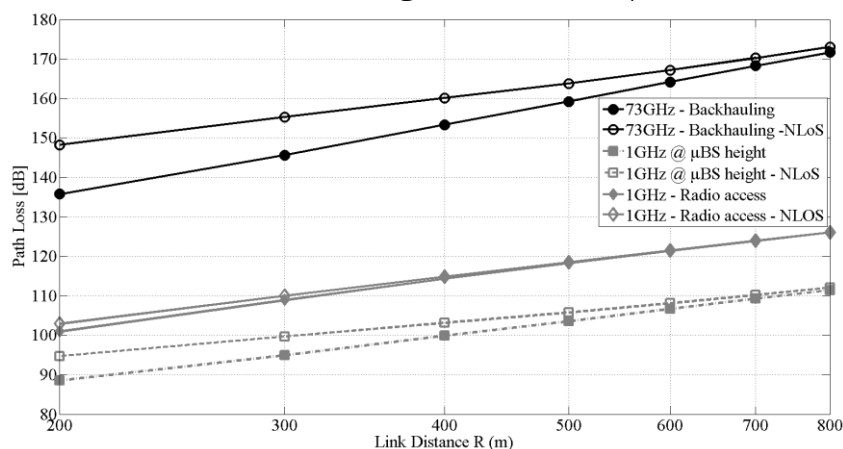


FIG. 3 – Wireless MB @ 73 GHz vs. macro-cellular radio access @ 1 GHz

Directive antennas (as the parabolic reflectors sketched in Fig. 1) may be introduced at the BH link ends to compensate for the heavy attenuations; nevertheless, such solution may result critical especially in NLoS conditions, where the selection of the optimal pointing direction could be not always straightforward.

IV. CONCLUSION

Wireless propagation for backhauling at millimeter frequencies is investigated in this work through a statistical approach and with special reference to NLoS conditions. Path loss values, as well as path loss exponents and attenuation std. deviations increase with frequencies and seem much higher if compared to frequency below 6 GHz so far considered for radio access in traditional wireless networks. Future developments should include experimental activities to check the outcomes of the statistical model with measured data gathered in real urban scenarios.

V. REFERENCES

- [1] U. Siddique, H. Tabassum, E. Hossain and D. I. Kim, "Wireless backhauling of 5G small cells: challenges and solution approaches," in *IEEE Wireless Communications*, vol. 22, no. 5, pp. 22-31, October 2015. doi: 10.1109/MWC.2015.7306534.
- [2] M. Shariat, M. Dianati, K. Seppänen, T. Suihko, J. Putkonen and V. Frascolla, "Enabling wireless backhauling for next generation mmWave networks," *Networks and Communications (EuCNC)*, 2015 European Conference on, Paris, 2015, pp. 164-168. doi: 10.1109/EuCNC.2015.7194061.
- [3] F. Fuschini, V. Degli Esposti, G. Falciasecca, "A Statistical Model for Over Rooftop Propagation", *IEEE Transactions on Antennas and Propagation*, vol. 52(1), pp. 230-239, Jan. 2004.
- [4] H. L. Bertoni, "Radio Propagation for Modern Wireless Systems", Prentice Hall 2000.

A FREQUENCY RECONFIGURABLE SELF-ADAPTING CONFORMAL ARRAY FOR CHANGING SURFACES

Giulia Mansutti⁽¹⁾, Muhammad Saeed Khan⁽¹⁾, Benjamin D. Braaten⁽²⁾,
Antonio-Daniele Capobianco⁽¹⁾,

⁽¹⁾ Department of Information Engineering, University of Padova
Via G. Gradenigo 6/B, 35131, Padova, Italy

⁽²⁾ Department of Electrical and Computer Engineering, North Dakota State University, Fargo, ND
58102 USA

Abstract

Conformal antennas placed on complex surfaces are gaining more attention as a method to increase coverage of modern wireless communication systems. Furthermore, frequency reconfigurable antennas are being used in the development of multi-band multi-radio wireless platforms to simplify design. In this work, a new 1x4 frequency reconfigurable self-adapting conformal antenna array that can be attached to changing surfaces is presented. This conformal array consists of four reconfigurable microstrip patch antennas, a reconfigurable sensor circuit used to measure the curvature of the conformal surface and voltage controlled phase shifters. Phase-compensation is implemented through the phase-shifters to autonomously recover the pattern in both bands of the reconfigurable 1x4 array as the wedge- and cylindrical-shaped surface on which the array is attached upon changes shape. Moreover a novel 1x6 Z-shaped conformal array antenna is designed and studied via full-wave numerical simulations, proving that the presented pattern recovery technique is effective also when the array is placed on a generic complex surface.

Index Terms – Conformal array, reconfigurable antennas.

I. INTRODUCTION

The applications of modern wireless communication systems are growing fast thus demanding antennas to satisfy evermore complex requirements, like for example wearable functionalities, load-bearing capabilities, vibration tolerances and extreme environmental immunity [1]. In order to meet some of the aforementioned requirements, designers have turned to the development of conformal antennas [2]-[4], thus facing the problem of unwanted pattern distortion caused by the deformation of the surface on which the antenna is attached upon [4]. Some preservation of the radiation pattern can be achieved by mechanical [5] and electrical [2],[6]-[7] compensation at a single frequency, however these pattern-correcting techniques have some drawbacks: they require extensive signal processing, narrowband correction algorithms and potentially complex sensor networks. Moreover, in addition to the aforementioned complex requirements that lead to the adoption of conformal antennas, also frequency reconfigurability is a desirable feature for modern antennas: in fact this enables to increase devices coverage and to access multi-band provider services such as GPS, Bluetooth, WiMax, WiFi and UWB services [8]-[9], avoiding the implementation of multiple antennas in a single device and exploiting the benefit of the resonant frequency of the antenna to avoid complicated and expensive multi-band filtering [8]. In this paper, the benefits of self-adapting conformal antennas and reconfigurability are combined into one design. In particular, the objective of this letter is to present the theoretical background on the autonomous self-adapting frequency reconfigurable conformal array shown in Fig. 1(a) on a changing wedge- and cylindrical-shaped conformal surface and a prototype for validation. Moreover a Z-shaped conformal array is designed and simulated in CST Microwave Studio, showing that the adopted phase-correcting technique is effective also on more complex conformal surfaces.

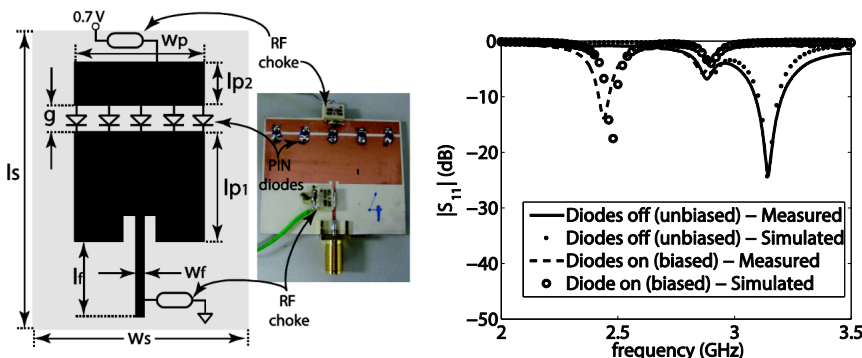


Fig. 1: (a) Drawing of the frequency reconfigurable microstrip patch element in the 1x4 array and a photograph of the prototype element ($l_s = 42$ mm, $w_s = 50.5$ mm, $l_{p1} = 17.7$ mm, $l_{p2} = 4.8$ mm, $w_p = 49$ mm, $l_f = 17.6$ mm and $w_f = 1.3$ mm) (b) reflection coefficient of the reconfigurable patch antenna.

II. THEORETICAL BACKGROUND

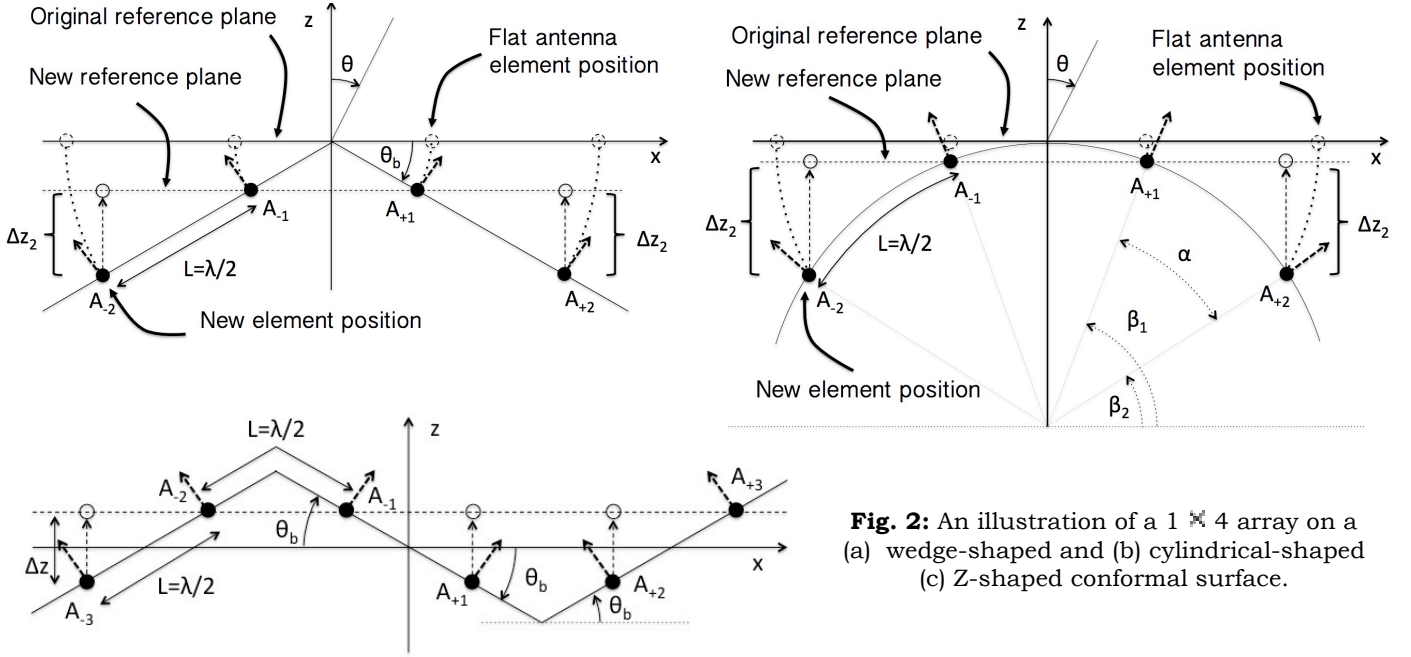


Fig. 2: An illustration of a 1×4 array on a (a) wedge-shaped and (b) cylindrical-shaped (c) Z-shaped conformal surface.

In order to determine the amount of required phase-compensation let us consider the problem described in Fig.2(a): the four antenna elements, denoted as $A_{\pm n}$ where $n = \pm 1$ and ± 2 , are on a wedge-shaped conformal surface with a bend angle θ_b . For this work, it is assumed that the direction of maximum radiation is along the z -axis (or $\phi_s = \pi/2$) and the inter-element spacing along the surface of the wedge is fixed at L . One method to ensure that radiation is along the z -axis in Fig. 2(a) is to add a phase shift to elements $A_{\pm 2}$ such that the fields from these elements arrive at the reference plane with the same phase as the fields radiated from elements $A_{\pm 1}$. This results in a broadside radiation to the reference plane. To determine the amount of phase required on elements $A_{\pm 2}$, the distance Δz_{wed} in Fig. 2(a) from the elements to the reference plane must be computed [2]. Then, Δz_{wed} can be used in the following equation to compute the amount of phase required to cancel the phase introduced by the free-space propagation from the elements $A_{\pm n}$ to the reference plane [2]:

$$\Delta\phi_{\pm 2} = k \Delta z_{wed} \quad (1)$$

where $\Delta z_{wed} = L n \sin \theta_b$, $0 \leq \theta_b \leq \pi/2$, $(x_{\pm 2}, y_{\pm 2})$ is the location of the $A_{\pm 2}$ elements, respectively, and k is the free-space wave number. Therefore to obtain the phase-shift at different frequencies of interest $f_1 f_2$ it is sufficient to evaluate k_1 and k_2 at these frequencies, thus obtaining Δz_1 and Δz_2 . As far as other conformal surfaces are concerned, the method to get the phase shift $\Delta\Phi$ is the same: the only difference lies in the evaluation of Δz : in the case of Fig.2(b) this is $\Delta z_{cyl} = r |\sin\beta_1 - \sin\beta_2|$ (where β_1, β_2 are defined in the figure). In the case of the Z-shaped surface depicted in Fig.3, we assumed that the bend angles are all equal to θ_b , so again the reasoning is the same that brought to (1), the only difference being that now the phase shift (1) has to be applied to elements $A_{-3} A_{+1} A_{+2}$.

III. RESULTS

Let us now examine the results obtained for the three configurations described in the previous section. Full-wave numerical simulations have been performed in HFSS and CST Microwave Studio for the three conformal arrays (wedge- cylindrical- and Z-shaped) with and without the introduction of the phase compensation $\Delta\Phi$ described in the previous section. Moreover for the wedge and cylindrical arrays measurements have been performed as well: four individual reconfigurable microstrip patch antennas (see Fig.1(b)) that switch between the two frequencies of interest $f_1=2.43$ GHz and $f_2=3.15$ GHz by changing the electrical length of the radiating patch were attached to the two conformal surfaces. Each patch antenna is individually connected to voltage

controlled phase shifters (Hittite Microwave Corporation part number: HMC928LP5E [10]) with identical SMA cables (flexible cables were chosen for placement on various surfaces). The wedge-

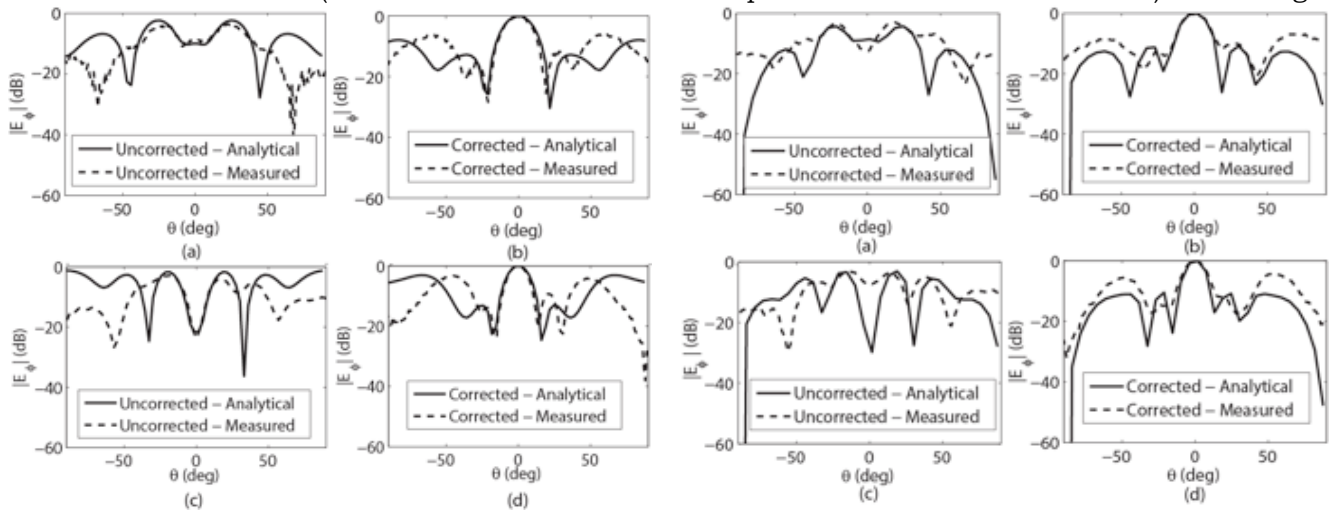


Fig.3: (a) Uncorrected and (b) corrected analytical and measured patterns of the reconfigurable self-adapting wedge-shaped array with $\theta_0 = 30^\circ$ at 2.43 GHz (f_1) and (c) uncorrected and (d) corrected analytical and measured patterns of the array at 3.15 GHz (f_2).

Fig.4: (a) Uncorrected and (b) corrected analytical and measured patterns of reconfigurable self-adapting cylindrical-shaped conformal array at 2.43 GHz (f_1) and (c) uncorrected and (d) corrected analytical and measured patterns of the array at 3.15 GHz (f_2).

and cylindrical-shaped surface deformation is measured by a resistive sensor (Spectra Symbol [11]: flat resistance=10KΩ and varies with bend; size=112.24x6.35 mm). This new reconfigurable sensing circuit doesn't require signal processing or complex algorithms and so the derived compensation algorithm can be autonomously implemented in the reconfigurable array using passive components and an opamp (AMPO4), which is much simpler and cost effective than a microprocessor. The circuit in turn provides an output voltage that drives the voltage controlled phase shifters to implement phase compensation [3] at both switching frequencies.

Fig. 3-4 report the results obtained when the self-adapting conformal array is placed on the wedge- and cylindrical- shaped surface: it can be seen how the radiation pattern can be recovered thanks to the compensation phase-shift. The effectiveness of this technique is visible especially around the direction of maximum, i.e., around 0° . Moreover it can be noticed that the simulations are in perfect agreement with the experimental measurements. As far as the Z-shaped surface is concerned, it is formed by six identical patch antennas each resonating at $f_3=2.45$ GHz. This conformal array was simulated in CST both with and without phase-compensation: again it can be seen from Fig.5 that the adopted pattern recovery technique is effective, especially around the direction of maximum 0° .

IV. CONCLUSIONS

The benefits of frequency reconfigurable antennas and self-adapting conformal antennas have been combined in this work. A new frequency reconfigurable sensor circuit that can measure the surface deformation and implement phase compensation theory at two frequencies without the need of

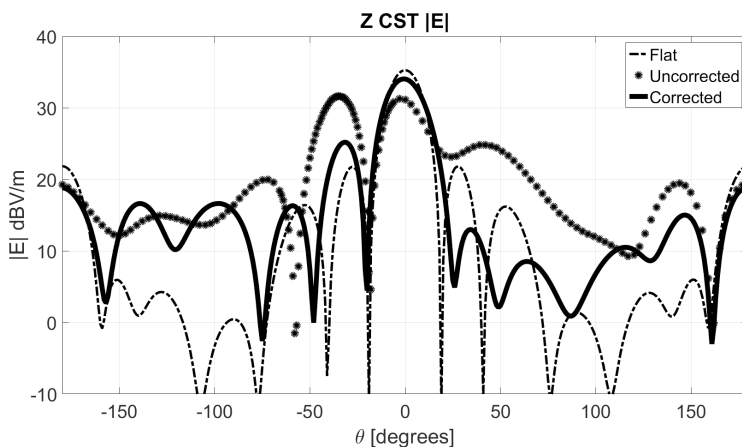


Fig.5: radiation pattern of a conformal array on a flat surface (dash-dotted line), on the Z-shaped surface without phase-compensation (dotted line) and with phase-compensation (solid line).

signal processing was shown. A prototype frequency reconfigurable self-adapting conformal array with switching frequencies of 2.43 GHz and 3.15 GHz was presented and used to successfully validate the phase-compensation expressions on the wedge- and cylindrical-shaped conformal surfaces. This showed that the conformal array could autonomously recover the radiation pattern at both switching frequencies. Moreover a more complex conformal array consisting of six patch antennas placed on a Z-shaped conformal surface was designed and studied through numerical simulations, proving that this new pattern recovery technique is effective also when the array is placed on more complicated surfaces, thus paving the way to a wide class of conformal arrays that could autonomously recover their radiation pattern when placed on a generic deformed surface. In the future we plan to realize a prototype of this array and to perform measurements on this design as those performed for the wedge- and cylindrical-shaped conformal arrays.

ACKNOWLEDGEMENTS

The authors acknowledge financial support from the University of Padova, project CPDA150022.

REFERENCES

- [1] Schippers, H., Verpoorte, H. J., Jorna, P., Hulzinga, A., Meijerink, A., Roeloffzen, C., Heideman, R. G., Leinse, A., and Wintels, M.: 'Conformal phased array with beam forming on airborne satellite communication', *Int. ITG Workshop on Smart Ant.*, Feb. 26-27 2008, pp. 343-350.
- [2] Braaten, B. D., Roy, S., Nariyal, S., Aziz, M. A., Chamberlain, N. F., Ullah, I., Reich, M. T., and Anagnostou, D. E.: 'A Self-Adapting Flexible (SELFLEX) Antenna Array for Changing Conformal Surface Applications', *IEEE Trans. Antennas Propag.*, Feb. 2013, 61, (2), pp. 655-665.
- [3] Haupt, R. L.: 'Antenna Arrays: A Computational Approach,' John Wiley and Sons, Ltd., Hoboken, New Jersey, 2010, pp. 287 - 315.
- [4] Wincza, K., and Gruszczynski.: 'Influence of curvature radius on radiation patterns in multibeam conformal antenna', *Proc. 36th Eur. Microw. Conf.*, Sep. 10-15, 2006, pp.1410-1413.
- [5] Huang, J.: 'Bandwidth study of microstrip reflectarray and a novel phased reflectarray concept', *Proc. of the IEEE Int. Symp. on Ant. and Propag.*, Newport Beach, CA, Jun. 18 - 23, 1995, pp. 582 - 585.
- [6] O'Donovan, P. L., and Rudge, A. W.: 'Adaptive control of a flexible linear array', *Electron. Lett.*, Mar. 22, 1973, 9, (6), pp.121-122.
- [7] Seidel, T. J., Rowe, W. S. T., and Ghorbani, K.: 'Passive compensation of beam shift in a bending array', *Prog. in Electrom. Research*, 2012, 29, pp. 41-53.
- [8] Anagnostou, D. E., Guizhen, Z., Chryssomallis, M. T., Lyke, J. C., Ponchak, G. E., Papapolymerou, J., and Christodoulou, C.G.: 'Design, fabrication, and measurements of an RF-MEMS-based self-similar reconfigurable antenna', *IEEE Trans. Antennas Propag.*, Feb. 2006, 54, (2), pp. 422-432.
- [9] Singh, M., Basu, A., and Koul, S. K.: 'Switchable frequency bands microstrip antennas', *iWAT*, Santa Monica CA, USA, Mar. 2 - 4, 2009.
- [10] Hittite Microwave Corporation, [online] www.hittite.com.
- [11] Spectra Symbol, [online] www.spectrasymbol.com.
- [12] Hinsz, L., and Braaten, B. D.: 'A Frequency Reconfigurable Transmitter Antenna with Autonomous Switching Capabilities', *IEEE Trans. Antennas Propag.*, Jul. 2014, 62, (7), pp. 3809 - 3813, Jul. 2014.

FRACTIONAL-CALCULUS-BASED FDTD MODEL FOR SIMULATING ARBITRARY DISPERSIVE DIELECTRIC MATERIALS

P. Bia⁽¹⁾, L. Mescia⁽¹⁾, D. Caratelli⁽²⁾

⁽¹⁾ Dipartimento di Ingegneria Elettrica e dell'Informazione,
Politecnico di Bari, Via E. Orabona 4, Bari, Italy.

⁽²⁾ The Antenna Company Nederland B.V., High Tech Campus, 5656
AE Eindhoven, The Netherlands.

luciano.mescia@poliba.it

Abstract

A novel Finite-Difference Time-Domain scheme (FDTD) for simulating electromagnetic pulse propagation in arbitrary dispersive biological media is illustrated. The proposed method is based on the fractional calculus theory and a general series expansion of the permittivity function. The effective medium theory (EMT) is also incorporated into the FDTD method. The resulting formulation is explicit, it has a second-order accuracy, and the need for additional storage variables is minimal.

Index Terms – Dispersive media, fractional calculus, finite difference method, effective media.

I. INTRODUCTION

In recent years, the feasibility of pulsed electromagnetic fields (PEFs) in RF and mm-wave frequency range, has been investigated in a variety of therapeutic and diagnostic applications [1]. This technology involves the interaction of electromagnetic fields with living tissues and as a result detailed theoretical modeling and computational techniques are essential to gain insight into the several phenomena occurring within the biological materials.

It is well known that the Debye model is not able to describe a wide class of relaxation processes occurring in biological materials. As a consequence, spectral models employing fractional power-law should be developed for accurately describing the dielectric response. In particular, taking into account that the dielectric response includes fractional powers of $j\omega$ the design of the FDTD algorithm requires special treatments [2-3]. To this aim, a novel FDTD approach for simulating ultra-wideband electromagnetic pulses propagating in arbitrary dispersive media is illustrated. In particular, using a general fractional polynomial series approximation, the fractional calculus theory and EMT formulation both the spatial and frequency dispersion characteristics of the dielectric response have been incorporated into the FDTD scheme. The comparison between the numerical results applying both the FDTD code and a fully analytical frequency-based approach demonstrates the accuracy of the proposed FDTD method.

II. FDTD SCHEME

In the developed FDTD scheme, a general relative electric permittivity function having the following fractional polynomial dispersion response has been implemented

$$\varepsilon(\omega) = \varepsilon_\infty + \Delta\varepsilon \frac{1 + \sum_{q=1}^M b_q (j\omega\tau)^{\beta_q}}{1 + \sum_{p=1}^N a_p (j\omega\tau)^{\gamma_p}} - j \frac{\sigma}{\omega\varepsilon_0} \quad (1)$$

where $\Delta\varepsilon$ and τ are the relaxation strength and time, respectively, ε_∞ is the relative permittivity at high frequency limit, σ is the static conductivity, $\gamma_p, \beta_q \geq 0$, $a_p, b_q \geq 0$ a real coefficients. Moreover, by using an optimization algorithm based on swarm intelligence [4] the parameters $\gamma_p, \beta_q, a_p, b_q$ can be recovered to suitably fit a generic frequency domain permittivity function. Taking into account the complex relative permittivity described by Eq. (1), the Ampere's law in time domain can be written as:

$$\nabla \times \mathbf{H} = \varepsilon_0 \varepsilon_\infty \frac{\partial \mathbf{E}}{\partial t} + \sigma \mathbf{E} + \mathbf{J} \quad (2)$$

where the auxiliary displacement current density \mathbf{J} satisfies the equation

$$\mathbf{J} + \mathcal{D}_t^J \mathbf{J} - \frac{\varepsilon_0 \Delta\varepsilon}{\tau} \mathcal{D}_t^E \mathbf{E} = \varepsilon_0 \Delta\varepsilon \frac{\partial \mathbf{E}}{\partial t} \quad (3)$$

with

$$\mathcal{D}_t^J = \sum_{p=1}^N a_p \tau^{\gamma_p} D_t^{\gamma_p} \quad (4)$$

$$\mathcal{D}_t^E = \sum_{q=1}^M b_q \tau^{1+\beta_q} D_t^{1+\beta_q} \quad (5)$$

Applying a second-order accurate finite-difference scheme at the time instant $t = m\Delta t$, the update equations for both electric and magnetic fields are

$$\mathbf{E}|^{m+1/2} = \mathbf{E}|^{m-1/2} + \frac{\Delta t}{\varepsilon_0 \Delta\varepsilon} \left(\mathbf{J} + \mathcal{D}_t^J \mathbf{J} - \frac{\varepsilon_0 \Delta\varepsilon}{\tau} \mathcal{D}_t^E \mathbf{E} \right) \Big|_t^m \quad (6)$$

$$\mathbf{H}|^{m+1} = \mathbf{H}|^m - \frac{\Delta t}{\mu_0} (\nabla \times \mathbf{E}) \Big|_t^{m+1/2} \quad (7)$$

where the finite-difference approximation of the generalized fractional derivative operators $\mathcal{D}_t^J, \mathcal{D}_t^E$ has been evaluated by applying the Riemann-Liouville theory [2-3].

III. NUMERICAL RESULTS

To test the developed numerical code, the 1-D layered model illustrated in Fig. 1 is considered. The system is irradiated by a plane wave propagating along the positive x-direction, with electric field linearly polarized along the z-axis and located at a given point $x = x_s$.

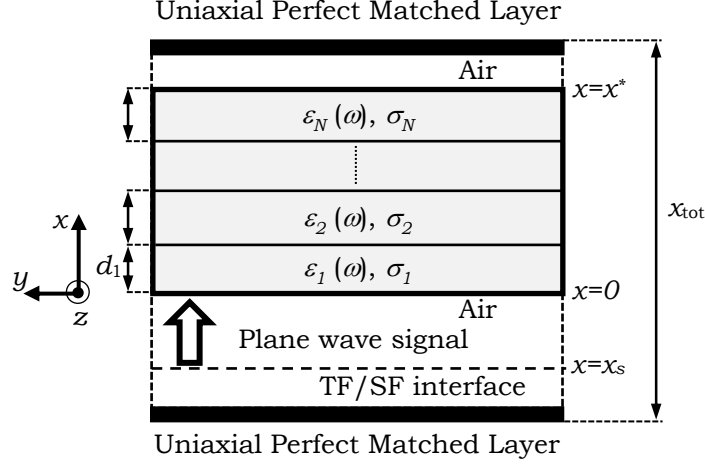


FIG. 1 – Layered model employed in the simulations.

The first test case pertains a single layer having thickness $d_1 = 10$ mm and relative electric permittivity

$$\varepsilon_1(\omega) = 2 + 60 \frac{1 + (j\omega\tau)^{0.2}}{1 + 9(j\omega\tau)^{0.3} + 2(j\omega\tau)^{0.5} + 10(j\omega\tau)^{0.9}} \quad (8)$$

$\sigma = 0.035$ S/m and $\tau = 318$ ps. The second one is a three layer having thickness $d_1 = 10$ mm, $d_2 = 30$ mm, $d_3 = 20$ mm and relative electric permittivity

$$\varepsilon_1(\omega) = 2.4 + 26 \frac{1 + 2(j\omega\tau_1)^{0.2}}{1 + 5(j\omega\tau_1)^{0.03} + 6.54(j\omega\tau_1)^{0.14} + 0.2(j\omega\tau_1)^{0.8} + 13(j\omega\tau_1)^{0.9}} \quad (9)$$

$$\varepsilon_2(\omega) = 4 + 44 \frac{1 + 3(j\omega\tau_2)^{0.3} + 2(j\omega\tau_2)^{0.4}}{1 + 5(j\omega\tau_2)^{0.14} + 8(j\omega\tau_2)^{0.7} + 6(j\omega\tau_2)^{0.8} + 2(j\omega\tau_2)^{0.83}} \quad (10)$$

$$\varepsilon_3(\omega) = 6 + 60 \frac{1 + 5(j\omega\tau_3)^{0.3}}{1 + 4(j\omega\tau_3)^{0.29} + 5(j\omega\tau_3)^{0.6} + 6(j\omega\tau_3)^{0.8}} \quad (11)$$

$\sigma_1 = 0.035$ S/m, $\sigma_2 = 0.05$ S/m, $\sigma_3 = 0.03$ S/m and $\tau_1 = 16$ ps, $\tau_2 = 5.91$ ps, $\tau_3 = 59.1$ ps.

Fig. 2 shows the reflectance and transmittance spectra as evaluated by using the proposed FDTD procedure and a fully analytical frequency-domain technique concerning (a) single layer and (b) three layers system. The excellent agreement between them fully validates the developed FDTD formulation.

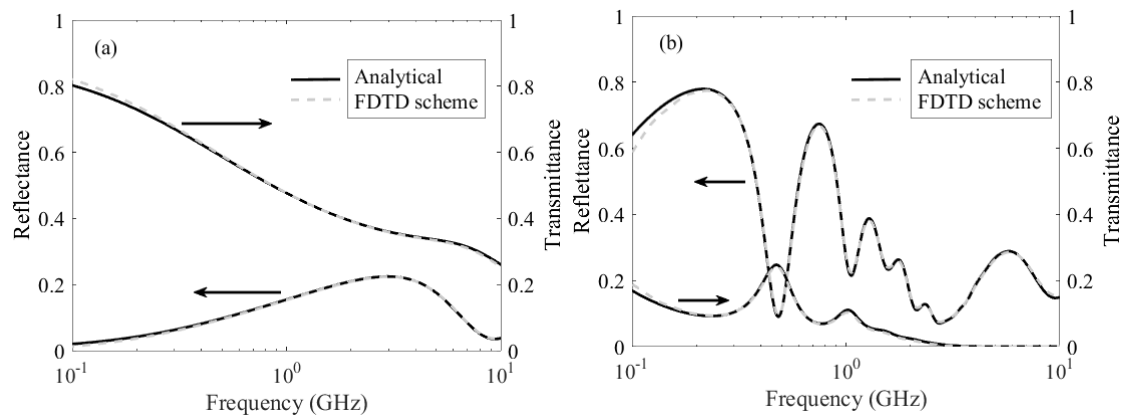


FIG. 2 – Reflectance and transmittance as a function of frequency of (a) single layer and (b) three layers dispersive media.

IV. CONCLUSION

An accurate FDTD model for simulating the pulse propagation in arbitrary dispersive media is proposed. Using the fractional derivative operator, the fractional part resulting from a general series expansion of the permittivity function of dispersive materials is directly incorporated into the FDTD scheme, avoiding the use of auxiliary differential equations. The comparison between simulation results and those evaluated by using an analytical method based on the Fourier transformation demonstrates the accuracy and effectiveness of the developed FDTD model.

ACKNOWLEDGEMENT

This work has been partially supported within the “Aiuti a Sostegno dei Cluster Tecnologici Regionali” plan: LPIJ9P2 PERFORM TECH-PUGLIA EMERGING FOOD TECHNOLOGY.

REFERENCES

- [1] M. Breton and L. Mir, “Microsecond and nanosecond electric pulses in cancer treatments,” *Bioelectromagnetics*, vol. 33, pp. 106-123, 2012.
- [2] L. Mescia, P. Bia, and D. Caratelli, “Fractional derivative based FDTD modeling of transient wave propagation in Havriliak–Negami media,” *IEEE Transactions on Microwave Theory and Techniques*, vol. 62, pp. 1920-1929, 2014.
- [3] P. Bia, D. Caratelli, L. Mescia, R. Cicchetti, G. Maione, and F. Prudenzeno, “A novel FDTD formulation based on fractional derivatives for dispersive Havriliak–Negami media,” *Signal Processing*, vol. 62, pp. 312-318, 2015.
- [4] P. Bia, D. Caratelli, L. Mescia, and J. Gielis, “Analysis and synthesis of supershaped dielectric lens antennas,” *IET Microwaves, Antennas and Propagation*, vol. 9, pp. 1497-1504, 2015.

A SIMPLIFIED RADIATION MODEL OF A WAVEGUIDE SLOT

G. Buonanno, G. Leone

Department of Industrial and Information Engineering
Second University of Naples
via Roma 29, Aversa, Italy
giovanni.leone@unina2.it

Abstract

The radiation of a waveguide slot requires the knowledge of the equivalent magnetic current, as the numerical solution of a coupling integral equation involving both internal and external Green's functions. An approximate solution for the external field is searched by resorting to the Babinet principle and the thin wire modeling of the slot. The behavior of the magnetic current agrees well with the slot fundamental mode both for non-resonant and resonant excited slots.

Index Terms– Babinet principle, Hallen approximation, Slot antenna.

I. INTRODUCTION

Waveguide slot arrays are largely employed in several applications due to the ease of fabrication. Due to the large number of radiators a full-wave numerical analysis is still resource demanding. Therefore it seems useful to resort to simplified models both for the external coupling evaluation and for the influence of the slot on the waveguide propagation. The analysis of the radiation of a slot cut over the upper wall of a rectangular waveguide requires the numerical solution of the integral equation resulting from imposing continuity conditions on the tangential magnetic field over the slot and solving for the equivalent magnetic current. Hereafter we are interested in providing a simplified appreciation of the general behavior of the solution by resorting to the application of the Babinet principle and the Hallen approximation. An analytic expression of the tangential magnetic field is so derived and compared with a numerical solution.

II. WAVEGUIDE EXCITATION

A $2l$ long and w large slot cut in the upper side of a perfectly electric conducting (PEC) infinite waveguide is considered according to the reference system of Fig. 1. It is assumed the propagation of the fundamental forward TE_{10} mode and that the slot is excited only by it, that is the influence of higher evanescent modes in proximity of the slot is neglected.

The only component of the electric field is $E_y = -\frac{\sqrt{2}V^+}{\sqrt{ab}} \cos\left[\frac{\pi}{a}(x + \alpha)\right] e^{-jk_z z}$, where V^+ is the amplitude of the equivalent voltage associated to the impinging mode, a and b are the transverse dimensions of the waveguide and k_z is the mode propagation constant. As well known the TE_{10} mode inside a rectangular waveguide can be decomposed into two TE_z plane waves with propagation vectors $\underline{k}_i = (\pm\pi/a, 0, k_z) = (\pm \sin\theta_i, 0, \cos\theta_i)$ and the problem of the evaluation of the external radiated field can be recast as the scattering of such plane waves by a slot cut into a PEC plane.

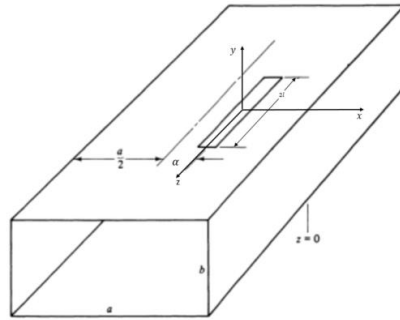


FIG. 1—The geometry of the problem.

Because of the Babinet principle such a field can be obtained by the solution of a complementary problem, that is the scattering of a PEC strip excited by a dual source, a TM_z plane wave in the present circumstance. In particular the solution for the tangential magnetic field over the strip, i.e. for the electric current over the strip, provides the behavior of the tangential electric field over the slot, from which both its radiation pattern and the influence on the waveguide propagation can be evaluated.

III. STRIP SCATTERING

If we assume a thin strip geometry $2l \gg w$, the concept of electrical equivalent radius [1] allows to treat its radiation and scattering as if it were an electrically small PEC cylinder of circular cross section and radius $a=w/4$. Adopting this approximation also for the problem at hand means to deal with the classical problem of the scattering of a thin cylinder by a plane wave of amplitude $E_0 = \frac{j}{\sqrt{2ab}} V^+ \frac{\beta}{k_z}$ (fig. 2)

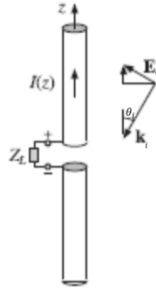


FIG. 2–Plane wave scattering by a wire

An approximate solution for the current density induced on the cylinder is provided by the Hallen approximation, which amounts to considering the current as flowing along the axis of the cylinder. We are interested in the short circuit solution that can be written as [2]

$$I(z) = 2I_{SC} \left\{ -\frac{\sin[\beta l(1 - \cos \theta_i)]}{2 \sin(\beta l)} e^{jk_0 z} - \frac{\sin[\beta l(1 + \cos \theta_i)]}{2 \sin(\beta l)} e^{-j\beta z} + \cos(\beta l) e^{-j\beta z \cos \theta_i} \right\} \frac{1}{\cos(\beta l) - \cos(\beta l \cos \theta_i)} \sin\left(\frac{\pi}{a} \alpha\right)$$

where I_{SC} is the current flowing in the $Z_L=0$ impedance for a single impinging plane wave. In turn the short circuit current can be cast as $I_{SC}=-V_{OC}/Z_A$ where V_{OC} is the open circuit voltage, that can be evaluated in terms of the transmission effective length of the wire and Z_A is the wire active impedance, when acting as an antenna. Fig 3 displays the results for different wire lengths and $\theta_i=\pi/4$.

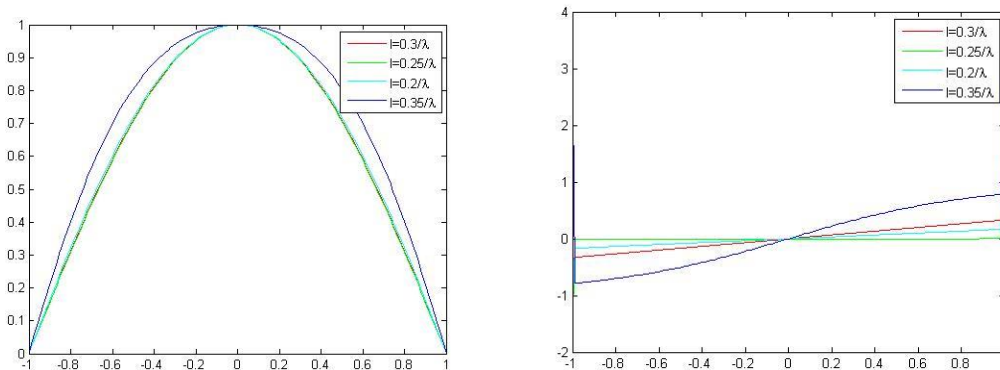


FIG. 3–Normalized modulus and phase of the current induced on a thin cylindrical scatterer under the Hallen approximation (abscissa is normalized to l/λ).

It can be appreciated that in most cases the current modulus resembles a cosine function and its phase varies very slowly. In particular if we expand the current function under the TE_{n0} modes of the slot, the energy of the fundamental mode is always larger than 80%

and close to 98% for most slot lengths of practical interest. This result agrees with the numerical solution of the relevant integral equation.

If the waveguide is closed on a PEC plane at $z=\pi/(2k_z)$, as it occurs in resonant slotted waveguide antennas, the approximate solution should account also for the backward TE_{10} mode propagation, which adds two more in-phase plane wave contributions to the induced current along the wire. The resulting current is provided by

$$\hat{I}(z) = 4I_{SC} \frac{\cos(\beta z) \cos(\beta l \cos \theta_i) - \cos(\beta l) \cos(\beta l z)}{\cos(\beta l \cos \theta_i) - \cos(\beta l)} \sin\left(\frac{\pi}{a} \alpha\right)$$

which is a purely real function agreeing always with a $\cos\left(\frac{\pi z}{2l}\right)$ function, i.e. the TE_{10} mode behavior of the slot, for more than 95% of its energy.

Finally the comparison with the numerical solution of the scattering equation for a strip is presented. The relevant Electric Field Integral Equation is solved as in [3] for a PEC strip with $w=0.05\lambda$ and plane wave impinging from $\theta_i=\pi/4$. The resulting longitudinal current is provided in fig. 4.

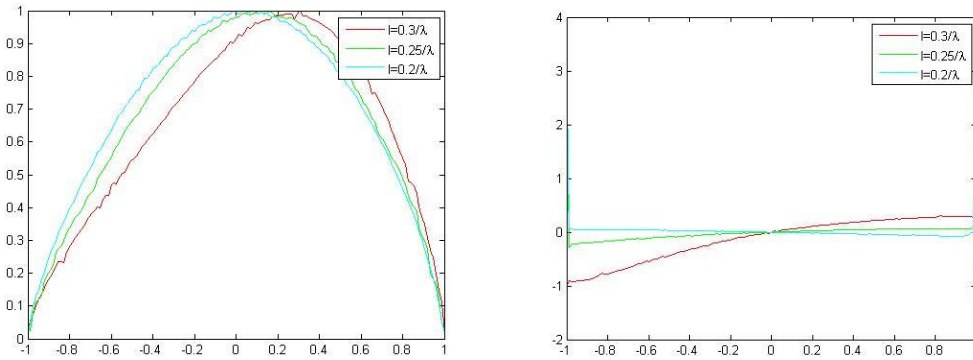


FIG. 4–Normalized modulus and phase of the current induced on a PEC strip (abscissa is normalized to l/λ).

IV. CONCLUSION

The simplified model of the excitation of a waveguide slot provides the basis to understand the numerical solution of the relevant integral equation and can be applied to determine the slot loading on the waveguide propagation via its scattering matrix and the external coupling within an array. The approach can be extended to examine the effects of waveguide higher mode and to oblique slots.

ACKNOWLEDGEMENT

This work has been partly sponsored by MBDA SpA under the "SIRena" (Sviluppo ed Industrializzazione di sistemi a Radiofrequenza e finestre elettromagnetiche) project, funded by the Italian MiSE.

REFERENCES

- [1] C. A. Balanis, "*Antenna Theory Analysis and Design*", Wiley-Interscience.
- [2] S. J. Orfanidis, "*Electromagnetic Waves and Antennas*", <http://eceweb1.rutgers.edu/~orfanidi/ewa/>
- [3] S. Makarov, "*Antenna and Electromagnetic Modeling with MATLAB*", Wiley-Interscience.

INVERSE SOURCE IMMERSSED IN INHOMOGENEOUS MEDIUM

M. A. Maisto⁽¹⁾, R. Solimene⁽¹⁾, R. Pierri⁽¹⁾

⁽¹⁾ Dipartimento di Ingegneria Industriale e dell'Informazione

Via Roma 29, Aversa (Ce), Italy

mariaantonio.maisto@unina2.it

Abstract

The role of a reflecting plane on the inverse source problem is analyzed via SVD.

Index Terms – Inverse source, resolution, NDF, inverse problems.

I. INTRODUCTION

In this paper, the case of a source radiating in proximity of a reflecting plane consisting of an interface which separates two half-space media with different electromagnetic properties is considered. The related inverse source and inverse scattering problems can benefit from reflections and scattering introduced by the hosting medium in that reflections and scattering effects can introduce a surplus of spatial diversity and can provide additional information about the probed scene. Therefore, it is our commitment to study the role played by those multipath effects by analyzing their impact on important figures as NDF and the resolution. Here, the achievable resolution is quantified as the principal lobe width of the point-spread function.

II. PERFORMANCE ANALYSIS

The geometry of the problem is sketched in Fig. 1. A reflecting plane consisting of an interface which separates two half-space media with different electromagnetic properties is located at $z = 0$. A strip of electric current J is present in the upper half-space and supported over the current domain $I = [z_1, z_2]$ along the z -axis. The source is oriented along the y -axis (i.e., along the axis of invariance). Denote with ε_1 and ε_2 the dielectric permittivity of the upper (i.e., with $z > 0$) and the lower half-spaces (i.e., with $z < 0$), respectively. For the sake of simplicity, the magnetic permeability is assumed equal to μ_0 everywhere. Also denote with k_1 and k_2 the corresponding wavenumbers. The observation domain is located in far zone in the upper half-space and the observation variable is $u = k_1 \cos \theta \in \Omega$ with $\Omega = [u_{\min}, u_{\max}]$ the observation angular corner. For the case at hand, the interface modifies the Green's function by introducing a second term that differently weighs the reflected plane-waves.

The presence of the interface is equivalent to an image source which is still symmetrically located (i.e., supported over $I' = [-z_2, -z_1]$) but now it has in general a complex amplitude. Let be \mathcal{A} the radiation operator in far zone.

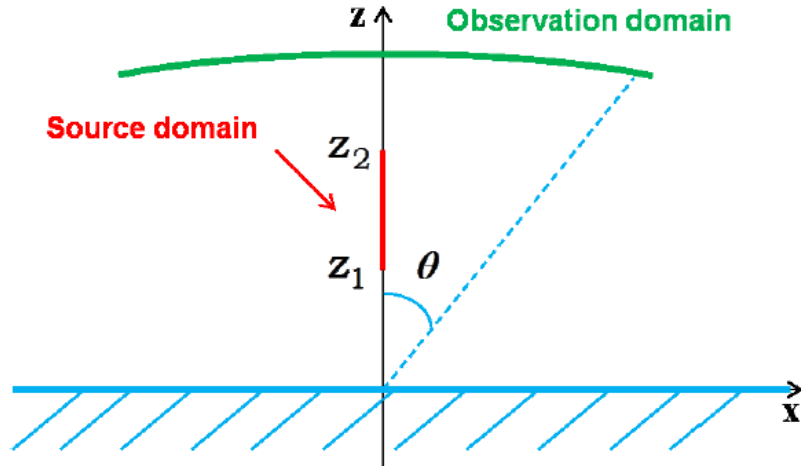


FIG. 1 – Pictorial view of the scattering configuration considered in this paper.

In [1] a procedure that allows to analytically estimate an upper and lower bound for the singular values of \mathcal{A} in terms of the once of two auxiliary operators is introduced. Accordingly, if $z_1 > \pi / \Delta$ (with $\Delta = u_{\max} - u_{\min}$) the reflection introduced by the dielectric interface shapes the singular values so that an increasing of the NDF is possible (with respect to the homogeneous background medium). However, now, this increasing depends on the dielectric jump (which dictates how fast $|\Gamma(u)|^2$ decreases) and on the chosen SVD threshold τ_{th} which in turn is linked to the stability requirements while considering the related inverse source problem. In any case, having fixed the truncation threshold, the higher the dielectric jump the larger the NDF. Of course, the perfect reflecting plane can be viewed as a limiting case .

It is interesting to note that when $\varepsilon_1 > \varepsilon_2$ a critical value $u_c = k_1 \sqrt{1 - \varepsilon_2 / \varepsilon_1}$ exists that corresponds to the so-called critical angle θ_c so that $\forall u \leq u_c$ it results $|\Gamma(u)| = 1$. This positively affects the achievable resolution.

So it is possible to assert that:

- if $u_{\max} \leq u_c$ then the singular values exhibit a step-like behavior being nearly constant and equal to $\sqrt{2\pi}$ up to the index N ; as consequence, an analytical estimation for the point-spread function can be given:

$$psf(z, z') = 2\pi \cos[u_{avg}(z - z')] \frac{\sin[\Delta(z - z') / 2]}{\pi(z - z')}$$

with $u_{avg} = \frac{u_{max} + u_{min}}{2}$. As can be seen, the reflecting plane introduces a modulating term that entails a narrowing of the main lobe of the psf but at the same time an increasing of the side-lobe level. More in detail, if $u_{min} = 0$ (this happens if the observation angular sector encompasses $\theta = \pi/2$) then the achievable resolution dz can be estimated by π/Δ and results halved (whereas the amplitude doubled) as compared to the case of no reflecting plane.

- if $u_{max} > u_c$ then the singular values stay nearly constant and equal to $\sqrt{2\pi}$ up to the index $N/2 + [(u_{max} - u_c)(z_2 - z_1)/2\pi]$. Beyond such an index the singular values decay according to the statement introduced in [1]. As concern the point-spread function, an analytical estimation cannot be given. Now, the actual bandwidth enlargement is threshold dependent. The reasoning described in [2] can be followed to get upper and lower estimations of the psf main-lobe and hence on resolution. The following estimate for the achievable resolution dz_ϵ can be deduced :

$$dz_\epsilon \leq dz_\epsilon \leq dz_\epsilon .$$

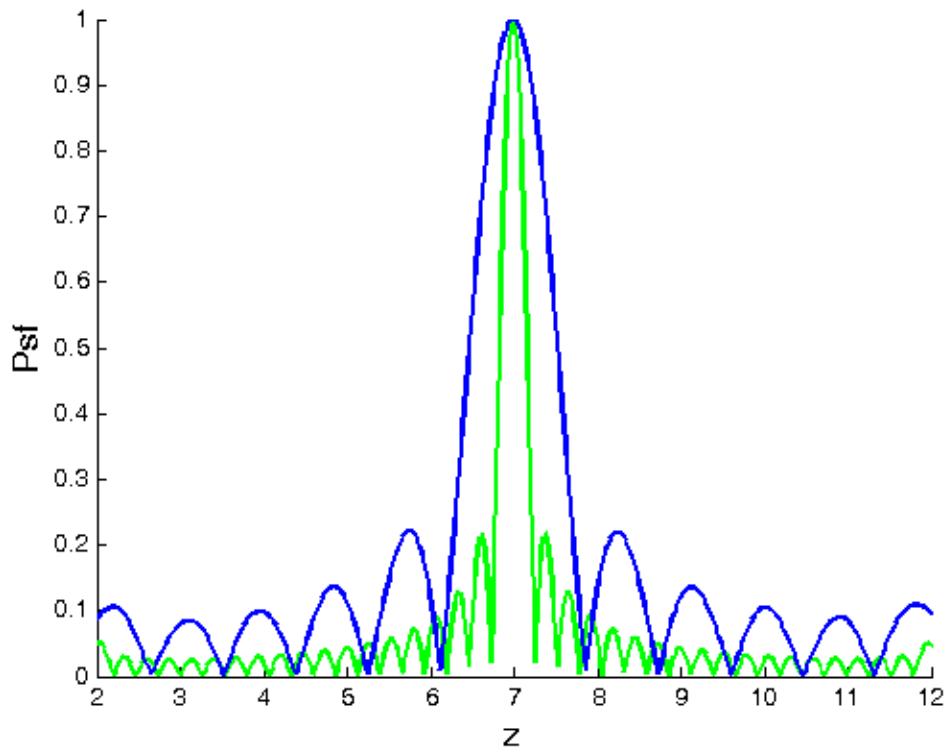


FIG. 2 – Normalized Psf amplitude for a source located at $z = z_{avg}$ with $I = [2,12]m$ and $\mathcal{G}_{max} = \frac{\pi}{2}$ and $\mathcal{G}_{min} = 0$. Blue line refers to the case where $\varepsilon_1 = \varepsilon_0$ and $\varepsilon_2 = 4\varepsilon_0$, while the green line to $\varepsilon_1 = 4\varepsilon_0$ and $\varepsilon_2 = \varepsilon_0$.

III. CONCLUSION

In this paper we studied the role played by a reflecting plane consisting of an interface which separates two half-space media on the achievable performance in the reconstruction of a strip source from far field measurements. The reflections shape the singular values so that an increasing of the NDF is possible. However, now, this increase depends on the dielectric jump (which dictates how fast $|\Gamma|^2$ decreases) and on the chosen SVD threshold τ_{th} . Accordingly, the NDF and the achievable resolution are noise-dependent. In particular, when $\varepsilon_1 > \varepsilon_2$, the singular value behaviour approaches the one of the conducting case and the achievable resolution respect to the case when $\varepsilon_1 < \varepsilon_2$ improves.

REFERENCES

- [1] R. Solimene, M. A. Maisto, R. Pierri, “Inverse source in presence of a reflecting plane for strip case,” *J. Opt. Soc. Am. A* 31, 2814-2820 (2014).
- [2] R. Solimene, M. A. Maisto, R. Pierri, “Inverse scattering in presence of a reflecting plane,” *Journal of Optics* 18, 2, 025603

COUPLING STRUCTURES FOR ON-CHIP MODE-DIVISION MULTIPLEXING SIGNAL PROCESSING

A. Parini⁽¹⁾, Y.G. Boucher⁽¹⁾, G. Bellanca⁽²⁾ C. Peucheret⁽¹⁾

⁽¹⁾ FOTON Laboratory, CNRS UMR 6082, 22305, Lannion, France

⁽²⁾ Department of Engineering, University of Ferrara, 44122, Ferrara,
Italy

alberto.parini@univ-rennes1.fr

Abstract

In this contribution, we review the operating principles of directional couplers enabling mode processing in on-chip mode-division multiplexing (MDM) interconnects. The capability of such structures to efficiently select and route specific spatial configurations of the electromagnetic field are demonstrated with the help of finite difference in time domain numerical simulations.

Index Terms – Directional couplers, mode-division multiplexing, optical networks-on-chip, photonic integrated circuits.

I. INTRODUCTION

The use of optical technologies for on-chip interconnects is proposed as a solution to meet the increasing bandwidth demand of multiple-core processor architectures, while keeping the power consumption of communication at an acceptable level.

The large majority of ONOC solutions explored so far rely for their operation on wavelength division multiplexing (WDM). However, one current limitation to the WDM approach for on-chip optical communications stems from the difficulty of integrating light sources on a silicon CMOS compatible platform. In fact, the weak maturity of the proposed integration technologies, and the contrasted performance of the fabricated devices, justify the study of an alternative approach, which will remain compatible with WDM once current integration issues are solved.

To reduce the number of sources or, in a complementary way, to optimize the use of the available ones, a possible solution relies on the exploitation of a further dimension inherent to optical communications, namely the spatial (modal) dimension. In mode-division multiplexing (MDM) techniques, communication channels are allocated, on the same wavelength, to the various propagation modes of a multi-mode waveguide. Used in conjunction with WDM, MDM not only can increase the aggregate communication bandwidth of an optical link, but also provide network designers with a new degree of freedom, the modal order, which can add further flexibility to on-chip integrated optical systems. From the experimental side, it is worth noting that point to point on-chip MDM links [1] and also multi-port topologies [2]

have been recently fabricated and characterized, showing promising performance.

II. ASYMMETRIC DIRECTIONAL COUPLERS

In MDM based circuits, multimode waveguides simultaneously transmit signals carried by different spatial modes at the same wavelength. This requires mode multiplexing and de-multiplexing devices, in order to selectively couple a channel to a specific mode. Mode multiplexing can be implemented by means of an asymmetric directional coupler between a narrow single mode waveguide and an adjacent wide multimode bus waveguide, as sketched in Fig. 1(a). In this configuration, by properly dimensioning the two waveguides widths, the effective refractive index of the fundamental TE_0 mode of the narrow waveguide is matched to the effective refractive index of the TE_N mode of the wider one, toward which we need to multiplex. Thanks to this index matching, power exchange can take place efficiently even between modes with different transverse spatial shapes. As stated before, in an asymmetric coupler, index matching is achieved by suitably choosing the widths of the two coupled waveguides. Therefore, such devices can be engineered with the help of the modal dispersion curves. To detail the design procedure, we refer to a silicon on insulator (SOI) technological platform in which waveguides have a core made of crystalline silicon ($n = 3.45$) with cross section $W \times H$ (width \times height), and are completely surrounded by silicon dioxide ($n = 1.45$). Fig. 1(b) shows the dispersion curves relating the effective indices of the TE_0 , TE_1 and TE_2 modes to the waveguide width W , at the wavelength of $\lambda = 1550$ nm and for $H = 250$ nm. By following the black-dashed arrows in panel (b), it can be observed how the TE_0 mode of a single mode waveguide of width $W_0 = 440$ nm presents the same effective index ($n_{\text{eff}} = 2.38$) as the TE_1 mode of a two-mode waveguide of width $W_1 = 900$ nm. This index matching condition thus ensures an efficient coupling between TE_0 and TE_1 modes. This approach can be scaled up to couple to higher order modes; in fact the TE_0 mode of the single mode (W_0) waveguide is also index matched to the TE_2 mode of a $W_2 = 1380$ nm three-mode waveguide. In Fig. 1(c) we report FDTD simulation results of the electric field propagation on a TE_0 to TE_1 mode multiplexer designed following the parameters extracted from Fig. 1(b). As one can note, the TE_0 mode (blue arrow) injected in the single mode W_0 waveguide is progressively converted to the TE_1 mode of the W_1 one (red arrow). The same behavior holds for a TE_0 to TE_2 mode multiplexer, as illustrated in Fig. 1(d).

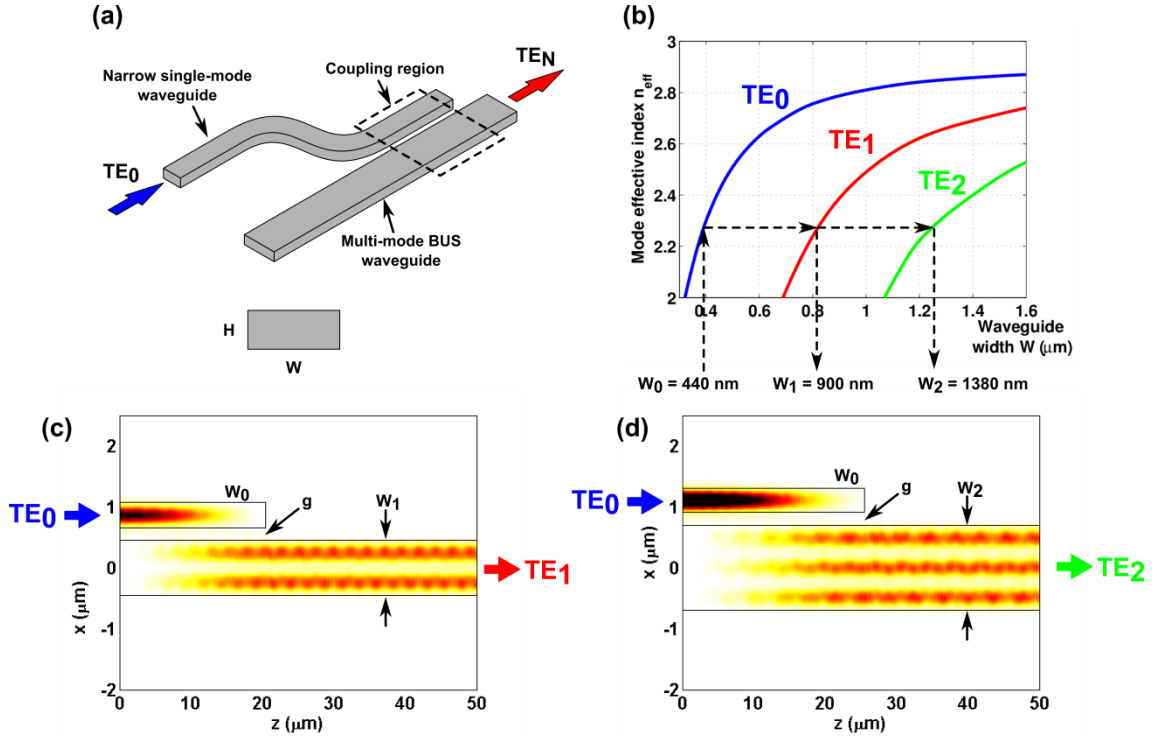


FIG. 1 – (a) 3D view of an asymmetric directional coupler where the TE_0 mode of a single-mode narrow waveguide is coupled to the TE_N mode of a multi-mode bus waveguide (the inset shows waveguide dimensions). (b) Dispersion curves for a $H = 250$ nm high waveguide relating the effective indices of the TE_0 , TE_1 and TE_2 modes to the waveguide width W . The black dashed arrows show that the fundamental TE_0 mode of a 440 nm (W_0) wide single-mode waveguide can be index-matched to the TE_1 mode of a 900 nm (W_1) wide two-mode waveguide or to the TE_2 mode of a 1380 nm (W_2) wide three mode waveguide. (c) Top view of the field evolution in an asymmetric directional coupler engineered to convert the fundamental TE_0 mode of a narrow single-mode W_0 waveguide to the TE_1 mode of a two-mode W_1 waveguide. (d) Field evolution for a TE_0 to TE_2 coupler. All the simulations refer to $\lambda = 1550$ nm.

III. SYMMETRIC TWO-MODE DIRECTIONAL COUPLER

In this section, we present a two-mode symmetric coupler enabling mode-selective routing between two multi mode bus waveguides. The layout is sketched in Fig. 2(a). Here, a two-mode bus waveguide (BUS 1) guiding the TE_0 and TE_1 modes, is placed beside a second identical waveguide (BUS 2) at a distance g . Due to symmetry TE_0 and TE_1 modes are periodically exchanged, with different coupling lengths, between the two bus. Panels (b) and (c) of Fig. 2 show the propagation of TE_0 and TE_1 modes, respectively, when they are injected individually in the coupler on BUS 1. Because of their different effective indices, the periodic power exchange of TE_1 takes place on a shorter spatial period than that of TE_0 . This inherent difference in the coupling lengths can be exploited to separate the modes if the length L of the coupler is suitably chosen. By comparing the field evolution of the two modes, one can note

that at the distance $Z = Z_s = 70 \mu\text{m}$ the TE_0 mode is present only on BUS 2, thus allowing a complete separation of the two modes: TE_1 is transmitted on BUS 1 while, at the same time the TE_0 is completely routed to BUS 2 (see Fig. 2(d)).

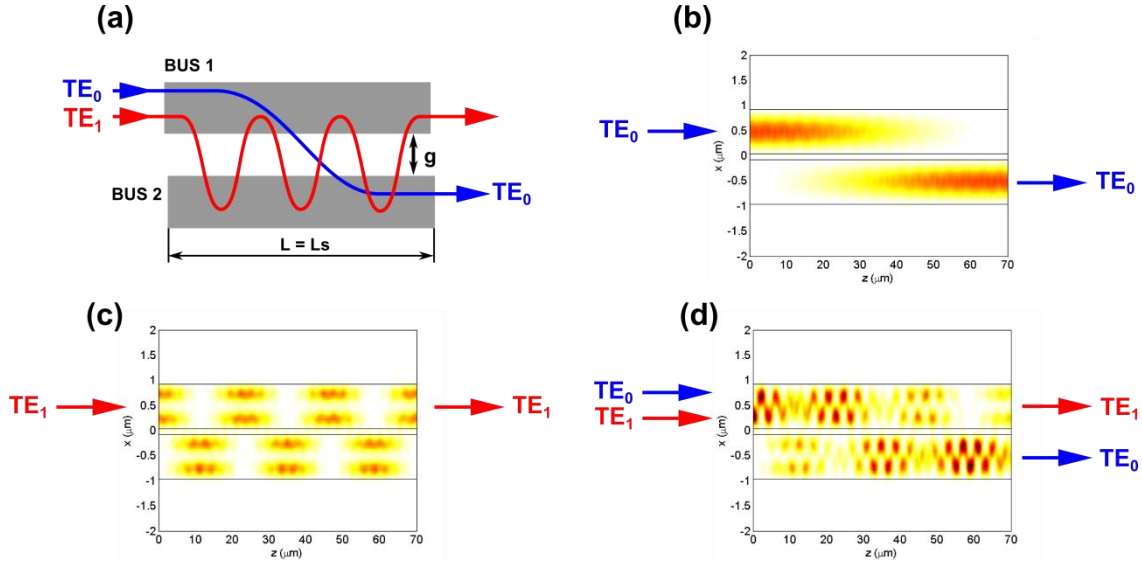


FIG. 2 – (a) Schematic of a two-mode directional coupling showing the de-multiplexing functionality. (b) Field evolution in the two-mode coupler when the mode injected in BUS 1 is the TE_0 mode, (c) the TE_1 mode, or (d) both modes. All the simulations refer to $\lambda = 1550 \text{ nm}$.

IV. CONCLUSION

In this contribution, starting from dispersion relations and modal index matching concepts, we reviewed the operating principles of directional couplers for on-chip mode division multiplexing (MDM). Those functional building blocks allow forming networks-on-chip where modal diversity is exploited in conjunction with wavelength multiplexing.

ACKNOWLEDGEMENT

This work is supported by the French National Research Agency program “Investing for the Future” ANR-10-LABX-07-01 within the framework of the “3D-Optical-ManyCores” project.

REFERENCES

- [1] Y. Ding, J. Xu, F. Da Ros, B. Huang, H. Ou, and C. Peucheret, “On-chip two-mode division multiplexing using tapered directional coupler based mode multiplexer and demultiplexer,” *Opt. Express* vol. 21, no. 8, pp. 10376-10382, Apr. 2013.
- [2] B. Stern, X. Zhu, C. P. Chen, L. D. Tzuang, J. Cardenas, K. Bergman, and M. Lipson, “On-chip mode division multiplexing switch,” *Optica*, vol. 2, no. 6, pp. 530-535, Jun. 2015.

Electromagnetic scattering by rotating axisymmetric objects

Praveen Kalarickel Ramakrishnan¹, Mirco Raffetto¹

¹ Department of Electrical, Electronic, Telecommunication
Engineering, and Naval Architecture (DITEN),
University of Genoa, Via Opera Pia 11a, 16145, Genoa, Italy
e-mail: 4079505@studenti.unige.it, raffetto@dibe.unige.it

Abstract

A three-dimensional finite element simulator has been generalized to solve time-harmonic electromagnetic problems involving bianisotropic media. Since moving objects are perceived as made up of bianisotropic media, the new code is exploited to solve electromagnetic scattering problems in the presence of rotating axisymmetric objects. Some considerations on the reliability of the simulator are presented, together with some preliminary numerical results.

Index Terms: electromagnetic scattering, moving media, rotating axisymmetric objects, finite element method.

I. Introduction

The importance of electromagnetic scattering by rotating axisymmetric objects is well recognized in several areas [1]. Unfortunately, any object is perceived as being made of a bianisotropic medium in any reference frame in which the object itself is not at rest [2], [3]. This could be the reason for the scarcity of numerical results for these problems.

We have recently generalized a three-dimensional finite element simulator. It is now able to approximately solve time-harmonic boundary value problems involving bianisotropic media [4]. Such a simulator can then be used to solve problems involving moving objects, when the boundaries of the moving objects are stationary [3]. It is able to deal, in particular, with the scattering by rotating axisymmetric objects.

In this paper we present the mathematical formulation of the problem of interest and of its finite element discretization, their main features and some preliminary numerical results.

II. Outline of Mathematical Formulation

The boundary value problem of interest for electromagnetic scattering is [4]:

$$\begin{cases} \operatorname{curl} \mathbf{H} - j\omega \mathbf{D} = \mathbf{J}_e & \text{in } \Omega \\ \operatorname{curl} \mathbf{E} + j\omega \mathbf{B} = -\mathbf{J}_m & \text{in } \Omega \\ \mathbf{H} \times \mathbf{n} - Y (\mathbf{n} \times \mathbf{E} \times \mathbf{n}) = \mathbf{f}_R & \text{on } \Gamma \end{cases} \quad (1)$$

where Ω is the region in which our problem is formulated, Γ is its boundary, \mathbf{J}_e and \mathbf{J}_m are, respectively, the electric and magnetic sources, Y is the boundary admittance and \mathbf{f}_R is the source term of the boundary condition enforced on Γ .

We assume that all media involved are linear and isotropic in their rest frames and there characterized by ε_r and μ_r . Unfortunately, in the presence of motion the constitutive equations become much more complex and assume the following form [3], [4]:

$$\begin{cases} \mathbf{D} = (1/c) \mathbf{P}\mathbf{E} + \mathbf{L}\mathbf{B} & \text{in } \Omega \\ \mathbf{H} = \mathbf{M}\mathbf{E} + c\mathbf{Q}\mathbf{B} & \text{in } \Omega \end{cases} \quad (2)$$

Here P , L , M and Q are matrices depending on ε_r , μ_r of the media in their rest frames and on their velocities. c is the speed of light.

The variational formulation equivalent to (1) and (2) refers to a space of fields U and is [4]:

$$\text{Find } \mathbf{E} \in U : a(\mathbf{E}, \mathbf{v}) = l(\mathbf{v}) \quad \forall \mathbf{v} \in U, \quad (3)$$

where:

$$\begin{aligned} a(\mathbf{u}, \mathbf{v}) = & c(Q \operatorname{curl} \mathbf{u}, \operatorname{curl} \mathbf{v})_{0,\Omega} - \frac{\omega^2}{c} (P \mathbf{u}, \mathbf{v})_{0,\Omega} - j\omega (M \mathbf{u}, \operatorname{curl} \mathbf{v})_{0,\Omega} \\ & - j\omega (L \operatorname{curl} \mathbf{u}, \mathbf{v})_{0,\Omega} + j\omega (Y (\mathbf{n} \times \mathbf{u} \times \mathbf{n}), \mathbf{n} \times \mathbf{v} \times \mathbf{n})_{0,\Gamma} \end{aligned} \quad (4)$$

$$l(\mathbf{v}) = -j\omega (\mathbf{J}_e, \mathbf{v})_{0,\Omega} - c(Q \mathbf{J}_m, \operatorname{curl} \mathbf{v})_{0,\Omega} + j\omega (L \mathbf{J}_m, \mathbf{v})_{0,\Omega} - j\omega (\mathbf{f}_R, \mathbf{n} \times \mathbf{v} \times \mathbf{n})_{0,\Gamma}. \quad (5)$$

Here the inner products are defined as $(\mathbf{u}, \mathbf{v})_{0,\Omega} = \int_{\Omega} \mathbf{v}^* \mathbf{u} dV$ and $(\mathbf{u}, \mathbf{v})_{0,\Gamma} = \int_{\Gamma} \mathbf{v}^* \mathbf{u} dS$. The above variational formulation can be approximated by a Galerkin finite element method by considering a suitable subspace U_h of U as follows:

$$\text{Find } \mathbf{E}_h \in U_h : a(\mathbf{E}_h, \mathbf{v}_h) = l(\mathbf{v}_h) \quad \forall \mathbf{v}_h \in U_h. \quad (6)$$

Our finite element simulator (which is based on (6)) has been generalized to compute (4) and (5) and is able to solve problems involving rotating axisymmetric objects. The user has to provide P , L , M and Q in Ω . Outside the rotating objects one easily gets $P = c\varepsilon_0\varepsilon_r I_3$, $Q = \frac{1}{c\mu_0\mu_r} I_3$, $L = M = 0$, where I_3 is the identity matrix. For rotating axisymmetric objects the determination of the matrices requires more work [2]. For example, for objects rotating about the z axis with angular velocity ω_r one gets $P_{xz} = P_{zx} = P_{yz} = P_{zy} = L_{xx} = L_{yy} = L_{zz} = L_{xy} = L_{yx} = Q_{xz} = Q_{zx} = Q_{yz} = Q_{zy} = 0$, and, with $k = \frac{\omega_r(\varepsilon_r\mu_r - 1)}{\mu_0\mu_r c(c^2 - \omega_r^2(x^2 + y^2))}$, $P_{xy} = P_{yx} = kxy$, $P_{xx} = \varepsilon_0\varepsilon_r c + kx^2$, $P_{yy} = \varepsilon_0\varepsilon_r c + ky^2$, $P_{zz} = \varepsilon_0\varepsilon_r c + k(x^2 + y^2)$, $Q_{xy} = Q_{yx} = -P_{xy}$, $Q_{xx} = \frac{1}{\mu_0\mu_r c} - kx^2$, $L_{xz} = -L_{zx} = kx$, $L_{yz} = -L_{zy} = ky$, $L = M$, $Q_{yy} = \frac{1}{\mu_0\mu_r c} - ky^2$, $Q_{zz} = \frac{1}{\mu_0\mu_r c} - k(x^2 + y^2)$. Other cases can be managed in similar ways referring to [2].

III. Well posedness of the problem of interest and convergence of the numerical approximation

All basic elements to get a result of well posedness of the problem of interest and of convergence of the finite element approximation seem to be available [5], [6]. As a matter of fact, these elements were exploited to obtain the indicated results

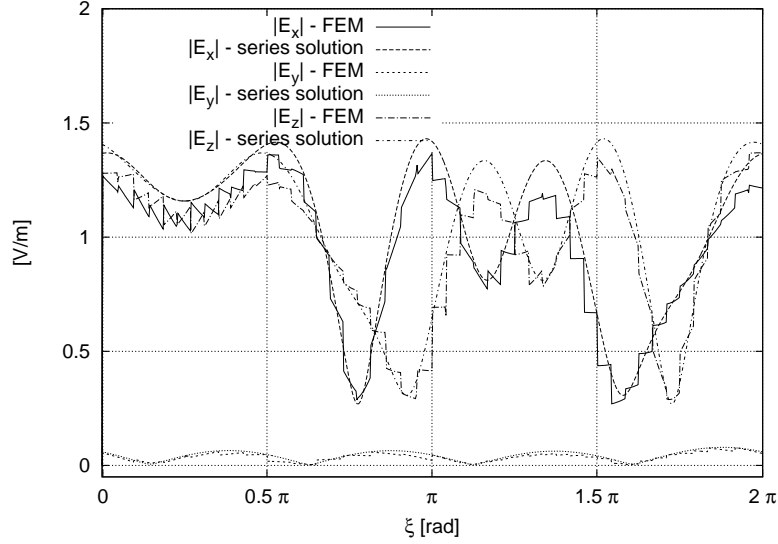


Figure 1: Magnitudes of electric field components along a circle in the (x, z) plane. The circle has radius 1.5 m and is centered at the origin. The angle is defined by $\xi = \theta + \frac{3\pi}{2}$, $\theta \in [0, \frac{\pi}{2}]$, $\varphi = \pi$; $\xi = \theta - \frac{\pi}{2}$, $\theta \in [\frac{\pi}{2}, \pi]$, $\varphi = \pi$; $\xi = -\theta + \frac{3\pi}{2}$, $\theta \in [0, \pi]$, $\varphi = 0$. The sphere is characterized by $R = 1$ m and by $\varepsilon_r = 4$ and $\mu_r = 2$ in its rest frame. It is hosted in vacuum and rotates with $\omega_r = 5 \cdot 10^{-3} c$ about the z axis. The illuminating plane wave has $f = 75$ MHz.

for electromagnetic boundary value problems involving axially moving cylinders [6]. Specific results of well posedness of the three-dimensional electromagnetic scattering problem and of convergence of the numerical approximation in the presence of rotating axisymmetric objects are still missing, however. We hope to be able to report additional information on this topic at the conference since, at present, we are working on it.

IV. Numerical results

Our simulator can manage problems involving several objects, rotating about different axes and having general axisymmetric geometries and constitutive parameters. However, since the convergence of the finite element approximation has not been proved so far, we begin by considering a simple case allowing the computation of the solution by a semi-analytical technique [1].

For this reason we consider a sphere (centered at the origin) of radius $R = 1$ m, made up of a medium having $\varepsilon_r = 4$ and $\mu_r = 2$ in its rest frame. It is hosted in vacuum and rotates with $\omega_r = 5 \cdot 10^{-3} c$ about the z axis. It is illuminated by a uniform plane wave of frequency $f = 75$ MHz, having $E_{x,incident} = -\frac{1}{\sqrt{2}} e^{-j\frac{\omega}{\sqrt{2}c}(x+z)}$, $E_{y,incident} = 0$, $E_{z,incident} = \frac{1}{\sqrt{2}} e^{-j\frac{\omega}{\sqrt{2}c}(x+z)}$.

In Figure 1 we show a comparison of the magnitudes of the electric field components computed using the two independent procedures along a circle centered at the origin of radius 1.5 m in the (x, z) plane. The numerical solution is computed by considering a spherical domain of numerical investigation of radius 4 m. It is

discretized by 40 spherical shells of thickness 0.1 m. The volumetric sources are set to zero and \mathbf{f}_R is determined by the incident field.

The results computed by our finite element simulator are in good agreement with the semi-analytical ones. Even the smallest of the three components is very well approximated.

It could be useful to observe that the x and z components of the electric field are not significantly affected by the rotation of the sphere. On the contrary, E_y is heavily changed. As a matter of fact, it is equal to zero in the motionless case and reaches a peak value of 0.08 [V/m] when $\omega_r = 5 \cdot 10^{-3} c$. These are the reasons why E_y provides more information on the rotational speed of the scatterer.

The accuracy that the finite element simulator seems to be able to guarantee for all components could be an important feature for inverse scattering procedures dealing with the reconstruction of the rotational speed of axisymmetric objects [7].

V. Conclusions

In this paper the numerical solution of time-harmonic electromagnetic boundary value problems involving rotating axisymmetric objects is discussed. The reliability of the numerical results is analyzed from a theoretical and a practical point of view. Some preliminary results and comparisons are provided.

References

- [1] D. D. Zutter, "Scattering by a rotating dielectric sphere," *IEEE Transactions on Antennas and Propagation*, vol. 28, pp. 643–651, September 1980.
- [2] A. Sommerfeld, *Electrodynamics*. Lectures on theoretical physics, Academic Press, 1959.
- [3] D. K. Cheng and J.-A. Kong, "Covariant descriptions of bianisotropic media," *Proceedings of the IEEE*, vol. 56, pp. 248–251, March 1968.
- [4] P. Fernandes and M. Raffetto, "Well posedness and finite element approximability of time-harmonic electromagnetic boundary value problems involving bianisotropic materials and metamaterials," *Mathematical Models and Methods in Applied Sciences*, vol. 19, pp. 2299–2335, December 2009. DOI No: 10.1142/S0218202509004121.
- [5] P. Fernandes, M. Ottonello, and M. Raffetto, "Regularity of time-harmonic electromagnetic fields in the interior of bianisotropic materials and metamaterials," *The IMA Journal of Applied Mathematics*, vol. 79, pp. 54–93, February 2014.
- [6] M. Brignone and M. Raffetto, "Well posedness and finite element approximability of two-dimensional time-harmonic electromagnetic problems involving non-conducting moving objects with stationary boundaries," *ESAIM: Mathematical Modelling and Numerical Analysis*, vol. 49, pp. 1157–1192, July-August 2015.
- [7] M. Pastorino, M. Raffetto, and A. Randazzo, "Electromagnetic inverse scattering of axially moving cylindrical targets," *IEEE Transactions on Geoscience and Remote Sensing*, vol. 53, pp. 1452–1462, March 2015.

A LOW-PROFILE ULTRAWIDEBAND ANTENNA FOR AUTOMOTIVE APPLICATIONS

A. Michel⁽¹⁾, V. Franchina⁽¹⁾, P. Nepa⁽¹⁾, G. Manara⁽¹⁾, M. Gallo⁽²⁾, I. Moro⁽²⁾, D. Zamberlan⁽²⁾

⁽¹⁾ Dept. of Information Engineering, University of Pisa
via Caruso 16, 56122, Pisa, Italy

⁽²⁾ Calearo Antenne S.p.A.
via Bacchiglione 49, Isola Vicentina (VI), Italy
e-mails: a.michel@iet.unipi.it, vittorio.franchina@gmail.com,
p.nepa@iet.unipi.it, g.manara@iet.unipi.it, mgallo@calearo.com,
imoro@calearo.com, dzamberlan@calearo.com

Abstract

A novel X-band antenna is proposed for automotive applications. In details, an array of two Vivaldi antennas has been designed in a back-to-back configuration for Vehicle to Infrastructure (V2I) system. Since the antenna is mounted on the metallic car roof, the antenna can be split in half to reduce the overall antenna size. A relatively high gain is obtained both in front and rear direction of the vehicle. Furthermore, thanks to the presence of a 180-degree hybrid coupler, the two antennas are excited with out-of-phase currents. As a consequence, the field radiation in the transversal direction is attenuated and the multipath effect due to the presence of buildings is decreased.

Index Terms—Automotive, wideband antenna, Vivaldi antenna, Vehicle to Infrastructure

I. INTRODUCTION

In the framework of automotive applications the number of infotainment communication and telematic services in the same vehicle is rapidly increasing to improve the driving safety and quality. At the same time, the increase of wireless functionalities results in a growing complexity of dedicated vehicular electronic systems, networks, and architectures [1], since wireless applications cover a large range of frequencies – from AM (535-1605 kHz) and FM (87.5-108 MHz) bands, to LTE/GSM/UMTS (690-960MHz, 1710-2170MHz, 2490-2690MHz) and WiFi (2400-2485 MHz) bands. In order to avoid significant changing of the car aesthetic and layout, the radiating elements are often miniaturized. In particular, for low-frequency applications such as AM/FM or DAB (174-240 MHz), the antenna available space is considerably smaller than the wavelength (electrically small radiating elements), and so a performance degradation is expected in terms of bandwidth and gain. With the technological progress of electronic devices, high-frequency applications are being considered and integrated in the same vehicle, as for example for C2C (5800-5900MHz) applications [2],[3]. Indeed, for high-frequency operating bands, the antenna size is physically small so that satisfactory performance in terms of gain and bandwidth is maintained. Nevertheless, more radiating elements can share the same available space, as in MIMO

systems. Among new high frequency applications, Vehicle to Infrastructure (V2I) communication systems in the X-band are attracting interest.

In the specific X-band V2I application considered in this paper, cars communicate with in front and behind vehicles to avoid rear-end collisions, and share information with ground V2I network nodes. Specifically, in this paper a novel antenna is presented, consisting in two Vivaldi antennas designed on the same substrate in a back-to-back configuration. Hence, a relatively high gain over the entire frequency band is achieved in both the frontal and rear direction. The required attenuation on the transverse plane is obtained by feeding the two ultra wideband (UWB) Vivaldi antennas with out-of-phase currents. Moreover, since the antenna is mounted on a large metallic car roof, the antenna height can be split in half, to better fill the limited available volume.

II. ANTENNA LAYOUT

The Vivaldi antenna proposed in [4] has been properly modified and miniaturized to fit the limited available space and to fulfill the European regulation on the maximum antenna height over the car's roof. In Fig. 1, the complete layout of the back-to-back Vivaldi antenna for X-Band (8.5-11 GHz) automotive applications is shown. The main antenna's dimensions are $A=6.8\text{mm}$, $B=2\text{mm}$, $C=2\text{mm}$, $h_v=8.2\text{mm}$, $L=31.5\text{mm}$, $L_v=29.3\text{mm}$, $R=4\text{mm}$, $R_v=1.5\text{mm}$, $W=68\text{mm}$. The antenna is printed on a $31.5\times 68\text{ mm}^2$ ($L\times W$) grounded 0.73mm-thick Rogers RO4350 ($\epsilon_r = 3.66$, $\text{tg}\delta = 0.004$) dielectric substrate.

In order to obtain a field attenuation in the direction transverse to the driving direction (z -axis in Fig. 1), the two slot Vivaldi Antennas are excited with out-of-phase currents through a 180° -hybrid T-Junction. In this way, due to the symmetry of the antenna, the overall antenna radiation pattern is characterized by a vanishing field on the transverse plane. The wideband 180° -hybrid T-Junction [5] has been optimized to fit the available space on the substrate. In Fig. 1a the hybrid T-junction is highlighted with a red color (dark), since it is etched on the top-layer of the substrate. Furthermore, meanders have been introduced to reduce the surface currents along the edges of the ground plane, which are responsible for the back radiation of each Vivaldi antenna [6]. Also, the overall antenna height can be reduced thanks to the Image Theorem, exploiting the presence of the metallic car's roof.

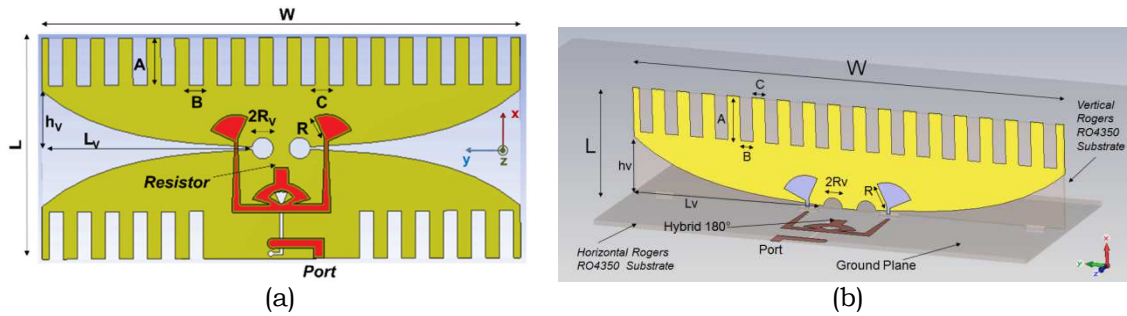


Fig. 1. (a) Complete layout of the proposed antenna that consists of two slotted Vivaldi antennas (yellow color, etched on the bottom of the substrate) and a miniaturized wideband 180° hybrid (red color, printed on the top of the substrate). The metallic car roof can be exploited to reduce the antenna size.

In Fig. 2a the simulated reflection coefficient of the antenna shown in Fig. 1b is plotted. In Fig. 2b the radiation pattern on the horizontal plane (YZ plane in Fig. 1) is shown at the frequency of 10.5GHz. By introducing the horizontal substrate with the 180-degree hybrid coupler, the layout symmetry is slightly perturbed, so that also the antenna radiation pattern is not perfectly symmetrical. Anyway, minima are visible along the transversal direction (z-axis in Fig. 2).

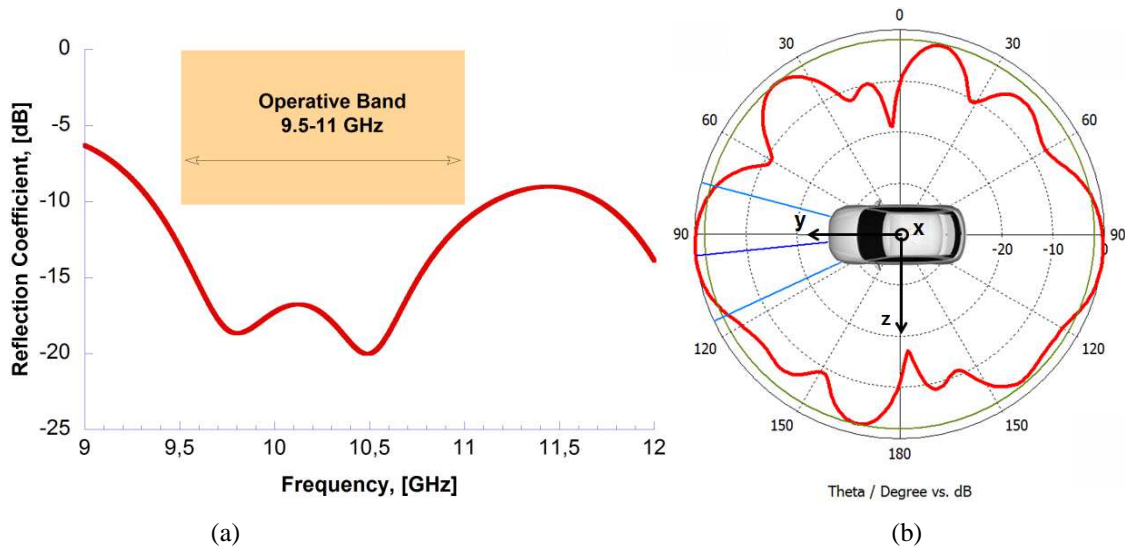


Fig. 2. Simulated (a) reflection coefficient and (b) radiation pattern on the horizontal plane (YZ plane in Fig. 1) computed at the frequency of 10.5GHz for the configuration shown in Fig. 1b.

III. CONCLUSION

An array of two Vivaldi antennas in a back-to-back configuration is here proposed for V2I applications in X-band (8.5-11GHz). A relatively high gain is obtained both in front and rear with respect to the car driving direction. A microstrip 180° hybrid has been properly miniaturized and

used to feed the two antennas with out-of-phase currents. Thus, thanks to the symmetry of the layout structure, a valuable field attenuation is obtained in the transverse plane, so attenuating multipath effects due to the wave reflections at the building surfaces in urban scenarios. Finally, the presence of the metallic car roof is exploited to split the antenna size in half according to the Image Theorem.

REFERENCES

- [1] D. Zamberlan, and M. PannoZZo, "Potential implications and road mapping of satellite bidirectional S-band antennas in the automotive market", *IEEE Antennas and Propagation Magazine*, vol.56, no.2, pp.240-250, April 2014
- [2] M. Gallo, S. Bruni, M. PannoZZo, D. Zamberlan, R. Caso, and P. Nepa, "Design and experimental validation of a windscreen patch array for C2C communications," *IEEE Antennas and Propagation Society International Symposium (APSURSI)*, pp.2063-2064, 7-13 July 2013
- [3] M. Gallo, S. Bruni, M. PannoZZo, and D. Zamberlan, "Performance evaluation of C2C antennas on car body," *7th European Conference on Antennas and Propagation (EuCAP)*, pp.3136-3139, 8-12 April 2013
- [4] Y. Yang, Y. Wang, and A. E. Fathy, "Design of compact Vivaldi Antenna Arrays for UWB see through wall applications", *Progress In Electromagnetic Research (PIER)*, Vol. 82, pp. 401-418, 2008.
- [5] M. E. Bialkowski and Y. Wang, "Wideband Microstrip 180° Hybrid Utilizing Ground slots", *IEEE Microwave And Wireless Components Letters*, Vol. 20, no. 9, September 2010.
- [6] K. Ma, Z. Q. Zhao, J. N. Wu, M. S. Ellis and Z. P. Nie, "A printed Vivaldi Antenna with improved radiation patterns by using two pairs of Eye-Shaped Slots for UWB applications", *Progress In Electromagnetic Research (PIER)*, Vol. 148, pp. 63-71, 2014.

NUMERICAL ANALYSIS OF THE RFID PRINTER ENCODER ANTENNAS PERFORMANCE

A. Michel, A. Buffi, P. Nepa, and G. Manara
Dept. of Information Engineering, University of Pisa
via Caruso 16, 56122, Pisa, Italy
[a.michel](mailto:a.michel@iet.unipi.it), [a.buffi](mailto:a.buffi@iet.unipi.it), [p.nepa](mailto:p.nepa@iet.unipi.it), [g.manara](mailto:g.manara@iet.unipi.it)

Abstract

An optimal antenna solution for UHF-RFID printer-encoder is discussed in this paper. Since, a printer-encoder antenna has to reliably communicate with only one targeted tag among a number of tightly spaced transponders in very close proximity, a numerical investigation is carried out in terms of spatial selectivity. Being the distance between the encoder antenna and the tags of a few millimeters only, antennas for UHF-RFID printer encoders are more similar to electromagnetic couplers and a specific analysis is required in terms of power transferred by the encoder to the transponder chip. A reader antenna identical to the tag antenna is proposed and a preliminary numerical investigation is here presented.

Index Terms – UHF-RFID printer-encoders, near-field coupling, near-field antenna, power transfer

I. INTRODUCTION

Near-field (NF) UHF-RFID systems are receiving a particular interest for item level tagging applications in smart shelves/drawers [1] and desktop readers [2]-[5] for retail or pharmaceutical industry. The field in close proximity to the reader antenna has to be as large as possible [6], while the far-field radiation must be limited to avoid false-positive issues and cross readings. In such framework, the RFID printer-encoder represents a specific application involving the near-field coupling between reader and transponder antennas [7]-[10]. The RFID printer-encoder manages smart labels composed by barcode and human-readable text (typically printed on paper or plastic substrates), combined with an UHF-RFID transponder that has to be encoded. The smart labels are typically attached on an adhesive roll and during encoding process, they approach very close to the reader antenna at a distance of only few millimeters, in order to maximize the power delivered to the RFID chip. Since the encoder antenna has to communicate with one RFID tag at a time, by limiting the interference with adjacent transponders, the encoder antenna selectivity represents a fundamental parameter for a RFID printer-encoder being the tagged labels close each other. In [8], such an antenna feature is named as spatial selectivity, that is the antenna capability to reliably communicate with the desired transponder without activating the surrounding ones. Moreover, the printer-encoder antenna must be compact to be easily integrated into the device mechanical structure.

Some solutions for antenna employed in commercial RFID printer-encoders have been patented [8]-[10] and they basically consist of

microstrip, stripline and double-conductor stripline technology, ended on open or matched loads. It is worth noting that, the capability of the encoder antenna to communicate selectively with only one specific tag among a number of tightly spaced transponders in very close proximity differentiates this typology of antennas from the others commonly used in NF UHF-RFID applications. In a certain sense, antennas for UHF-RFID printer-encoders result more similar to electromagnetic couplers than to antennas and a specific analysis is required in terms of power transferred by the encoder to the transponder chip.

In this paper, an optimal antenna solution for the RFID printer-encoder is discussed, which is represented by the so-called *matched antenna* configuration (namely, a reader antenna equal to the tag antenna). An equivalent electric circuit is considered to numerically evaluate the power delivered to the RFID chip when using commercial UHF-RFID tags layout. The antenna performance is evaluated in terms of the level and spatial selectivity of the power delivered to the transponder chip.

II. PRELIMINARY NUMERICAL RESULTS

In a typical RFID printer-encoder scenario, the encoder antenna (*i.e.* reader antenna) and the transponder planes are parallel to each other. For sake of simplicity, the mutual coupling effect due to the presence of several tags close each other has been neglected in the present analysis, and only one smart label slides along the rectilinear feed direction, at a distance of $d=5$ mm from the reader antenna (Fig. 1a). The offset between the reader and transponder antennas, measured along the feed direction, is denoted by Δ . In Fig. 1b the equivalent circuit of the overall system is shown. The reader is represented by a 1 V voltage generator with a 50- Ω internal resistance and the tag antenna is connected to an impedance load equal to the chip impedance value at the working frequency of 915 MHz, as stated by the chip producer (Z_{chip}). The impedance matrix \underline{Z} for the two-port network made by the encoder and transponder antennas, and the air space between them is obtained by means of the commercial numerical tool CST Microwave Studio[®], at the working frequency. An L-shaped matching circuit made of two reactive loads X_A , X_B , has been included in the circuit to maximize the power transferred by the reader to the chip when the reader antenna and the transponder are perfectly aligned ($\Delta=0$ mm). Firstly, a full-wave simulation is performed when the reader antenna and the transponder are perfectly aligned ($\Delta=0$ mm). By extracting the impedance matrix \underline{Z} for the two-port network, the values of X_A , X_B are set to maximize the power transferred to the tag chip (P_{chip}). Then, P_{chip} is calculated as a function of the offset Δ – for each value of the offset, additional numerical simulations are performed to evaluate the new impedance matrix - while keeping X_A , X_B unchanged. As far as the encoder antenna is concerned, numerical results are shown for the optimal reader antenna configuration presented in [7], namely a reader antenna equal to the tag antenna (*matched antenna*). As stated by the authors in [11] and by

$T_{sirline}$ in [8], a field distribution similar to that one of the RFID tag is effective to maximize the coupling with a transponder, on the basis of the reciprocity theorem.

Preliminary numerical results have been presented in [6] for a dipole-like tag and here extended to a hybrid loop-dipole configuration (LAB-ID UH113 RFID tag, $Z_{chip}=32-j216 \Omega$) that is characterized by high orientation insensitivity and good near-field performance. When the tag slides along the roll feeding direction, in front of the reader antenna, the geometrical Δ is varying. In Fig. 2, the power delivered to the chip is shown as a function of the offset (Δ), for both the UH113 and UH100 tags. In both the configurations, a maximum power transfer to the load is achieved when the two antennas are aligned ($\Delta=0$ mm), since the matching networks are optimized to meet the impedance matching condition. When Δ varies, the system efficiency (*i.e.* the ratio between the power delivered to the load and the reader available power) decreases. The -3 dB width of the power curve qualitatively indicates the achievable antenna spatial selectivity obtained with a specific encoder antenna in case of short smart labels and small pitch distances. The simulated -3 dB width is 4.3 mm and 4.8 mm for the UH100 and UH113 tags, respectively. Additional numerical tests will include other commercial tag layouts, as well as reader antenna configurations typically used in UHF-RFID printer-encoders [8]-[10].

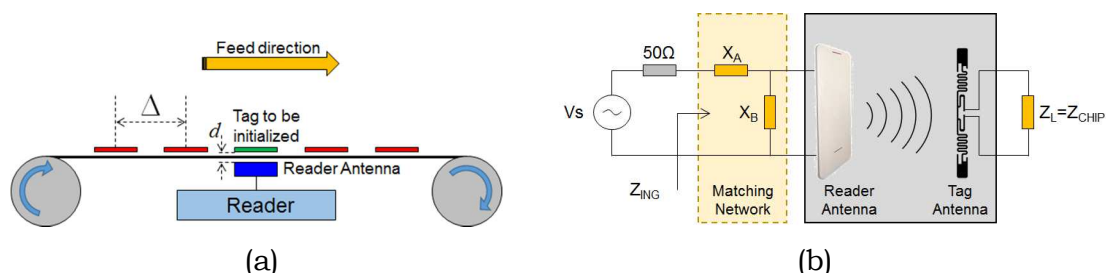


FIG. 1 - (a) A schematic view of a printer-encoder. The distance between adjacent transponders is denoted as Δ and (b) the electric equivalent circuit of the encoder-transponder network.

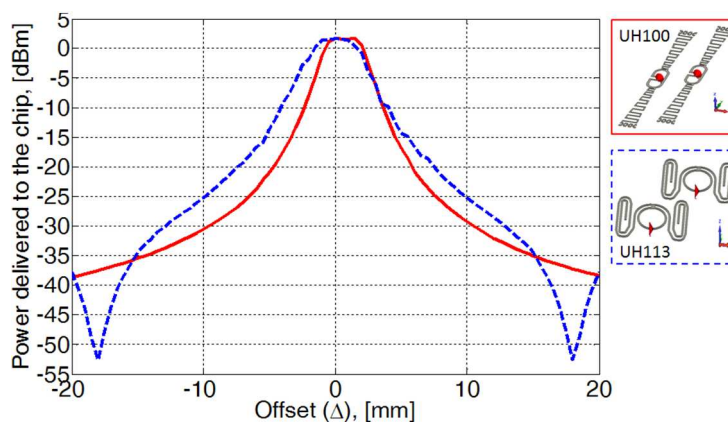


FIG. 2 - (a) Power delivered to the tag chip, as a function of the offset (Δ) when the reader antenna is equal to LAB-ID UH100 (red curve) and LAB-ID UH113 tag antenna (blue curve). The reader available power is -4 dBm.

III. CONCLUSION

In this paper, the mutual coupling between an UHF-RFID printer-encoder antenna and the RFID tag is investigated. Preliminary numerical results have been presented by considering two commercial tag layouts, the LAB-ID Inlay UH113 and the LAB-ID Inlay UH100. As a figure of merit, the achievable spatial selectivity and the amount of power delivered to the transponder chip have been considered. From this analysis, the proposed configuration with the reader antenna equal to the tag antenna allows for a narrow spatial selectivity, resulting in a good candidate for printer-encoders in case of short smart labels and small pitch distances.

REFERENCES

- [1] A. S. Andrenko, "Optimized near-field antenna for UHF RFID smart shelf applications", *IEEE Ant. Prop. Society Int. Symp. (APSURSI)*, Vancouver, BC, pp. 1576-1577, 19-24 July 2015.
- [2] A. Michel, A. Buffi, R. Caso, P. Nepa, G. Isola, and H. T. Chou, "Design and performance analysis of a planar antenna for near-field UHF-RFID desktop readers," *Asia-Pacific Microwave Conference Proceedings (APMC)*, Kaohsiung, pp. 1019-1021, 2012.
- [3] A. Michel, R. Caso, A. Buffi, P. Nepa, and G. Isola, "Meandered TWAS array for near-field UHF RFID applications", *Electronic Letters*, vol. 50, no. 1, pp. 17-18, January 2014.
- [4] C. R. Medeiros, J. R. Costa, and C. A. Fernandes, "RFID Reader Antennas for Tag Detection in Self-Confined Volumes at UHF", *IEEE Antennas and Propagation Magazine*, vol. 53, no. 2, pp. 39-50, April 2011.
- [5] A. Michel, R. Caso, A. Buffi, P. Nepa, and G. Isola, "Modular antenna for reactive and radiative near-field regions of UHF-RFID desktop readers," *XXXIth URSI General Assembly and Scientific Symposium (URSI GASS)*, pp. 1-4, 2014.
- [6] A. Michel, and P. Nepa, "UHF-RFID Desktop Reader Antennas: Performance Analysis in the Near-Field Region", to appear on *IEEE Antennas and Wireless Propagation Letters*.
- [7] A. Michel, A. Buffi, P. Nepa, and G. Manara, "Antennas for UHF-RFID printer-encoders", *2015 IEEE 15th Mediterranean Microwave Symposium (MMS)*, pp. 1-4, Nov. 30 2015-Dec. 2 2015.
- [8] B.Y. Tsirlin, "UHF RFID Antennas for Printer-Encoders-Part 1: System Requirements -Part 1", *High Frequency Electronics*, vol. 6, no. 9, pp. 28-39, September, 2007.
- [9] B. Y. Tsirlin, C. P. Hohberger, R. Gawelczyk, and D. F. Donato, "Spatially selective UHF near field microstrip coupler device and RFID systems using device", US7650114 B2, 19-Jan-2010.
- [10] B. Y. Tsirlin, K. Torchalski, "RFID near-field antenna and associated systems", US 20090152353 A1, 18-Jun-2009.
- [11] A. Buffi, A. Michel, R. Caso, and P. Nepa, "Near-field coupling in UHF-RFID systems", *Proceedings of 2013 URSI International Symposium on Electromagnetic Theory (EMTS)*, pp. 408-411, 2013.

SIMPLE TOOLS FOR UNDERSTANDING THE LIMITATIONS OF ORBITAL ANGULAR MOMENTUM ANTENNAS

A. F. Morabito⁽¹⁾ and L. Di Donato⁽²⁾

⁽¹⁾ DIIES Department, University of Reggio Calabria, Via Graziella, Loc. Feo di Vito, I-89124 Reggio Calabria, Italy, and CNIT Consortium, viale G.P. Usberti, n. 181/A, I-43124 Parma, Italy

⁽²⁾ DIEEI Department, Università degli Studi di Catania, Viale A. Doria 6, 95125 Catania, Italy.

andrea.morabito@unirc.it; loreto.didonato@dieei.unict.it

Abstract

A new strategy is proposed for the understanding of the ultimate limitations of Orbital Angular Momentum antennas when applied to enhance the transmission data rate in a wireless communication system. The introduced tools rely on the Hankel transform properties and on the Singular Value Decomposition of the radiation operator at hand. The developed theory is supported by numerical results concerning scenarios and synthesis problems of actual interest.

Index Terms – Antenna theory, Orbital Angular Momentum.

I. INTRODUCTION

Due to the limited radio spectrum, one of the main challenges for modern wireless communication systems is that of enhancing the transmission data-rate. Amongst the novel techniques developed for utilizing the radio spectrum with maximum efficiency, great attention has been recently devoted to Orbital Angular Momentum (OAM) antennas [1]-[5]. Such systems have been in some cases proposed as means to improve almost “indefinitely” [1] the channel capacity in a link amongst two antennas.

Roughly speaking, the idea is to take profit from the fact that an antenna could simultaneously generate different fields each associated to a different amount of ‘orbital momentum’, i.e., to a different angular variation of the phase such as $e^{j\phi}$, $e^{2j\phi}$, and so on, ϕ denoting the azimuth angle in the observation domain. Then, by associating a different information to each of these patterns, one could eventually enlarge “at his will” [1] the channel capacity.

As the debate is still open (see for example [2]-[4]), we aim at furnishing in the following some additional points of view and tools on the subject. In particular, by considering the case of aperture antennas, we focus on the possibility to get an arbitrary multiplication of channels in the far-field zone. To this aim, we exploit in Sections II and III, respectively, some crucial properties of the Hankel transform and the Singular Value Decomposition (SVD) of the radiation operator relating the ‘field vortices’ to the corresponding sources.

II. A MATHEMATICAL SETTING IN TERMS OF HANKEL TRANSFORMS

As the far field of an aperture antenna is proportional to the Fourier transform of the aperture field [6], a convenient mathematical setting is furnished by the Hankel transform [7]. In fact, with respect to our specific problem, such a tool can be exploited as follows.

Let $f(\rho', \phi')$ denote the component of interest of the aperture field, ρ' and ϕ' respectively being the radial and angular variables spanning the aperture. By virtue of eq. (9.14) in [7], $f(\rho', \phi')$ can be expanded in a multipole series as:

$$f(\rho', \phi') = \sum_{m=-\infty}^{\infty} f_m(\rho') e^{jm\phi'} \quad \text{with} \quad f_m(\rho') = \frac{1}{2\pi} \int_0^{2\pi} f(\rho', \phi') e^{-jm\phi'} d\phi' \quad (1)$$

Then, by exploiting the theory in [7], if k and ϕ respectively denote the radial and azimuth coordinates in the observation domain then the Fourier transform of the source (1) can be written as follows:

$$F(k, \phi) = \sum_{m=-\infty}^{\infty} F_m(k) e^{jm\phi} \quad \text{with} \quad F_m(k) = \int_0^{\infty} f_m(\rho') J_m(k\rho') \rho' d\rho' = H_m[f_m(\rho')] \quad (2)$$

wherein H_m and J_m respectively denote the m -order Hankel transform and the m -order Bessel function of first kind.

It is worth noting that, by denoting with θ the observation elevation angle with respect to boresight and introducing the spectral variables $u = \beta \sin \theta \cos \phi$ and $v = \beta \sin \theta \sin \phi$ (β denoting the wavenumber), it results $k = (u^2 + v^2)^{1/2} = \beta \sin \theta$. Therefore, relations (1), (2) entail that:

- i. an angular variation of order m of the source in terms of the ϕ' variable corresponds to an angular variation of order m of the far field in terms of the ϕ variable;
- ii. for any fixed m order of angular variation, the function $f_m(\rho')$ univocally determines the corresponding function $F_m(k)$ and vice versa. Both the forward and backward relations are ruled by an Hankel transform of order m ;
- iii. since in (2) no terms having a variable amplitude are present in front of $F_m(k) e^{jm\phi}$, the Hankel transform relationship also determines the power pattern associated to each source component $f_m(\rho') e^{jm\phi'}$.

Point iii above has the following crucial consequence. Since Bessel functions J_m present a m -order zero around the origin [8], whatever the source at hand the corresponding far field will have a null in the boresight direction. Such a hole will have increasing size and depth with m . Under such circumstances, assuming a receiver positioned at the broadside direction is able to detect and understand the (weaker and weaker) signal associated to the m -order vortex, a huge price is paid. In fact, the majority of the power radiated by the transmitting antenna is moved out of the broadside direction, with two related consequences. First, the field level is uselessly large in a number of spatial directions.

Second, spectral resources are wasted, as a number of potential space channels are occupied by the toroidal patterns associated to the vortices. Numerical examples concerning such circumstances will be shown at the Conference.

III. THE SVD ANALYSIS OF THE RADIATION OPERATOR

In order to get an even deeper understanding of OAM antennas limitations, we analyzed the SVD of the radiation operator relating, through (2), the ‘field vortices’ to the corresponding sources. We show in Fig. 1(a) the singular values of a source of radius of 4λ (λ denoting the wavelength in free space) for different values of the m . In addition to the step-like behavior typical of compact operators and related to the degrees of freedom of scattered fields [9], it is easy to note that, as m increases, the singular values’ decay begins for lower and lower values of the n index. Since the left-hand and right-hand singular functions of the radiation operator respectively represent a basis for the expansions of the source and the far field [10], and the singular values can be thought as scalar (gain) factors by which each source is multiplied to give the corresponding far field, distribution shown Fig. 1(a) has an important consequence: realizing OAM antennas without incurring into superdirective solutions becomes progressively harder as the requested order of angular variations increases.

By exploiting further tools which will be presented at the Conference, we used the SVD of the radiation operator also to evaluate the aperture power required to generate a far-field distribution guaranteeing at the same time a given m -order vortex and a fixed signal amplitude to a receiver positioned in the broadside direction. The results of this study, which are summarized in Fig. 1(b), entail that, whatever the transmitting and receiving antennas’ size, producing a small increase of m requires a huge increase of the aperture power.

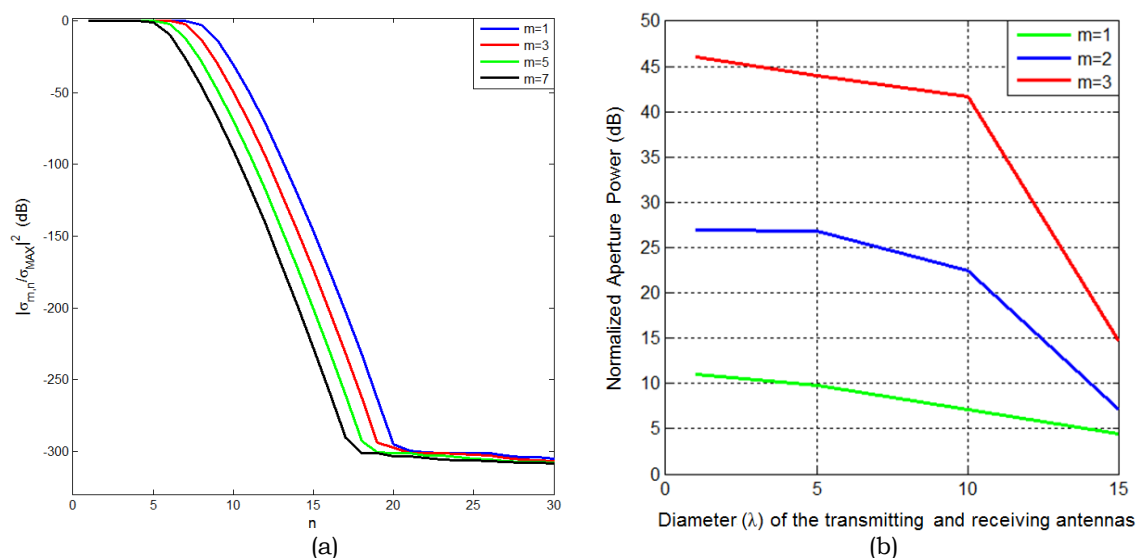


FIG. 1 – Singular values of the radiation operator (a) and outcomes of an ad-hoc synthesis problem aimed at minimizing the input power of a source guaranteeing a fixed level of signal to a receiver located at the Fraunhofer distance and having the same size of the transmitter (b).

IV. CONCLUSION

A deep analysis of OAM antennas' ultimate limitations has been provided with reference to their application to the enhancement of the transmission data rate in a wireless communication system. The provided results confirm the observations made in some notable recent contributions about the OAM antennas' disadvantages when used in long-range communications links.

ACKNOWLEDGEMENT

The authors acknowledge very interesting and fruitful discussions with Professor Tommaso Isernia.

REFERENCES

- [1] F. Tamburini, E. Mari, A. Sponselli, F. Romanato, B. Thide, A. Bianchini, L. Palmieri, and C. G. Someda, "Encoding many channels on the same frequency through radio vorticity: First experimental test," *New Journal of Physics*, vol. 14, 033001, 2012.
- [2] M. Tamagnone, C. Craeye, and J. Perruisseau-Carrier, "Comment on 'Encoding many channels on the same frequency through radio vorticity: First experimental test'," *New Journal of Physics*, vol. 14, p. 118001, 2012.
- [3] F. Tamburini, B. Thidé, E. Mari, A. Sponselli, A. Bianchini, and F. Romanato, "Reply to Comment on 'Encoding many channels on the same frequency through radio vorticity: First experimental test'," *New Journal of Physics*, vol. 14, p. 118002, 2012.
- [4] M. Tamagnone, C. Craeye, and J. Perruisseau-Carrier, "Comment on Reply to Comments on 'Encoding many channels on the same frequency through radio vorticity: First experimental test'," *New Journal of Physics*, vol. 15, p. 118001, 2013.
- [5] C. Craeye, "On the Transmittance Between OAM Antennas," *IEEE Transactions on Antennas and Propagation*, vol. 64, no. 1, pp. 336-339, 2016.
- [6] C. A. Balanis, "Aperture Antennas," §12 in *Antenna Theory, Analysis, and Design*, Third Edition, John Wiley & Sons, 2005.
- [7] R. Piessens, "The Hankel Transform," §9 in *The Transforms and Applications Handbook*, Second Edition, Alexander D. Poularikas, Boca Raton: CRC Press LLC, 2000.
- [8] M. Abramowitz and I. A. Stegun, "Bessel Functions J and Y ," §9.1 in *Handbook of Mathematical Functions with Formulas, Graphs, and Mathematical Tables*, 9th printing. New York: Dover, pp. 358-364, 1972.
- [9] O. M. Bucci and G. Franceschetti, "On the degrees of freedom of scattered fields," *IEEE Transactions on Antennas and Propagation*, vol. 37, n. 7, pp. 918-926, 1989.
- [10] M. Bertero and P. Boccacci, "Singular Value Decomposition," §9 in *Introduction to Inverse Problems in Imaging*, First Edition, CRC Press, pp. 220-246, 1998.

A NEW APPROACH TO THE DIAGNOSTICS OF ARRAY ANTENNAS BY MEANS OF A SMALL NUMBER OF PHASELESS MEASUREMENTS

A. F. Morabito and R. Palmeri

DIIES Department, University of Reggio Calabria, Via Graziella, Loc. Feo di Vito, I-89124 Reggio Calabria, Italy, and CNIT Consortium, viale G.P. Usberti, n. 181/A, I-43124 Parma, Italy
andrea.morabito@unirc.it; roberta.palmeri@unirc.it

Abstract

We introduce a new approach to the diagnostics of fixed-geometry array antennas by means of amplitude-only far-field measurements. Although the overall problem is a non-linear one, the developed technique is able to take decisive advantage from the Compressive Sensing theory. In case of low percentages of faulty elements, the diagnostics is reduced to a Convex Programming problem. An extensive numerical assessment is provided in such a way to identify the minimum number of measurements required to successfully perform the diagnostics of arrays excited by either real or complex coefficients.

Index Terms – Antenna diagnostics, compressive sensing, phase retrieval.

I. INTRODUCTION

In several applications, including antennas characterization in Submillimeter and Terahertz bands [1], diagnostics of reflectors for radio astronomy [2], array excitations retrieval [3], near field-far field transformations [4], and ‘on site’ antenna radiation evaluation by means of unmanned aerial vehicles [5], *phaseless* measurements are proposed as an effective alternative to *amplitude and phase* measurements.

In particular, a relevant problem is represented by the diagnostics of array antennas through amplitude-only measurements [6],[7]. Notably, we have not been able to find any contribution suggesting the exploitation of Compressive Sensing (CS) to solve it. This is fully coherent with the fact that CS theory is well developed and assessed only for *linear* problems, which is not the case at hand.

In the following, we show that the array antenna diagnostics by using phaseless measurements can be effectively performed by means of a CS-inspired procedure and that, under few reasonable hypotheses, the minimum required number of measurements can be identified by means of a simple and fast Convex Programming (CP) optimization.

II. PROBLEM STATEMENT AND REDUCTION TO CONVEX PROGRAMMING

Let us suppose to know the ‘nominal’ far-field pattern expected to be radiated by the Array Under Test (AUT) when all elements are correctly working. By the sake of simplicity, let us also consider the case where the array is linear and all elements are identical, equally oriented, and uniformly spaced (with a constant distance equal to d), so that the problem can be conveniently analyzed in terms of an array factor. Also,

let us denote by N , θ and λ the overall number of array elements, the observation angle with respect to the array axis, and the wavelength, respectively. Then, the ‘nominal’ or ‘expected’ field will be given by:

$$F^E(u) = \sum_{n=1}^N a_n^E e^{jnu} \quad \text{with } u = \frac{2\pi}{\lambda} d \cos\theta \quad (1)$$

where a_1^E, \dots, a_N^E are the known ‘nominal’ excitations. In case some element is not correctly working, if a_1^A, \dots, a_N^A denote the unknown ‘actual’ excitations then the ‘actual’ field will be given by:

$$F^A(u) = \sum_{n=1}^N a_n^A e^{jnu} \quad (2)$$

Therefore, the difference between the ‘nominal’ and ‘actual’ fields results:

$$\Delta F(u) = F^E(u) - F^A(u) = \sum_{n=1}^N \Delta a_n e^{jnu} \quad \text{with } \Delta a_n = a_n^E - a_n^A \quad n = 1, \dots, N \quad (3)$$

Let us now consider the case where only phaseless measurements are available and denote by P^E and P^A the square amplitudes of F^E and of F^A , respectively. Then, in a measurement point u_m one achieves:

$$P^A(u_m) - P^E(u_m) = -2\text{Re}[F^E(u_m)\Delta F^*(u_m)] + |\Delta F(u_m)|^2 \quad m = 1, \dots, M \quad (4)$$

wherein $*$ denotes complex conjugation.

Let us now suppose that the number of faulty elements, i.e., the number of elements whose excitation is different from the ‘nominal’ one, say S , is small with respect to N . Under this assumption, ΔF can be considered S -sparse when represented in terms of $\Delta a_1, \dots, \Delta a_N$ [8],[9] and the CS theory can be profitably exploited. In particular, the diagnostics problem from phaseless measurements can be solved as:

$$\min_{\Delta a_1, \dots, \Delta a_N} \|\underline{\Delta a}\|_1 \quad (5)$$

$$\text{subject to } \|\underline{\Delta x}\|_2 \leq \epsilon \quad (6)$$

wherein ϵ is a constant concerning the desired diagnostics’ accuracy level, the subscripts 1 and 2 respectively stand for ℓ_1 and ℓ_2 norms, $\underline{\Delta a} = [\Delta a_1 \dots \Delta a_N]$, and $\underline{\Delta x} = [\Delta x_1 \dots \Delta x_M]$, with:

$$\Delta x_m = P^A(u_m) - P^E(u_m) + 2\text{Re}[F^E(u_m)\Delta F^*(u_m)] - |\Delta F(u_m)|^2 \quad (7)$$

As discussed in [8],[9], condition (5) is meant to enforce sparsity, and an accurate recovery is granted for the corresponding linear problems provided a number of conditions on M , S , N are fulfilled [10].

Notably, if S is low and the M measurements are performed in those points where the signal F^E (which is known) has a large intensity, the second term at the right-hand member of (4) will be small with respect to the first one, and constraint (6) will practically result quadratic. Under such hypotheses, problem (5),(6) can be effectively solved as a CP one.

III. NUMERICAL ASSESSMENT

We analyze the performance achievable in case of noiseless data by considering ‘successful’ only those simulation giving a Mean Squared Error (MSE) between the ‘actual’ and recovered excitation sets, i.e.,

$$MSE = \frac{1}{N} \sum_{n=1}^N |a_n^A - a_n^R|^2 \quad (8)$$

not larger than -30dB (denoting with a_n^R the recovered value of the n -th actual excitation). All presented results concern linear arrays with a constant $\lambda/2$ inter-element spacing. According to the reasonings made in Section II about linearization of relation (4), only those u values corresponding to a nominal power pattern’s normalized value larger than -25 dB have been randomly sampled.

In a first class of numerical experiments, we used an AUT composed by $N=20$ elements and chose the nominal excitations as the Chebyshev coefficients providing a -20 dB equiripple far-field pattern. In a second class of simulations, in order to validate the approach also in case of complex reference excitations, we considered an AUT composed by $N=16$ elements and used as nominal excitations the coefficients reported at page 1131 of [11]. For each AUT, we assessed the actual capabilities of the approach by repeatedly varying M and S . At least 100 simulations have been performed for each couple (M,S) .

The results pertaining to the two classes of experiments are summarized in Fig. 1. As it can be seen, as long as the percentage of faulty elements is not ‘too large’ (i.e., $S/N \leq 0.15$) the minimum number of measurements allowing an ‘almost sure’ successful reconstruction (i.e., $RSER > 95\%$) is $M=6S$ in both cases of real and complex nominal excitations. For larger percentages of faulty elements (i.e., $S/N=0.25$), $M=8S$ phaseless measurements have been sufficient to guarantee a $RSER$ at least in the order of 90%. It is also worth noting that, whatever the number of failures, the $RSER$ (expected) growth for increasing values of M is very intense as long as M is lower than $4S$. Such a circumstance agrees with the theoretical results in [10]. For larger values of M , the $RSER$ curve becomes smoother. This kind of asymptotic behavior is very similar to the one shown in [8].

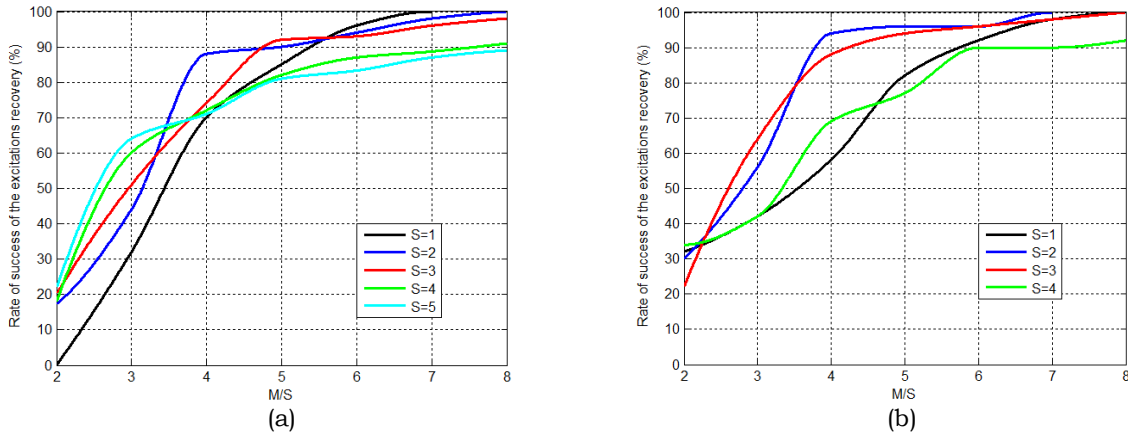


FIG. 1 – Results achieved in case of Chebyshev (a) and Elliott (b) nominal excitations.

IV. CONCLUSION

An innovative and effective approach to the array antennas diagnostics by means of magnitude-only measurements, exploiting at best the CS theory, has been introduced and assessed. Further numerical examples concerning the effects of the noise on the data and of 'on-site' measurement strategies will be presented at the Conference.

ACKNOWLEDGEMENT

The authors acknowledge very interesting and fruitful discussions with Professor Tommaso Isernia.

REFERENCES

- [1] G. Junkin, "Planar near-field phase retrieval using GPUs for Accurate THz far-field prediction," *IEEE Trans. Antennas Propag.*, vol. 61, n. 4, pp. 1763-1776, 2013.
- [2] D. Morris, "Phase retrieval in the radio holography of reflector antennas and radio telescopes," *IEEE Trans. Antennas Propag.*, vol. 33, pp. 749-755, 1985.
- [3] B. Fuchs and L. Le Coq, "Excitation retrieval of microwave linear arrays from phaseless far-field data," *IEEE Trans. Antennas Propag.*, vol. 63, n. 2, pp. 748-754, 2015.
- [4] A. P. Anderson and G. Junkin, "Near-field far-field predictions from single-intensity-planar-scan phase retrieval," *Electron. Lett.*, vol. 25, n. 8, pp. 519-520, 1989.
- [5] F. Üstüner, E. Aydemir, E. Güleç, M. İlarıslan, M. Çelebi, and E. Demirel, "Antenna radiation pattern measurement using an unmanned aerial vehicle," *31st URSI General Assembly and Scientific Symp.*, Beijing, Aug. 2014.
- [6] O. M. Bucci et al., "Diagnosis of array faults from far-field amplitude-only data," *IEEE Trans. Antennas Propag.*, vol. 48, n. 5, pp. 647-652, 2000.
- [7] J. A. Rodriguez-Gonzalez et al., "Rapid method for finding faulty elements in antenna arrays using far field pattern samples," *IEEE Trans. Antennas Propag.*, vol. 57, n. 6, pp. 1679-1683, 2009.
- [8] M. D. Migliore, "Array diagnosis from far-field data using the theory of random partial Fourier matrices," *IEEE Antennas and Wireless Propagation Letters*, vol. 12, pp. 745-748, 2013.
- [9] G. Oliveri, P. Rocca, and A. Massa, "Reliable diagnosis of large linear arrays: a Bayesian Compressive Sensing approach," *IEEE Trans. Antennas Propag.*, vol. 60, n. 10, pp. 4627-4636, 2012.
- [10] M. Akçakaya and V. Tarokh, "Sparse signal recovery from a mixture of linear and magnitude-only measurements," *IEEE Signal Processing Letters*, vol. 22, n. 9, pp. 1220-1223, 2015.
- [11] R. S. Elliot and G. J. Stern, "A new technique for shaped beam synthesis of equispaced arrays," *IEEE Trans. Antennas Propag.*, vol. AP-32, n. 10, pp. 1129-1133, 1984.

FURTHER APPROACH TO PHASE RETRIEVAL THROUGH CONSTRAINED POWER INFLATION AND FLIPPING

A. R. Laganà⁽¹⁾, T. Isernia⁽¹⁾

⁽¹⁾ LEMMA Research Group @ DIIES Università Mediterranea di Reggio Calabria, Via Graziella, Loc. Feo di Vito, 89122, Italy
(antonia.lagana, tommaso.isernia)@unirc.it

Abstract

A new approach to the recovery of the far field of a discrete source starting from the knowledge of far-field phaseless data is proposed and discussed. In particular, the problem is formulated as a ‘constrained power inflation’, which leads to two different interesting strategies allowing alternative points of view for the problem at hand. The approach and the corresponding procedures can be extended in a straightforward fashion to generic phase retrieval problems.

Index Terms – phase retrieval problem, convex programming, false solutions.

I. INTRODUCTION

The phase retrieval problem (PR) is of significant interest in many areas of theoretical and applied science such as electron microscopy, astronomy, Crystallography and Optics, antenna characterization and diagnostics, inverse scattering, and in many other fields where the full knowledge of a complex function is needed, but phase measurements are not available or not convenient. Over the years, very many different approaches have been proposed for solving phase retrieval problems, but the so called ‘hybrid input-output’ procedure by Fienup [1] continues to be the most popular. In the following, we introduce an innovative formulation of the problem as a (constrained) local maximization of a cost functional, which allows an alternative point of view to the problem of ‘false solutions’ [2] and new possible solution procedures.

II. STATEMENT OF THE PROBLEM AND FORMULATION AS A ‘CONSTRAINED POWER INFLATION’ PROBLEM

A very general formulation of phase retrieval problems can be given as follows.

If $f(x)$ is a 1-D, 2-D or even a higher dimensional unknown complex signal, and T is a linear operator performing some transformation of the unknown signal, the phase retrieval problem consists of determining $f(x)$, from $|F(u)|$, where:

$$F(u) = |F(u)|\exp[j\varphi(u)] = T[f(x)] \quad (1)$$

Notably, some additional information on $f(x)$ (or some property of T) are usually required in order to guarantee the uniqueness of a solution, which is anyway assumed in the following. In the case at hand, $f(x)$ is a discrete source (such as for instance a uniformly spaced array), and T is a Fourier Transform, so that $F(u)$ can be eventually interpreted as the corresponding array factor. However, all the presented ideas and procedures can be extended in a conceptually easy fashion to continuous sources, as well as to generic radiation operators (including the case of near field measurements) and to many other cases.

Our alternative approach to generic Phase Retrieval problems is as follows:

Find $f(x)$ such that:

$$OF = \sum_0^s |T[f(x)]|_s^2 \tag{2}$$

is maximized while fulfilling:

$$|T[f(x)]|^2 \leq M^2(u) \tag{3}$$

where the index s in Eq. (2) denotes a sample of the corresponding quantity, and constrains in Eq. (3), (which will be discretized in any practical instance), allows to avoid divergence of the procedure. Finally, $M^2(u)$ is the far-field phaseless data.

Interestingly, the proposed procedure can be interpreted as an inflation of the function $|T[f(x)]|^2$ until it reaches the right values corresponding to a perfect fitting (equivalence) of the two functions $|T[f(x)]|^2$ and $M^2(u)$. Obviously, the difficulties related to the non-linearity of the problem are still present. In fact, the maximization of a quadratic function in a convex set is known to be an NP hard problem [8], which witnesses the difficulty of the problem.

On the other side, both the physical interpretation as an ‘inflation’ technique, as well as the mathematical structure of the problem, offer at least two different possibilities which are analyzed in the Sections which follow.

III. A ‘SIGNUM FLIPPING’ TUNNELING STRATEGY

As a first possibility, let us note that the cost function to be maximized can be written (in all 1-D, 2D and/or near field cases) as a Positive Definite Quadratic Form as:

$$OF = \sum_0^{2N-2} \sigma_i^2(x_i)^2 \quad (4)$$

where x_i are suitable real auxiliary variables deriving from transforming the original quadratic form into its canonical form, and σ_i^2 are positive real quantities. In the particular case of linear arrays with elements spaced half a wavelength these auxiliary variables correspond (by virtue of the Parseval theorem) to the real and imaginary part of the excitations I_i , and $\sigma_i^2 = 1 \forall i$.

Then, a possible strategy to optimize the objective function is as follows:

- i. in a first step, starting from a random point, optimize by means of a local optimization technique function (4) subject to constraints deriving from the discretization of (3);
- ii. then, if the $M^2(u)$ data are not satisfactorily fitted, change the sign of one (or more) of the x_i variables. Such a step can be interpreted as a ‘tunneling’ of the cost function meant to jump into a different attraction basin. In fact, the ‘signum flipping’ operation will leave the value of the cost function unaltered;
- iii. iterate the procedure if needed.

Interestingly, numerical examples (for the case of 1-D arrays) have shown that a few flipping (operated according to a well defined criterion) allows a correct retrieval of the actual ground truth solution.

IV. PHASE RETRIEVAL AS A COMBINATION OF CONVEX PROBLEMS

As a second possibility, let us supposed to use the samples of $T[f(x)]$ as the unknowns of our problem. Then, let us also suppose to relax the (L2) norm of data into a (L1) norm. As a consequence, the cost function to be optimized (under the same constraints as above) becomes:

$$\sum_n [|\text{Re}\{T[f(x)]\}|_n + |\text{Im}\{T[f(x)]\}|_n] \quad (5)$$

and where some care has to be taken in choosing the number of samples to be considered. In particular, we suppose herein to use a number of samples equal to the number of degrees of freedom of the field. Quite interestingly maximization of (5) subject to constraints (3) is a Convex Programming Problem in any ‘hyperquadrant’ defined by any possible combination of:

$$\left\{ \begin{array}{lll} \operatorname{Re}\{T[f(x)]_1\} \leq 0 & \text{or} & \operatorname{Re}\{T[f(x)]_1\} \geq 0 \\ \operatorname{Im}\{T[f(x)]_1\} \leq 0 & \text{or} & \operatorname{Im}\{T[f(x)]_1\} \geq 0 \\ & \dots & \\ \operatorname{Re}\{T[f(x)]_N\} \leq 0 & \text{or} & \operatorname{Re}\{T[f(x)]_N\} \geq 0 \\ \operatorname{Im}\{T[f(x)]_N\} \leq 0 & \text{or} & \operatorname{Im}\{T[f(x)]_N\} \geq 0 \end{array} \right. \quad (6)$$

As a consequence, the PR problem can be formulated in terms of the solution of (very many) Convex Programming Problems, wherein at the end of each Convex Programming problem one can eventually turn back to the original Objective Function (1).

Obviously, consideration of all the different problems arising from the combinations of (6), while guaranteeing somehow global optimality, would lead to a computational complexity growing exponentially with the number of unknowns. Hence, some clever strategy is required in order to reduce such a complexity. A possibility starts from the consideration that the largest samples have of course a major impact on the value of the cost function (either (5) or (1)) In fact, consideration of the combinations arising from the larger samples (while not considering any constraint of the kind (6) on the smaller samples) has revealed a very effective strategy.

III. CONCLUSIONS

A different point of view to Phase Retrieval has been introduced which allows the introduction of new strategies. A large number of numerical examples dealing with 1D problems where theoretical uniqueness is somehow granted confirm the interest of the approach.

Further details and numerical examples will be given at the Conference.

REFERENCES

- [1] J. R. Fienup, "Phase retrieval algorithms: a comparison," *Appl. Opt.* 21, 2758-2769 (1982).
- [2] T. Isernia, G. Leone, R. Pierri, and F. Soldovieri, "On the local minima in phase reconstruction algorithms," *Radio Science*, 31, 1887-1899 (1996).

LATTICE OPTIMIZATION FOR A MULTI-ARRAY ANTENNA SYSTEM AIMED AT SPACE DEBRIS SURVEILLANCE

Giuseppe Siciliano⁽¹⁾, Magdalena Mendijur⁽²⁾, Piermario Besso⁽²⁾, Marco Pasian⁽¹⁾, Maurizio Bozzi⁽¹⁾, Luca Perregrini⁽¹⁾

⁽¹⁾ Dept. of Electrical, Electronic and Biomedical Engineering, University of Pavia, Pavia, Italy

giuseppe.siciliano01@universitadipavia.it, marco.pasian@unipv.it,
maurizio.bozzi@unipv.it, luca.perregrini@unipv.it

⁽²⁾ Dept. of Ground Stations and Operations, European Space Operations Center (ESOC), Darmstadt, Germany

magdalena.mendijur@esa.int, pier.mario.besso@esa.int

Abstract

The European Space Agency (ESA) is developing surveillance radars, based on phased-array antennas, for detecting and cataloguing space debris objects. The number of elementary radiators (array elements) in the phased arrays has a strong impact on the cost of the final antenna.

This work shows the preliminary design of a multi-array antenna system, given a rectangular-sectioned window to be scanned, called Field of Regard (FoR). The array orientations in terms of polar coordinate angles will be provided in a local coordinate system, having z axis directed along the zenith. Then, the geometrical lattice of each array, analytically optimized for the minimization of the number of elements, will be explicitly derived in terms of array lattice parameters (horizontal and vertical distance, and skew angle).

Index Terms – array lattice optimization, field of regard, grating lobes, multi-array system, phased array, pyramidal scanning, space debris, surveillance radar.

I. INTRODUCTION

This paper presents the design process of a phased-array antenna system for rectangular pyramidal scan (Fig. 1), i.e. the region of interest, called Field of Regard (FoR), is delimited by a rectangular section, whose scan limits are determined by two angles measured in the sense of elevation and azimuth (Fig. 1). In this work, we present the uniform sectorization of the rectangular pyramidal FoR in the azimuthal direction and the assignation of each sector to a separate array antenna.

A multi-array system is designed and the orientation of each array provided in terms of azimuth and elevation angles of the array axis in a local coordinate system, where zenith coincides with the z axis, and x and y axes lie in the plane of the horizon. After calculating the orientation of each array in the multi-array system, an array-lattice optimization procedure is applied. In particular, the array lattice is optimized in order to minimize the number of radiating elements in the array, without

allowing grating lobes to show up in the array factor, while maintaining a regular lattice. Eventually, analytical formulas for the main array-lattice parameters will be provided.

II. A MULTI-ARRAY SYSTEM

This section shows the calculation of the orientation of each array in a multi-array system. The orientation is provided in terms of a couple of polar angles defining the direction of the array axis, where such angles are measured in a local coordinate system (xyz) having z axis coinciding with the local zenith. Let the FoR, as in Fig. 1, be placed at an elevation of $90^\circ - \delta$ and defined between $-A'$ and A' in azimuth direction. Now, let the FoR be divided into N_s identical sectors. Each array axis \mathbf{v}_n in a multi-array system will point orthogonally to its sector of the FoR. An example of a two-array system is depicted in Fig. 2a.

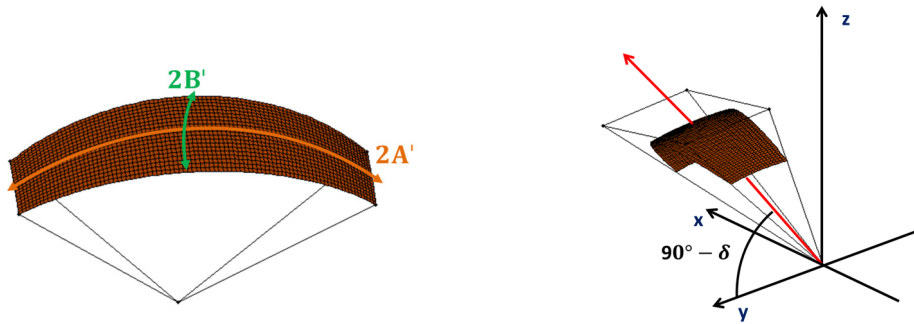


FIG. 1 - Definition of the Field of Regard (FoR).

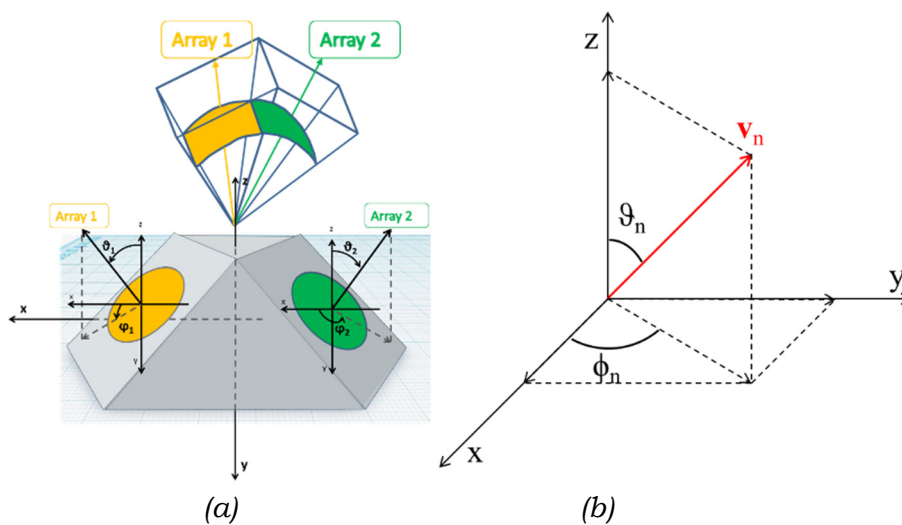


FIG. 2 – (a) example of a two-array system; and (b) definition of array axis.

The actual FoR can be seen as the same FoR centered at zenith and sectorized in azimuth, then rotated at the right elevation. After applying a couple of rotations, the right polar angles for each array axis, shown in Fig. 2b, are computed as [1]:

$$\vartheta_n = \cos^{-1}(\cos \alpha_n \cos \delta)$$

$$\varphi_n = \begin{cases} \tan^{-1}\left(\frac{\cos \alpha_n \sin \delta}{\sin \alpha_n}\right) + \pi & \text{if } -\frac{\pi}{2} \leq \alpha_n < 0 \\ \frac{\pi}{2} & \text{if } \alpha_n = 0 \\ \tan^{-1}\left(\frac{\cos \alpha_n \sin \delta}{\sin \alpha_n}\right) & \text{if } 0 < \alpha_n \leq \frac{\pi}{2} \end{cases}$$

where $\alpha_n = -A' + \frac{A'}{N_s} + 2(n-1)\frac{A'}{N_s}$.

III. ARRAY LATTICE OPTIMIZATION

The array lattice can be optimized for a rectangular pyramidal scan (or FoR) to minimize the required number of elements, while maintaining a regular lattice, shown in Fig. 3b, described by three parameters a , b , and γ . To ease the analysis of the array and better understand the aspects related to grating lobes, it is more convenient to pass from the angle space to the so-called UV space, through the following mathematical relations: $u = \sin \theta \cos \varphi$, $v = \sin \theta \sin \varphi$.

It can be proven that the rectangular pyramidal sector, as in Fig. 3a, is mapped into the interception of two mutually orthogonal ellipses (Fig. 4a), one having the semi-major axis vertically oriented (vertical ellipse), and the other horizontally oriented (horizontal ellipse) [2].

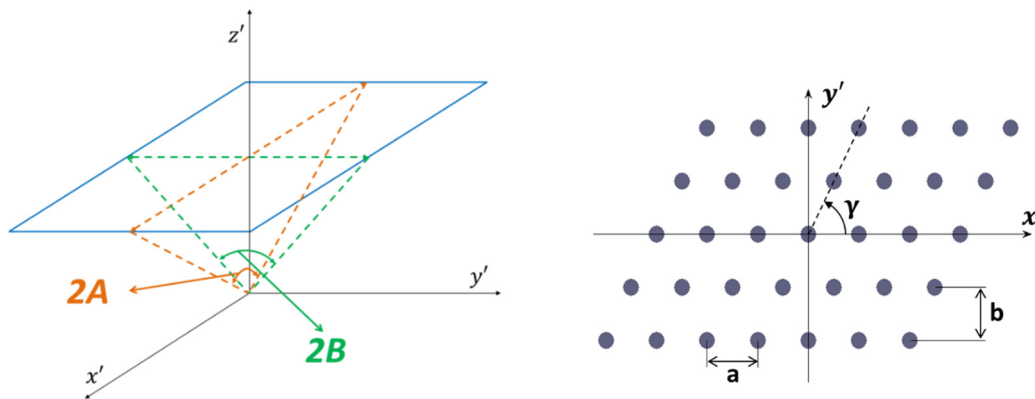


FIG. 3 – (a) FoR sector with the array lying in the $x'y'$ plane; and (b) general array lattice.

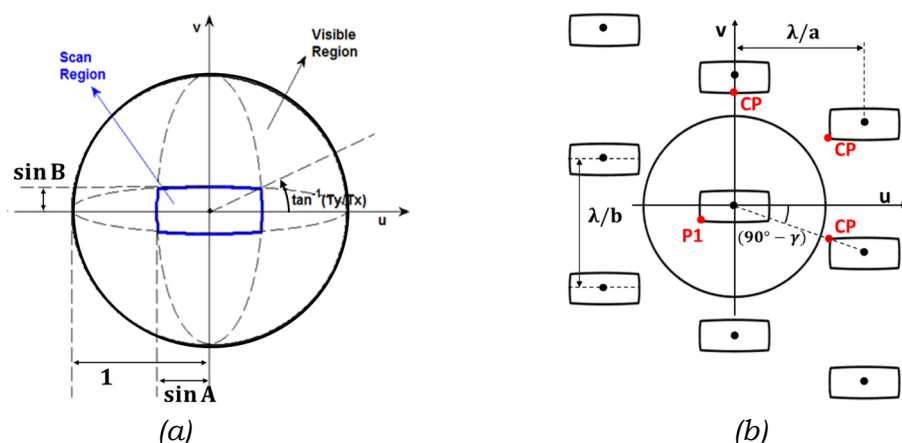


FIG. 4 – (a) Mapping of a rectangular scan in the UV plane; and (b) UV mapping of grating lobe contours.

Instead, Fig. 4b shows the UV mapping of grating lobes (GL) [1] for the general array lattice of Fig. 3b, from the GL locations reported in [1] and [3]. The analysis of grating lobes was performed in the UV space, by considering the tangential condition for the closest grating lobe contours. This condition imposes that grating lobe contours must not enter but at most be tangent to the unit circle.

The array skew angle, the vertical spacing and the horizontal spacing (respectively parameters γ , b , and a) can be computed by imposing that all critical points (CP) in Fig. 4b are tangent to the unit circle. This condition ensures that, for all possible scan angles experienced by each array, GLs are always out of visibility or at worse with their peaks exactly on the boundary of the visibility region. Such criterion translates into the following simple and analytical formulas for the three array-lattice parameters [1],[2]:

$$\gamma = \tan^{-1}\left(\frac{2b}{a}\right) \quad b = \frac{\lambda}{1 + \sin B} \quad a = \frac{\lambda}{\sqrt{1 - \left(v_{P1} + \frac{\lambda}{2b}\right)^2 - u_{P1}^2}}$$

where the coordinates of point P1 (u_{P1} and v_{P1}) are provided in [1].

REFERENCES

- [1] G. Siciliano, M. Pasian, M. Mendijur, P. Besso, M. Bozzi, and L. Perregrini, "A Multi-Array Antenna System with Optimal Lattice for Rectangular Pyramidal Scanning of Space Debris", *EuCAP 2016*, Davos, Switzerland, April 10-15, 2016.
- [2] S. Zinka, I.-B. Jeong, J.-H. Chun and J.-P. Kim, "A novel geometrical technique for determining optimal array antenna lattice configuration", *IEEE Trans. Antennas Propagat.*, vol. 58, no. 2, pp. 404-412, 2010.
- [3] A. Bhattacharyya, "Phased Array Antennas, Floquet Analysis, Synthesis, BFNs, and Active Array Systems." Hoboken, NJ: Wiley-Interscience, 2006.

ADDITIVE MANUFACTURING OF SUBSTRATE INTEGRATED WAVEGUIDE COMPONENTS

E. Massoni, L. Silvestri, S. Moscato, M. Pasian, M. Bozzi, L. Perregrini

Dept. of Electrical, Computer and Biomedical Engineering
University of Pavia, Pavia, Italy

Abstract

This paper presents the recent advances in the implementation of substrate integrated waveguide (SIW) components and circuits by additive manufacturing (AM) techniques. The use of AM allows introducing novel features in the design of SIW structures, ranging from fully three-dimensional geometries (impossibly to obtain with standard planar circuits technologies), to the local modification of the dielectric permittivity and loss tangent of the 3D-printed material (which allows for novel classes of components and resonant cavities with modified quality factor). The material characterization is described, along with the design and implementation of several 3D-printed SIW components.

Index Terms – Additive manufacturing, 3D printing, dielectric material characterization, substrate integrated waveguide (SIW).

I. INTRODUCTION

The deployment of the Internet of Things (IoT) demands for the implementation of microwave components with innovative features in terms of low cost, compact size, light weight, flexibility, and environmental compliance. Moreover, the need to manufacture a very large number of wireless systems expected for IoT applications requires the identification of an efficient manufacturing technology and a suitable integration method.

Among the emerging fabrication technologies, the additive manufacturing based on 3D printing results particularly interesting, as it allows realizing complex and fully three-dimensional devices [1]. Commercial 3D printers allow high resolutions and fast prototyping: in particular, the fused deposition modeling (FDM) presents a good compromise between low cost and reasonable accuracy.

Among the integration technologies, the substrate integrated waveguide (SIW) has received increasing attention in the last decade for the implementation of active and passive components and antennas, as well as for the integration of complete systems at microwave and mm-wave frequencies [2].

This paper summarizes the recent advances in the implementation of SIW components by adopting a 3D-printing process based on FDM [3]-[6]. Different materials filaments (ABS, t-glase, Ninjaflex) have been characterized and adopted. The implementation of several SIW components is described and discussed.

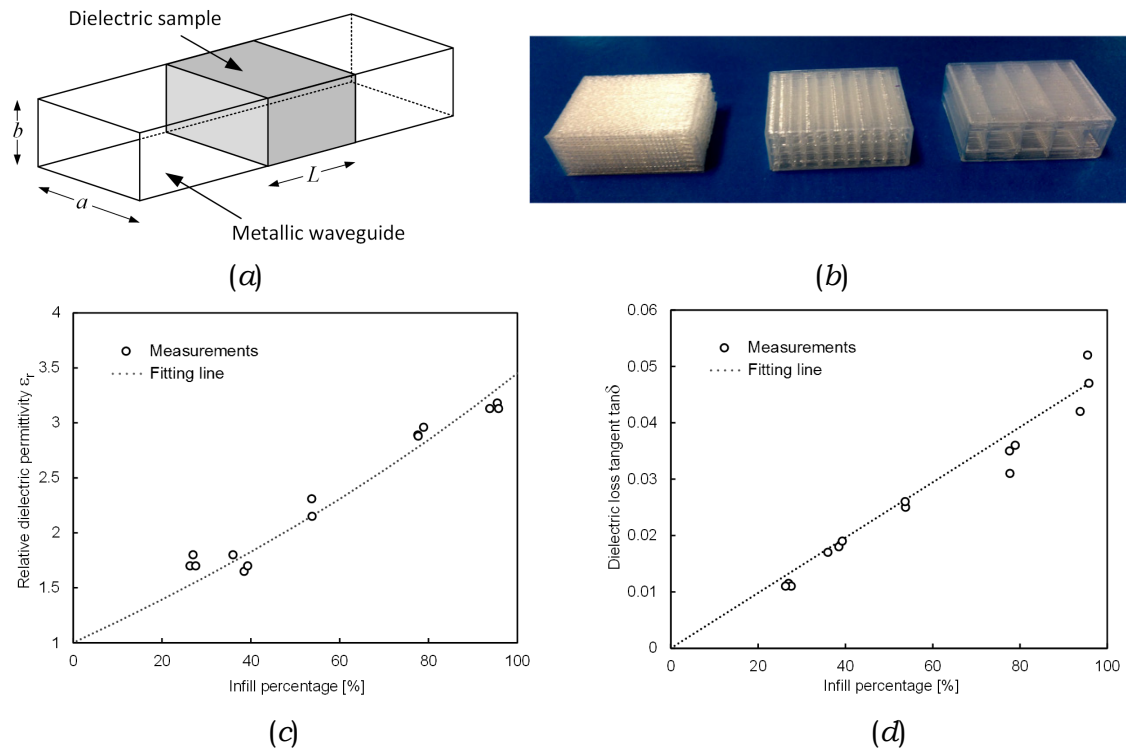


FIG. 1 – Electromagnetic characteristics of 3D-printed material:
 (a) measurement setup for waveguide-based material characterization;
 (b) photograph of 3D-printed dielectric samples with different infill percentage;
 (c) measured dielectric permittivity ϵ_r versus infill percentage;
 (d) measured dielectric loss tangent $\tan\delta$ versus infill percentage.

II. 3D-PRINTED MATERIAL CHARACTERIZATION

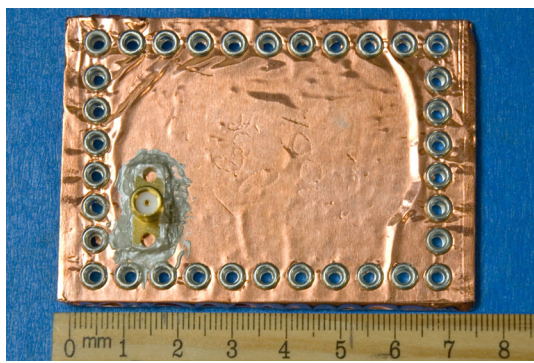
The electromagnetic characterization of 3D-printed materials can be performed by adopting two different techniques: the former based on a metallic waveguide (for accurate narrow-band information); the latter based on a microstrip line (which provides broadband information).

Waveguide measurements have been performed in the X band, by adopting a standard WR-90 waveguide (Fig. 1a). Dielectric samples have been 3D-printed by using a thermoplastic polyurethane called Ninjaflex®, with different infill ranging from 25% to 95% (Fig. 1b).

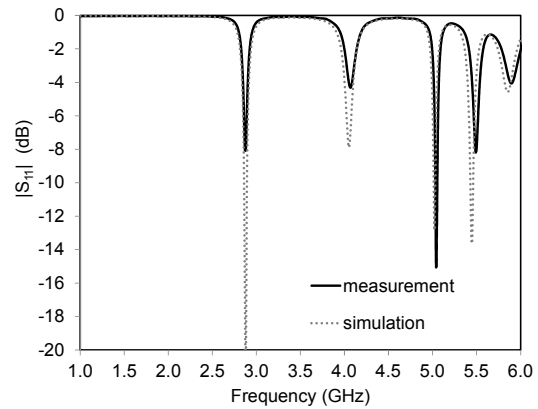
The measured results for relative dielectric permittivity ϵ_r and loss tangent $\tan\delta$ are shown in Figs. 1c and 1d, respectively, versus the infill percentage. The measured values (dotted symbols) well agree with the fitting curve (dashed line) obtained from the Maxwell-Garnett equation.

III. 3D-PRINTED SIW COMPONENTS

The AM has been first adopted for the implementation of an SIW resonant cavity, operating with fundamental mode at about 3 GHz, based on a t-glase filament [3]. The implementation of the top and bottom ground planes of the SIW cavity was obtained by adopting

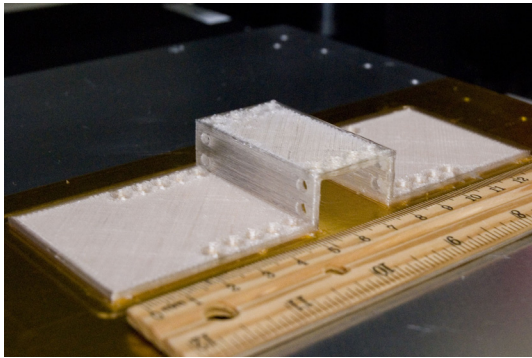


(a)

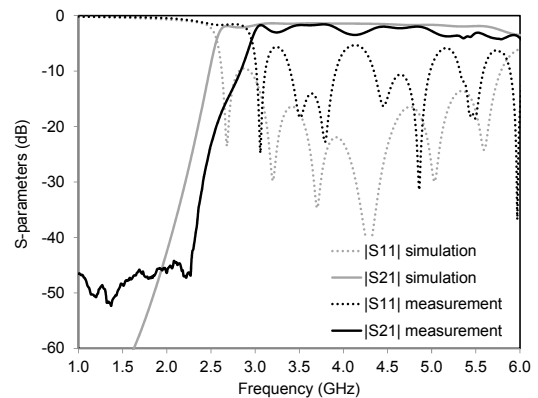


(b)

FIG. 2 – 3D-printed SIW cavity based on t-glass filament: (a) photograph of the prototype; (b) simulated and measured scattering parameters (from [3]).



(a)



(b)

FIG. 3 – 3D-printed SIW interconnect based on t-glass filament: (a) photograph of the prototype (before metallization); (b) simulated and measured scattering parameters (from [3]).

standard copper tape, pasted at both sides of the 3D-printed substrate (Fig. 2). The metal vias defining the sidewalls of the SIW resonant cavity were realized by using brass rivets.

A three-dimensional SIW interconnect was manufactured by adopting a t-glass filament, to fully exploit the capabilities of 3D printing fabrication process [3]. The structure consists of an SIW interconnect with four bends in the E-plane (Fig. 3). The fabrication of the suspended bridge section was performed without any support material: during this fabrication step, a fan behind the extruder was turned on to quickly solidify the filament.

Fig. 4a shows an SIW cavity based on Ninjaflex® and used for a microfluidic sensor. It consists of a square SIW cavity with a pattern of thin tubes directly embedded in the substrate, with two vertical exits on the top of the substrate. The two vertical exits are designed in order to guarantee a continuous flow of fluid within the pipe. The presence and characteristics of the liquid determined a frequency shift of the cavity resonant modes (Fig. 4b).

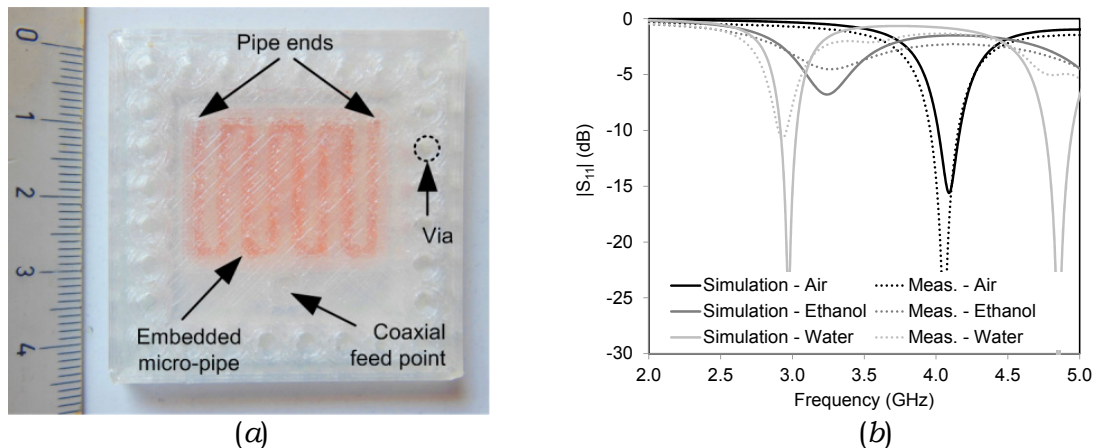


FIG. 4 – 3D-printed microfluidic sensor based on Ninjaflex: (a) photograph, with colored water to highlight the embedded micro-pipe; (b) simulated and measured scattering parameters with air, pure ethanol, and distilled water [4].

IV. CONCLUSION

This paper has presented some recent achievements in the additive manufacturing of substrate integrated waveguide components. After an accurate material characterization, 3D printing has been adopted for implementing a variety of structures, including components with three-dimensional shape, SIW cavities and filters, and microfluidic sensors.

ACKNOWLEDGEMENT

The authors gratefully acknowledge Prof. Manos Tentzeris and his group at the Georgia Institute of Technology, and Prof. Ferdinando Auricchio and his coworkers at the University of Pavia, for their collaboration in the development of 3D printed components.

REFERENCES

- [1] D. Giusto, A. Iera, G. Morabito, L. Atzori (Eds.), *The Internet of Things*, Springer, 2010.
- [2] M. Bozzi, A. Georgiadis, and K. Wu, "Review of Substrate Integrated Waveguide (SIW) Circuits and Antennas," *IET Microwaves, Antennas and Propagation*, Vol. 5, No. 8, pp. 909–920, June 2011.
- [3] S. Moscato, R. Bahr, T. Le, M. Pasian, M. Bozzi, L. Perregrini, and M.M. Tentzeris, "Additive Manufacturing of 3D Substrate Integrated Waveguide Components," *Electronics Letters*, Vol. 51, No. 18, pp. 1426–1428, Sept. 2015.
- [4] S. Moscato, M. Pasian, M. Bozzi, L. Perregrini, R. Bahr, T. Le, and M. Tentzeris, "Exploiting 3D Printed Substrate for Microfluidic SIW Sensor," *45th European Microwave Conference (EuMC2015)*, Paris, France, Sept. 7–10, 2015.
- [5] S. Moscato, R. Bahr, T. Le, M. Pasian, M. Bozzi, L. Perregrini, and M.M. Tentzeris, "Infill Dependent 3D-Printed Material Based on NinjaFlex Filament for Antenna Applications," *IEEE Antennas and Wireless Propagation Letters*, Vol. 15, 2016.
- [6] C. Tomassoni, R. Bahr, M. Bozzi, L. Perregrini, and M. Tentzeris, "3D Printed Substrate Integrated Waveguide Filters with Locally Controlled Dielectric Permittivity," *46th European Microwave Conference (EuMC2016)*, London, UK, Oct. 3–7, 2016.

RADIATION OF AN APERTURE ON THE FACE OF A PERFECTLY ELECTRIC CONDUCTING WEDGE-SHAPED SCREEN

Monica Righini

Department of Information Engineering, University of Florence.
Via S. Marta 3, 50139 Florence, Italy

monica.righini@unifi.it

Abstract

The scattering problem of a slot on the face of a wedge-shaped perfectly electric conducting screen is presented. In this contribution the aperture is treated via an application of the equivalence theorem so as to decouple the problem in an outer and an inner part. The electromagnetic field radiated in the external wedge region is computed via the Method of Moments relying on an exact analytic solution, which expresses the Sommerfeld spectral integral in terms of an infinite summation.

Index Terms – Electromagnetic wedge diffraction, apertures, High-frequency approximation.

I. INTRODUCTION

The problem of the computation of the electromagnetic field generated by an aperture over a perfectly electric conductor wedge is a problem of remarkable practical relevance, since it is the building brick for the accurate analysis of many kind of antennas as, among the others, arrays of slots. Considering the general problem of an aperture on a perfect electric conductor wedge-shaped screen (Fig. 1), this can be analyzed with the equivalence theorem in the Harrington and Mautz formulation [1], by, splitting the original problem into two equivalent sub-problems, one relative to the exterior of the wedge and one to the inner part (Fig. 2), coupling being enforced via magnetic equivalent currents where the original aperture was.

The main issue here is the evaluation of the radiation of the equivalent currents in a wedge shaped region. Issues of this type has been studied in the past within the framework of high-frequency techniques, and in particular, within the Geometrical Theory of Diffraction (GTD) and its Uniform version (Uniform Geometrical Theory of Diffraction - UTD) [2]. However, if the slot is close to the wedge the accuracy of the high-frequency techniques rapidly deteriorates.

The present contribution aims at evaluating the field radiated by a single slot on a wedge face, using a particular series expression for Green's function in a wedge-shaped region of recent publication [3]. The main

advantage of this formulation is that the infinite summation is the exact solution of the electromagnetic problem for any source or observation point in the wedge-shaped region.

The paper is organized as follows: Section II briefly presents the formulation of the exterior problem. Section III shows some preliminary simulation results and finally, Section IV draws some conclusions.

II. ELECTROMAGNETIC PROBLEM

The problem of computing the electromagnetic field radiated by an aperture over a perfectly conducting wedge is presented, Fig. 1.

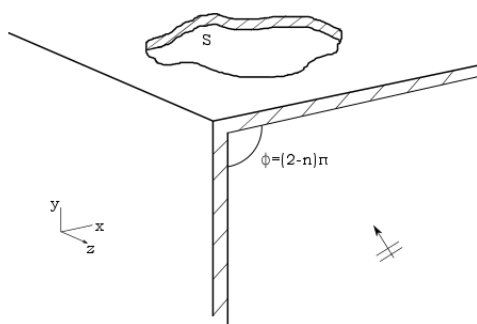


FIG. 1 - General problem of an aperture over a perfectly electric conductor wedge, with an impinging plane wave from the inside.

On the basis of the Harrington-Mautz formulation of the equivalence theorem, this problem can be split into two equivalent problems: an inner (represented by region A) and outer one (represented by region B), Fig 2.

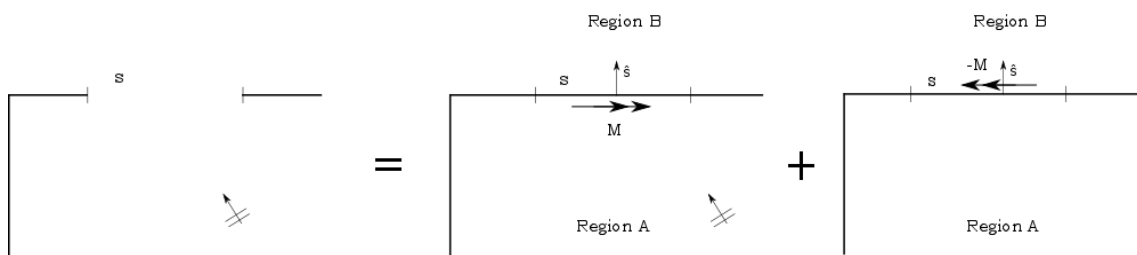


FIG. 2 - This figure shows the two parts composing the main problem. On the left the inner problem (region A) is illustrated while, on the right, there is the outer one (region B).

These two regions are coupled through the aperture (surface S), where both the electric and magnetic field tangential components must be continuous. The condition on the electric field is guaranteed by enforcing a surface magnetic current distribution \mathbf{M} in the inner problem, and $-\mathbf{M}$ in the outer problem according to:

$$\mathbf{M} = \hat{n} \times \mathbf{E} \tag{1}$$

whereas the continuity of magnetic field tangential component is explicitly imposed by:

$$\mathbf{H}_t^a(\mathbf{M}) + \mathbf{H}_t^b(\mathbf{M}) = -\mathbf{H}_t^i \quad (2)$$

Eq. (2) can be numerically solved by employing the Method of Moments (MoM), [4], which uses the dyadic Green's function which, in a wedge shaped region, are given in [3]. In that reference, starting from the Hertz's potential spectral integral representation, an expression of the potential, and hence of the fields, is obtained in terms of infinite summation. For example, the expression of the z -component of the electric potential for a magnetic dipole of moment $p^{(m)}$ parallel to the edge of the wedge is:

$$\Pi_z^e = \frac{jp^{(m)}\sin\chi}{8\pi\mu n} \sqrt{\frac{2\pi k}{R}} \left\{ \sum_{m=0}^{\infty} \cos\left(\frac{m}{n}\phi_0\right) \cos\left(\frac{m}{n}\phi\right) \sum_{p=0}^{\infty} \frac{H_{m/n+2p+1/2}^{(2)}\left(\frac{k\rho\rho_0}{2R}\right)^{m/n+2p}}{p!\left(\frac{m}{n}+p+1\right)} + \right. \\ \left. - \frac{1}{2} \sum_{p=0}^{\infty} \frac{H_{2p+1/2}^{(2)}\left(\frac{k\rho\rho_0}{2R}\right)^{2p}}{p!(p+1)} \right\} \quad (3)$$

III. ANALYSIS OF EXTERIOR PROBLEM

In the case in which the aperture is a single thin slot, the inner problem can be reduced to that of a rectangular waveguide, where a modal expansion can be enforced to represent the fields at the aperture.

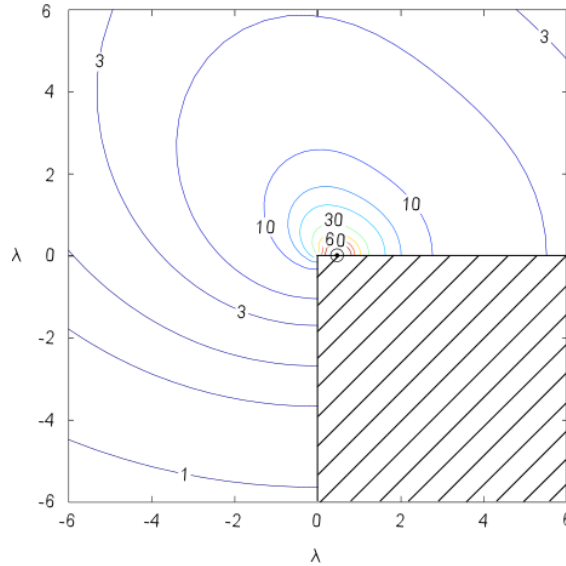


FIG. 3 - Simulation of the z -component of the magnetic field (A/m) radiated by a magnetic current of intensity 1V placed over a perfectly conducting wedge and parallel to its edge. The wedge internal angle is $\phi = \pi/2$ and the source is placed at 0.25λ from the edge of the wedge.

Hence, as a preliminary result, the radiation of the equivalent magnetic currents relative to the rectangular waveguide modes will be presented here. In fact, if the slot is thin, the fundamental TE_{10} mode behaves as a single magnetic dipole on the perfectly electric conductor wedge.

In Fig. 2, the amplitude of the z -component of the magnetic field is shown. This result has been obtained considering the sinusoidal tapering of the current bound to the TE_{10} field distribution, having a 1 V-amplitude at the slot center. The slot, and hence the magnetic dipole, is parallel to the edge of the wedge and placed a quarter wavelength from it.

IV. CONCLUSION

The issue of computing the electromagnetic field radiated by an aperture in a perfectly conducting wedge has been presented. Using the Harrington-Mautz formulation the problem has been divided into two sub-problems, coupled via surface magnetic currents computable via MoM. In order to compute the electromagnetic field in the wedge-shaped regions, a novel Green's function expression has been used.

Preliminary numerical results for the radiation of a single thin slot, represented by a magnetic dipole, has been presented.

Although this is a preliminary analysis, its result is very important because it represents the first step for the accurate analysis of generic apertures or slot arrays.

REFERENCES

- [1] R. Harrington and J. Mautz, "A generalized network formulation for aperture problems," *IEEE Transactions on Antennas and Propagation* vol. 24, no. 6, pp. 870-873, Nov. 1976.
- [2] R.J. Kouyoumjian and P.H. Pathak, "A Uniform Geometrical Theory of Diffraction for an Edge in a Perfectly Conducting Surface," *Proceedings of the IEEE*, vol. 62, no. 11, pp. 1448-1461, Nov. 1974.
- [3] G. G. Gentili, G. Pelosi, M. Righini and S. Selleri, "Electromagnetic scattering of a dipole field by a perfectly conducting wedge," *IEEE Transactions on Antennas and Propagation*, vol. 63, no. 9, pp. 4081-4090, Sep. 2015.
- [4] R. F. Harrington, *Time-Harmonic Electromagnetic Fields*, McGraw-Hill, New York, USA, 1961.

A BACK PROJECTION ALGORITHM TO FOCUS SYNTHETIC APERTURE RADAR DATA ACQUIRED FROM STRONGLY NON-RECTILINEAR TRAJECTORIES

Stefano Perna^(1, 2), Antonio Natale⁽²⁾, Paolo Berardino⁽²⁾

⁽¹⁾ DI, Università degli Studi di Napoli “Parthenope”, Centro
Direzionale Isola C4, Napoli, Italy

⁽²⁾ IREA – CNR, Via Diocleziano 328, Napoli, Italy

perna@uniparthenope.it, natale.a@irea.cnr.it, berardino.p@irea.cnr.it

Abstract

In this work we devise a Back Projection (BP) strategy for precise focusing of data acquired by Synthetic Aperture Radar (SAR) sensors moving along highly non-rectilinear trajectories. In order to reduce the computational burden typical of each BP procedure, the proposed approach consists of two processing steps. The first one performs, in a computationally efficient fashion, a rough compensation of the effects induced on the received radar echoes by the non-rectilinear shape of the sensor trajectory. The residual effects not compensated through the first step are accommodated, without any approximation, by the second processing step, which splits the synthetic antenna in a number of adjacent sub-arrays with the aim of further improving the computational efficiency of the overall focusing procedure. The algorithm has been tested on a helicopterborne data set collected by a P-band SAR of the Italian Space Agency.

Index Terms – Back Projection, Motion Compensation, SAR data focusing.

I. INTRODUCTION

Synthetic Aperture Radar (SAR) imaging is a powerful tool for Earth’s observation, in all weather conditions and with high space resolutions [1]. SAR systems are mounted on moving platforms, such as satellites, airplanes, helicopters. Indeed, the sensor movement allows synthesizing a fictitious array whose dimension is much greater than that of the physical radar antenna. This makes it possible to obtain high spatial resolution in the along-track direction provided that, for each point of the observed scene, coherent summation of the corresponding backscattered radar echoes is properly performed. This operation, which is referred to as SAR focusing in the literature [1], requires proper compensation of the phase terms that depend on the so-called range history, i.e., the distance between the considered point of the observed scene and the phase center of the moving radar antenna. This because, in a typical SAR acquisition scenario, the generic observed target belongs to the Fraunhofer region of the radar antenna, but not to that of the synthetic array.

In the case of spaceborne SAR sensors, the satellites move along very stable (locally) rectilinear orbits. In this case, the synthetic array turns

out to be rectilinear and uniformly spaced. This allows calculating the range history of each target of the observed scene without any external information on the terrain topography [1]. Differently, when the SAR sensors are mounted onboard airplanes or helicopters, the unavoidable presence of atmospheric turbulences induces deviations from an ideal rectilinear flight track. In this case, the synthetic array turns out to be non-rectilinear. Moreover, the range history of each observed target becomes dependent on both the terrain topography and the track deviation. Accordingly, the precise focusing of SAR data acquired by airplanes or helicopters requires the exploitation of external Digital Elevation Models (DEMs) of the observed area, as well as the flight data recorded by the navigation system mounted onboard [1].

In the last decades a number of accurate and computationally efficient algorithms, which operate in the spectral domain, have been devised to focus satellite SAR data [1]. These algorithms take benefit from the assumption that in the satellite case the synthetic array is a uniformly spaced linear one. To widen the range of applicability of these algorithms also to airborne or helicopterborne SAR data, it is necessary the additional implementation of the so-called MOTion COmpensation (MOCO) procedures, which are aimed at dealing with non-rectilinear synthetic arrays [2]-[3]. However, such MOCO procedures involve some approximations [4] necessary to preserve the high computational efficiency typical of the focusing algorithms that operate in the spectral domain. In particular, these approximations become unsuitable in the presence of large trajectory deviations, thus impairing the accuracy of the focusing procedure [4]. This may represent a key limit for natural disaster monitoring, where the exploitation of flexible – possibly unmanned – SAR platforms, such as small airplanes or helicopters, is particularly appropriate to guarantee a quick response, but it is typically associated to strongly non-rectilinear flight tracks.

To circumvent these kinds of problems, in this work we present a Back Projection (BP) focusing algorithm, which operates in the time domain and, differently from the spectral domain approaches, does not carry out any approximation, even when the synthetic array is strongly non-rectilinear. The proposed algorithm includes a bulk MOCO step followed by a sub-aperture approach to reduce the high computational burden common to each BP procedure. The effectiveness of the proposed approach has been evaluated on real data acquired by a helicopterborne P-band SAR sensor of the Italian Space Agency (ASI).

II. RATIONALE OF THE PROPOSED BACK PROJECTION FOCUSING ALGORITHM

Let us consider a SAR system that moves along an arbitrary trajectory. The position of a generic scattering target P lying in the observed scene is described by the vector \vec{P} . The position of the radar antenna phase center during the acquisition is instead described by the vector $\vec{P}_A(t)$, where t represents the time. Let us suppose that the generic target P is *seen* within the main lobe of the radar antenna in the

times $\{t_1, \dots, t_n, \dots, t_N\}$, where t_n is the transmission time of the n^{th} pulse. The antennas of our synthetic array (which is not necessarily a linear and periodic one) are located in $\{\bar{P}_A(t_1), \dots, \bar{P}_A(t_n), \dots, \bar{P}_A(t_N)\}$. In order to focus such a generic target P into a pixel $i(P)$ of the SAR image, we have to carry out the following coherent summation:

$$i(P) = \sum_{n=1}^N s_n h_n e^{j\frac{4\pi}{\lambda}|\bar{P}_A(t_n) - \bar{P}|} \quad , \quad (1)$$

which is referred in the literature to as SAR Back Projection (BP) of the target P . In Eq. (1) λ is the operating wavelength, s_n is the radar echo relevant to the considered target and received by the n^{th} antenna of the synthetic array, while h_n is a weighting function which takes into account both the antenna pattern and the round-trip attenuation. Note that the exponential term in Eq. (1) compensates for the phase-delay of the received echoes relevant to the considered target, which typically does not belong to the Fraunhofer region of the synthetic array. It is also recalled that in the case of non-rectilinear synthetic arrays, computation of the terms of Eq. (1) requires the exploitation of an external DEM of the observed area, as well as the flight data recorded by the navigation system [1]-[3].

Unfortunately, due to the Range Cell Migration (RCM) effect [1], the terms s_n in Eq. (1) are typically not aligned in the SAR raw data (that is, the two dimensional radar signal recorded onboard) [1]. They rather distribute over a raw data patch, whose extension depends on the target range history. Accordingly, to compute the terms s_n in Eq. (1) it is necessary to compensate, for each observed target, the RCM effect through a raw data interpolation/resampling step. To this regard, it can be shown that the severer the flight track deviations, the stronger the RCM effect and the higher the number of numerical operations required to accurately compute the terms s_n .

To limit this problem, which is particularly stringent in the presence of strongly non-rectilinear synthetic arrays, we have to find a smart, computationally efficient, procedure aimed at reducing as much as possible the RCM of the radar echoes, before the implementation of the summation in Eq.(1). To this aim, in our approach we first apply a Bulk MOCO (BM) that carries out a rough correction of the RCM for all the targets of the observed scene. Such a BM step is carried out in a computationally efficient fashion based on the spectral domain algorithms in [2]-[3]. Then, to accurately accommodate, for each observed target, the residual RCM not compensated by such BM step, we take benefit from the additional consideration that the excursion of the RCM within the overall synthetic array is typically greater than that occurring in a generic portion of the array itself. Accordingly, we split our synthetic antenna in a number of smaller, adjacent, sub-arrays, and for each of them we compensate, without approximations, the residual RCM not compensated by the BM step. Final computation of the BP focusing in Eq. (1) follows straightforwardly.

III. EXPERIMENTAL RESULTS

Here we show the focusing results obtained on P-band data acquired in 2013 on the Molise region, Italy, by a helicopterborne SAR of the ASI. Although the helicopter exhibited strong trajectory deviations (up to 140 meters in a flight track of about 90 seconds), the proposed BP algorithm allowed us to get accurate focusing results. Due to space limitation, further details will be provided at conference time; here we just stress that the obtained geometrical resolution evaluated on bright points is practically coincident with the theoretical expected one (see Fig.1).

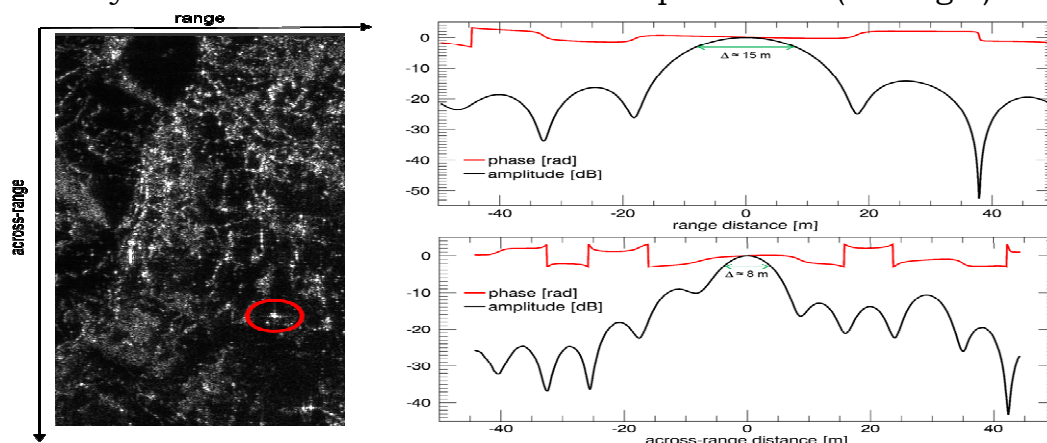


FIG. 1 – Left : a patch of the focused image. Right: range (up) and across-range (down) cuts relevant to the bright point marked in the red circle. Green arrows represent the expected theoretical resolutions.

IV. CONCLUSION

In this work we proposed a BP strategy for the accurate focusing of SAR data acquired from platforms that move along highly non-rectilinear trajectories. The algorithm has been tested on actual data collected by a helicopterborne SAR sensor. The obtained results clearly demonstrate the effectiveness of the proposed strategy.

ACKNOWLEDGEMENT

The work has been partly supported by ASI in the frame of the contract “Evoluzione Tecnologica e sperimentazione, tramite piattaforma aerea, di un sensore Radar nelle bande VHF e UHF (frequenze inferiori ad 1 GHz)”, signed by ASI and CNR-IREA.

REFERENCES

- [1] G. Franceschetti and R.Lanari, “Synthetic Aperture Radar Processing”, CRC PRESS, New York, 1999.
- [2] A. Moreira, Y. Huang, “Airborne SAR Processing of Highly Squinted Data Using a Chirp Scaling Approach with Integrated Motion Compensation”, *IEEE Trans. Geosci. Remote Sensing*, vol. 32, pp.1029-1040, July 1994.
- [3] G. Fornaro, “Trajectory Deviations in Airborne SAR: Analysis and Compensation”, *IEEE Trans. Aerospace and Electron. Syst.*, vol. 35, pp.997-1009, July 1999.
- [4] G. Fornaro, G. Franceschetti, S. Perna, “On Center-Beam Approximation in SAR Motion Compensation”, *IEEE Geosci. Remote Sensing Lett.*, vol. 3, pp. 276-280, April 2006.

INVESTIGATION OF THE PATH REDUCTION FACTOR ON TERRESTRIAL LINKS FOR THE DEVELOPMENT OF A PHYSICALLY-BASED RAIN ATTENUATION MODEL

R. Ghiani ⁽¹⁾, L. Luini ⁽²⁾ ⁽³⁾, A. Fanti ⁽¹⁾

⁽¹⁾ DIEE, Università di Cagliari, Cagliari, Italy

⁽²⁾ DEIB, Politecnico di Milano, Milano, Italy

⁽³⁾ IEIIT, Consiglio Nazionale delle Ricerche (CNR), Milano, Italy R.
alessandro.fanti@diee.unica.it

Abstract

This contribution investigates the path reduction factor (PF) on terrestrial links, a typical element of rain attenuation prediction models, introduced to take into due account the spatial inhomogeneity of rainfall. A large number of PF values are calculated by simulating the interaction of a hypothetical terrestrial link with a set of realistic rain fields synthesized by MultiEXCELL. The dependence of PF on different quantities such as the path length, the operational frequency, and the rain rate measured at the transmitter, is addressed. Based on that, the contribution also illustrates the preliminary modeling steps oriented to the development of a new analytical methodology for the physically-based prediction of the rain attenuation affecting terrestrial links.

Index Terms – Eletromagnetic wave propagation, rainfall effects, prediction models.

I. INTRODUCTION

In the near future, the global data volume exchange is expected to increase dramatically, on one side, due to the gradual enrichment of high data rate broadcast and multimedia services offered to users and, on the other side, owing to the exponential increase in the number of devices connected to the Internet [1]. This calls for the enhancement of existing telecommunication networks and/or for the deployment of new infrastructures. A viable way to tackle this problem, especially in regions where laying wires and optical fibers is cumbersome or very expensive (e.g. remote areas), is to install wireless links at high frequencies (e.g. millimeter waves), which offer the large bandwidth necessary to support the required high data rates (e.g. in future 5G systems [2]). As is well-known, the impairments induced by the atmosphere on millimeter waves steeply increase with the operational frequency, mainly because of hydrometeors, which cause strong absorption and scattering of the impinging electromagnetic energy [3]. As a result, accurate models able to predict rain attenuation affecting terrestrial links are of paramount importance for the design of reliable communication systems. This is more and more true when the frequency increases considerably: as scarce or no experimental data are

available beyond 40 GHz, the increased reliability offered by physically-based models [4] should be preferred to (semi-)empirical and semi-empirical methods in designing new links, being the accuracy of latter typically more critical when applied outside the frequency range of the data used to regress their (often several) parameters [5]. This contribution investigates the path reduction factor (PF), a typical element of rain attenuation prediction models (both for terrestrial links and Earth-space paths), introduced to take into due account, in an effective way, the spatial inhomogeneity of rainfall. Specifically, values of PF are calculated by simulating the interaction of a hypothetical terrestrial link with a set of realistic rain fields synthesized by MultiEXCELL [6]. The dependence of PF on different quantities such as the path length, the operational frequency, the rain rate measured at the transmitter, is addressed. Moreover, based on the calculated PF values, the paper illustrates the preliminary modeling results oriented to the development of a new analytical methodology for the physically-based prediction of the rain attenuation affecting terrestrial links.

II. METHODOLOGY AND RESULTS

The results presented in this contribution rely on MultiEXCELL, a global rainfall model oriented to the analysis and prediction of the atmospheric impairments affecting the propagation of electromagnetic waves [6]. MultiEXCELL generates a set of synthetic rain fields (spatial resolution of 1 km×1 km and dimension of 250 km×250 km), whose ensemble preserves the local rainfall statistics and reproduces the correct rainfall spatial correlation. MultiEXCELL was successfully used to simulate the interaction of rain fields with millimeter wave communication systems in different scenarios, including terrestrial links. Results reported in [4] show a good performance in predicting statistics of rain attenuation A affecting terrestrial links, achieved by numerically integrating the specific attenuation along the link as follows:

$$A = \int_L k R(l)^\alpha dl \quad (1)$$

In (1), L is the length of the link, k and α are rain-to-specific attenuation conversion coefficients extracted from recommendation ITU-R P.838-3 [7], whilst $R(l)$ is the rain rate at position l along the path, associated to a pixel of the rain map (refer to Fig.1). The long-term goal of this work is the definition of an analytical model combining the good prediction performance achieved in [4] with a handier analytical approach relying on the concept of path reduction factor PF: :

$$A = (k R_{tx}^\alpha L) PF \quad (2)$$

In (2), A is calculated by applying (1) for different positions of the terrestrial links across the rain map, RTX is the rain rate “measured” at the transmitter, while PF is introduced to account for the inhomogeneity of the rain intensity along the link (as also clearly shown in the example of Fig. 1).

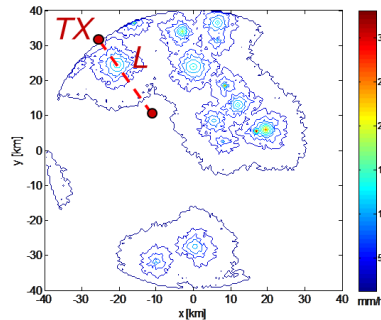


FIG. 1 – Calculation of the path attenuation along a terrestrial link using MultiEXCELL.

A large number of PF values were obtained considering all the rain maps generated by MultiEXCELL. Starting from such values, the path reduction factor was investigated in terms of its dependence on the path length ($1 \text{ km} \leq L \leq 50 \text{ km}$), the rain rate ($1 \text{ km} \leq RTX \leq 50 \text{ km}$) and the operational frequencies ($10 \text{ GHz} \leq f \leq 80 \text{ GHz}$). Moreover, results on PF as obtained according to this approach were compared with the path reduction factor as defined in several prediction models available in the literature. As an example Fig.2 shows all the PF values as a function of RTX obtained for a 20 GHz link of 15 km (565 rain maps), together with the trend of PF adopted in the ITU-R P.530-16 [8] and Brazilian [9]. models. Finally, based on such results, the contribution describes some preliminary steps aiming at devising a new analytical methodology for the physically-based prediction of the rain attenuation affecting terrestrial links.

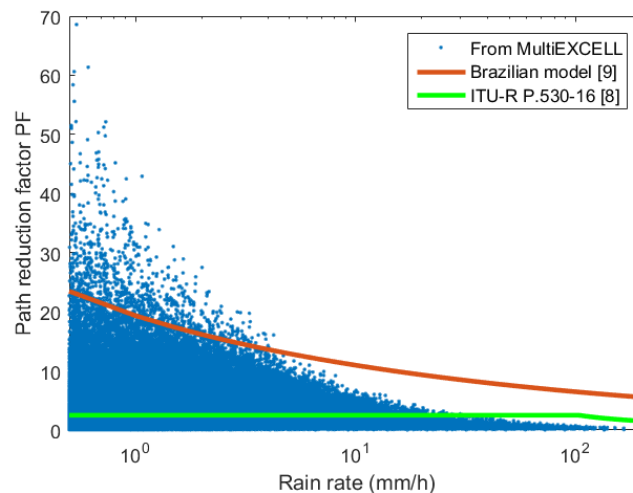


FIG. 2 – Path reduction factor values derived from MultiEXCELL (see Fig.1) compared to the trend of PF adopted in the ITU-R P.530-16 [8] and Brazilian [9] models.

REFERENCES

- [1] C. Dehos, J. L. González, A. De Domenico, D. Kténas, L. Dussopt, “Millimeter-Wave Access and Backhauling: The Solution to the Exponential Data Traffic Increase in 5G Mobile Communications Systems?”, *IEEE Communications Magazine*, Year: 2014, Volume: 52, Issue: 9, Pages: 88 – 95.
- [2] T. S. Rappaport, Shu Sun, R. Mayzus, Hang ZhaoY. Azar, K. Wang, G. N. Wong, J. K. Schulz, M. Samimi, F. Gutierrez, “Millimeter Wave Mobile Communications for 5G Cellular: It Will Work!”, *IEEE Access*, Year: 2013, Volume: 1, Pages: 335 – 349.
- [3] T. S. Rappaport, Shu Sun, R. Mayzus, Hang ZhaoY. Azar, K. Wang, G. N. Wong, J. K. Schulz, M. Samimi, F. Gutierrez, “Millimeter Wave Mobile Communications for 5G Cellular: It Will Work!”, *IEEE Access*, Year: 2013, Volume: 1, Pages: 335 – 349
- [4] R. K. Crane, “*Electromagnetic Wave Propagation Through Rain*,” Wiley, 1996.
- [5] L. Luini, C. Capsoni, “A physically based methodology for the evaluation of the rain attenuation on terrestrial radio links”, *EuCAP 2010*, pp. 1-5, 12th-16th April 2010, Barcelona, Spain.
- [6] Doc. 3M/25-E, *Modelling and prediction methods of rain attenuation statistics, China*, 26 May 2008.
- [7] L. Luini, C. Capsoni, “MultiEXCELL: a new rain field model for propagation applications”, *IEEE Transactions on Antennas and Propagation*, vol. 59, no. 11, Page(s): 4286 - 4300, November 2011.
- [8] ITU-R Recommendation P.838-3, Specific attenuation model for rain for use in prediction methods, *Propagation in Non-Ionized Media*, Geneva, 2003.
- [9] ITU-R, Recommendation P.530-16, “*Propagation data and prediction methods required for the design of terrestrial line-of-sight systems*”, Geneva, 2015.
- [10] L. A. R Silva Mello, M. S. Pontes, “Prediction of rain attenuation in terrestrial links with the full rainfall distribution”, *EuCAP 2007*, 11-16 November, 2007, EICC, Edinburgh, UK.

MICROWAVE BESSEL BEAM LAUNCHER FOR PLANETARY DRILLING OPERATIONS

S. Costanzo¹, G. Di Massa¹, A. Borgia¹, A. Raffo¹

¹ DIMES – University of Calabria , 87036 Rende (CS), Italy
costanzo@dimes.unical.it

Abstract

The adoption of non-diffracting Bessel beam is proposed in this work to realize a near-field concentrator with high penetration depth, to be successfully integrated in drilling tools used for planetary surfaces exploration. The design, realization and test of a microwave Bessel beam launcher is discussed, and preliminary experimental results on analog rock materials are reported, which reveal beneficial effects for drilling operations.

Index Terms – Bessel beam, diffraction-free, planetary exploration, high penetration.

I. INTRODUCTION

Drilling operations are required to capture soil samples useful for the analysis of planetary compositions. ESA's planned ExoMars explorer is fitted with a drill and a sampling system, specifically designed to reach down to 2 meter depth using a rod extension mechanism [1]. Drilling operations are usually performed by adopting a mechanical device, which however can give some drawbacks, as requiring fast rotating parts (huge power) and suffering for the presence of vibrations on the drill machine, which can give some damages when working on very hard materials (e.g. planetary rocks). To overcome the above difficulties, an alternative method has been recently proposed which exploits the use of localized microwave energy to perform drilling operations [2]. In this first attempt, a frequency equal to 2.45 GHz is adopted to exploit the absorption mechanism as in a microwave oven, thus limiting the application to non-conductive materials exhibiting high water content, but not so usefully applicable to Mars/Lunar soil. Furthermore, research conducted till now [3] have revealed drawbacks related to the low penetration depth (only a few cm) and the large power requirement (above 1KW). In the present work, the investigation of microwave-assisted drilling tools, based on a near-field concentrator approach, is performed with the aim to reach enhanced penetration depth, but requiring lower power than existing techniques.

II. MICROWAVE BESSEL BEAM LAUNCHER

To obtain enhanced penetration depth, we propose the adoption of microwave Bessel beams, which are non-diffracting solutions of the Helmholtz equation [6], whose transverse localization is independent on the propagation distance. A Bessel beam can be described by the zero-order Bessel function of the first kind, namely [4]:

$$E(r, \varphi, z) = A_o e^{-jk_z z} J_0(k_r r) \quad (1)$$

k_z , k_r being the longitudinal and the radial wave vectors, respectively.

The particular feature of the Bessel beam to appear not as a single spot, but rather as a series of concentric rings, leads to a first advantageous property for microwave drilling, namely the ability to reconstruct after an obstruction ('self-healing'). But the main advantage is related to the enhanced penetration depth of a Bessel beam propagating inside a hole in a bulk material, when compared to that achievable with a conventional beam (e.g. a Gaussian beam). Following the approach outlined in [4], a microwave Bessel beam is designed in this work as the aperture field at the open-end of a metallic circular waveguide. The schematic configuration of the designed X-band Bessel beam launcher is reported in Fig. 1, where a single loop antenna is adopted to properly excite the field inside the circular waveguide.



FIG. 1 – Microwave Bessel beam launcher: (a) side view and (b) front view.

III. EXPERIMENTAL RESULTS

The proper behavior of X-band Bessel beam launcher is successfully validated by performing both return loss as well as near-field measurements into the anechoic chamber of the Microwave Laboratory at University of Calabria. To verify the optimum power transfer of the launcher when acting on planetary surfaces, the return loss is measured by assuming three different propagation media, namely air, basalt and marble, these last two materials having similar compositions to Mars/Lunar soils. A very good matching condition (about -40 dB) can

be observed in Fig. 3 around the design frequency $f_0 = 8.7$ GHz, thus assuring the good power injection capability of the designed Bessel beam launcher.

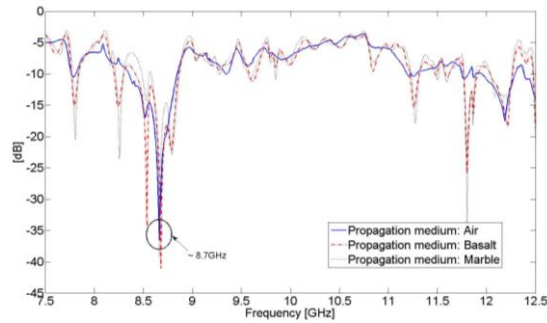


FIG. 3 – Measured return loss of X-band Bessel beam launcher in air and in the presence of analog rock materials.

Furthermore, in order to verify the high penetration features, near-field measurements are performed on different planes placed at parallel distances from the circular aperture of the launcher, from 1.5 cm (strictly near the aperture) up to 14 cm. As illustrative examples, the measured near-field amplitudes at 8 cm and 10 cm distances are reported in Fig. 4.

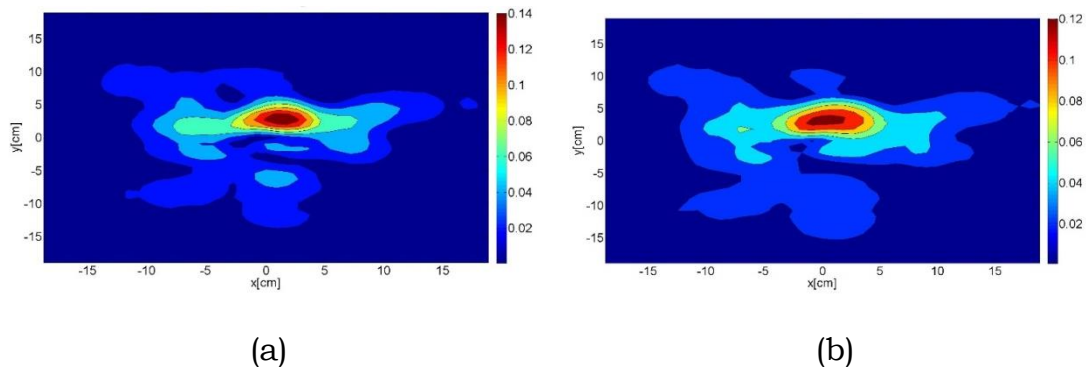


FIG. 4 – Near-field intensity on a plane (a) 8 cm and (b) 10 cm away from the Bessel beam launcher.

IV. RESULTS ON ROCK MATERIALS

To investigate the potential application of Bessel beam launcher in microwave-assisted drilling, irradiation experiments are conducted on analog rock materials, namely basalt and marble, by highlighting the effect of microwave Bessel beam heating on the dielectric constant of these materials and the consequent effect on their mechanical hardness. Test samples are illuminated by a Bessel beam with a 100 W power, by monitoring the temperature increase and the variation of dielectric constant before and after irradiation. To perform dielectric

measurements, a standard open-ended coaxial probe is adopted. A photograph showing the setup adopted for the irradiation experiments on basalt samples is reported in Fig. 5, while the measured dielectric profile is illustrated in Fig.6. It can be observed that 45 min after irradiation occur to have a decrease in the dielectric constant, and thus a beneficial effect on reducing the material hardness. This time interval is required to reach a zero thermal gradient inside the rock (Fig. 8), thus re-obtaining a homogeneous material, with a (almost) unique permittivity along the thickness direction.



FIG. 5 – Test setup for microwave Bessel beam irradiations: (a) equipments and (b) Bessel beam launcher acting on the rock material.

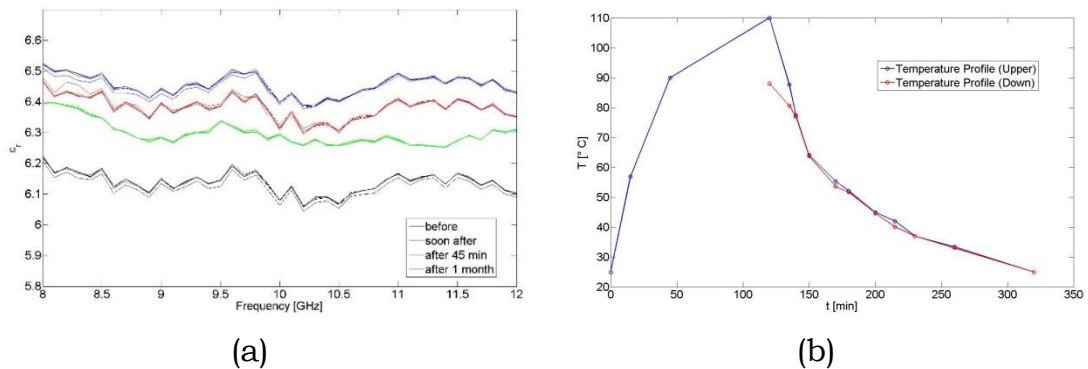


FIG. 6 – Measured (a) dielectric and (b) temperature profile on basalt surfaces before and after irradiation.

REFERENCES

- [1] D. Rodionov, O. Witasse, J. L. Vago, “Exomars: overview of scientific programme,” in 40th COSPAR Scientific Assembly, vol. 40 of COSPAR Meeting, 2014.
- [2] E. Jerby, “The microwave drill”, Science, vol. 298, pp. 587-589, 2002.
- [3] E. Jerby, V. Dikhtyar, O. Aktushev, “Microwave drill for ceramics,” Ceramic Bulletin, vol. 82, 2003.
- [4] M. Salem, E. Niver, “Launching transverse-electric localized waves from a circular waveguide,” 2001 IEEE AP-S/URSI Symposium.

DI-SILICATE DENTAL CERAMIC SURFACE PREPARATION BY FIBER LASER: ULTRASTRUCTURAL ANALYSIS

Carlo Fornaini^{(1),(2)}, Federica Poli⁽¹⁾, Elisabetta Merigo⁽²⁾, Marco Valentini⁽³⁾, Luca Romoli⁽³⁾, Federica Bondioli⁽³⁾, Stefano Selleri⁽¹⁾, Annamaria Cucinotta⁽¹⁾

⁽¹⁾ Department of Information Engineering, Parma University
Parco Area delle Scienze 181/A, Parma, Italy

⁽²⁾ Micoralis Laboratory, Faculty of Dentistry, University of Nice,
24, Avenue des Diabes Bleus, Nice, France

⁽³⁾ Department of Industrial Engineering, Parma University, Parco
Area delle Scienze 181/A, Parma, Italy

carlo.fornaini@nemo.unipr.it

Abstract

Lithium di-silicate ceramics offer a high level of accuracy when used in prosthetic dentistry. Their bonding, using different resins, is highly dependent on micro-mechanical interlocking and adhesive chemical bonding. Investigation of the performances of high strength ceramics when their surface is modified for chemical and mechanical bonding is so required. The aim of this study was to investigate the possibility of using fiber lasers for surface treatment of Lithium di-silicate ceramics thus improving their mechanical and chemical properties. Samples were irradiated by a pulsed fiber laser at 1064 nm with different parameters and the surface modifications were analysed by optic microscope and SEM. The observation of the irradiated surface showed a roughness increase with small areas of melting and carbonization. Even if further studies will be necessary to confirm the results, fiber laser irradiation may be considered a good help to increase the adhesion of Lithium di-silicate ceramics.

Index Terms – Lithium di-silicate ceramics, dentistry, laser texturing, fiber laser, SEM

I. INTRODUCTION

The demand of ceramic restorations has become increasingly common in dentistry and the continuous need of precisions is still a challenge to be achieved. The internal surface of the ceramic restoration must be prepared to optimize micro-mechanical retention of the cement into the ceramic micro roughness. Surface treatment of the ceramic increases the surface in contact with the tooth structure creating micro-porosities and enhancing the potential for mechanical retention of the cement [1]. Different surface treatment methods have been proposed to provide roughness and promote micro-mechanical retention [2]. The search for non-destructive methods to treat inert ceramics and modify their mechanical and chemical properties helps to produce an activated surface. Surface treatment (laser irradiation) has been previously

engaged in the industrial field using high power lasers and represents a controllable and flexible technique aiming to modify the surface properties of different materials [3]. Laser processing parameters during such surface modifications are expected to influence the surface microstructure [4].

Fiber lasers are sources where the active medium is an optical fiber with core doped by active ions, such as Nd (neodymium), Yb (ytterbium), Er (erbium), Tm (thulium) [5]. The fundamental difference between traditional solid-state lasers and fiber ones lies in the form of the gain medium. In fact, while bulk crystal lasers are typically based on conventional rod or slab geometries, in fiber lasers active ions are added into the core of an optical fiber, often with a length of many metres [6]. This laser family emits in a wide wavelength range, depending on dopants and host materials, operates in continuous wave (CW) or pulsed mode. CW output powers of several kW [7] and pulse energies up to around 30 mJ [8],[9] can be currently obtained with Yb-doped fiber lasers.

The aim of this study was to characterize Lithium di-silicate ceramic specimens irradiated with a 1064 nm pulsed fiber laser. The characterization of the surfaces before and after laser irradiation using Scanning Electron Microscopy (SEM) could help to observe the morphological changes and eventual zones of melting and cracks.

II. METHOD

The circular faces of twelve cylinders of Lithium di-silicate ceramics (e.max Press, Ivoclar, Italy) with 10 mm diameter and 8 mm height were processed in three 3 x 3 mm square zones using a 1064 nm pulsed fiber laser (AREX 20) provided by Datalogic, Italy. The source has a maximum average output power of 20 W and a fixed pulse duration of 100 ns. Each square zone on the sample faces has been processed with different laser parameters. In particular, the output power has been changed from 100% to 30%, the repetition rate from 100 to 20 kHz and the speed from 50 to 5 mm/s. The specimens were observed by an optic microscope (Olympus MTV-3, Japan), then metallized and subsequently analysed by SEM (Ion sputter Jeol JFC 1100E, USA).

III. RESULTS

As demonstrated in Fig. 1-3, the SEM observation of metallized surface irradiated samples showed two types of surfaces, smooth and rough ones. Some areas of melting and burning were shown at the highest energy used, due to the cumulative effect of the laser irradiation. Also the presence of some cracks with variable intensities related to the thermal effects of laser irradiation has been noticed. The laser parameters which seem to be the most effective for surface conditioning without damages for the material are 60% of output power, repetition rate of 20 kHz and speed of 50 mm/s, as shown in Fig. 3 (right).

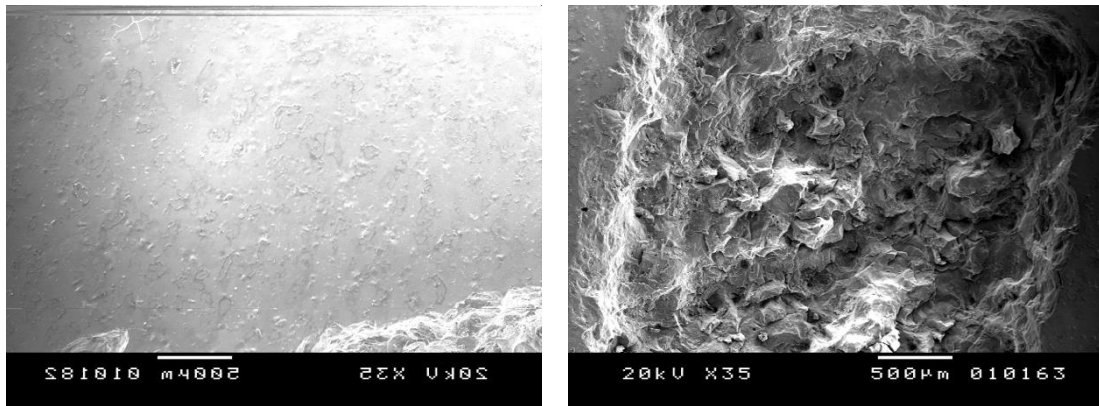


FIG. 1 – (Left) Non-irradiated sample. (Right) Sample obtained with the following laser parameters: 100% of output power, repetition rate of 20 kHz, speed of 10 mm/s.

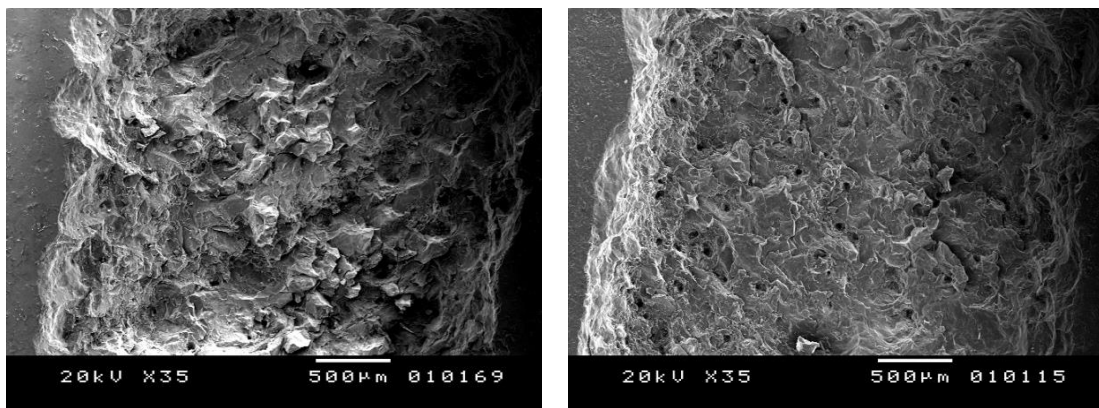


FIG. 2 – Samples obtained with the following laser parameters: (left) 100% of output power, repetition rate of 20 kHz, speed of 5 mm/s; (right) 100% of output power, repetition rate of 20 kHz, speed of 30 mm/s.

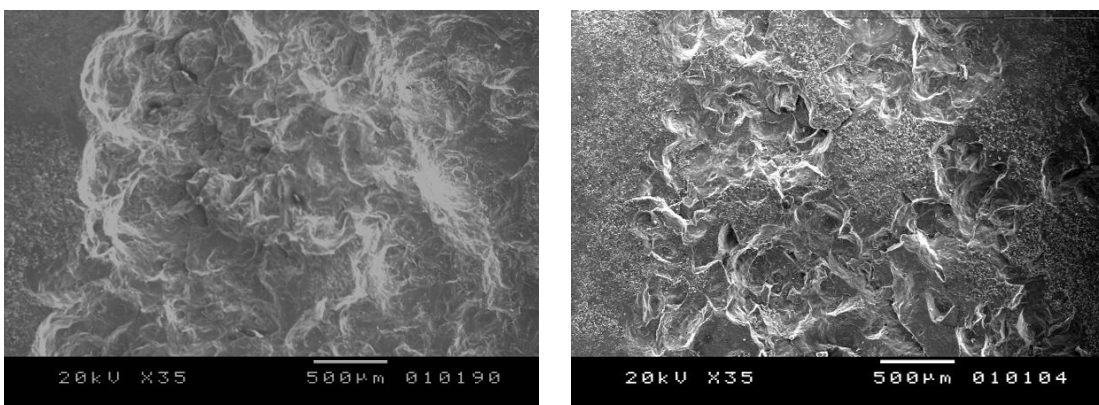


FIG. 3 – Samples obtained with the following laser parameters: (left) 75% of output power, repetition rate of 20 kHz, speed of 50 mm/s; (right) 60% of output power, repetition rate of 20 kHz, speed of 50 mm/s.

IV. CONCLUSION

Even if this study must be considered as preliminary, due to the small number of samples treated, however it may open a new perspective on the utilization of fiber lasers for the Lithium di-silicate ceramics surface conditioning.

Further studies should be performed to analyse the mechanical properties of irradiated ceramic surface (micro-hardness, roughness) and the adhesion characteristics after ceramic sealing (wettability, shear bond strength and micro-leakage).

ACKNOWLEDGEMENT

The Authors would like to thank Datalogic S.p.A. and in particular Dr. Lorenzo Bassi for providing the fiber laser source.

REFERENCES

- [1] R. Giordano R and E.A. McLaren EA, "Ceramics overview: classification by microstructure and processing methods", *Compend Contin Educ Dent*, 2010;31:682-4.
- [2] M. Albakry, M. Guazzato and M.V. Swain, "Biaxial flexural strength, elastic moduli, and x-ray diffraction characterization of three pressable all-ceramic material", *J Prosthet Dent*, 2003;89:374-80.
- [3] W. Holand, M. Schweiger, M. Frank and V. Rheinberger, "A comparison of the microstructure and properties of the IPS empress 2 and the IPS empress glass ceramics", *J Biomed Mater Res*, 2000;53:297-303.
- [4] A. Piwowarczyk, P. Ottil, H.C. Lauer and T. Kuretzky, "A clinical report and overview of scientific studies and clinical procedures conducted on the 3 M ESPE lava allceramic system", *J Prosthodont* 2005;14:39-45.
- [5] V. Tuchin, *Biomedical Optics and Biophotonics*, SPIE Press, USA, 2012
- [6] M. Pierce, S. Jackson, P. Golding, B. Dickinson, M. Dickinson, T. King and P. Sloan, "Development and application of fibre lasers for medical applications", *Proc. SPIE 4253*, Optical Fibers and Sensors for Medical Applications, 144 (June 4, 2001); doi:10.1117/12.427916.
- [7] B. Shiner, "The Impact of Fiber Laser Technology on the World Wide Material Processing Market", CLEO: 2013, OSA Technical Digest (online) (Optical Society of America, 2013), paper AF2J.1.
- [8] C. Zheng, H. Zhang, P. Yan, M. Gong, "Low repetition rate broadband high energy and peak power nanosecond pulsed Yb-doped fiber amplifier", *Optics & Laser Technology*, vol. 49, pp. 284-287, July 2013.
- [9] F. Stutzki, F. Jansen, A. Liem, C. Jauregui, J. Limpert, and A. Tünnermann, "26 mJ, 130 W Q-switched fiber-laser system with near-diffraction-limited beam quality", *Optics Letters*, vol. 37, pp. 1073-1075, 2012.

OPTIMIZATION OF STRAIGHT AMPLIFIER ERBIUM DOPED WAVEGUIDES WITH THE IMPLEMENTATION OF AN ADIABATIC INPUT TAPER

V. Vaiti

Department of Information Engineering, Parma University
Viale delle Scienze 181/A, Parma, Italy
valentina.vaiti@studenti.unipr.it

Abstract

In order to increase the coupling of pump and signal light into the high contrast erbium doped potassium double tungstate waveguides, two different amplifiers input models are investigated. The first one is the straight waveguide model, in which the confinement of the electromagnetic field permits large erbium concentration to be inverted with relatively low input pump power. The second one is an adiabatic input taper, which is theoretically designed and optimized. A comparison of the results of the total net gain in two different cases (MFD = 4 μm , MFD = 10 μm) with a straight waveguide model is carried out in order to demonstrate the efficiency of this designed structures.

Index Terms – Erbium, waveguide amplifiers, mode field diameter, adiabatic input taper.

I. INTRODUCTION

Original investigations of rare-earth began in 1839, when a French physicist, A.E. Becquerel, observed the photovoltaic effects for the first time [1]. Throughout the next 70 years rare-earth-doped crystal spectra were extensively investigated and theories were developed to accurately explain their optical properties. The field of luminescence from rare-earth ions has been one of the steady growth during the past decade, principally due to the ever-increasing demand for optical sources and amplifiers operating at a wavelength compatible with fiber communications technology [2]. The fortunate coincidence between the Er^{3+} emission band around 1550 nm and the principal low-loss and low-dispersion window of optical fibers has been the main driving force behind much of the recent work on erbium-doped materials [3].

In this paper, the amplifier model in high contrast erbium doped potassium tungstate waveguide is presented. In order to calculate the total net gain and the losses at the output of the channel, several assumptions about two fundamental aspects, the simplified 3-level rate equation model and the erbium laser emitting spectral range, are required. The total net gain, the saturation output power and the gain bandwidth are calculated as a function of three different parameters: the amplifier length, the pump power and the rate of the erbium concentration. With the purpose of increasing the coupling of pump and signal light into the high contrast waveguide amplifiers, input adiabatic

tapers are considered. A comparison of the theoretical results of the total net gain in two different cases (MFD = 4 μm , MFD = 10 μm) with a straight waveguide model is carried out in order to demonstrate the efficiency of this designed structure.

II. TOTAL GAIN CALCULATION

The optimization of an amplifier model relies on different important design parameters: the geometrical waveguide cross-section providing the fundamental mode operation, the pump and the signal wavelengths and, lastly, the launched pump power range. In our case, the waveguide cross-section amplifiers consisted of a 2 μm -thick by 2 μm -wide KYW channel with a range height of 1.5 μm . This geometry allows high field confinement in straight and taper sections of the waveguide.

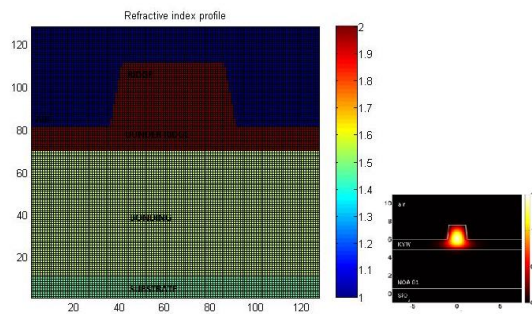


FIG. 1 – Waveguide amplifier cross-section and stimulated signal mode profile.

Thanks to the *PhoeniX Field Designer Software* [4], the mode-field simulations at pump and signal wavelength are performed, using the Finite Difference (FD) algorithm. In Fig. 1 the waveguide cross-section, the materials used and the corresponding different refractive-index values are shown. A relevant feature is the discretization of the model. The idea is to create a two-dimensional grid, to improve the accuracy of the calculation of the ion population distribution. Specifically, the x-axis and y-axis are both divided in 129 sections with non-uniform space distribution: more concentrated (few space between one grid and the other) in the doped region amplifier, conversely in the “peripheral” section.

III. INPUT ADIABATIC TAPER

In order to increase the coupling of pump and signal light into the high contrast waveguide amplifiers, input tapers with various tapering angles (from 0.5° to 5°) are investigated. The study and the results of an adiabatic taper (adiabatic condition: angle = 0.5°) for different ridge width dimensions are reported, in accordance with the convergence tests concluded before the taper research. The idea is to simulate a linear

adiabatic taper, decrementing the width from the initial to the final dimension (from 6 μm and 5 μm to 2 μm). For each value of the width, it is necessary to create the pump profile, signal profile and refractive index profile in *PhoeniX Field Designer* and then export them in the *Matlab* script. The Gaussian Overlap calculation is very important and it is made using the Mode Field Diameter (MFD), or rather the measure of the beam width of light propagating in a single mode fiber.

Normally the MFD is larger than the actual core material, because some of the light travels through the cladding [8]. According to the laser beam present in the Optical Science laboratories, the choice is to use two different MFDs for our range pump and signal power with the purpose of measuring the higher internal net gain in different conditions. The MFDs selected are MFD = 4 μm and MFD = 10 μm . According to the theoretical results, the initial taper width is fixed to the dimension of the MFD selected.

TABLE I - PARAMETERS AND VALUES APPLIED TO THE INPUT ADIABATIC TAPER SIMULATION.

Adiabatic Taper $\theta=0.5$			Gaussian Overlap		
MFD	10	4		Taper	Straight
Winp [μm]	6	5	MFD = 10	20%	10%
Wout [μm]	2	2	MFD = 4	68%	48%
Taper Length [mm]	0,458	0,343			

All the parameters used in the total internal net gain calculation, required for an input adiabatic taper, are listed in Table 1. In order to determine to which extent an input taper is useful, it is important to compare the designed structure with a straight waveguide, in which the input ridge width is equal to the final ridge width (2 μm). We decide to measure the gain in dB for different pump power values and to evaluate the results at the end of a length of 0.7 cm, according to the chip dimensions (1 cm x 1 cm). The trend of the total internal gain in dB for different pump power values is reported in Fig. 2(a) and Fig. 2(b). Using a MFD = 10 μm , an adiabatic taper structure permits to reach good performances, leading to a gain of 40 mW, which is around 3 dB higher with respect to a straight structure. For high pump power values (200 mW), the graph converges towards the same results in both cases. The performances obtained using a MFD = 4 μm , shown in Fig. 2(b), suggest that an input adiabatic taper implementation is not useful, because we can reach a total gain of 20 mW for both taper and straight waveguides, with relatively low pump power.

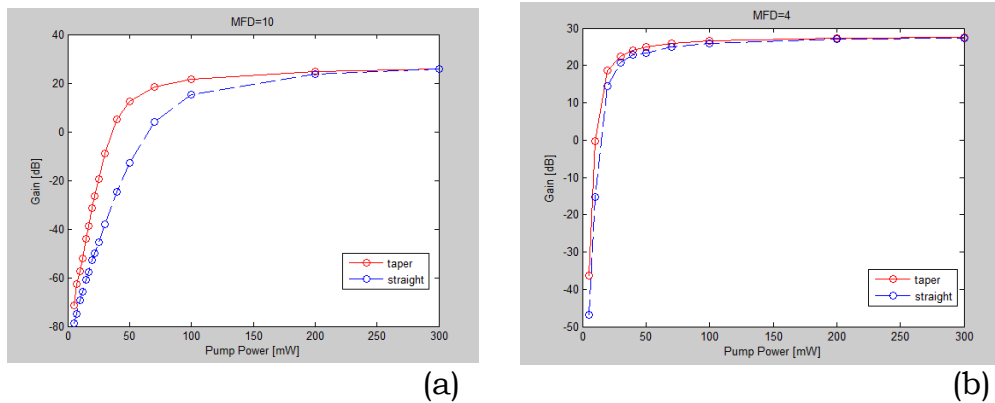


FIG. 2 – Measured internal net gain at different pump power values for 0.7 cm-long Er³⁺ doped waveguide: simulations with (red curves) and without (blue curve) using an input adiabatic taper, considering MFD=10 μm (a) and MFD=4 μm (b).

IV. CONCLUSION

The total internal net gain is the key factor in order to select the implementation of an adiabatic linear taper or a straight waveguide at the beginning of a waveguide amplifier doped with erbium. We have theoretically demonstrated that with MFD = 10 μm a good performance and gain value is obtained using an adiabatic input taper. In the MFD = 4 μm scenario, an implementation of the designed structure is not useful and a straight waveguide is advised.

Future works may involve the percentage of erbium concentration, always considering an optimization of the structure of the amplifier model, that means the dimensions and the structure of the doped channel waveguide.

REFERENCES

- [1] Antoine César Becquerel, “Éléments de physique terrestre et de météorologie”, Paris : Firmin-Didot frères, 1847.
- [2] J. Bradley, “Al₂O₃:Er³⁺ as a gain platform for integrated optics”, thesis, 2009.
- [3] A.J. Kenyon, “Recent developments in rare-earth doped materials for optoelectronics”, Department of Electronic and Electrical Engineering, University College London, October 2002.
- [4] A.M. Guzmán, “Simplified slab waveguide three-level model for short length EDFA pumped at 1.48 μm”, Universidad Nacional de Colombia Departamento de Física, Bogotá, Colombia, vol.33 no.1 São Paulo Mar. 2003.

PLASMONIC NANOANTENNA FOR POSSIBLE CMOS INTEGRATION

M. Celli⁽¹⁾, A. Polemi^(1,2), and L. Vincetti⁽¹⁾

⁽¹⁾ Department of Engineering “Enzo Ferrari”, University of Modena, Modena, Italy

⁽²⁾ Department of Material Science and Engineering, Drexel University, Philadelphia, USA alessia.polemi@unimore.it

Abstract

Plasmonic nanoantennas have gained interest in several environments like integrated photonics, biosensing, microscopy and solar cells, due to their capability in collecting and conveying the electromagnetic radiation in the visible and in the near visible regions. However, examples of antennas applied to integrated circuits are conspicuously rare even if they are able to provide a solution to the bandwidth shortage problem. In this paper, we show a new plasmonic nanoantenna configuration for easy coupling with plasmonic transmission line in order to enable the direct on-chip connection with modulators and demodulators of a communication system. The antenna shows tunable capabilities that allow for bidirectional communications without the use of complex time division duplex (TDD) techniques. The size of the antenna and the materials employed are all suitable for future CMOS integration

Index Terms – Plasmonics, nanoantennas, on-chip, CMOS, nitride.

I. INTRODUCTION

Nowadays, one of the most limiting factor in the computational power demand is represented by slow interconnects. In a modern CPU architecture, there are billions of transistors that cannot efficiently communicate through the traditional integrated transmission system based upon metallic lines, since they are not able to increase their bandwidth at the growth rate of transistors. Silicon photonics transmission lines could deliver a sufficient bandwidth to avoid the interconnection bottleneck, but their dimensions are far from those that an ultra-scaled process requires.

Plasmonic devices provide scaled dimensions and high bandwidth, taking the best from both worlds of electronics and photonics. The main drawback for plasmonics devices still remain the short propagation length, which does not represent an obstacle given the nanoscale dimensions of integrated circuits. All constituent blocks of a typical transmission scheme (sources, transmission lines, modulators...) have already been characterized for a plasmonic setup as shown in literature [1]-[3]. Among plasmonic devices, nanoantennas play an important role in the overall communication scheme. Many scientific papers explore different configurations [4],[5] but not many examples are present that

successfully address the problem of on-chip and possibly CMOS integration [6],[7]. This kind of integration, not only requires the usual plasmonic resonant features, but also an accurate selection of materials. In fact, plasmonic nanoantennas for infrared and visible domain are usually made of noble metals, mostly gold and silver, which offer good resonant conditions and relatively low losses. However, these materials are not well suited for CMOS manufacturing process due to their high reactivity with silicon (silver) and to their high diffusivity (gold).

In this paper, we present a new plasmonic nanoantenna design able to guarantee high frequency communication that satisfies the high density integration requirements imposed by a modern CMOS process and the employment of compatible materials. In particular, we use here TiN, which has been already used within CMOS technology and also shows good plasmonic properties [2]. The antenna also shows capabilities for bidirectional communications, thanks to its multiple resonances.

II. DESCRIPTION AND RESULTS

Starting from the advent of high-k metal gate transistors, titanium nitride is widely adopted in CMOS devices thanks to its electrical properties and to the good integration with the manufacturing process. Its employment in plasmonics is still low. TiN is usually deposited at low temperatures through atomic layer deposition (ALD) in order to satisfy the power budget limits imposed by the CMOS process, but low temperatures cause the contamination with oxygen and carbon that introduces not negligible losses [8]. However, a CMOS compatible deposition technique for TiN has been shown [9] and optical properties are able to compete with that of gold (see Fig. 1(a)).

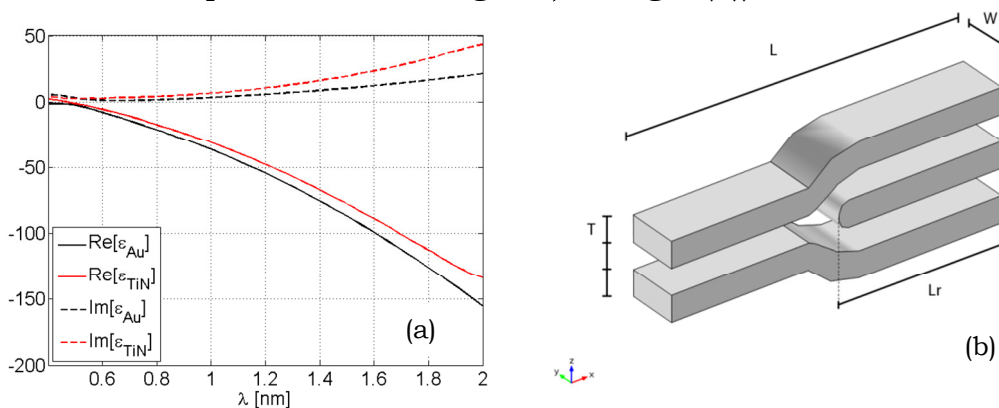


FIG. 1 – (a) Real and imaginary part of the dielectric constant of gold and TiN. (b) 3D view of the antenna. The dimensions are: $L = 97$ nm, $W = 15$ nm, $T = 7.5$ nm. L_r can be changed to give tunable properties at the antenna.

With the aim of CMOS integration, we have designed a frequency agile and compact nanoantenna, as depicted in Fig. 1(b), based on TiN. Because of the peculiar shape, we refer to this configuration to as diapasoon nanoantenna. The antenna dimensions are selected in order

to have a resonance at 1.55 μm . This particular geometry, if compared to an equivalent plasmonic dipole nanoantenna, shows much smaller size, about 3 times.

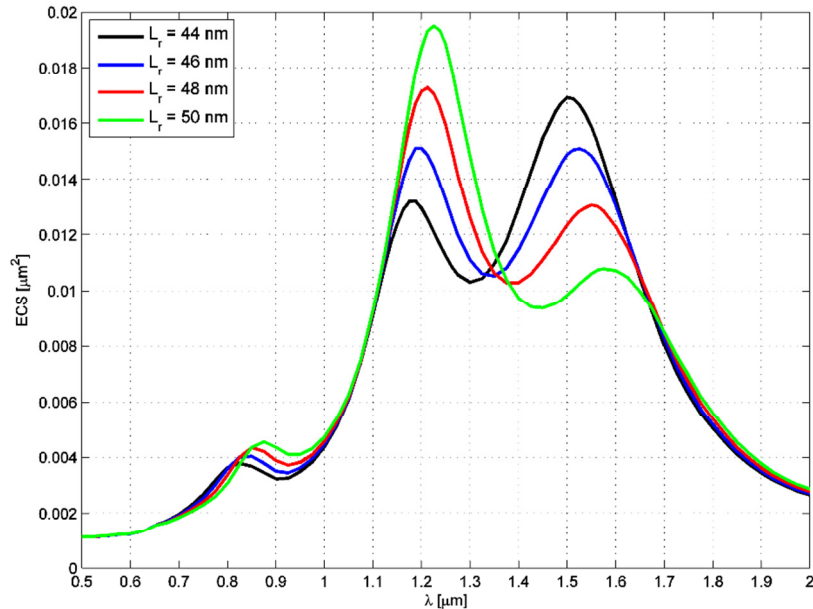


FIG. 2 – Extinction cross-section in μm^2 for different central arm lengths.

Furthermore, the presence of the central arm provides the capability of tuning a second resonance by changing its length, as shown in Fig.2. In particular, the outer arms of the diapasone control the resonance at higher wavelength, while the central arm changes the lower wavelength. The presence of two well separated resonances enables the possibility to have a bidirectional communication avoiding the need of using a TDD techniques that only adds complexity at the transmission scheme. One of the issues of many plasmonic nanoantennas is how to feed them. We show here (Fig. 3(a)) how we can easily couple a plasmonic transmission line to the diapasone nanoantenna. The simplicity in the coupling scheme is crucial for a communication setup in order to avoid losses. The radiation pattern of the antenna is also shown in Fig. 3(b), showing the typical dipole characteristic with very good uniformity.

I. CONCLUSION

The plasmonic nanoantenna proposed in this work is a promising candidate for full integration into a traditional CMOS process without the need of changes during the manufacturing of a silicon chip. The particular geometry saves area and grants an easy connection with the other fundamental blocks required to build a photonic transmission scheme. The particular diapasone shape allows for controlling of multiple resonance that can be helpful for bidirectional communications.

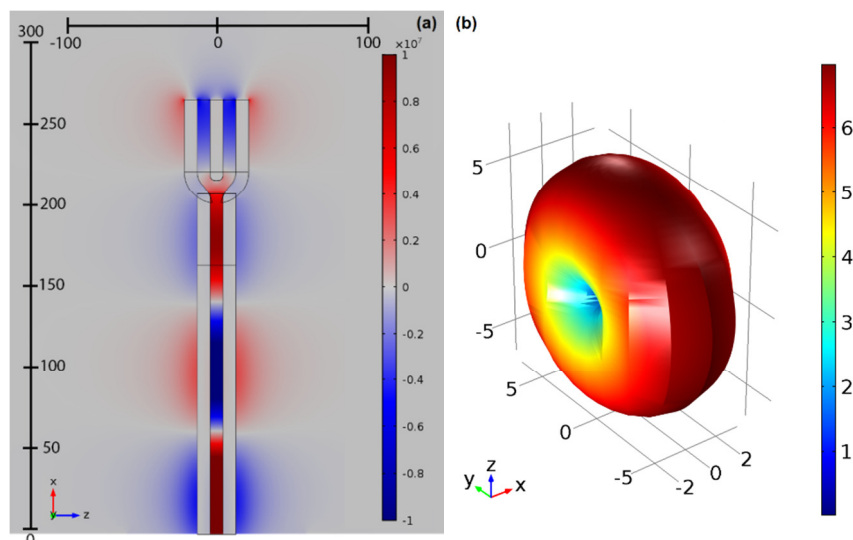


FIG. 3 – (a) Z component of the electric field in V/m when the antenna is coupled to a parallel plate transmission line. On the top and on the left of the figure are shown the x and y coordinates in nm. (b) Radiation characteristic of the nanoantenna (a.u.)

REFERENCES

- [1] Rupert F. Oulton, Volker J. Sorger et al, *Nature* 461, pp 629-632 (2009).
- [2] Viktoriia E. Babicheva et al, *Optics Express*, Vol. 21, Issue 22, pp. 27326-27337, (2013).
- [3] R. F. Oulton, V. J. Sorger et al, *Nature Photonics* 2, 496 - 500 (2008).
- [4] Ronen Adato, Ahmet A Yanik, and Hatice Altug, *Nano Lett.*, 2011, 11 (12), pp 5219–5226.
- [5] Maciej Klemm, *International Journal of Optics*, Volume 2012 (2012), Article ID 348306.
- [6] Moshik Cohen et al, *Scientific Reports* 5, Article number: 17562 (2015).
- [7] Leila Yousefi and Amy C. Foster, *Optics Express*, Vol. 20, Issue 16, pp. 18326-18335 (2012).
- [8] Justin A. Briggs, Gururaj V. Naik et al, *Applied Physics Letters* 108, 051110 (2016).
- [9] Naik GV, Shalaev VM, Boltasseva A., *Adv. Mater.*, 2013 Jun 25;25(24):3264-94.

REDUCTION OF HARMONIC DISTORTION IN RADIO OVER FIBER LINKS THROUGH DIGITAL PREPROCESSING

F.Fuochi, M.U.Hadi, J.Nanni, P.A. Traverso, G.Tartarini
Department of Electrical, Electronic and Information Engineering (DEI),
University of Bologna
Viale Risorgimento 2, Bologna, Italy
{Filippo.Fuochi.1990, usmanhadi}@ieee.org
{jacopo.nanni3, pierandrea.traverso, giovanni.tartarini}@unibo.it

Abstract

Radio over Fiber (RoF) networks have been taking more space as substitutes to wireless networks and are often used in Distributed Antenna System (DAS) to increase coverage in particular situations. However, significant bounds on the technology usability are set by the harmonic distortion, which, in the case of RoF links exploiting Directly Modulated Lasers (DML), has the combined effect of laser's chirp and optical fiber's dispersion among its major causes. In this paper, a signal pre distortion circuit, which can lower these detrimental effects, is proposed. A detailed description of its functional model is given, and its attractive features both in terms of quality improvement of the received signal, and cost effectiveness of the system are illustrated.

Index Terms – Directly Modulated Laser, Harmonic Distortion, Laser Inversion, Nonlinear Distortion.

I. INTRODUCTION

Fiber Optic links constitute mainstay of speedy data communication, both in digital form and in the form of radio signals, due to their high bandwidth and low attenuation. However, system nonlinearities can lead to signal distortions, which collocate the signal badly and, in the case of Radio over Fiber (RoF) systems, may result in a non-compliance with the Spectrum Emission Mask. Various solutions to significantly improve the transmission rendition by compensating these problems have been proposed, see, e.g., [1], [2]. In this paper a particularly cost effective approach is presented, which can be realized through a Field Programmable Gate Array with typical characteristics. Since the laser's chirp and the optical fiber's dispersion are major causes which generate harmonic distortion, a solution is proposed, based on the operations of Analog to Digital (ADC) conversion, digital predistortion and subsequent Digital to Analog (DAC) conversion, to reduce their effect. Simulations are then performed based on a rigorous theoretical model which allow to appreciate the advantages of the proposed solution.

II. PROPOSED APPROACH

The predistortion scheme is presented in Fig. (1). The input analog current is converted into a digital one. Then, the effect of the laser is simulated using its mathematical model, the optical fiber's chromatic

dispersion is compensated and the laser function is inverted to correct the current samples, before reconverting the current in analog form and subsequently modulate the real laser. So, the predistortion circuit firstly converts the Radio Frequency (RF) signal to a digital one. Then it works with its samples $i(t_k)$ to find the field, $e(t_k)$ transmitted by the laser. The corrected field which will entirely compensate for fiber's dispersion effect is $e_{corr}(t_k)$.

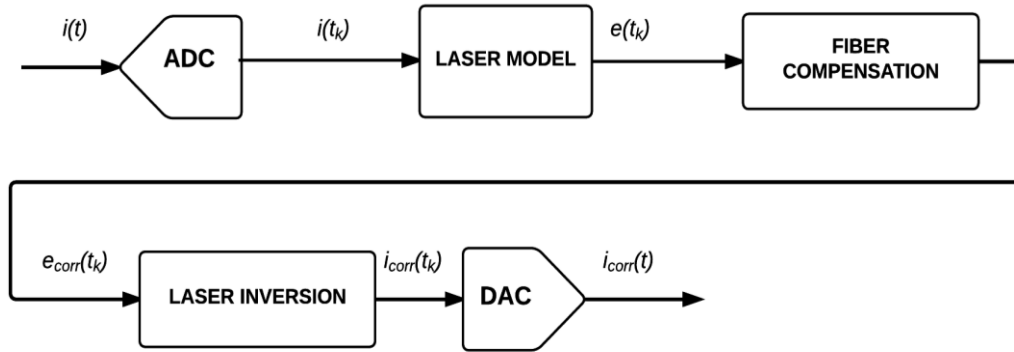


FIG.1- Block scheme of the predistortion circuit proposed.

The Conjugate of the Optical fiber's impulsive response which is related to the chromatic dispersion permits to fully compensate for the chromatic dispersion effects. It can be calculated starting from the fiber's transfer function and exploiting the commutative property of the Fourier transforms. Fig.2 shows the time domain dispersion compensation function. The impulse response function which can compensate for optical fiber's dispersion effect is complex and unlimited in both time and frequency. The blue waveform shows the real part while in red there is its imaginary part.

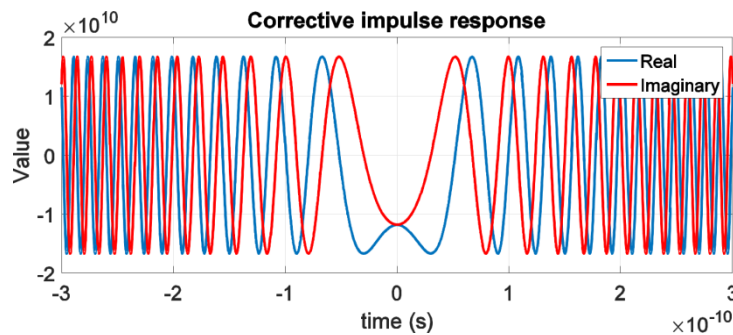


FIG.2 - Time domain dispersion compensation function.

The fiber's input field is convolved with the compensating function. Finally, before performing the digital to analog conversion, the "Laser Inversion" block will calculate the corrected samples of current $i_{corr}(t_k)$, that will lead to an electric field as close as possible to $e_{corr}(t_k)$, once used as laser's input signal. The laser inversion procedure consists in

finding the minimum distance, sample by sample, between a function contained in the laser's codomain and the corrected field. This operation can be fulfilled by minimizing the function:

$$f(i_{corr}(t_k)) = \sqrt{f_{\Re}^2(i_{corr}(t_k)) + f_{\Im}^2(i_{corr}(t_k))} \quad (1)$$

This minimizing function in Eq. (1) has been proposed by exploiting the starting function from [3]

Where

$$f_{\Re}(i_{corr}(t_k)) = \Re \left[\left[E_0 \sqrt{1 + c_I i_{corr}(t_k)} e^{j c_F \int_{-\infty}^{t_k} i_{corr}(\tau)} \right] - [e_{corr}(t_k)] \right] \quad (2)$$

and

$$f_{\Im}(i_{corr}(t_k)) = \Im \left[\left[E_0 \sqrt{1 + c_I i_{corr}(t_k)} e^{j c_F \int_{-\infty}^{t_k} i_{corr}(\tau)} \right] - [e_{corr}(t_k)] \right] \quad (3)$$

Where c_F and c_I are the intensity and frequency modulation coefficients respectively and with the notations $\Re[*]$ and $\Im[*]$ it is meant respectively that the real part and the imaginary part of $[*]$ is taken. In order to find minima of Eq. (1), it is necessary to find the zeros of its derivative.

The above mentioned solutions have been found using the MATLAB numeric solver ***vpasolve(eqn,var,init_guess)***, which returns one solution inside a fixed value's range. As can be seen in Fig. (3), there's no real solution but it's possible to find approximate solution which will partially compensate for Fiber Dispersion. Therefore, this solution's interval has been iteratively halved until no solution is found. Then, it is possible to retrieve the last valid value and check in Eq. (1) if it is either a maximum or a minimum. Clearly, if that solution is a minimum, then the algorithm ends. Otherwise, if it is not, then the search process will continue arranging the interval to find the second nearest solution, which will be a minimum.

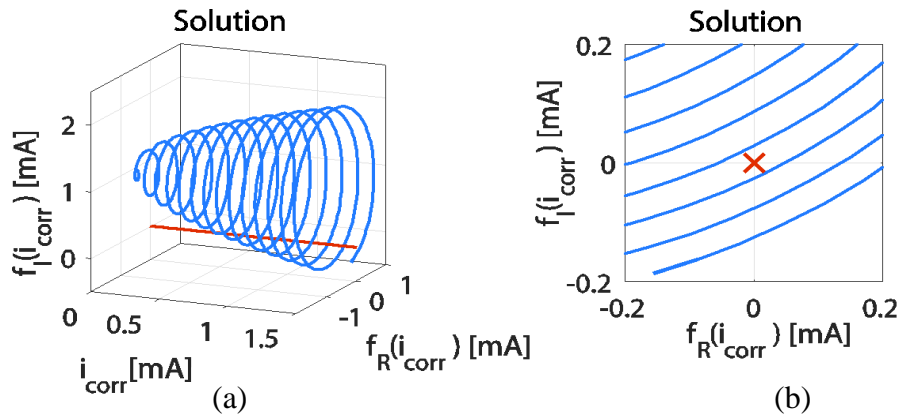


Fig.3 – The difference between electric field and corrected field, which will fully compensate for fiber's dispersion in a fixed time instant t_k , as a function of $i_{corr}(t_k)$ is shown in blue, while in red is presented $i_{corr}(t_k)$ itself. The general set of solutions is presented in (a), while (b) represents the graph projection on the complex plane, which highlights that there is no real current which can generate the field $e_{corr}(t_k)$.

III. RESULTS

As described earlier in the proposed approach, it is possible to use the digital preprocessing technique in order to lower the Harmonic distortion effects. The improvement has been confirmed in the simulations. As an example, Fig.4 reports the behavior of the quantity C/HD2, which is the difference, expressed in dB, between the power received at the frequency of the modulated signal and the power received at the double frequency.

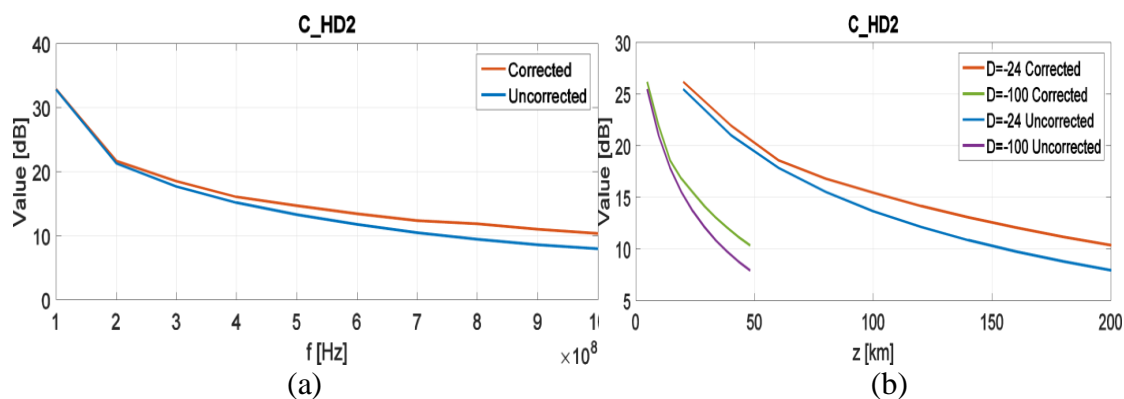


Fig.4 - Improvement in terms of C/HD2 (dB) using a laser emitting at a wavelength of 1310 nm, with adiabatic chirp coefficient $k_f = 130 \frac{\text{MHz}}{\text{mA}}$. In (a) the link is constituted by $L=200$ km of G.655 (dispersion $D = -24 \frac{\text{ps}}{\text{nm Km}}$) and C/HD2 is plotted versus frequency. In (b) the frequency is fixed to $f=1\text{GHz}$ and the distance L varies from 20 to 200 km. The blue and red simulation refer to the G655 fiber. Additional results are reported, referred to a fiber with $D = -100 \frac{\text{ps}}{\text{nm Km}}$ to show that the level of improvement due to the technique proposed depends on the product DL .

CONCLUSION

The functional model of a cost effective signal predistortion circuit has been implemented that can lower the detrimental combined effect of laser chirp and chromatic dispersion in Radio over Fiber links. The improvements due to the proposed compensation technique increase for increasing values of the product between level of dispersion and link length.

Through an improvement of the global system description, like the introduction of laser and photodiode nonlinearities, the implemented methodology can constitute an important cost-effective solution in the field of RoF predistortion technologies.

REFERENCES

- [1] H. Al-Raweshidy and S. Komaki, Eds., *Radio over Fiber Technologies for Mobile Communications Networks*. Norwood MA: Artech House, 2002.
- [2] Fibre optic networks for distributed, extendible heterogeneous radio architectures and service provisioning. FUTON project. [Online]. Available: <http://www.ict-futon.eu/>.
- [3] Davide Visani, Giovanni Tartarini, Luigi Tarlazzi, and Pier Faccin. "Transmission of UMTS and WIMAX signals over cost-effective radio over fiber systems," *IEEE Microwave and Wireless Components Letters*, 19(12):831-833, 2009.

DYSPROSIUM-DOPED CHALCOGENIDE FIBER LASER FOR MEDICAL APPLICATIONS

M. C. Falconi⁽¹⁾, G. Palma⁽¹⁾, F. Starecki⁽²⁾, V. Nazabal⁽²⁾, J. Troles⁽²⁾, S. Taccheo⁽³⁾, M. Ferrari⁽⁴⁾, F. Prudenzano⁽¹⁾

(1) Department of Electrical and Information Engineering, Politecnico di Bari, Via E. Orabona 4, 70125 Bari, Italy

(2) Institut des Sciences Chimiques de Rennes, UMR 6226, Université de Rennes 1-CNRS 263 Avenue du Général Leclerc, 35042 Rennes Cedex, France

(3) Institute of Advanced Telecommunications, Swansea University, Fabian Way, Crymlyn Burrows, Swansea SA1 8EN, Wales U.K.

(4) CSMFO Laboratory, Consiglio Nazionale delle Ricerche Istituto di Fotonica e Nanotecnologie, Via alla Cascata 56/C Povo, 38123 Trento, Italy

francesco.prudenzano@poliba.it

Abstract

A medium infrared (Mid-IR) laser exploiting a novel pumping scheme is designed. A photonic crystal fiber (PCF) made of chalcogenide glass doped with dysprosium ions is optimized to obtain laser emission at the wavelength $\lambda_s = 4384$ nm. Two different pumping beams #1 and #2, at the wavelengths $\lambda_{p1} = 2850$ nm and $\lambda_{p2} = 4092$ nm are used to populate the upper laser level. Both forward and backward pumping configurations are considered for each pumping beam. A slope efficiency of about $\eta = 32.5\%$ is simulated for pump #1 power $P_{p1} = 50$ mW and pump #2 $P_{p2} = 200$ mW, in the forward scheme. Slope efficiencies about three times higher than those reported in literature are simulated for the proposed configuration.

Index Terms – chalcogenide glass, dysprosium, laser, medium infrared.

I. INTRODUCTION

During the last decade, medium infrared (Mid-IR) light sources have attracted a lot of interest since they can find application in the field of medicine, global positioning and environmental monitoring [1]-[5]. Typical applications include active sensing, laser therapy ablation and imaging. Chalcogenide glasses have been proven to be good candidates for the fabrication of rare earth-doped fiber lasers and amplifiers [6]-[8]. In this work, dysprosium is exploited to obtain laser emission at the wavelength $\lambda_s = 4384$ nm. The major shortcoming of this rare earth is the long lifetime of the lower laser level, which leads to poor overall efficiencies. Many approaches, such as cascade lasing [1], [2], have been proposed in literature to overcome this problem, but they require high fabrication complexity. In this work, a novel pumping configuration is

numerically investigated. Slope efficiencies higher than those reported in literature are calculated.

II. ELECTROMAGNETIC DESIGN

The device exploits a pumping configuration based on two optical pumps, which are coupled to the Dy³⁺:Ga₅Ge₂₀Sb₁₀S₆₅ PCF fiber by means of an optical combiner. The fiber cross-section includes three rings of air holes surrounding the rare earth-doped solid core [6], [7]. Two fiber Bragg gratings, inscribed into the core, allow to obtain the optical cavity resonating at the wavelength $\lambda_s = 4384$ nm.

The rare earth interacting with light is modelled as a three level laser system. Absorption and stimulated emission are considered for the signal and the two pump beams, while Amplified Spontaneous Emission (ASE) is negligible. The model takes into account both forward and backward propagating beams. The optical and spectroscopic parameters employed in the simulations refer to glass samples preliminarily characterized. The calculations are performed by considering the pump #1 wavelength $\lambda_{p1} = 2850$ nm, pump #2 wavelength $\lambda_{p2} = 4092$ nm, signal wavelength $\lambda_s = 4384$ nm, pump #1 absorption cross section $\sigma_{12p} = 1.33 \times 10^{-24}$ m², pump #1 emission cross section $\sigma_{21p} = 9.79 \times 10^{-25}$ m², pump #2 absorption cross section $\sigma_{23p} = 3.39 \times 10^{-25}$ m², pump #2 emission cross section $\sigma_{32p} = 2.10 \times 10^{-25}$ m², signal absorption cross section $\sigma_{23s} = 7.32 \times 10^{-25}$ m², signal emission cross section $\sigma_{32s} = 1.09 \times 10^{-24}$ m², lifetime of level 3 $\tau_3 = 1.5$ ms, lifetime of level 2 $\tau_2 = 7.0$ ms, branching ratio for 3 \rightarrow 2 transition $\beta_{32} = 0.088$, fiber losses at all wavelengths $\alpha = 3$ dB/m.

Fig. 1 illustrates the optical signal power P_s of the Dy³⁺-doped fiber laser versus input pump #1 forward power $P_{p1}^+(0)$ and backward power $P_{p1}^-(L)$. The input pump #2 forward power is $P_{p2}^+(0) = 1000$ mW, the optical cavity length is $L = 0.5$ m, the dopant concentration is $N_{Dy} = 4 \times 10^{25}$ ions/m³, the first mirror reflectivity is $R_1 = 99\%$ and the second mirror reflectivity is $R_2 = 30\%$. The output signal power plot is almost symmetric with respect to the forward and backward powers, although the former yields a slightly larger output signal power. Moreover, the surface slope is very low for pump #1 powers higher than 45-50 mW.

Fig. 2 illustrates the optical signal power P_s of the Dy³⁺-doped fiber laser versus input pump #2 forward power $P_{p2}^+(0)$ and backward power $P_{p2}^-(L)$. The input pump #1 forward power is $P_{p1}^+(0) = 50$ mW, while the other laser parameters are the same of Fig. 1. The laser characteristics are linear with respect to both forward and backward pump #2 powers. Again, the forward pumping scheme operates slightly better than the backward one. The best achievable slope efficiency is about 32.5%.

The slope efficiency may be improved by optimizing the laser cavity by means of algorithms such as Particle Swarm Optimization (PSO) and Backtracking approaches.

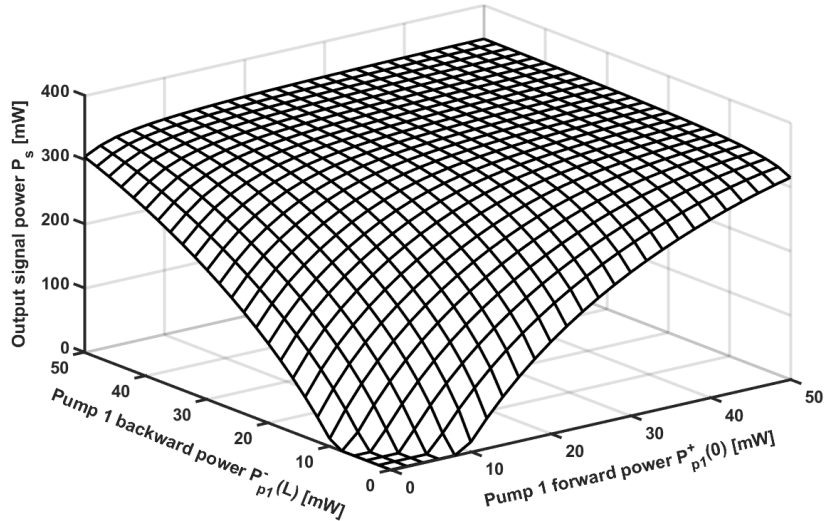


FIG. 1 – Optical signal power P_s of the Dy^{3+} -doped PCF laser versus input pump #1 forward power $P_{p1}^+(0)$ and backward power $P_{p1}^-(L)$. Input pump #2 forward power $P_{p2}^+(0) = 1000$ mW; optical cavity length $L = 0.5$ m; dopant concentration $N_{\text{Dy}} = 4 \times 10^{25}$ ions/m³; first mirror reflectivity $R_1 = 99\%$; second mirror reflectivity $R_2 = 30\%$.

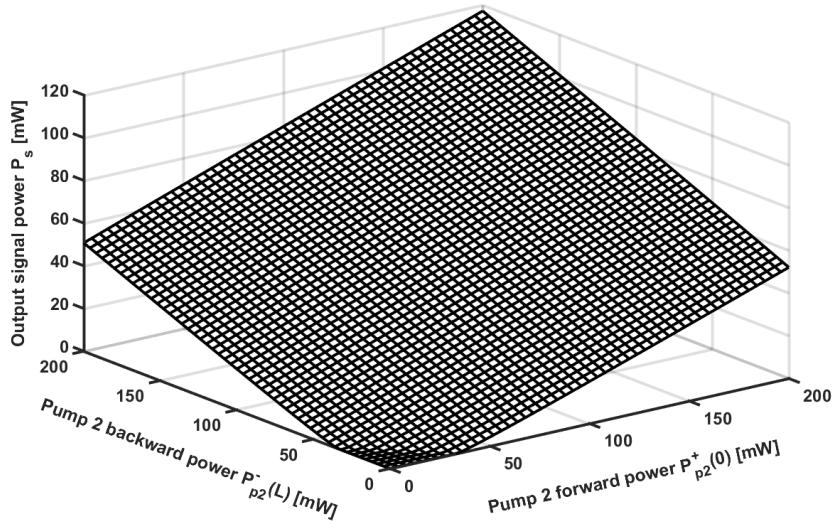


FIG. 2 – Optical signal power P_s of the Dy^{3+} -doped PCF laser versus input pump #2 forward power $P_{p2}^+(0)$ and backward power $P_{p2}^-(L)$. Input pump #1 forward power $P_{p1}^+(0) = 50$ mW; optical cavity length $L = 0.5$ m; dopant concentration $N_{\text{Dy}} = 4 \times 10^{25}$ ions/m³; first mirror reflectivity $R_1 = 99\%$; second mirror reflectivity $R_2 = 30\%$.

III. CONCLUSION

A novel pumping configuration for a Mid-IR Dy^{3+} -doped fiber laser is proposed and numerically investigated. A slope efficiency of 32.5% is calculated for the input pump #1 forward power of 50 mW and the

input pump #2 forward power of 200 mW, this indicates the goodness of this pumping scheme. Future works may include the employment of other rare earths and energy transitions to investigate the feasibility of fiber lasers at different wavelengths in medium infrared.

ACKNOWLEDGEMENT

This research was performed within MIUR plans: PON01 01224 “Sviluppo di tecnologie in guida d’onda integrata (SIW) per applicazioni ICT a microonde”; PONa3 00298 “Potenziamento delle strutture e delle dotazioni scientifiche e tecnologiche del polo scientifico e tecnologico Magna Grecia”; PON02 00576 3329762 “Sistemi avanzati mini-invasivi di diagnosi e radioterapia” AMIDERHA; COST Action MP1401.

REFERENCES

- [1] S. Sujecki, L. Sojka, E. Beres-Pawlik, Z. Tang, D. Furniss, A. Seddon, and T. Benson, “Modelling of a simple Dy³⁺ doped chalcogenide glass fibre laser for mid-infrared light generation,” *Optical and Quantum Electronics*, vol. 42, no. 2, pp. 69 – 79, 2010.
- [2] R. Quimby, L. Shaw, J. Sanghera, and I. Aggarwal, “Modeling of Cascade Lasing in Dy : Chalcogenide Glass Fiber Laser With Efficient Output at 4.5 μm ,” *Photonics Technology Letters, IEEE*, vol. 20, no. 2, pp. 123 – 125, Jan 2008.
- [3] D. D. Hudson, “Short pulse generation in mid-IR fiber lasers,” *Optical Fiber Technology*, vol. 20, no. 6, pp. 631 – 641, 2014.
- [4] F. Starecki, F. Charpentier, J.-L. Doualan, L. Quetel, K. Michel, R. Chahal, J. Troles, B. Bureau, A. Braud, P. Camy, V. Moizan, and V. Nazabal, “Mid-IR optical sensor for CO₂ detection based on fluorescence absorbance of Dy³⁺:Ga₅Ge₂₀Sb₁₀S₆₅ fibers,” *Sensors and Actuators B: Chemical*, vol. 207, Part A, pp. 518 – 525, 2015.
- [5] M. Ebrahim-Zadeh, S. Chaitanya Kumar, and K. Devi, “Yb-Fiber-Laser-Pumped Continuous-Wave Frequency Conversion Sources from the Mid-Infrared to the Ultraviolet,” *Selected Topics in Quantum Electronics, IEEE Journal of*, vol. 20, no. 5, pp. 350 – 372, Sept 2014.
- [6] F. Prudenzano, L. Mescia, L. Allegretti, M. De Sario, T. Palmisano, F. Smektala, V. Moizan, V. Nazabal, and J. Troles, “Design of Er³⁺-doped chalcogenide glass laser for MID-IR application,” *Journal of Non-Crystalline Solids*, vol. 355, no. 1821, pp. 1145 – 1148, 2009.
- [7] M. De Sario, L. Mescia, F. Prudenzano, F. Smektala, F. Deseveday, V. Nazabal, J. Troles, and L. Brilland, “Feasibility of Er³⁺-doped, Ga₅Ge₂₀Sb₁₀S₆₅ chalcogenide microstructured optical fiber amplifiers,” *Optics & Laser Technology*, vol. 41, no. 1, pp. 99 – 106, 2009.
- [8] L. Mescia, P. Bia, O. Losito, and F. Prudenzano, “Design of Mid-IR Er³⁺-Doped Microsphere Laser,” *Photonics Journal, IEEE*, vol. 5, no. 4, Aug 2013.

MULTI-MODE PROPAGATION IN OPTICAL FIBERS FOR SPACE-DIVISION MULTIPLEX TRANSMISSION

C. Antonelli⁽¹⁾, A. Mecozzi⁽¹⁾, and M. Shtaif⁽²⁾

⁽¹⁾ Department of Physical and Chemical Sciences, University of L'Aquila, via Vetoio 1, L'Aquila, Italy

⁽²⁾ Department of Physical Electronics, Tel Aviv University, Ramat Aviv, Tel Aviv, Israel
cristian.antonelli@univaq.it

Abstract

Space-division multiplexed transmission over multi-mode fiber structures is considered one of the most promising approaches to prevent the capacity crunch of the global fiber-optic transport network. In this paper we present the extension to the multi-mode case of the Stokes-space formalism that was originally developed for the study of polarization effects in single-mode fibers. The generalized Stokes-space formalism is shown to provide a convenient description of random mode coupling and modal dispersion, which are key propagation effects in the context of space-division multiplexed transmission. In particular, we show that in the regime of strong mode coupling the duration of the fiber intensity impulse response is proportional to the average length of the newly introduced mode-dispersion vector.

Index Terms – Fiber optics communications, Mode coupling, Modal dispersion, Space-division multiplexing.

I. INTRODUCTION

Over the past two decades, the world has experienced a steadily exponential increase in the demand for transmitted data, with growth rates peaking at above 100% per year. The telecom industry has been able to satisfy such increasing demand through a number of technological revolutions, including primarily the invention of wavelength-division multiplexing, and the implementation of coherent fiber-optic transmission supported by digital signal processing (DSP). Yet, in recent years a reduction in the growth-rate of the spectral efficiency has started to be sensed, with studies on the Shannon capacity of the optical transport networks suggesting that the capacity limit is only about a factor of two higher than what system experiments have been able to achieve [1]. In the search for scalable and cost-effective solutions to avoid an imminent capacity crunch [2], the optical communication community has started to consider a new and revolutionary approach - spatially multiplexed transmission in multi-mode or in multi-core fiber structures, supported by multiple-input multiple-output (MIMO) DSP. The explosion of this field of research has entailed numerous challenges, starting from fundamental issues related to light propagation in multiple modes of non-ideal fiber-optic

structures that are relevant for space division multiplexed (SDM) transmission.

In this paper we review some of work that we have recently performed on the modeling of linear propagation in SDM fibers. More specifically, we discuss the generalization of the Stokes space formalism that was originally developed for the study of polarization-related phenomena in single-mode fibers [3]. The generalized Stokes-space formalism is a powerful tool for the study of mode coupling [3], [4], and allows a compact and elegant representation of modal dispersion in SDM fibers [4]-[6], which is the primary phenomenon responsible for setting the complexity of MIMO-DSP receivers needed in SDM systems.

II. STOKES-SPACE REPRESENTATION OF MULTI-MODE FIELD EVOLUTION

We focus on the case of linear unitary multi-mode propagation, while neglecting non-unitary effects such as mode-dependent loss, whose characterization can be found in [7] and therein referenced papers (the presence of mode-averaged loss is, on the other hand, immaterial to the analysis). We consider transmission in $2N$ fiber modes, where the factor of 2 accounts for the polarization degeneracy of the individual spatial modes. The optical field at the angular frequency ω at a given point z along the optical fiber can be conveniently represented by a column vector $|s\rangle$ with $2N$ complex components, each representing the excitation of the a space and polarization (scalar) mode. The optical power is equal to the scalar product $\langle s|s\rangle$, which for convenience is set to 1, and where we use the notation $\langle s|$ to denote the conjugate transpose vector. Linear unitary propagation between positions z_0 and z along the fiber is represented by a $2N \times 2N$ frequency dependent unitary matrix $\mathbf{U}(z, z_0)$, such that $|s(z)\rangle = \mathbf{U}(z, z_0)|s(z_0)\rangle$, and $\mathbf{U}\mathbf{U}^\dagger = \mathbf{U}^\dagger\mathbf{U} = \mathbf{I}$, where the dagger denotes Hermitian conjugation, and where \mathbf{I} is the $2N \times 2N$ identity matrix. The space evolution of \mathbf{U} can be expressed as

$$\frac{\partial \mathbf{U}}{\partial z} = i \left(\beta_0 \mathbf{I} + \frac{\vec{\beta} \cdot \vec{\Lambda}}{2N} \right) \mathbf{U}, \quad (1)$$

where β_0 is the mode-averaged propagation constant. The quantities $\vec{\beta} \cdot \vec{\Lambda}$ is a traceless Hermitian matrix, where $\vec{\beta}$ is a D -dimensional real valued vectors, with $D = 4N^2 - 1$, and $\vec{\Lambda}$ is a vector collecting a set of D traceless matrices Λ_n which, when supplemented with the identity matrix, constitutes a basis for the linear space of $2N \times 2N$ Hermitian matrices. The scalar product $\vec{b} \cdot \vec{\Lambda}$ is hence to be interpreted as $\vec{b} \cdot \vec{\Lambda} = \sum_{n=1}^D b_n \Lambda_n$. The matrices Λ_n are a generalization of the Pauli matrices to the multi-dimensional case and they can be constructed as detailed in [3]. Use of this notation yields the following evolution equation for the state vector $|s\rangle$

$$\frac{\partial |s\rangle}{\partial z} = i\beta_0 |s\rangle + i \frac{\vec{\beta} \cdot \vec{\Lambda}}{2N} |s\rangle. \quad (2)$$

which is formally identical to the one obtained for polarized single-mode fields [8]. The vector $\vec{\beta}$ describes the local coupling between the various modes. It is a generalization of the birefringence vector of single-mode fibers [8] and it can be directly related to the physical mechanisms that are responsible for mode coupling [6], [9]. The intuitive meaning of the birefringence vector $\vec{\beta}$ of single-mode fibers comes from the notion that unitary evolution can be described as rotations of the Stokes vector of the field \vec{s} around $\vec{\beta}$, according to the equation

$$\frac{\partial \vec{s}}{\partial z} = \vec{\beta} \times \vec{s}. \quad (3)$$

A major finding of [3] is that Eq. (3) applies to the multi-dimensional case as well. The generalized Stokes representation \vec{s} of the multi-mode field is defined through the identity

$$|s\rangle\langle s| = \frac{1}{2N} (\mathbf{I} + \vec{s} \cdot \vec{\Lambda}), \quad (4)$$

where the components of \vec{s} are given by $s_j = \langle s | \Lambda_j | s \rangle$, and the definition of product vector between generalized Stokes vectors is

$$(\vec{a} \times \vec{b})_k = \sum_{i,j=1}^D f_{ijk} a_i b_j, \quad f_{ijk} = \text{trace}\{\Lambda_k (\Lambda_i \Lambda_j - \Lambda_j \Lambda_i)\}, \quad (5)$$

which yields the usual definition in the single-mode case ($D = 3$).

III. MODAL DISPERSION AND MIMO-DSP COMPLEXITY IV.

Modal birefringence implies that the information transmitted over multiple modes travelling in the fiber is dispersed in time when it reaches the receiver. In the presence of random mode coupling this phenomenon implies that long signal frames from all modes need to be processed at the receiver, thus increasing the complexity (memory) of the MIMO-DSP receiver. The signal duration that needs to be accommodated is equal to the duration of the fiber intensity impulse response (IIR). The IIR is the sum of the intensities received in all modes, obtained by separately exciting each of the spatial channels by a short optical pulse [10]. In the regime of strong coupling between modes, the IIR duration was shown in [5] to be equal to $T = \langle |\vec{\tau}|^2 \rangle^{1/2} / 2N$, where $\vec{\tau}$ is what we defined the modal dispersion (MD) vector [3] and where by brackets we denote ensemble averaging. The MD vector is a generalization of the famous polarization mode dispersion (PMD) vector [8], and its accumulation along the fiber obeys the equation

$$\frac{\partial \vec{\tau}}{\partial z} = \frac{\partial \vec{\beta}}{\partial \omega} + \vec{\beta} \times \vec{\tau}, \quad (6)$$

which is also formally identical to the evolution equation of the PMD vector [8]. In the regime of strong mode coupling, the root-mean-square length of the MD vector is proportional to the square-root of the

propagation distance, and so is the IIR duration, namely $T = \kappa\sqrt{z}$. The dependence of the proportionality coefficient κ on the fiber parameters and perturbations statistics is a key aspect in the design of SDM fibers, which we have recently addressed in [6].

V. CONCLUSION

We reviewed the Stokes-space representation of multi-mode optical fields, and discussed its use for studying mode coupling and modal dispersion in multi-mode fiber structures for SDM transmission.

ACKNOWLEDGEMENT

C. Antonelli and A. Mecozzi acknowledge financial support from the Italian Government under Cipe Resolution 135 (December 21, 2012), project INnovating City Planning through Information and Communication Technologies

REFERENCES

- [1] P.J. Winzer, “*Making spatial multiplexing a reality*,” Nature Photonics vol. pp. 345–348, April 2014.
- [2] A. R. Chraplyvy, “*The coming capacity crunch*,” European Conference on Optical Communication 2009 (ECOC09), plenary talk (2009).
- [3] C. Antonelli, A. Mecozzi, M. Shtaif, and P. J. Winzer, “*Stokes-space analysis of modal dispersion in fibers with multiple mode transmission*,” Optics Express vol. 20, pp. 11718–11733, April 2012.
- [4] C. Antonelli, A. Mecozzi, M. Shtaif, and P. J. Winzer, “*Random coupling between groups of degenerate fiber modes in mode multiplexed transmission*,” Optics Express vol. 21, pp. 9484–9490, March 2013.
- [5] A. Mecozzi, C. Antonelli, and M. Shtaif, “*Intensity impulse response of SDM links*,” Optics Express, vol. 23, pp. 5738–5743, March 2015.
- [6] C. Antonelli, A. Mecozzi, and M. Shtaif, “*The delay spread in fibers for SDM transmission: dependence on fiber parameters and perturbations*,” Optics Express vol. 23, pp. 2196–2202, Jan. 2015.
- [7] C. Antonelli, A. Mecozzi, M. Shtaif, and P. J. Winzer “*Modeling and performance metrics of MIMO-SDM systems with different amplification schemes in the presence of mode-dependent loss*,” Opt. Express vol. 23, pp. 2203–2219, Jan. 2015.
- [8] J. P. Gordon and H. Kogelnik, “*PMD fundamentals: polarization mode dispersion in optical fibers*,” Proceedings of the National Academy of Sciences of the USA vol. 97, pp. 4541–4550, Feb. 2000.
- [9] L. Palmieri and A. Galtarossa, “*Coupling effects among degenerate modes in multimode optical fibers*,” IEEE Photonics Journal vol. 6, pp. 0600408 (1–9), Dec. 2014.
- [10] R. Ryf *et al.*, “*SDM Transmission over 4200-km 3-Core Microstructured Fiber*,” Optical Fiber Communications Conference 2011 (OFC11), Paper PDP5C.2 (2011).

A PRELIMINARY NUMERICAL ANALYSIS OF THE DIFFERENTIAL GROUP DELAY OF A 6-SPATIAL-MODES SPUN FIBER

Luca Palmieri, Gianluca Guerra, Leonardo Marcon,
Marco Santagiustina, Andrea Galtarossa

Department of Information Engineering, University of Padova, Italy
luca.palmieri@dei.unipd.it

Abstract

The differential group delay of a spun fiber supporting the first 4 LP groups (for a total of 12 spatial-polarization modes) has been numerically analyzed. Results suggest that spin may reduce modal dispersion.

Index Terms – Fiber optic, few-mode fibers, mode coupling, spinning.

I. INTRODUCTION

The use of few-mode optical fibers is one of the approaches pursued to implement spatial division multiplexing (SDM). [1] One of the parameters that most influences the complexity of such systems is the modal dispersion accumulated along the link, for the higher this dispersion, the more complex the MIMO equalizer required at the receiver. [2]

Spin is well known to be able to substantially reduce polarization mode dispersion in single-mode fibers. [3] Similarly, we recently showed that spin can reduce also the modal dispersion among the modes of quasi-degenerate LP groups (hereinafter “LP groups” for short) in the case of weak coupling. [4] Whether a similar spin-induced reduction can be achieved also in the case where LP groups strongly couples each other is still a wide open question. In this work, we report some preliminary results about the modal dispersion of a spun fiber supporting the first 4 LP groups of quasi-degenerate modes. The analysis shows that spin can be effective only if the fiber is affected by core ellipticity; however, the achieved level of reduction may have modest practical interest.

II. THEORETICAL MODEL

The propagation along a fiber can be described by its generalized $N \times N$ Jones matrix $U(z)$, [5] whose dependence on z is governed by the equation $U_z = -j[D + K(z)]U$, where the subscript x indicates hereinafter derivation with respect to x , $D = \text{diag}(\beta_1, \dots, \beta_N)$ is a diagonal matrix with the propagation constants β_n of modes, and $K(z)$ is an Hermitian matrix describing mode coupling. [6] Similarly, modal dispersion is related to the dependence of U on the optical frequency ω , which is known to be $U_\omega = -jQU$. In particular, the real eigenvalues τ_n of the Hermitian matrix Q are the group delays of the principal modes of propagation, and the difference between their maximum and minimum is the differential group

delay $\Delta\tau$ (DGD, also known as the maximum delay spread). [5] Matrix Q depends on both D and K and on their ω -derivative. [5] In this work we assume that $D_\omega = D/\omega$ and $K_\omega = K/\omega$. The overall effects of the spin can then be summarized by the *spin-induced reduction factor* (SIRF), which is the ratio of the mean DGD of the spun fiber, over the mean DGD that same fiber would have if it were not spun.

The analysis of spin effects is intimately related to an accurate description of the coupling mechanisms occurring in the fiber. In the vast majority of cases spin is thought as a way to mitigate intrinsic mode coupling, which can be only of two kinds: [7] stress birefringence (induced by core eccentricity and core and/or cladding ellipticity) and geometrical asymmetries (typically core ellipticity). Therefore, hereinafter we will consider only these two effects. It can be shown [6] that stress birefringence causes coupling only within each LP group separately. In this case, spin changes coupling conditions within each group, but it does not induce coupling among different groups. As a consequence, as long as the fiber is affected only by stress birefringence, spin is largely ineffective. This situation is however not realistic, since intrinsic stress birefringence is always caused by geometrical asymmetries. [7]

Differently, core ellipticity can induce coupling among different LP groups, as summarized in Fig. 1(a). [6] Specifically, coupling may occur either through the transverse components of the field (dark blue boxes) or through the longitudinal ones (light blue boxes); as a result, the former kind of coupling causes a much stronger effect, up to several hundreds of times higher than the other. In particular, note that for a given ellipticity, coupling between modes such as the $LP_{2,1}$ and $LP_{0,1}$ or $LP_{2,1}$ and $LP_{0,2}$, or within the $LP_{1,1}$ is more than two orders of magnitude stronger than the coupling within $LP_{0,1}$. The detailed expression of the corresponding coupling matrices is quite cumbersome and will be reported elsewhere. By changing the orientation of the ellipticity, the spin may modify the coupling condition among those modes and hence may affect the accumulated modal dispersion.

III. NUMERICAL RESULTS

The effects of spin on few-mode fibers have been evaluated by means of Monte Carlo simulations. The reference fiber is step-index, with core radius $8\ \mu\text{m}$ and numerical aperture 0.148; at 1550 nm it supports the propagation of 4 LP groups: $LP_{0,1}$, $LP_{1,1}$, $LP_{2,1}$ and $LP_{0,2}$ (for a total of 12 spatial-polarization modes). Following the above argumentation, we assume that only core ellipticity affects the fiber; we also assume that the ellipticity is fixed along the fiber, but core orientation varies due to both intrinsic randomness and the deterministic action of the spin. The angle of the random intrinsic orientation is described by a Wiener process, [8] with a coupling correlation length, L_F , of 10 m in all cases.

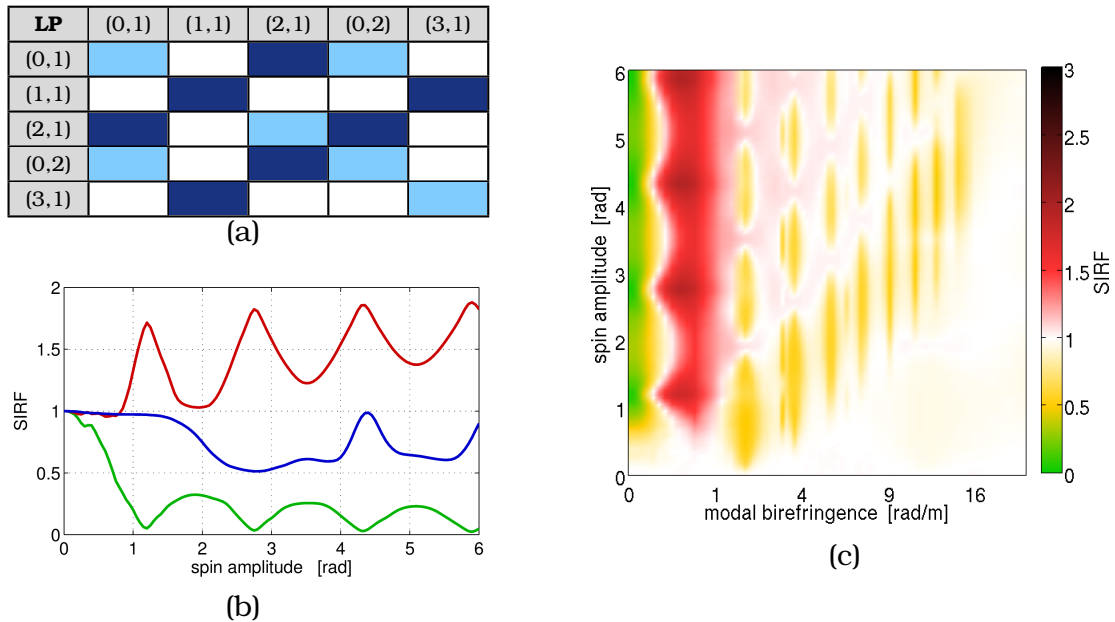


FIG. 1 – (a) Schematic representation of coupling among the first few LP modes due to core ellipticity. Darker (lighter) color indicates stronger (weaker) coupling. (b) SIRF vs. spin amplitude for modal birefringence equal to 0, 0.25 and 9 rad/m (green, red and blue, respectively). (c) SIRF vs. modal birefringence and spin amplitude. The horizontal axis is nonlinearly distorted to highlight features.

To reduce the burden of numerical simulations, for this preliminary analysis we have rescaled the maximum modal birefringence of the fiber (defined as the maximum difference among the propagation constants of modes) to about 20 rad/m and set the coupling birefringence (defined as the difference between the maximum and the minimum eigenvalues of K) to 0.5 rad/m, while preserving the ratios between the elements of D and K as given by the reference fiber. The spin is sinusoidal, with period 4 m and amplitude ranging from 0 (unspun fiber) to 6 rad; this corresponds to a maximum spin rate of about 9.5 rad/m. Simulations have been performed with the waveplate model, using an integration step of 1 cm, so to build a statistical ensemble of 500 1-km-long fibers.

Results are reported in fig. 1(c), where the SIRF is shown as a function of modal birefringence and spin amplitude. As an extreme reference, let consider the unrealistic case when modal birefringence is 0, which represents a fiber with 12 degenerate modes. The SIRF is well below 1 and, as shown in fig. 1(b) (lower green curve), it has the marked local minima already observed in single mode fibers. [3] As the modal birefringence increases, the SIRF enters a region where it goes well above 1, indicating that the spin is actually increasing the DGD, rather than reducing it. This quite peculiar result has been already observed for intra-modal DGD, [4] and is more clearly shown in fig. 1(b) (higher red curve). This effect is likely due to the fact that in this regime the spin is contrasting the beneficial effects of random mode coupling; this is suggested by the correspondence between the SIRF peaks of this case and the SIRF minima of

the degenerate case. As the modal birefringence is further increased, the SIRF goes back below 1, but less markedly. In general, we still observe optimal regions where the spin is locally minimum, but these minima are above 0.5 (see also the middle blue curve in fig. 1(b)). The large white area in the lower right portion of the graph confirms that the spin has to be fast enough to be effective.

IV. CONCLUSIONS

The preliminary numerical results reported here shows that spin may reduce the DGD of few-mode fibers. It has to be remarked, however, that simulations refer to a downscaled model, where modal and coupling birefringence are smaller than what encounter in practice nowadays. Nonetheless, a rather low spin rate of 9.5 rad/m has been considered, whereas spin rates larger than 150 rad/m can be routinely applied to standard telecommunication fibers. Considering this scaling factor and the strong effort currently put in reducing modal dispersion of graded-index fibers, it seems reasonable that the spin might contribute to a further reduction of modal dispersion.

V. ACKNOWLEDGMENTS

This research has been partially supported by the Italian Ministry of University (project ROAD-NGN, PRIN 20102KAZKN_005) and has been held within the agreement with ISCTI, Rome, Italy.

REFERENCES

- [1] Richardson, D. J., Fini, J. M., and Nelson, L. E., "Space-division multiplexing in optical fibres," *Nature Photonics* **7**, 354–362 (May 2013). 00057.
- [2] Arik, S., Askarov, D., and Kahn, J., "Effect of Mode Coupling on Signal Processing Complexity in Mode-Division Multiplexing," *Journal of Lightwave Technology* **31**(3), 423–431 (2013).
- [3] Palmieri, L., "Polarization Properties of Spun Single-Mode Fibers," *J. Lightwave Technol.* **24**(11), 4075–4088 (2006).
- [4] Palmieri, L., "Modal Dispersion Properties of Few-Mode Spun Fibers," in [Optical Fiber Communication Conference], *OSA Technical Digest (online)*, Tu2D.4, Optical Society of America, Los Angeles, CA, USA (Mar. 2015). 00000.
- [5] Antonelli, C., Mecozzi, A., Shtaif, M., and Winzer, P. J., "Stokes-space analysis of modal dispersion in fibers with multiple mode transmission," *Optics Express* **20**(11), 11718–11733 (2012).
- [6] Palmieri, L., "Coupling mechanism in multimode fibers," in [Photonics West OPTO], **9009**, 90090G–90090G–9, SPIE, San Francisco (US-CA) (2014).
- [7] Chowdhury, D. and Wilcox, D., "Comparison between optical fiber birefringence induced by stress anisotropy and geometric deformation," *IEEE J. Sel. Top. Quantum Electron.* **6**(2), 227–232 (2000). Journal Article.
- [8] Wai, P. and Menyuk, C., "Polarization mode dispersion, decorrelation, and diffusion in optical fibers with randomly varying birefringence," *Journal of Lightwave Technology* **14**, 148–157 (Feb. 1996). 00340.

INFLUENCE OF INNER CLADDING GEOMETRY ON SYMMETRY-FREE PHOTONIC CRYSTAL FIBER PROPERTIES UNDER SEVERE HEAT LOAD

F. Poli, G. Ciletti, E. Coscelli, A. Cucinotta, S. Selleri

Information Engineering Department, University of Parma
Parco Area delle Scienze 181/A, 43124 Parma, Italy
federica.poli@unipr.it

Abstract

The inner cladding influence on the guiding properties of Yb-doped symmetry-free photonic crystal fibers in different heating conditions has been investigated using simulation tools based on the finite element method. Results have demonstrated that, by properly modifying the inner cladding radius and the air-hole spacing and diameter, it is possible to facilitate the coupling of the guided modes with the cladding ones, thus affecting their confinement in the doped core and the fiber single-mode regime under severe heat load.

Index Terms – Finite element method, large mode area, thermal effects, Yb-doped symmetry-free fibers

I. INTRODUCTION

The continuous power scaling of fiber lasers, which has been driven in the last years by the significant advantages provided by Yb-doped double-cladding Photonic Crystal Fibers (PCFs) [1], is currently hindered mainly by thermal effects, which negatively affect the fiber Single-Mode (SM) behavior. In particular, beyond a certain average power threshold, the laser beam quality worsens because of the unwanted energy transfer from the Fundamental Mode (FM) to the Higher-Order Modes (HOMs), usually referred as Transverse Mode Instability (TMI) [2]. Since this effect is favored by the thermally-driven improvement of the HOM confinement in the fiber core, an effective strategy to increase the TMI power threshold is to design Yb-doped double-cladding PCFs which provide a strong HOM delocalization even under severe heat load conditions [3]. Among them, Symmetry-Free PCFs (SF-PCFs), characterized by the absence of any mirror symmetry in the inner cladding, have shown interesting properties in terms of resilience to thermal effects [4],[5].

In this paper the influence of the main inner cladding characteristics on the guided mode confinement in Yb-doped PCFs in presence of severe thermal effects has been analyzed with a full-vector modal solver based on the finite element method [5]. The aim is to find a fiber design that facilitates the first HOM coupling with the cladding modes, thus making the fiber SM behaviour more robust. Simulation results have shown which heat load value causes a thermally-induced refractive index change high enough to radically modify the SF-PCF guiding mechanism.

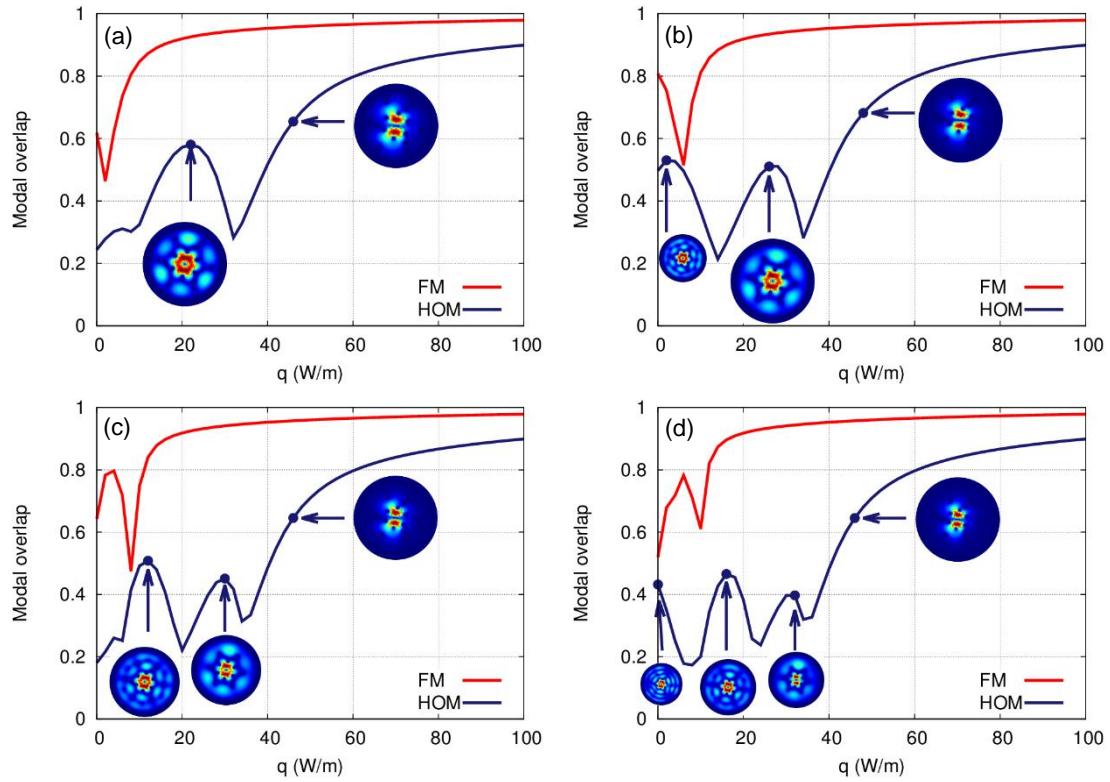


FIG. 1 – FM and HOM overlap integral as a function of q for SF-PCF with (a) $d_{AC}=15\Lambda$, (b) $d_{AC}=17\Lambda$, (c) $d_{AC}=19\Lambda$ and (d) $d_{AC}=21\Lambda$. (Inset) HOM electric field modulus at the SM range limit and at the modal overlap maximum.

II. SIMULATION RESULTS

The Yb-doped SF-PCF considered in this analysis [4] is built over a triangular lattice stack with pitch Λ . Its 19-cell Yb-doped core is surrounded by air-holes with diameter d , distributed according to a C_3 symmetry. The inner cladding is enclosed by an air-cladding with inner diameter d_{AC} and thickness of $7\ \mu\text{m}$. A commercial full-vector modal solver based on the finite element method has been used to calculate the thermally-induced refractive index change over the SF-PCF cross-section, and, then, to evaluate the guided modes at $1032\ \text{nm}$ [5]. 150 modes have been calculated for heat load q values between 0 and $100\ \text{W/m}$. In particular, the confinement of the FM and the first HOM, that is the guided modes involved in the definition of the fiber SM regime, has been analyzed by calculating their overlap integral on the doped core [6]. Simulation results obtained for SF-PCFs with $\Lambda = 15, 20, 25\ \mu\text{m}$, $d/\Lambda = 0.5, 0.4, 0.3$, and $d_{AC} = 15\Lambda, 17\Lambda, 19\Lambda$ and 21Λ are reported in this paper.

Fig. 1 shows the FM and the first HOM overlap integral curve as a function of the heat load q for the SF-PCFs with $d/\Lambda = 0.5$, $\Lambda = 15\ \mu\text{m}$ and different air-cladding inner diameter. The first HOM is defined as the LP_{11} -like mode with the highest overlap integral value at a certain heat load. Notice that, regardless the inner cladding radius, both the guided modes become increasingly confined at higher q values.

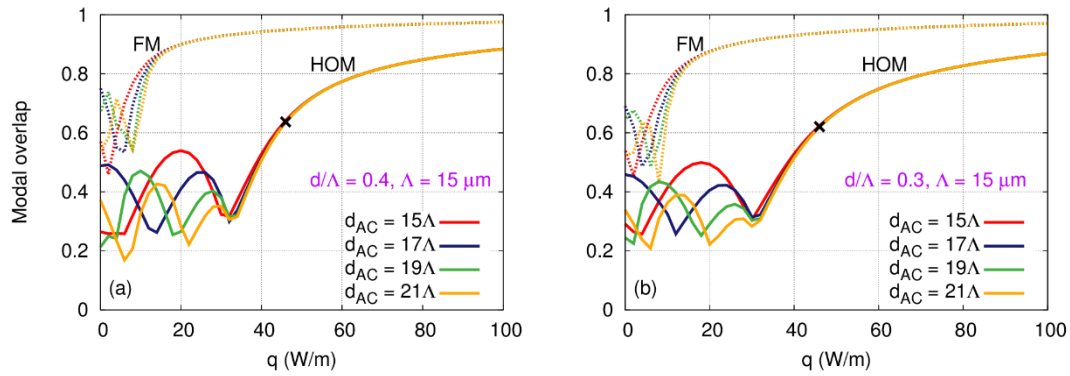


FIG. 2 – FM (dotted lines) and HOM (solid lines) overlap integral as a function of heat load q for SF-PCFs with $\Lambda = 15 \mu\text{m}$, different d_{AC} values and (a) $d/\Lambda=0.4$, or (b) $d/\Lambda=0.3$.

Differently from the FM, the first HOM is barely guided into the core at low q values. By comparing results reported in Fig. 1(a)-(d), it is possible to notice that the HOM coupling with the cladding modes becomes stronger when the inner cladding size increases from 15Λ to 21Λ . Therefore, more peaks appear in the HOM overlap curve for low heat load values, that is for $q < 35 \text{ W/m}$. The HOM field distributions added as inset in Fig. 1 demonstrate that the maximum overlap integral for a certain LP_{11} -like mode in this heat load range becomes lower and shifts to higher q values as the inner cladding enlarges. In particular, the peak of the HOM overlap integral which is about 0.58 at $q = 22 \text{ W/m}$ for the fiber with the smallest inner cladding, decreases to about 0.4 and moves to $q = 32 \text{ W/m}$ for the fiber with the largest d_{AC} . However, it is interesting to underline that the HOM delocalization in the cladding is not significantly affected by d_{AC} value in the SF-PCF considered in the present study. In fact, the maximum heat load q_{max} which guarantees the SM regime, that is an overlap integral difference between FM and HOM of 0.3 [4],[5], is around 46 W/m regardless the inner cladding size. At q_{max} the HOM overlap integral is around 0.65 and its field distribution is almost the same, as shown in Fig. 1, for all the SF-PCFs analyzed.

The HOM delocalization has been studied also for SF-PCFs characterized by a lower air-filling fraction in the inner cladding. In particular, the normalized air-hole diameter has been decreased to 0.4 and 0.3, while keeping fixed the pitch value. Results are reported in Fig. 2 for fibers with different inner cladding size. Notice that the overlap integral behavior is very similar to the one obtained for the fiber with $d/\Lambda = 0.5$. The air-hole size affects the overlap integral curves of the HOM only at low heat load, since fewer peaks can be found as the air-filling fraction decreases. Consequently, the SM regime boundary is almost unaffected by the d/Λ decrease, being still $q_{max} = 46 \text{ W/m}$. The HOM overlap integral at q_{max} becomes slightly lower, being about 0.64 and 0.62 for the SF-PCFs with $d/\Lambda = 0.4$ and 0.3, respectively.

Finally, the effect of the pitch on the SF-PCF SM regime has been taken into account, by fixing $d/\Lambda = 0.5$ and enlarging Λ to 20 and 25 μm .

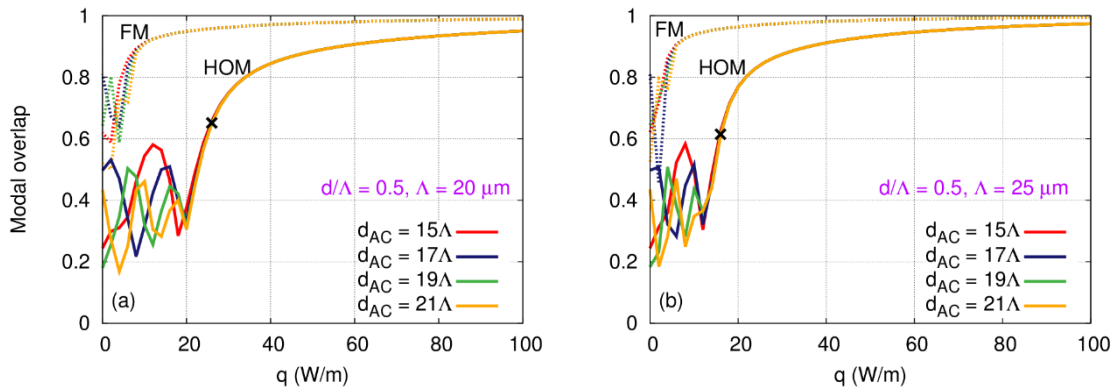


FIG. 3 – FM (dotted lines) and HOM (solid lines) overlap integral as a function of q for SF-PCFs with $d/\Lambda=0.5$, different d_{AC} and (a) $\Lambda=20\ \mu\text{m}$, or (b) $\Lambda=25\ \mu\text{m}$.

As shown in Fig. 3, the influence of the inner cladding size becomes negligible as the pitch enlarges, since the low heat load region where the HOM delocalization can be obtained shrinks significantly with respect to the fiber with $\Lambda = 15\ \mu\text{m}$. Moreover, the SM regime is negatively affected by the hole-to-hole spacing increase, being q_{max} about 26 W/m and 16 W/m for the SF-PCF with $\Lambda = 20\ \mu\text{m}$ and $\Lambda = 25\ \mu\text{m}$, respectively.

III. CONCLUSION

The guiding properties of Yb-doped SF-PCFs under severe heat load have been thoroughly analyzed with simulation tools based on the finite element method, taking into account the influence of the main inner cladding characteristics. Results have demonstrated that the fiber SM regime resilience to thermal effect worsens as the pitch enlarges, being on the contrary almost unaffected by the normalized air-hole diameter and the inner cladding size. The latter influences the coupling of the guided modes with the cladding ones only in the low heat load region.

REFERENCES

- [1] M.N. Zervas and C.A. Codemard, “High power fiber lasers: a review”, *IEEE J. of Sel. Topics in Quant. Electronics*, vol. 20(5), p. 0904123, Sep./Oct. 2014.
- [2] A.V. Smith and J.J. Smith, “Mode instability in high power fiber amplifiers”, *Optics Express*, vol. 19(11), pp. 10180-10192, May 2011.
- [3] R. Dauliat, D. Gaponov, A. Benoit, F. Salin, K. Schuster, R. Jamier, and P. Roy, “Inner cladding microstructuring based on symmetry reduction for improvement of singlemode robustness in VLMA fiber”, *Optics Express*, vol. 21(16), pp. 18927-18926, Aug. 2013.
- [4] F. Poli, E. Coscelli, A. Cucinotta, S. Selleri, and F. Salin, “Single-mode propagation in Yb-doped large mode area fibers with reduced cladding symmetry”, *IEEE Phot. Tech. Letters*, vol. 26(24), pp. 2454-2457, Dec. 2014.
- [5] E. Coscelli, R. Dauliat, F. Poli, D. Darwich, A. Cucinotta, S. Selleri, K. Schuster, A. Benoit, R. Jamier, P. Roy and F. Salin, “Analysis of the modal content into large-mode-area photonic crystal fibers under heat load”, *IEEE J. of Sel. Topics in Quant. Electronics*, vol. 22(2), p. 4900808, Mar./Apr. 2016.

A QUASI-DISTRIBUTED OPTICAL FIBER LOAD SENSOR

L. Schenato⁽¹⁾, A. Pasuto⁽¹⁾, A. Galtarossa^{(2),(3)}, L. Palmieri⁽²⁾

- ⁽¹⁾ Research Institute for Geo-Hydrological Protection, National Research Council, Padova, Corso Stati Uniti 4, Padova, Italy
- ⁽²⁾ Department of Information Engineering, University of Padova
Via Gradenigo 6/B, Padova, Italy
- ⁽³⁾ IIUSE, Southeast University, Nanjing, China
luca.schenato@cnr.it

Abstract

This paper describes a quasi-distributed optical fiber load sensor based on the concatenation of sections with positive Poisson's ratio with sections with negative Poisson's ratio. Any load applied to a certain position along the structure induce a precise strain exerted on the different sections of fiber anchored along the axis of the structure. By interrogating the fiber by a suitable optical technique capable of measuring such strain with sufficient resolution, e.g. optical frequency domain reflectometry, is then possible to measure the applied load.

Index Terms – Load sensing, Quasi-distributed sensing, Optical frequency domain reflectometry.

I. INTRODUCTION

Generally it would seem obvious that when a material is loaded in one direction, it expands in the transverse direction and vice versa. Such behavior is quantitatively regulated by the Poisson's ratio, defined as $\nu = -\varepsilon_T/\varepsilon_L$, where ε_L is the strain in the load direction and ε_T is the strain in the direction perpendicular to the load. Usually, ε_L and ε_T have opposite signs and, therefore, the Poisson's ratio is in general positive.

Counter-intuitively, there exist materials that if stretched in one direction, expand in the transversal direction and vice versa: these materials, with negative Poisson's ratio, are referred as auxetic ones [1].

Combination of materials with opposite Poisson's ratio has been also proposed to the aim of obtaining uncommon mechanical behavior: such solid, referred as positional semi-auxetic solid [2], if stretched in one direction, will not deform in the transversal direction, because the auxetic part compensates the non-auxetic one. Here, we propose to integrate an optical fiber into a semi-auxetic structure, obtained by the concatenation of hexagonal and re-entrant cells, to be used as a quasi-distributed optical fiber load sensor.

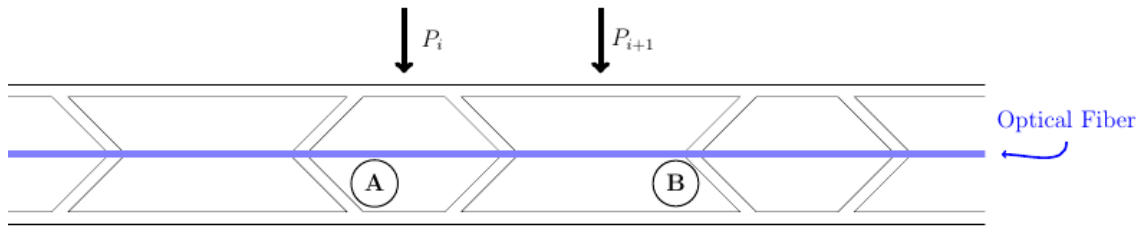


FIG. 1 – Structure of the semi-auxetic sensor (cross section) made of a concatenation of hexagonal cells (A) and of re-entrant auxetic cells (B).

II. SENSOR: WORKING MECHANISM AND PROTOTYPE

The scheme of the sensor structure is shown in Fig. 1. In the structure, an hexagonal cell (A) follows a re-entrant one (B) to constitute a longitudinal structure of several units. The sensing fiber is fixed at the walls of each cell along the longitudinal axis of the structure.

Hexagonal cells behave as common solids, with positive Poisson's ratio; under transversal loading they expand transversally and pull the section of fiber clamped at their walls. Re-entrant cells behave instead as auxetic solids and contract in the direction perpendicular to the load, determining a negative strain to the fiber section anchored at their walls. Due to concatenation, the lateral expansion of a loaded hexagonal cell induces the contraction of the adjacent re-entrant cells and vice versa and the mechanical interaction between cells extends up to some cells far from the position under load, in a reproducible way.

A sensor prototype has been built by assembling flat and L-shaped polyvinyl chloride plastic (PVC) rods and it is shown in Fig. 2. The fiber used in the sensor is a polyimide coated single mode fiber (OFS Geosil), anchored at the PVC cells walls by means of two part epoxy cement. To avoid curvature of the fiber in the re-entrant cells when large load is applied, it has been pre-tensioned with 200 g before gluing. The fiber has been interrogated by means of an Optical Backscatter Reflectometer (OBR) from Luna Innovations Incorporated, implementing

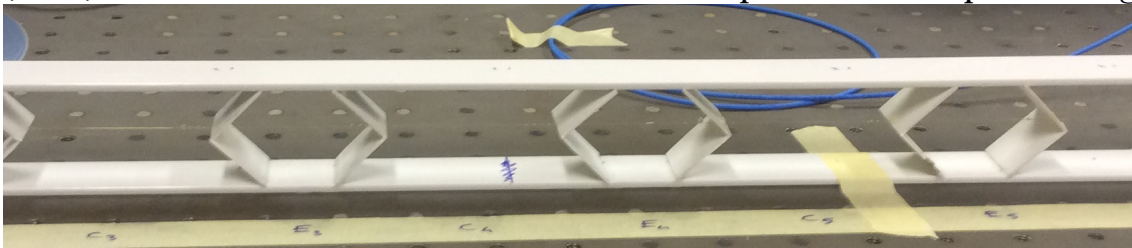


FIG. 2 – Detail of sensor prototype (material is PVC; thickness of bearing structure/cell walls is 3 mm/1 mm; walls angle is 45°; cell height is 35.4 mm; lateral width is 24 mm; cells length at the central axis is 60.35 mm).

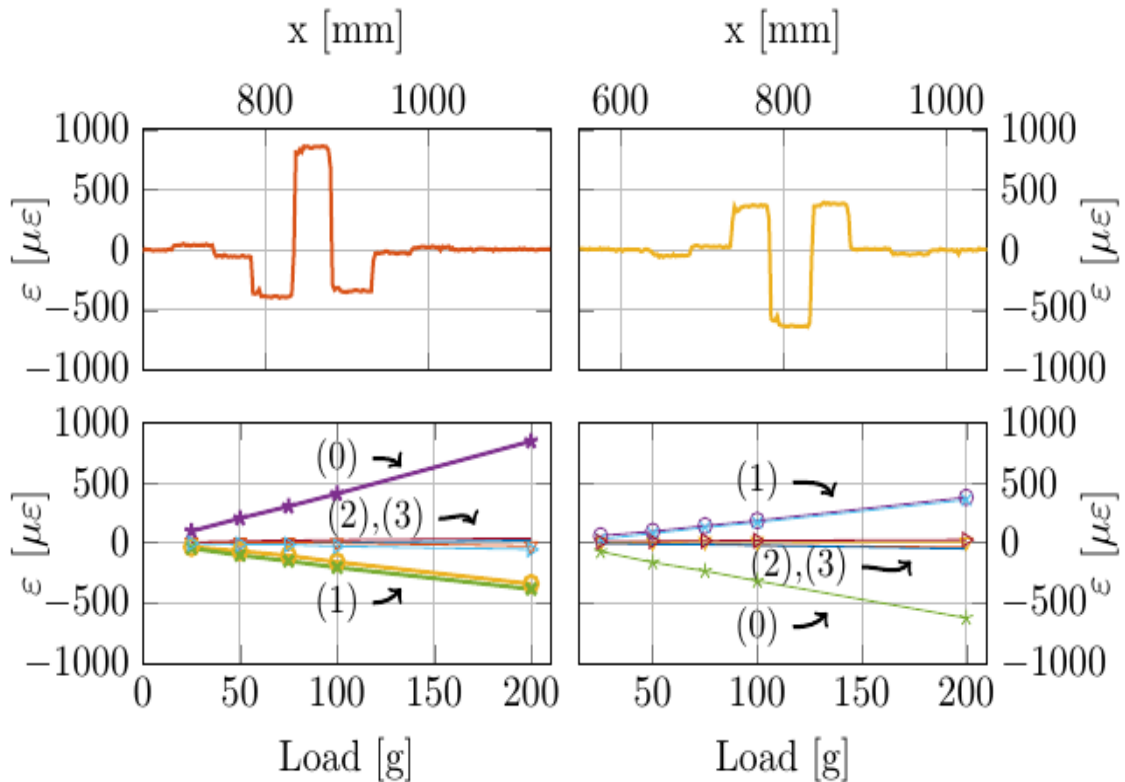


FIG. 3 – Upper plots: Strain on the fiber by a load of 200 g applied on an hexagonal/re-entrant cell (left/right plot). Lower plots: Strain vs. load of the hexagonal/re-entrant (left/right plot) cells and of the adjacent cells.

optical frequency domain reflectometry (OFDR) [3].

The prototype response has been characterized by loading each cell with 25, 50, 75, 100 and 200 g. As examples, the strain measured by the OBR with load of 200 g on an hexagonal and a re-entrant cell is represented in the upper plots of Fig. 3, left and right plots, respectively. Corresponding responses of the cell under load and of adjacent cells vs. load are represented in the lower plots of the same figure.

Lower left[right] plot refer to the load of the hexagonal[re-entrant] cell: curve (0) is the strain vs. load curve measured in the same hexagonal[re-entrant] cell, (1) the strain vs. load measured at the two next re-entrant[hexagonal] cells, (2) the strain vs. load at the two following adjacent hexagonal[re-entrant] cells and (3) at the next re-entrant[hexagonal] cells. As one can note, the response is linear in all the cells and the overlap of curves (1), (2) and (3) confirms the symmetric response of the cell.

Slopes of these load-strain curves describe the overall sensor response: the response of a sensor made of n -cells consists in fact of a set of n -strain measurements taken at each cell and these

measurements can be linearly related to the n-loads applied on each cell via these load-strain slope coefficients.

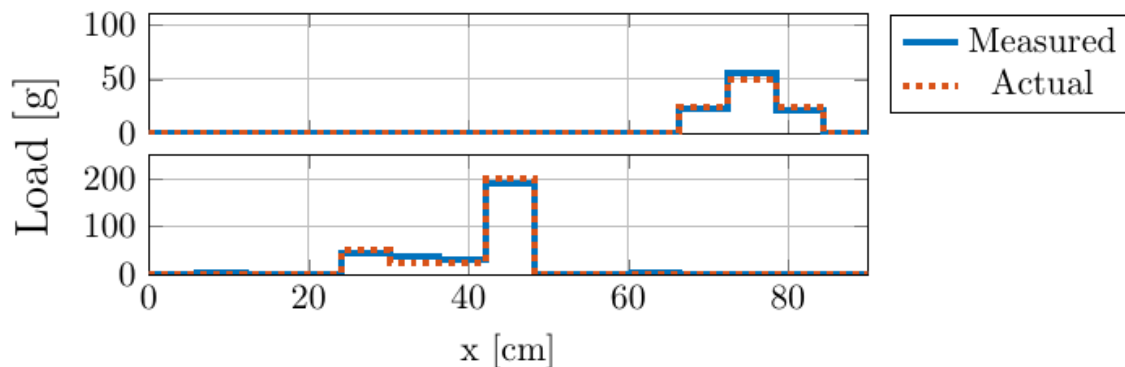


FIG. 4 – Examples of measured load profile compared to actual load.

The sensor has been tested by applying some unknown loads distributed along the sensor and then estimating them from the measured strain values. Results is shown in Fig. 4, where blue solid and red dashed curves refer to measured and actual loads, respectively; measurements errors are limited to few grams, confirming the viability of the proposed concept.

III. CONCLUSION

A novel quasi-distributed optical fiber load sensor has been proposed and investigated. The concept has been experimentally proved with a prototype and successfully interrogated by means of OFDR.

ACKNOWLEDGEMENT

The European Commission (Horizon 2020) and the Italian Ministry of Instruction, University and Research are acknowledged for financial support within the Water JPI and the WaterWork2014 Cofunded Call (project DOMINO).

REFERENCES

- [1] Evans, K. E., “Auxetic polymers: a new range of materials,” *Endeavour* 15(4), pp. 170–174, 1991.
- [2] Lim, T.-C., “Auxetic Materials and Structures”, Engineering Materials, Springer-Verlag Singapur, Singapore, 2015.
- [3] Palmieri, L. and Schenato, L., “Distributed optical fiber sensing based on Rayleigh scattering,” *The Open Optics Journal* (7), pp. 104–127, 2013.

DEVELOPING A LOW COST MULTIPURPOSE X-BAND FMICW RADAR

C. Lucianaz⁽¹⁾, S. Bertoldo⁽¹⁾, P. Petrini⁽¹⁾, M. Allegretti⁽²⁾

⁽¹⁾ Department of Electronics and Telecommunications (DET),
Politecnico di Torino

Corso Castelfidardo 39, 10129 Torino, Italy

{[claudio.lucianaz](mailto:claudio.lucianaz@polito.it), [silvano.bertoldo](mailto:silvano.bertoldo@polito.it), [paolo.petrini](mailto:paolo.petrini@polito.it)}@polito.it

⁽²⁾ CINFAI (Consorzio Interuniversitario Nazionale per la Fisica
delle Atmosfere e delle Idrosfere) c/o Politecnico di Torino

Corso Castelfidardo 39, 10129 Torino, Italy

marco.allegretti@polito.it

Abstract

In the framework of a series of research projects a first prototype of an X-band FMCW (Frequency Modulated Interrupted Continuous Wave) was developed. Its main characteristics are the low cost and the complete software programmability, making it a multipurpose and versatile instrument. Without any hardware modifications and by simply varying the software for data acquisition and processing, it can be used for target detection, as radar altimeter and also for atmospheric monitoring operations (e.g. for rainfall estimation).

The present work briefly describes the radar standard electronics and presents the interfaces of the processing software. Some results are also given.

Index Terms – FMCW radar, X-band, multipurpose radar, low cost, atmospheric monitoring, target detection, radar altimeter.

I. INTRODUCTION

Frequency Modulated Continuous Wave (FMCW) radars have been always used in many applications, since both target range and speed can be detected analyzing the frequency spectrum of the received signal, using particular modulations, and adequate signal processing techniques.

The developed prototype of FMCW radar here presented is monostatic: it uses a single antenna to transmit radiofrequency signal and receive backscattered echoes. Single antenna operation could be achieved by using a circulator to isolate the transmitter from the receiver. Usually, the problem with this technique is that the circulator has limited isolation capability and forward energy may be reflected from the antenna and leak into the receiver path. The solution implemented in this prototypal radar exploits the possibility to switch the transmitter signal on and off. When the transmitter is off the receiver is switched on recording the received signal. A radar exploiting this technique is also called Frequency Modulated Interrupted Continuous Wave (FMICW). The effects of this gating are numerous and are well discussed in [1]. The most important ones for our applications are of course the reduction of the transmitted power, and the limitation

in range resolution due to the gating. However they do not heavily affect the desired performance for the system here described.

II. HARDWARE DESCRIPTION

The prototypal FMICW radar hardware (Fig. 1) can be divided into different modules: synthesizer, power amplifier, receiver, filter, control unit, power supply and eventually the Oven Controlled Cristal Oscillator (OCXO). All of them are realized with electronic components as low cost as possible.

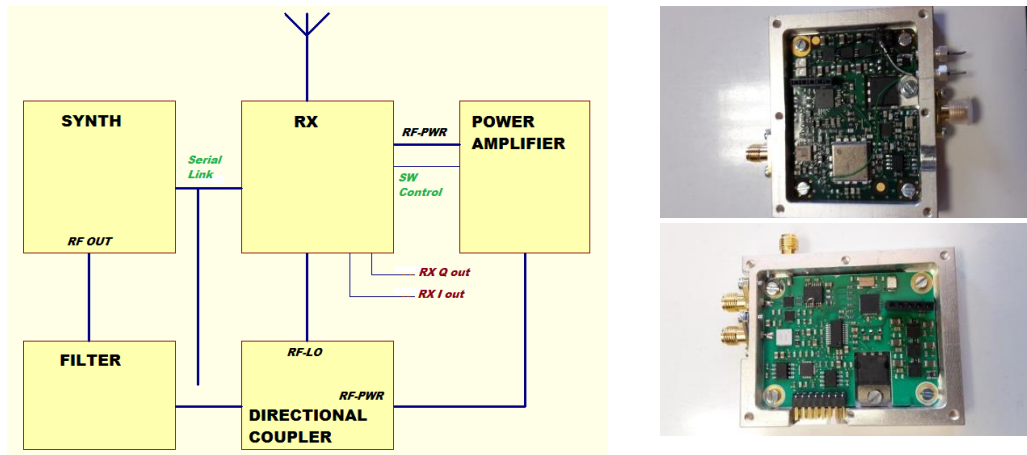


FIG. 1 – FMICW radar electronics block scheme (left). Realized synthesizer and receiver modules (right)

The synthesizer is based onto an ADF4158 integrated circuit autonomously capable to produce FMCW signals with linear or parabolic ramp, tunable from 4700 to 4900 MHz, followed by a frequency doubler. This signal is then filtered and delivered to the receiver, for mixing operations and to the power amplifier.

The radar is equipped with 2D slotted array antenna with a Half Power Beam Width (HPBW) of 5 degrees which can be moved on the horizontal plane, keeping fixed the elevation.

The receiver module includes a low loss antenna switch operated by a 64 MHz microcontroller in order to operate as monostatic radar. The total noise figure is lower than 3 dB.

The LNA drives an active I/Q mixer which is followed by a dual channel variable gain amplifier. The acquired signal is then sent to the micro PC which acquires the signal using its own audio card properly programmed and then runs the control and processing software.

The control of the radar is done by a micro PC, model PIPO X7 running Windows 10© where the developed control software dialogs with the main microcontroller (MCU) of the radar. The MCU runs the ad-hoc developed firmware.

A power module produces all the voltages needed by the circuits, which are the stabilized ± 5 V and ± 12 V voltage.



FIG. 2 – The realized prototype of multipurpose low cost FMICW radar.

III. CONTROL AND ACQUISITION/PROCESSING SOFTWARE

It is possible to identify three different software sections: firmware, control and acquisition/processing software. The ad-hoc firmware is developed in embedded C and is resident on the MCU. The control and acquisition/processing software are developed in C# in a unique full package installed on the control PC. The control software allows users to properly program the prototype of FMICW radar to optimize the parameters (e.g. sweep time, bandwidth, transmitted frequency, etc.) needed to perform a specific operation. It sends the parameters to the radar exploiting the RS-232 interface. The control software package includes also the module to control the motion of the antenna. The acquisition/processing software allows acquiring the signal with the PC audio card and performing primary processing operations. It is possible to configure radar to act as target detection system by properly settings distance and power level thresholds, or weather radar by setting proper values for radar equations for meteorological target. Acquired data can be visualized and saved to file. As soon as the system is turns on, it can automatically start working for the desired and programmed application using the parameters stored in well formatted XML files.

IV. SOME EXPERIMENTAL RESULTS

The first results aimed to test the radar proper working as a target detection system. At first a single corner reflector of known RCS was moved at different distance from the radar in order to verify the correct received power values (Fig. 3). A second test was then performed to show the radar resolution; according to theoretical calculation based on settled radar parameters, the FMICW radar resolution was 3.2 m, which was therefore the minimum distance at which the system can distinguish two different targets. The resolution was confirmed by experimental tests.

Other tests have been performed to verify the proper working as weather radar. Received power is converted into radar reflectivity factor and then into rain rate. Fig. 4 shows the comparisons between the rain rate measured by the FMICW radar (spatial resolution of 7.4 m) and an

extracted zoomed portion of a radar instantaneous map acquired by a calibrated X-band mini weather radar installed on the roof of the Politecnico di Torino. The reference track is highlighted in black. The FMICW radar underestimates rain with a bias of more than 5 dB. It means that further improvements and calibration procedures are required to use the radar as weather radar (adding also the automatic movement on the horizontal plane in order to obtain polar maps) or even a “microwave rain gauge” (the radar pointed in a single fixed direction).

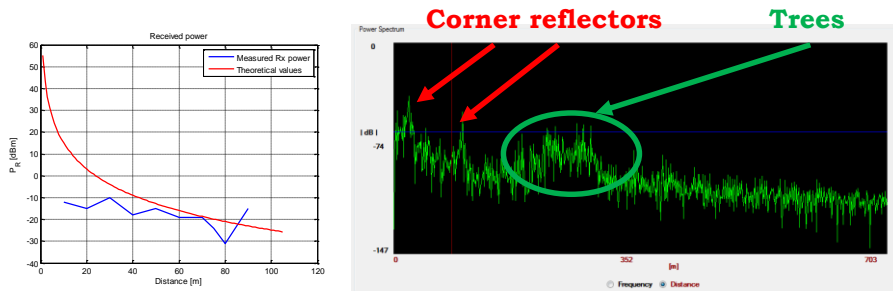


FIG. 3 – Received power compared with theoretical values (left). Power spectrum acquired for radar resolution verification (right): first and second spikes are related to corner reflector. The peak power values before 350 m are related to trees at the end of the area where the tests were performed.

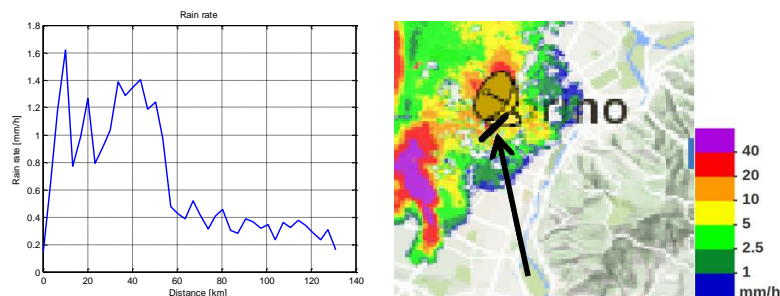


FIG. 4 – Rain rate estimate with FMICW radar measurements (left) compared with zoomed portion of instantaneous radar map (right).

V. CONCLUSIONS AND OUTLOOKS

The presented prototypal low cost and multipurpose FMICW radar shows good and encouraging results in different fields of applications. Future works will focus on improvement of radar performances for what concern both HW and SW. Main effort will be dedicated to use the system for atmospheric monitoring and meteorological purposes.

REFERENCES

- [1] S. E. Hamran, T. Berger, L. Hanssen and M. J. Oyan, "Gated FMCW SAR system," *Proceedings of European Radar Conference (EuRAD)*, Amsterdam, 2008, pp. 487-490, doi: 10.1109/EUMC.2008.4751788.

ELECTROMAGNETIC SCATTERING AND A NEW PERSPECTIVE IN SAR DESPECKLING

G. Di Martino⁽¹⁾, A. Di Simone⁽¹⁾, A. Iodice⁽¹⁾, D. Riccio⁽¹⁾, G. Ruello⁽¹⁾

⁽¹⁾ Department of Information Technology and Electrical Engineering, University of Naples Federico II
Via Claudio 21, Naples, Italy
{gerardo.dimartino; alessio.disimone; iodice; daniele.riccio; ruello}@unina.it

Abstract

Remotely sensed data acquired by Synthetic Aperture Radar (SAR) systems represent an essential and useful tool in Earth observation and monitoring, as well as for the study and the analysis of other celestial bodies. However, readability of SAR images is greatly affected by the multiplicative speckle noise, typical of coherent acquisition systems, like SAR sensors. Speckle noise degrades significantly the appearance of the SAR images and affects the performance of both scene analysis and interpretation by SAR expert users and information extraction performed by computer programs. Despeckling is therefore an essential preprocessing step, since a despeckling algorithm can, at least in principle, dramatically improve SAR data readability and interpretation also for non-SAR expert users. In this paper, the possibility to introduce electromagnetic scattering concepts in the despeckling problem is presented and two different scattering-based filters are discussed. Relevant experimental results are also shown.

Index Terms – Despeckling, Electromagnetic Scattering, Fractals, Synthetic Aperture Radar.

I. INTRODUCTION

Synthetic Aperture Radar (SAR) imagery represents an essential tool for natural resource monitoring and environmental hazard management and control. However, despite their potentialities, SAR data interpretation is restricted to SAR-expert users, due to the multiplicative noise, named speckle, typical of SAR sensors. Therefore, an accurate image interpretation by human users and processing by algorithms is very difficult unless a despeckling preprocessing step is carried out. However, removal (or reduction) of speckle effects is not at all an easy task, as witnessed by the huge related literature. During the last three decades, several methods and approaches have been developed, each with its own potentials and drawbacks [1]-[4]. However, the main limitation of the state of the art is the disregard of the physical phenomena hidden in the SAR image formation. Most of the developed techniques treats the despeckling problem in a purely statistical framework, ignoring the electromagnetic scattering phenomena generating speckle noise. Very

recently, some of the authors developed a novel approach to despeckling based on the knowledge of the scattering behavior of the surface [5]-[7]. In this paper, an overall discussion of scattering-based despeckling is presented. The two main approaches, namely the Scattering Based Probabilistic-Patch-Based SB-PPB filter and the SB-SARBM3D one are described and relevant results are shown.

II. SCATTERING-BASED DESPECKLING

In order to deal with a scattering-based despeckling approach, a scattering model of the surface is required. To this aim, a natural surface is modeled via fractal geometry and the Small Perturbation Method (SPM) suitable for fractal surfaces is used to model the single bounce scattering behavior of the surface. Therefore, the backscattering coefficient σ^0 reads as [6]

$$\sigma^0 = 2\pi 8k^4 S_0 |\beta|^2 \frac{\cos^4 \theta}{(2k \sin \theta)^{2+2H}} \quad (1)$$

where k is the electromagnetic wavenumber of the incident field; S^0 and H are the fractal parameters of the surface; β is a coefficient related to the polarization of the incident and reflected waves; θ is the local incidence angle.

The scattering behavior of the surface is estimated via Eq. (1) and assuming the knowledge of the local incidence angle derived from a Digital Elevation Model (DEM) of the surface. For the remaining parameters, reference values typical for natural surfaces are used. In particular, SB-PPB is a patch-based nonlocal algorithm derived from the PPB filter [2]. Filter weights are formally expressed as the weights of the iterative PPB (see Eq. (4) of [6]), substituting the previous estimate of the backscattering coefficient with the one estimated via Eq. (1). SB-SARBM3D uses the estimated backscattering coefficient to refine the initial estimate of the despeckled image provided by the first step of the original SARBM3D [3]. For more details the reader is referred to [6], [7].

III. EXPERIMENTAL RESULTS

The SB-PPB and SB-SARBM3D are applied to a 2000x2000 subset of a COSMO-SkyMed single-look stripmap SAR image of the Vesuvius volcano close to Naples (Italy) (Fig. 1). Fig. 1(a) shows the single-look image used as input for both the algorithms. A quantitative analysis of the despeckling capabilities of the filters is provided in Table I in which some performance parameters are evaluated. For the definition of the parameters the reader is referred to [6]. The reference image (Fig. 1(b)) has been obtained via a temporal multi-look of 42 images. As both Fig. 1 and Table I show, owing to the scattering a priori information, a

significant speckle suppression is reached without details smearing. Furthermore, even if the techniques were primarily designed for natural surfaces, the weighting procedure in SB-SARBM3D and the noniterative PPB weight in SB-PPB (see Eqs. (5) and (12) in [6]) extend the applicability of the proposed algorithms also to SAR images with sparse man-made structures.

IV. CONCLUSION

The paper discusses the performance improvements of despeckling algorithms by exploiting some a priori information about the scattering behavior of the surface. In particular, two recently proposed scattering-based despeckling techniques, namely SB-PPB and SB-SARBM3D are presented and their performances are compared for the first time. The a priori scattering information used within the filters is estimated by assuming a fractal scattering model and exploiting a DEM of the surface. The possibility to estimate the scattering information directly from the single SAR image is currently under investigation by the authors. This will avoid the need for such extra information.

REFERENCES

- [1] J. S. Lee, "Digital Image Enhancement and Noise Filtering by Use of Local Statistics," *IEEE Transactions on Pattern Analysis and Machine Intelligence*, vol. PAMI-2(2), pp. 165-168, Mar. 1980.
- [2] C.-A. Deledalle, L. Denis, and F. Tupin, "Iterative Weighted Maximum Likelihood Denoising With Probabilistic Patch-Based Weights," *IEEE Transactions on Image Processing*, vol. 18(12), pp. 2661-2672, Dec. 2009.
- [3] S. Parrilli, M. Poderico, C. V. Angelino, and L. Verdoliva, "A Nonlocal SAR Image Denoising Algorithm Based on LLMMSE Wavelet Shrinkage," *IEEE Transactions on Geoscience and Remote Sensing*, vol. 50(2), pp. 606-616, Feb. 2012.
- [4] F. Argenti, A. Lapini, T. Bianchi, and L. Alparone, "A Tutorial on Speckle Reduction in Synthetic Aperture Radar Images," *IEEE Geoscience and Remote Sensing Magazine*, vol. 1(3), pp. 6-35, Sep. 2013.
- [5] G. Di Martino, A. Di Simone, A. Iodice, D. Riccio, and G. Ruello, "Non-Local Means SAR Despeckling Based on Scattering," *IEEE International Geoscience and Remote Sensing Symposium (IGARSS)*, pp. 3172-3174, Milan, Jul. 2015.
- [6] G. Di Martino, A. Di Simone, A. Iodice, and D. Riccio, "Scattering-Based Non-Local Means SAR Despeckling," *IEEE Transactions on Geoscience and Remote Sensing* (in print), 2016.
- [7] G. Di Martino, A. Di Simone, A. Iodice, G. Poggi, D. Riccio, and L. Verdoliva, "Scattering-Based SARBM3D," *IEEE Journal of Selected Topics in Applied Earth Observations and Remote Sensing* (in print), 2016.

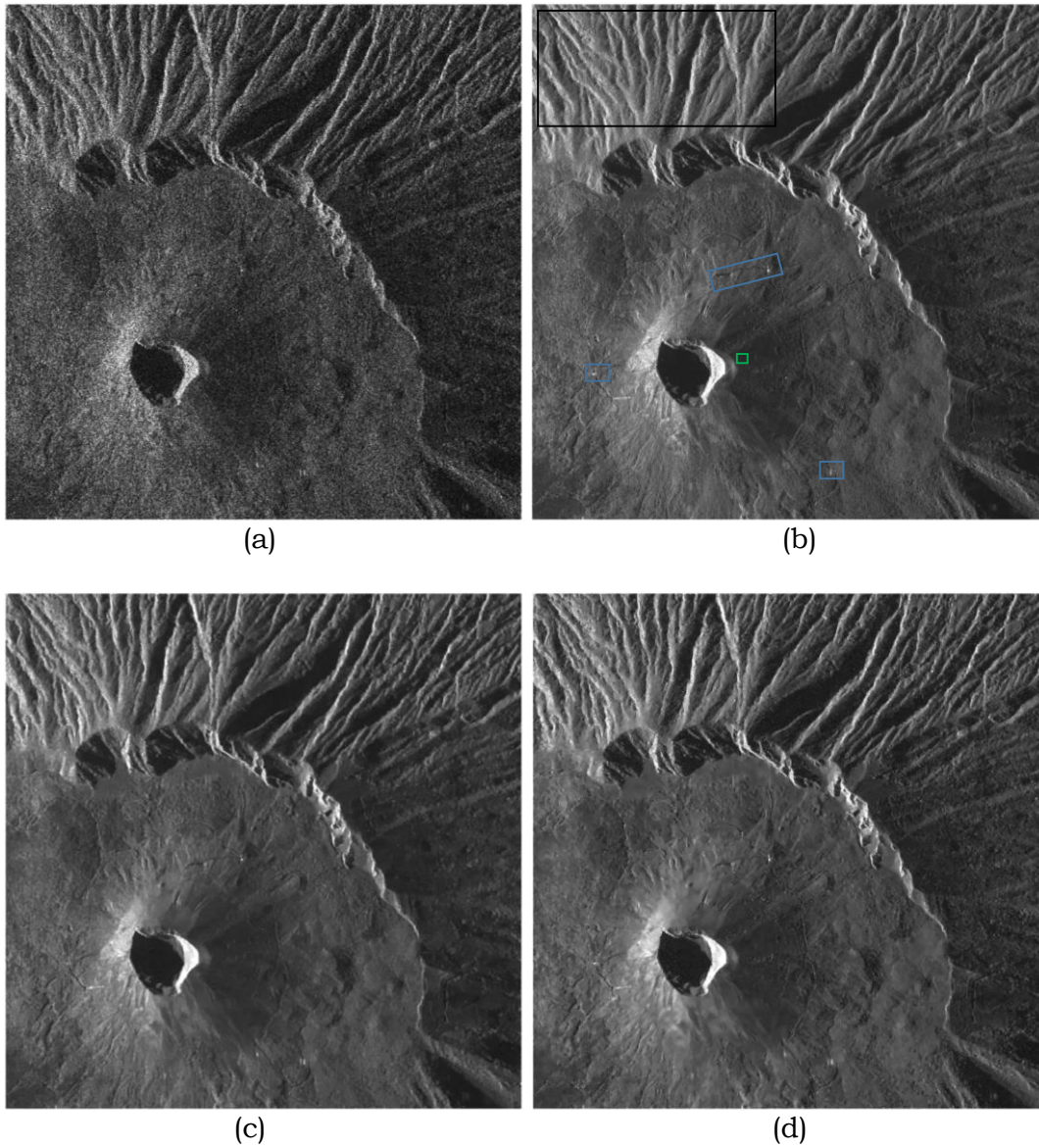


FIG. 1 – (a) 2000×2000 subset of a COSMO-SkyMed single-look stripmap SAR image of the Vesuvius volcano close to Naples (Italy); (b) reference image obtained via a temporal multilook of 42 SAR images. Black, and green boxes indicate the areas selected for coefficient of variation, and Equivalent Number of Looks computation, respectively. Blue boxes show some man-made features correctly retained by the filters; (c) SB-SARBM3D (d) SB-PPB.

TABLE I – PERFORMANCE PARAMETERS

	MoI	VoR	SNR	C_x	MSSIM	ENL
Reference	1.000	1.000	∞	1.054	1.000	19.70
Noisy	1.000	-	-1.470	1.795	0.962	0.93
SB-PPB	0.994	0.707	4.787	1.002	0.990	60.45
SB-SARBM3D	0.970	1.029	5.475	0.940	0.991	71.02

OPTIMAL TILING FOR NEW GENERATION RADAR SYSTEMS

N. Anselmi⁽¹⁾

⁽¹⁾ELEDIA Research Center (ELEDIA@UniTN, University of Trento)
via Sommarive 5, 38123 Trento, Italy
nicola.anselmi@eledia.org

Abstract

In this paper, an innovative tiling methodology for next generation radar systems is presented. Domino tiling for phased array antennas are obtained by means of a Genetic Algorithm (GA) optimization procedure that are optimal in terms of aperture covering and radiation performances. A simple illustrative example is reported, showing the effectiveness of the proposed approach.

Index Terms – tile array, array clustering, sub-array, wideband array, domino tiling.

I. INTRODUCTION

Phased arrays are antenna technology that can afford a multitude of interesting functionalities, such as fast-beam scanning, high-directivity, adaptive beam forming and multi-beam sensing, that are very attractive for next generation radar applications. Unfortunately these systems are very expensive, because of the high costs of the transmission/receive modules (TRM) [1]. Therefore lowering the number of TRM in the beam-forming network can significantly reduce the antenna implementative costs. To overcome such an issue, several methodologies have been proposed in the literature, like sparse, thinned and clustered arrays [2]. In this framework, clustered array architectures allow to achieve good trade-offs between the costs and complexity of the beam-forming network, by grouping more than one element over a single TRM and still keeping the modularity of standard fully-populated phased arrays. The main drawback in case of sub-arrayed architecture is the presence of quantization lobes, arising when periodic errors are introduced in the quantization of the aperture illumination [3]. Polyomino-based clustering methods [4], [5] have been proposed to reduce the level of quantization lobes. Nevertheless these approaches cannot assure optimal coverings (i.e., the region is not entirely covered by elements).

Optimal coverings are also known as tiling problems. The tiling of a finite region is not a trivial mathematical problem [6]. However in [7], for simple 1×2 tiles (also known as *dominoes*) an optimal tiling algorithm is proposed, that allows to generate exhaustively all the possible domino tilings of a finite region. Unfortunately even for simple small squared regions, the number of admissible tilings is very high (as example, a 10×10 region, can be tiled in more than 10^{11} different ways [8]). Consequently, an exhaustive search leads to prohibitive computational timings for medium/big antenna apertures. In this work, the search

space is reduced by means of a GA optimizer [9] that is used to find the best possible aperture tiling with respect to a predefined cost function. The use of a GA optimizer is allowed by the possibility to encode into a string of integers a tiling configuration, as explained in [7]. In a limited time, the tiling can be optimized, affording a clustering configuration that is optimal in terms of aperture covering and performances of the radiated power pattern.

II. MATHEMATICAL FORMULATION

The array factor of a rectangular $M \times N$ planar array of isotropic elements, clustered into $Q < M \times N$ sub-arrays, is obtained as [2]:

$$AF(\theta, \phi) = \sum_{m=1}^M \sum_{n=1}^N \sum_{q=1}^Q \omega_q \delta_{c_{m,n}}^{(q)} e^{jk(d_x u + d_y v)} \quad (1)$$

where $k = 2\pi/\lambda$ is the wavenumber, λ being the wavelength, d_x and d_y are the elements spacing along the x and y axes, respectively, $u = \sin(\theta)\cos(\phi)$ and $v = \sin(\theta)\sin(\phi)$. Moreover, ω_q ($q = 1, \dots, Q$) are the sub-array control points, while $\delta_{c_{m,n}}^{(q)}$ is the Kronecker delta function that defines the clustering of the array elements, being $c_{m,n} \in [1, Q]$ ($m = 1, \dots, M$, $n = 1, \dots, N$) a set of integer values that univocally identify the sub-array for each element. In Eq. (1) $\delta_{c_{m,n}}^{(q)} = 1$ when $c_{m,n} = q$ (i.e. the (m, n) -th element is grouped into the q -th sub-array), otherwise if $c_{m,n} \neq q$, $\delta_{c_{m,n}}^{(q)} = 0$. The amplifiers gains A_q ($q = 1, \dots, Q$), connected to the sub-arrays output ports, are obtained, starting from a reference amplitude tapering $A_{m,n}^{(REF)}$ ($m = 1, \dots, M$, $n = 1, \dots, N$), by averaging the amplitudes that belong to the q -th cluster, as:

$$A_q = \frac{1}{C_q} \sum_{m=1}^M \sum_{n=1}^N A_{m,n}^{(REF)} \delta_{c_{m,n}}^{(q)} \quad (2)$$

where in Eq. (2) $C_q = \sum_{m=1}^M \sum_{n=1}^N \delta_{c_{m,n}}^{(q)}$ is the number of elements clustered into the q -th sub-array. During the design of such architectures, a natural question arises: how to cluster the elements together in order to minimize the quantization lobes height? It is well known that a trivial tiling like the one shown in Fig. 1(a) is not the best choice [3]. The aim of this work is to provide optimal domino tilings that minimize the impact of quantization errors on the measured side-lobe level (SLL) of the radiated power pattern ($P(\theta, \phi) = |AF(\theta, \phi)|^2$). The method proposed in [6], where domino tilings are encoded by string of positive integer numbers, called tiling words, is exploited. The discrete representation of the unknowns, allow to use a GA optimizer for finding

the best, among all the admissible tilings. The GA initial population is obtained generating P tiling words T_i^p ($p = 1, \dots, P$), using the exhaustive algorithm proposed in [7]. The initial population is then evaluated by means of the cost function:

$$\Omega(k, p) = SLL\{P(\theta, \phi)_k^p\} \quad (3)$$

where $P(\theta, \phi)_k^p$ is the power pattern of the clustered array obtained using Eq. (1) and Eq. (2) and the tiling T_k^p , while $SLL\{\cdot\}$ is the respective measured side-lobe level. Standard GA operators [9] are then applied for the generation of new admissible individuals. Then the fitness is computed by evaluating the cost of each individual using Eq. (3), and the best solution is preserved until the maximum number of iterations K is reached.

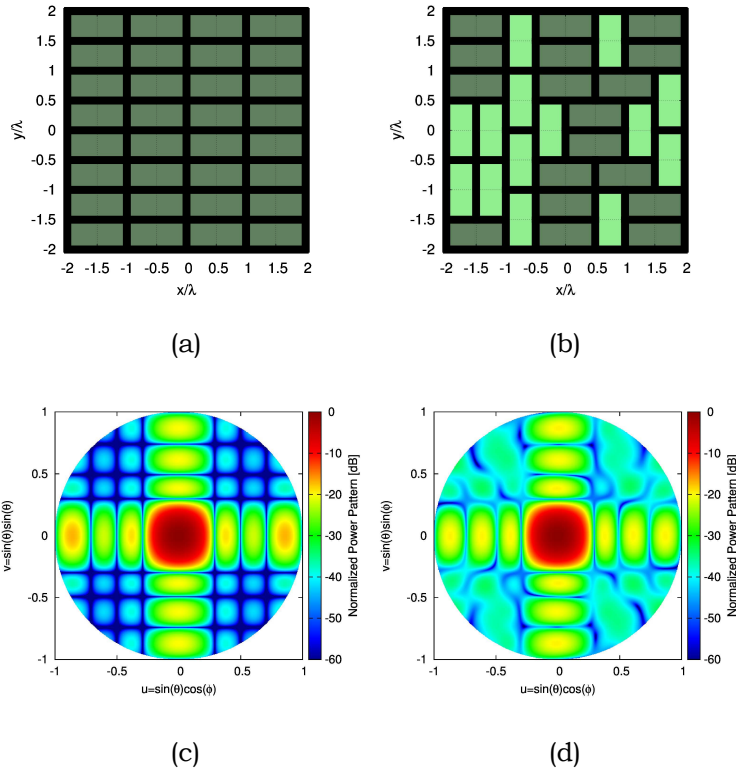


FIG. 1 – [$M \times N = 8 \times 8$, $Q = 32$, $C_q = 2$, $d_x = d_y = 0.5\lambda$, $SLL^{REF} = -20$ dB]
- Periodic (a) and GA-optimized (b) array aperture tiling, and the respective normalized power patterns (c) and (d).

III. NUMERICAL RESULT

Let us consider a $4\lambda \times 4\lambda$ aperture subdivided into 64 cells by a regular squared lattice. In each cell barycenter an isotropic radiator is positioned obtaining a planar array of $M \times N = 8 \times 8$ elements grouped into $Q = 32$ clusters ($C_q = 2$). A Dolph-Chebyshev amplitude tapering

generating a power pattern with $SLL^{REF} = -20 \text{ dB}$ is chosen as reference. A simple tiling can be obtained by placing all the tiles in the same orientation, as shown in Fig. 1(a), where only horizontal dominoes are used. In this case the SLL of the generated power pattern increases up to $SLL = -17.05 \text{ dB}$, because of the two quantization lobes arising along the $\nu = 0.0$ cut of the normalized power pattern of Figure 1(c). On the contrary, the GA optimized tiling configuration reported in Fig. 1(b) shows an aperiodic tiles configuration and consequently the generated power pattern shown in Fig. (d) has lower quantization lobes ($SLL = -19.51 \text{ dB}$) with respect to Fig 1(c) obtaining an improvement of almost 2.5 dB .

IV. CONCLUSION

In this work an innovative optimization strategy for phased array tiling has been presented. The proposed methodology, based on a GA optimization, and a smart tilings encoding, is able to find optimal domino tilings that can be used for phased array clustering. A simple numerical example shows the advantages of the provided optimized solution, which radiates a power patterns with lower SLL with respect to a trivial periodic clustering.

REFERENCES

- [1] J. S. Herd, and M. D. Conway, "The Evolution to Modern Phased Array Architectures," *Proc. IEEE*, vol. 104, no. 3, pp. 519-529, Mar. 2016.
- [2] P. Rocca, G. Oliveri, R. J. Mailloux, and A. Massa, "Unconventional phased array architectures and design methodologies - A review," *Proc. IEEE*, vol. 104, no. 3, pp. 544-560, Mar. 2016.
- [3] R. J. Mailloux, "Array grating lobes due to periodic phase, amplitude and time delay quantization," *IEEE Trans. Antennas Propag.*, vol. 32, no. 12, pp. 1364-1368, Dec. 1984.
- [4] R. J. Mailloux, S. G. Santarelli, T. M. Roberts, and D. Luu, "Irregular polyomino-shaped subarrays for space-based active arrays," *Int. J. Antennas Propag.*, vol. 2009, Article ID 956524, 2009.
- [5] P. Rocca, R. J. Mailloux, and G. Toso, "GA-based optimization of irregular subarray layouts for wideband phased array design," *IEEE Antennas Wireless Propag. Lett.*, vol. 14, pp. 131-134, 2015.
- [6] J. H. Conway, and J. C. Lagarias, "Tiling with Polyominoes and Combinatorial Group Theory," *J. of Combinatorial Theory*, Series A 53, 183-208, 1990.
- [7] S. Desreux, and E. Remila, "An optimal algorithm to generate tilings," *J. of Discrete Algorithms*, vol. 4, pp. 168-180, 2006.
- [8] P. W. Kastelyn, "The Statistics of Dimers on a Lattice," *Physica*, vol. 27, pp. 1209-1225, 1961.
- [9] P. Rocca, M. Benedetti, M. Donelli, D. Franceschini, and A. Massa, "Evolutionary optimization as applied to inverse scattering problems," *Inu. Prob.*, vol. 24, pp. 1-41, 2009.

EXPERIMENTAL ASSESSMENT OF SOFTWARE DEFINED RADAR FOR LANDSLIDE EARLY WARNING

S. Costanzo⁽¹⁾, G. Di Massa⁽¹⁾, A. Costanzo⁽¹⁾, A. Borgia⁽¹⁾, A. Raffo⁽¹⁾

DIMES – University of Calabria
87036 Rende (CS), Italy
costanzo@dimes.unical.it

Abstract

A low cost L-band Software Defined Radar, operating into an Integrated Landslides Early Warning System, is developed and tested in a real scenario. An overall description of the monitoring system and the architecture of the L-band radar device are briefly provided. A novel estimator, based on a measured High Range Resolution profile variation, is further discussed and experimentally validated in order to detect significant movements in the monitoring scenario.

Index Terms – Software Defined Radar, Landslides Early Warning.

I. INTRODUCTION

Hydrogeological factors, morphological aspects, sudden weather trend changes and inappropriate human intervention may lead to various typologies of ground movements (mud flows, rock fails and debris precipitation); as a consequence, landslide events are difficult to be predicted, real time monitored and aptly tackled. Since a large set of physical parameters related to the phenomenon have to be taken into account for a possible evolution of a risk event, the knowledge in several heterogeneous fields is required for monitoring a risk scenario.

One of the main goal of an Early Warning approach is the possibility of replacing a structural intervention where financial resources are too limited to properly face the problem in a permanent way. Since several typology of heterogeneous sensor may be integrated in the system, the cost reduction of each device gives a serious constraint.

In order to avoid most of the cost associated to hardware devices, a Software Defined Radar, working at L-Band frequencies, has been designed, tested, and further included into an “Integrated System for Landslide Monitoring, Early Warning and Risk Mitigation along Lifelines” (LEWIS) project. The development of the full monitoring system is inserted in the framework of the National Operational Programme 2007-13. The aim of the project, involving several industrial companies and research centers, is the development of an infrastructure able to detect landslide risks and transmit an affordable alert for a mitigation action.

II. L-BAND SOFTWARE DEFINED RADAR INTEGRATED IN A LANDSLIDE EARLY WARNING SYSTEM

The Landslide Early Warning Integrated System is composed of several heterogeneous subsystems which support different operations (Fig. 1). A set of punctual sensors are placed directly in the monitoring points, while areal systems are properly located in order to control an overall scenario. Data flows generated by these monitoring systems are sent to a data collection and processing center through a network with a multithread based architecture, using an ad hoc communication protocol and a flexible middleware. Information are stored in real time and further elaborated using specific mathematic models evaluating landslide movements. If critical variations are detected, a warning is transmitted to a control and mitigation center, in which appropriate operative decisions are taken.

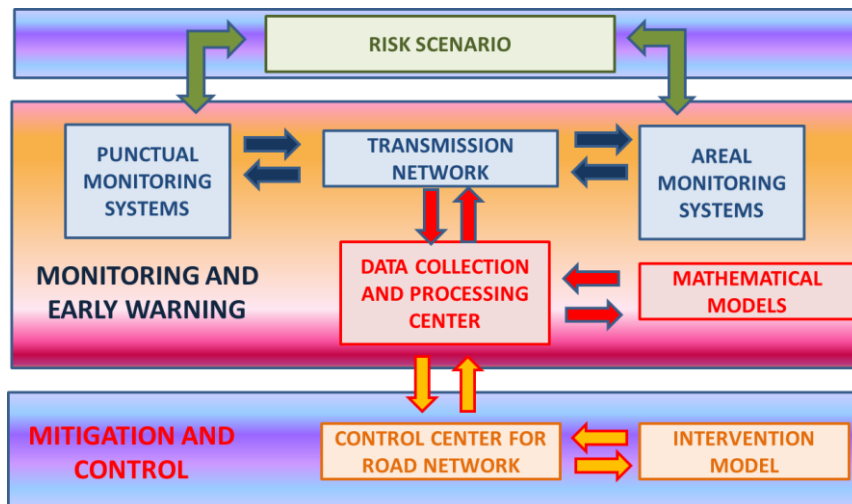


FIG. 1 – Landslides Early Warning Integrated System architecture.

L-Band Software Defined Radar Module, which represents the most significant areal sensor of the LEWIS system, has been developed and experimentally validated into the Microwave Laboratory at University of Calabria (Fig. 2).

A Universal Software Radio Peripheral transceiver (NI USRP 2920) is adopted to replace most of the hardware operations (e.g. modulation, demodulation, signal generation) through software implementation, thus achieving significant cost savings with respect to classical radar implementation. A Lab-View code, implemented on a compact PC (MXE 5302), controls the overall USRP operation, while two GSM modules are used for the communication with the control center, by adopting a protocol shared with the other devices of the LEWIS system. A fixed horn antenna is employed in the TX path, while a patch array, moved by a stepped motor, is used in the receiving path.

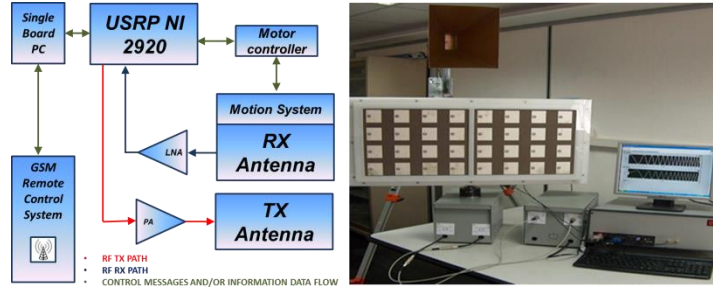


FIG. 2 – L-Band Software Defined Radar System: block diagram (a) and prototype configuration (b)

III. EXPERIMENTAL RESULTS

A specific hill area (Mancarelli, Cosenza), crossed by national A3 highway and recently involved in landslides events, is currently monitored by the proposed L-Band Software Defined Radar (Fig. 3).

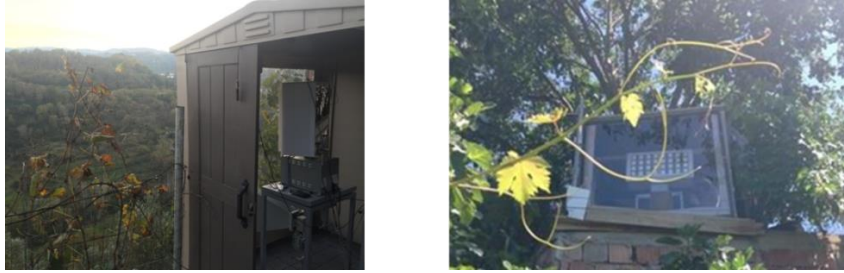


FIG. 3 – Monitored area (a) and radar picture (b).

The scene is divided into 5 sectors, with an azimuthal 10° scan angle between two successive positions over a time step of 1 minute. High Range Resolution (HRR) profiles, obtained through a stretch processing technique [1-2], are elaborated in real time, stored and transmitted to the control center. Since absolute variations in the HRR profile are related to changes in the scene, a novel estimator, quantitatively taking into account these variations, is proposed into Eq. (1), where $S_i(r)$ is the HRR profile measured at distance r by the i^{th} scan.

$$\xi_i(r) = \varepsilon_i(r) \hat{s}_i(r) \hat{d}(r)^{-2} \quad (1)$$

$$\varepsilon_i(r) = \frac{S_i(r)^2 - S_{i-1}(r)^2}{S_{i-1}(r)^2} \quad (2)$$

$$\hat{s}_i(r) = \frac{S_i(r)^2}{\max\{S_i(r)^2\}} \quad (3)$$

$$\hat{d}(r) = \frac{r}{\max\{r\}} \quad (4)$$

The three factors involved in the computation represent, respectively, the relative power variation between two range profiles (Eq. (2)), the normalized power (Eq. (3)) and the normalized distance with respect to the total observation range (Eq. (4)). The evolution of the estimator ξ between two successive measurement, during a 30 minutes duration campaign (7 scans for each sector), is extracted (Fig. 4) and a threshold equal to the 50% of the estimator variation is associated to a critical evolution of HRR profile at the corresponding sector and range.

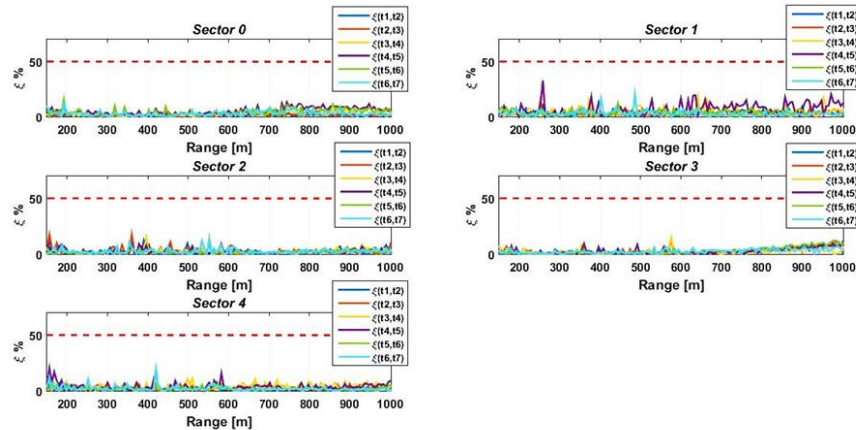


FIG. 4 – Evolution of the estimator ξ over a measurement of 30 minutes.

Some variations can be mainly observed in the range profiles elaborations for the Sectors 1-2, namely those directly facing the landslide scenario, but dynamic changes cannot be attributed to possible significant landslide movements, as all estimator values maintain below the prescribed limit of 50% variation.

IV. CONCLUSIONS

Experimental tests of a low cost L-Band Software Defined Radar working in a real monitoring scenario and completely integrated into the LEWIS system have been performed. A novel mathematical estimator has been defined and applied to measured range profiles in order to detect possible critical variations in the scenario.

A more extensive measurement campaign and a comparison with theoretical models for landslides prediction and analysis will be carried out in a future work.

REFERENCES

- [1] B. R. Mahafza, A. Z. Elsherbeni, “Simulations for Radar Systems Design”, *Chapman and Hall/Crc*, 2003.
- [2] S. Costanzo, F. Spadafora, A. Borgia, O. H. Moreno, A. Costanzo, G. Di Massa, “High resolution software defined radar system for target detection,” *Journal of Electrical and Computer Engineering*, Article ID 573217, 2013.

COLOR-CODING OF SAR IMAGES USING MULTITEMPORAL

D. Amitrano⁽¹⁾, G. Di Martino⁽¹⁾, A. Iodice⁽¹⁾, D. Riccio⁽¹⁾, G. Ruello⁽¹⁾

⁽¹⁾ University of Napoli Federico II, Department of Electrical
Engineering and Information Technology
Via Claudio 21, 80125, Napoli, Italy

Abstract

In this paper, we present an innovative, human-centered framework for color-coding of multitemporal SAR images. The objective is to provide ready-to-use images for applications and characterized by a high degree of interpretability, even for non-expert users, and the possibility to be processed with simple, end-user-oriented algorithms for information extraction.

Index Terms – image interpretation, synthetic aperture radar

I. INTRODUCTION

In order to favor the dissemination of SAR data, it is very important to take care of users' experience, both from the standpoint of visualization and processing [1]. In fact, despite the huge investments made by the international community to develop and launch new sensors, the use of SAR data in applications is still rather limited. Therefore, there is a strong necessity to design end-user-oriented frameworks putting users at the center of the processing chain [2].

In this paper, we present an innovative, human-centered framework for RGB composition of time-series SAR images. The aim is to provide ready-to-use images characterized by a high degree of interpretability (even for non-expert users) and the possibility to be processed with simple techniques/algorithms for the extraction of meaningful physical information [3]. In such way, the idea (widely diffused in among multidisciplinary users) that SAR images are too complicated to be understood and processed is overcome.

II. METHODS AND PRODUCTS

The MAP3 framework exploits a rigorous multitemporal processing for making explicit the semantic of SAR images using an end-user-oriented RGB presentation. The framework is composed by three major processing blocks aimed at:

- Radiometric calibration and geometric registration, in order to make images of the time series comparable each other. Despeckling is also a key activity in this phase to enhance image presentation and improve objects discrimination;

- Selection of the best variables involved in the fusion process. This choice will determine the output product;
- Data fusion,

The outputs of the MAP3 framework are two classes of RGB products we named as Level-1 α [1] and Level-1 β [4]. These products have different rationale:

- Level-1 α products are bi-temporal images oriented to change-detection applications. In this case, we exploit two SAR images and their interferometric coherence to enhance changes with respect to a suitable reference situation.
- Level-1 β products summarize in a unique RGB frame the information content of a SAR multitemporal series. In this case, the RGB channels are constituted by temporal variables (mean backscattering, mean interferometric coherence, saturation index, time-series variance) opportunely combined. These products are particularly well suited for classification applications, since objects' appearance in the RGB image depends on their characteristic dynamics.

The principal characteristic of both Level-1 α and Level-1 β products is that the association color-object, being physical-based, is stable. Moreover, the RGB composition is designed in such way to recall the natural color palette, at least for some image features.

In Fig. 1, we show a Level-1 α product depicting a rural area of Burkina Faso. This area is characterized by a semi-arid climate. This means that, at the top of the dry season, the environment is completely bare. This represents a good reference situation for change-detection, i.e. to monitor the evolution of the scene by comparing the electromagnetic response of a test image with that of the reference one.

However, the characteristics of this product allow for easily recognize water bodies and vegetation without having any information about the product composition. This is possible because these features are rendered in natural colors, giving the possibility even to non-expert users the possibility to easily reconstruct the scene semantic. Obviously, this is a false-color image. Therefore, other features are rendered in a color which depends on their electromagnetic response during the acquisitions composing the product. As an example, trees all around the lake are rendered in cyan due to their temporal backscattering stability.

As stated above, the proposed RGB products, are characterized by a physical-based and stable color-object association. Therefore, the variation of the scene does not affect the rendering of image features. This can be clarified by considering Fig. 2. In this case, the Level-1 α product depicts a scene acquired over the city of Castel Volturno (Italy), i.e. in a temperate Mediterranean climate. However, the features' colorimetric response is constant (vegetation-green, bare soil-prussian blue, shadows/permanent water-black, etc.).

In Fig.3a and Fig. 3b, two images extracted from a Level-1 β product concerning the city of Dresden is shown. The considerations made above about Level-1 α products hold. In fact, even in this case, the color-object association is stable varying the scene and the climatic condition. Obviously, this association is different, since in this kind of images the rendering depends on objects' temporal behavior rather than their change with respect to a reference situation.

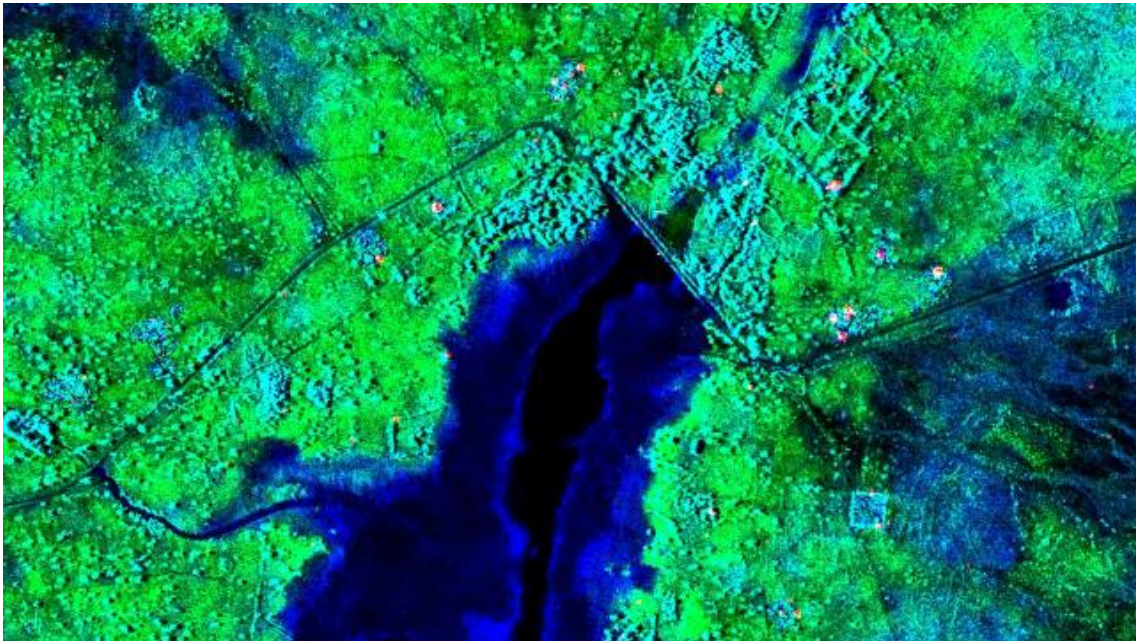


Figure 1. Burkina Faso, change-detection-oriented Level-1 α product.



Figure 2. Castel Volturno (Italy), change-detection-oriented Level-1 α product.

Both Level-1 α and Level- β products demonstrated their suitability in applicative contexts, as illustrated, as in example, in [5] and [4].

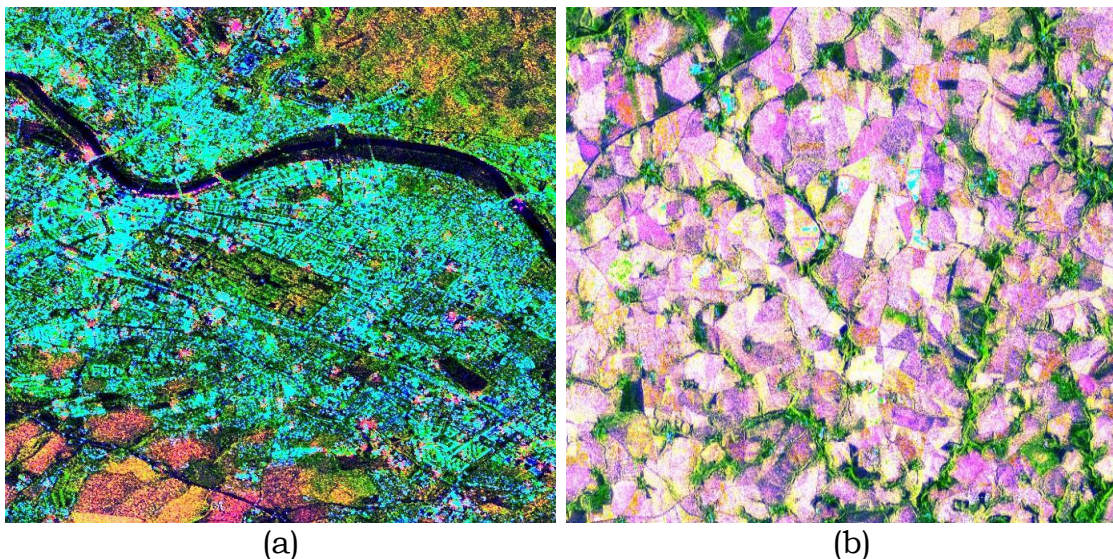


Figure 3. Dresden (Germany), Level-1 β product: (a) urban area, and (b) growing crops.

III. CONCLUSIONS

In this paper, we presented an innovative framework for RGB composition of multitemporal SAR images. The aim is to provide ready-to-use images characterized by a high degree of interpretability and the possibility to be processed with simple algorithms for information extraction. The framework is particularly oriented toward end-users with the objective to improve their experience with SAR data.

REFERENCES

- [1] D. Amitrano, G. Di Martino, A. Iodice, D. Riccio, and G. Ruello, "A New Framework for SAR Multitemporal Data RGB Representation: Rationale and Products," *IEEE Trans. Geosci. Remote Sens.*, vol. 53, no. 1, pp. 117–133, 2015.
- [2] M. Datcu and K. Seidel, "Human Centered Concepts for Exploration and Understanding of Earth Observation Images," *IEEE Trans. Geosci. Remote Sens.*, vol. 43, no. 3, pp. 52–59, 2005.
- [3] D. Amitrano, G. Di Martino, A. Iodice, D. Riccio, and G. Ruello, "An end-user oriented framework for the classification of multitemporal SAR images," *Int. J. Remote Sens.*, vol. 37, no. 1, pp. 248–261, 2016.
- [4] D. Amitrano, F. Cecinati, G. Di Martino, A. Iodice, D. Riccio, and G. Ruello, "Sentinel-1 Multitemporal SAR Products," in *IEEE International Geoscience and Remote Sensing Symposium*, 2015.
- [5] D. Amitrano, F. Cecinati, G. Di Martino, and A. Iodice, "Urban areas extraction from RGB SAR images using interferometric coherence and textural information," in *ESA FRINGE Workshop*, 2015.

NEURAL NETWORKS ARCHITECTURES FOR OIL SPILL MONITORING USING FULLY POLARIMETRIC SAR DATA

V. Scappiti ⁽¹⁾, D. Latini ⁽¹⁾, A. Ghezzi ⁽¹⁾ F. Del Frate ⁽¹⁾ G. Schiavon ⁽¹⁾

⁽¹⁾ Department of Civil Engineering and Computer Science
Engineering, University of Rome Tor Vergata,
Via del Politecnico, 1, 00133 Roma, Italy.
amendola@uniroma2.it

Abstract

Due to the launch of Radarsat-2 and ALOS missions the availability of fully polarimetric SAR data is significantly increased and such a trend will continue with the next generation of satellite instruments. This claims for the possibility of using suitable and adequate tools for image processing, so as not to miss a significant percentage of the information contained in the acquired images. To achieve this task, as far as oil spill detection from SAR is concerned, in this paper we combine different topologies of neural networks (NN) in order to design an effective processing system characterized at the same time by a high level of automation. In this context we introduce the application of a novel approach for target polarimetric decomposition based on the use of Autoassociative Neural Network (AANN). The AANN implementation precedes the other needed steps, in particular object extraction and object classification, which are performed using a Pulse Couple NN (PCNN) and a Multi-layer Perceptron NN (MLP-NN), respectively.

Index Terms – Polarimetric SAR, Neural Networks, Oil Spill Detection.

I. INTRODUCTION

The presence of an oil film on the sea surface damps the small waves due to the increased viscosity of the top layer and drastically reduces the measured backscattering energy, resulting in darker areas in SAR imagery [1]. However, the identification of hydrocarbon over the sea surface is not easy due to many natural phenomena, for instance, when the wind is weak the electromagnetic response is similar to that of natural films, which are a source of ambiguity [2]. Polarimetry has been demonstrated to be a valuable tool for interpreting and separating different scattering mechanism present in an observation area. These can be separated exploiting phase and amplitudes relations between the different polarimetric channels which can be represented through the computation of the scattering matrix or covariance matrix [3].

The aim of this study is to design new algorithms for the oil spill detection taking advantage of the polarimetric Radarsat-2 data features. The polarimetric information is exploited using a new statistical

decomposition method based on AANN. Thanks to the AANN the original image is represented in terms of Nonlinear principal components. Such components will be considered for the subsequent object extraction, characterization and classification steps.

II. POLARIMETRIC DECOMPOSITION WITH AANN

AANN's have feed-forward connections and sigmoidal nodal transfer functions, trained by back-propagation or similar algorithms. The implemented network architecture has three hidden layers, including an internal “bottleneck” layer of smaller dimension than either input or output (Fig. 1). The network is trained to perform the identity mapping, where the input is approximated by the output. Since the number of units in the bottleneck layer is lower than those in both input and output, the bottleneck nodes are able to encode the input information for subsequent reconstruction in the output. This process results in a feature extraction from the input vector. As input of the AANN the HH, HV, VV polarizations and two phases’ differences VV-HH and HV-HH have been considered in this work.

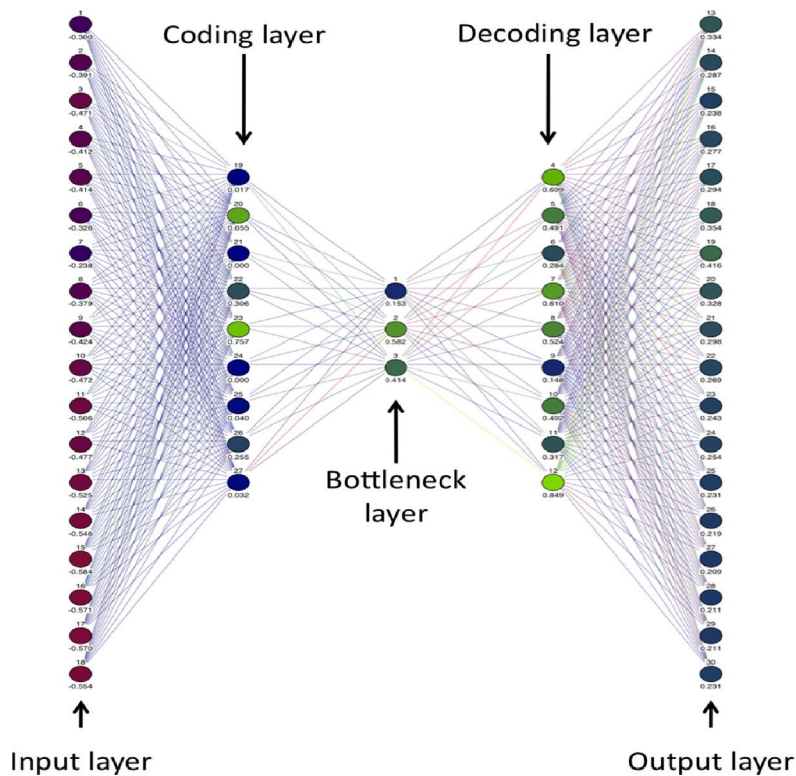


FIG. 1 – Auto-associative neural network topology

III. METHODOLOGY

The complete scheme for the oil spill detection, once the polarimetric image has been given as input to the system, consists of the following

steps: 1) polarimetric decomposition, 2) object extraction, 3) object characterization, 4) object classification. As shown in Fig. 2, three different NN topologies have been considered for the implementation of steps 1), 2), 4). We have already described in the previous section the use of AANN for the first step.

In step 2) the extraction of the candidate oil spill object is processed through a PCNN algorithm [4]. PCNNs are unsupervised and context sensitive algorithms. A PCNN is an NN algorithm that, when applied to image processing, yields a series of binary pulsed signals, each associated to one pixel or to a cluster of pixels. It belongs to the class of unsupervised artificial NNs in the sense that it does not need to be trained. The network consists of nodes with spiking behavior interacting each other within a predefined grid. The architecture of the net is rather simpler than most other NN implementations. PCNNs only have one layer of neurons, which receive input directly from the original image, and form a resulting “pulse” image. These characteristics make PCNN a rather suitable algorithm for image edge detection.

Once the object is extracted, a number of morphological and physical parameters are computed. The features extracted from the dark object are given as input to a classifier that estimates its probability of being an oil slick. Normally these features consider the geometry of the dark object in terms of its extension and of its shape, as well as the physical behavior in terms of the characteristics of the backscattering intensity of the pixels belonging to the object, to the background, and to the area around the border. In our study also the statistical polarimetric features computed from the NLPC images have been considered. The classification task is performed using a MLP-NN. These are feedforward networks, where the input flows only in one direction to the output, and each neuron of a layer is connected to all neurons of the successive layer but has no feedback to neurons in the previous layers.

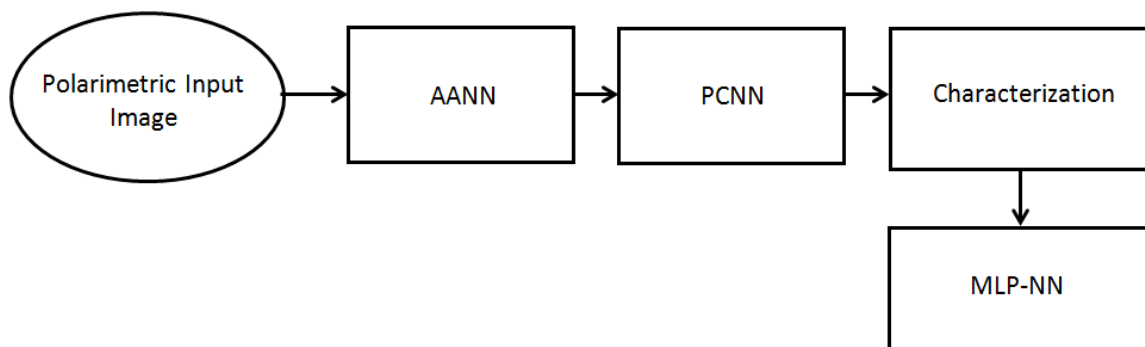


Fig. 2 – Oil spill detection scheme based on NN

In Fig. 3 an example extracted from the data set of Radarsat-2 image collection (VV polarization) is shown together with one of the components obtained through the AANN analysis. After having applying

the procedure to a significant number of cases we observed that the use of the nonlinear components rather than of the original images increases the effectiveness of the whole procedure.

IV. CONCLUSIONS

An ensemble of NN characterized by a different architecture has been designed for detecting oil spills in full polarimetric SAR images. The NN are shown to effectively play various roles, in particular: decomposition, object extraction and classification, increasing significantly the level of automatic processing of the image.

ACKNOWLEDGEMENT

Radarsat-2 data are provided by Canadian Space Agency: RADARSAT-2 Data and Products © 790 MacDonald, Dettwiler and Associates Ltd. (2010) – All Rights Reserved. RADARSAT is an 791 official trademark of the Canadian Space Agency

REFERENCES

- [1] Alpers, W., & H. Hühnerfuss (1988), Radar signatures of oil films floating on the sea surface and 801 the Marangoni effect, *J. Geophys. Res.*, 93(C4), 3642–3648
- [2] Camilla Brekke^{a,b,*}, Anne H.S. Solberg^b Oil spill detection by satellite remote sensing, *Remote Sensing of Environment* 95 (2005) 1–13
- [3] Minchew, B., Jones, C. E., & Holt, B. (2012). Polarimetric analysis of backscatter from the Deepwater Horizon oil spill using L-band synthetic aperture radar. *IEEE Transactions on Geoscience and Remote Sensing*, 50(10), 3812–3830
- [4] Taravat A., Latini D., Del Frate F., “Fully automatic dark-spot detection from SAR imagery with the combination of NonAdaptive Weibull Multiplicative Model and Pulsed-Coupled Neural Networks,” *IEEE Transactions on Geoscience and Remote Sensing*, vol. 52, n. 5, pp. 2427–2435, May 2014

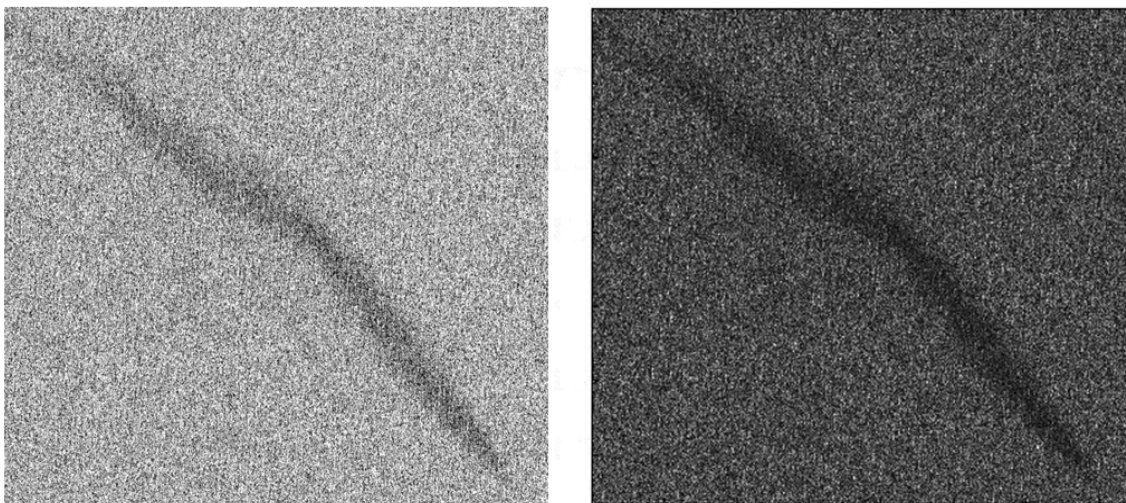


Fig. 3 – Original VV polarization image (left) and nonlinear component obtained via AANN analysis (right)

A PORTABLE WIRELESS CHARGER FOR THIN-FILM BATTERIES

G. Monti, L. Corchia, E. De Benedetto, L. Tarricone

University of Salento – Department of Engineering for Innovation,
Complesso Ecotekne, via Monteroni, Lecce, Italy
giuseppina.monti@unisalento.it

Abstract

In this paper, a wireless charger for low-capacity thin-film batteries is presented. The proposed device consists of a near-field wireless energy link and a power management unit. Experimental data referring to a prototype operating in the ISM band, centered at 434 MHz, are presented and discussed.

A conductive fabric on a leather layer was used for the fabrication of the wireless energy link, thus resulting into a prototype that can be easily embedded into apparel and accessories, such as handbags or suitcases.

From experimental data, it is demonstrated that, at 434 MHz, the RF-to-RF power transfer efficiency of the link is approximately 69.3 %. As for the performance of the system as a whole, the proposed portable charger exhibits a total efficiency of about 29.7 % when an RF power of 7.5 dBm is provided at the input port.

Index Terms – Wireless Resonant Energy Link, wearable, charger, thin-film batteries.

I. INTRODUCTION

Wearable electronics (WE) is becoming increasingly popular, thanks to the benefits offered by this technology in several application fields (e.g., military, gaming, health care). The embedding of electronic circuitry in clothes and/or apparel accessories, however, must not compromise the usability of the product and must not interfere with the freedom of movement of the user. In this regard, either near-field [1] or far-field [2] wireless technologies may effectively serve the purpose both for data and power transmission. Nevertheless, it is crucial that the necessary electronic devices and antennas be seamlessly integrated in wearable and portable accessories. In fact, the use of WE must not compromise the appearance/appeal of the product, must be lightweight, comfortable and long-lasting. To satisfy all the aforementioned requirements, it is crucial to implement WE by selecting appropriate fabrication techniques and materials, such as textile materials, conductive threads, electro-textile fabrics and non-woven conductive fabrics.

On the bases of the aforementioned considerations and starting from the prototype presented in [3], in this work, a wireless battery charger for application in clothing industry is presented. More in detail, the Wireless Resonant Energy Link (WREL) proposed in this work was exploited for implementing a wireless charger [1] for low-capacity thin-film batteries. As illustrated in Fig. 1a, the proposed system consists of: 1) two planar resonators that were optimized and fabricated to be embedded in portable leather accessories; and a 2) Power Management Unit (PMU).

Fig. 1b shows a sketch of a possible practical application: the secondary resonator (which is connected to the PMU) is embedded into a bag, while the primary resonator (i.e., the resonator connected to the power source) is embedded into a pad where the bag should be placed on for charging battery. Details on the design of the charger and experimental data are provided in the following sections.

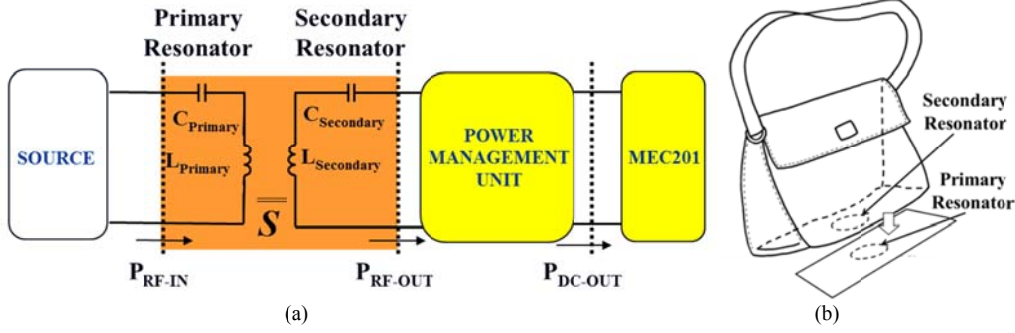


FIG. 1 – Proposed wireless charger. (a) Schematic representation: the link consists of a wireless resonant energy link and of a PMU. (b) Example of application.

II. WPT LINK

The proposed WPT link exploits a magnetic coupling between two identical resonators, each one consisting of a distributed inductance loaded by a lumped capacitor. The configuration adopted for the link and the geometry of the resonators is illustrated in Figure 2.

From Figure 2(a), it can be seen that each resonator consists of an elliptical loop loaded by a smaller one. The two resonators are rotated by 180° with respect to each other (on the x-y plane), and they are also aligned with the centre of the external elliptical loop. Two lumped capacitors, C_1 and C_2 , guarantee the resonance at the desired operating frequency.

Starting from a simple elliptical loop, the geometry of the resonators was optimized, by means of full-wave simulations, to obtain an operating frequency in the ISM band (433.05 – 434.79 MHz) and an input impedance of 50Ω . The final geometry and its dimensions are reported in Fig. 2a, while photographs of the realized prototype are given in Fig. 2b.

In order to facilitate the integration in clothes and accessories (such as leather handbags), an adhesive non-woven conductive fabric with a surface resistivity of $0.04 \Omega/\text{sq}$ on a 1.65 mm thick layer of leather with a relative dielectric permittivity (ϵ_r) of 3 was adopted for fabrication. As for the lumped capacitors, C_1 and C_2 , surface mounted capacitors were used. Figure 3 shows the scattering parameters measured through a vector network analyzer R&S ZVA50. A transmission coefficient better than -3 dB in the frequency range 318.70 – 523.67 MHz, corresponding to a relative bandwidth of about 48.7 %, was obtained.

We refer to the following definition for the RF-to-RF power transfer efficiency of the link (see Fig. 1):

$$\eta_{RF-RF} = \frac{P_{RF-OUT}}{P_{RF-IN}} = \frac{P_{RF-IN} \cdot |S_{21}|^2}{P_{RF-IN}} = |S_{21}|^2 \quad (1)$$

where P_{RF-IN} is the power available from the source, and P_{RF-OUT} is the power delivered by the secondary resonator to the PMU unit. Fig. 3b shows the η_{RF-RF} of the

fabricated prototype, evaluated according to Equation (1). A maximum of 71.3 % was obtained at 403.97 MHz, while values higher than 69.3 % were obtained in the ISM band (433.05 - 434.79 MHz).

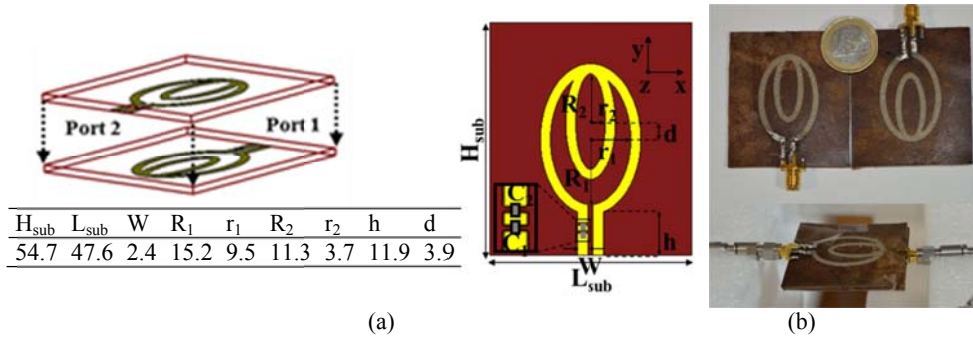


FIG. 2 – (a) Geometry and dimensions of the resonators (dimensions in the table are in mm). (b) Photographs of the fabricated prototype and of the experimental setup adopted for the measurements of the scattering parameters.

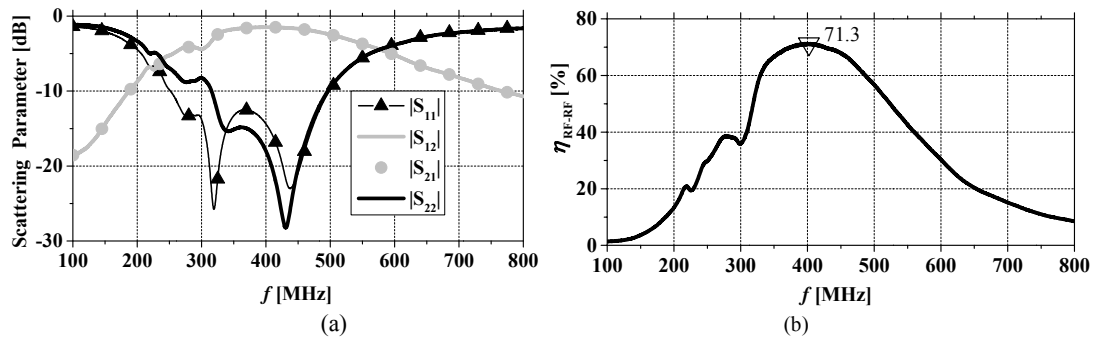


FIG. 3 – Experimental results obtained for: (a) the scattering parameters, (b) the RF-to-RF power transfer efficiency (η_{RF-RF}).

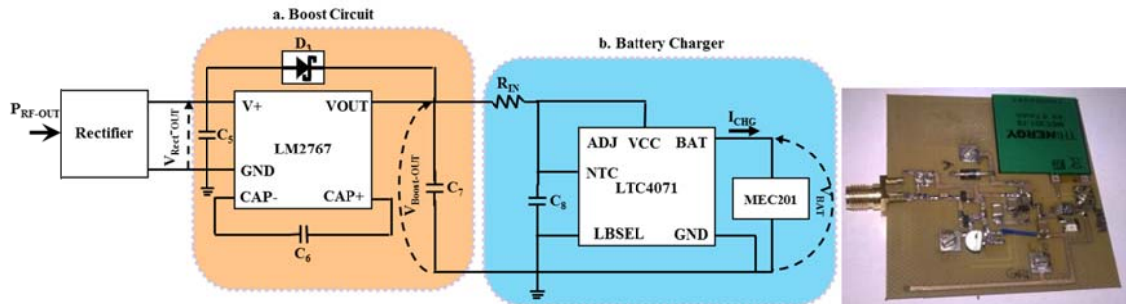


FIG. 4 – PMU: schematic representation and photograph of the fabricated prototype.

III. PORTABLE WIRELESS CHARGER

In order to verify the feasibility of using the WPT link presented in the previous section for implementing a portable wireless charger, a PMU that converts the RF power received by the secondary resonator into a DC power that can be directly delivered to a battery was also designed. Fig. 4 illustrates the schematic representation and a photograph of the fabricated prototype on a double side FR4 board; the PMU is 55 x 55 mm² and consists of three blocks: a) a voltage doubler rectifier, b) a boost circuit, and c) a battery charger. A photograph of a prototype fabricated (relative

dielectric permittivity equal to 4.1 and thickness of 0.4 mm) is shown in Fig. 10. The performance of the proposed portable battery charger consisting of the WREL illustrated in Fig. 2 connected to the PMU of Fig. 4, was experimentally investigated. Tests were performed in order to evaluate both the total efficiency of the wireless charger ($\eta_{\text{TOT}} = P_{\text{DC-OUT}}/P_{\text{RF-IN}}$) and the time necessary to recharge the THINERGY MEC201 battery (t_{CHG}).

A signal generator (VSG R&S FSW26) was used for providing an RF input power at 434 MHz ($P_{\text{RF-IN}}$) to the charger. Figures 5(a) and 5(b) show the results for η_{TOT} and t_{CHG} , respectively. It can be seen that the proposed wireless charger exhibits a maximum η_{TOT} of about 29.7 % for an RF input power of 7.5 dBm. As for the charging time, experimental tests showed *i)* that values of $P_{\text{RF-IN}}$ higher than 1.5 dBm are necessary to recharge the considered battery; and *ii)* that for $P_{\text{RF-IN}}$ higher than 6 dBm, the time necessary to recharge the battery is shorter than 50 minutes.

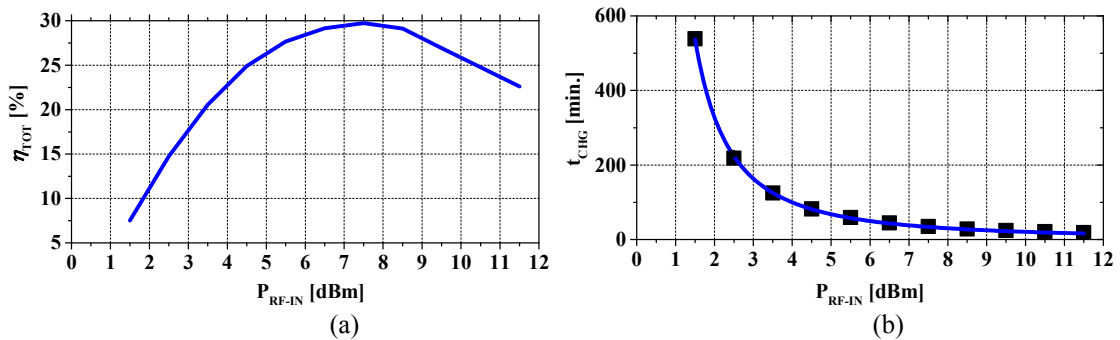


FIG. 5 – Experimental data obtained for the total efficiency and the charging time.

IV. CONCLUSIONS

A wireless charger for low-capacity thin-film batteries was presented. The proposed device exploits a non-radiative WREL for power transmission. A prototype operating in the ISM band centered at 434 MHz and optimized to be easily embedded in wearable accessories (such as handbags) was designed, fabricated and experimentally characterized. Experimental data showed that the fabricated power link exhibits a maximum of the RF-to-RF power transfer efficiency of about 69.3 %. As for the battery charger, a total efficiency of approximately 29.7 % was demonstrated. It was also shown that, by providing an input power higher than 6 dBm, a time charging shorter than 50 minutes is required for recharging a thin-film battery THINERGY MEC201.

REFERENCES

- [1] W. Kwun-Chiu, X. Quan, L. Xun, and S.Y. Hui, "Passive radiofrequency repeater for enhancing signal reception and transmission in a wireless charging platform," *IEEE Trans. on Industrial Electr.*, vol. 61, no. 4, pp. 1750-1757, April 2014.
- [2] A. Costanzo, M. Dionigi, D. Masotti, M. Mongiardo, G. Monti, L. Tarricone, and R. Sorrentino, "Electromagnetic energy harvesting and wireless power transmission: A unified approach," *Proceedings of the IEEE*, vol. 102, no. 11, pp. 1692-1711, 2014.
- [3] G. Monti, L. Corchia, L. Tarricone, "A Wearable Wireless Energy Link," in 45th EuMC, 2015, pp.143-146, 7- 10 Sept. 2015.

A PRELIMINARY STUDY OF EBG HOLLOW-CORE STRUCTURES FOR HIGH VOLTAGE APPLICATION

O. Leonardi⁽¹⁾, G. Castorina⁽²⁾, G. Sorbello⁽²⁾, G. Torrasi⁽¹⁾, L. Di Donato⁽²⁾,
L. Celona⁽¹⁾ and S. Gammino⁽¹⁾

⁽¹⁾ Istituto Nazionale di Fisica Nucleare - Laboratori Nazionali del Sud
Via S. Sofia 62, Catania, Italia

⁽²⁾ Università degli Studi di Catania, DIEEI,
Viale Andrea Doria 6, 95125, Catania, Italia
ornella.leonardi@lns.infn.it

Abstract

Microwave ion sources are usually located on high voltage platform to allow the beam extraction. The link between the ion source and the microwave generator, usually placed a ground, needs to accomplish two basic aspects: the microwave should be efficiently transferred to the plasma chamber and no DC-path must exist between the ion source and RF power generator; moreover any dielectric breakdown due to static electric fields in the DC-break should be avoided. This paper presents the preliminary study and design of an EBG Hollow-Core structure handling a maximum microwave power of 1.5 kW and fulfilling a DC insulation requirement of 50 kV.

Index Terms – DC-break, Electromagnetic Band Gap (EBG), HV application, Microwave Ion Source.

I. INTRODUCTION

Microwave ion sources are currently the most efficient devices used in facilities dedicated to nuclear physics because of their ability to generate intense beams with high reproducibility, stability and brightness [1]. Usually they are located on high voltage platform to allow the beam extraction, while the microwave power is provided by amplifiers placed at ground potential. Therefore, an electric insulator is needed between the high voltage region and the microwave generator.

Up to now, the adopted solution usually consists of a DC-break composed by several section of standard waveguide interlinked by dielectric windows [2] which requires a voltage divider in order to fix the total resistance of the whole structures [3] and to fulfil the typically required insulation voltage value of 50 kV.

This solution presents some drawbacks especially in terms of microwave leakage due to finite discontinuity between waveguides and dielectrics, and high costs for the low permittivity and low loss tangent insulator procurement. Hereinafter an innovative alternative with respect to the classical solution will be presented.

II. ELECTROMAGNETICS BAND GAP STRUCTURES

Photonic crystals (PC) are composed of periodic dielectric or metal-dielectric structures that affect electromagnetic wave propagation. The electromagnetic field in PC can exist only at prescribed frequencies and configuration. Forbidden bands of wavelengths are called Electromagnetic Band Gaps (EBG).

By perturbing a lattice it possible to create a single localized mode or a set of closely spaced modes that have frequencies within the gap [4]. Typical application are EBG-waveguide achieved by introducing a linear defect into the periodic structure (*in-plane propagation*). An EBG-cavity can be created by altering the periodic structure for one or few elementary cells creating a region where the electromagnetic mode is confined. Recently dielectric EBG-cavities have been applied to accelerator structures due to their good frequency selectivity [5].

In this paper we carry out a preliminary study and design of a dielectric EBG hollow-core structure, supporting out-of-plane propagation [4], which acts as natural DC-break. This structure can effectively guide the RF power into an ion source keeping the insulation between the plasma chamber at high voltage and the microwave generators at ground.

The simplest EBG structure which presents full band gap are 2D triangular lattices of air columns in a dielectric substrate [4], as shown in Fig.1 (a), where the unit cell is framed with dashed line. Figure 1 (b) depicts the reciprocal lattice in the wave-vector \mathbf{k} -plane where the hexagon is the first Brillouin zone of the lattice. The propagation characteristics of electromagnetic waves through the lattice can be solved as described in [6] and minima and maxima of a given band as function of the wave-vector \mathbf{k} usually occur on the boundary of the irreducible Brillouin zone, grey region in Fig.1 (b).

The gap's existence and frequency bandwidth depends on the dielectric constant and the ratio r/a , where r is the rod radius and a is the rods spacing.

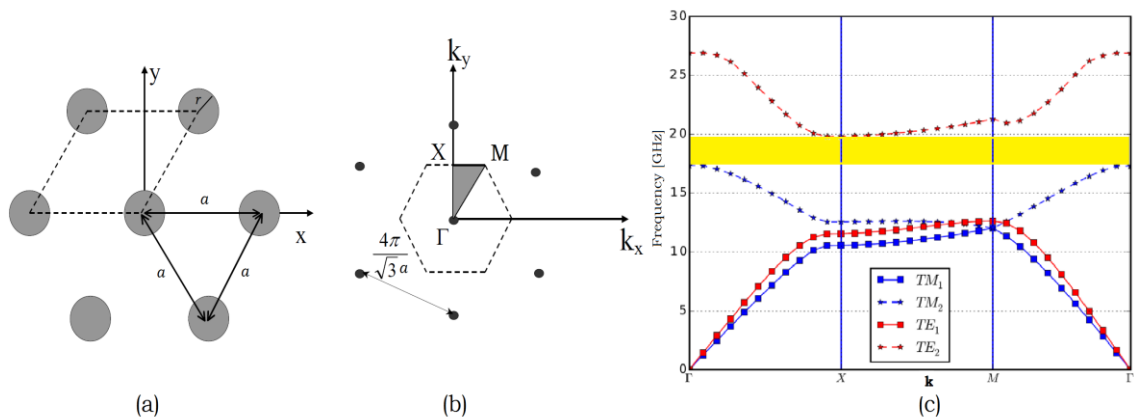


FIG. 1 – (a) 2D triangular lattice and (b) reciprocal lattice. (c) Dispersion diagram of air columns in a dielectric substrate of alumina for $k_z=0$ with $a=7.4\text{mm}$ rods spacing ratio $r/a=0.44$. The band gap is marked in yellow.

By properly dimensioning the lattice's parameters, a total band gap exactly in the frequency band of the injected microwave can be achieved. In this paper we focused on the AISHa ion source injection frequencies [17.3-18.4] GHz in order to enable the Frequency Tuning Effect mechanism [7]. The dispersion diagram for a triangular lattice of air columns in a dielectric substrate of alumina Al_2O_3 ($\epsilon_r=9.7$) is shown in Fig. 1 (c). The band gap, marked in yellow, indicate that the band gap is in AISHa injection range.

III. EBG HOLLOW-CORE WAVEGUIDE

The final device is achieved by finite repetition of the fundamental cell and by thickening of the lattice along the z -direction. A local defect is created by taking out some rods from the centre, as illustrated in Fig. 2 (a) for an optimal transition between the circular metallic and the dielectric hollow core EBG waveguide. The radius of defect, $r_d=7.4$ mm, was chosen equal to rods spacing and slightly larger than radius of standard metallic waveguide operating around 18 GHz. We have used seven repetition of the elementary cell around the defect for better mode confinement and a finite thickness of dielectric equal to 35 mm to prevent discharges in air. The device has been simulated by means of a full 3D electromagnetic simulator to take in account any mismatch loss between metallic waveguide and EBG section. In Fig. 2 (b) the simulated transmission loss (S_{21}) of the EBG device is compared to the conventional waveguide DC-break one. The two structures provide comparable S_{21} although the EBG device seems to be frequency selective since the metallic- to EBG-waveguide transition is not yet optimized and multiple reflections between input and output of the EBG section occur.

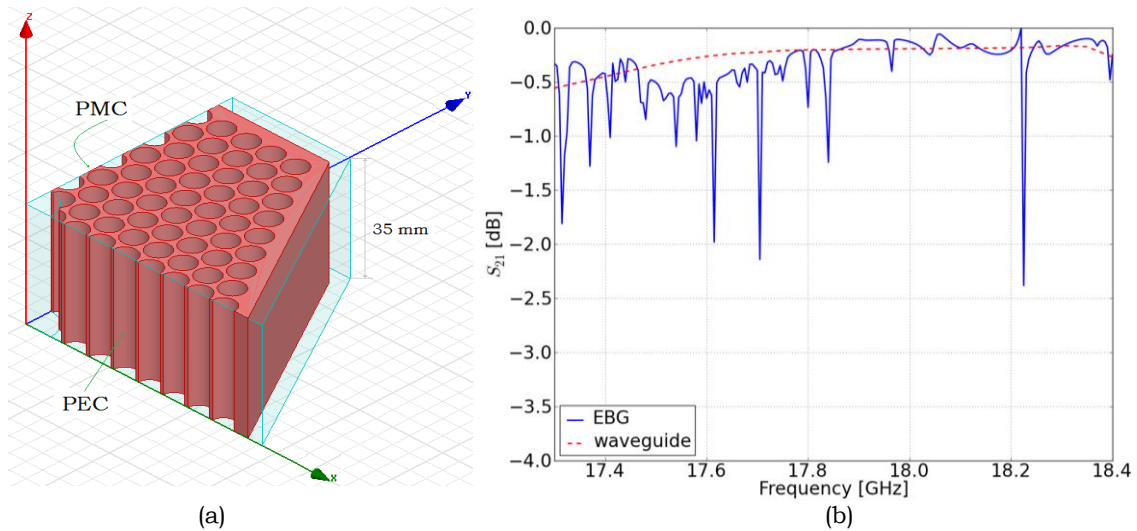


FIG. 2 – (a) A section of EBG device and (b) simulated transmission losses compared with those of the conventional waveguide DC-break

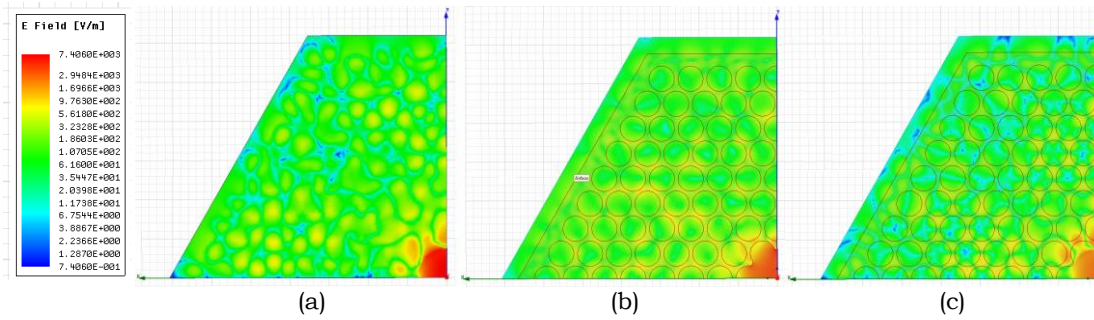


FIG. 3 – Magnitude of electric field at different z -section along the device.
(a) $z=0$ mm, (b) $z=17.5$ mm and (c) $z=35$ mm

The magnitude of electric field at different z -section along the device is shown in Fig. 3, where the good confinement of the electromagnetic field by the EBG waveguide is apparent.

IV. CONCLUSION

The hollow core structure has been designed and modelled for studying its propagation characteristics. The 3D numerical simulations show that the electromagnetic field is well confined by the EBG-dielectric waveguide with $S_{21} = -0.12$ dB at $f = 18$ GHz. Hence, it could be a suitable candidate as DC-break circuit into ion sources waveguide branching due to the easy implementation and coupling with conventional metallic waveguides.

REFERENCES

- [1] Ian G. Brown, "The physics and technology of ion sources", John Wiley & Sons, 2006.
- [2] S. Gammino, et al., "Tests of the versatile ion source (vis) for high power proton beam production", *XIX ECRIS Workshop*, Grenoble, August 2010.
- [3] Y. S. Cho, et al., "Compact Microwave Ion Source for Industrial Applications", *Rev. Sci. Instrum.*, vol. 83, 02B914, 2012
- [4] J. D. Joannopoulos et al., "Photonic crystals: molding the flow of light", second edition, Princeton, 2008.
- [5] M.A. Shapiro et al., "Theoretical analysis of overmodes dielectric photonic band gap structures for accelerator applications", PAC'03, IEEE Conf. Prof., pp.1255-1257 (2003).
- [6] Frédéric Zolla et al., "Foundations of Photonic Crystal Fibres", Imperial College Press, 2005.
- [7] L. Celona et al., "A Compact Multiply Charged Ion Source for Hadrontherapy Facility", *IPAC'15*, Richmond, VA, USA, pp. 2563-2565, 2015.

A UHF PASSIVE SENSING LINK IN A NEAR-FIELD WIRELESS POWER TRANSFER SYSTEM

R. Trevisan⁽¹⁾, A. Costanzo⁽²⁾

⁽¹⁾ Innovation R&D – IMA SpA
Via Emilia 428-448, Ozzano dell'Emilia (BO), Italy
TrevisanR@ima.it

⁽²⁾ Department of Electrical, Electronic and Information Engineering,
“Guglielmo Marconi,” University of Bologna,
Viale Risorgimento, 2, Bologna, Italy
alessandra.costanzo@unibo.it

Abstract

This paper is based on the results obtained during a high-apprentice PhD carried out with the University of Bologna and IMA SpA, Bologna, Italy. It focuses on a nonconventional exploitation of a self-resonant near-field link at UHF for data communication, to be combined in a compact inductive wireless power transfer system. At LF, the inductive channel is designed to deliver up to 1.3 kW to a resistive rotary heater. At UHF, sensing capabilities are made possible by exploiting self-resonant structures, such as split-ring resonators, one at each far-end side of the link. This network is used in a passive sensing system, to convert the data of a remote temperature sensor, representing the system variable load. The reflected power variations at the transmitter side, due to the dc load variations, are successfully used to perform the sensor readout.

Index Terms – passive sensing, near-field RFID, wireless power transfer.

I. INTRODUCTION

The trend toward wireless solutions embrace a wide set of solution, including remote powering an sensing. Some complex industrial equipment, as automatic machines, for example, demand for wirelessly powered actuators that are controlled through complex feedback loops. In these cases, remote sensors may be located in proximity of actuators, but require independent energy supply and communication links physically decoupled from the actuator power link due to robustness and safety requirements.

A simultaneous wireless transmission of power and data in an automatic machine environment is then required to realize contactless feedback systems. In such scenario, the system can be divided into two main parts. First, the actuator supply, where electric power is modulated by a switching dc/ac converter and wirelessly delivered to the actuator (e.g. a heater) by an inductive unit. Second, the feedback path of the sensor data: the readout is conditioned, digitalized, elaborated and sent back to the controller through a secondary wireless

interface. Many contactless industrial applications do not necessarily involve large air gaps between the energy source and the electric load (sensor, actuator, etc.). This allows to investigate the use of UHF signals in the near-field range for passive sensing purposes.

II. CONTACTLESS ENERGY TRANSFER

Traditionally, electrical joints between static and rotatable parts of automatic machinery are realized by mean of sliding contacts, usually slip rings. Contactless rotatable joints may widely replace the unreliable slip rings employed in rotary organs of automatic machines. A proposed system, which provides the geometrical constraints of the UHF sensing link, is based on a pot-core rotatable transformer. The magnetically coupled windings are placed in the cavities of the pot core halves and realize a contactless energy transfer (CET) device as described in [1].

III. PASSIVE SENSING

In case of resistive or capacitive measurements, chipless passive RFID sensing has some advantages compared to its tag- or chip-enabled counterpart. In some cases, the readout can be simply achieved by estimating the reflected power by the sensor at the reader output port for a given frequency; in this case, if channel is short, invariant, and well known, the measure uncertainty can be minimized.

For high-temperature industrial equipment, for example, resistive temperature sensors, or RTDs, are used. At the far end of a near-field wireless resonant link the RTD acts as the variable resistive load of the link, and the reflection coefficient Γ_L variations can be retrieved at the transmitter side by measuring the reflected power [2]. In matched conditions, the reflected power is minimum; far from the conjugate matching, however, the sensitivity of the reflected power with respect to load variation is emphasized. In particular, for

$$R_L = R_g \cdot (2 \pm \sqrt{3}), \quad (1)$$

where R_L represents a resistive load and R_g the source impedance, the sensitivity is maximum, as explained in [3].

IV. NEAR-FIELD RESONATING LINK

In a previous work [4], the possibility to integrate independent power and sensing links into a single WPT device was presented. The proposed solution was based on the integration of a 50-kHz inductive link and a 13.56-MHz capacitive link for power and data transfer respectively,

included in a single pot-core -based semi-rotating unit. The design presented several drawbacks related to the losses and frequency uncertainty introduced by the external resonating inductors required.

In order to provide a more reliable solution, a different approach is presented. First, the link operating frequency is shifted up to 868 MHz; second, the capacitive plates are modified into a pair of split ring resonators (SRRs). These choices represent an uncommon design for a near-field solution, though fully compliant with RFID standards.

A UHF near-field link can be efficiently realized by exploiting two faced SRRs, whose geometries are optimized by EM simulations, to realize a resonant link at 868 MHz. A rendering of the final link arrangement is shown in Fig. 2(a). The input and output ports of the link are connected to unbalanced feeding lines by means of two baluns, B_1 and B_2 . Each side of the near-field link, composed by the SRR and its own ground plane, is free to rotate with respect to the other. This can be used to center the resonance frequency. The fine tuning of the SRRs-based link is then carried out by using CST Studio Suite. The final EM-derived circuit model of Fig. 2(a) is then analyzed at the circuit level and its port parameters are compared with the experimental measurements on the printed-circuit boards.

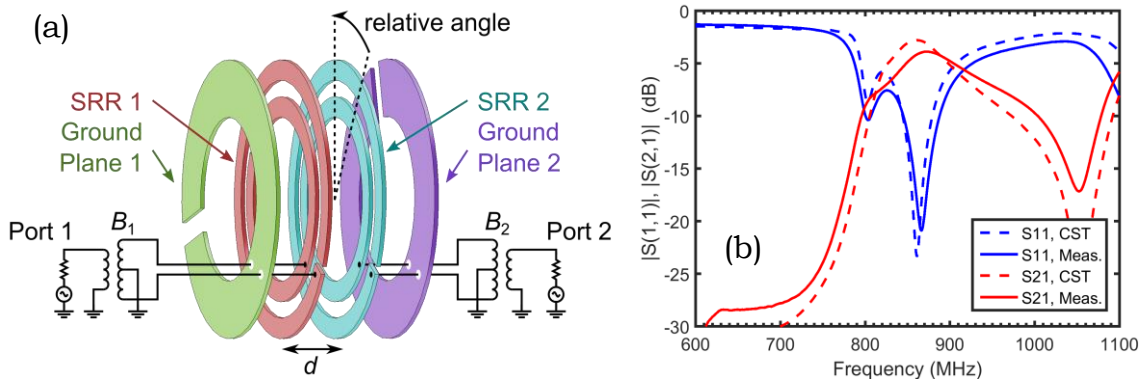


FIG. 2 – Link structure and results. (a): stack up of the SRR link; (b): comparison of reflection transmission coefficients (CST simulation, results).

V. EXPERIMENTAL SETUP AND RESULTS

Prototypes of SRRs have been manufactured. The distance d equals 0.6 mm, the relative angle between the two sides is 45° . The adopted substrate is FR4 Panasonic 4-layer R1566/R1551. A set of measurements have been carried out to verify the frequency behavior of the two faced coupled SRRs. Results are shown in Fig. 2(b).

The SRR link is employed as near-field channel in a passive sensing system, whose block diagram is shown in Fig. 3. On the left of the channel, the coupler allows to isolate the reflected power, which is evaluated by the power detector; on the right, C_m and L_m realize the mismatching network to obtain the equivalent load expressed by Eq. (1);

the rectifier is required to provide a dc supply to the resistive temperature probe represented by R_{RTD} .

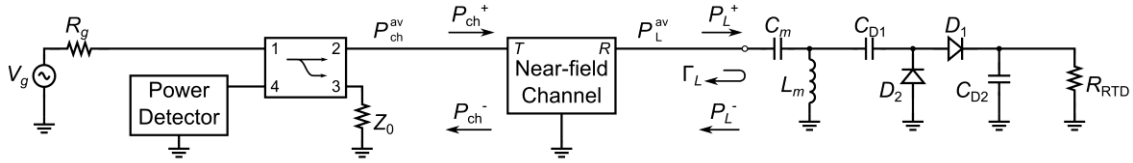


FIG. 3 – Block diagram of the sensing system, as proposed in [3].

Experimental results show that by supplying the system with $P^{av} = 10$ dBm, the reflection due to the nonlinear network is minimized, whereas the reflected power with respect to load variations is maximized. The power detector output reading shows that the temperature range of $[0, 300]$ °C corresponds to a voltage variation of 105 mV, with an average sensitivity of 0.35 mV/°C.

VI. CONCLUSION

An innovative UHF near-field application intended to achieve wireless passive sensing of remotely-located resistive temperature probes has been presented. The experiments demonstrate that the adoption of self-resonant structures, realized by near-field SRRs in the UHF band, allows to obtain high accuracy and repeatability of measures, while complying with the geometry constraints for simultaneous power and data transfer in CET systems.

REFERENCES

- [1] R. Trevisan and A. Costanzo, "A 1-kW contactless energy transfer system based on a rotary transformer for sealing rollers," *IEEE Trans. Ind. Electron.*, vol. 61, no. 11, pp. 6337-6345, Nov 2014.
- [2] D. Masotti, A. Costanzo, P. Francia, M. Filippi, and A. Romani, "A load-modulated rectifier for RF micropower harvesting with start-up strategies," *IEEE Trans. Microw. Theory Techn.*, vol. 62, no. 4, pp. 994-1004, Apr. 2014.
- [3] R. Trevisan and A. Costanzo, "A UHF near-field link for passive sensing in industrial wireless power transfer systems," *IEEE Trans. Microw. Theory Techn.*, early access available.
- [4] R. Trevisan and A. Costanzo, "Wireless sensing and power transfer in a rotary tool," in *Proc. 2015 IEEE MTT-S Int. Microwave Symp.*, Phoenix, AZ, May 2015, pp.1-4.

INTERLEAVED ISOPHORIC ARRAY ARCHITECTURES FOR RECONFIGURABLE FULL-EARTH COVERAGE FROM GEO SATELLITES

O.M. Bucci^{(1),(4)}, S. Perna^{(2),(3),(4)}, D. Pinchera^{(3),(4)}

⁽¹⁾ IREA, Consiglio Nazionale delle Ricerche,
Via Diocleziano 328, Napoli, Italy
bucci@unina.it

⁽²⁾ DI, Università degli Studi di Napoli “Parthenope”,
Centro Direzionale Isola C4, Napoli, Italy
perna@uniparthenope.it

⁽³⁾ DIEI, Università degli Studi di Cassino e del Lazio Meridionale,
Via G. Di Biasio 43, Cassino, Italy
pinchera@unicas.it

⁽⁴⁾ CNIT,
Viale G.P. Usberti, n. 181/A 43124 Parma, Italy

Abstract

This work addresses the synthesis of isophoric, i.e., equi-amplitude, sparse ring arrays capable of guaranteeing full Earth coverage from GEO satellites by means of steerable beams, switchable between two different widths. In particular, the required reconfigurability is obtained by radiating two different beams with two interleaved sparse arrays deployed over the available circular aperture. More specifically, two different architectures, achieved by means of a synthesis procedure based on a (computationally) very efficient deterministic approach, are proposed. In one case, the two interleaved arrays are separate; in the other case, they share a common part of their layouts.

Index Terms – Array synthesis, deterministic density tapering approach, isophoric arrays, sparse arrays.

I. INTRODUCTION

Direct Radiating Arrays (DRAs) represent appealing architectures for next satellite telecommunication antennas. Within such class of antennas, the so called isophoric sparse DRAs, namely non-periodic arrays employing equi-amplitude radiators [1]-[3] are particularly attractive.

However, their synthesis is a non-trivial problem that, in cases of practical interest, can be addressed only through smart approaches [4]-[10] aimed at finding effective sub-optimal solutions.

With particular reference to the satellite applications, in recent years exploitation of some of these approaches [4]-[8] has allowed us to find sound solutions capable of fulfilling the requirements listed by the European Space Agency (ESA) through the Invitation To Tenders (ITTs)

in [2]-[3]. In particular, in [8] we have addressed the synthesis of sparse ring arrays capable of satisfying the specifications listed in [3], that is, capable of guaranteeing full Earth coverage from GEO satellites by means of multiple beams, steerable up to about 8° and switchable between two widths (0.65° and 3.25°). More specifically, in [8] both the narrow and the wide beams are radiated by the same array and the required beam zooming/shrinking is achieved by means of a phase-only control.

In this work, in order to reduce the number of control points of the sparse array obtained in [8], we propose the use of two interleaved sparse arrays, one for each beam-width, deployed over the available circular aperture. To this aim, we consider two novel sparse architectures: the first one consists of two separate arrays, whereas the second one consists of two arrays that share a common part of their layouts. For both the proposed architectures, the two interleaved array layouts are obtained through a synthesis procedure based on the Deterministic Approach (DA) originally presented in [4] and further developed in [6]-[7].

The main rationale of the synthesis approach (described in Section II) as well as the results (discussed in Section III) are extracted from the work in [11].

II. MAIN RATIONALE OF THE SYNTHESIS APPROACH

The main rationale of the proposed synthesis approach is based on the quite natural consideration that the size of the layout tailored to the wide beam can be smaller than that required to radiate the narrow beam. Accordingly, the array layout that radiates the wide beam can be profitably located in the core part of the available aperture. This, in turns, suggests a synthesis scheme very easy to implement, which calculates the two interleaved layouts through the cascade of two separate steps.

The first step carries out the synthesis of the inner sparse layout tailored to the wide beam, without enforcing any geometrical constraint related to the presence of the other layout to be synthesized.

The second step performs the synthesis of the sparse layout tailored to the narrow beam by taking into account that some areas of the available aperture are already occupied by the feeds of the layout synthesized through the first step. To this regard, we propose two options, which lead to two different antenna architectures. The first possibility is to exploit for the narrow beam radiation only the circular crown not occupied by the inner array tailored to the wide beam. The second option is instead to exploit for the narrow beam radiation the entire circular aperture comprising the elements synthesized in the first step. For both the steps, we exploit a synthesis procedure based on the Deterministic Approach (DA) originally presented in [4] and further developed in [7] to allow the 8° beam steerability needed to guarantee

full Earth coverage.

III. RESULTS

With reference to the application scenario in [3], the required constraints can be summarized in a given directivity mask [8]. As described above, two zoomable architectures are proposed. For both the architectures, to radiate the wide beam we have synthesized the 43-elements layout reported in Fig. 1a. As for the narrow beam, for the first proposed architecture we have synthesized the 460-elements layout reported in Fig. 1b, which does not include the core layout of Fig. 1. Accordingly, in this case the overall zoomable sparse array consists of $460+43=503$ elements, that is, 25% less elements with respect to the sparse array obtained in [8] (with comparable side lobe level performances).

For the second proposed architecture we have synthesized the 424-elements layout reported in Fig. 1c. It is remarked that this layout includes also the core layout of Fig. 1a. In this case, we employ 44% less elements with respect to the sparse array obtained in [8] with comparable side lobe level performances.

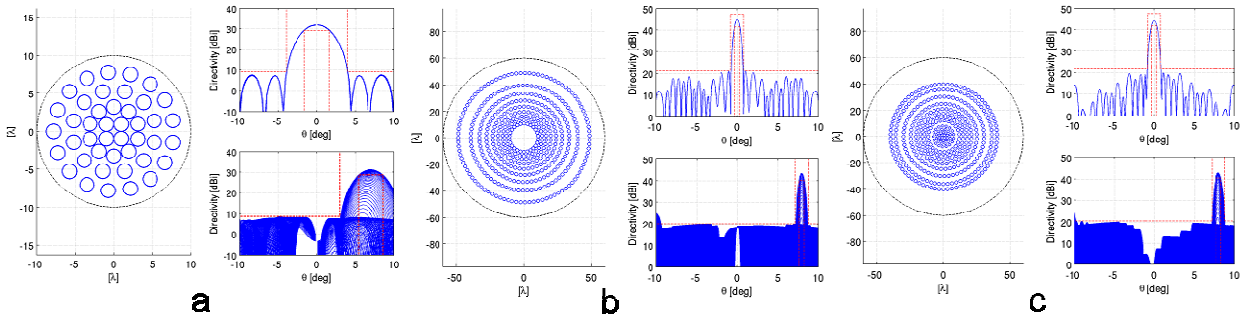


Figure 1 (a) 43-elements layout (employing circular feeds of 1.9λ diameter) tailored to the wide beam case. (b) 460-elements layout (employing circular feeds of 2.5λ diameter) tailored to the narrow beam case. (c) 424-elements layout (employing 43 circular feeds of 1.9λ diameter and 381 circular feeds of 2.5λ diameter) tailored to the narrow beam case. For each figure, left panels show the layout whereas right panels show the superposition of the array directivity φ -cuts for the boresight (top) and the maximally scanned (bottom) beams.

IV. CONCLUSION

In this work we have addressed the synthesis of isophoric sparse ring arrays capable of guaranteeing full Earth coverage from GEO satellites with a modification of the beamwidth of the radiated pattern. To this aim, we have proposed two slightly different antenna architectures: in one case, the two beams are radiated by two separate interleaved arrays; in the other case, the two beams are instead radiated by two interleaved arrays that share a common part of their layouts. The synthesis of the two architectures has been obtained by means of a computationally very efficient deterministic approach; the shown layouts allow a reduction of the overall numbers of feed of 25% and 44%

with respect to the reference reconfigurable sparse architecture in [8], which is based on a phase-only control and it has been obtained by means of a non-deterministic, computationally less efficient, approach.

REFERENCES

- [1] G. Toso, R. Mailloux, "Guest Editorial for the Special Issue on Innovative Phased Array Antennas Based on Non-Regular Lattices and Overlapped Subarrays," *IEEE Trans. Antennas and Propagat.*, vol. 62, n. 4, Part 1, pp. 1546-1548, 2014.
- [2] ESA/ESTEC Tender AO/1-5598/08/NL/ST, "Innovative Architectures For Reducing The Number Of Controls Of Multiple Beam Telecommunications Antennas". [Online]. Available: www.esa.int.
- [3] ESA/ESTEC Tender AO/1-6338/09/NL/JD, "Active Multibeam Sparse Array Demonstrator". [Online]. Available: www.esa.int.
- [4] O. M. Bucci, S. Perna, "A deterministic two dimensional density taper approach for fast design of uniform amplitude pencil beams arrays," *IEEE Trans. Antennas and Propagat.*, vol. 59, n. 8, pp. 2952-2861, 2011.
- [5] O. M. Bucci, D. Pinchera, "A Generalized Hybrid Approach for the Synthesis of Uniform Amplitude Pencil Beam Ring-Arrays," *IEEE Trans. Antennas and Propagat.*, Jan. 2012.
- [6] O.M., Bucci, S. Perna, D. Pinchera, "Advances in the Deterministic Synthesis of Uniform Amplitude Pencil Beam Concentric Ring Arrays," *IEEE Trans. Antennas and Propagat.*, vol. 60, n. 7, pp. 3504-3509 , 2012.
- [7] O.M.Bucci, T.Isernia, S.Perna, D.Pinchera, "Isophoric Sparse Arrays Ensuring Global Coverage in Satellite Communications," *IEEE Trans. Antennas and Propagat.*, 62, 4, 1607-1618, 2014.
- [8] O.M.Bucci, S.Perna, D.Pinchera; "Synthesis of Isophoric Sparse Arrays Allowing Zoomable Beams and Arbitrary Coverage in Satellite Communications," *IEEE Trans. Antennas and Propagat.*, vol. 63, Issue 5, pp. 1445 - 1457, 2015.
- [9] P. Angeletti, G. Toso, G. Ruggerini, "Array Antennas With Jointly Optimized Elements Positions and Dimensions Part II: Planar Circular Arrays," *IEEE Trans. Antennas and Propagat.*, vol. 62, n. 4, Part 1, pp. 1627-1639, 2014.
- [10] M. Carlin, G. Oliveri, A. Massa, "Hybrid BCS-Deterministic Approach for Sparse Concentric Ring Isophoric Arrays," *IEEE Trans. Antennas and Propagat.*, vol. 63, n. 1, pp. 378-383, 2015.
- [11] O.M., Bucci, S. Perna, D. Pinchera, "Interleaved Isophoric Sparse Arrays for the Radiation of Steerable and Switchable Beams in Satellite Communications," submitted to *IEEE Transactions on Antennas and Propagation*.

UNMANNED AERIAL VEHICLE FOR THE MEASUREMENT OF 3D ELECTROMAGNETIC FIELDS DISTRIBUTION

D. Latini⁽¹⁾, F. Carbone⁽²⁾, J. Bulli⁽³⁾, A. Saitto⁽⁴⁾,
F. Del Frate⁽¹⁾ and G. Schiavon⁽¹⁾

⁽¹⁾Earth Observation Laboratory, Department of Civil Engineering and Computer Science Engineering, University of Rome Tor Vergata, Rome.

⁽²⁾GEO-K s.r.l., Via Del Politecnico 1, Rome, <http://www.geo-k.co/co/>.

⁽³⁾Mpb s.r.l., Via G. Peroni 400, Rome, <http://www.gruppompb.com/>.

⁽⁴⁾ Consorzio NITEL, Via Spalato 1, Rome, <http://www.nitel.it/>.

Abstract

A new technique for the 3D measurement of electromagnetic fields is presented. The technique consists in mounting selective electric triaxial probes on Unmanned Aerial Vehicles of suitable weight and characteristics. The paper reports the system set-up and the different phases of validation which has been so far carried out. The results obtained for a selected test site containing a tower with telecommunication antennas are also reported.

Index Terms – 3D EMF measurement, SEP, drones and UAV, Electromagnetic Compatibility, Safety, Pollution.

I. INTRODUCTION

The measurement of three-dimensional (3D) spatial Electromagnetic Fields (EMF) can be a very crucial activity in various sectors ranging from radiation pattern analysis to electromagnetic safety, compatibility and pollution. For measuring the spatial distributions of EMF, it is very important to track a measuring position and for this purpose conventional techniques used so far may need large scale systems, such as those including robot-arms, or a great amount of time and manpower. Moreover, this kind of approaches have significant constraints in terms of the dimension of the volume considered for the measurements. In this paper we presents a novel technique to the 3D EMF distribution based on Unmanned Aerial Vehicles (UAV) and optimized field probes. We describe the different phases that have been so far considered for setting-up the system and report the results obtained in some preliminary tests.

II. OVERVIEW ON THE SYSTEM

During the last decade, the use of UAV under 25 kg has known an exponential growth in an extended range of applications [2]. However, their application for the measurement of EMF is a very innovative application never addressed in Italy. The system is based on the

integration of SEP [3] (Selective Electric Triaxial Antenna) onboard of a proper equipped drone and a ground station controlling the flight parameters and the electromagnetic fields measured by the SEP. The present configuration exploits an hex-rotor drone (Fig.1a) ensuring payload until 6kg and able to accomplish autonomous mission previously planned by the operators. It ensure flight time of about 18min with the most innovative fail-safe technologies and high degree of stability also on severe wind condition. Moreover, as strictly required in Italy, it has been certified by ENAC (National Agency for Civil Aviation) for operations in critical scenarios. The SEP instrument (Fig. 1b) is developed and distributed by Mpb group. It allows selective and automatic real time measurement of the electromagnetic field in a frequency range between 10 MHz and 3 GHz. It has been designed to mitigate the problems of the traditional spectrum analyzers (use of the coaxial ferrite cable, isotropy error, calibration complexity), offering an “all-in one” instrument of small dimensions and weight (370g) with power supplied by rechargeable battery. The signal from the isotropic antenna is analyzed and stored directly in the ground station through a safe fiber optic connection. The ground station is equipped with the software for controlling the mission and the signals from SEP. The flight planner (Fig. 1c) allows the user to plan, upload and manage the mission that will be accomplished by the APR. Moreover, it keeps track of the telemetry data from the Inertial Measurement Unity (IMU) in order to control the flight preventing any failures. The SEP software (Fig. 1d) allows to make measurements in real time, offering the possibility to apply filters, display signal with three overlaid axes, set markers and adapt the graphics settings for each measurement.

III. SET-UP AND PRELIMINARY TEST

The system set-up has been carried out considering three main phases before the test. In order to keep invariant the drone barycenter and ensure the low signal interference with SEP, the first phase has regarded the study of weights and the position of the sensor in relation to the on board installation. A specific support has been designed and applied using glass-fiber material with no-magnetic and no-reflective properties. The second phase has regarded the system interference analysis and calibration inside the anechoic chamber. The latter is a specific test environment for radio frequency signals (RF) and microwaves (MW), used to make measurements of electromagnetic fields without letting in any interference from outside. The measured electric field intensity generated by the drone in operative configuration with motor running, telemetry Rx/Tx on, Pilot controller Rx/Tx on (Fig 2.a) was 0.1 V/m (Fig 2.b). With respect to the signal that we expect to measure, this kind of interference is negligible and it doesn't compromise the quality of the signal intercepted by the SEP. The third phase has regarded the data transfer between SEP and ground station.

At present, the link is established through an optic fiber which reaches 80 meters of length. This solution preserves from any risk of attenuation, reflection or distortion of the signal from the SEP, but can be a limitation for high range operation (if allowed by the authorities).

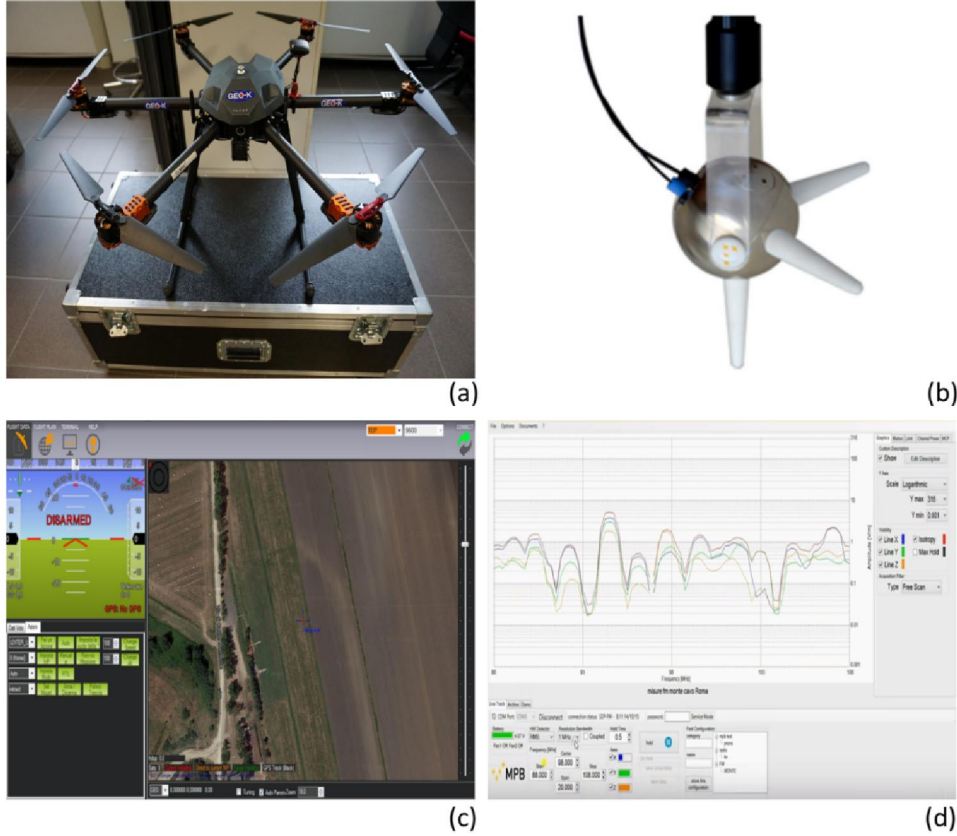


Fig. 1 System Elements: (a) Hexa-rotor drone, (b) SEP (Selective Electric Triaxial Antenna), (c) Mission Planner software and (d) SEP signal analyzer software.

After the system set-up, a preliminary flight aiming at simulating a real applicative scenario has been carried out as shown in Fig. 3(a). Exploiting the presence of a tower for broadcasting telecommunication systems, Fig. 3(b), at a distance of about 300 meters, the electromagnetic field intensities has been measured and evaluated at different altitudes, from ground to 20 meters. As expected, scanning a frequency range between 750 MHz and 950 MHz, the observations, Fig. 3(c), have confirmed the presence of peaks in the GSM bands (around 800 MHz) having amplitude values that respect the normative limits. No anomalous electromagnetic fields effects have been observed during the test.

IV. CONCLUSIONS

We have described preliminary assessment and validation activities that have been successfully performed using a new system based on UAV and SEP for 3D characterization of EMF in volumes of large dimensions.

The results are encouraging and the system seems to have significant potential especially for measurement operations that might be carried out in critical conditions, for example in dangerous or not easily accessible areas. The validation activities, with an upgrade of the system using a radio data-link between SEP and the ground station, will continue considering new and more complex test sites and also in view of the measurements tasks that will be required in the coming Galileo scenario.

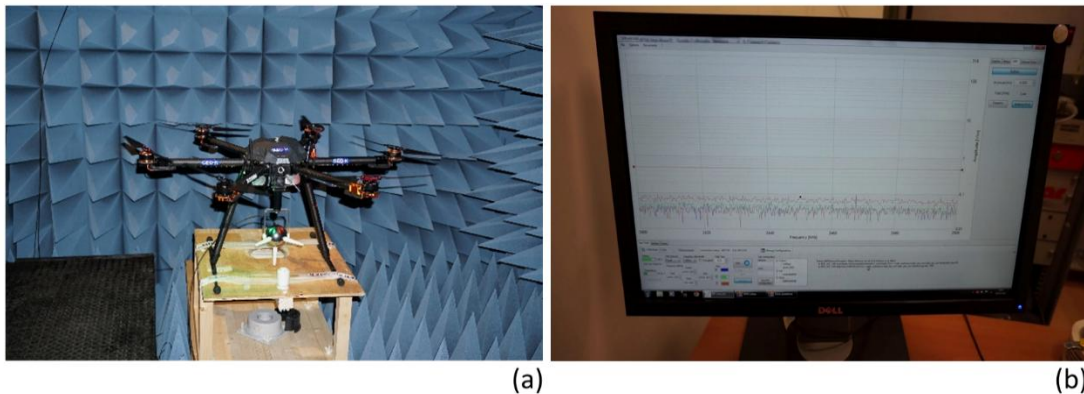


Fig. 2 System set-up: (a) Drone equipped with SEP inside anechoic chamber and (b) the measured electromagnetic fields of system in operative configuration.

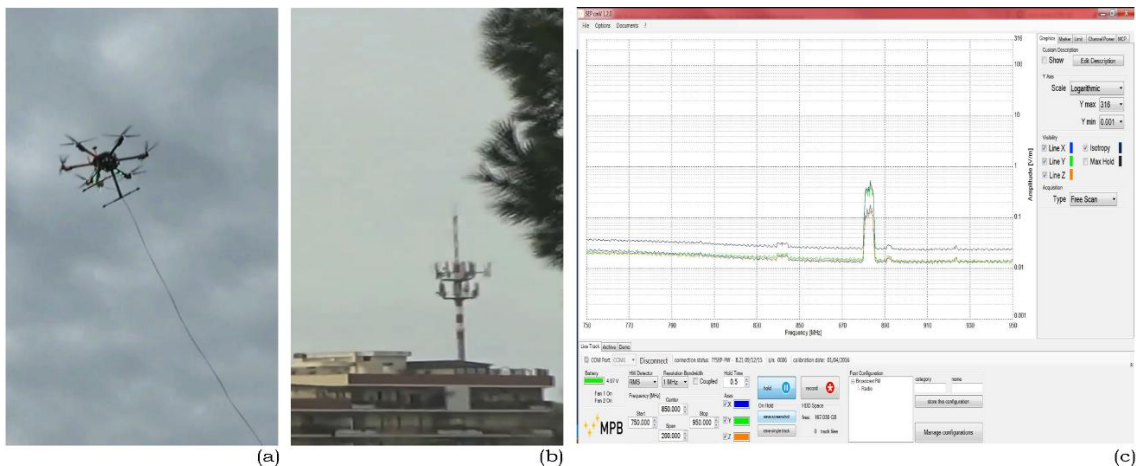


Fig. 3 Test activities of Drone+SEP system (a) near a tower with telecom antennas (b) and corresponding measurements (c).

REFERENCES

- [1] K. Sato, Y. Kashimura, and Y. Yamimura, "A Real-time Measuring Method of 3D EMF Distributions Using the Wiimote," *Proc. of the 2013 International Symposium on Electromagnetic Compatibility (EMC Europe 2013)*, Brugge, Belgium, September 2-6, 2013
- [2] A.C. Watts, V.G. Ambrosia, and E.A. Hinkley, "Unmanned aircraft systems in remote sensing and scientific research: Classification and considerations of use." *Remote Sensing* 4.6, pp. 1671-1692, 2012
- [3] SEP Selective Electric Triaxial Antenna, http://www.gruppompb.uk.com/product.asp?ID_Prodotto=602.

SOIL MOISTURE RETRIEVALS FROM RADAR DATA AT L-BAND THROUGH A MULTI-TEMPORAL APPROACH

F. Fascetti⁽¹⁾, N. Pierdicca⁽¹⁾, L. Pulvirenti⁽²⁾

⁽¹⁾ Sapienza, Dept. Information Engineering, Electronics and Telecommunications, Via Eudossiana 18, Rome, Italy

⁽²⁾ Cima Research Foundation, via Armando Magliotto, Savona, Italy
fabiofasc@virgilio.it

Abstract

In this work, a multitemporal algorithm, originally conceived for the C-Band radar aboard the Sentinel-1 satellite, was updated in order to retrieve soil moisture from L-Band radar data, such as those provided by the NASA Soil Moisture Active/Passive (SMAP) mission. A dense time series of radar measurements is combined to invert a forward backscattering model. The calibration and validation tasks was accomplished by using the data collected during the SMAP Validation Experiment 12 campaign, which consists of in situ soil moisture data, measurements of vegetation parameters and L-Band images collected by the UAVSAR sensor, during the growing season of several crops. Moreover, a simple vegetation scattering model was tuned considering two different classes of vegetation: those producing mainly single scattering effects, and those characterized by a significant multiple scattering involving terrain surface and vegetation elements interaction.

Index Terms – L-Band, multitemporal approach, soil moisture, SMAP.

I. INTRODUCTION

Soil moisture (*SM*) is a key environmental variable for a large number of disciplines and its knowledge is essential for several applications, such as drought and flood predictions, meteorology, agronomy and climatology. At microwave bands, the dielectric constant of soils is sensitive to *SM*, and sensors operating in the low-frequency portion of the microwave spectrum (L-, C- band) are able to measure *SM* within a suitable depth (~ 5 cm or shorter). However, the radar return is sensitive not only to soil moisture, but also to surface roughness and, in presence of vegetation, to vegetation parameters.

The multitemporal algorithms may mitigate these problems and deliver frequent and accurate soil moisture maps, assuming that the variations of vegetation and soil roughness occur at longer temporal scales with respect to the soil moisture. The multitemporal algorithm [1] (hereafter denoted as *MLTA*) was initially conceived for deriving a soil moisture product from the data provided by the European Space Agency (ESA) Sentinel-1 (S-1) mission. The *MLTA* was adapted to work at L-band and to take advantage of the multipolarization (HH, VV, and HV), such as the measurements provided by the Soil Moisture Active/Passive (SMAP [2]) satellite mission, which is able to deliver SAR images with very short revisit (in the order of three days). Unfortunately, the SMAP radar stopped

operating since the beginning of July 2015; nevertheless, a few months of data acquisition can be exploited to assess its potential.

In this work, the outcomes of a preliminary test of the *MLTA* soil moisture retrieval based on L-band data are presented. The analysis was accomplished taking advantage of the data available from the SMAPVEX12 campaign, which consists of in situ measurements and L-band radar images starting from June 6th to July 7th, 2012.

II. MULTI-TEMPORAL ALGORITHM

The *MLTA* prototype was designed in the framework of the “GMES Sentinel-1 Soil Moisture Algorithm Development” project, funded by the European Space Agency. The proposed approach retrieves soil moisture from a sequence of SAR acquisitions using a multitemporal Bayesian decision criterion that Maximizes the “A Posteriori probability” (*MAP*) of soil parameters (i.e., moisture and roughness). In general, the *MAP* estimator inverts a forward soil backscattering model relating the backscattering coefficient to the bare soil parameters. More specific details about the *MLTA* can be found in [1].

III. BARE SOIL ANALYSIS

The Oh and Sarabandi semi-empirical model [3] was considered to simulate the backscattering of bare soils. The model was analyzed at L-band over several bare soils, selected among the SMAPVEX12 fields using a threshold on the Vegetation Water Content (*VWC* less than 0.5 kg/m²). An error dependence on the roughness standard deviations *s* [cm] and soil moisture [m³/m³] was observed in the comparison of the modelled and measured backscattering. Then, a first degree empirical polynomial function (Eq. 1), dependent on *s* and *SM*, was fitted to reduce such error dependence.

$$\sigma_{\text{mod}}^0 | \text{dB} - \sigma_{\text{meas}}^0 | \text{dB} = a + bSM + cs \quad (1)$$

Subsequently, the *MLTA* was first assessed over bare soil fields, using a threshold on *VWC* provided by the ground campaign. In this case, the retrieval results present a good degree of correlation (0.73) with the soil moisture measured on ground, and a root mean square difference of about 0.045 m³/m³.

IV. VEGETATED SOIL ANALYSIS

Afterwards, the *MLTA* was tested also over vegetated areas, considering wheat and soybean fields independently. It was attempted to group the crops in order to use a common model to describe the interactions with the radar signal, but unfortunately, it was not possible without worsening too much the retrieval performances. As a first step, the wheat fields were

considered. For this kind of crop, the canopy backscattering was simulated through the Water Cloud Model (*WCM* [4]), which was tuned using the *SMAPVEX12* data through a Matlab© fitting script. The Normalized Difference Vegetation Index (*NDVI*), provided by MODIS, was used as an indicator of the vegetation state. Testing the *MLTA* over single wheat fields, the soil moisture temporal trend of each field was fairly well reproduced (not shown); considering the whole comparison (all the seven fields together, reported in Fig. 1), the results were not extremely good in terms of RMSD, which was around $0.077 \text{ m}^3/\text{m}^3$.

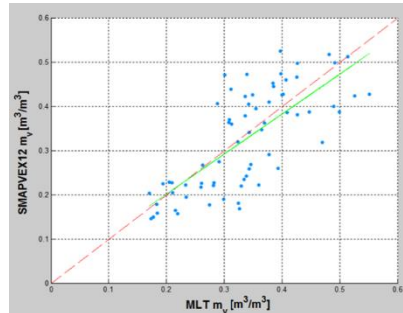


FIG. 1 – Soil moisture retrieved by the algorithm and those measured over wheat fields. Dashed red and green lines refer to the perfect agreement and the best fitting line, respectively.

However, if the data of each field were normalized in order to make the temporal variability have a common mean, the results become promising with an RMSD around $0.05 \text{ m}^3/\text{m}^3$. Local effects on the scattering response of the targeted fields have to be carefully accounted for; a task that will be better investigated in future work.

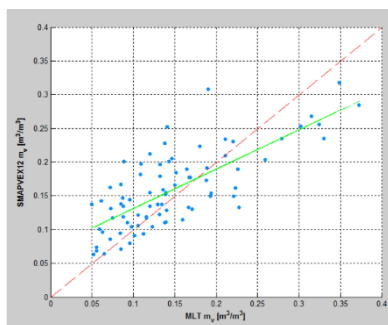


FIG. 2 – Comparison between the retrieved and in situ measured soil moisture over soybean crops. Dashed red and green lines represent the perfect agreement and the best fitting line, respectively.

As for soybean crops the fitting of the *WCM* did not provide satisfactory results, as the forward model needs to take into account of other backscattering mechanisms, such as the interaction between the soil and the vegetation. In this work the ratio (*RRI*) between the soil and canopy measured backscattering was related to few parameters describing the canopy conditions which can be considered quite effective and easily available (as the *NDVI*), as done in [5]. Here, an exponential

relationship between these parameters was observed and was fitted through a Matlab© script. After applying such vegetation correction, the *MLTA* results over soybean fields show good performances; the temporal trend of soil moisture is well reproduced, as reported in Fig. 2, with an RMSD around $0.05 \text{ m}^3/\text{m}^3$.

V. CONCLUSION

In this work, a study describing the potential of the multitemporal approach for soil moisture retrieval was performed. A Multi-Temporal Algorithm was updated in order to analyze radar data at L-Band, such as those provided by SMAP mission. A semi-empirical backscattering model for bare surface was modified to match campaign measurements at L-band provided by the SMAPVEX12 experiment. In bare soil conditions the *MLTA* shows fairly good performances. As for the vegetated fields, simple semi-empirical backscattering models were considered and tuned using the SMAPVEX12 data. The results show an RMSD in the order of 5% for the soybean crops, while for wheat some unexplained biases among different fields were observed. Removing such biases, the results in term of RMSD go down from 7.7% to 5%.

ACKNOWLEDGEMENT

The authors acknowledge the SMAPVEX12 project to share the SMAPVEX12 dataset with the scientific community.

REFERENCES

- [1] N. Pierdicca, L. Pulvirenti, G. Pace, "A Prototype Software Package to Retrieve Soil Moisture from Sentinel 1 Data by Using a Bayesian Multitemporal Algorithm," *IEEE Journal of Selected Topics in Applied Earth Observations and Remote Sensing*, vol.7, pp.153-166, 2014.
- [2] D. Entekhabi, E.G. Njoku, P.E. O'Neill, K.H. Kellog, "The Soil Moisture Active Passive (SMAP) Mission," *Proceedings of the IEEE*, vol. 98, pp. 704-716, 2010.
- [3] Y. Oh, K. Sarabandi, F.T. Ulaby, "Semi-empirical model of the ensemble-averaged differential Mueller matrix for microwave backscattering from bare soil surfaces," *IEEE Trans. Geosci. Remote Sens.*, vol.40, pp.1348-1355, 2002.
- [4] E.P.W. Attema, F.T Ulaby,, "Vegetation Modeled as a water cloud," *Radio Science*, vol.13, pp.357-364, 1978.
- [5] A.T. Joseph, R. van der Velde, P.E. O'Neill, R.H. Lang, T. Gish, "Soil Moisture Retrieval During a Corn Growth Cycle Using L-Band (1.6 GHz) Radar Observations," *IEEE Trans. on Geosci. and Remote Sens.*, vol.46, 2008.

SUPERPARAMAGNETIC SCAFFOLDS FOR TISSUE ENGINEERING

M. B. Lodi⁽¹⁾, A. Fanti⁽¹⁾, B. Bisceglia⁽²⁾, G. Mazzarella⁽¹⁾

⁽¹⁾ Department of Electric and Electronic Engineering, University of Cagliari, Via Marengo , Cagliari, Italy

⁽²⁾ Department of Industrial Engineering, University of Salerno, Fisciano (SA), Italy, 84084
alessandro.fanti@diee.unica.it

Abstract

Regenerative medicine and Tissue Engineering are exploiting engineered magnetic nanoparticles (MNPs), because they can be functionalized and controlled by an external magnetic field, integrating therapeutic and diagnostic applications. Modifying traditional bone tissue engineering materials (bioactive ceramics and polymers) for scaffolds and turning them into magnetic object using MNPs, opened a number of possibilities to help healing, reparation and regeneration of bone tissue. Magnetic therapeutic scaffolds pretend to be an attractor of magnetic bio-agent, which could exert chemotaxis on different cell populations. This application of magnetic scaffold is studied and analyzed in the present work. Moreover, we developed a minimum chemotaxis model to quantify and show the great therapeutic potential of magnetic scaffold.

Index Terms – Magnetic Nanoparticles, Magnetic Targeting, Nanomedicine, Tissue Engineering

I. INTRODUCTION

Contemporary medicine is looking for tools able to integrate therapeutic and diagnostic applications, i.e. theragnostic devices, in order to expand and advance clinical and surgical possibilities, making it possible to individualize medicine[1]. Magnetic nanoparticles represent a powerful object for such purpose[1],[2].

Since Tissue Engineering integrates engineering principles and life science to develop biological substitute that regenerate, restore or improve the function of a tissue[3], in orthopedic practice valuable results have been achieved using biophysical stimulation through magnetic fields: they enhance osteogenesis, support healing of fracture and favour the integration of prosthetic implants[4]. Recently scientific community focused on the mechanism of interaction between magnetic fields and scaffolds to understand the observed benefits[5], but the problem is still not solved.

Hence, modifying *ad hoc* at the nanoscale traditional materials for tissue engineering using MNPs, new magnetic scaffold were produced:

super-paramagnetic nanoparticles of iron oxide (MNP) were adsorbed on Hydroxyapatite (HA) and/or PCL surface, or they were nucleated on Collagen fibers through ionic addition in apatite crystals[6]. Such innovative class of orthopaedic scaffolds act as a therapeutic device because, when an external field is applied, they can attract magnetic agents that transport biological molecule[7].

The aim of our work is to study and analyze the behaviour of a spherical superparamagnetic scaffold, similar to the one in [8], under the action of a static magnetic field applied along the z axis, in order to demonstrate how it can direct on itself magnetic carriers functionalized with growth factors, which are able to control and direct cellular migration of angiogenic and osteogenic cell populations.

II. THE MODEL

We used *Magnetic Fields No Current Module (COMSOL Multiphysics)* in order to study how the spatial distribution of the magnetic field could be altered and how the presence of the scaffold could determine a local field amplification, in comparison to traditional paramagnetic scaffolds, thanks to his non-linear magnetization, according to Langevin equation for a volume where MNPs are monodisperse in size[9].

Because the magnetic nanoparticles (MNP) to attract usually have a radius of 135nm and a saturation magnetization of 310kA/m, we evaluated the magnetic density flux gradients, the magnetic forces and the velocity on them. So that it was possible to check if, in presence of the scaffold, the value of 1.3T/m could be overcome, because this value it's actually related to the weight of the MNPs[10]; to verify if the magnetic force was on the order of pN and if the velocity was in the experimental range of mm/h [11].

Then, using *Transport of Dilute Species Module*, we coupled a drift-diffusion equation to establish how the concentration profile of MNP was altered by the magnetic force, defined as[12]:

$$F_m = \nabla \mu_{mnp,2} B = \frac{M_{s,2}^2 V_{mnp,2}}{6k_b T} (\nabla |B|^2) \quad (2)$$

Considering the MNPs to attract in saturation state, $M_{s,2}$ is the saturation magnetization of the MNP to attract and $V_{mnp,2}$ is its volume. So, solving a chemotaxis mass balance with a minimum model[3], it was possible to describe how cellular migration pattern are influenced indirectly using an external magnetic field and acting on magnetic material properties.

III. RESULTS

The intrinsic magnetic scaffold of Tampieri et al.[4] is able to reach 1.6T/m, whereas the deep coated scaffolds showed higher values such as 24.3T/m for high volumetric fraction of MNPs. Then, to overcome

random motion due to thermal noise, from our analysis, a magnetic field of 0.5T is required in most cases to make the convective term higher than the diffusive one, so that it is possible to drift MNPs towards the prosthetic implant. The impregnated scaffolds reach high value of magnetization, leading to a field distribution similar to a uniformly magnetized sphere. If diffusive and convective fluxes are not balanced MNPs in the system are drifted following magnetic field flux lines, as in Fig. 1.

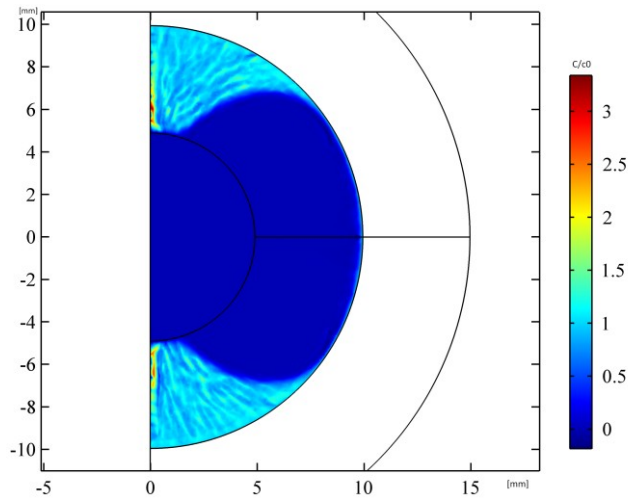


FIG. 1 – MNPs concentration profile in the presence of a superparamagnetic scaffold

If these MNPs are carrying biological information, they can direct cellular migration. So, defining the chemotactic strength parameter as the ratio of the cell's mobility coefficient and the concentration of nanoparticles directly injected into the tissue(c_0), the concentration profile of cell population is modified as in fig.2.

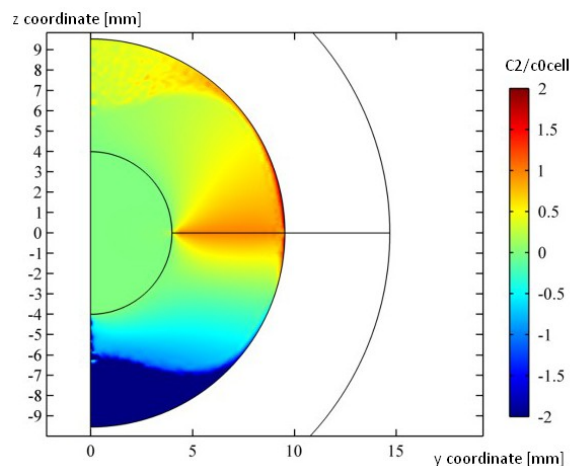


FIG. 2 – Chemotaxis flux drifts cells from the surroundings to the pole in the field direction, where B field reach a maximum

But it is shown how superparamagnetic scaffolds could be used in regenerative medicine and bone tissue engineering, thanks to their potential to be remotely controlled, in a non-invasive way, leading to the seeding of biological agent with magnetic nanoparticles for bone reconstruction and to the population of the implant, with the valuable result to forecast a new and better way to repair and regenerate bone tissue.

REFERENCES

- [1] V. I. Shubayev, T. R. Pisanic II, S. Jin, "Magnetic nanoparticles for theragnostic", *Advanced Drug Delivery Reviews*, vol. 61, pp. 467-477, Apr. 2009
- [2] Q. A. Pankhurst, J. Connolly, S. K. Jones, J. Dobson, "Applications of Magnetic Nanoparticles in Biomedicine", *Journal of Physics D: Applied Physics*, vol. 36, no. 13, pp. 167-181, Jun. 2003
- [3] W. M. Saltzman, *Tissue Engineering: Principles for the design of replacement organs and tissues*, 1st. ed., W. M. Saltzman, New York, U.S.A: Oxford University Press, 2004.
- [4] R. Cadossi and S. Setti, "Low-frequency pulsed electromagnetic fields in orthopedic practice: bone and cartilage repair," in *General Assembly and Scientific Symposium, XXXth URSI*, 2011
- [5] B. Bisceglia, "Effects of Magnetic Field (MF) on Alkaline Phosphatase Activity of Human Osteosarcoma Cells", III *ICEMB*, 2014
- [6] M. Banobre-Lopez, Y. Pineiro-Redondo, M. Sandri, A. Tampieri, R. De Santis, V. A. Dediu, J. Rivas, "Hyperthermia induced in magnetic scaffolds for bone tissue engineering", *IEEE Transaction on Magnetics*, vol.50, no.11, Nov. 2014
- [7] A. Tampieri, N. Bock, A. Riminucci, A. Russo, E. Landi, V. A. Goranov, M. Marcacci, V. Dediu, "A novel route in bone tissue engineering: magnetic biomimetic scaffolds", *Acta Biomaterialia*, vol. 6, pp. 786-796, 2009
- [8] J. Meng, B. Xiao, Y. Zhang, J. Liu, H. Xue, J. Lei, H.Kong, Y. Huang, Z. Jin, N. Gu, H. Xu, "Super-paramagnetic responsive nanofibrous scaffolds under static magnetic field enhance osteogenesis for bone repair in vivo", *Scientific Reports*, vol.3, 2655, 2013.
- [9] D. L. Leslie-Pelecky, R. D. Rieke, "Magnetic Properties of Nanostructured Materials", *Chem. Mater.*, vol. 8, pp. 1770-1783, 1996.
- [10] S. K. Samal, V. Goranov, A. Russo, T. Shelyakova, A. Riminucci, T. Herrmannsdorfer, V. Dediu, D. L. Kaplan, M. Uhlarz et al., "Multilayered Magnetic Gelatin Membrane Scaffolds", *Applied Materials & Interfaces*, vol.7, pp. 23098-23109, 2015
- [11] S. J. Kuhn, D. E. Hallahan, Todd D. Giorgio, "Characterization of Superparamagnetic Nanoparticles Interactions with Extracellular Matrix in an in Vitro System", *Annals of Biomedical Engineering*, vol. 34, no.1, Jan. 2006
- [12] A. D. Grief, G. Richardson, "Mathematical Modeling of Magnetically Targeted Drug Delivery", *Journal of Magnetism and Magnetic Materials*, vol.293, pp. 455-463, 2005

INDUCTIVE LINK FOR RECHARGEABLE PULSE GENERATORS IMPLANTED IN THE CHEST

G. Monti, M. V. De Paolis, L.Tarricone

Department of Engineering for Innovation, University of Salento, via per
Monteroni, Lecce, 73100, Italy.
giuseppina.monti@unisalento.it

Abstract

In this paper a near-field wireless energy link for recharging medical devices implanted in the chest is presented. The power transfer is realized by two magnetically coupled planar resonators. Experimental and numerical data referring to a prototype working in the MedRadio band are presented and discussed. A maximum of the measured power transfer efficiency of about 20.54 % is demonstrated and the compliance with safety regulations is verified.

Index Terms – Deep Brain Stimulation, implantable pulse generator, Wireless Resonant Energy Link, wireless power transmission.

I. INTRODUCTION

Deep Brain Stimulation (DBS) is one of the most important treatment for movement disorders such as Parkinson's disease, essential tremor, and dystonia in patients who are refractory to medical therapies.[1]

A typical DBS includes an Implanted Pulse Generator (IPG) that is located near the collarbone or in lateral chest wall [2]. Common IPGs are powered by a battery having a limited lifetime (2 ~ 5 years) [3] and have to be periodically replaced through surgery. Recently, some IPGs equipped with wirelessly rechargeable batteries have been proposed [4]; these IPGs exploit wireless power transmission (WPT) technologies for achieving longer lifetime (up to 10-20 years).

In particular, these rechargeable IPGs use an inductive coupling between an external and an implanted coils. As for the operating frequency, in order to minimize the EM energy absorption in human tissues which increases as the frequency increases, most of the WPT links for IMD that have been proposed up to now in the literature operate at very low frequencies not reserved to medical devices. However, this choice has important drawbacks: 1) it imposes the use of different devices for power and data transmission, and 2) the power link is exposed to and may generate interferences.

In order to overcome these problems, in [5] the possibility of recharging a medical implant by using the MedRadio (Medical Device Radiocommunications Service) core band reserved to medical devices [6] was investigated. Additionally, the solution proposed in [5] adopts a resonant scheme (i.e., a Wireless Resonant Energy Link - WREL) for maximizing the power transfer efficiency [7].

By defining the RF-to-RF power transfer efficiency as the ratio between the power delivered by the secondary resonator (P_{RX}) to the medical implant and the power provided to the primary resonator (P_G):

$$\eta_{RF-RF}[\%] = \frac{P_{RX}}{P_G} \times 100 = |S_{21}|^2 \quad (1)$$

the WPT link presented in [5] has a measured power transfer efficiency of about 15.27 %.

In this paper, taking into account experimental results presented in [5], an improved version of the link is presented.

From experimental tests the prototype here presented exhibits a power transfer efficiency of about 20.54 %.

II. RESONATOR GEOMETRY AND NUMERICAL RESULTS

The proposed WPT link exploits a magnetic coupling between two planar resonators on an Arlon DiClad 880 substrate ($\epsilon_r = 2.17$, $\tan\delta = 0.0009$) with a thickness of 0.508 mm.

The configuration of the link is the same considered in [5] and it is illustrated in Fig. 1c: it is assumed that the transmitting resonator (primary resonator) operates in direct contact with the skin and that the receiving resonator (secondary resonator) is implanted in the muscle, at a depth of 1 mm (i.e., $d_t = 1$ mm), below a 2 mm-layer of skin and fat (d_{skin} and d_{fat}). The overall distance between the two resonators is equal to 5 mm (d) (see Fig. 1c).

The values assumed for the electromagnetic parameters of human tissues were taken by the IT'IS Foundation database [8].

The starting point of the design process of the resonators was the geometry presented in [5]. In particular, taking into account numerical and experimental data reported in [5], the primary and the secondary resonators were optimized in order to improve both the matching and the power transfer efficiency at 403 MHz (i.e., at the central frequency of the MedRadio band). The final geometries guaranteeing the best results are illustrated in Figs. 1a and 1b.

The link here presented adopts a different geometry for the primary and the secondary resonator. In more detail, the secondary resonator has the same geometry described in [5] with optimized dimensions. As for the primary resonator, the solution here presented is a single face design consisting of three concentric loops.

As in [5], for both the primary and the secondary resonator a lumped capacitor and an Arlon AR1000 superstrate ($\epsilon_r = 9.7$, and $\tan\delta = 0.003$, thickness = 0.610 mm) were used to tune the frequency of resonance to the desired value and to improve the magnetic coupling, respectively.

The primary resonator occupies an area of 20.48 mm x 20.48 mm, while the secondary resonator occupies an area of 15.48 mm x 15.48 mm. The thickness of the resonators is equal to 1.18 mm and 1.15 mm for the primary and the secondary resonator, respectively.

Fig. 3e shows the numerical data obtained for the scattering parameters. The values calculated at 403 MHz are: $|S_{11}| = -17.10$ dB, $|S_{21}| = -6.83$ dB, and $|S_{22}| = -20.04$ dB. According to the definition given in (1), from numerical data the RF-to-RF power transfer efficiency is equal to 20.74 % at 403 MHz.

III. COMPLIANCE WITH SAFETY REGULATIONS

The compliance of the proposed WPT link with safety regulations has also been investigated.

In the frequency range of interest, safety guidelines on exposure to electromagnetic fields provide restrictions in terms of the Specific Absorption Rate (SAR) [9, 10]. In particular, for head and trunk areas, the exposure limit considering a mass of 10-g is 2 W/kg.

In more detail, it was assumed that the secondary resonator is connected to the IPG by means of a rectifier with an RF-to-DC conversion efficiency expressed by:

$$\eta_{RF-DC}[\%] = \frac{P_{DC}}{P_{RF}} \times 100 \quad (2)$$

Where P_{DC} is the DC power at the output port of the rectifier and P_{RF} is the RF power at its input port (i.e., the RF power at the output port of the secondary resonator). The power delivered by the link to the IPG is given by:

$$P_{DC}[\%] = P_G \times \frac{\eta_{RF-RF}}{100} \times \frac{\eta_{RF-DC}}{100} \quad (3)$$

Simulations were performed by setting the power delivered to the primary resonator (i.e., P_G) at the value guaranteeing a DC power delivered to the IPG higher than 1 mW. In order to perform calculations, a reasonable value of 50 % was assumed for η_{RF-DC} . As for the η_{RF-RF} , the

value of 20.74 % calculated by numerical data was adopted. Accordingly, P_G was set to 9.64 mW.

Figure 2 illustrates the simulated 10-g average SAR distribution calculated by means of full-wave simulations at 403 MHz. As it can be observed, a maximum value of about 0.49 W/kg was achieved, thus proving the compliance of the proposed WPT link with safety regulations. In fact, this value is decisively below the 2 W/kg limit imposed by safety regulations.

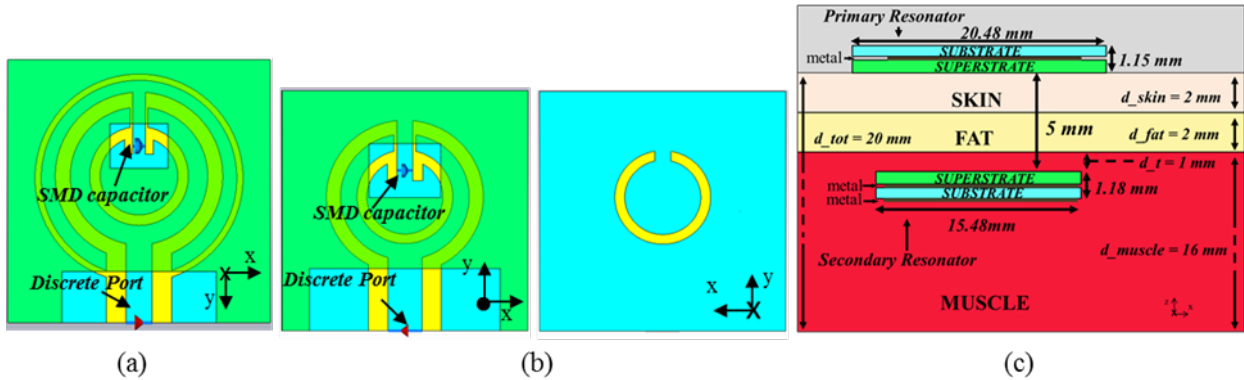


FIG. 1 - (a) Geometry of the primary resonator, (b) Front and back view of the secondary resonator, (c) Configuration of the wireless resonant inductive link. The multilayer tissue model consists of three layers: skin ($d_{skin} = 2$ mm), fat ($d_{fat} = 2$ mm), muscle ($d_{muscle} = 16$ mm). The whole thickness of these three biological tissues is equal to 20 mm (d_{tot}).

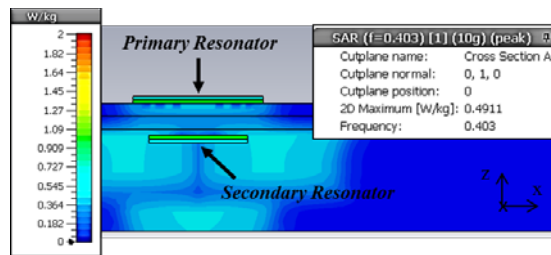


FIG. 2 - Simulated 10-g average SAR distribution at 403 MHz when P_G was equal to 9.64 mW.

IV. EXPERIMENTAL RESULTS

A prototype of both the primary and the secondary resonator was fabricated by using the LPKF ProMat S103 circuit board plotter. Photographs are given in Figs. 3a and 3b.

The experimental setup shown in Figs. 3c and 3d was adopted for verifying the results obtained by means of full-wave simulations. In order to mimic the presence of human tissues minced pork was employed [11].

Measurements of the scattering parameters were performed by using the vector network analyzer R&S® ZVL6. A comparison between numerical and experimental results is given in Fig. 3e, an overall good agreement can be observed.

The values measured at 403 MHz for the S-parameters are: $|S_{11}| = -11.96$ dB, $|S_{21}| = -6.87$ dB, and $|S_{22}| = -8.84$ dB. In particular, Figure 3f compares the transfer efficiency corresponding to measured data with the one calculated by simulations. From measurements the maximum of η_{RF-RF} is centered at 403 MHz and it is of about 20.54 %.

V. CONCLUSION

A wireless power link for energizing medical devices implanted in the chest has been presented. The proposed solution adopts a resonant scheme and operates in the MEDRADIO band reserved to medical applications. From experimental tests a power transfer efficiency of about 20.54 % is demonstrated.

According to the results presented in this paper, the proposed link is able to wirelessly provide the implantable medical device with a DC power higher than 1 mW while inducing a 10-g average Specific Absorption Rate decisively below the 2 W/Kg imposed by safety regulations.

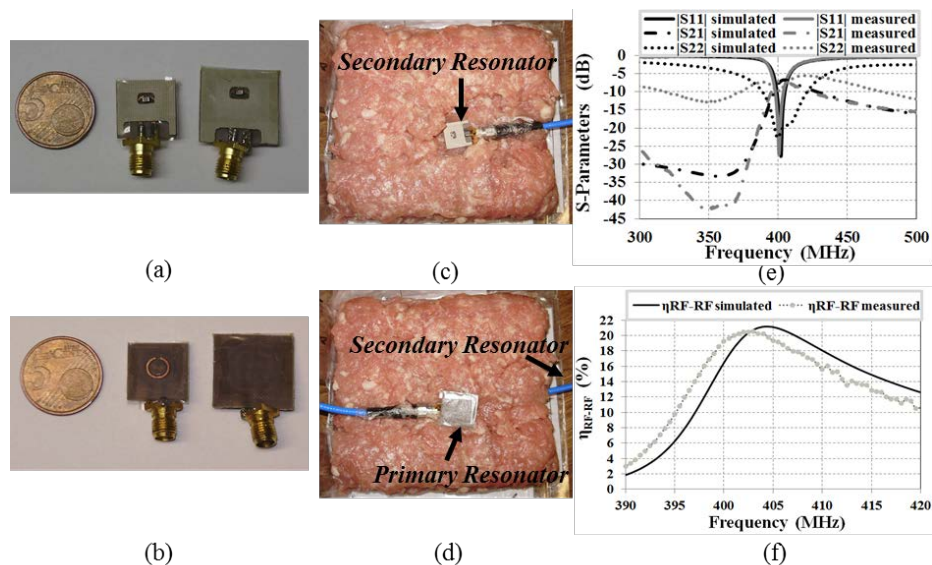


FIG. 3 - Front (a) and back view (b) of the two prototypes; Experimental setup: (c) Placement of the secondary resonator inside minced pork and whole setup (d); Comparison between numerical and experimental data obtained for the S-parameters (e) and the η_{RF-RF} (f) of the proposed WPT link.

REFERENCES

- [1] Elias W.J., et al.: Deep Brain Stimulation: The Spectrum of Application, *Neurosurg Focus.*, **29**(2), 2010.
- [2] Hosain M. K., et al.: Compact stacked planar inverted-F antenna for passive deep brain stimulation implants, *Conference of the IEEE in EMBC*, 2012.
- [3] Lee H. M., et al.: A power-efficient wireless system with adaptive supply control for deep brain stimulation, *IEEE Journal of Solid-State Circuits*, **48**(2013), 2203–16.
- [4] Boston scientific. Vercise™ Deep Brain Stimulation System [Online]. Available: <http://www.vercise.com/vercise-and-guide-dbs-systems/vercise-dbs/>
- [5] Monti G., et al.: Wireless power transfer link for rechargeable deep brain stimulators, *IEEE 15th MMS, Lecce*, 2015.
- [6] FCC, Washington, DC, USA, 2012 [Online]. Available: <http://www.fcc.gov>
- [7] Zhang Y. et al.: Quantitative Analysis of System Efficiency and Output Power of Four-Coil Resonant Wireless Power Transfer, *IEEE Journal of Emerging and Selected Topics in Power Electronics*, 3 (2015),184-190.
- [8] <http://www.itis.ethz.ch/itis-for-health/tissue-properties/database/>
- [9] IEEE Stand. for Safety with Respect to Human Exposure to Radio Frequency Electromagnetic Fields, 3 kHz to 300 GHz, *IEEE Standard C95.1-1991*, 1999.
- [10] ICNIRP, “Guidelines for limiting exposure to time-varying electric, magnetic, and electromagnetic fields (up to 300 GHz)”, *Health Phys.*, **74** (1998), 494–522.
- [11] Monti G., et al.: Resonant Inductive Link for Remote Powering of Pacemakers, *IEEE Transactions on MTT*, 63 (2015), 3814-3822.

TISSUE SHRINKAGE IN MICROWAVE THERMAL ABLATION

L. Farina⁽¹⁾, M. Cavagnaro⁽¹⁾

⁽¹⁾ Department of Information Engineering, Electronics and Telecommunications, Sapienza University of Rome
Via Eudossiana 18, 00184, Rome, Italy
farina@diet.uniroma1.it

Abstract

This work focuses on the tissue shrinkage occurring during a Microwave Thermal Ablation procedure, and on the importance of deeply comprehend and characterize it, in correlation with the changes occurring in dielectric and thermal properties of the treated tissue. Two experimental set ups are proposed to study the phenomenon, and to investigate and model it.

Index Terms – *Ex vivo* Study, Microwave Thermal Ablation, Tissue Shrinkage.

I. INTRODUCTION

Microwave Thermal Ablation (MTA) is a minimally invasive technique widely used in interventional radiology to treat tumorous diseases. It exploits the interaction between the biological tissue and the electromagnetic (EM) field deployed from an interstitial antenna at microwave frequencies (usually 915 MHz or 2.45 GHz) to induce a cytotoxic temperature increase in the target. To cause an irreversible thermal damage, 55 °C are required at minimum, however temperature up to 100 °C and beyond can be achieved during the treatment in the tissue close to the radiating antenna [1]. In the thermally ablated tissue, it is possible to visually discern two regions linked to the physical status of the tissue: a black zone, close to the antenna, and a light brown area surrounding the previous one. The black region corresponds to the carbonized tissue that undergoes temperatures higher than 100 °C and appears highly dehydrated and rigid, while the light-brown region (often referred to as “white” area for sake of brevity) corresponds to the coagulated tissue that undergoes temperatures between 55-60 °C and 100 °C [2]. Recently, it was evidenced that the two regions, constituting the so-called necrosis or thermally ablated area, are characterized by different dielectric and thermal properties due to changes in the physical and structural characteristics occurring in the biological tissue treated with MTA. In particular, modifications in the thermal and dielectric properties have been observed in correlation with the temperature increase and with the denaturation process that leads the target cells to coagulate [3]–[6]. Likewise, a complex phenomenon of tissue shrinkage was observed in the ablated tissue in the very last years [7]–[11].

Understanding, modeling and characterizing these changes is fundamental to have complete control over the interventional procedure and provide the physician with the safest operating conditions.

In recent years, studies have been conducted to try to characterize, model and quantify the tissue shrinkage. In the present work, two methods are proposed and the corresponding set-up optimized, for the evaluation of the process.

II. METHODS

The first method (Fig. 1a) consists in ablating restricted samples of biological tissue of cuboid shape and of variable size, mimicking the amount of treated tissue. Increasing cuboid dimensions it is possible to represent portions of tissue undergoing only the carbonization process or the carbonization plus the coagulation one, and thus to discriminate shrinkage in the two different tissue statuses. The set up developed and optimized for the purpose was made up of an agar phantom that guarantees electromagnetic and thermal continuity, in which the *ex vivo* bovine liver cuboids were embedded. The samples were ablated for different times (up to 10 minutes) with a MW (2.45 GHz) interstitial antenna operating at 60 W. Measurements of cuboid dimensions before and after the procedure were performed with a ruler and the final contraction evaluated.

The second method (Fig. 1b) foresaw a Computed Tomography (CT) scan for the real-time monitoring of the displacement of fiducial spherical markers placed into the tissue surrounding the MTA applicator. A plastic box transparent to the EM field was realized with holes in its walls to guarantee a reliable positioning of antenna and markers. Fiber-optic sensors were also placed in the region of the expected necrosis to measure the tissue temperature at different distances from the antenna axis. The 2.45 GHz antenna was supplied with 60 W for 10 minutes and images of the procedure were recorded every 30 s. Then, a dedicated MATLAB program was developed to elaborate the collected data.

III. RESULTS

The first set of experiments allows measuring the shrinkage discriminating between carbonized and coagulated tissue. The maximum achievable shrinkage was observed in the carbonized tissue (about 40 % of the initial dimension), whereas a gradient of less consistent shrinkage was measured in the coagulated one. This evaluation permits to quantify the shrinkage occurring in a MTA treated tissue and to model it, in correlation with the rate of tissue coagulation, and with the time of ablation, i.e. with the given thermal dose.

The second set of experiments allows dynamically evaluating the tissue modification occurring in the tissue and resulting in the final shrinkage of the tissue; and allows correlating the markers' displacement with the variation of the tissue temperature. A first analysis showed a similar kinetic behavior between the temperature increase rate and the shrinkage rate. The results of the CT-monitored experiments could be useful to validate and generalize the quantification analysis performed with the cuboids experiments.

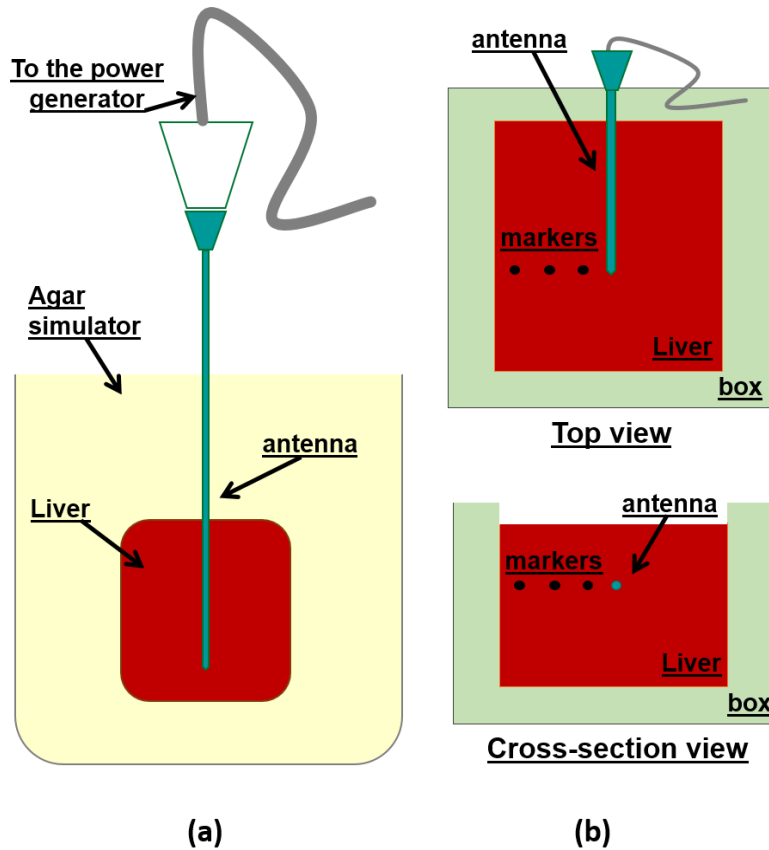


FIG. 1 – Set ups for the evaluation of the tissue shrinkage: (a) quantitative analysis on restricted specimens, (b) real-time analysis of the markers' displacement.

IV. CONCLUSION

Tissue shrinkage occurring during a MTA procedure is a complex phenomenon: it is correlated to the temperature increase and with the deployed EM energy. The shrinkage influences the treatment outcomes, and thus accounting it during the clinical practice through a reliable model would be highly recommended.

ACKNOWLEDGEMENT

The authors acknowledge the Division of Health Protection Technologies, of ENEA Casaccia Research Centre, Rome, Italy; the R&D Unit of HS Hospital Service S.p.A., Rome, Italy; the Medical Physics Laboratory of Regina Elena National Cancer Institute, Rome, Italy; and Prof. S. Nahum Goldberg of Hadassah Hebrew University Medical Center, Jerusalem, Israel, for their technical and scientific support and collaboration.

REFERENCES

- [1] M. Ahmed, C.L. Brace, F.T. Lee Jr, S.N. Goldberg, "Principles of and advances in percutaneous ablation," *Radiology*, vol. 258, pp. 351–369, 2011.
- [2] M. Ahmed, L. Solbiati, C.L. Brace, D.J. Breen, M.R. Callstrom, *et al.*, "Image-guided tumor ablation: standardization of terminology and reporting criteria—a 10-year update," *J Vasc Interv Radiol*, vol. 25(11), pp. 1691–1705, 2014.
- [3] D. Yang, M.C. Converse, D.M. Mahvi, J.G. Webster, "Measurement and analysis of tissue temperature during microwave liver ablation," *IEEE trans Biomed Eng*, vol. 54, pp. 150–155, 2007.
- [4] Z. Ji, C.L. Brace, "Expanded modelling of temperature-dependent dielectric properties for microwave thermal ablation," *Phys Med Biol*, vol. 56, pp. 5249–5264, 2011.
- [5] V. Lopresto, R. Pinto, G.A. Lovisolo, M. Cavagnaro, "Changes in the dielectric properties of ex vivo bovine liver during microwave thermal ablation at 2.45 GHz," *Phys Med Biol*, vol. 57, pp. 2309–2327, 2012.
- [6] V. Lopresto, R. Pinto, M. Cavagnaro, "Experimental characterisation of the thermal lesion induced by microwave ablation," *Int J Hyperthermia*, vol. 30, pp. 110–118, 2014.
- [7] C.L. Brace, T.A. Diaz, J.L. Hinshaw, F.T. Lee Jr, "Tissue contraction caused by radiofrequency and microwave ablation: A laboratory study in liver and lung," *J Vasc Interv Radiol*, vol. 21, pp. 1280–1286, 2010.
- [8] D. Liu, C.L. Brace. "CT imaging during microwave ablation: analysis of spatial and temporal tissue contraction," *Med Phys*, vol. 41(11), pp. 113303-1–9, 2014.
- [9] C.M. Sommer, S.A. Sommer, T. Mokry, T. Gockner, D. Gnutzmann, *et al.*, "Quantification of tissue shrinkage and dehydration caused by microwave ablation: experimental study in kidneys for the estimation of effective coagulation volume," *J Vasc Interv Radiol*, vol. 24, pp. 1241–1248, 2013.
- [10] C. Rossmann, E. Garrett-Mayer, F. Rattay, D. Haemmerich, "Dynamics of tissue shrinkage during ablative temperature exposures," *Physiol Meas*, vol. 35, pp. 55–67, 2014.
- [11] L. Farina, N. Weiss, Y. Nissenbaum, M. Cavagnaro, V. Lopresto, *et al.*, "Characterisation of tissue shrinkage during microwave thermal ablation," *Int. J. Hyperthermia*, vol. 30, pp. 419–428, 2014.

EPIDERMAL UHF ANTENNAS FOR SKIN SENSING: FUNDAMENTAL LIMITATIONS AND OPTIMAL PERFORMANCE

S. Amendola ⁽¹⁾, G. Marrocco ⁽¹⁾

⁽¹⁾ Department of Civil Engineering and Informatics
University of Rome Tor Vergata,
Via del Politecnico, 1, 00133 Roma, Italy.
amendola@uniroma2.it

Abstract

Skin-mounted electronics is the next wave beyond the wearable technology for bodycentric monitoring systems. In designing epidermal wireless devices, the presence of the human body cannot be ignored due to strong electromagnetic interactions. This contribution provides a systematic investigation on the performance of canonical UHF low-profile antennas suitable to the direct application over the skin. Both numerical and experimental analyses highlight non-monotonic relationship between efficiency/gain and size for radiators placed over lossy medium. As a consequence, an optimal size, which depends on the specific layout, can be defined for epidermal antennas, while the upper bounds in the maximum achievable gain is an invariant for size-optimized radiators.

Index Terms – Epidermal UHF Antennas, Skin Sensors, RFID technology.

I. INTRODUCTION

The latest advancements in flexible and stretchable electronics led to the development of ultrathin conformable sensors, which are perfectly integrated to the body surface and unobtrusively monitor vital signs over the skin. The Radiofrequency Identification Technology offers innovative ways to provide this new class of stick-to-skin devices with wireless interfaces for data communication and power harvesting, which will represent in the near future the fundamental breakthrough for the real usability of epidermal technologies. Although strongly influenced by high dielectric targets like the human body, UHF antennas has the potential of providing activation ranges up to one meter and more [1]. The UHF-RFID standard (860 - 960 MHz) is hence particularly attractive over the near-field coupling at 13.56 MHz (HF-RFID, NFC [2]) for pervasive applications where uncooperative users are continuously monitored by scanners placed within smart environments (smart home, hospitals, control gates at airports).

This contribution is aimed at deriving fundamental Limitations and optimal Performance of UHF RFID antennas, which are conceived to work at a very small (micrometrical) distance from the lossy body whose electromagnetic interaction cannot be mitigated by means of shielding planes or thick spacing, as in the case of conventional wearable tag.

II. THEORETICAL ANALYSIS

An extensive numerical analysis was performed with the multi-fold purpose of: (i) analyzing the correlation between the antenna performance (efficiency, gain) and the radiator size, and (ii) identifying the geometry that suits best to epidermal transponders by comparing the performance of different layouts, (iii) investigating the role of the quality of the conductors on the performance of epidermal antennas. Single-layer radiators (dipole, loop and their complementary slotted counterparts), which are fully compatible with ultra-low profile “tattoo-like” devices, were modeled over a homogenous human phantom ($\epsilon_{ph}=43$ and $\sigma_{ph}=0.9$ S/m).

a) Gain vs. Size

Simulations based on MOM method revealed that, unlike in free-space, the radiation efficiency of dipoles and loops over lossy medium exhibits a bell-shaped behavior (Fig. 1). After an initial monotonic region with nearly linear relationship between maximum gain/efficiency and size, there are peak values for the two antennas of sizes $L=30$ mm and $L=50$ mm for the loop and the dipole, respectively. In both cases, the significant losses of the tissues resulted in extremely poor values for the radiation gain ($G \approx -20$ dB). Beyond the peak value, the maximum gain remained rather stable, while the radiation efficiency degraded significantly. Similar trends were achieved for slotted antennas. The non-monotonic relationship between the gain/efficiency and physical size of antennas is the result of two counteracting effects: the radiation resistance, which is proportional to the overall length of the antenna, and the power dissipation on the conducting traces and into the surrounding tissues, which increases with the radiator size, too. As a consequence, enlarging the antenna beyond its optimal size is not only undesirable for epidermal applications, which require small and unobtrusive devices, but it even produces a negative impact on radiation properties.

The results in Table I show that efficiency and maximum gain are almost the same for all the considered configurations and the optimal performance decreases slightly with the increase in the area of the conductor (and hence in the surface current). Contrary to the general belief, the loop has no tangible advantage over the dipole as epidermal

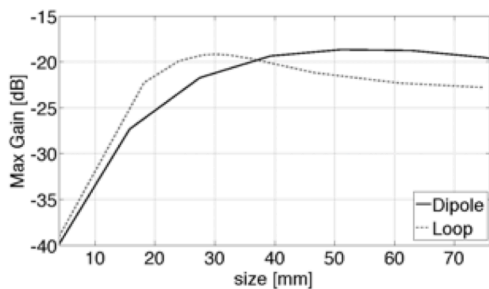


FIG. 1 – Dipole and Loop over body-like medium: Radiation gain at 870 MHz as a function of the external radiator’s size.

TABLE I – ELECTROMAGNETIC PERFORMANCE OF REFERENCE EPIDERMAL ANTENNAS AT 870 MHz

Antenna	η [%]	G [dB]	L_{opt} [cm]	A_{metal} [cm ²]
	0.3	-18.7	5	0.5
	0.3	-19.1	3	0.9
	0.3	-19.4	6	27.6
	0.3	-19.5	8	46.7

tag, in terms of gain and efficiency, even though it has overall smaller optimal size.

b) Gain vs. Conductivity

Fabrication of epidermal devices demands for cost-effective and easily accessible methods to deposit conductive traces over thin specialized flexible films. Viable solutions come from ink-jet printing or stencil-based techniques (screen printing) with conducting paints and nanoparticle inks. Those materials have conductivity sensibly lower than bulk metals, which cause a not negligible efficiency loss in the case of antennas radiating in the free space. Instead, epidermal antennas behave in a rather different manner. Fig. 2 shows the gain of the optimum-sized dipole and loop placed in direct contact with the body, when the conductivity of the metal trace was decreased from 10^8 S/m (good conductor) down to 10^2 S/m (poor conductor). No visible variation was noticed in the radiation performance, provided that $\sigma > 10^4$ S/m. Furthermore, even by reducing the conductivity down to 1000 S/m, the gain dropped by less than 2 dB. This result is not trivial and is a consequence of the power losses of the hosting human body.

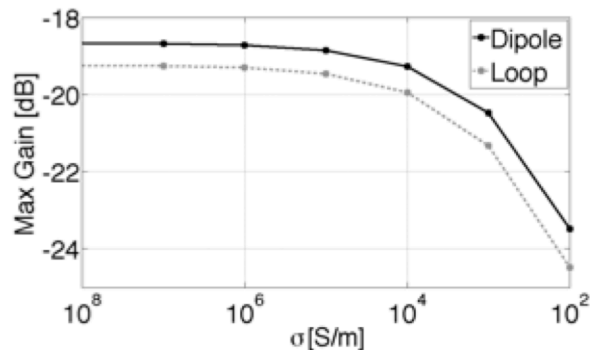


FIG. 2 – Maximum Gain of a 50x1 mm dipole and a 30x1mm loop at 870 MHz versus the finite conductivity of the trace.

III. EXPERIMENTAL VALIDATION

The measurement technique involved a couplet of transmitting and receiving antennas connected to a calibrated 2-port vector network analyzer. The reference lossy biological region was a cooked box-shaped pork shoulder ($\epsilon_r=55$, $\sigma=1.8$ S/m). To simplify the antenna-probe interconnection, an image-plane configuration was used (Fig. 1a). The transmitting antenna thus consisted of a quarter-wave planar monopole, whose input impedance was matched to 50Ω at 870 MHz. The close interaction between the epidermal antenna over the phantom and the monopole probe was described by the formalism of the two-ports network so that the performance of the antenna can be conveniently evaluated in terms of the scattering matrix of the system that accounts for channel path loss, reflection, diffraction and power absorption by the hosting medium. An easily measurable performance parameter of the epidermal antenna is the following *system gain* (not directly comparable with the radiation gain):

$$g = \frac{P_{out,av}}{P_{in}} \frac{|S_{21}|^2}{(1-|S_{11}|^2)(1-|S_{22}|^2)} \quad (1)$$

where P_{in} is the net power entering the transmitting monopole and $P_{out,av}$ is the maximum available power the network may deliver to the load of the epidermal antenna in case of proper impedance matching.

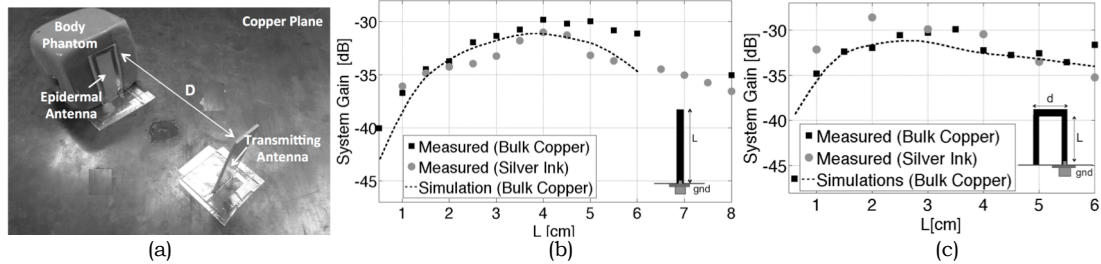


Fig. 3 – (a) Experimental setup for characterization of epidermal antennas. Measured and simulated system gains g , defined as in (1), at 870 MHz for the (b) monopoles and (c) half loops made of adhesive copper and silver nano-ink.

This performance parameter is independent of the impedance matching of the two antennas, and hence it characterizes the radiation properties of the epidermal antennas over the lossy medium. Planar layouts (monopole and a half rectangular loop) were fabricated by adhesive copper film (good conductor, $\sigma=5.7e7$ S/m) and by self-sintering Ag ink [3] (bad conductor $\sigma=2.2e4$ S/m) deposited by desktop printer. Measurements results, together with the corresponding numerical simulations in Fig. 3, clearly confirm the presence of the optimal size for the epidermal antennas as well as the presence of rather similar peak values of system gain. The behaviors of copper and the inkjet-printed antennas are comparable, despite of the poorer conductivity of the silver nanoparticle ink. The smaller optimal layout is the half loop ($L_{h,loop} \approx 3$ cm, $L_{monop} \approx 4$ cm) as expected from the numerical analysis.

IV. CONCLUSION

The presented findings define fundamental limitations in the performance of epidermal antennas, and may be used as a reference benchmark for the optimal design of real RFID epidermal transponders. Design examples and real-life temperature sensing applications will be shown at the conference.

REFERENCES

- [1] S. Amendola, S. Milici, G. Marrocco, "Performance of Epidermal RFID Dual-loop Tag and On-skin Retuning", *IEEE Trans. Antennas and Propagat.*, Vol. 63, no. 8, August 2015.
- [2] J. Kim, *et al.*, "Epidermal Electronics with Advanced Capabilities in Near-Field Communication", *Small*, Vol. 11, no. 8, pp. 906–912, Feb. 2015.
- [3] NBSIJ Diamond Jet Silver Nanoparticle Ink, Mitsubishi Imaging (MPM), Inc., Available [online] <http://diamond-jet.com/silvernanoparticleink-2.aspx>.

A FEASIBILITY STUDY ON THE USE OF MICROWAVE TOMOGRAPHY FOR TEMPERATURE MONITORING IN ABLATION TREATMENTS

R. Scapaticci⁽¹⁾, G.G. Bellizzi^(1,2), O.M. Bucci^(1,3), M. Cavagnaro⁽⁴⁾, L. Crocco⁽¹⁾, V. Lopresto⁽⁵⁾,

⁽¹⁾IREA, National Council of Research of Italy, Naples, Italy
scapaticci.r, bellizzi.g, crocco.l@irea.cnr.it, bucci@unina.it

⁽²⁾DIIES, Mediterranea Univ. of Reggio Calabria, Reggio Calabria, Italy

⁽³⁾CNIT - National Interuniversity Consortium on Telecommunications

⁽⁴⁾DIET, Sapienza University of Rome, Rome, Italy
cavagnaro@diet.uniroma1.it

⁽⁵⁾ENEA, Division of Health Protection Technologies, Rome, Italy
vanni.lopresto@enea.it

Abstract

Microwave ablation is a cancer treatment based on local heating of tumor cells to induce coagulative necrosis. This technique would be sensibly more effective if paired with a system for the real-time monitoring of the evolving dimension and shape of the thermally ablated area. This work explores the possibility of using microwave imaging as a non-invasive methodology to monitor the overall treatment evolution, by tracking variations of the electromagnetic properties of ablated tissue and surrounding regions. In particular, a preliminary feasibility study based on full-wave numerical simulations is herein presented.

Index Terms – Liver cancer, Microwave ablation, Microwave Imaging, Temperature Monitoring.

I. INTRODUCTION

Thermal ablation consists in heating cancerous tissues (and a surrounding "safety area" of about 5-10 mm) at temperatures higher than 60°C. This produces coagulative necrosis, which represents the actual therapeutic effect.

The mostly exploited heating modality is radiofrequency (RF), in which the heating occurs in the near proximity of an electrode, a larger area being actually ablated thanks to thermal conduction. Besides RF ablation, microwave ablation (MWA), typically using frequencies in the ISM band (915MHz or 2.45GHz), has been recently considered [1]. Different from RF ablation, MWA exploits dielectric heating and relies on the propagation of an electromagnetic field in tissues with different water content [2]. As such, microwave (MW) induced heating occurs in a volume that surrounds the antenna, and not just in its proximity. Such a circumstance entails the capability of treating larger volumes in a shorter time, which in turn leads to a reduced sensitivity to blood perfusion heat sinks.

Since in MWA the heating occurs in a volume, which should be defined by the treatment protocol (MW power and duration of treatment), it is crucial to have proper tools for the monitoring of the evolution of temperature in the ablated and surrounding tissues. Typically, the temperature in the region of interest is monitored by local thermometric probes. However, these latter suffer of being invasive and only capable of providing local information.

This motivates the interest in alternative techniques; a possible candidate in this respect is MW tomography, which relies on low-cost and portable equipment and could directly track the variations of the electromagnetic properties of the treated tissue occurring due to temperature increase [3-7].

In [5], we have presented a first feasibility study concerning the use of MW tomography as a tool to monitor changes of electromagnetic properties (and therefore of temperature) during ablation, concerned with an ideal configuration (i.e., a very simplified scenario geometrically invariant along an axis and ideal probes). Based on the positive outcome of that study, in this communication we present the results of a full-wave numerical study aimed at validating the idea proposed in [5] in a more realistic scenario, as the one of *ex vivo* experiments.

II. MATERIALS AND METHODS

An ablation process occurring in *ex vivo* bovine liver has been considered for our study, being this case a typical scenario for validations. In particular, the first 180s of the treatment have been simulated, since in the vicinity of the applicator the main changes occur in this time window. Simulations have been performed with CST MICROWAVE STUDIO®.

Exploiting previous studies on the relationship between electromagnetic and thermal parameters of liver tissues, it has been modeled the variation of electromagnetic properties during an ablation treatment. These studies, based on experimental results, evidenced an irreversible temperature-dependent change in the dielectric parameters [4,6]. The sample is assumed to have a rotational symmetry around the axis of the antenna applicator, which is an a-symmetrical dipole equipped with a mini-choke [7], working at 2.45GHz and radiating a power of 60W.

The exploited image reconstruction algorithm is a differential tomographic approach based on the Distorted Born Approximation (DBA). The approach is described in [8], although therein it is applied to a different imaging problem. Such an approach is computationally effective and robust against noise on data. However, the DBA requires contrast variations to be of low magnitude ($\ll 1$) and small as compared to the probing wavelength. Since these assumptions are not fulfilled in the scenario at hand, the tomographic processing cannot provide quantitative results, but only qualitative information related to the size and position of the occurring variations.

III. RESULTS AND DISCUSSIONS

We report in this section the results obtained applying the differential tomographic processing to the scattered field data simulated for the four considered time instants of ablation procedure. The considered measurement configuration, consists of 13 dipole antennas, evenly spaced on a plane parallel to the major axis of the MWA applicator. Note that this configuration would be compatible with the scenario actually dealt with in ex-vivo experiments. The same frequency used for the ablation (i.e., 2.45GHz) has been adopted also for imaging purposes. Moreover, to test the reliability of the inversion procedure with respect to noise, the simulated scattered fields have been corrupted with an additive white gaussian noise, with SNR equal to 20dB.

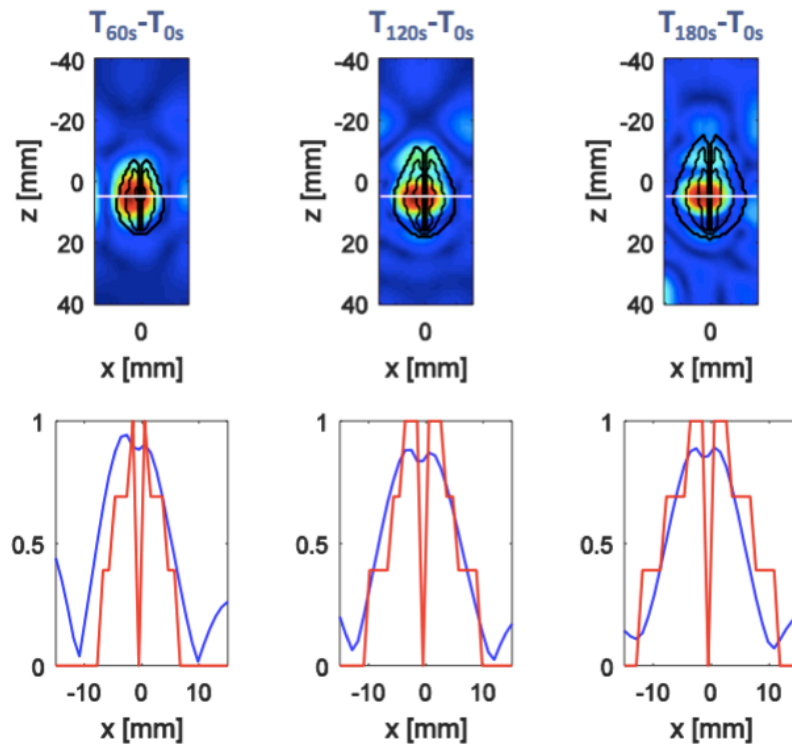


FIG. 2 – Reconstructions of the normalized modulus of the contrast function $\delta\chi$ at different time instants. The bottom row shows the cuts of the reconstructions at $z=5\text{mm}$.

The outcome of the analysis is summarized in Fig.2, wherein we compare the actual differential contrast variations occurring during the ablation between the three considered time instants and the initial state ($t = 0$ s), with the corresponding tomographic images. Given the non-quantitative nature of the adopted approach, we only report the normalized amplitude of the retrieved contrast function, which provides information on the extent of the portion of the sample wherein electromagnetic properties are changing.

IV. CONCLUSIONS

We have presented a full-wave numerical study concerning the feasibility of MW tomography as a real-time noninvasive tool to monitor the evolution of a MWA procedure. To this end, we have exploited the electromagnetic properties variations obtained in an ex-vivo liver sample during the ablation [4], and then tailored a differential tomographic approach [8] to the scenario at hand. The achieved results suggest that a differential tomography approach can track the variations of the complex permittivity, by determining the main features of the complex permittivity variation: namely its extent along the applicator axis and its maximum distance from the applicator.

Based on these initial encouraging observations, the activity is planned to progress along several directions. First, ablation of liver tissues with a tighter temporal sampling will be simulated to better match the DBA assumptions. Finally, we plan to develop a more complex inversion procedure for quantitatively estimating the variations of the electric properties.

REFERENCES

- [1] K. F. Chu and D. E. Dupuy, "Thermal ablation of tumours: biological mechanisms and advances in therapy", *Nature Reviews Cancer*, vol. 14, pp. 199-208, 2014.
- [2] C. L. Brace, "Radiofrequency and Microwave Ablation of the Liver, Lung, Kidney, and Bone: What Are the Differences?", *Curr. Probl. Diagn. Radiol.*, vol. 38, pp. 135-143, 2009.
- [3] Z. Jiand C. L. Brace, "Expanded modeling of temperature-dependent dielectric properties for microwave thermal ablation", *Phys. Med. Biol.*, vol. 56, pp. 52495264, 2011
- [4] V. Lopresto, R. Pinto and M. Cavagnaro, "Experimental characterisation of the thermal lesion induced by microwave ablation", *Int. J. Hyperth.*, vol. 30, pp. 110118, 2014.
- [5] O. M. Bucci, M. Cavagnaro, L. Crocco, V. Lopresto, R. Scapaticci, "Microwave Ablation Monitoring via Microwave Tomography: a Numerical Feasibility Assessment", *EuCAP*, Davos, 2016.
- [6] M. Cavagnaro, R. Pinto and V. Lopresto, "Numerical models to evaluate the temperature increase induced by ex vivo microwave thermal ablation", *Phys. Med. Biol.*, vol. 60, pp. 3287?3311, 2015.
- [7] M. Cavagnaro, C. Amabile, P. Bernardi, S. Pisa and N. Tosoratti, "A minimally invasive antenna for microwave ablation therapies: design, performances, and experimental assessment", *IEEE Trans. Biomed. Eng.*, vol. 58, pp. 949959, 2011.
- [8] R. Scapaticci, O. M. Bucci, I. Catapano, and L. Crocco, "Differential Microwave Imaging for Brain Stroke Follow-up", *International Journal of Antennas and Propagation*, vol. 2014, Article ID 312528, 11 pages, 2014

MICROWAVE HYPERTHERMIA OF PHOENIX CANARIENSIS FOR RED PALM WEEVIL PEST CONTROL

R.Massa¹, M.D.Migliore², G.Panariello², D.Pinchera², F.Schettino²,
E.Caprio³, R.Griffo⁴

- (¹) Physics Department “Ettore Pancini”, Un. of Naples Federico II, CMSA, Via Cintia, 80128, Naples, Italy, massa@unina.it
- (²) DIEI, Un. of Cassino and Southern Lazio, Cassino, Italy, V. G. Di Biasio, Cassino, Italy, mdmiglio@unicas.it, panariello@unicas.it; pinchera@unicas.it; schettino@unicas.it;
- (³) Department of Agricultural Sciences, Un. of Naples Federico II, V. Università 100, Portici, Naples, Italy, emcaprio@unina.it
- (⁴) Plant Protection Service of Campania Region, V. G. Porzio, Naples, Italy, raffaele.griffo@regione.campania.it

Abstract

This paper introduces the feasibility and effectiveness of microwave treatments of Phoenix Canariensis palms to help the control of Rhynchophorus ferrugineus (red palm weevil) that is currently one of the major threats to palms in the Mediterranean area. We developed a model for the evaluation of the temperature enhancement induced in the infested palm by a microwave ring applicator. The model relies on the measurements of relevant thermal, electromagnetics and biological parameters. It allows to reach the insect lethal temperature without damaging the palm tissues. The main advantage of microwaves is their eco-compatibility, and results of their application to Rhynchophorus ferrugineus control are very promising.

Index Terms – Microwave treatment, palm, *Rhynchophorus ferrugineus* (red palm weevil)

I. INTRODUCTION

The invasive red palm weevil (RPW), *Rhynchophorus ferrugineus* (Olivier 1790) (Coleoptera: Curculionidae) has become the major pest of palms in the Mediterranean area, where it has spread slowly during the mid-1990s and very quickly during the last 10 years, affecting mainly *Phoenix canariensis* Hort. ex Chabaud. These plants are the main ornamental palms planted in the gardens and in the streets of the Mediterranean coast cities. Some monumental specimens had very high values, especially those at historic sites, some of them including in the UNESCO World Heritage [1]. Within an integrated pest management strategy phytosanitation, which involves cutting down and burning infested palms, use of insecticides and use of pheromone traps, for adult monitoring and mass trapping, are the main actions. However environmental concerns related to the use of pesticides seriously

impede chemical preventative and curative procedures and legislation restricts their use [2]. Aim of the present research is to show the feasibility and effectiveness of the eco-compatible microwave heating of *Phoenix Canariensis* palms in order to control RPW pest, being microwaves able either to induce the lethal temperatures of the insect in different life stages without damaging the host plant or to affect survived insects.

II. THE INSECT

Originally from tropical Asia, the RPW (Fig.1a) has spread to Africa, Europe and recently USA. Females deposit about 300-500 eggs in holes, that they realize while searching for food, or in cracks or wounds in the palm. Eggs hatch over a period of 2-5 days. The neonate larvae are able to create burrow from the axils of the leaves to the crown, where they feed voraciously. Into the palm larvae may pass through 3-7 instars. At the end of the larval period development (1 to 3 months), larvae emerge from the trunk, realize a pupal case of fiber extracted from the galleries inside the palm and undergo metamorphosis into adults (pre-pupal stage of 3 days and pupal period of 12-20 days). Tests on estimation of the time to 100% kill of eggs [3], larvae and adults at a fixed temperature [4] indicate that typically they failed to survive when leaving for 30 min at 50°C. In particular, results indicate that the adult insects are much more sensitive to heat than the larger larvae (weight 5-6 g), at 50 °C adults are killed after 20 min, larger larvae after 30 min, while 15 min are enough to cause the death of smaller larvae (2-3 g). From the electromagnetic point of view, permittivity measurements of the RPW in different developmental stages (larva, pupal chamber, adult) [5] show that at 2.45 GHz the conductivity on the surface of the adult (0.38 S/m) is much lower than that of the larva (1.4 S/m), due to the reduced water content of the insect at this stage compared to the larva, and the penetration depth in the chamber is of many centimeters thus allowing the microwaves to reach the larva/adult depending on the stage of the metamorphosis.

III. THE HOST

Results of the permittivity measurements of healthy and damaged palm tissues show a penetration depth of the order of a couple of centimeters at 2.45 GHz in the damaged palm tissues, and a slightly lower depth in the healthy palm. By applying Ulaby model to our data [5], the volume fraction of free water resulted higher than that of the bulk vegetation-bound water mixture in the damaged tissues, and the ionic conductivity of the free water solution was lower in the damaged tissues compared to that in the healthy tissues. The high water content entails the very high loss factor of palm tissues and only the external section of the palm can be heated directly by the microwaves. The thermal conductivity and the specific heat capacity were evaluated to be 1.5 W/m²K and 3100 J/kg²K respectively by calorimetric measurements carried out during

microwave exposure of an healthy palm. On the basis of these results and considering an average density of 844 kg/m^3 , a time rate of initial temperature rise of $0.3 \text{ }^\circ\text{C/s}$ in the case of 1000 V/m electric field in the healthy palm tissues was estimated.

IV. EFFECTIVENESS OF MICROWAVE HEATING TO CONTRAST RPW PEST

The low penetration depth and thermal conductivity indicate that the external region of the palm is deeply involved in the microwave heating. In this portion eggs, small larvae, cocoons and adults are directly reached by the electromagnetic radiation and a rapid increase of the temperature is expected due to both the insect and palm tissues heating. The results obtained in greenhouse [4] and in semi-field tests confirmed the analysis. In particular, microwave treatments of *Phoenix Canariensis* palms, opportunely infested, were carried out by means of Ecopalm applicator (Bi.Elle s.r.l.) (Fig. 1b)

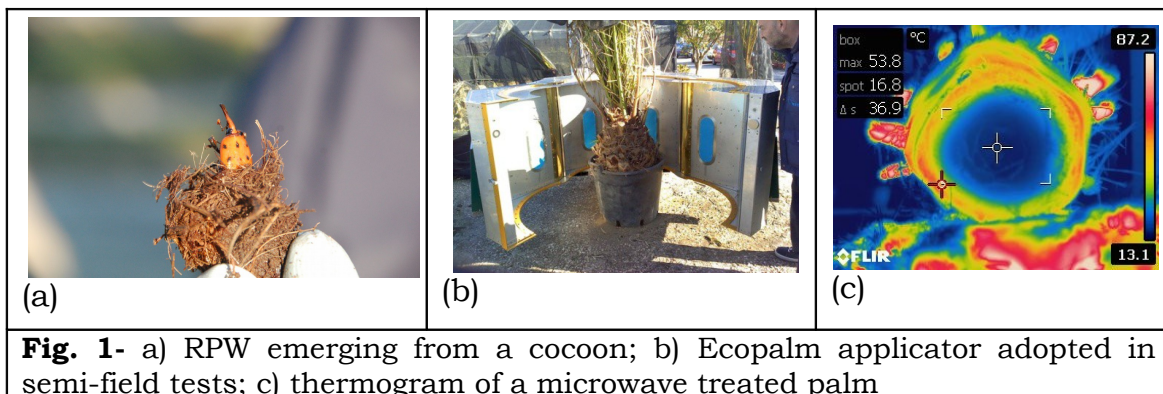


Fig. 1- a) RPW emerging from a cocoon; b) Ecopalm applicator adopted in semi-field tests; c) thermogram of a microwave treated palm

It consists in 12 magnetrons (each one 1 kW nominal power) arranged in a ring that surrounds the trunk of the palm, allowing an illumination circularly symmetric of the plant, that was really observed by means IR thermographic monitoring recorded immediately after the microwave exposure of a palm opportunely cut along the radial section (Fig. 1c). Thermal measurements confirmed that only the surface layers are involved in the heating process and the core of the palm remains at lower temperature. Considering the insects found alive and died after the irradiation of palms, opportunely infested, the effectiveness of the treatment turned out between 60% and 87%. In particular 100% of died insects into pupal cases were achieved in three over four palms. Additional laboratory tests on adults survived and processed for anatomical and histological analysis showed histological lesions of female and male reproductive system which increased with the increase of irradiation time (200 W, 5-15-30 sec.), indicating that microwave exposure reduce or remove completely the reproductive capacity in the survived insects [6].

V. THERMAL MODEL OF A THE MICROWAVE HEATING

On the basis of the overall results described in the previous sections an effort was devoted to obtain an electromagnetic-thermal code able to predict the thickness of the annular area in “living” palms wherein the

temperature reaches the lethal temperature for RPW, and how long it should stay in order to have a high probability that the treatment is successful, without damaging the palm core that is the most relevant area for the life of the palm itself. Good agreement was found when we compared the results of the code with the ones obtained with a multiphysics full-wave commercial software (Ansys HFSS). The model resulted simple and user friendly. It can be easily adopted by not skilled operator in order to establish the power, modulation and duration of the treatment, once the dimension of the palm, the ambient temperature and wind conditions are set.

VI. CONCLUSIONS

To the best of our knowledge this is the first time that an “hyperthermia” treatment of an alive plant is dealt with. The measurements of thermal and electromagnetic parameters of the tissues involved (both insect and plant host), the evaluation of the effect of the radiation on the insect (in different stage of development), the numerical simulations and the evaluation of the performance of the applicator that actually is on the market indicate that microwave heating of *Phoenix Canariensis* palm resulted an efficient, cheap and eco-compatible method to control RPW without affecting the plant.

ACKNOWLEDGEMENTS

Project MIPALM (PSR Campania 2007 - 2013 Misura 12 CUP N.B95C12000040004). We would like to thank the Agriculture and Food Commission of the Italian Senato for the interest in the research and Bi.Elle s.r.l., ComFlomer and Dr. A. Greco for their technical support.

REFERENCES

- [1] UNESCO World Heritage. 2010 <http://whc.unesco.org/en/list/930>.
- [2] EU Directives 91/414EEC, 2011.
- [3] Li L, Qin WQ, Ma ZL, Yan W, Huang SC & Peng ZQ, “ Effect of temperature on the population growth of *Rhynchophorus ferrugineus* (Coleoptera: Curculionidae) on sugarcane”. *Env. Entomology*, 39 (3), 999–1003, 2010.
- [4] R. Massa, E. Caprio, M. De Sanctis, R. Griffo, M.D. Migliore, G. Panariello D. Pinchera, P. Spigno, “Microwave Treatment for pest control: the case of *Rhynchophorus ferrugineus* in *Phoenix canariensis*” *EPPO Bulletin*, vol. 41(2), pp. 128-135, August 2011.
- [5] R. Massa, M. D. Migliore, G. Panariello, D. Pinchera, F. Schettino, E. Caprio, and R. Griffo “Wide Band Permittivity Measurements of Palm (*P. canariensis*) and *Rhynchophorus ferrugineus* (Coleoptera Curculionidae) for RF Pest Control.” *J.Microwave Power and Electrom Energy*, vol. 48(3), pp. 158-169, 2014.
- [6] M. Martano, R. Massa, I. Pagano, A. Greco, G. De Leva, A. Linguadoca, P. Maiolino “ Histological Findings of the male and female reproductive system of the RPW (*Rhynchophorus ferrugineus*) irradiated with microwaves”, IX International Symposium on Wild Fauna, Slovakia, 2015

FIBER-BASED BIOSENSORS FOR DNA DETECTION

M. Barozzi⁽¹⁾, Sarah K. M. Al-Hayali⁽²⁾, A. Candiani⁽³⁾, A. Vannucci⁽¹⁾,
A. Hadi Al- Janabi ⁽²⁾, A. Cucinotta ⁽¹⁾, S. Selleri ⁽¹⁾

⁽¹⁾Department of Information Engineering, University of Parma
Viale delle Scienze 181/A, Parma, Italy

⁽²⁾Institute of laser for postgraduate studies, University of Baghdad
Jadriya Complex, Baghdad, Iraq

⁽³⁾DNAPhone s.r.l.

matteo.barozzi82@gmail.com

Abstract

This paper describes a bio-sensor based on a functionalized microstructured optical fiber with a Bragg grating, for specific DNA target sequences detection. The inner surface of the fiber has been functionalized using PNA probes that allows hybridization of the target DNA. To achieve sensing enhancement, functionalized gold nanoparticles were used. Experimental measurements show the high selectivity and sensitivity of the bio-sensor.

Index Terms – Biosensors; fiber sensors; label-free DNA detection.

I. INTRODUCTION

The need for new, fast, and cheap technologies for medical and healthcare diagnostic equipment has been driving interest and investment in biosensor technology and research [1]. Among the different principles of detection, optical fiber-based bio-sensing is one of the most widely investigated transduction methods. Optical bio-sensors can be classified in two main categories: labelled sensors [2], and label-free sensors. While in a labelled detection scheme the target molecules are modified by adding a tag element, a label-free sensor allows the direct sensing of the target DNA without markers. Most of the label-free detection schemes exploit a refractive index change related to the target presence/concentration.

In particular, microstructured optical fibers (MOFs), in addition to intrinsic advantages of the standard fiber-based sensors (small and flexible shape, in situ sensing, etc.), allow the infiltration of the solution to be tested inside their capillaries. In this way, small biological samples inside the holes can be used. In general, for DNA detection, a *functionalization* process, i.e., a chemical treatment of the fiber surface, is needed, so that the optically sensitive surface is able to bind the specific DNA sequence (*DNA hybridization*). In this work we summarize results obtained with a DNA sensing approach based on a peptide nucleic acid (PNA)-functionalized MOF Bragg grating.

II. EXPERIMENTAL SET-UP

Two MOFs with a Bragg grating inscribed were used: a Penta fiber (Fig. 1a) and an LMA-10 (Fig. 1b). Penta is a multimode fiber whose grating reflects few modes [3], while LMA-10 is single mode fiber [4]. Both fibers have been functionalized with a PNA sequence complementary to the target DNA, according to the procedure described in [4]. The experimental setup (Fig. 1c), consisted of an amplified spontaneous emission (ASE) source connected to a fiber optic circulator. Light was coupled to the MOFs and the signal reflected by the grating was sent to an optical spectrum analyzer (OSA). The fiber was placed on two tri-axial micro-positioning devices, to keep it fixed during the measurements and to allow a good coupling in air with the light. From one fiber end, DNA solution was infiltrated through a syringe pump. The system was finally connected to a high pressure nitrogen line, to empty and dry the fiber after infiltration.

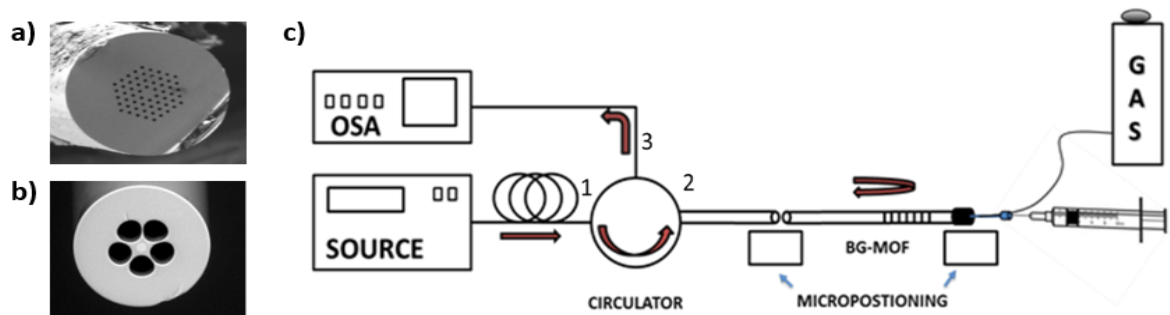


FIG. 1 – SEM images of: (a) Penta fiber (b) LMA-10 suspended-core PCF. (c) Schematic experimental Set-up

II. APPLICATIONS: DNA LABEL-FREE DETECTION USING PNA PROBES

PNAs are artificial nucleic acid mimics in which the natural nucleobases are linked to a poly-amidic backbone instead of the sugar-phosphate scaffold naturally present in DNA or RNA systems. The advantages of using PNA instead of DNA or other oligonucleotide mimics are linked to their high DNA affinity, which allows properly designed PNA molecules to perform strand invasion of the double stranded DNA [4], and sequence-specificity, in particular their ability to discriminate even a single base mismatch.

In recent years, we explored the possibility to combine the advantages provided by PCF (small analysis volumes; possibility to perform label-free detection) with the great performances in the PNAs (sequence selectivity and stability), for the realization of systems able to perform qualitative or quantitative analysis. Two example applications are described in the following, along with the obtained experimental results. The first example developed in our laboratories, focused on the detection of the single point mutation W1282X, associated with cystic fibrosis (CF) disease, was performed using a multi-mode Penta fiber with a Bragg grating inscribed within its core [3]. The sandwich-like scheme of detection adopted in this study, derived from previous studies conducted with different optical

techniques, was designed in order to avoid the use of labelled target DNA as well as a system to enhance the spectral shift exploiting the higher refractive index of gold compared to that of air or organic layers. The label-free detection experiment was performed using longer oligonucleotides sequences having the point mutation target sequence (full matched DNA) or the sequence of the wild type gene (single mismatched DNA). After a subsequent nanoparticles infiltration step, the reflected spectra were analyzed showing a significant shift in the high order Bragg mode only were target DNA was used (Fig. 2b and Fig. 2c).

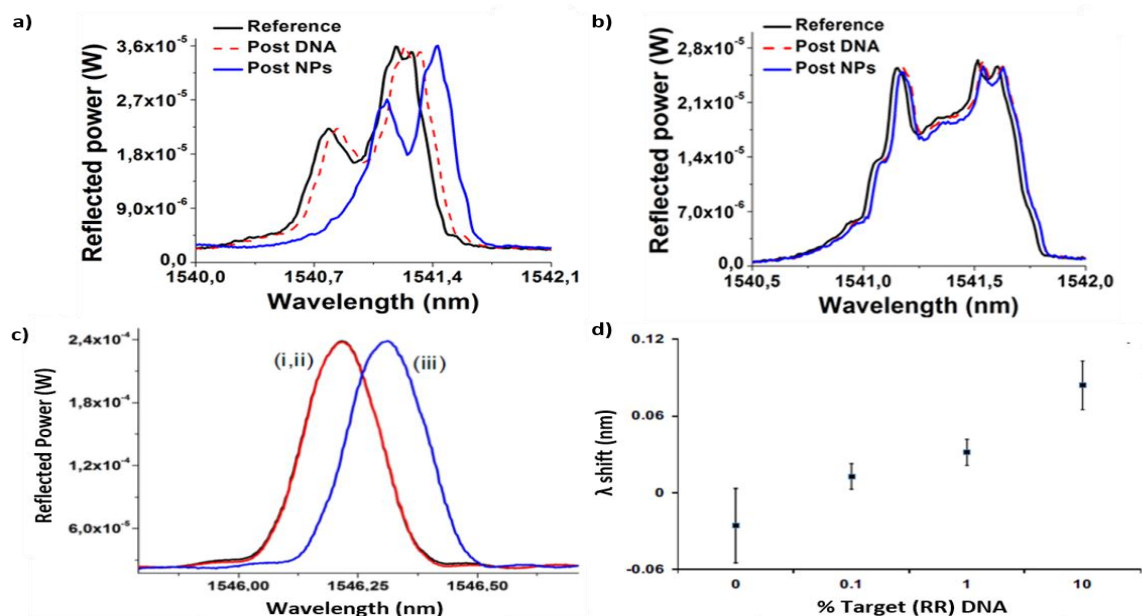


FIG. 2 – (a) shift in the high order band induced by infiltration of target sample; (b) shift in the high order band induced by infiltration of non-target sample; (c) wavelength shift in the reflection mode obtained for the LMA10-PNA fibers (i) before (blackline), (ii) after DNA (redline), and (iii) after ON-AuNPs infiltration (blue line), using 10% GMO DNA sample; (d) optical shifts obtained using DNA at the same concentration but with different GMO% (vertical bars represent standard deviation).

Later we moved our attention to the possibility to apply this approach to a PCR-free detection for the identification of Read up Ready Soy GMO contaminants in soy flour [4]. In this case, a single mode LMA-10 fiber (with a Bragg grating inscribed within its core) and DNA samples directly extracted from food matrices were used. Compared to the previous case in which Penta fibers were used, this new type of fibers has the advantage of having only one reflected mode, so that the evaluation of the variation induced by the recognition events was clear and sharp. The detection scheme was the same as applied before and it was possible to detect small percentages of target DNA (1% and 10%) in the presence of a large excess of non-target DNA, using only a small amount (3 ng) of sample. Fig. 2d shows the spectral shift obtained using a 10% target containing sample and the shift obtained using solution with different percentages of target. Selectivity of the analysis was assessed using a blank soy flour sample as well as an unrelated calf thymus

sample, resulting in no significant shift. In this latter experiment, we exploited the great stability of the PNA: DNA complexes for the realization of quantitative detection of contaminants in food matrices. The great sensitivity eliminates the need for Polymerase Chain Reaction (PCR), typically required to *multiply* small amounts of DNA to a detectable level. This reduces the time and costs required for the analysis and enables the application of this kind of devices for a faster screening of contaminants in raw materials or in the food processing chain. In both studies the reproducibility of the detection was confirmed by repeating the measurement after a preliminary washing step, and only a small memory effect was observed in accordance with previous experiments, confirming the possibility to apply this kind of detection in the realization of devices.

III. CONCLUSION

In this work, fiber-based biosensors for DNA detection has been presented. A small shift of the reflected high order Bragg mode observed when DNA molecules, complementary to the PNA probes, were infiltrated into the MOF; however, by “decoration” of the captured DNA with gold nanoparticle, a significant shift was observed only in the case of full match DNA. This first demonstration proves the feasibility of realizing a sensor for biological measurements by observing the optical signal reflected by a Bragg grating, utilizing the fiber itself as a probe. The fibers used in the experiment shows a good compromise between size of the holes, sensitivity and relative ease of inscription of the grating. Other recognition elements are possible, that are able to bind target analytes, such as proteins or contaminants, using the same strategy as described here, thus making this technology suitable for powerful and versatile bio-sensing platforms.

IV. REFERENCES

- [1] Y. Cao, T. Guo, X. Wang, D. Sun, Y. Ran, X. Feng, and B. Guan, “Resolution-improved in situ DNA hybridization detection based on microwave photonic interrogation,” *Opt. Express*, vol. 23(21), pp. 27061–27070, 2015.
- [2] E. Coscelli, M. Sozzi, F. Poli, D. Passaro, a. Cucinotta, S. Selleri, R. Corradini, and R. Marchelli, “Toward A Highly Specific DNA Biosensor: PNA-Modified Suspended-Core Photonic Crystal Fibers,” *IEEE J. Sel. Top. Quantum Electron.*, vol. 16(4), pp. 1–6, July 2010.
- [3] A. Candiani, A. Bertucci, S. Giannetti, M. Konstantaki, A. Manicardi, S. Pissadakis, A. Cucinotta, R. Corradini, and S. Selleri, “Label-free DNA biosensor based on a peptide nucleic acid-functionalized microstructured optical fiber-Bragg grating.,” *J. Biomed. Opt.*, vol. 18 (5), p. 57004, 2013.
- [4] A. Bertucci, A. Manicardi, A. Candiani, S. Giannetti, A. Cucinotta, G. Spoto, M. Konstantaki, S. Pissadakis, S. Selleri, and R. Corradini, “Detection of unamplified genomic DNA by a PNA-based microstructured optical fiber (MOF) Bragg-grating optofluidic system,” *Biosens. Bioelectron.*, vol. 63, pp. 248–254, 2015.

